Experimental and Theoretical Studies of Combustion Rates at High Pressure

By:

Ali Saied Al-Shahrany

BSc, MSc

Submitted in accordance with the requirements for the degree of Doctor of philosophy

The University of Leeds
Department of Mechanical Engineering

June 2004

The candidate confirms that the work submitted is his own and that appropriate credit has been given where reference has been made to the work of others.

Abstract

The thesis reports experimental and theoretical studies of premixed combustion rates at high pressure and temperature. It focuses on measurements of laminar and turbulent burning velocities at high pressures and temperatures approaching those in engines, with emphasis on flame instabilities. To encourage the development of such instabilities, mixtures with negative Markstein numbers were employed. Three different methods were used to measure burning velocities in a spherical bomb. The bomb was fitted with windows for observing flame propagation at the centre of the bomb and a transducer to measure pressure. Four fans at the wall of the bomb were employed for mixing and the generation of turbulence. The first two methods of measuring burning velocities were well established and involved central ignition. The third method was new and involved implosions of two flame kernels that originated at spark plugs mounted near the wall. It enabled the later stages of burning at the high pressures to be observed and burning velocities to be measured. The first method depended on high-speed schlieren photographic measurements of the flame speed, dr/dt, at different radii, r, supplemented by pressure measurements. The second method was employed when the flame front has propagated beyond the boundaries of the window and could no longer be observed. The expression for the burning velocity rested upon the assumption that the flame was spherical and the fractional pressure rise was equal to the fractional mass burned.

Two different approaches were employed for the new third method, one was based on geometrical considerations, the other on the fractional pressure rise. A knowledge of the flame area and the appropriate geometrical analysis enabled two expressions to be obtained for the burning velocity. The agreement between the two different approaches for obtaining burning velocities, and the general consistency of the results for both initially laminar and turbulent flames, showed the technique to be accurate and suitable for obtaining burning velocities at high pressure. As a result, burning velocities, initially laminar, were measured for iso-octane – air at equivalence ratios ranging from 0.8 to 1.6 at initial pressures of 0.5 and 1.0 MPa. They were also measured for hydrogen – air mixtures at equivalence ratios of 0.3 to 0.5. Modification of the linear theory of flame instability of Bechtold and Matalon enabled the laminar burning velocity to be obtained from the values of unstable burning velocities. Enhancements of the laminar burning velocity of up to six fold were measured.

Turbulent burning velocities were measured over a range of rms turbulent velocities ranging from 0.25 to 3 m/s. It was found that these values of burning velocity were higher than those predicted from earlier expressions, derived predominantly from more stable flames close to atmospheric pressure. The possibility that turbulent burning velocities might be enhanced, not only by the effect of flame stretch at negative Markstein numbers, but also by flamelet instabilities was also investigated at high pressures and with mixtures with very low Markstein numbers. Stoichiometric and rich iso-octane-air flames were selected for this study and mixtures were ignited at initial pressures of 0.5 and 1.0 MPa. This enabled burning velocities to be measured up to 6 MPa.

Acknowledgments

I would like to forward my thanks to my supervisors Prof. Bradley, D. and Dr. Lawes, M. for their support, directions, and valuable discussions throughout the period of this study and during the preparation of the thesis.

My thanks are also forward to Dr. Woolley for his valuable assistance and discussions during the period of conducting the experimental work.

My thanks are forward to all of the staff in the Thermodynamics Laboratory and to all of the combustion group members for their help, assistance and friendship.

I also would like to forward my thanks to the Saudi Arabian Government for granting me this valuable chance and the financial support is greatly acknowledged.

Finally, I would like to express my deep thanks and love to my parents and my family for their love and encouragement through out the period of my study.

Publications

The work in the thesis has given rise to the first two publications. A third is in preparation.

- "Measurements of Laminar Burning Velocities in Explosions and Implosion in a Spherical Bomb". Presented by the author at the Fourth International Seminar: Fire and Explosions Hazard, London Derry, Belfast (2003). Accepted for Publication in the Seminar Proceedings.

- "Measurement of Unstable Burning Velocities of Iso-octane-air Mixtures at High Pressure and the Derivation of Laminar Burning Velocities". To be presented at the Thirtieth Symposium (International) on Combustion, The Combustion Institute Chicago, July (2004). Accepted for Publication in the Proceedings of the Combustion Institute.

- "Turbulent Burning Velocities of Stoichiometric and Rich Iso-octane-air Mixtures at High Pressures", in preparation.

Table of Contents

Abstract..... i

Acknowledgments..... ii

Publications..... iii

Table of Contents..... iv

List of Tables..... ix

List of Figures..... x

Nomenclature xix

Chapter 1. Introduction 1

1.1 General 1

1.2 Laminar Flames..... 2

1.3 Laminar Burning Velocity 3

1.4 Effects of Flame Stretch on Burning Velocities Perditions..... 4

1.5 Instability..... 7

1.6 The Twin Kernel Explosion (Implosion) Technique 8

1.7 Turbulent Flames 9

1.8 Achievements of the Present Studies..... 10

Chapter 2. Experimental: Apparatus and Techniques 12

2.1 Introduction..... 12

2.2 Explosion Vessel 13

2.3 Auxiliary Systems..... 14

2.3.1 Ignition System..... 15

2.3.2 Pressure Measurement..... 16

2.3.3 Temperature Control and Measurement..... 17

2.4 Preparation of Mixtures..... 17

2.5 Optical Arrangements for Schlieren Photography..... 18

2.5.1 Central Ignition..... 18

2.5.2 Twin Ignition..... 19

2.6 Methods of Processing..... 19

2.6.1 Central Ignition..... 19

2.6.2 Twin Ignition..... 21

2.6.2.1 Hand Based Method 21

2.6.2.2 Computer Based Method 25

2.7 Thermodynamic Properties..... 27

2.8 Practical Considerations – Geometrical Complexity..... 28

Chapter 3. Measurement of Burning Velocities in Spherical Explosions with Central Ignition 30

3.1 Introduction..... 30

3.2 Optically Based Measurements..... 30

3.3 Pressure Based Measurements..... 32

3.4 The Effect of Flame Thickness..... 33

3.5 Experimental Results for Central Ignition..... 34

3.5.1 Measurements of Pressure and Flame Radius..... 34

3.5.2 Influences of Flame Stretch..... 38

3.5.3 Derivation of Laminar Burning Velocities by the Two Methods... 41

3.6 Evolution of Cellular Structure in Laminar Flames..... 43

3.7 Pressure Measurements in Turbulent Flames..... 43

Chapter 4. Theory of Two Hemispherical Imploding Spherical Flame Surfaces 48

4.1 Introduction..... 48

4.2 Geometrical Considerations and Burned Gas Volume..... 49

4.3 Burning Rate..... 52

4.4 Volume Burned and Pressure Rise..... 55

4.5 Assessment of Method..... 56

4.5.1 Sphericity of the Flame Front..... 56

4.5.2 Effects of V_r for Laminar Flames..... 59

4.5.3 Comparison of Laminar Burning Velocity Obtained by the Two Expressions..... 60

4.5.4 Effects of V_r for Turbulent Flames..... 61

4.5.5 Burned Gas Volume and Flame Area Correction for Turbulent Conditions..... 62

4.5.6 Correction to Turbulent Burning Velocities Measured with Radii Centred at the Wall..... 66

Chapter 5. Development of Laminar Flame Instabilities and their Effect on Burning Velocities 68

5.1 Causes of Instabilities..... 68

5.2 More Recent Fundamental Studies of Flame Instabilities..... 70

5.3 Prediction of Burning Velocity of Initially Laminar Unstable Flames..... 73

Chapter 6. Results from Initially Laminar Imploding Flames 78

6.1 Introduction..... 78

6.2 Measurements of Burning Velocity Using Imploding Method..... 78

6.3 Derivation of Laminar Burning Velocity, u_l, from u_n..... 80

Chapter 7. Results From Turbulent Imploding Flames 119

7.1 Introduction..... 119

7.2 Measurements of Turbulent Burning Velocity Using Imploding Method..... 119

7.3 Derivation of Effective rms Turbulent Velocity, u'_k, Acting on the Flame Kernel..... 122

7.4 Corrected Values of u_t and Effects of High p and T..... 125

Chapter 8. Discussion 175

8.1 Introduction..... 175

8.2 Laminar Burning: Central and Twin Ignition..... 175

8.3 Validity of the Twin Kernel Implosion Technique for Initially Laminar Flames..... 177

8.4 Values of Laminar Burning Velocity..... 177

8.5 The Rapid Increase in u_n for Unstable Iso-octane Rich Mixtures..... 183

8.6 Correlations of Turbulent Burning Velocity..... 186

8.7 Predicted Values of u_t..... 194

8.8 Laminar and Turbulent Instabilities..... 196

Chapter 9. Conclusions and Recommendations 204

9.1 Conclusions..... 204

9.2 Recommendations..... 207

Appendix A. Typical Computational Results for Flame Radius from Edge Fortran program..... 209

Appendix B. Additional Results from Initially laminar Explosions..... 212

Appendix C. Additional Results from Turbulent Explosion..... 238

References..... 284

List of Tables

2.1 Specifications of the Kistler 701, 7261, and 810 pressure transducers..... 16

6.1 Schedules of all laminar explosions during which measurements were made..... 79

6.2 Chosen mixtures to assess the reliability of deriving values of u_ℓ..... 80

6.3 Data for predication of unstable burning velocity, u_n, from laminar burning velocity u_ℓ, using instability theory. CH_4 – air, ϕ = 1.0, initial pressure and temperature, 0.1 MPa and 298 K..... 83

6.4 Schedule of all laminar implosions for which values of u_ℓ were obtained from the measured values of u_n, using the modified Bechtold – Matalon theory..... 86

7.1 Summary of conditions for different values of u' for all turbulent explosions during which measurements were made for iso-octane – air mixtures. p_o and T_o are initial pressures and temperatures..... 120

7.2 Summary of all turbulent explosions during which measurements were made for hydrogen – air mixtures, ϕ = 0.3 and ϕ = 0.4. p_o and T_o are initial pressures and temperatures..... 121

8.1 Initial conditions and corresponding turbulence parameters for iso-octane - air mixtures, ϕ = 1.0, p_o = 0.5 MPa, T_o = 358 K..... 198

8.2 Initial conditions and corresponding turbulence parameters for iso-octane - air mixtures, ϕ = 1.4, p_o = 0.5 MPa, T_o = 358 K..... 199

8.3 Initial conditions and corresponding turbulence parameters for iso-octane - air mixtures, ϕ = 1.0, p_o = 1 MPa, T_o = 358 K..... 200

8.4 Initial conditions and corresponding turbulence parameters for iso-octane - air mixtures, ϕ = 1.4, p_o = 1 MPa, T_o = 358 K..... 201

8.5 Initial conditions and corresponding turbulence parameters for hydrogen - air mixtures, ϕ = 0.3, p_o = 0.5 MPa, T_o = 358 K..... 202

8.6 Initial conditions and corresponding turbulence parameters for hydrogen - air mixtures, ϕ = 0.4, p_o = 0.5 MPa, T_o = 358 K..... 203

List of Figures

1.1 Concentration and temperature profiles associated with one-dimensional, premixed adiabatic flame..... 3

1.2 Maximum measured burning velocities of methane-air mixtures (initial ambient conditions) since 1915..... 6

1.3 Photographic images of: (a) stable lean butane/air flame, and (b) unstable lean hydrogen/air flame..... 7

2.1 Schematic of the apparatus used, for central ignition, (light source: He-Ne laser, camera: Hitachi 16 HM high-speed cine camera) and twin ignition, (light source: 20W tungest element lamp, camera: 545-4D High-speed Phantom digital camera)..... 12

2.2 Explosion vessel..... 13

2.3 Twin ignition arrangement..... 15

2.4 Fuel system..... 17

2.5 Sequence of schlieren images of laminar flames for different methane-air mixtures at the indicated times after spark ignition. The initial pressure was 0.5 MPa and the temperature was 358 K..... 20

2.6 Sequence of schlieren images of laminar imploded flames for different iso-octane-air mixtures. The initial pressure was 0.5 MPa and the temperature was 358 K..... 22

2.7 Sequence of schlieren images laminar imploded flames for methane-air mixture, $\phi = 1.0$. The initial pressure was 0.1 MPa and the temperature was 298 K..... 23

2.8 Stages of image processing. (a) Laminar stoichiometric iso-octan-air mixture at an initial pressure of 0.5 MPa and temperature of 358 K. b Turbulent stoichiometric iso-octane-air mixture at an initial pressure of 1 MPa and temperature of 358K, ($u' = 2.5$ ms)..... 24

2.9 Hand-measurement method. 25

2.10 Positions of flame fronts relative to X and Y-axis..... 26

2.11 Comparison between the two methods used to obtain the flame radii..... 27

2.12 View of inside the combustion vessel showing spark plug, window recess and fans..... 28

3.1 Pressure records for (a) methane – air and, (b) iso-octane - air mixtures, p_o = 0.5 MPa and T_o = 358 K. Explosions at three equivalence ratios..... 35

3.2 Flame radii obtained directly and deduced from pressure for (a) methane-air and (b) iso-octane-air mixture. p_0 = 0. 5 MPa, T_0 = 358 K..... 36

3.3 Gas velocities just ahead of the flame for (a) methane – air and (b) iso-octane – air mixtures, at p_0 = 0. 5 MPa, T_0 = 358 K, for different equivalence ratios. 37

3.4 Plots of flame speed against total flame stretch for (a) methane - air and (b) iso-octane – air mixtures at p_0 = 0.5 MPa, T_0 = 358 K, three equivalence ratios, optical measurements..... 40

3.5 Burning velocities from optical and pressure measurement techniques for (a) methane - air and (b) iso-octane – air mixtures at p_0 = 0.5 MPa and T_0 = 358 K. ϕ = 0.8, 1.0 and 1.2. 42

3.6 Variations of laminar burning velocities with pressure during isentropic compression for stoichiometric methane and iso-octane mixtures at p_0 = 0.5 MPa, T_0 = 358 K..... 43

3.7 Cellular flame image for stoichiometric methane-air mixture, at initial pressure of 0.5 MPa and temperature of 358 K, 31.73 ms, from ignition... 44

3.8 Cellular flame image for stoichiometric iso-octane - air mixture, at initial pressure of 0.5 MPa and temperature of 358 K, 25.48 ms, from ignition..... 44

3.9 Pressure records for turbulent iso-octane – air flames, ϕ = 1.5, p_o = 0.25 MPa, T_o = 358 K, u' in m/s..... 45

3.10 Burning velocities against time for iso-octane – air flames at ϕ = 1.5, p_0 = 0.25 MPa, T_0 = 358 K, at different values of u' in m/s, using pressure measurements Eq. 3.22. X indicates when the flame reaches the fans..... 46

3.11 Flame radius against time for iso-octane – air flames at ϕ = 1.5, p_0 = 0.25 MPa, T_0 = 358 K, at different values of u' in m/s. Pressure measurements, Eq. 3.17..... 46

3.12 Gas velocities for iso-octane – air flames at ϕ = 1.5, p_0 = 0.25 MPa, T_0 = 358 K at different values of u' in m/s, using Eq. 3.12. X indicates when the flame reaches the fans..... 47

4.1 Derivation of volume of a cusp. 49

4.2 Burned gas contained in two cusps, volume (a and b)..... 50

4.3 Derivation of flame front area. 52

4.4 Volume of window recess and volume occupied by fans..... 53

4.5 Normalized rms flame front radii for twin imploding laminar flames, for iso-octane – air mixture, $\phi = 1$, $p_o = 1$ MPa, $T_o = 358$ K..... 57

4.6 Normalized rms flame front radii for twin imploding laminar flames, for methane – air mixture, $\phi = 1$, $p_o = 0.1$ MPa, $T_o = 298$ K..... 57

4.7 Normalized rms flame front radii for twin imploding turbulent flames, for iso-octane – mixture, $\phi = 1.4$, $p_o = 0.5$ MPa, $T_o = 358$ K, $u' = 0.25$ m/s. 58

4.8 Normalized rms flame front radii for twin imploding turbulent flames for iso-octane – mixture, $\phi = 1.4$, $p_o = 0.5$MPa, $T_o = 358$ K, $u' = 1$ m/s..... 58

4.9 Normalized rms flame front radii for twin imploding turbulent flames for iso-octane – air mixture, $\phi = 1.4$, $p_o = 0.5$ MPa, $T_o = 358$ K, $u' = 3$ m/s..... 59

4.10 Variation of $\overline{V}_r$ with mean normalized radius for initially laminar flames of stoichiometric iso-octane – air, at different initial pressures and an initial temperature of 358 K..... 60

4.11 Variations of burning velocity with time from ignition for iso-octane mixture, $\phi = 0.8$, $p_o = 0.5$ MPa, $T_o = 358$ K, using Eqs. (4.14) and (4.19). Broken curves: no allowance for V_r..... 61

4.12 Variation of $\overline{V}_r$ with mean radius in turbulent flames for different values of u' (m/s), $p_o = 0.75$ MPa, $T_o = 358$ K. 62

4.13 Flame front correction for turbulent conditions..... 63

4.14 Flame area correction chart for turbulent conditions, Full lines give $\bar{r}$ 67

5.1 Photographic image of a cellular rich propane/air/nitrogen flame..... 68

5.2 Schematic mechanism of diffusional–thermal cellular instability..... 69

5.3 Theoretical wave number, n, at limits of stability for different Ma_{sr}, as a function of Peclet number..... 72

5.4 Instability peninsula, with limiting wave numbers fn_s and n_l. The critical, cellular, Peclet number, Pe_{cl} is at the tip of the peninsula..... 73

6.1 Iso-octane – air implosion, $\phi = 0.8$, $p_o = 0.5$ MPa, $T_o = 358$ K..... 88

6.2 Iso-octane – air implosion, $\phi = 0.8$, $p_o = 1$ MPa, $T_o = 358$ K. 89

6.3 Iso-octane – air implosion, $\phi = 0.9$, $p_o = 0.5$ MPa, $T_o = 358$ K. 90

6.4 Iso-octane – air implosion, $\phi = 0.9$, $p_o = 1$ MPa, $T_o = 358$ K. 91

6.5 Iso-octane – air implosion, $\phi = 1$, $p_o = 0.5$ MPa, $T_o = 358$ K. 92

6.6 Iso-octane – air implosion, $\phi = 1$, $p_o = 1$ MPa, $T_o = 358$ K. 93

6.7 Iso-octane – air implosion, $\phi = 1.1$, $p_o = 0.5$ MPa, $T_o = 358$ K. 94

6.8 Iso-octane – air implosion, $\phi = 1.1$, $p_o = 1$ MPa, $T_o = 358$ K. 95

6.9 Iso-octane – air implosion, $\phi = 1.2$, $p_o = 0.5$ MPa, $T_o = 358$ K..... 96

6.10 Iso-octane – air implosion, $\phi = 1.2$, $p_o = 1$ MPa, $T_o = 358$ K. 97

6.11 Iso-octane – air implosion, $\phi = 1.3$, $p_o = 0.5$ MPa, $T_o = 358$ K. 98

6.12 Iso-octane – air implosion, $\phi = 1.3$, $p_o = 1$ MPa, $T_o = 358$ K. 99

6.13 Iso-octane – air implosion, $\phi = 1.4$, $p_o = 0.5$ MPa, $T_o = 358$ K. 100

6.14 Iso-octane – air implosion, $\phi = 1.4$, $p_o = 1$ MPa, $T_o = 358$ K. 101

6.15 Iso-octane – air implosion, $\phi = 1.5$, $p_o = 0.5$ MPa, $T_o = 358$ K. 102

6.16 Iso-octane – air implosion, $\phi = 1.5$, $p_o = 1$ MPa, $T_o = 358$ K. 103

6.17 Iso-octane – air implosion, $\phi = 1.6$, $p_o = 0.5$ MPa, $T_o = 358$ K. 104

6.18 Iso-octane – air implosion, $\phi = 1.6$, $p_o = 1$ MPa, $T_o = 358$ K. 105

6.19 Iso-octane – air implosion, $\phi = 1$, $p_o = 0.75$ MPa, $T_o = 358$ K. 106

6.20 Iso-octane – air implosion, $\phi = 1.4$, $p_o = 0.75$ MPa, $T_o = 358$ K. 107

6.21 Methane – air implosion, $\phi = 1$, $p_o = 0.1$ MPa, $T_o = 298$ K. 108

6.22 Methane – air implosion, $\phi = 1$, $p_o = 0.5$ MPa, $T_o = 358$ K. 109

6.23 Hydrogen – air implosion, $\phi = 0.3$, $p_o = 0.5$ MPa, $T_o = 358$ K..... 110

6.24 Hydrogen – air implosion, $\phi = 0.4$, $p_o = 0.5$ MPa, $T_o = 358$ K..... 111

6.25 Hydrogen – air implosion, $\phi = 0.5$, $p_o = 0.5$ MPa, $T_o = 358$ K..... 112

6.26 Schlieren images of the two kernels close to making contact of stoichiometric CH_4-air initially at 0.1 MPa and 298 K, ($p = 0.37$ MPa, $T = 430$ K, $t = 104.86$ ms)..... 81

6.27 Symbols: experimental values of u_n from two explosions of stoichiometric CH_4-air initially at 0.1 MPa and 298 K. Broken curve, values of u_ℓ from Gu *et al.* (2000), full line curve, predicted unstable burning velocities, u_n. 82

6.28 Symbols: experimental values of u_n from two implosions of stoichiometric iso-octane-air initially at 0.5 MPa and 358 K, (upper symbols). Lower symbols show values of u_ℓ predicted from these compared with values from Bradley *et al.* (1998) (broken curve)..... 84

6.29 Symbols: experimental values of u_n from two implosions of of lean (ϕ = 0.8) iso-octane-air initially at 0.5 MPa and 358 K, (upper symbols). Lower symbols show values of u_ℓ predicted from these, compared with values from Bradley *et al.* (1998) (broken curve)..... 85

6.30 Experimental values of u_n from two implosions of (a) lean (ϕ = 0.8) iso-octane-air initially at 1.0 MPa, (b) for stoichiometric iso-octane initially 1.0 MPa, both at initial temperature of 358 K (upper symbols). Lower symbols show values of u_ℓ predicted from these..... 113

6.31 Experimental values of u_n from two implosions of lean (ϕ = 0.9) iso-octane-air initially at (a) 0.5 MPa, (b) 1 MPa and 358 K (upper symbols). Lower symbols show values of u_ℓ predicted from these..... 114

6.32 Experimental values of u_n from two implosions of rich (ϕ = 1.1) iso-octane-air initially at (a) 0.5 MPa, (b) 1 MPa and 358 K (upper symbols). Lower symbols show values of u_ℓ predicted from these..... 115

6.33 Experimental values of u_n from two implosions of rich (ϕ = 1.2) iso-octane-air initially at (a) 0.5 MPa, (b) 1 MPa and 358 K (upper symbols). Lower symbols show values of u_ℓ predicted from these..... 116

6.34 Experimental values of u_n from two implosions of rich (ϕ = 1.3) iso-octane-air initially at (a) 0.5 MPa, (b) 1 MPa and 358 K (upper symbols). Lower symbols show values of u_ℓ predicted from these..... 117

6.35 Experimental values of u_n from two implosions of rich (ϕ = 1.4) iso-octane-air initially at (a) 0.5 MPa, (b) 1 MPa and 358 K (upper symbols). Lower symbols show values of u_ℓ predicted from these..... 118

7.1 Iso-octane - air implosion, $\phi = 1$, $p_o = 0.5$ MPa, To = 358 K, $u' = 0.25$..... 129

7.2 Iso-octane - air implosion, $\phi = 1$, $p_o = 0.5$ MPa, To = 358 K, $u' = 0.50$..... 130

7.3 Iso-octane - air implosion, $\phi = 1$, $p_o = 0.5$ MPa, To = 358 K, $u' = 0.75$..... 131

7.4 Iso-octane - air implosion, $\phi = 1$, $p_o = 0.5$ MPa, To = 358 K, $u' = 1.0$..... 132

7.5 Iso-octane - air implosion, $\phi = 1$, $p_o = 0.5$ MPa, To = 358 K, $u' = 2.0$..... 133

7.6 Iso-octane - air implosion, $\phi = 1$, $p_o = 0.5$ MPa, To = 358 K, $u' = 3.0$..... 134

7.7 Iso-octane - air implosion, $\phi = 1.4$, $p_o = 0.5$ MPa, To = 358 K, $u' = 0.25$... 135

7.8 Iso-octane - air implosion, $\phi = 1.4$, $p_o = 0.5$ MPa, To = 358 K, $u' = 0.50$... 136

7.9 Iso-octane - air implosion, $\phi = 1.4$, $p_o = 0.5$ MPa, To = 358 K, $u' = 0.75$... 137

7.10 Iso-octane - air implosion, $\phi = 1.4$, $p_o = 0.5$ MPa, To = 358 K, $u' = 1.0$.... 138

7.11 Iso-octane - air implosion, $\phi = 1.4$, $p_o = 0.5$ MPa, To = 358 K, $u' = 2.0$.... 139

7.12 Iso-octane - air implosion, $\phi = 1.4$, $p_o = 0.5$ MPa, To = 358 K, $u' = 3.0$.... 140

7.13 Iso-octane - air implosion, $\phi = 1$, $p_o = 0.75$ MPa, $T_o = 358$ K, $u' = 0.25$.... 141

7.14 Iso-octane - air implosion, $\phi = 1$, $p_o = 0.75$ MPa, $T_o = 358$ K, $u' = 0.50$.... 142

7.15 Iso-octane - air implosion, $\phi = 1$, $p_o = 0.75$ MPa, $T_o = 358$ K, $u' = 0.75$.... 143

7.16 Iso-octane - air implosion, $\phi = 1$, $p_o = 0.75$ MPa, $T_o = 358$ K, $u' = 1.0$..... 144

7.17 Iso-octane - air implosion, $\phi = 1$, $p_o = 0.75$ MPa, $T_o = 358$ K, $u' = 2.0$..... 145

7.18 Iso-octane - air implosion, $\phi = 1$, $p_o = 0.75$ MPa, $T_o = 358$ K, $u' = 3.0$..... 146

7.19 Iso-octane - air implosion, $\phi = 1.4$, $p_o = 0.75$ MPa, $T_o = 358$ K, $u' = 0.25$.. 147

7.20 Iso-octane - air implosion, $\phi = 1.4$, $p_o = 0.75$ MPa, $T_o = 358$ K, $u' = 0.50$.. 148

7.21 Iso-octane - air implosion, $\phi = 1.4$, $p_o = 0.75$ MPa, $T_o = 358$ K, $u' = 0.75$.. 149

7.22 Iso-octane - air implosion, $\phi = 1.4$, $p_o = 0.75$ MPa, $T_o = 358$ K, $u' = 1.0$... 150

7.23 Iso-octane - air implosion, $\phi = 1.4$, $p_o = 0.75$ MPa, $T_o = 358$ K, $u' = 2.0$... 151

7.24 Iso-octane - air implosion, $\phi = 1.4$, $p_o = 0.75$ MPa, $T_o = 358$ K, $u' = 3.0$... 152

7.25 Iso-octane - air implosion, $\phi = 1$, $p_o = 1$ MPa, $T_o = 358$ K, $u' = 0.25$..... 153

7.26 Iso-octane - air implosion, $\phi = 1$, $p_o = 1$ MPa, $T_o = 358$ K, $u' = 0.50$..... 154

7.27 Iso-octane - air implosion, $\phi = 1$, $p_o = 1$ MPa, $T_o = 358$ K, $u' = 0.75$..... 155

7.28 Iso-octane - air implosion, $\phi = 1$, $p_o = 1$ MPa, $T_o = 358$ K, $u' = 1.0$..... 156

7.29 Iso-octane - air implosion, $\phi = 1$, $p_o = 1$ MPa, $T_o = 358$ K, $u' = 2.0$..... 157

7.30 Iso-octane - air implosion, $\phi = 1$, $p_o = 1$ MPa, $T_o = 358$ K, $u' = 3.0$..... 158

7.31 Iso-octane - air implosion, $\phi = 1.4$, $p_o = 1$ MPa, $T_o = 358$ K, $u' = 0.25$..... 159

7.32 Iso-octane - air implosion, $\phi = 1.4$, $p_o = 1$ MPa, $T_o = 358$ K, $u' = 0.50$..... 160

7.33 Iso-octane - air implosion, $\phi = 1.4$, $p_o = 1$ MPa, $T_o = 358$ K, $u' = 0.75$..... 161

7.34 Iso-octane - air implosion, $\phi = 1.4$, $p_o = 1$ MPa, $T_o = 358$ K, $u' = 1.0$..... 162

7.35 Iso-octane - air implosion, $\phi = 1.4$, $p_o = 1$ MPa, $T_o = 358$ K, $u' = 2.0$..... 163

7.36 Iso-octane - air implosion, $\phi = 1.4$, $p_o = 1$ MPa, $T_o = 358$ K, $u' = 3.0$..... 164

7.37 Hydrogen - air implosion, $\phi = 0.3$, $p_o = 0.5$ MPa, $T_o = 358$ K, $u' = 0.25$... 165

7.38 Hydrogen - air implosion, $\phi = 0.3$, $p_o = 0.5$ MPa, $T_o = 358$ K, $u' = 0.50$... 166

7.39 Hydrogen - air implosion, $\phi = 0.3$, $p_o = 0.5$ MPa, $T_o = 358$ K, $u' = 0.75$... 167

7.40 Hydrogen - air implosion, $\phi = 0.3$, $p_o = 0.5$ MPa, $T_o = 358$ K, $u' = 1.0$..... 168

7.41 Hydrogen - air implosion, $\phi = 0.3$, $p_o = 0.5$ MPa, $T_o = 358$ K, $u' = 2.0$..... 169

7.42 Hydrogen - air implosion, $\phi = 0.3$, $p_o = 0.5$ MPa, $T_o = 358$ K, $u' = 0.25$... 170

7.43 Hydrogen - air implosion, $\phi = 0.3$, $p_o = 0.5$ MPa, $T_o = 358$ K, $u' = 0.50$... 171

7.44 Hydrogen - air implosion, $\phi = 0.3$, $p_o = 0.5$ MPa, $T_o = 358$ K, $u' = 0.75$... 172

7.45 Hydrogen - air implosion, $\phi = 0.3$, $p_o = 0.5$ MPa, $T_o = 358$ K, $u' = 1.0$..... 173

7.46 Hydrogen - air implosion, $\phi = 0.3$, $p_o = 0.5$ MPa, $T_o = 358$ K, $u' = 2.0$..... 174

7.47 Schlieren image of the two kernels close to making contact of lean (ϕ = 0.3) H_2-air initially at 0.5 MPa and 358 K, $u' = 1$ m/s..... 122

7.48 Development of effective rms turbulent velocity (Haq, 1998). 124

7.49 Temporal development of u'_k/u', in iso-octane –air mixture, $\phi = 1.0$ and $\phi = 1.4$..... 125

7.50 Corrected values of u_t for iso-octane - air implosions, (a) $\phi = 1$ (b) $\phi = 1.4$, at $p_o = 0.5$ MPa, $T_o = 358$ K..... 126

7.51 Corrected values of u_t for iso-octane - air implosions, (a) $\phi = 1$ (b) $\phi = 1.4$, at $p_o = 1$ MPa, $T_o = 358$ K..... 127

7.52 Corrected values of u_t for hydrogen - air implosions, (a) $\phi = 0.3$, (b) $\phi = 0.4$, at $p_o = 0.5$ MPa, $T_o = 358$ K..... 128

8.1 Values of u_n derived from three different methods for stoichiometric iso-octane-air mixture (filled symbols) and methane – air mixture (open symbols), at $p_o = 0.5$ MPa and $T_o = 358$ K. Triangle symbols indicate double kernel values..... 176

8.2 Values of u_ℓ derived from twin kernel measurements for different values of u_n for iso-octane-air. Initial conditions 0.5 MPa and 358 K..... 178

8.3 Values of u_ℓ derived from twin kernel measurements for different values of ϕ for iso-octane-air. Initial conditions 1.0 MPa and 358 K..... 179

8.4 Variations of u_n, F and u_ℓ with equivalence ratio at 2.0 MPa and 427 K. Iso-octane-air, initial conditions 1.0 MPa and 358 K..... 180

8.5 Laminar burning velocity at two different pressures and temperatures in isentropic compression from 0.5 MPa and 358 K. Pressures in MPa followed by temperature. Topmost curve are values from Davis and Law, (1998) under atmospheric conditions..... 181

8.6 Laminar burning velocity at five different pressures and temperatures in isentropic compression from 1.0 MPa and 358 K. Pressures in MPa followed by temperature..... 181

8.7 Experimental values of u_n from two implosions of lean hydrogen-air initially at 0.5 MPa and 358 K, (a) $\phi = 0.3$, (b) $\phi = 0.4$ and (c) $\phi = 0.5$ (upper symbols). Lower symbols show values of u_ℓ predicted from these, compared with computed values from Verhelsts *et al.*, (2004) (broken curves)..... 182

8.8 Experimental values of u_n from one implosion of rich ($\phi = 1.5$) iso-octane - air initially at 0.5 MPa, and 358 K (upper symbols). Lower symbols show apparent values of u_ℓ derived from these..... 184

8.9 Ignition delay times for stoichiometic n-heptane mixtures at different pressures, Peters *et al.* (2002)..... 185

8.10 Integral values, *i*, for laminar iso-octane flame, ϕ = 1.5, p_o = 1 MPa, T_o = 358 K at the appropriate p and T and u_n values for which measurements were made..... 185

8.11 Integral values, *i*, for laminar iso-octane flame, ϕ = 1.6, p_o = 1 MPa, T_o = 358 K at the appropriate p, T and u_n values for which measurements were made..... 186

8.12 Normalized u_t against K for iso-octane-air mixture at different pressures and temperatures. (a) ϕ = 1.0, (b) ϕ = 1.4, at p_o = 0.5 MPa, T_o = 358 K.... 187

8.13 Normalized u_t against K for iso-octane - air mixture at different pressures and temperatures. (a) ϕ = 1.0, (b) ϕ = 1.4, at p_o = 1.0 MPa, T_o = 358 K.... 188

8.14 Normalized u_t against K for hydrogen - air mixture at different pressures and temperatures. (a) ϕ = 0.3, (b) ϕ = 0.4, at p_o = 0.5 MPa, T_o = 358 K.... 189

8.15 Normalized u_t against K for iso-octane - air mixture at different pressures and temperatures. (a) ϕ = 1.0, (b) ϕ = 1.4, at p_o = 0.5 MPa, T_o = 358 K..... 191

8.16 Normalized u_t against K for iso-octane - air mixture at different pressures and temperatures. (a) ϕ = 1.0, (b) ϕ = 1.4, at p_o = 1.0 MPa, T_o = 358 K..... 192

8.17 Normalized u_t against K for hydrogn - air mixture at different pressures and temperatures. (a) ϕ = 0.3, (b) ϕ = 0.4, at p_o = 0.5 MPa, T_o = 358 K..... 193

8.18 Variation of U with Ma_{sr} for K=0.025 and 0.15 (filled symbol)..... 194

8.19 Values of U at 1.0 and 2.0 MPa. a and c, ϕ = 1.0; b and d, ϕ = 1.4. Symbols, measured values from the present work; dotted curve, Bradley *et al.* (1992); bold curves, flamelet instability theory, (Sedaghat)..... 196

Nomenclature

A	flame area
a	volume of burned gas contained in the upper cusp
A'	flame area associated with flame radius r_v
B	enhancement burned volume factor
b	volume of burned gas contained in the lower cusp
D	thermal diffusivity
D	fractal dimension
f	instability lag factor for wave number
F	burning velocity enhancement factor
h	cusp height in Eq. 4.3
K	Karlovitz stretch factor
L	integral length scale
L_b	burned gas Markstein length
L_c, L_s, L_{cr}, L_{sr}	Markstein lengths, (L_c, L_s, associated with curvature and strain respectively for stretched laminar burning velocity, L_{cr}, L_{sr}, associated with curvature and strain respectively for stretched mass burning velocity).
Le	Lewis number
Ma_c, Ma_s, Ma_{cr}, Ma_{sr}	Markstein numbers, (Ma_c, Ma_s, associated with curvature and strain respectively for stretched laminar burning velocity, Ma_{cr}, Ma_{sr} associated with curvature and strain respectively for stretched mass burning velocity).
m_b	mass of burned gas
m_u	mass of unburned gas
N	experimental wave number of large unstable cells
n	theoretical wave number
n_{cl}	unstable wave number at, n_l, at Pe_{cl}
n_{cr}	critical unstable wave number at Pe_{cr}
n_l	wave number at longest unstable wavelength
N_s	experimental wave number of small unstable cells
n_s	wave number at shortest unstable wavelength

p	pressure
p_e	end pressure
Pe	Peclet number
Pe_{cl}	second (cellular) critical Peclet number
Pe_{cr}	first critical Peclet number
p_o	initial pressure
R	explosion vessel radius
r	mean radius
r'	r.m.s values for mean radius, r
R_λ	Reynolds number for Taylor scale ($R_\lambda = 4R_\ell^{0.5}$)
r_1	bottom flame radius
r_2	tope flame radius
r_b	flame radius
R_ℓ	Reynolds number ($R_\ell = u'L/\nu$)
r_o	arbitrary flame radius at $t = 0$
r_{sch}	schlieren flame front radius
r_u	cold flame radius defined in equation (3.28)
r_v	flame radius centered outside the vessel wall
S	flame speed factor
S_n	stretched flame speed
S_s	unstretched flame speed
S_u	burning velocity
t	time from ignition
T_o	initial temperature
T_u	unburned gas temperature
u'	r.m.s turbulent velocity
u_g	gas velocity ahead of the flame
u'_k	effective r.m.s turbulent burning velocity
u_l	unstretched laminar burning velocity
u_n	stretched laminar burning velocity
u_t	corrected turbulent burning velocity
u'_t	uncorrected turbulent burning velocity
V	volume of combustion vessel

V_r	residual volume of unburned gas
V_{rt}	net volume of residual unburned gas in turbulent flame
$V_{r\ell}$	net volume of residual unburned gas in laminar flame
V_{ut}	volume of unburned gas in turbulent explosion
$V_{u\ell}$	volume of unburned gas in laminar explosion
$\overline{V}_r$	normalized residual volume of unburned gas

Greek Symbols

Λ_s	wave number for a localized cell
η	Kolmogorov scale
α	flame stretch rate
α_c	stretch rate due to flame curvature
α_s	stretch rate due to flame strain
δ_ℓ	laminar flame thickness
δ_x	thickness of a segment of the cusp defined in Fig. 4.1
ϕ	equivalence ratio
ρ_b	burned gas density
ρ_u	unburned gas density
γ	ratio of specific heats
λ	Taylor turbulent length scale
ν	kinematic viscosity
$\tau_{(T,\,p)}$	ignition delay time at the instantaneous value of T and p
θ	angle by which the extent of the cusp is defined in Fig 4.1
φ	defined angle in Fig. 4.1
α'	defined angle in Fig. 4.13
θ'	defined angle in Fig. 4.13

Chapter 1

Introduction

1.1 General

The study of combustion and its control is ultimately important and even essential for modern civilisation. Throughout the world, combustion still provides more than 95% of the energy consumed. Fuels for practical combustion can be stored conveniently and their energy is readily released. This is particularly so for the fuels used in transportation (Griffiths and Barnard, 1995). Most of the researches in this field analyse fundamental aspects such as ignition, burn rate, decomposition of mixtures, stretch effects on flame propagation, and other parameters. Yet our understanding is still incomplete. According to Webster's Dictionary, (Turns 1996) combustion is a "rapid oxidation generating heat, or both light and heat; also, slow oxidation accompanied by relatively little heat and no light". Others define it as the interaction of chemical reactions, which occur between the fuel and oxidant (normally air), involving transport processes and fluid motion, (Griffiths and Barnard, 1995).

The propagation of a reaction front takes two major forms. Deflagration involves the molecular transport processes of conduction and diffusion of species and a comparatively thin reaction zone. There are large temperature and species concentration gradients and the flame may be laminar or turbulent. The second form is autoignitive. Here, most of the mixture ignites after the autoignition delay time has elapsed and molecular transport processes are less important. In this form a shock wave may be created that generates temperatures and pressures sufficient for rapid chemical reaction. The shock and reaction fronts then move in tandem as a detonation front. The main physical – chemical parameter for deflagration is the laminar burning velocity: that for autoignition is the ignition delay time.

In practice, most of the chemical reactions that occur in flames do so in the gaseous phase. All flames can be classified as either premixed or non-premixed. In premixed flames the fuel and oxidant are mixed prior to the combustion, whereas in non-premixed

flames mixing takes place close to the reaction zone. Flames can also be either laminar or turbulent. For intensive burning in power systems the combustion is usually turbulent. If the fuel is not completely vaporised or devolatilised before entering the reaction zone, then combustion is two phased. The focus in this study is on premixed gaseous combustion in both laminar and turbulent flames.

1.2 Laminar Flames

This type of flame occurs in residential and some commercial heating systems. It is important to study laminar flames not only for this reason but also to help our basic understanding of combustion, including turbulent combustion. In flamelet modelling it is often assumed that a turbulent flame is an array of laminar flames (Peters 2000). Mallard and Le Chatelier, (1883), were the first to develop a coherent picture of laminar flame structure. They proposed that the back-propagation of heat from the hot gas to the cold on-coming mixture was a controlling mechanism in flame propagation. They identified two zones separated at the point where the second zone ignites. However, this early thermal theory presented some difficulties, as it required the concept of an ignition temperature, a difficult parameter to identify or measure.

Later research led to better understanding of the molecular transport pressures, chain reactions and heat release rates, particularly in the theory of Zeldovich and Frank-Kamenetskii (1938). Zeldovich (1959) in his classical paper allowed for conduction, species diffusion and chemical reaction and obtained a reliable expression for the laminar burning velocity. The chemistry became more complex with the growing understanding of chain reactions, as a result of the seminal studies of Semenov and Hinshelwood.

The present understanding of the laminar flame structure is demonstrated in Fig. 1.1 (Griffiths and Barnard, 1995). The temperature profile is divided into four zones: cold reactants, preflame, reaction and products. The temperature increases initially by conduction, from the initial to the final state. Such a one dimensional flame, for given conditions, will have a unique value of the laminar burning velocity.

1.3 Laminar Burning Velocities

The burning velocity is influenced by the chemical kinetics of the chain reactions, diffusion coefficients of species and thermal conductivity. It is dependent on the pressure, temperature and mixture. It is defined as the relative velocity of the unburned

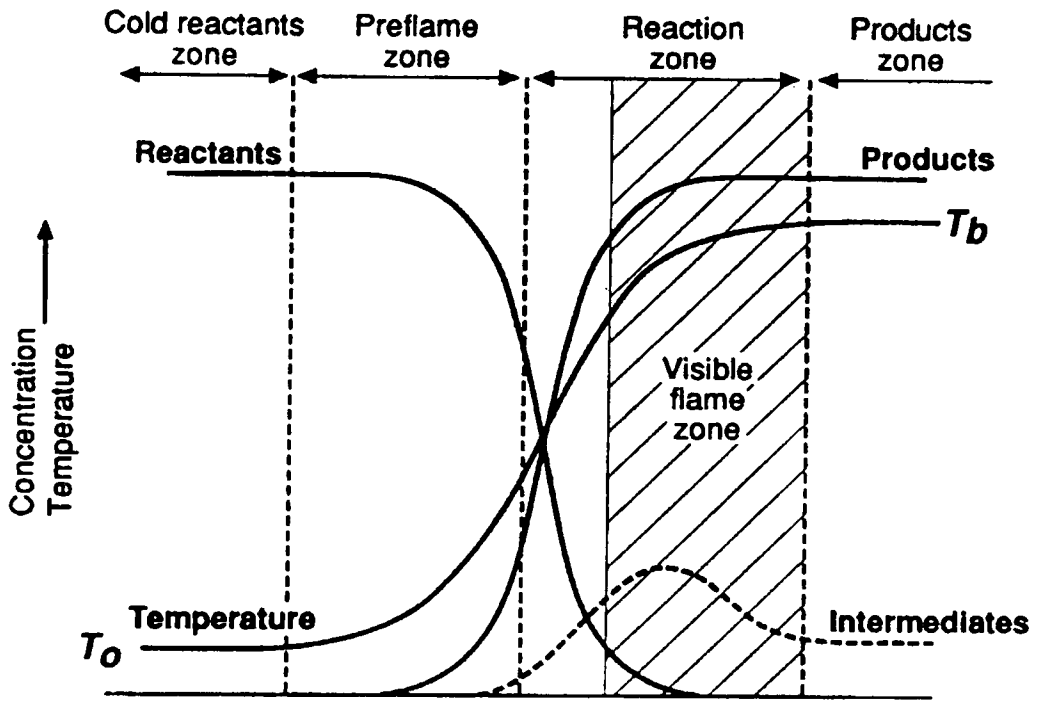

Fig. 1.1. Concentration and temperature profiles associated with one-dimensional, premixed adiabatic flame (Griffiths and Barnard, 1995).

gas, relative to and into a planar, one-dimensional flame along the normal to its surface. Its value has been studied for over a century, and yet there is still a lack of consensus both as to the most effective method for its measurement and the reliability of the published data. The different experimental methods of measuring it have been reviewed by Andrews and Bradley (1972), and Rallis and Garforth (1980). There are two categories for measurements, involving burner and explosion bomb methods. Burner methods have evolved, so that at the present time one of the most accurate methods involves two opposed counterflow burners with unburned gas velocities into the planar flame measured by laser Doppler velocimetry. A particular advantage of this technique is that it also enables the flame stretch rate (see Section 1.4) to be adjusted and

measured (Wu and Law, 1984, Yamaoka and Tsuji, 1984, Law, 1988, Law and Sung, 2000).

With regard to explosion methods, Mallard and Le Chatelier, (1883), showed that, a cylindrical tube closed at one end with ignition at the other, open end was probably the best method for achieving a constant flame speed over a distance sufficient to measure the laminar burning velocity. Thereafter, the flame developed oscillations especially with lean methane, hydrogen and rich hydrocarbon mixtures with air, and then assumed a cellular structure with an enhanced flame speed (Guénoche, 1964). Guénoche and Laffitte (1946) reduced the effects of potential acoustic oscillation by fitting an orifice to vent the burned gas at the open end of the tube. The vertical open tube method became a strongly recommended one for measuring burning velocity (Combourieu, 1961 and Laffitte, 1961).

The most common explosion method is to employ spherical explosion kernels with central ignition (Lewis and von Elbe, 1987). Some of the different techniques based on this are described in Chapter 3.5. Many experimental studies have been conducted to investigate spherical flames under a variety of conditions. This method has many advantages over others. Small quantities of combustible mixture are required, pressure, temperature and mixture composition are controllable over wide ranges, there are no surface interaction effects and the heat loss is negligible. The double kernel method introduced by Raezer and Olsen (1962) involved measuring the closing velocity between two explosion kernels. It has also been used by Andrews and Bradley (1972), Abdel-Gayed *et al.* (1984) and Koroll *et al.* (1993) to obtain, by direct measurements, the laminar burning velocity at the limit where the two kernels merge.

Another flame kernel method was developed by Dery (1949), and used by Bolz (1955) and Burlage (1960). They measured the flame radius from an equivalent sphere for the flame area as a flame kernel was carried downstream in a laminar combustible gas stream. The burning velocity was found from knowledge of the unburned / burned gas density ratio determined from thermo-chemical calculations. This method has the advantage of eliminating the effects of spark electrodes but produces a rather complex flame–front shape since the kernel is not spherical. Burning velocities also can be measured by explosions within a soap-bubble (Stevens, 1929 and 1932), a method

developed further by Fiock and Roeder (1935), and Linnett *et al.* (1951). A disadvantage of this method is that if water–based soap solutions are used, dry mixtures cannot be tested, (Rallis and Garforth, 1980, Simon and Wong, 1954).

1.4 Effects of Flame Stretch on Burning Velocities Predictions

In recent years the understanding of how flame stretch affects the laminar burning velocity has been consolidated. Bradley (2000), following Andrews and Bradley (1972), plotted the various measured values of maximum burning velocities against the year of publication in the literature for methane-air mixtures and this plot is reproduced in Fig. 1.2. The flame stretch rate can be complex and be a combination of curvature and strain rate effects. In dimensionless terms the effect of flame stretch rate on the laminar burning velocity, u_ℓ, has been given as (Bradley *et al.*, 1992 and Bradley *et al.*, 1996):

$$\frac{u_\ell - u_n}{u_\ell} = K_\ell Ma \qquad (1.1)$$

where K_ℓ is the laminar Karlovitch stretch factor. For a positive Markstein number, Ma, an increase in stretch rate reduces the stretched burning velocity, u_n, below u_ℓ. This is described in detail in Chapter 3.5. Both counterflow burners and spherical explosions have yielded, not only values of u_ℓ but also of Markstein numbers.

On Fig. 1.2 the method of measurement employed for each point in the plot is identified either in Andrews and Bradley (1972) or in Bradley (2000). It can be seen that in the last decade the scatter between results has been reduced, principally due to the recognition of the importance of allowing for the effects of the flame stretch rate. It is interesting to note the consistency of results from the open tube method of measurement.

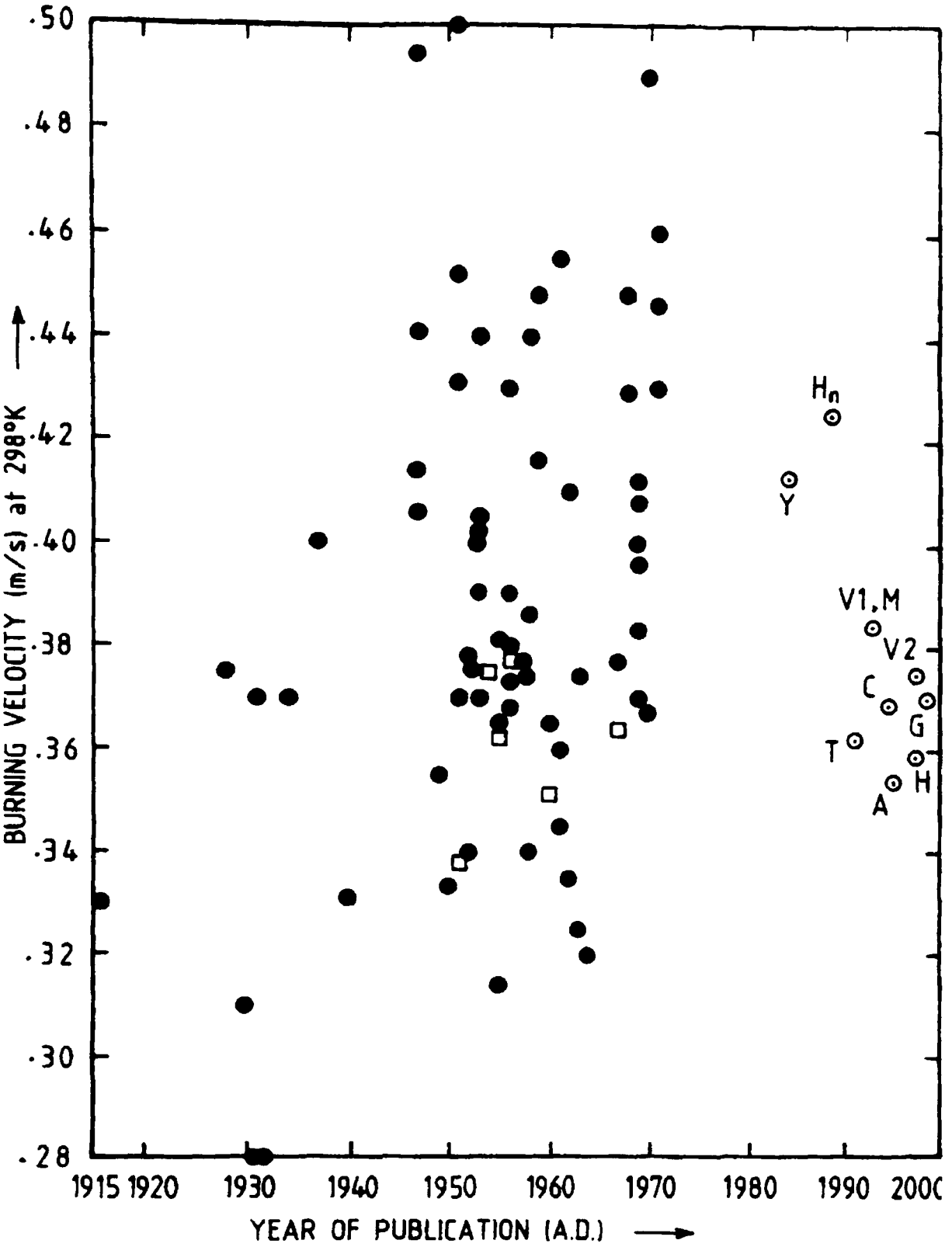

Fig. 1.2. Maximum measured burning velocities of methane-air mixtures (initial ambient conditions – 0.1 MPa) since 1915. For key to data before 1972 see Andrews and Bradley, 1972. Square symbol indicates open-tube method. Reference for later data are: A Aunge *et al.* (1995) C Clarke *et al.* (1995) G Gu *et al.* (2000) H Hassan *et al.* (1998) Hn Haniff *et al.* (1989) M Van Maaren *et al.* (1994) T Taylor (1991) V1 Vagelopoulos *et al.* (1994) V2 Vagelopoulos *et al.* (1998) Y Yamaoka and Tsuji. (1984). Source: Bradley (2000).

1.5 Instabilities

The flame instabilities observed by Guénoche (1946) were the results of low values of K_ℓ and Ma and it is shown in Chapter 5 how thermo-diffusive instabilities can arise under these conditions. In addition, and predating them in terms of our understanding, hydrodynamic instabilities can arise at a reaction front (Darrieus, 1938, Landau, 1944). The generation of instabilities is favoured by large flames and high pressures. Figure 1.3 shows two different outwardly propagating flames, one stable (a, lean butane/air. mixture), the other unstable (b, lean hydrogen/air mixture), (Law *et.al.*, 2000). The ensuing flame wrinkling can cause appreciable increases in the burning velocity. This is particularly marked for negative values of *Ma*.

(a) (b)

Fig. 1.3. Photographic images of: (a) stable lean butane/air flame, and (b) unstable lean hydrogen/air flame (Law *et al.*, 2000).

Such explosive flames propagate instabilities, in the form of cells and ridges and these develop over an increasing range of wavelengths. Basic understanding of the development of instabilities in explosion flames has advanced in recent years as a result of experimental studies, (Groff, 1982, Kwon *et al.* 1992, Bradley *et al.* 1998, Gu *et al.* 2000), and theoretical studies, (Bechtold and Matallon 1987, Bradley 1999, Addabbo *et al.* 2003). Some of these have shown that laminar spherical explosion flames are unstable above a critical Peclet number (the flame radius, r, normalised by the flame

thickness) that depends upon *Ma*. The burning velocity continues to increases with an increase in the flame wrinkling. Once the flame becomes unstable it is difficult to determine the key physico-chemical parameter, the laminar burning velocity. The present work addresses this problem and reports a detailed experimental study of these influences, using a modified version of the laminar instability theory of Bechtold and Matalon (1987).

Large values of *Pe* can arise in large atmospheric explosions. They also can arise at higher pressures, such as occur in engines, due to the smaller flame thickness. A higher pressure also decreases Ma_{sr}, (Bradley *et al.* 1998, Gu *et al* 2000, Bradley *et al.* 1996, and Aung *et al* 2002). The associated instabilities create a continually increasing burning velocity and early tentative estimates of the magnitudes of this, due to increases in both flame radius and pressure were given by Bradley *et al.*, (2000).

1.6 The Twin Kernel Explosion (Implosion) Technique

Large flame kernels with high pressures and negative Markstein numbers increase instabilities. Spherical bomb explosions, with central ignition have been widely employed to measure burning velocities and Markstein numbers of gaseous mixtures and sprays and observe the early stages of instabilities. The provision of strong windows facilitates such observations. Unfortunately, these central observations are not at the highest pressure and the flame moves out of the field of view as the pressure increases and the safe working pressure of the vessel must be designed to be much greater than the pressure at which measurements are made. The Princeton group (Tse *et al.*, 2000), has overcome this difficulty by employing two concentric cylinders, an inner one containing the combustible mixture with an annulus between them that is filled with inert gas at the same pressure. Just prior to ignition an encasing sleeve of the inner cylinder is moved to align holes that then connect the inner vessel and annulus. By this means the flame is quenched in the annulus after initial propagation in the inner vessel at the initial pressure, close to the maximum value.

An alternative approach would be to implode the mixture after ignition over the entire spherical wall of the bomb and make measurements in the final high-pressure stage

through central windows. Although spherical implosions have been modelled mathematically (Bradley *et al.*, 1996), they are impractical. As an alternative, in the course of the present studies a technique was developed that utilised two inwardly propagating flame kernels. Spark ignition occurred at diametrical opposite points at the wall of a spherical bomb and the two flame fronts met at the centre of the bomb where flame fronts could be observed. In this way, burning velocities were measured closer to the maximum pressure, rather than earlier at low pressure. This and the relatively large flame kernels were conducive to the development of flame instabilities and increased flame wrinkling. This resulted in increased measured burning velocities, compared with those in the absence of instabilities. With the emphasis on unstable flames, this method was advantageous in that Peclet numbers were maximised and stretch rate minimized by large flame radii and small flame thickness.

1.7 Turbulent Flames

Most practical flames are turbulent. By wrinkling the flame, turbulence increases the rate of volumetric heat release in combustion chambers of all types. Recent experimental and theoretical studies of turbulent combustion are reported in Peters (2000). However, most fundamental studies of turbulent flame propagation have been at atmospheric pressure whereas, in practice, reciprocating engines and gas turbines operate at elevated pressures in the region of 4 MPa. Consequently, there are few accurate data on turbulent and laminar burning velocities at these pressures.

Bradley *et al.* (1992) attempted to generalise results of 1650 diverse measurements of turbulent burning velocity, u_t, from a variety of sources with the expression:

$$\frac{u_t}{u'_k} = 1.01(KLe)^{-.0.3} \tag{1.2}$$

where $K = 0.25\left(\frac{u'}{u_\ell}\right)^2 \frac{1}{R_\ell^{0.5}}$ and $R_\ell = \frac{u'L}{\upsilon}$

here, u'_k is the effective rms velocity, Le the Lewis number, L the integral length scale, ν the kinematic viscosity and K the turbulent Karlovitz stretch factor. This expression

attempts to allow for flame stretch rate effects. Another expression is that of Gülder (1991):

$$\frac{u_t}{u'} = \frac{u_\ell}{u'} + 0.62\left(\frac{u_\ell}{u'}\right)^{0.5} R_l^{0.25} \qquad (1.3)$$

Uniquely, Kobayashi and his group (Kobayashi *et al.*, 1996) have measured turbulent burning velocities on a burner at pressures of up to 3 MPa. These measurements suggested significant enhancement in turbulent burning velocities over the values obtained from correlations predominantly derived for atmospheric pressure. That this enhancement might be attributed to Darieus-Landau and thermo-diffusive instabilities in the laminar flamelets has been confirmed by planar laser-induced fluorescence images of flame wrinkling, Kobayashi and Kawazoe, (2000). There is a growing realisation that these effects are more important at high pressure in turbulent flames, particularly at low values of the strain rate Markstein number, Ma_{sr}, the turbulent Karlovitz stretch factor, K, and at high values of the turbulent Reynolds number, R_{ℓ} (Boughanem and Trouvé, 1998, Bradley *et al.*, 2003). Any increased flamelet wrinkling due to instabilities would result in a further increase in the turbulent burning velocity.

With an anticipated increase in turbulent burning velocities at high pressure due to smaller flame thicknesses and Markstein numbers it was decided to use the two kernel implosion technique to measure them. The bomb was equipped with four fans of controllable speed to generate uniform, isotropic turbulence. Studies of turbulent burning in fan-stirred bombs originated at the Institute of Chemical Physics in Moscow (Karpov *et al.*, 1959). This technique avoids some of the problems of continuous combustion in high-pressure burners, but presents some other problems. The provision of windows is essential, but with central ignition observations are limited to combustion at, or close to, the initial pressure. This limitation is overcome with the two kernel implosion technique.

1.8 Achievements of the Present Studies

The main findings of the work are the evaluations of laminar and turbulent burning velocities principally of iso-octane mixtures, but also of those of H_2 – air and CH_4 – air.

Of particular importance have been studies of the effects of high pressure and temperature, approaching those in engines. In the case of turbulent burning velocities one of the objectives was to ascertain the effects of high pressure and any flamelet instabilities.

In the early studies, central ignition was employed and measurements were made with laminar burning in the early stage of combustion (pre-pressure period and with little increase in pressure). This was followed by measurements as the pressure increased. These two methods are well established. The third novel technique then was developed involving two implosions originating at spark plugs mounted near the wall. This enabled the later stages of burning at the higher pressures to be observed and burning velocities to be measured. It was applied in preliminary studies to both laminar and turbulent burning velocities.

Chapter Two describes the experimental apparatus and techniques, including the methods used to measure flames radii and the image processing. Chapter Three describes the theories for obtaining burning velocities with the central ignition technique, and these are applied to measure burning velocities. Chapter Four develops the theory for the twin ignition (implosion) technique. In Chapter Five flame instabilities in originally quiescent mixtures and their effect on burning velocities are discussed theoretically and an expression developed for the enhancements in burning velocity to be expected due to instabilities. Chapter Six presents the measured burning velocities, which increase with time and, from these, derives the laminar burning velocities at different temperatures and pressures. Chapter Seven reports the measured turbulent burning velocities. Results are discussed in Chapter Eight and an attempt is made to generalise the turbulent burning velocities, which are higher than those suggested by Eqs. (1.2) and (1.3). The generalisations involve the earlier deduced values of u_ℓ, free from instabilities. Chapter Nine reports conclusions extracted from the work, with some recommendations for future work.

Chapter 2

Experimental: Apparatus and Techniques

2.1 Introduction

The present work utilised existing apparatus in a novel way. Therefore, only brief descriptions, of the apparatus are given because full descriptions are given elsewhere. Full descriptions of the data processing techniques are given in Chapters 6 and 7. A general arrangement of the apparatus is shown in Fig. 2.1. It consisted of an optically accessed spherical explosion vessel instrumented with pressure transducers (Section 2.3.2), thermocouples (Section2.3.3), necessary piping and valves, and an ADC system. Two arrangements for explosion studies were utilised. The first involved central ignition to obtain laminar measurements at pressure up to 0.6 MPa.

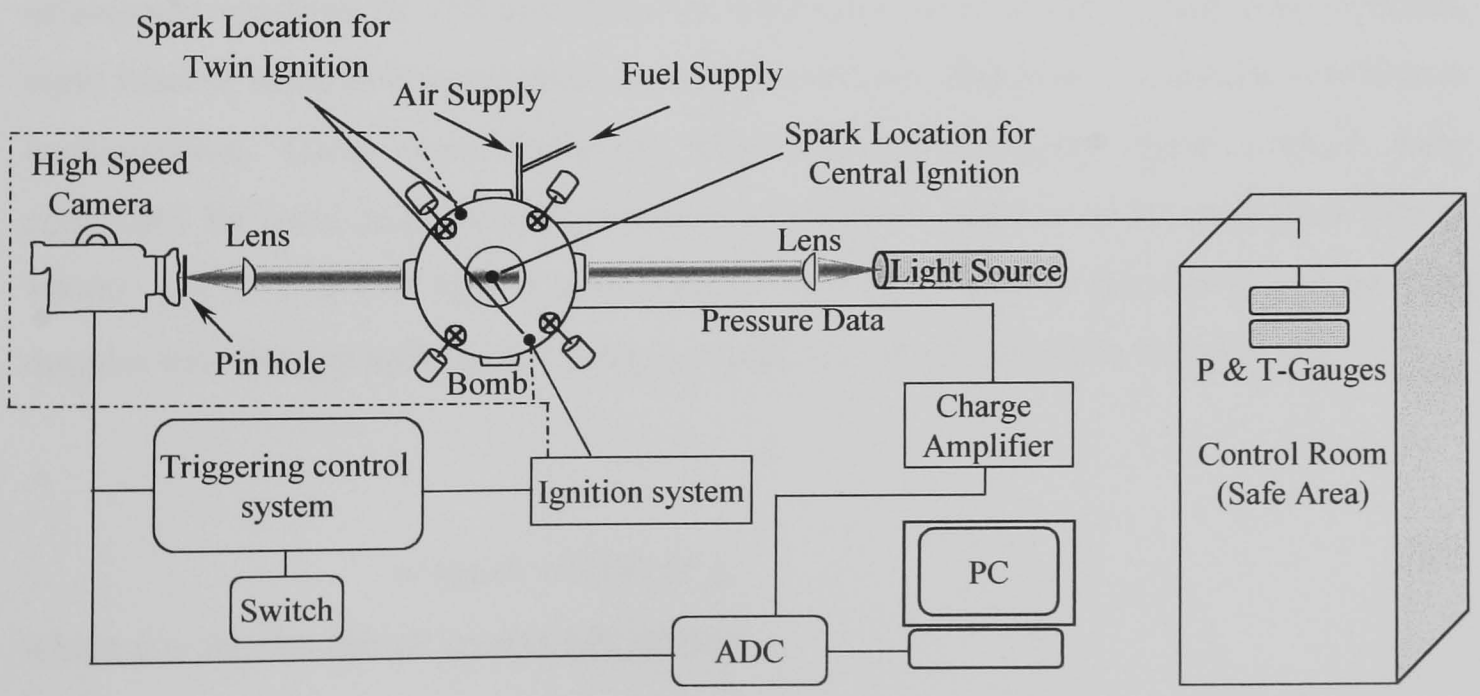

Fig. 2.1. Schematic of the apparatus used, for central ignition, (light source: He-Ne laser, camera: Hitachi 16 HM high-speed cine camera) and twin ignition, (light source: 20W tungsten element lamp, camera: 545-4D High-speed Phantom digital camera).

The second technique, developed by the present author, involved two spark plugs located diametrically opposite each other close to the vessel wall as indicated by the chain dashed lines in Fig. 2.1 and these yielded measurements at pressure up to 6 MPa. These experiments occurred later than the single kernel ones and, by this time, improved equipment had become available (Section 2.5.2). Methane, iso-octane and hydrogen premixtures were ignited at different conditions. Turbulent and laminar flames were studied with more emphasis, than with the single kernel work, on the effects of instabilities. Further details of each component and experimental techniques are given in the following sections.

2.2 Explosion Vessel

The explosion vessel known as ´the bomb` is shown in Fig. 2.2 and is fully described in Haq (1998) and Bradley *et al.* (1998). It comprised a 380 mm diameter spherical stainless steel vessel, capable of withstanding initial pressures of up to 1.5 MPa and initial temperatures of up to 600 K, with extensive optical access through 3 pairs of orthogonal windows of 150 mm diameter. The vessel was equipped with four identical, eight bladed, separately controlled, fans symmetrically disposed in a regular tetrahedron configuration. These were driven by adjustable speed electric motors, which were controlled by solid state variable frequency converter units, over a range from 200 to 10000 rpm (3.3 to 176 Hz). The turbulence was measured by Haq (1998) using laser doppler velocimetry and the rms turbulent velocity, u', was found to be given by:

$$u'\,(\text{m/s}) = 0.00119\,n \qquad 2.1$$

where n is the fan speeds in revs per minute.

The integral length scale, L, measured by two point correlation, was 20 mm (Bradley *et al.*, 1996a), for all the present conditions. For laminar studies, the fans were used only for mixing the reactants.

2.3 Auxiliary Systems

The combustion rig was mounted with several sub-systems for ignition, mixture preparation and diagnostic purposes. These included pressure transducers, an ignition source, and a data collection and digitising system (PC-ADC). The laboratory was equipped with a triggering system which synchronised the operation of such items as the spark, PC-ADC, camera and laser systems. It also included three emergency stop buttons, which were located in different places in the laboratory.

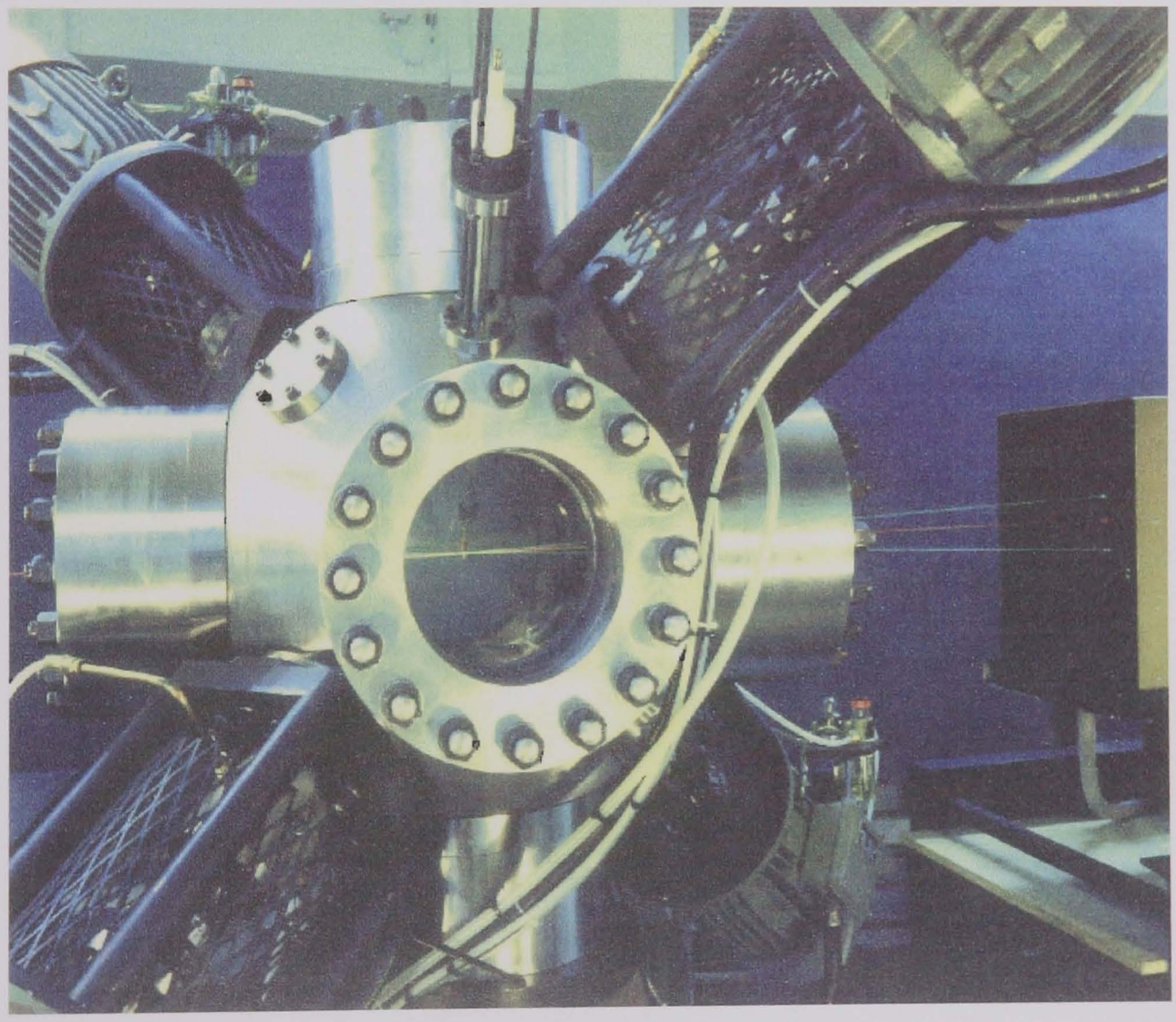

Fig. 2.2. Explosion vessel.

By pushing any of these buttons the fans, laser and the ignition system were turned off. The laboratory contained a ´safe area` located by the door. This was protected from flying debris, which might result from an explosion vessel failure, by a steel reinforced wall. Most controls and one of the emergency stop buttons were located in the safe area in which all personal stayed while conducting an explosion.

2.3.1 Ignition System

Two ignition arrangements were employed. One for the central ignition technique and the other for the twin ignition technique. For central ignition, a standard 6.35 mm Minimag spark plug was supported at the vessel centre by a 6mm diameter stainless steel tube. The electrical supply was provided by 12 V transistorised automotive ignition coil which was connected to the spark electrode assembly. Further details are provided in Haq (1998). The average spark energy generated by this system was estimated by Bradley *et al.* (1998) to be about 23 mJ.

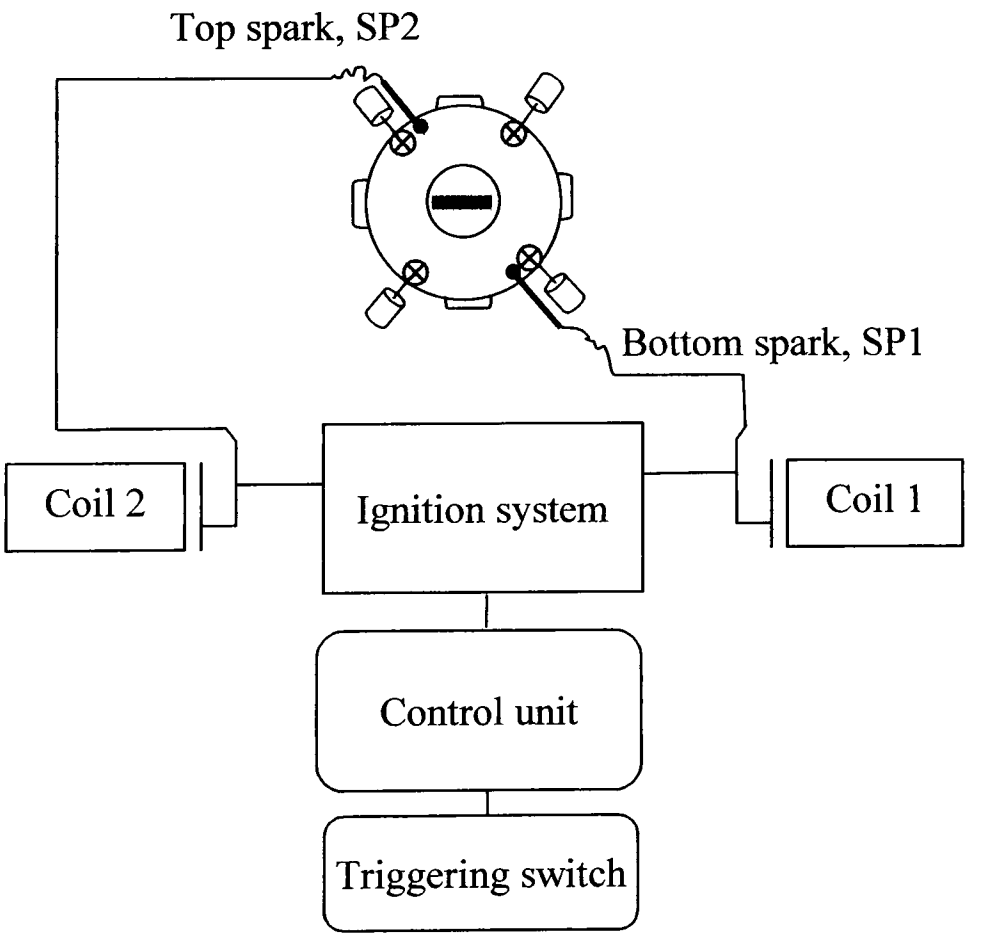

Fig. 2.3. Twin ignition arrangement.

Shown in Fig. 2.3 is the arrangement for the twin ignition technique. Essentially, it was the same as for the single kernel except that two coils and two spark plugs were used, the spark plugs being located diametrically opposite each other close to the vessel wall, and were synchronized so that ignition occurred simultaneously.

2.3.2 Pressure Measurement

Measurements of pressure were required at a wide range of conditions and this necessitated the use of three types of transducer, details of which are shown in Table 2.1. The initial unburned gas pressure was measured by a Druck PDCR 810 transducer. This was located in the air inlet pipe outside the bomb behind a valve and was isolated from the bomb for protection purposes before the unburned mixture was ignited. During explosions at initial pressures higher than 0.1 MPa a Kistler 701 transducer was used to record the transient pressure.

Type	701	7261	810
Measuring Range (MPa) - gauge	0 – 25	0 – 1	-0.1 - 1.5
Max.Pressure (MPa) - gauge	25	1.2	3
Measurements setting (MPa/volt)	0.1, 1.0	0.01	0.1
Resonant frequency kHz	> 70	13	> 28
Operating Temp. Range ° C	-150 to 240	-40 to 240	-20 to 80

Table 2.1 Specifications of the Kistler 701, 7261, and 810 pressure transducers.

The main problem with the Kistler 701 transducer was the difficulty in obtaining an accurate reading of the pressure in the first 10-15 ms during which the pressure rise was small. This is possibly attributable to the electrical interference generated by the fans and their a.c. motors. Therefore, for explosions at low initial pressures of up to 0.1 MPa, a Kistler 7261 was used because of its greater sensitivity.

All pressure against time records were monitored via PC-ADC system. The raw data were captured as voltage signals which were converted to binary format by the PC-ADC and then converted into an ASCII output file using the computer program FAMOS provided by Keithley Instrumentations Ltd. This voltage data was then processed to yield the variation of pressure with time, initially by a Fortran program written by Woolley (2001) and subsequently by an approved one, written in C++ by Wu (2003).

2.3.3 Temperature Control and Measurement

The temperature of the premixture was measured by a sheathed K type Chromel-Alumel thermocouple. For reactant temperatures up to 400 °C, two 2 kW electric bar heaters, attached to the inside of the access cover of the vessel, were used to warm up and to fine-tune the temperature of the vessel to the desired level. Temperatures above this range were attained by a larger 6kW electric bank of heaters, located on the access cover. The heaters were interlocked such that they would operate only while all four fans are running. This ensured good heat distribution inside the vessel, protected the heaters from burning out and minimised possible pre-combustion reactions associated with hot spots.

2.4 Preparation of Mixtures

After warming the vessel to the desired temperature (358K $\pm$ 5K for all mixtures ignited at an initial pressure of 0.5, 0.75 and 0.1 MPa, and 298K $\pm$5 K for methane – air mixture

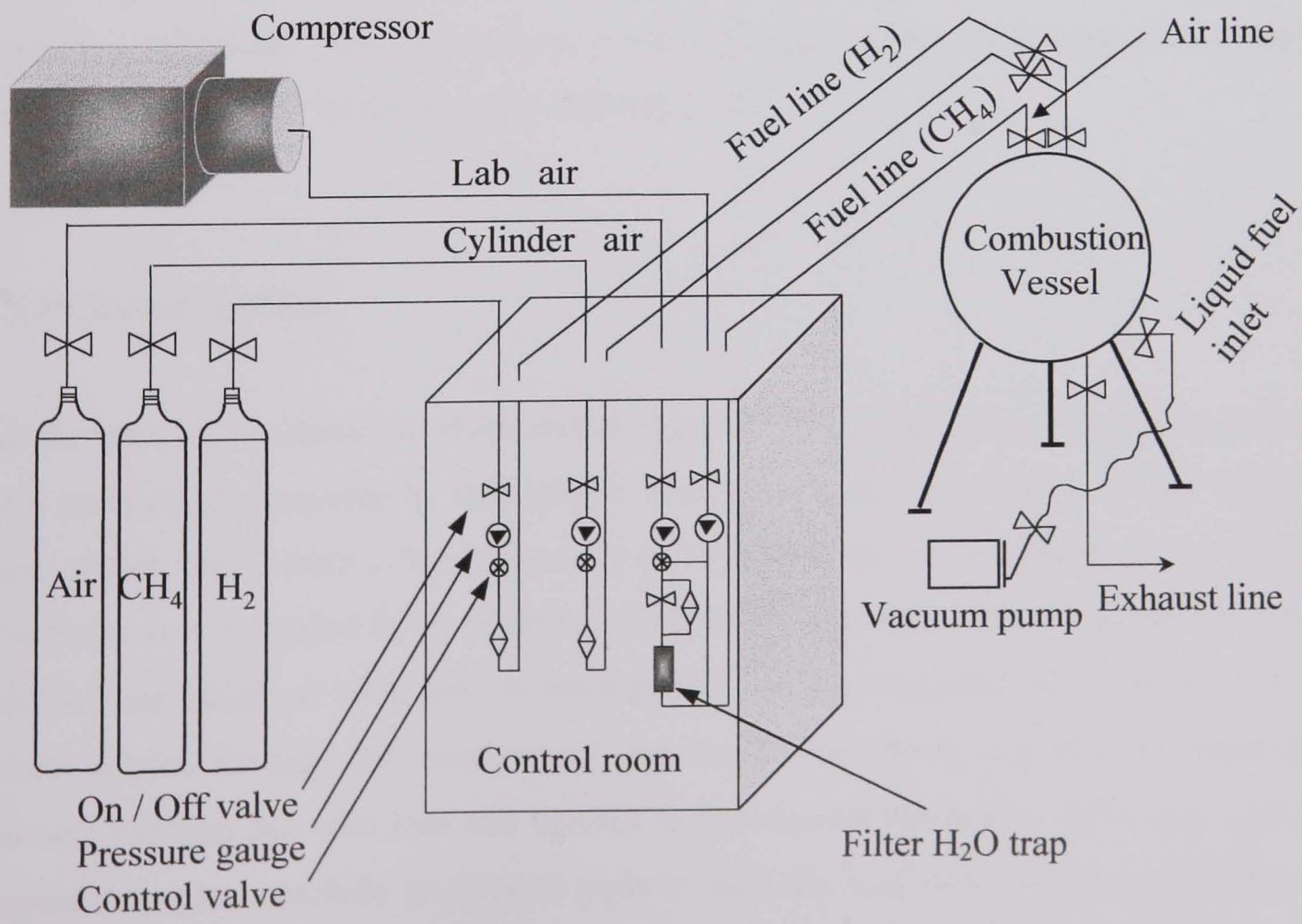

Fig. 2.4. Fuel system

at an initial pressure of 0.1 MPa), prior to filling the vessel with the mixtures, the vessel was evacuated to a pressure of less than 0.1 MPa and flushed twice with lab air from previous explosions to remove any residual products from previous explosions (Haq, 1998). After further evacuation, the mixture components were added, fuel first, to its respective partial pressure and then the vessel was filled to the required initial pressure with dry cylinder air. Shown in Fig. 2.4 is a schematic of the complete arrangement for the fuel system used in this study. For laminar flames, the fans remained running during the filling process for mixing purposes and then were turned off for one minute before ignition to ensure a quiescent premixture. For turbulent flames the fans remained running during mixture preparation, ignition and the subsequent combustion event. For this, the speed was maintained at within $\pm$ 20 rpm of that required.

2.5 Optical Arrangement for Schlieren Photography

Two different arrangements were used. For central ignition studies, which were undertaken early in the project, the light source was a laser, and the camera was a high-speed cine camera, as discussed in Section 2.5.1. However, by the time at which twin ignition experiments were undertaken, a more effective schlieren photography system had become available as discussed in Section 2.5.2.

2.5.1 Central Ignition

All the main components are illustrated in Fig. 2.1. The arrangement is the same as that used and fully documented by Haq (1998). The light source comprised a 10 mW He-Ne laser model 106-1, with a beam diameter of 0.65 mm and a wavelength of 632.8 nm. The beam was expanded by an Olympus A 40 microscope onto a 150 mm diameter lens with a focal length of 1000 mm, to produce the 150 mm diameter parallel laser beam, which passed through the windows of the bomb. The beam was then received by another 150 mm diameter lens and focused to the original diameter of 0.65 mm. It then passed through a carefully positioned pinhole onto the lens of a Hitachi 16 HM high-speed cine camera, which was operated at 6000 frames/s. Flame growth sequences were recorded on Ilford FP4 16 mm high-speed monochrome film. Typical sequences of

flame images are shown in Fig. 2.5. The high-speed camera was equipped with a timing mechanism to produce a timing mark on the film at intervals of one ms, and by measuring the distance between each timing mark, the camera framing rate was derived Haq (1998).

2.5.2 Twin Ignition

The arrangement for this technique is shown in Fig. 2.1. A high speed, model 545-4D Phantom digital camera with 256 megabytes integral image memory was used, at a framing rate of 3,700 frames/s and a resolution of 256 × 256 pixels. This camera was optically more sensitive than the Hitachi 16 HM camera, described above and produced better quality images. Although the spatial resolution was lower than for the16 mm film above (2000x2000), it was quite adequate for the present work. Further, the digital camera had the very significant advantage of producing digital images, which could be observed immediately after an experiment. This is in marked contrast with the wet film explained in Section 2.6.1. The light beam was generated by a 20W tungsten element lamp source instead of the He-Ne laser. The flame growth sequences were recorded and stored using the software that was supplied the camera.

2.6 Methods of Processing

The different techniques for data processing employed in this study, are described in Section 2.6.1 and 2.6.2. The analysis of data obtained from the first technique is presented in Chapter 3, and that from the twin kernel technique in Chapter 6 and 7.

2.6.1 Central Ignition

The exposed films were developed by the author in a dark room and placed in a bray film chemical processor to produce the final flame images. All processed films were viewed on a Vanguard back projector, which was equipped with a translucent screen with a projection screen size of 30x50 cm (Haq, 1998). For the present work, it was found not necessary to measure every frame because there was little variation in the

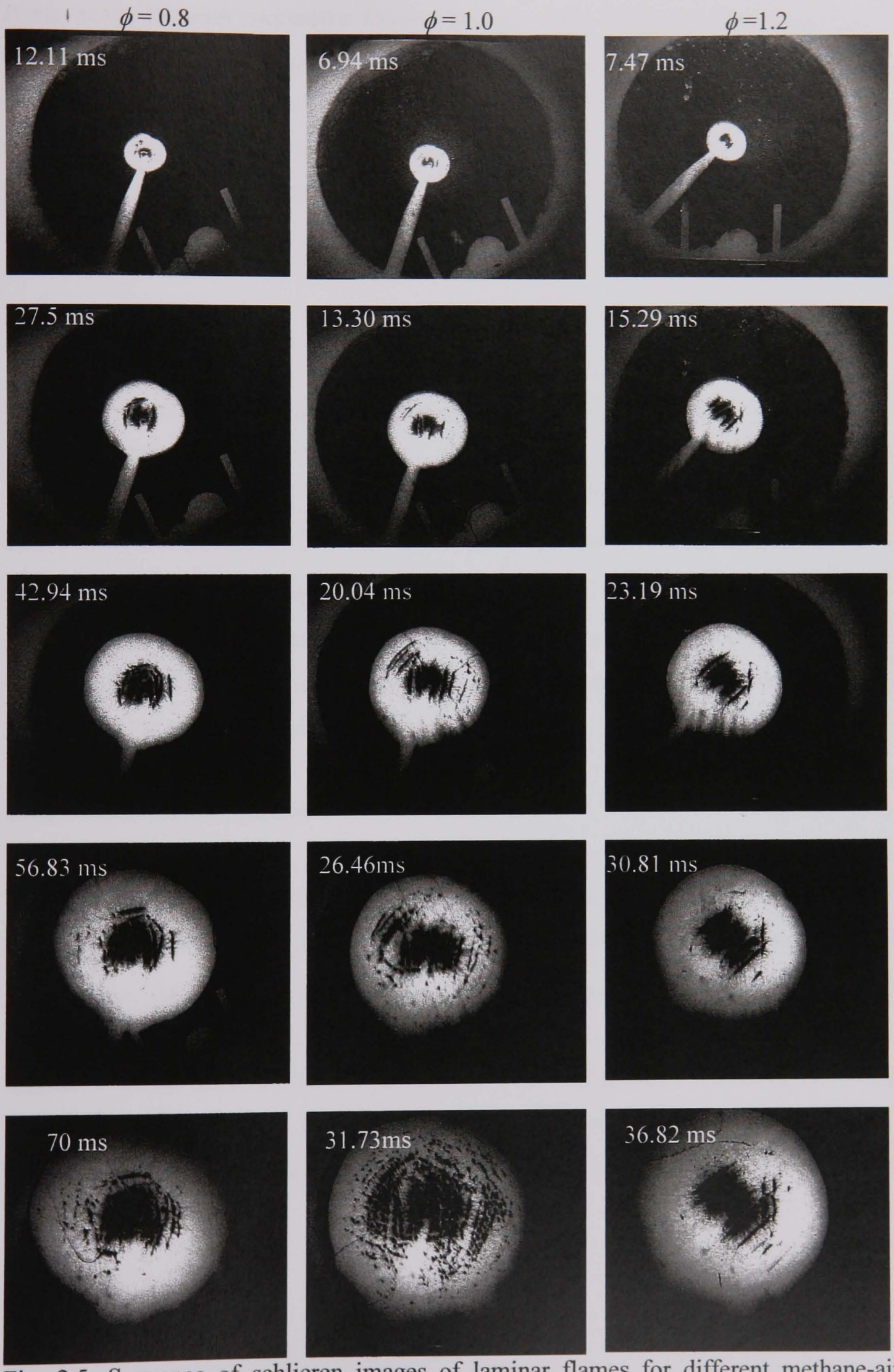

Fig. 2.5. Sequence of schlieren images of laminar flames for different methane-air mixtures at the indicated times after spark ignition. The initial pressure was 0.5 MPa and the temperature was 358 K.

flame image between successive frames. Instead, flame diameters were measured in increments of 6 frames, reducing processing time and producing an effective recording rate of 1000 fps. The flames were not perfectly circular. Therefore, the flame diameter from each image was obtained as the average from three measurements, taken vertically, horizontally and diagonally.

2.6.2 Twin Ignition

Since there were two inwardly propagating flames, initiated from two hidden spark plugs mounted at the walls of the vessel, great care was required to measure accurately the radii. Typical sequences of digital flame images for iso-octane-air and methane-air mixtures are shown in Fig. 2.6 and Fig. 2.7. Prior to quantifying the propagation rate, these images were pre-processed using the software ´Adobe Photoshop`, supplied by Adobe Systems Incorporated, to yield binary images as illustrated in Fig 2.8. Two methods of measurement were implemented: one was a manual process using a pair of compasses; the other was done electronically.

2.6.2.1 Hand-Based Method

This method utilized a hard copy of the binary image of the flame and a pair of compasses to strike off the flame radius as shown in Fig. 2.9. This was repeated for each flame image, (at each time increment). Although this method was time consuming, it allowed for full operator control and interpretation. For the processing of laminar flames, it served as a validation exercise to give confidence in the computer-based procedure discussed below. However, due to uncertainties in the computer analysis of turbulent flames (Section 2.6.2.2) this hand-based method was used to analyse all turbulent flames.

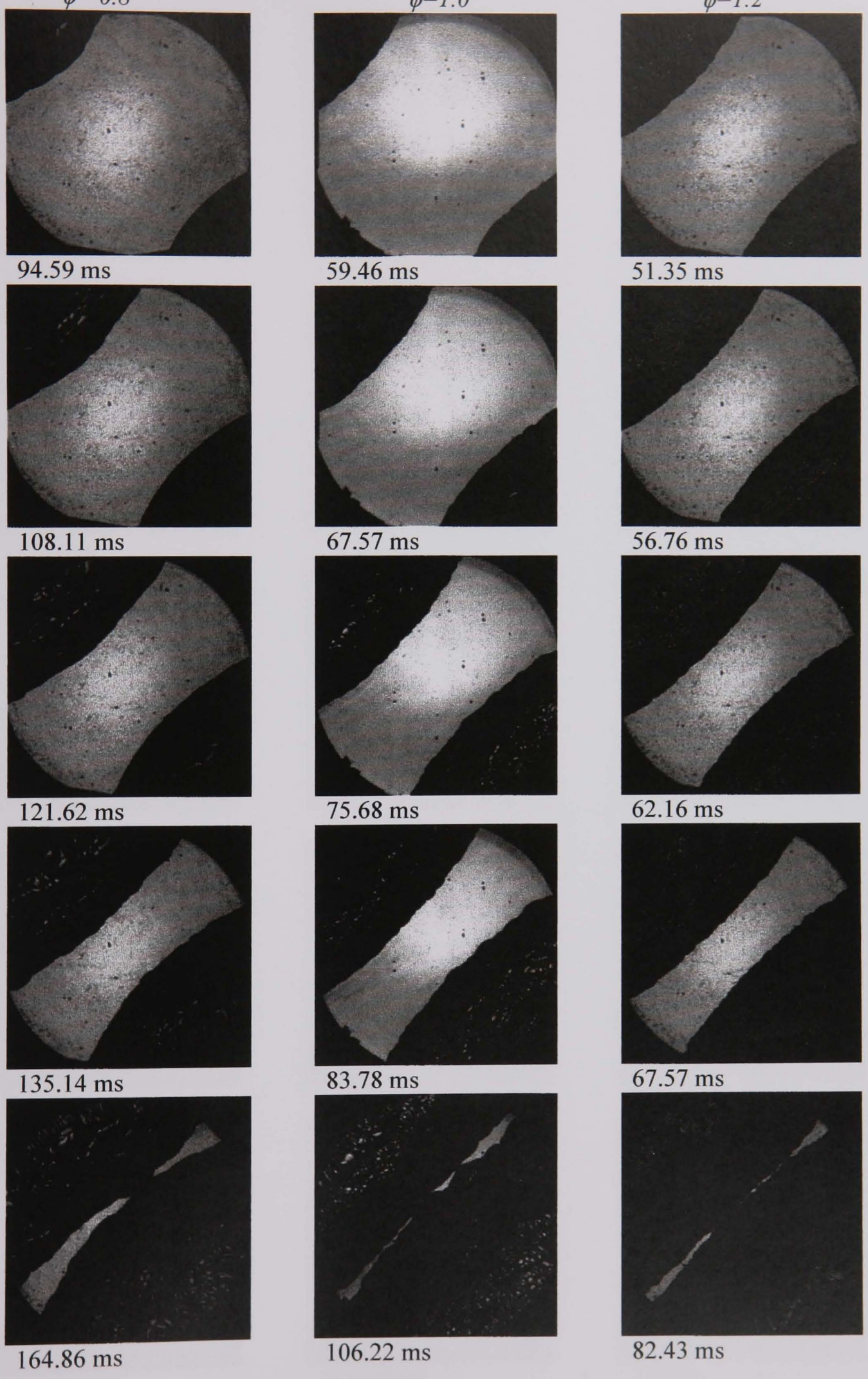

Fig. 2.6. Sequence of schlieren images of laminar imploding flames for different iso-octane-air mixtures. The initial pressure was 0.5 MPa and the temperature was 358 K.

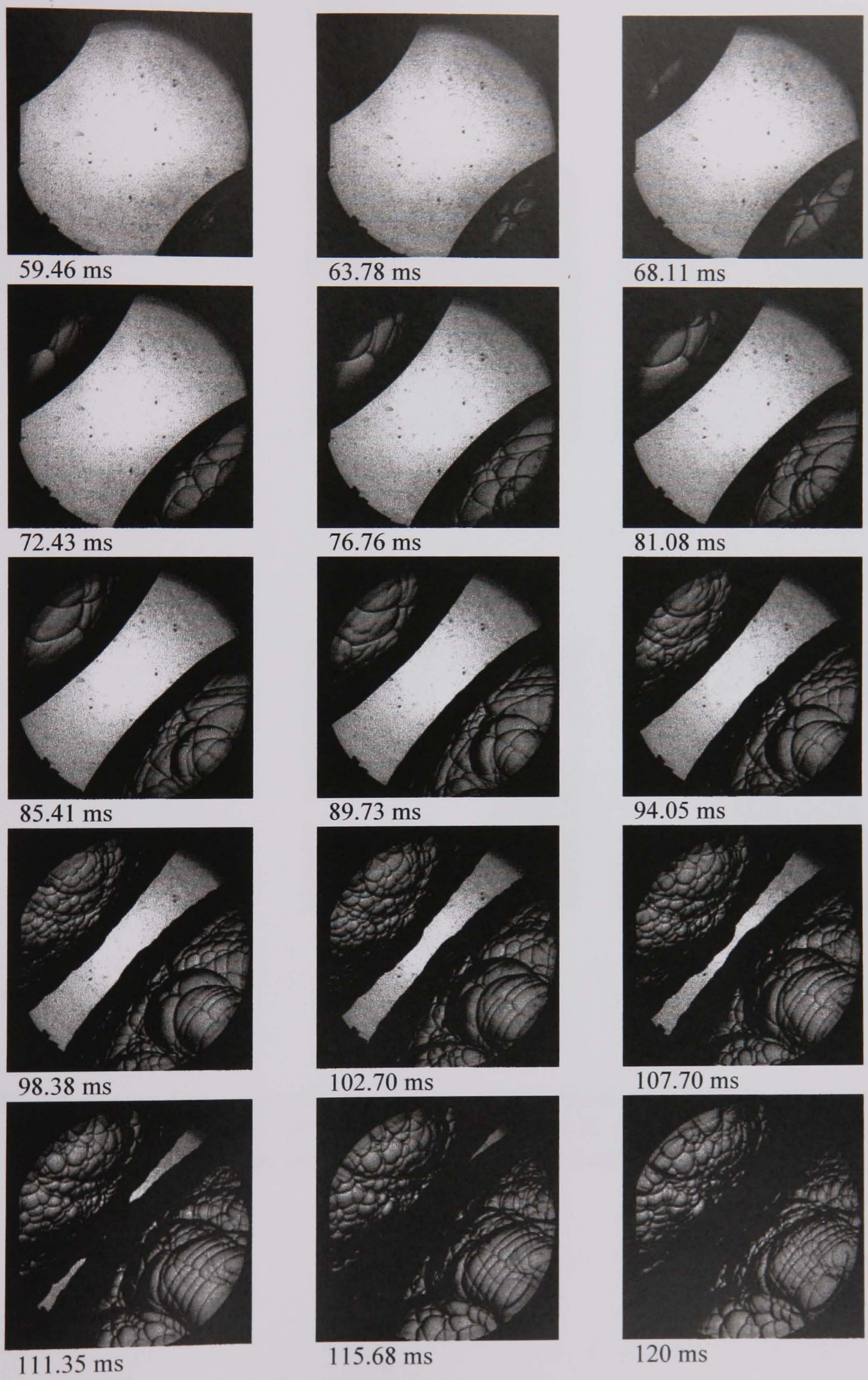

Fig. 2.7. Sequence of schlieren images laminar implodeing flames for methane-air mixture, $\phi = 1.0$. The initial pressure was 0.1 MPa and the temperature was 298 K.

Stage one

Captured flame image, either on film or digital

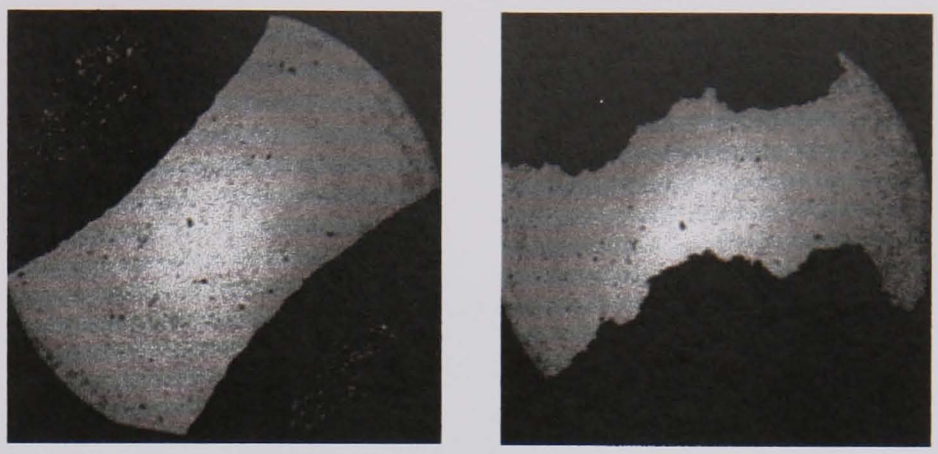

Stage two

Processed binary image

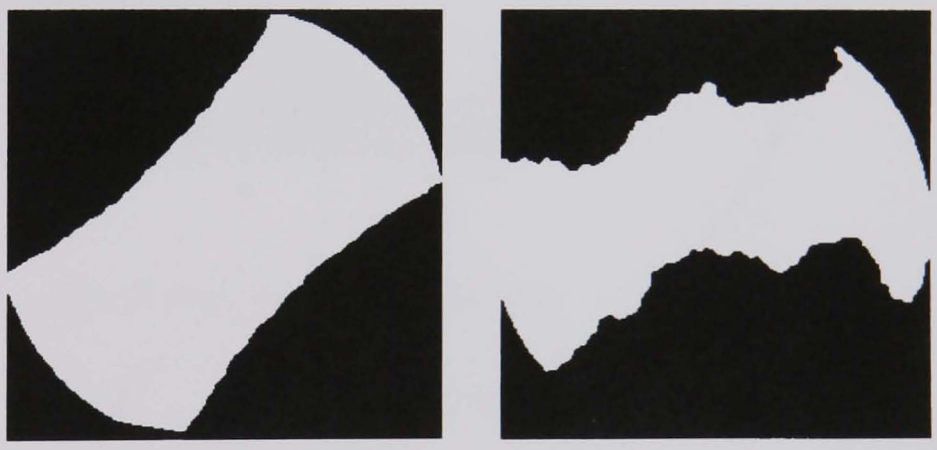

a b

Fig. 2.8. Stages of image processing. (a) Laminar stoichiometric iso-octane - air mixture at an initial pressure of 0.5 MPa and temperature of 358 K. (b) Turbulent stoichiometric iso-octane-air mixture at an initial pressure of 1 MPa and temperature of 358K, (u' = 2.5 ms).

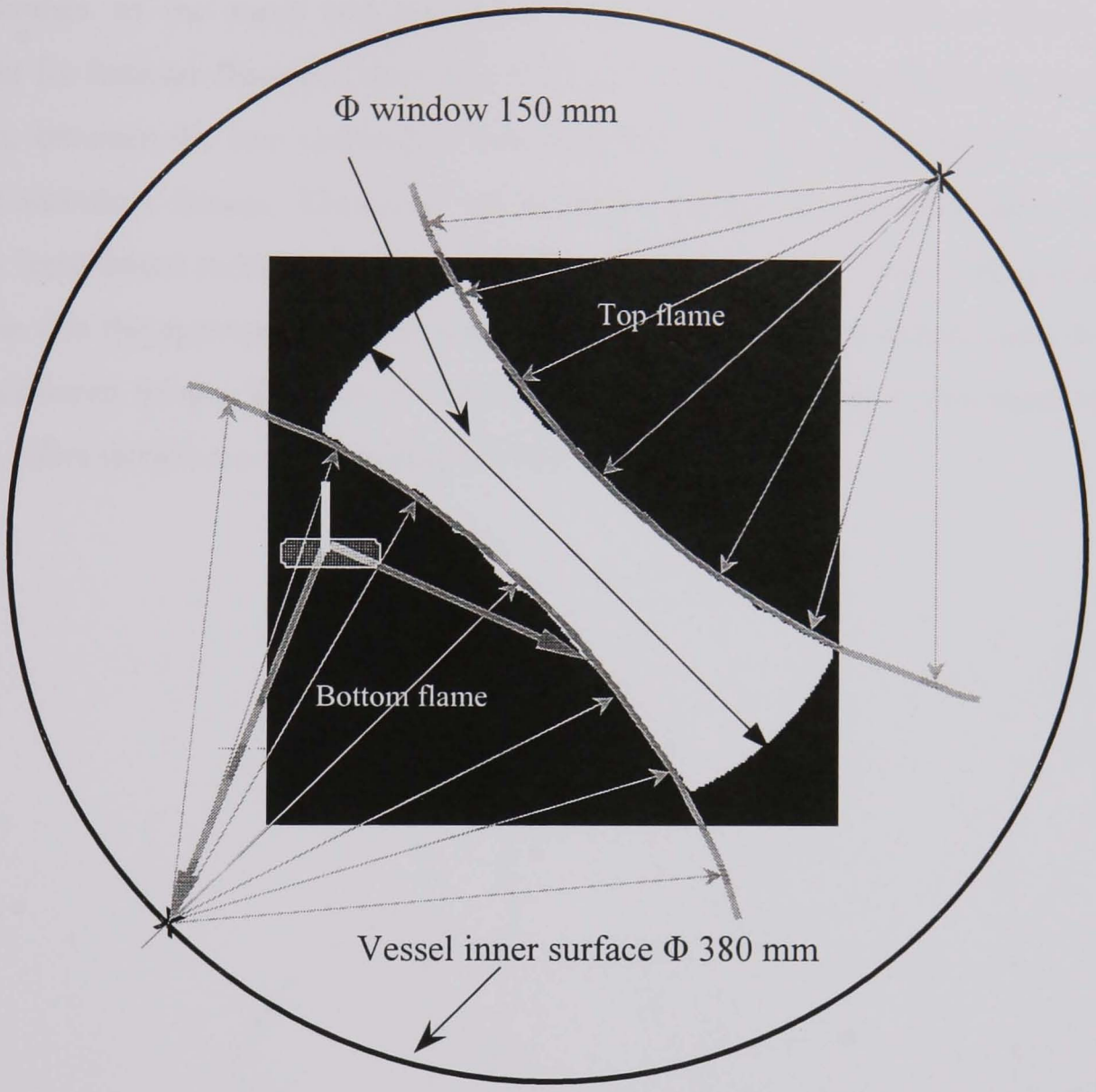

Fig. 2.9. Hand-measurement method.

2.6.2.2 Computer Based method

The processed binary images were used in a Fortran program, ´Edge`, developed by Kitagawa and Woolley (2003), to yield the X and Y coordinates for the flame front (and a portion of the edge of the vessel window), as shown in Fig. 2.10. From these, the program calculated the mean flame radius for each flame in each image. The outputs were two files containing radius against time information for each flame. Sample

calculations, program output and a brief description of the evaluation method are shown in Appendix A.

The outcomes of the hand and computer methods were compared to check their agreement for laminar flames as shown in Fig. 2.11. Results indicated that the averaged difference between the two methods is less than 1%. However, agreement was not so good for turbulent flames. Therefore, all turbulent flames in this work were treated using the hand-based method since considerable care was required due to their complex shape. For this the appropriate flame radius was taken to be that of sphere such that, on the 2D schlieren image, the area of unburned gas outside the sphere was equal to that within it. More details are given in Haq (1998).

.

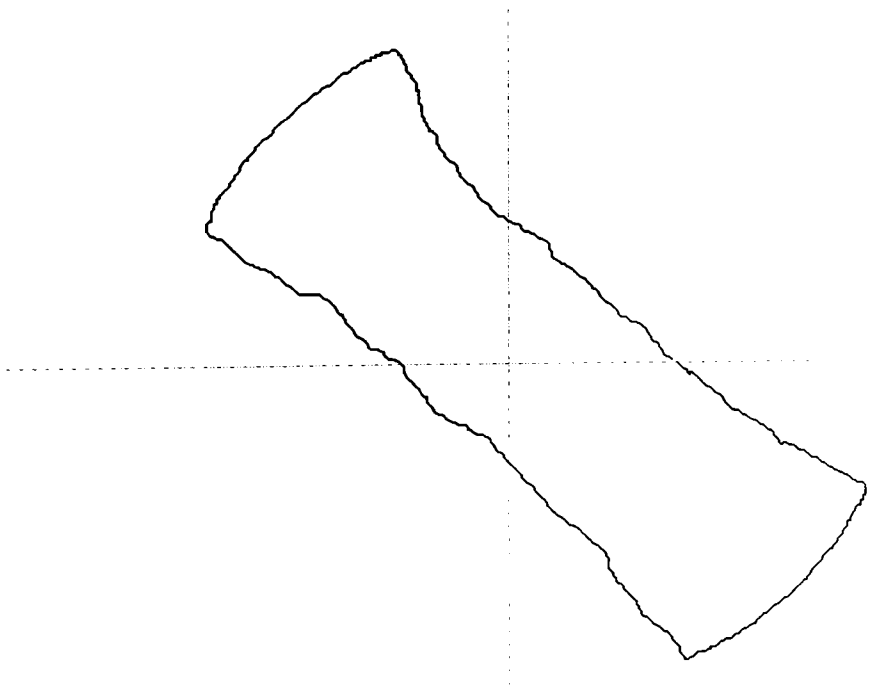

Fig. 2.10. Positions of flame fronts relative to X and Y-axis.

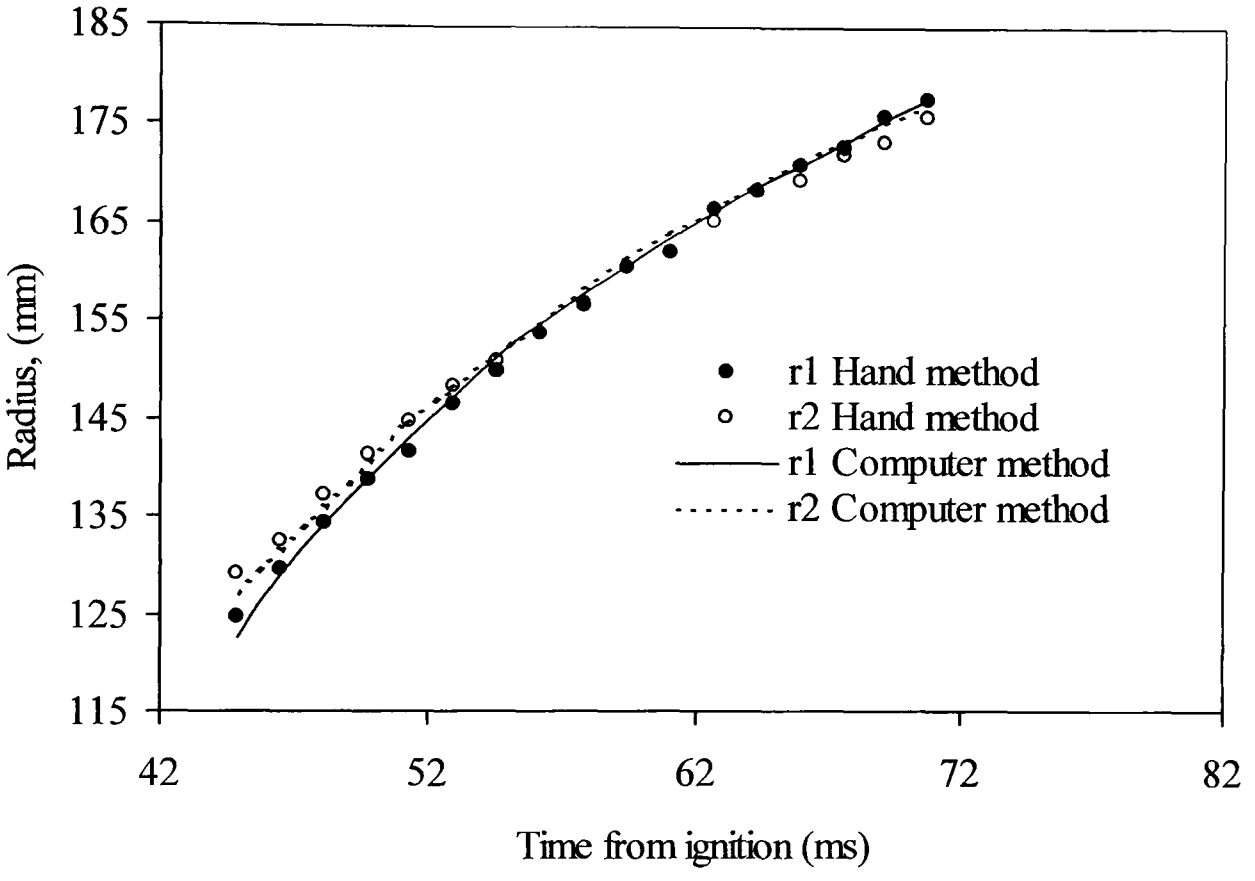

Fig. 2.11. Comparison between the hand and computer methods used to obtain the radii of twin laminar flames.

2.7 Thermodynamic Properties

For single kernel experiments, all measurements were made during the pre-pressure period. Hence, thermodynamic properties of the reactants were assumed to be constant. However, this was not so for twin kernel measurements. The analysis of twin flames (Chapter 6 and 7) required knowledge of the thermodynamic properties of the unburned gas during flame development. During this period, the pressure and temperature were changing and hence, so were other unburned gas properties such as, gas density, ρ_u, gas temperature, T_u, specific heat ratio, γ_u, and kinematic viscosity, ν_u. A computer program, GASEQ, developed by Morley (2001) was used to obtain these values.

2.8 Practical Considerations – Geometrical Complexity

The combustion vessel is equipped with internal accessories such as fans, windows, ignition sparks, and other components, as shown in Fig. 2.12. This results in difficulties in estimating the net true burned and unburned gas volumes, which are required for burning rate calculations, due to the shape complexity. There was an increase in the total vessel volume due to the window recesses and a decrease in the volume due to fans. This issue is discussed in detail in Chapter 4 in which an expression for evaluating

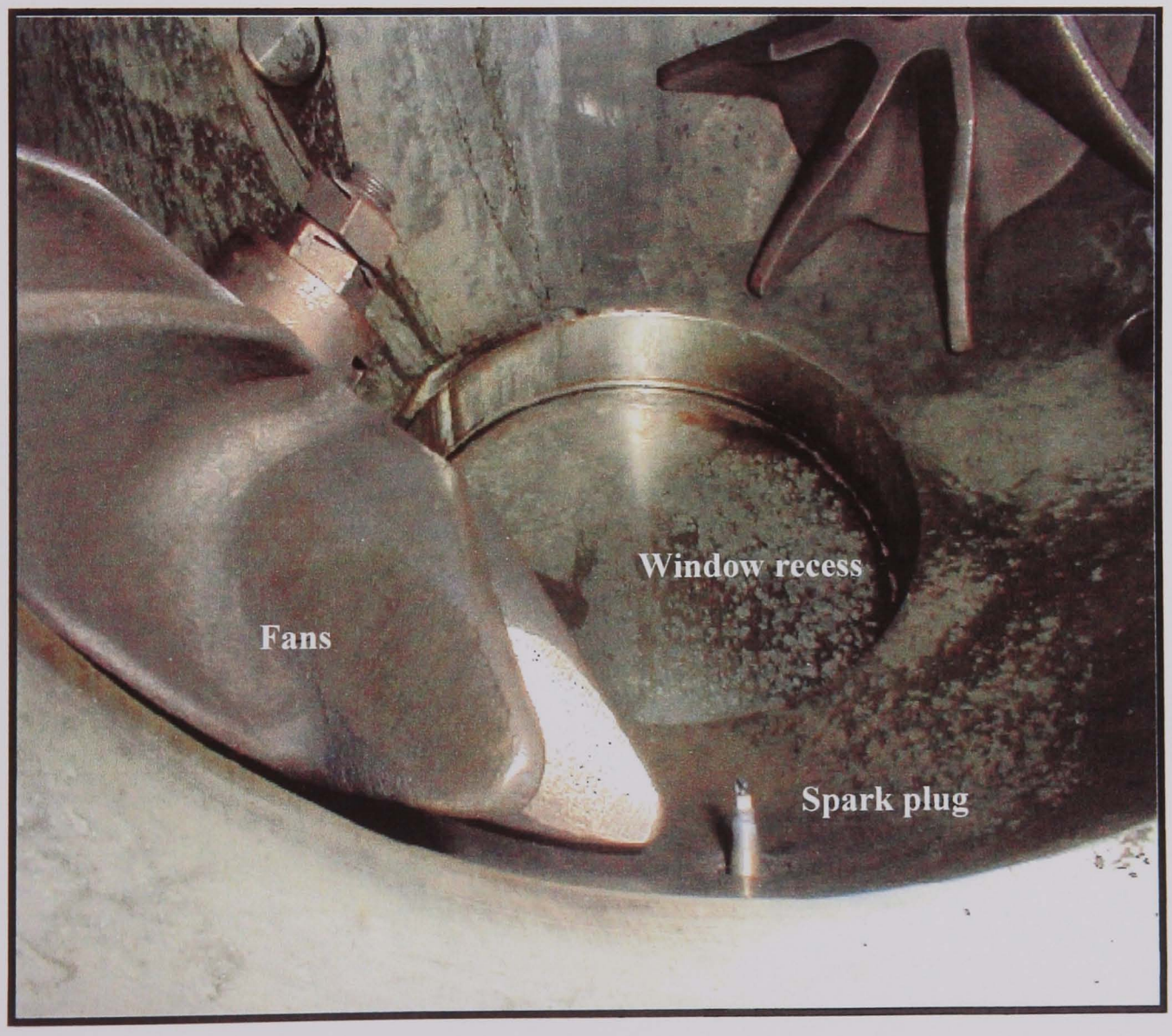

Fig. 2.12. View of inside the combustion vessel showing spark plug, window recess and fans.

the volume correction is developed. It is of particular interest to mention here that the true volume of the vessel was measured, by filling it with water, to be 0.0310 m^3 .

Chapter 3

Measurement of Burning Velocities in Spherical Explosions with Central Ignition

3.1 Introduction

For explosion flames there are two main categories of such measurements. The first one involves an optical technique, to trace the propagation of the flames during the early stages. When such observations are not optically possible in the later stages of combustion, recourse, is made to pressure-time measurements. The theoretical bases of these approaches follow. The assumptions are:

1. There are no heat losses to the walls of the vessel.
2. All flames propagate spherically toward the walls of the spherical vessel.
3. Either unburned or burned gases are compressed isentropically.
4. The pressure is equalized throughout the vessel.
5. The flame is infinitesimally thin.

First, expressions are derived for the burning velocity, then these are applied to experimental measurements.

3.2 Optically Based Measurements

Let the radius of the spherical vessel be R, and the radius of the assumed flame be r_b. At any instant the masses of unburned, m_u, and burned gas, m_b, are given by:

$$m_u = \frac{4\pi}{3}\left(R^3 - r_b^{\,3}\right)\rho_u \tag{3.1}$$

$$m_b = \frac{4\pi}{3} r_b^{\,3} \rho_b \tag{3.2}$$

Here ρ_u and ρ_b are the densities of unburned and burned gas.

The mass conservation equations and the definition of burning velocity, S_u, give

$$\frac{dm_b}{dt} = -\frac{dm_u}{dt} = 4\pi r_b^{\,2} S_u \rho_u \tag{3.3}$$

In addition, if isentropic compression is assumed:

$$\frac{p}{\rho^{\gamma}} = const. \tag{3.4}$$

$$\frac{\partial \rho}{\partial t} = \frac{\rho}{p\gamma}\frac{\partial p}{\partial t} \tag{3.5}$$

From Eqs. (3.2) and (3.3) :

$$\frac{dm_b}{dt} = \frac{4\pi}{3}\left(\frac{\partial \rho_b}{\partial t} r^3{}_b + \rho_b 3 r_b^{\,2}\frac{\partial r_b}{\partial t}\right) = 4\pi r_b^{\,2} S_u \rho_u \tag{3.6}$$

If it is assumed that the burned gases are compressed isentropically, substituting Eq. (3.5) into Eq. (3.6) gives

$$\frac{r_b}{3}\frac{\rho_b}{p\gamma_b}\frac{\partial p}{\partial t} + \rho_b \frac{\partial r_b}{\partial t} = S_u \rho_u \tag{3.7}$$

$$\therefore S_u = \frac{\rho_b}{\rho_u}\left[\frac{\partial r_b}{\partial t} + \frac{r_b}{3p\gamma_b}\frac{\partial p}{\partial t}\right] \tag{3.8}$$

This expression is often used for the laminar burning velocity when there is no change in pressure and the second term on the right can be neglected. The density ratio, ρ_b/ρ_u, is evaluated from equilibrium calculations.

In the early stages of an explosion the burned gas density, ρ_b, does not change greatly with flame radius, but in the later stages of an explosion it does and the first burned gas has a lower value of ρ_b . Hence the assumption of constant, ρ_b at all radii is invalid. This difficulty is overcome if the burning velocity is defined in terms of the unburned gas, when Eq. (3.1) in preferred to Eq. (3.2).

Hence, from Eqs. (3.1) and (3.3):

$$\frac{d\frac{4}{3}\pi\left(R^3 - r_b^{\,3}\right)\rho_u}{dt} = -4\pi r_b^{\,2} S_u \rho_u \tag{3.9}$$

$$\left(R^3 - r^3\right)\frac{\partial \rho_u}{\partial t} - \rho_u 3 r_b^{\,2}\frac{dr_b}{dt} = -3 r_b^{\,2}\rho_u S_u \tag{3.10}$$

By substituting Eq. (3.5), more accurately applied to unburned gas, into Eq. (3.10)

$$\left(R^3 - r^3\right)\frac{\rho_u}{p\gamma_u}\frac{\partial p}{\partial t} - \rho_u 3 r_b^{\,2}\frac{\partial r_b}{\partial t} = -3 r_b^{\,2}\rho_u S_u \tag{3.11}$$

Therefore:

$$S_u = \frac{dr_b}{dt} - \left(\frac{R^3 - r_b^{\,3}}{3p\gamma_u r_b^{\,2}}\right)\frac{dp}{dt} \tag{3.12}$$

The second term on the right represents the gas velocity just ahead of the flame. The disadvantage of this expression is that this term is fairly close in value to the first term on the right and, consequently, both must be evaluated accurately.

3.3 Pressure Based Measurements

When the flame front cannot be observed, the burning rate can only be measured from the pressure record. Following Bradley and Mitcheson (1976), for measurements that depend solely on pressure, it usually is assumed that the fractional pressure rise is proportional to the fractional mass burned (Lewis and Von Elbe, 1987):

$$m_b = (m_u + m_b)\left(\frac{p - p_0}{p_e - p_o}\right) \tag{3.13}$$

Here, p_e is the final pressure after complete combustion and p_o is the initial pressure. Bradley and Mitcheson confirmed this assumption from more detailed computations. The treatment here follows that given by these workers. Hence, with ρ_o the initial density of the gas in the sphere, Eq. (3.13) gives

$$\frac{4\pi R^3}{3}\rho_o - \frac{4\pi}{3}\left(R^3 - r_b^{\,3}\right)\rho_u = \frac{4\pi}{3}R^3\rho_0\left(\frac{p - p_0}{p_e - p_0}\right) \tag{3.14}$$

From Eq. (3.14)

$$R^3\rho_o\left[1 - \left(\frac{p - p_o}{p_e - p_o}\right)\right] = \left(R^3 - r_b^{\,3}\right)\rho_u \tag{3.15}$$

with $\rho_o/\rho_u = (p_o/p)^{1/\gamma_u}$, Eq. (3.15) becomes

$$r^3{}_b = R^3 - R^3\left(\frac{p_0}{p}\right)^{1/\gamma_u}\left(\frac{p_e - p}{p_e - p_o}\right) \tag{3.16}$$

$$r_b^{\,2} = R^2\left\{1 - \left(\frac{p_o}{p}\right)^{1/\gamma_u}\left[\frac{p_e - p}{p_e - p_o}\right]\right\}^{\frac{2}{3}} \tag{3.17}$$

This expression is useful in giving the flame radius in terms of the pressure rise.

From Eq. (3.13)

$$\frac{dm_b}{dt} = \frac{d(m_u + m_b)}{dt}\left[\frac{p - p_o}{p_e - p_o}\right] + \left(\frac{m_u + m_b}{p_e - p_o}\right)\frac{dp}{dt} \tag{3.18}$$

The first term on the right is zero, because the total mass does not change. Hence

$$\frac{dm_b}{dt} = -\frac{dm_u}{dt} = \frac{4}{3}\frac{\pi R^3 \rho_o}{(p_e - p_o)}\frac{dp}{dt} \tag{3.19}$$

From the definition of burning velocity

$$\frac{dm_u}{dt} = -4\pi r_b^{\,2} S_u \rho_u \tag{3.20}$$

From Eqs. (3.17), (3.19), (3.20)

$$-\frac{dm_u}{dt} = 4\pi S_u \rho_u R^2 \left\{1 - \left(\frac{p_o}{p}\right)^{\frac{1}{\gamma_u}}\left[\frac{p_e - p}{p_e - p_o}\right]\right\}^{\frac{2}{3}} = \frac{4}{3}\frac{\pi R^3 \rho_o}{(p_e - p_o)}\frac{dp}{dt} \tag{3.21}$$

$$S_u = \frac{R\left(\frac{p_0}{p}\right)^{\frac{1}{\gamma_u}}\frac{dp}{dt}}{3(p_e - p_o)\left\{1 - \left(\frac{p_o}{p}\right)^{\frac{1}{\gamma_u}}\left[\frac{p_e - p}{p_e - p_o}\right]\right\}^{\frac{2}{3}}} \tag{3.22}$$

This expression is used to obtain the burning velocity when it not possible to measure the flame radius directly. With $\gamma_u = \gamma$, this is the expression derived by Liu *et al.* (2001).

3.4 The Effect of Flame Thickness

It has been assumed that all the completely burned and hot gas is contained within a sphere of radius r_b. In practice the front, upon which the definition of burning velocity is based, will be a flame of 'thickness' δ_ℓ ahead of this.

Hence

$$\frac{dm_u}{dt} = -4\pi r(r_b + \delta_l)^2 S_u \rho_u \tag{3.23}$$

Now from Eq. (3.17):

$$(r_b + \delta_\ell) = R\left\{1 - \left(\frac{p_o}{p}\right)^{\frac{1}{\gamma_u}}\left[\frac{p_e - p}{p_e - p_o}\right]\right\}^{\frac{1}{3}} + \delta_\ell \tag{3.24}$$

Hence from Eqs. (3.19), (3.23) and (3.24)

$$4\pi S_u \rho_u \left[R\left\{1-\left(\frac{p_0}{p}\right)^{\frac{1}{\gamma_u}}\left[\frac{p_e-p}{p_e-p_o}\right]\right\}^{\frac{1}{3}}+\delta_\ell \right]^2 = \frac{4}{3}\frac{\pi R^3 \rho_o}{(p_e-p_o)}\frac{dp}{dt} \tag{3.25}$$

and

$$S_u = \frac{R\left(\frac{p_0}{p}\right)^{\frac{1}{\gamma_u}}\frac{dp}{dt}}{3(p_e-p_o)\left[\left\{1-\left(\frac{p_0}{p}\right)^{\frac{1}{\gamma_u}}\left[\frac{p_e-p}{p_e-p_o}\right]\right\}^{\frac{1}{3}}+\frac{\delta_\ell}{R}\right]^2} \tag{3.26}$$

Comparison with Eq. (3.22) shows the effect of flame thickness on the measured burning velocity.

3.5 Experimental Results for Central Ignition

Schlieren ciné films of the propagating laminar flames were obtained with the Hitachi 16HM high-speed camera. The pressure rise was simultaneously recorded by the pressure transducer mentioned in Chapter 2.

3.5.1 Measurements of Pressure and Flame Radius

All the results are for methane – air and iso-octane – air mixtures, initially at 0.5 MPa and 358 K and cover equivalence ratios, ϕ, of 0.8, 1.0, and 1.2. Shown in Figs. 3.1 (a) and (b) are the variations of pressure with time from ignition for all the mixtures. Figures 3.2 (a) and (b) show the variations of flame radii for the same mixtures under the same conditions. Radii were evaluated from two different approaches; one rested upon optical measurements obtained from schlieren photography and has been discussed earlier in Section 2.6. The other rested upon the recorded pressure-time history for each explosion and employed Eq. (3.17). Figure 3.2 shows reasonable agreement in the later stages between the radii derived by the two methods. In the earlier stages the pressure measurements were not sensitive enough relative to the background noise to obtain reliable values of the radii.

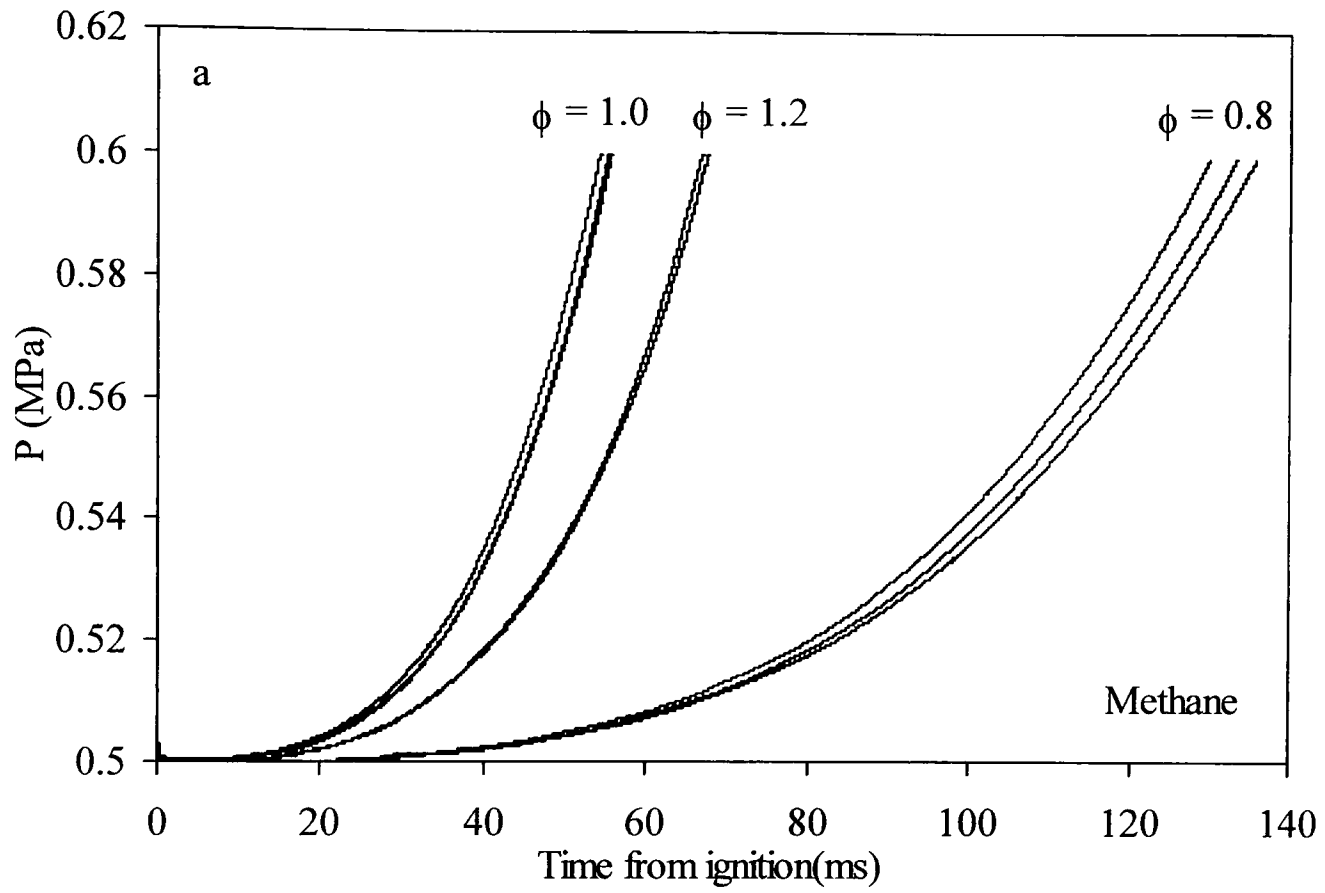

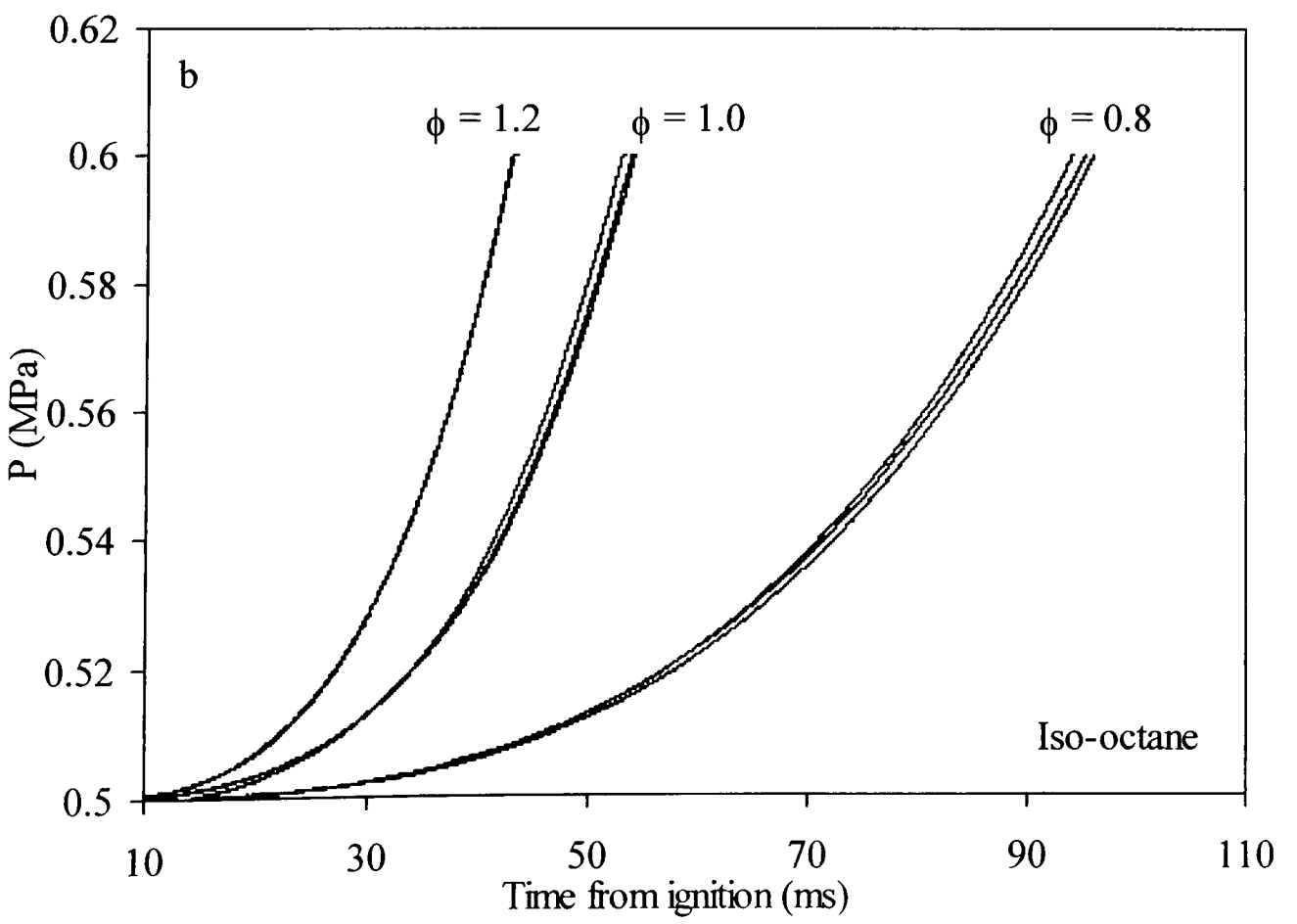

Fig. 3.1. Pressure records for (a) methane – air and, (b) iso-octane - air mixtures, p_o = 0.5 MPa and T_o = 358 K. Explosions at three equivalence ratios.

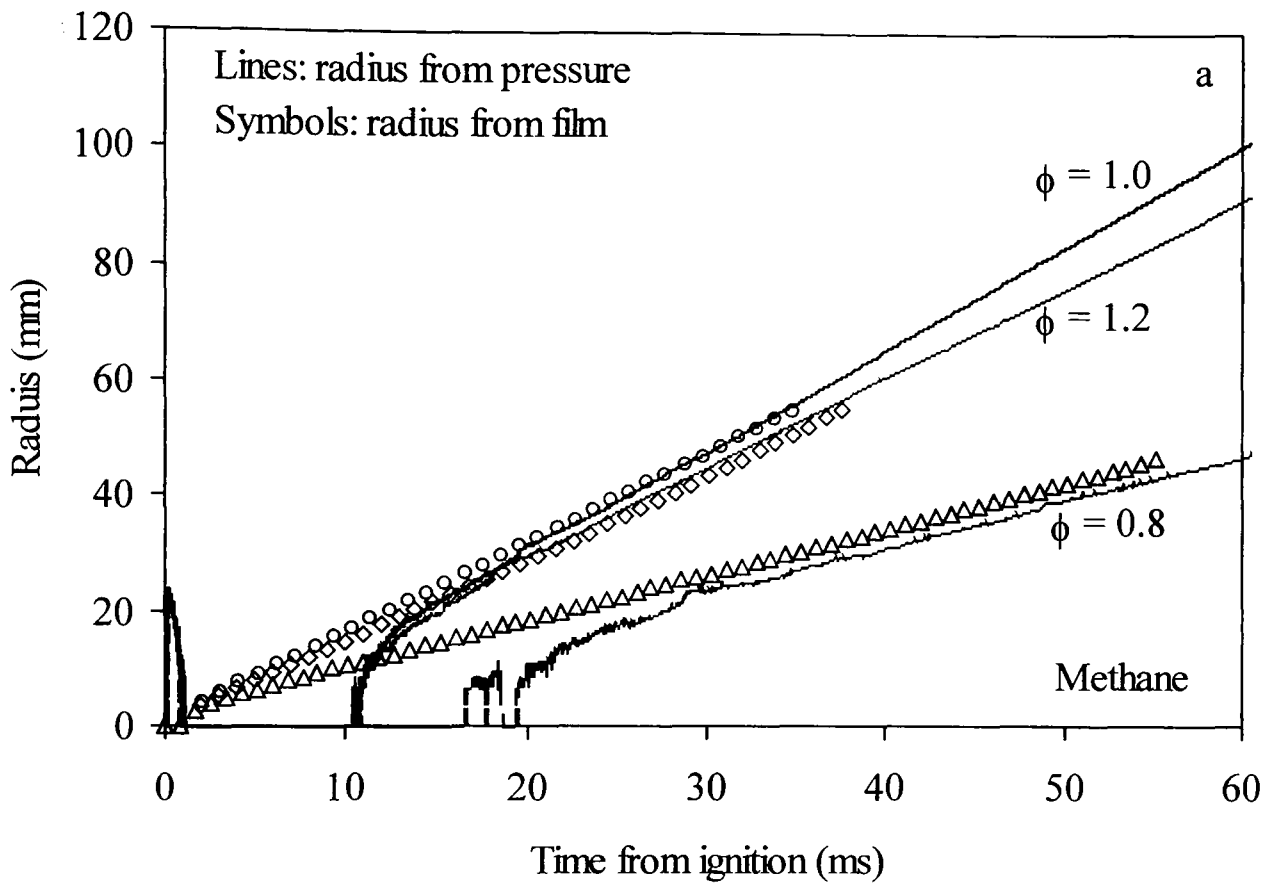

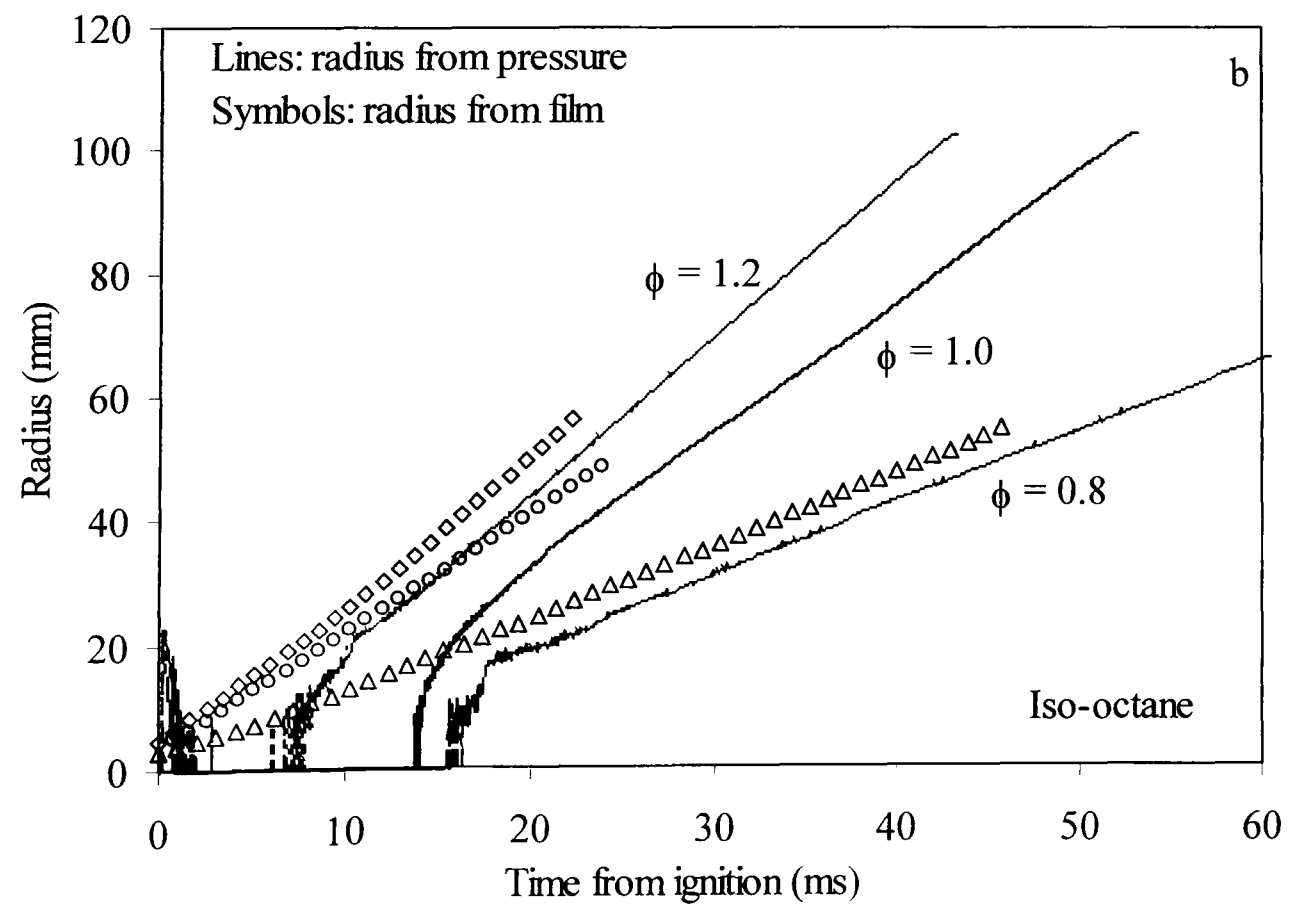

Fig. 3.2. Flame radii obtained directly and deduced from pressure for (a) methane-air and (b) iso-octane-air mixture. p_0 = 0. 5 MPa, T_0 = 358 K.

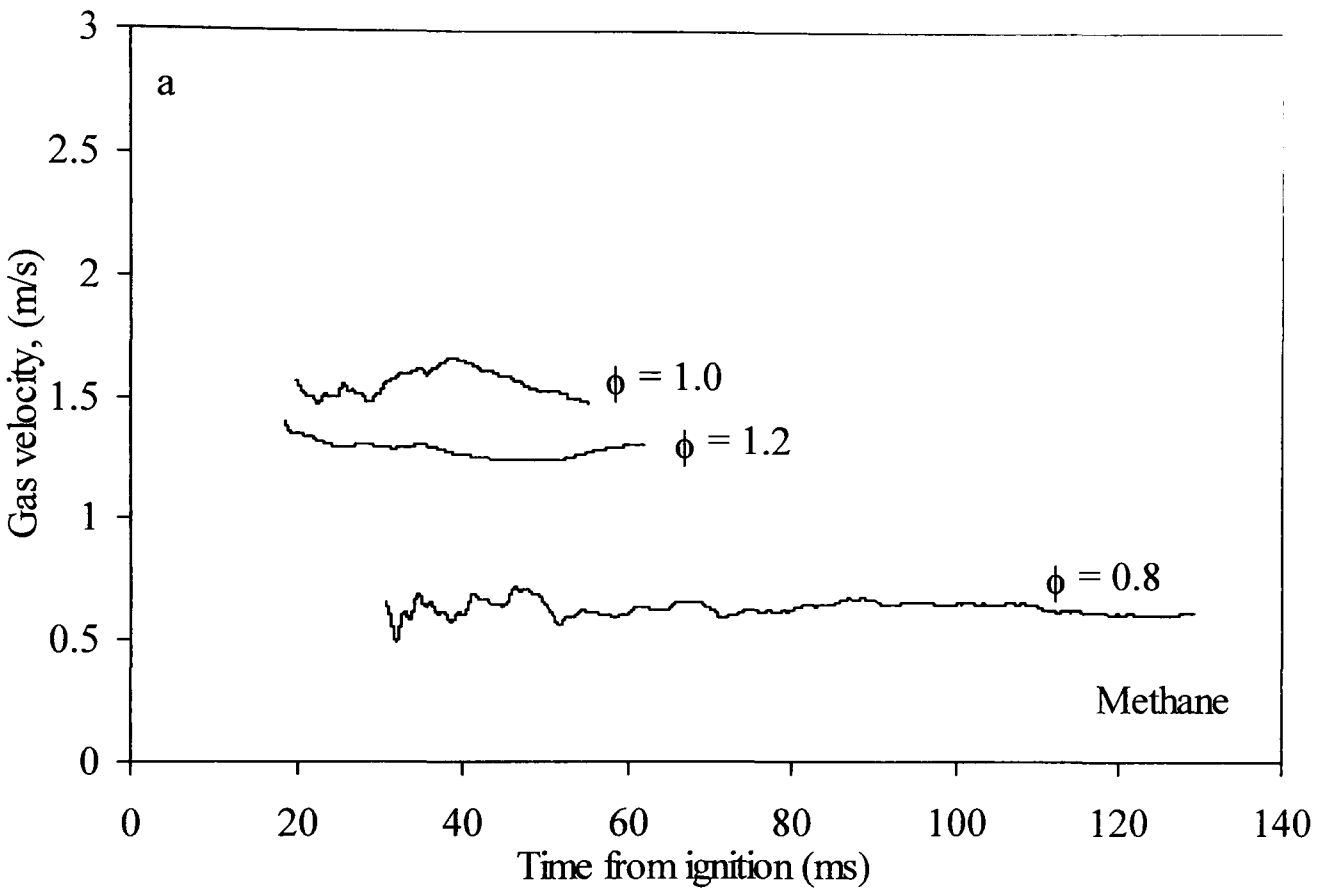

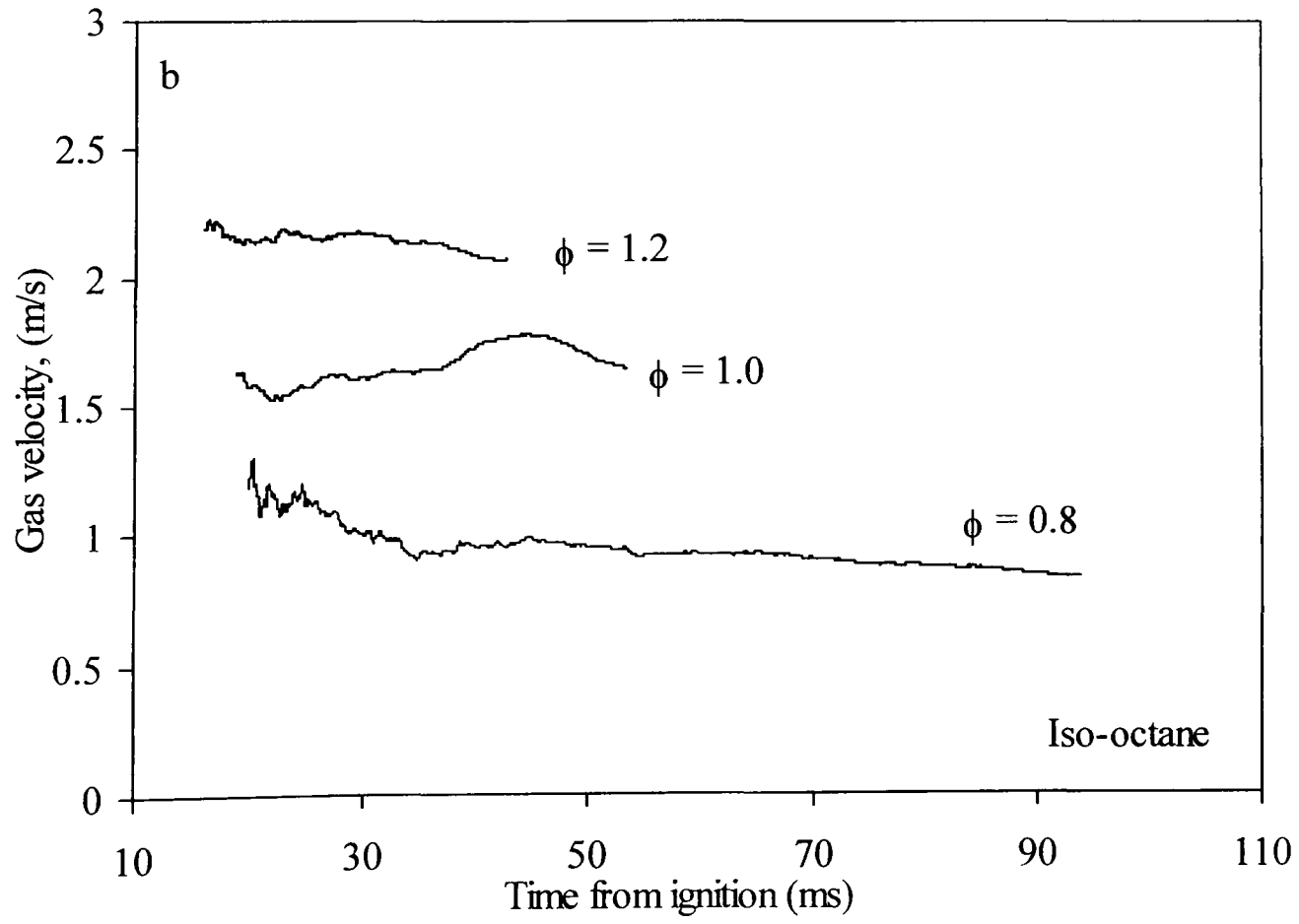

Fig. 3.3. Gas velocities just ahead of the flame for (a) methane – air and (b) iso-octane – air mixtures, at p_0 = 0. 5 MPa, T_0 = 358 K, for different equivalence ratios.

Gas velocities just ahead of the flame, u_g, were found from the second term on the right of Eq. 3.12. It represents the difference between flame speed and burning velocity. The results are shown in Fig 3.3 (a) and (b) for methane-air and for iso-octane –air mixtures, respectively. Not surprisingly, for the initial stages of an explosion, these do not change much as the flame propagates.

3.5.2 Influences of Flame Stretch

In the initial stages of burning, before the development of any flame instabilities, the flame stretch rate influences the burning velocities. The initially higher stretch rate can stabilise the flame. At any point on the flame surface, the stretch rate, α, is the Lagrangian time derivative of the logarithm of the area, A, of an infinitesimal element of the surface surrounding that point (Williams, 1985):

$$\alpha = \frac{d \ln A}{dt} = \frac{1}{A}\frac{dA}{dt} \tag{3.27}$$

Following Bradley *et al.* (1996), the flame stretch rate has curvature and strain rate components, given by:

$$\alpha_c = \frac{2u_n}{r_u} \qquad \alpha_s = \frac{2u_g}{r_u} \tag{3.28}$$

Here r_u is the cold front radius of the flame, where u_n is the stretched laminar burning velocity based on the propagation of the flame front and u_g is the gas velocity due to the flame expansion at r_u.

$$S_n = u_g + u_n \tag{3.29}$$

The total stretch rate is given by:

$$\alpha = \alpha_c + \alpha_s = 2S_n / r_u \tag{3.30}$$

The Markstein lengths, which express the effect of stretch rate on the burning velocity, are related by:

$$u_\ell - u_n = L_c\alpha_c + L_s\alpha_s \tag{3.31}$$

where L_c and L_s are the Markstein lengths associated with curvature and strain, respectively. The relationship between cold flame r_u radius and the observed schlieren flame front radius, r_{sch}, has been studied by Bradley *et al.* (1996). They related the two by

$$r_u = r_{sch} + 1.95\delta_\ell \left(\frac{\rho_u}{\rho_b}\right)^{0.5} \tag{3.32}$$

The flame speed is found from

$$S_n = \frac{dr_u}{dt} \tag{3.33}$$

and S_n is related to u_n by:

$$S_n = \frac{u_n \rho_u}{S\rho_b} \tag{3.34}$$

where S is a factor which depends on the flame radius and the density ratio and accounts for the flame thickness. It is given by Bradley *et al.* (1996):

$$S = 1 + 1.2\left[\frac{\delta_\ell}{r_u}\left(\frac{\rho_u}{\rho_b}\right)^{2.2}\right] - 0.15\left[\frac{\delta_\ell}{r_u}\left(\frac{\rho_u}{\rho_b}\right)^{2.2}\right]^2 \tag{3.35}$$

The burned gas Markstein length L_b quantifies the influence of flame stretch on the flame speed (Gu *et al.,* 2000, Clavin, 1985) by:

$$S_s - S_n = L_b \alpha \tag{3.36}$$

Here S_s is the unstretched flame speed and is obtained as the intercept of S_n at $\alpha = 0$, in the plot of S_n against α (Gu *et al.,* 2000). The gradient of the best straight-line fit to the experimental data gives L_b and the unstretched laminar burning velocity u_ℓ is evaluated from Eq. (3.8). When *dp/dt* is very small the second term on the right of Eq. (3.8) can be neglected.

Shown in Figs 3.4. (a) and (b), are plots of the flame speed, S_n, against the total flame stretch rate, α, given by Eq. (3.30). Reference to Eq. (3.36) shows the burned gas Markstein length, L_b, is negative for the lean mixture of methane–air, but shifts to positive for the rich mixtures. For the iso-octane–air mixture L_b is always positive, increasingly so for leaner mixtures. At the lower values of α, cellular flames developed in four of the mixtures. The points at which the cellularity began are indicated and the associated increase in flame speed is apparent.

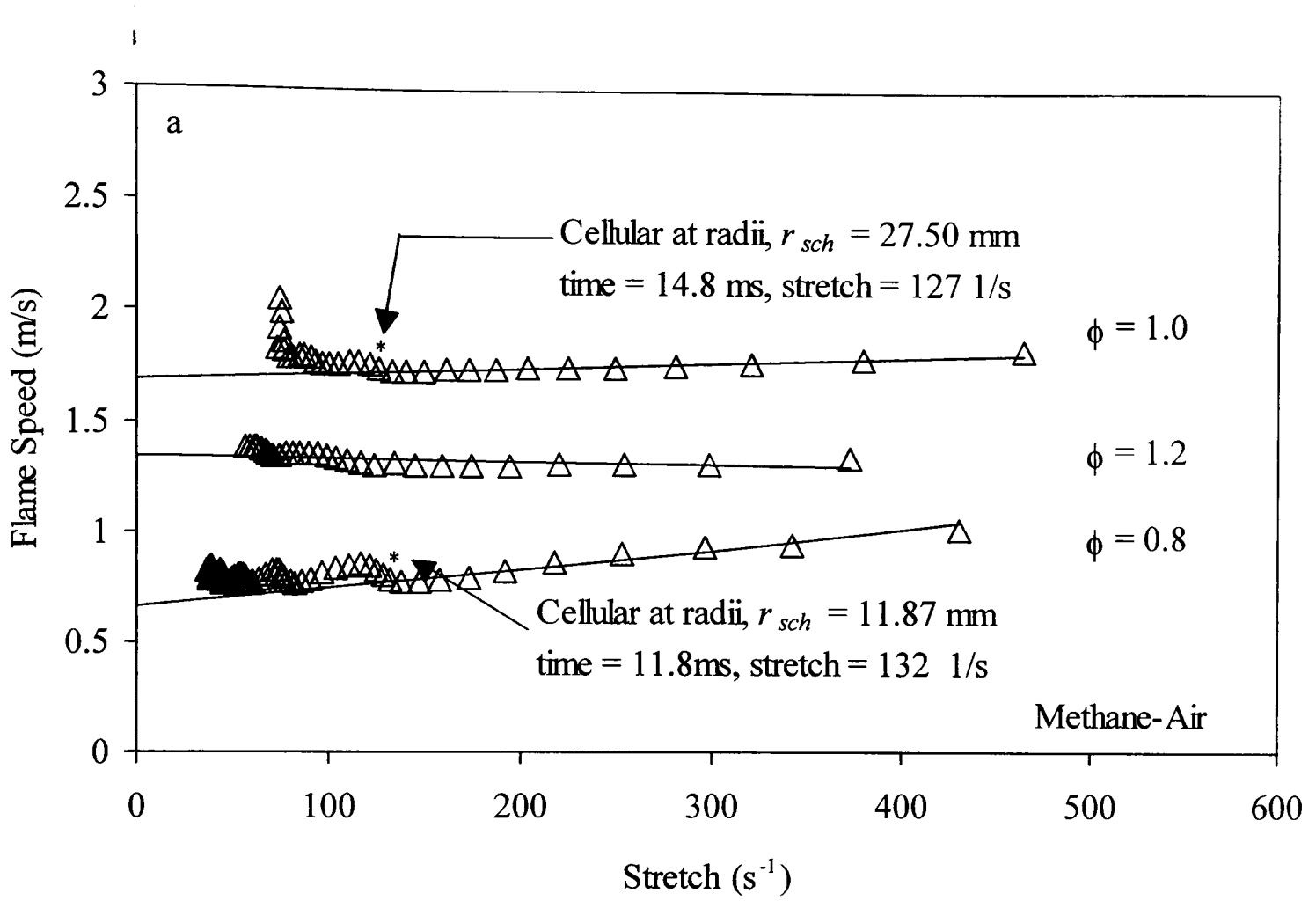

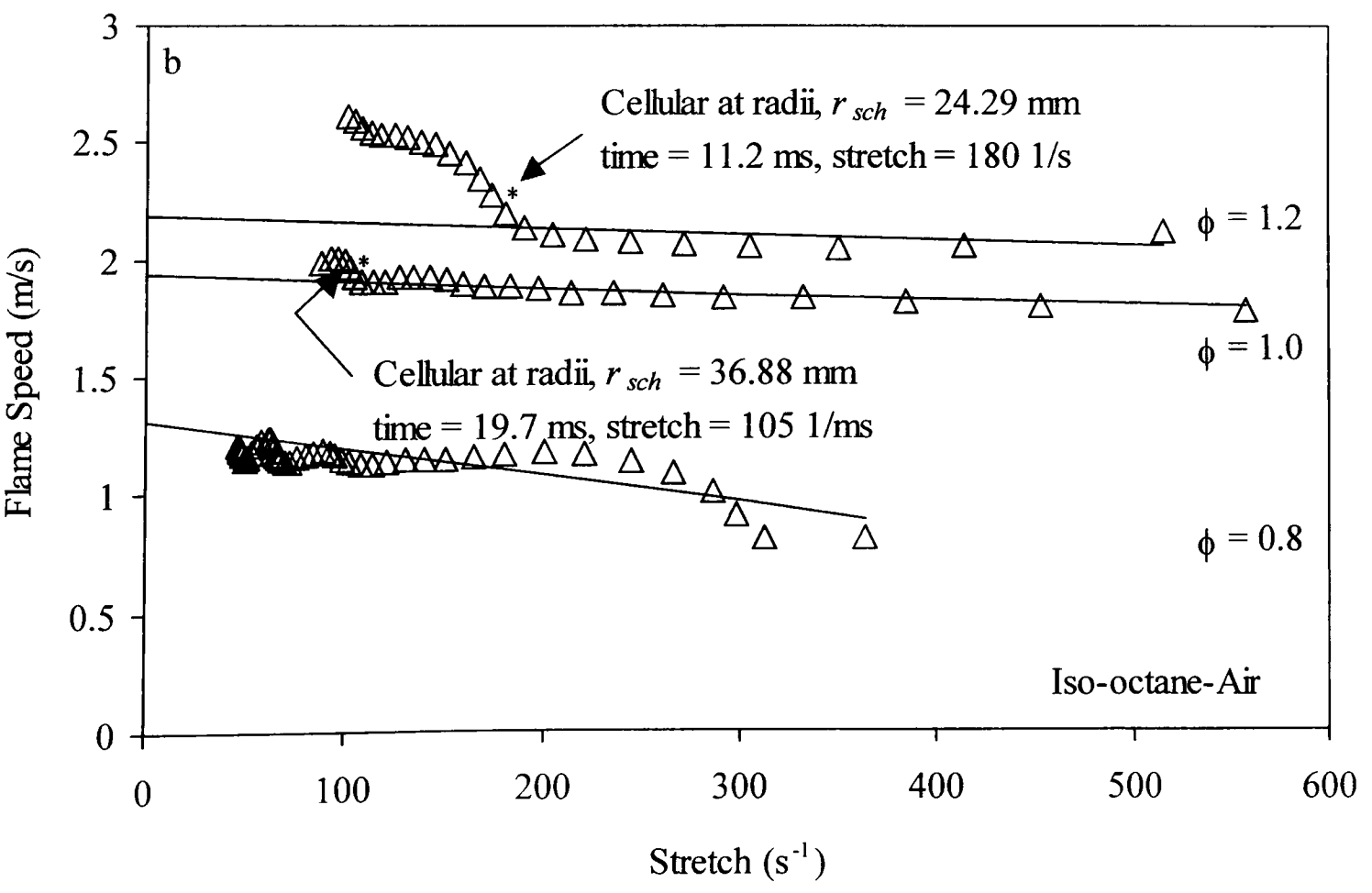

Fig. 3.4. Plots of flame speed against total flame stretch for (a) methane - air and (b) iso-octane – air mixtures at p_0 = 0.5 MPa, T_0 = 358 K, three equivalence ratios, optical measurements.

3.5.3 Derivation of Laminar Burning Velocities by the Two Methods

The first method is optical and uses Eq. (3.8). The *dp/dt* term is negligible. The second method rests on pressure measurements and uses Eq. (3.22), usually when the flame front has propagated beyond the window boundaries. Results involving both methods for measuring burning velocities, u_n, at different times are shown in Figs 3.5 (a) for methane - air and (b) for isooctane – air mixtures, both for ϕ = 0.8, 1.0 and 1.2. Values of u_n depend on the stretch rate, and, at low values of it, flame instabilities develop. Symbols in the figure indicate values from the optical method, while bold lines indicate values from the pressure method. Full lines indicate the pressure traces for the different values of ϕ. There is good continuity between both methods, with flame speeds and burning velocities increasing with the development of flame instabilities.

During the pre-pressure period, before the onset of instabilities, the changes in u_n correspond to the changes in S_n in Fig. 3.4, and are due to the effects of the changing stretch rate. The fastest flame for methane was at ϕ=1.0 and for iso-octane was at ϕ=1.2. Thereafter, the values of u_n increased in iso-octane mixtures, ϕ= 1.0 and 1.2, due to the flame instabilities.

Shown in Fig. 3.6 for both methane and iso-octane mixtures, originally at 0.5 MPa and 358 K, are plots of u_n against the pressure, increasing due to isentropic compression. The optical method was only employed in the initial "pre-pressure" period. The pressure method gave values at different times until the pressure had risen to about 0.58 MPa. Values of u_ℓ (zero stretch rate) were found as described in Section 3.5.2, and the two values are shown for 0.5 MPa. Shown by the full lines are values of u_ℓ obtained using the optical method for iso-octane - air (Bradley *et al.*, 1998), and methane - air (Gu *et al.*, 2000). These were found from the measured pressures, with allowance for the increased temperatures. As the pressure and the flame cellularity developed the measured values of u_n, shown by the symbols and full line curves, increasingly became higher than the corresponding values of u_ℓ.

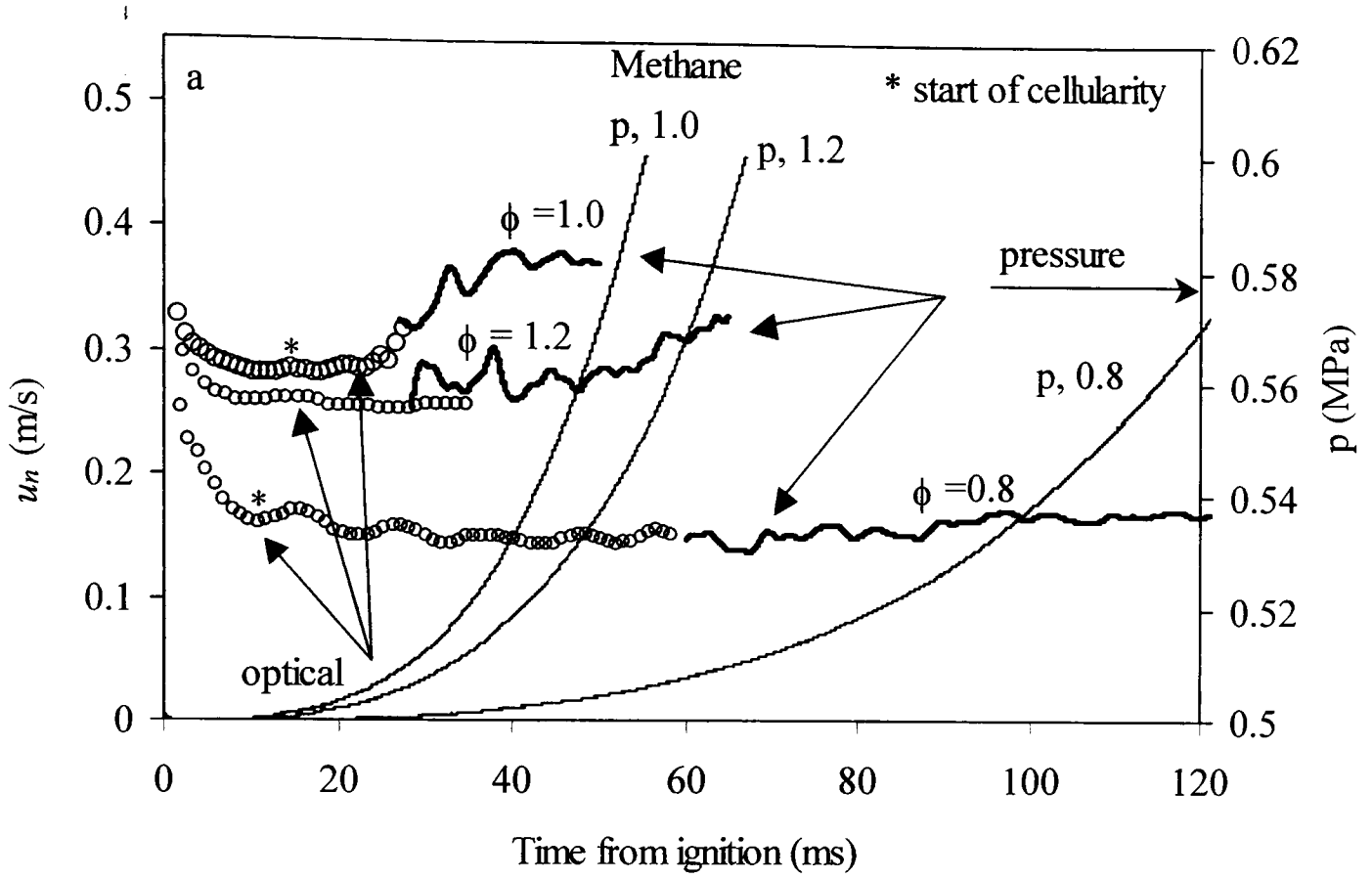

Fig. 3.5. Burning velocities from optical and pressure measurement techniques for (a) methane - air and (b) iso-octane – air mixtures at p_0 = 0.5 MPa and T_0 = 358 K. ϕ = 0.8, 1.0 and 1.2.

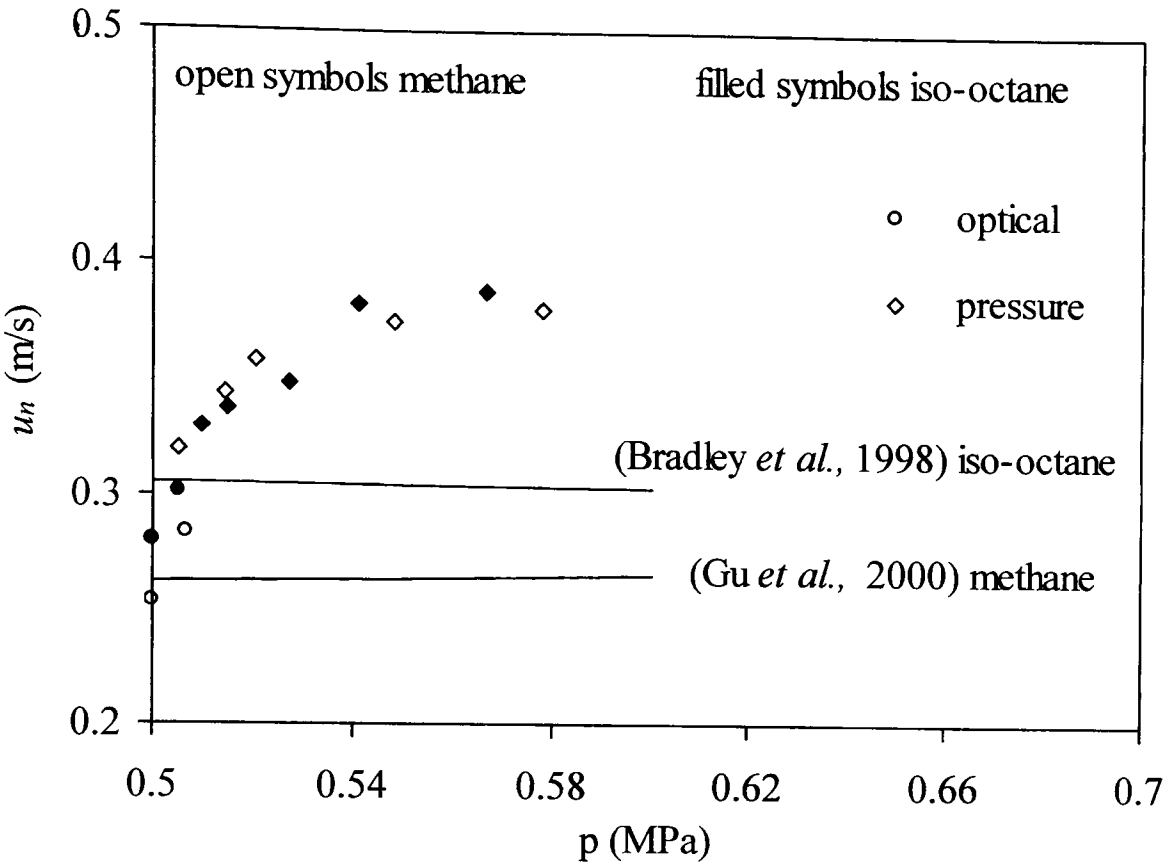

Fig. 3.6. Variations of laminar burning velocities with pressure during isentropic compression for stoichiometric methane and iso-octane mixtures at p_0 = 0.5 MPa, T_0 = 358 K.

3.6 Evolution of Cellular Structure in Laminar Flames

The evidence for flame cellularity must be optical and the cellular structure was observed from the captured images from schlieren photography. Typical images are shown in Figs. 3.7 and 3.8. The most marked cellularity was observed for the iso-octane – air mixture, ϕ = 1.2. Cells started as cracks in the flame structure and evolved to a cellularity that covered the entire surface as the stretch rate decreased. This caused a change in the flame frontal area, which increased the flame propagation speeds and burning velocities. This behaviour is quite clear in Figs. 3.5 (a) and (b).

These experiments showed the importance of high pressure and negative Markstein numbers in enhancing burning rates due to flame instabilities and also the importance of flame photography in observing them. This led to the developments of the implosion techniques, described in the next Chapter.

3.7 Pressure Measurements in Turbulent Flames

As a preliminary to more detailed studies of turbulent flames, pressure records were taken for the unstable iso-octane – air mixture, ϕ = 1.5, initially at 0.25 MPa and 358 K. Ignition was

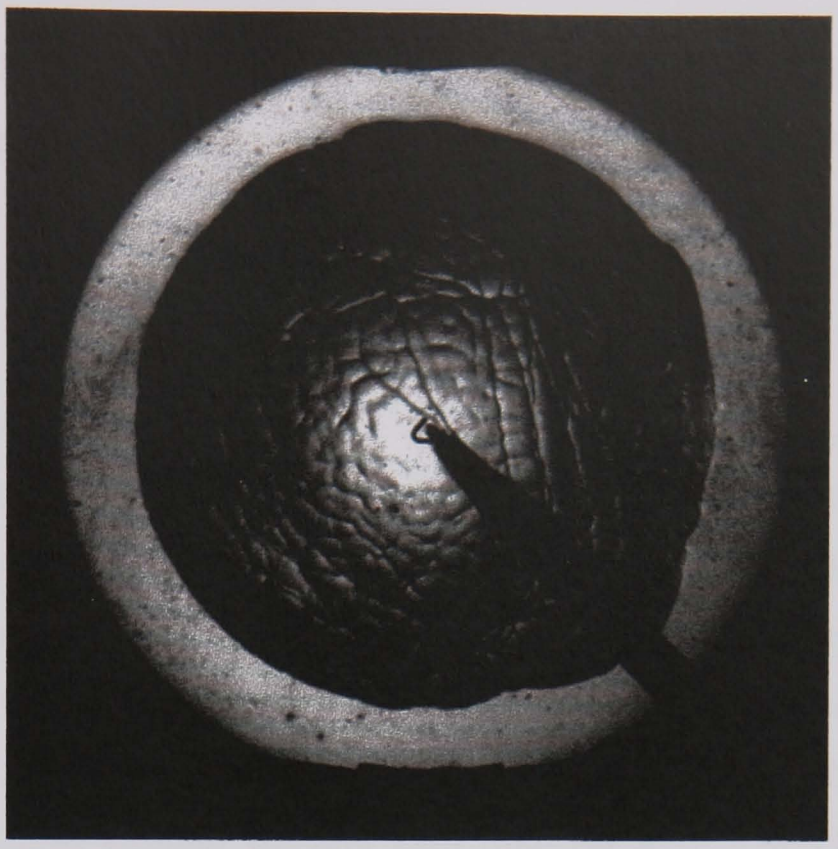

Fig. 3.7. Cellular flame image for stoichiometric methane-air mixture, at initial pressure of 0.5 MPa and temperature of 358 K, 31.73 ms, from ignition.

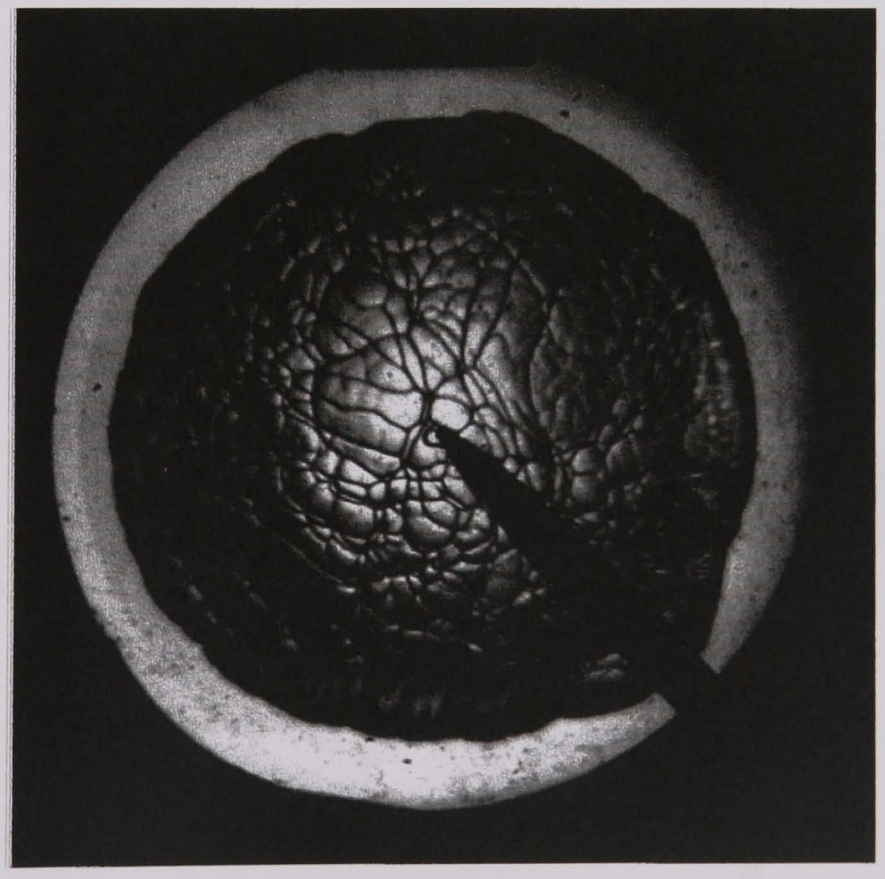

Fig. 3.8. Cellular flame image for stoichiometric iso-octane - air mixture, at initial pressure of 0.5 MPa and temperature of 358 K, 25.48 ms, from ignition.

central and rms turbulent velocities, u', ranged from 0 to 4.0 m/s, as fan speeds increased from zero. More details of acoustic oscillations in unstable flames can be found in Bradley *et al.* (2001). The pressure records at different values of u' are shown in Fig. 3.9. Not surprisingly,

as u' increased, so did the rate of burning. More interesting were the acoustic oscillations associated with the flames. The most severe oscillations occured with the fans at rest, $u' = 0$, and such explosions were the most noisy. It would appear that increased turbulence reduced the severity of the oscillations.

The burning velocities and flame radii were calculated using Eq. 3.22, based on pressure records, with the results shown in Figs. 3.10 and 3.11. The effect of flame brush thickness is neglected. For $u' = 0$ at about 75 ms after ignition the flame radius and the burning velocity suddenly increased, with the onset of strong pressure oscillations. These might have increased the flame front area, beyond that due to Darrieus-Landau and thermo-diffusive instabilities probably on account of Taylor instabilities, in turn to increase further the burning velocity. The continuing increase in burning velocity with time for $u' \geq 2$ m/s is more difficult to understand and motivated further study with the twin kernel implosion technique (see Chapter 7). The gas velocities ahead of each flame were found from the right hand term in Eq. 3.12, for all turbulent flames and are shown in Figs. 3.12 and 3.13 for different values of u'. The gas velocities were influenced by the rms turbulent velocities, in a similar manner to the burning velocities.

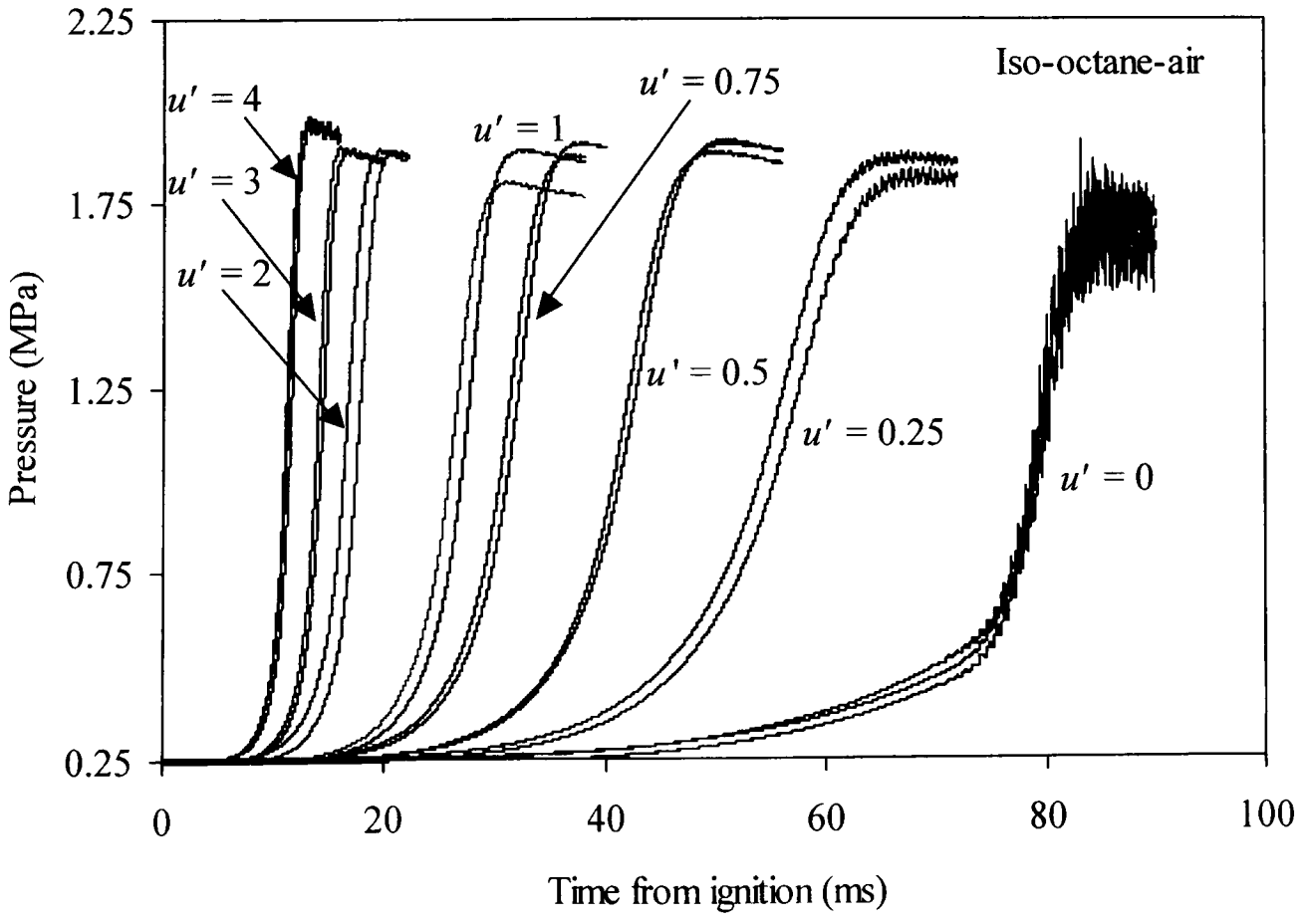

Fig. 3.9. Pressure records for turbulent iso-octane – air flames, $\phi = 1.5$, $p_o = 0.25$ MPa, $T_o = 358$ K, u' in m/s.

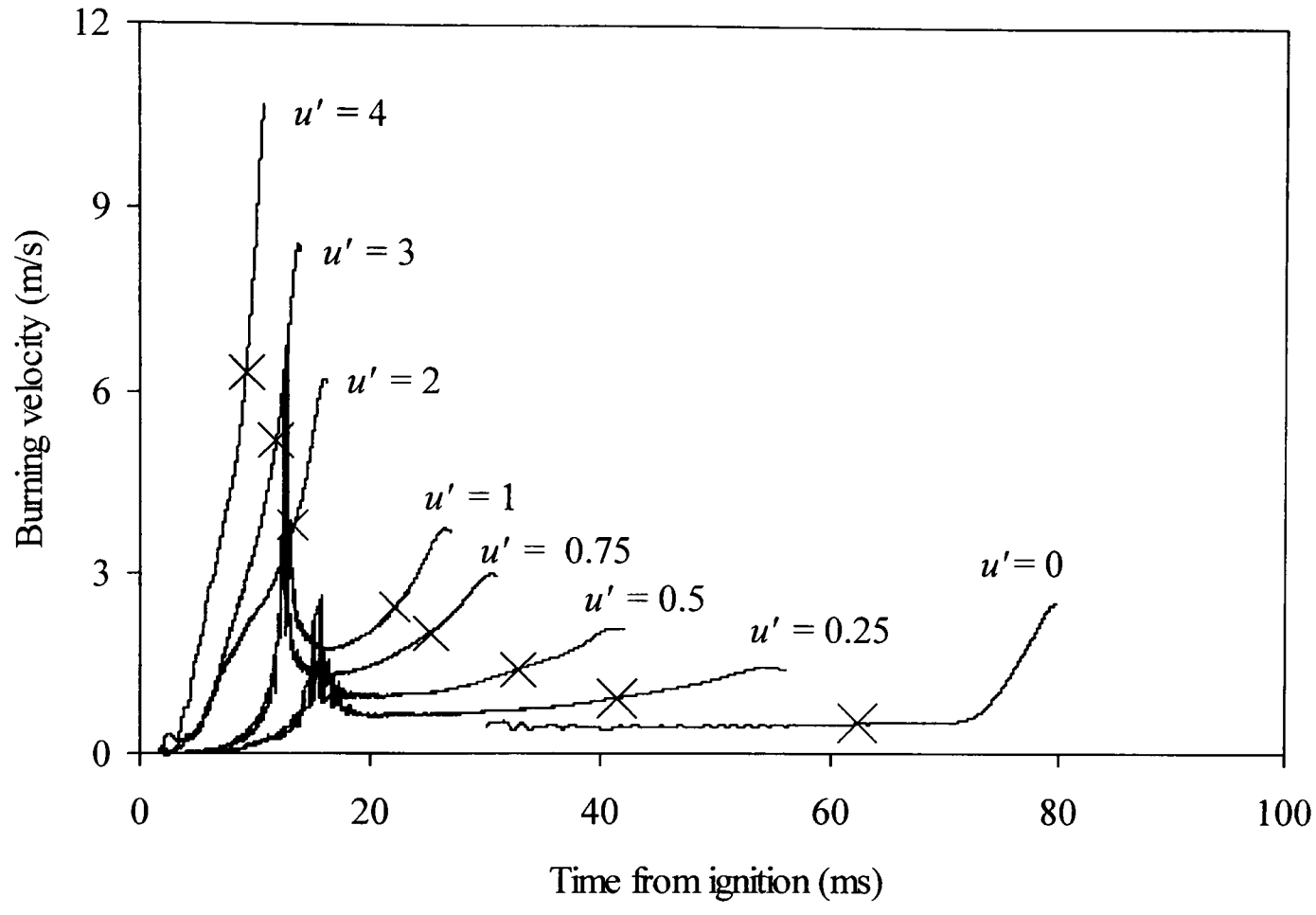

Fig. 3.10. Burning velocities against time for iso-octane – air flames at $\phi = 1.5$, $p_0 = 0.25$ MPa, $T_0 = 358$ K, at different values of u' in m/s, using pressure measurements Eq. 3.22. X indicates when the flame reaches the fans.

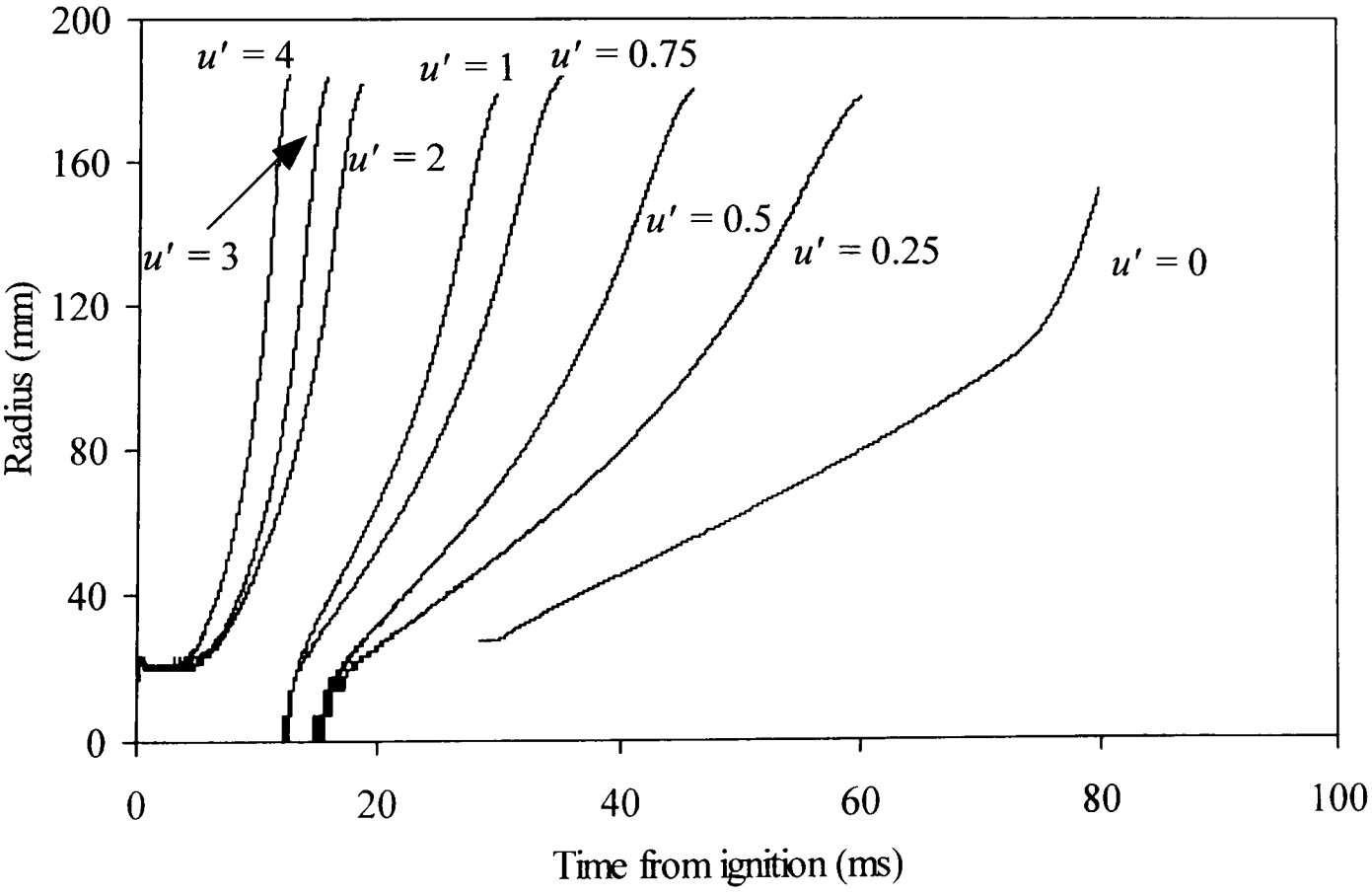

Fig. 3.11. Flame radius against time for iso-octane – air flames at $\phi = 1.5$, $p_0 = 0.25$ MPa, $T_0 = 358$ K, at different values of u' in m/s. Pressure measurements, Eq. 3.17.

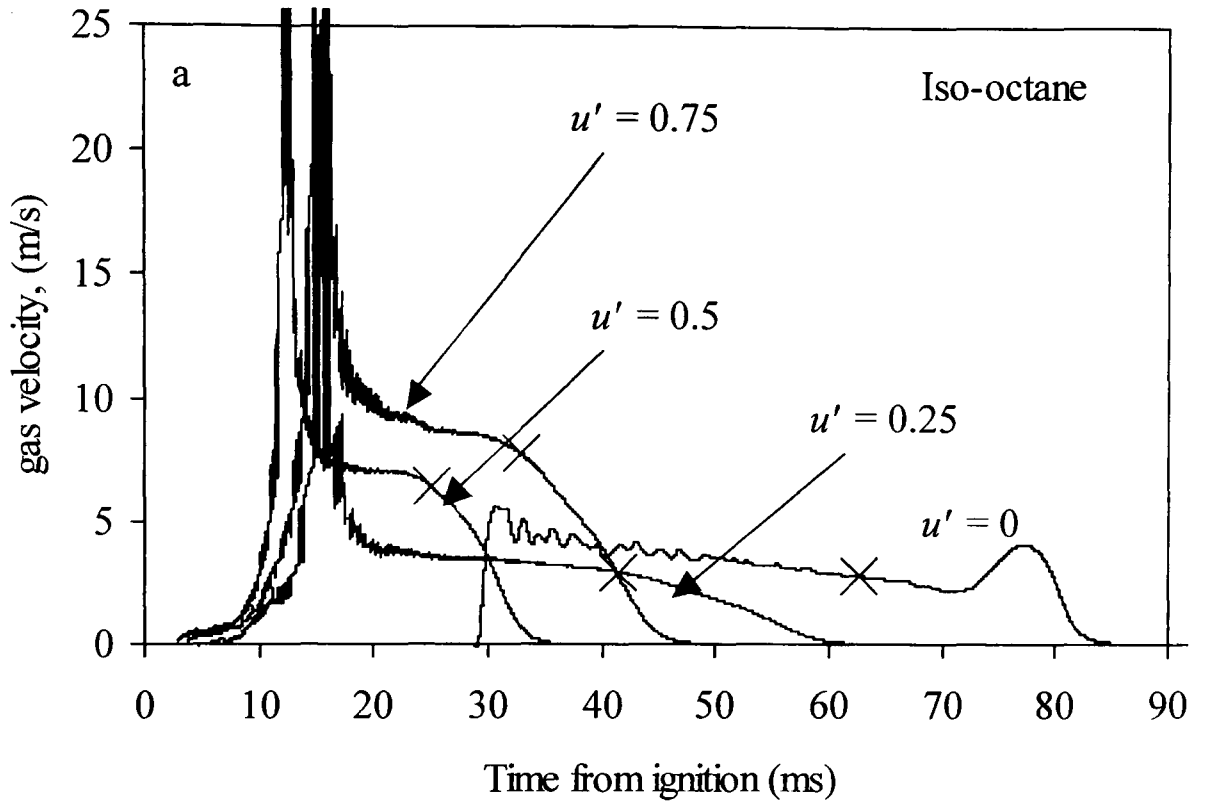

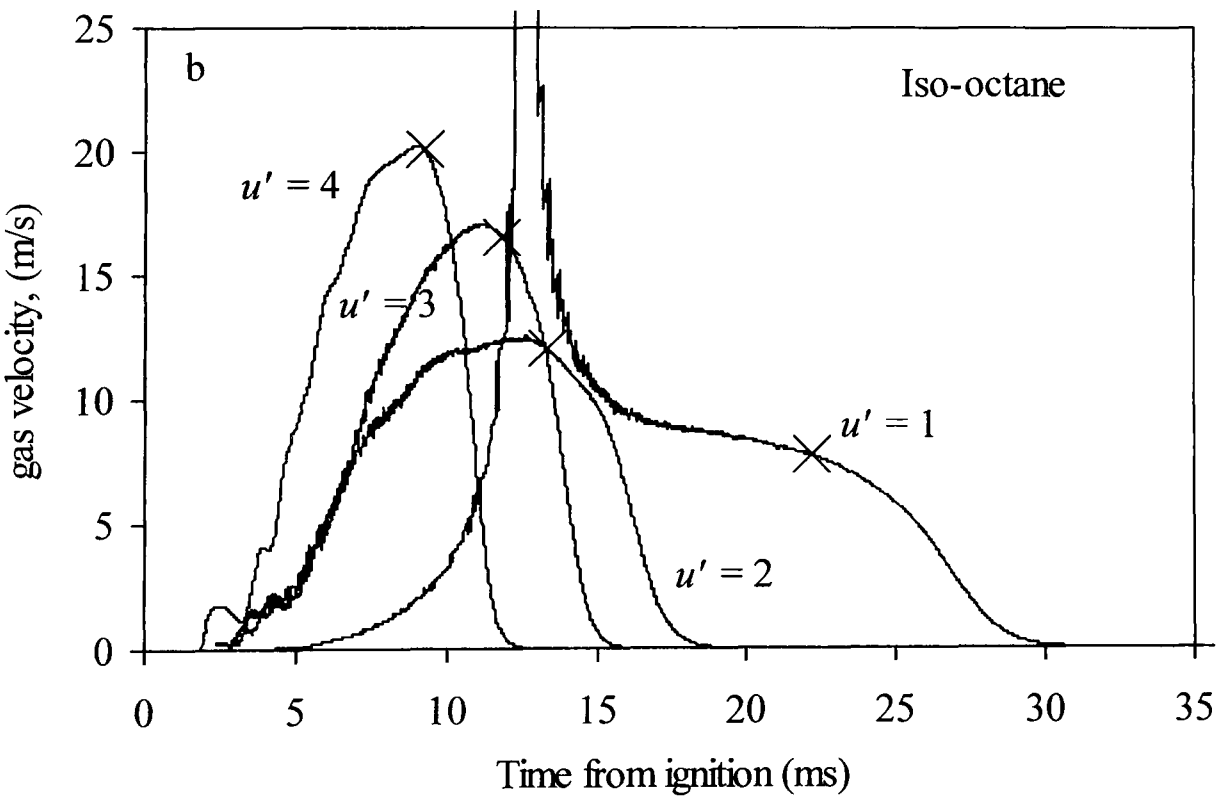

Fig. 3.12. Gas velocities for iso-octane – air flames at $\phi = 1.5$, $p_0 = 0.25$ MPa, $T_0 = 358$ K at different values of u' in m/s, using Eq. 3.12. X indicates when the flame reaches the fans.

Chapter 4

Theory of Two Hemispherical Imploding Spherical Flame Surfaces

4.1 Introduction

There are many advantages in simultaneously measuring the pressure during spherical explosions and observing the progress of the propagating flame. This technique enables more accurate values of burning velocity to be attained and the onset of any instabilities to be observed. However, with central ignition and windows located to view the early flame, it is not possible in practice to view the propagating flame at the highest pressures, as it will have moved out of view. This is a significant disadvantage. The bomb must be designed to withstand the highest pressure yet no experimental data are obtained at the higher pressure.

One way of overcoming this limitation is to ignite the mixture uniformly at the inside face of the bomb to generate an implosion, the final stages of which can be observed through windows located to view the centre of the bomb. Although such implosions have been simulated computationally (Bradley e*t al.,* 1996), in practice uniform ignition at the outer spherical boundary is impossible.

An alternative approach was therefore developed. It was decided to generate implosions from two diametrical opposite spark gaps mounted close to the wall. The two imploding flames that developed and their structure could be observed as they moved towards each other at the centre of the bomb and their burning velocities derived. Furthermore, as they closed together in the final stages burning velocities could be attained by the double kernel method.

The methods for deriving both laminar and turbulent burning velocities under these circumstances are described below. It is first necessary to obtain an expression for the volume of burned gas. A knowledge of the flame area then enables expressions to be obtained for the burning velocity. It is assumed that:

(i) The flames propagate radially inwards towards the centre of the vessel, as surfaces of spheres, but with different radii.

(ii) Pressures are equalized throughout the vessel.

(iii) Unburned gases are compressed isentropically and there is no heat loses from the bomb.

(iv) Homogenous, isotropic turbulence throughout the vessel even in outer (fan) regions.

First a theory is presented for flame radii centred at the vessel wall. This is followed by one, relevant to turbulent flames, for radii centred beyond the wall.

4.2 Geometrical Considerations and Burned Gas Volume

It is first necessary to find the volume of burned gas and the area of the assumed part-hemispherical flame front. Consider a cusp, height h, of a sphere of radius R, as shown in Fig. 4.1. The extent of the cusp is also defined by the angle, θ. Consider a segment of the cusp at a height x and thickness δx subtending an angle ϕ.

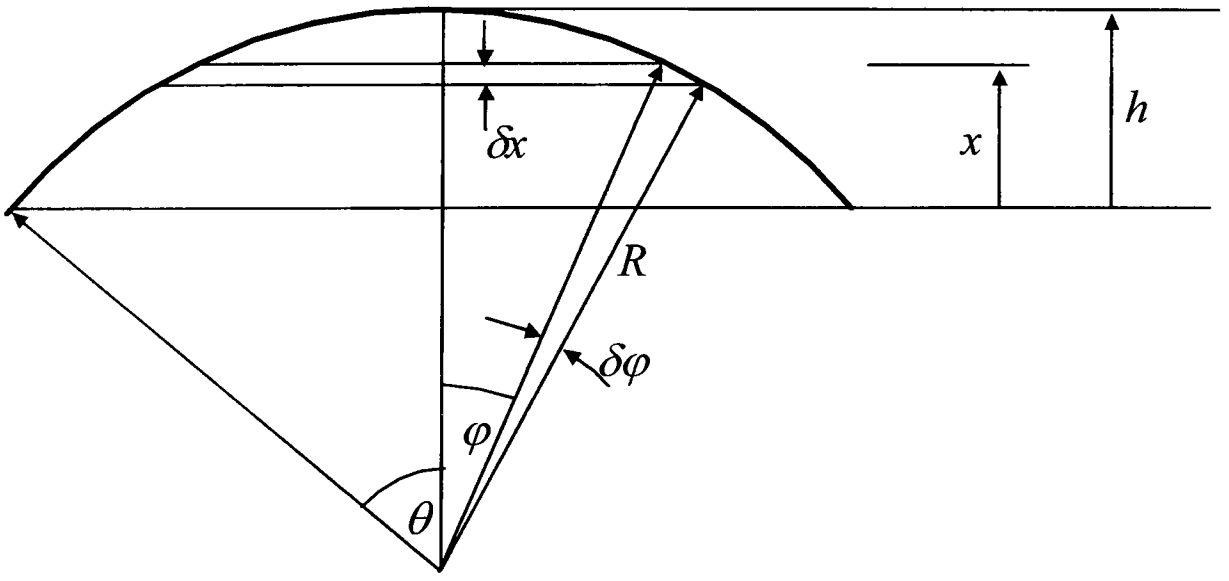

Fig. 4.1. Derivation of volume of a cusp.

The area of the segment $A = \pi R^2 \sin^2 \phi$. (4.1)

The associated volume of the segment $= \pi R^2 \sin^2 \phi \, \delta x$. (4.2)

Now $R\cos\phi - x + h = R$ (4.3)

and $-R\sin\phi = \dfrac{dx}{d\phi}$, as h and R are fixed.

The total volume of the cusp $= \int_{\phi=\theta}^{\phi=0} -\pi R^3 \sin^3\phi \, d\phi = + \int_{\phi=\theta}^{\phi=0} \pi R^3 \left(1-\cos^2\phi\right) d\cos\phi$

$$= \pi R^3 \left[\cos\phi - \frac{\cos^3\phi}{3}\right]_{\theta}^{0} = \pi R^3 \left[1 - \frac{1}{3} - \cos\theta + \frac{\cos^3\theta}{3}\right]$$

$$= \frac{\pi R^3}{3}\left[2 - \cos\theta\left(3 - \cos^2\theta\right)\right]. \tag{4.4}$$

Now consider the volume of burned gas. This is shown shaded in Fig. 4.2. The flame radius after ignition at the walls is, r. The burned gas is contained within two cusps of volumes a and b.

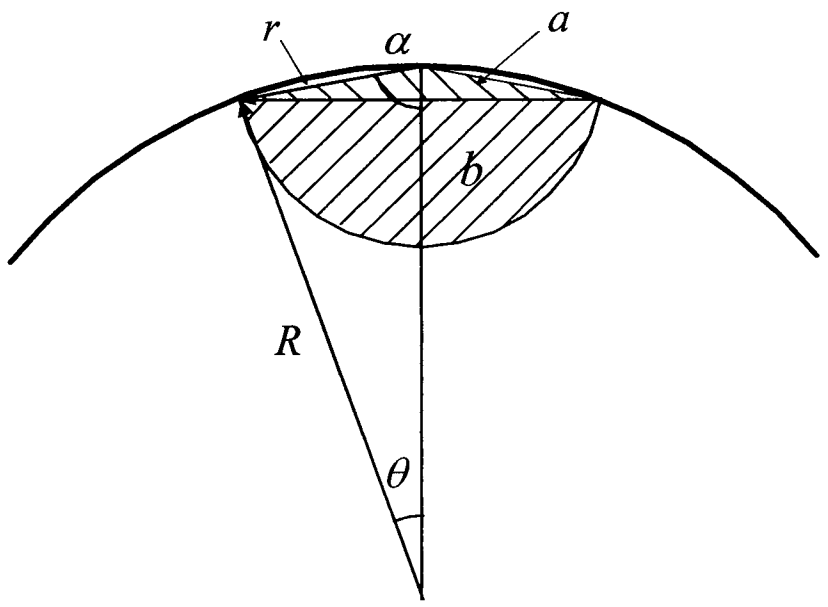

Fig. 4.2. Burned gas contained in two cusps, volume (a and b).

From Eq. (4.4):

$$a = \frac{\pi R^3}{3}\left[2 - \cos\theta\left(3 - \cos^2\theta\right)\right].$$

Similarly, the volume of the second cusp, b, is given by

$$b = \frac{\pi r^3}{3}\left[2 - \cos\alpha\left(3 - \cos^2\alpha\right)\right].$$

The relationship between r and R is found from

$$r^2 = \left(R - R\cos\theta\right)^2 + R^2\sin^2\theta = R^2 - 2R^2\cos\theta + R^2\cos^2\theta + R^2\sin^2\theta$$

$$= 2R^2(1-\cos\theta)$$

$$\therefore \quad \cos\theta = 1 - \frac{r^2}{2R^2} \tag{4.5}$$

Now $r\sin\alpha = R\sin\theta \qquad \therefore\ r^2\sin^2\alpha = R^2\sin^2\theta \quad = R^2(1-\cos^2\theta)$

and $\bar{r}^2\left(1-\cos^2\alpha\right)=\left(1-\cos^2\theta\right)$, where $\bar{r}=r/R$.

From Eq. (4.5) $[\bar{r}]^2\left(1-\cos^2\alpha\right)=1-\left(1-\dfrac{\bar{r}^2}{2}\right)^2 \quad =1-1+\bar{r}^2-\dfrac{\bar{r}^4}{4}$

$\therefore 1-\cos^2\alpha = 1-\dfrac{r^2}{4} \qquad \therefore \cos\alpha = \dfrac{\bar{r}}{2}.$

Substituting for *cos* θ, from Eq. (4.5), in the previous expression for *a*,

$$a = \frac{\pi R^3}{3}\left[2-\left(1-\frac{\bar{r}^2}{2}\right)\left(3-\left[1-\frac{\bar{r}^2}{2}\right]^2\right)\right] \quad = \frac{\pi R^3}{3}\left[2-\left(1-\frac{\bar{r}^2}{2}\right)\left(3-\left[1-\bar{r}^2+\frac{\bar{r}^4}{4}\right]\right)\right]$$

$$= \frac{\pi R^3}{3}\left[2-\left(1-\frac{\bar{r}^2}{2}\right)\left(2+\bar{r}^2-\frac{\bar{r}^4}{4}\right)\right] \qquad = \frac{\pi R^3}{3}\left[2-2-\bar{r}^2+\frac{\bar{r}^4}{4}+\bar{r}^2+\frac{\bar{r}^4}{2}-\frac{\bar{r}^6}{8}\right]$$

$$= \frac{\pi R^3}{3}\left[\frac{3}{4}\bar{r}^4-\frac{\bar{r}^6}{8}\right]. \tag{4.6}$$

Similarly, by substituting for *cos* α in the previous expression for *b* gives

$$b = \frac{\pi r^3}{3}\left[2-\frac{\bar{r}}{2}\left(3-\frac{\bar{r}^2}{4}\right)\right] \quad = \frac{\pi R^3\bar{r}^3}{3}\left[2-\frac{3\bar{r}}{2}+\frac{\bar{r}^3}{8}\right]$$

$$= \frac{\pi R^3}{3}\left[2\bar{r}^3-\frac{3\bar{r}^4}{2}+\frac{\bar{r}^6}{8}\right]. \tag{4.7}$$

The total volume of burned gas is (*a* + *b*) and

$$(a+b) \ = \frac{\pi R^3}{3}\left[2\bar{r}^3-\frac{3\bar{r}^4}{4}\right]. \tag{4.8}$$

The rate at which the volume changes with time is needed to express the burning rate, and

$$\frac{\partial(a+b)}{\partial t} \quad = \frac{\pi R^3}{3}\left[6\bar{r}^2-3\bar{r}^3\right]\frac{\partial\bar{r}}{\partial t} \quad = \pi R^3\left[2\bar{r}^2-\bar{r}^3\right]\frac{\partial\bar{r}}{\partial t} \tag{4.9}$$

The area of the flame front, *A*, also is needed, to find the burning velocity. Referring to Fig. 4.3:

$$A = \int_{\phi=0}^{\phi=\alpha} 2\pi r\sin\phi\, r\,\delta\phi$$

$$= \left[-2\pi r^2 \cos\phi\right]_0^{\alpha} \quad = 2\pi r^2 \left[1 - \cos\alpha\right]$$

$$= 2\pi r^2 \left[1 - \frac{\bar{r}}{2}\right]. \tag{4.10}$$

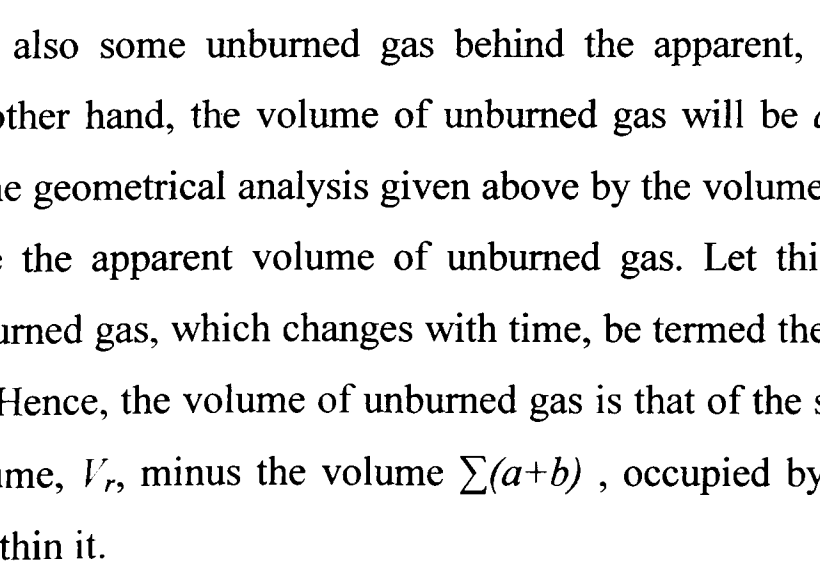

Fig. 4.3. Derivation of flame front area.

4.3 Burning Rate

It is assumed that the two flames surfaces continue to be of spherical form until they mutually begin to flatten at the leading fronts. A turbulent flame was represented by a smoothed spherical surface such that on the 2 D schlieren image the area of unburned gas outside the surface was equal to that within it, as in Bradley *et al.* (2003). The radius of the containing spherical bomb is R. In practice, the unburned gas volume is *increased* above $4\pi R^3/3$ by some small recessed volumes at windows and spark plugs. There may be also some unburned gas behind the apparent, photographed, flame front. On the other hand, the volume of unburned gas will be *decreased* below that suggested by the geometrical analysis given above by the volume occupied by parts of the fans inside the apparent volume of unburned gas. Let this total net increased volume of unburned gas, which changes with time, be termed the residual volume, V_r, at any instant. Hence, the volume of unburned gas is that of the sphere, supplemented by the net volume, V_r, minus the volume $\sum(a+b)$, occupied by burned gas and any parts of fans within it.

The mass of unburned gas, m_u, is found by multiplying these volumes by the unburned gas density, ρ_u.

$$\therefore m_u = \frac{4}{3}\pi R^3 \rho_u + V_r \rho_u - \sum (a+b)\,\rho_u \qquad (4.11)$$

here $\sum (a+b)$ is sum of the two separated burned gas volumes originating from the two diametrically opposed spark gaps. In general, the two flame radii will be different.

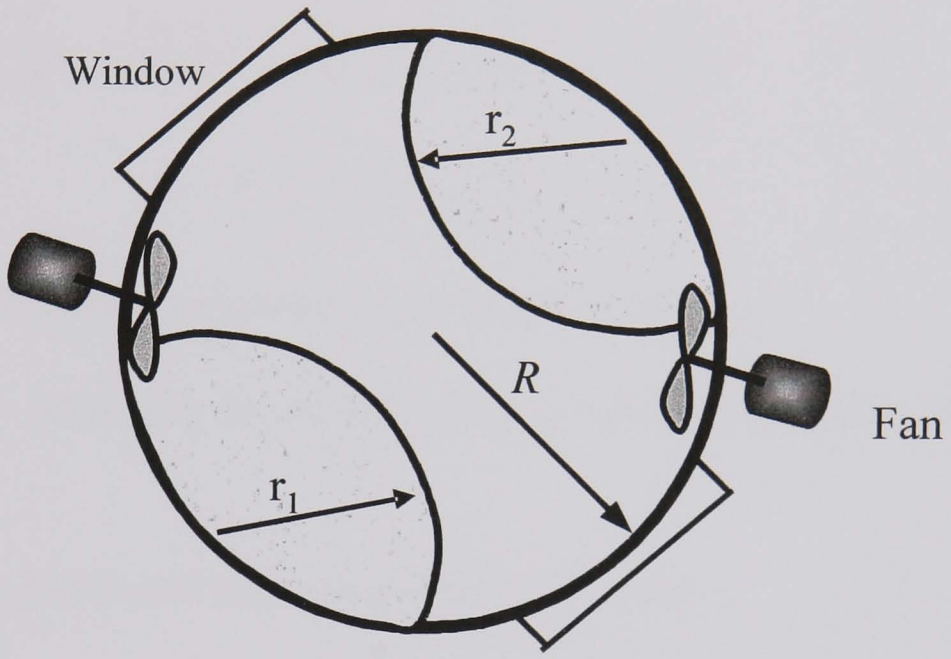

Fig. 4.4. Volume of window recess and volume occupied by fans.

The area of the flame front, given by Eq. (4.10) for a single front is, multiplied by the burning velocity, S_u , and the unburned gas density to give the mass rate of burning . This is

$S_u \rho_u \sum 2\pi r^2 (1-\bar{r}/2)$, and is equal to $-\partial m_u/\partial t$. Here, $\sum 2\pi r^2 (1-\bar{r}/2)$ is the sum of the two separate flame areas. From Eq. (4.11)

$$\frac{\partial m_u}{\partial t} = \frac{4}{3}\pi R^3 \frac{\partial \rho_u}{\partial t} + \rho_u \frac{\partial V_r}{\partial t} + V_r \frac{\partial \rho_u}{\partial t} - \sum (a+b)\frac{\partial \rho_u}{\partial t} - \frac{\rho_u \partial \sum (a+b)}{\partial t}.$$

Hence, using Eqs. (4.8) and (4.9),

$$\frac{\partial \rho_u}{\partial t}\left[\frac{4\pi R^3}{3} + V_r - \frac{\pi R^3}{3}\sum\left(2\bar{r}^3 - \frac{3\bar{r}^4}{4}\right)\right] + \rho_u \frac{\partial V_r}{\partial t} - \rho_u \pi R^3 \sum \left(2\bar{r}^2 - \bar{r}^3\right)\frac{\partial \bar{r}}{\partial t}$$

$$= -\bar{S}_u \rho_u \sum 2\pi \bar{r}^2 \left(1 - \frac{\bar{r}}{2}\right) R^3 \qquad \text{where} \quad \bar{S}_u = S_u / R \tag{4.12}$$

here $\sum$ indicates sums over both, flame areas and volumes. This definition of burning velocity includes the rate of burning of any unburned gas behind the defined flame front.

If both sides of this equation are divided by $\rho_u \pi R^3$

$$\therefore \frac{1}{\rho_u}\frac{\partial \rho_u}{\partial t}\left[\frac{4}{3} + \frac{V_r}{\pi R^3} - \frac{1}{3}\sum\left(2\bar{r}^3 - \frac{3}{4}\bar{r}^4\right)\right] + \frac{1}{\pi R^3}\frac{\partial V_r}{\partial t} - \sum\left(2\bar{r}^2 - \bar{r}^3\right)\frac{\partial \bar{r}}{\partial t}$$
$$= -\bar{S}_u \sum 2\bar{r}^2\left(1 - \frac{\bar{r}}{2}\right). \tag{4.13}$$

The assumption of isentropic compression of unburned gas gives

$\frac{\partial \rho_u}{\partial t} = \frac{\rho_u}{p\gamma_u}\frac{\partial p}{\partial t}$, where p is the pressure and γ_u is ratio of the specific heats of that gas.

In general, the two flames will have two different radii, $\bar{r}_1$ and $\bar{r}_2$.

$$\therefore \frac{1}{p\gamma_u}\frac{\partial p}{\partial t}\left[\frac{2}{3} + \frac{V_r}{2\pi R^3} - \left(\frac{\bar{r}_1^3}{3} - \frac{\bar{r}_1^4}{8}\right) - \left(\frac{\bar{r}_2^3}{3} - \frac{\bar{r}_2^4}{8}\right)\right] + \frac{1}{2\pi R^3}\frac{\partial V_r}{\partial t}$$
$$-\left(\bar{r}_1^2 - \frac{\bar{r}_1^3}{2}\right)\frac{\partial \bar{r}_1}{\partial t} - \left(\bar{r}_2^2 - \frac{\bar{r}_2^3}{2}\right)\frac{\partial \bar{r}_2}{\partial t} = -\bar{S}_u\left[\left(\bar{r}_1^2 - \frac{\bar{r}_1^3}{2}\right) + \left(\bar{r}_2^2 - \frac{\bar{r}_2^3}{2}\right)\right]$$

$$\therefore \bar{S}_u = \frac{\left(\bar{r}_1^2 - \frac{\bar{r}_1^3}{2}\right)\frac{\partial \bar{r}_1}{\partial t} + \left(\bar{r}_2^2 - \frac{\bar{r}_2^3}{2}\right)\frac{\partial \bar{r}_2}{\partial t}}{\left[\left(\bar{r}_1^2 - \frac{\bar{r}_1^3}{2}\right) + \left(\bar{r}_2^2 - \frac{\bar{r}_2^3}{2}\right)\right]} - \frac{\frac{1}{2\pi R^3}\frac{\partial V_r}{\partial t}}{\left[\left(\bar{r}_1^2 - \frac{\bar{r}_1^3}{2}\right) + \left(\bar{r}_2^2 - \frac{\bar{r}_2^3}{2}\right)\right]} \tag{4.14}$$
$$- \frac{\frac{1}{p\gamma_u}\frac{\partial p}{\partial t}\left[\frac{2}{3} + \frac{V_r}{2\pi R^3} - \left(\frac{\bar{r}_1^3}{3} - \frac{\bar{r}_1^4}{8}\right) - \left(\frac{\bar{r}_2^3}{3} - \frac{\bar{r}_2^4}{8}\right)\right]}{\left[\left(\bar{r}_1^2 - \frac{\bar{r}_1^3}{2}\right) + \left(\bar{r}_2^2 - \frac{\bar{r}_2^3}{2}\right)\right]}.$$

This is an equation in which all units of lengths are normalized by R, but units of time are in seconds. Evaluation of V_r is discussed in the next section.

4.4 Volume Burned and Pressure Rise

Because V_r, $\bar{r}_1$, and $\bar{r}_2$ are continually changing and have different values in different explosions, it is clear that V_r cannot be derived directly without a grate deal of difficulty. The procedure adopted, therefore, was to obtain V_r from a combination of geometrical expressions and the following assumption concerning fractional mass burned. The widely used assumption, supported by some detailed computations, (Bradley and Mitcheson, 1976) of the equality of fractional mass burned and fractional pressure rise enables another expression to be obtained for S_u, based more directly on the pressure record. The assumption gives:

$$\frac{m_b}{m_u + m_b} = \frac{p - p_o}{p_e - p_0} \tag{4.15}$$

here m_b is the mass burned, p_0 is the initial pressure in the bomb and p_e the final pressure at the end of the explosion. If ρ_o is the initial density just prior to exploding,

$$m_u + m_b = \frac{4}{3}\pi R_0^3 \rho_0 \tag{4.16}$$

where R_o is the equivalent radius of a sphere with the same total internal volume as the actual bomb, allowing for recesses and fans. From Eqs. (4.15) and (4.16)

$m_b = \frac{4}{3}\pi R_o^3\ \rho_o - \ m_u = \frac{4}{3}\pi R_o^3 \rho_o \left(\frac{p - p_o}{p_e - p_o}\right)$. With m_u given by Eq. (4.11):

$$\frac{4}{3}\pi R_0^3 \rho_o - \frac{4}{3}\pi R^3 \rho_u - V_r \rho_u + \left(a_1 + a_2 + b_1 + b_2\right)\rho_u = \frac{4}{3}\pi R_o^3 \rho_o \left(\frac{p - p_o}{p_e - p_o}\right). \tag{4.17}$$

This equation enables the residual volume, V_r, to be evaluated at different times during the explosion. From Eq. (4.7) and (4.17) and by dividing by $4/3\pi R^3 \rho_u$

$$\frac{V_r}{\frac{4}{3}\pi R^3} = \left(\frac{R_0}{R}\right)^3 \frac{\rho_0}{\rho_u} - 1 + \left[\frac{\bar{r}_1^3}{2} - \frac{3\bar{r}_1^4}{16}\right] + \left[\frac{\bar{r}_2^3}{2} - \frac{3\bar{r}_2^4}{16}\right] - \left(\frac{R_0}{R}\right)^3 \frac{\rho_0}{\rho_u}\left(\frac{p - p_o}{p_e - p_o}\right). \tag{4.18}$$

It has been shown that the mass burning rate is given by $S_u \rho_u \sum 2\pi r^2 \left(1 - \bar{r}/2\right)$. This is equal to $= \frac{-\partial m_u}{\partial t} = \frac{\partial m_b}{\partial t}$. By invoking Eqs. (4.15) and (4.16)

$$S_u \rho_u \left\{2\pi r_1^2 \left[1 - \frac{\bar{r}_1}{2}\right] + 2\pi r_2^2 \left[1 - \frac{\bar{r}_2}{2}\right]\right\} = \frac{dm_b}{dt} = \frac{d\left(m_u + m_b\right)\frac{\left(p - p_0\right)}{\left(p_e - p_0\right)}}{dt}$$

$$= \frac{4}{3}\frac{\pi R_0^3 \rho_0}{(p_e - p_0)}\frac{\partial p}{\partial t}.$$

If both sides of the equation are divided by $2\pi R^3 \rho_u$, then

$$\bar{S}_u \left\{\left(\bar{r}_1^2 - \frac{\bar{r}_1^3}{2}\right) + \left(\bar{r}_2^2 - \frac{\bar{r}_2^3}{2}\right)\right\} = \frac{2}{3}\left(\frac{R_0}{R}\right)^3\left(\frac{\rho_0}{\rho_u}\right)\frac{1}{(p_e - p_0)}\frac{\partial p}{\partial t}$$

$$\therefore \bar{S}_u = \frac{\frac{2}{3}\left(\frac{R_0}{R}\right)^3\left(\frac{\rho_0}{\rho_u}\right)\frac{1}{(p_e - p_0)}\frac{\partial p}{\partial t}}{\left\{\left(\bar{r}_1^2 - \frac{\bar{r}_1^3}{2}\right) + \left(\bar{r}_2^2 - \frac{\bar{r}_2^3}{2}\right)\right\}} \qquad (4.19)$$

4.5 Assessment of the Method

Three aspects of the imploding flames technique require careful assessment. First, whether each of the two flame front are of spherical shape, second whether the treatment of the residual unburned gas volume, V_r, is satisfactory and third whether the two expressions, Eqs. (4.14) and (4.19), give similar results for S_u. The measuring techniques for the flames radius and fans immersed volume have been discussed in Sections 2.6.2 and 4.3. Here, the three aspects are discussed in the proceeding paragraphs.

4.5.1 Sphericity of the Flame Fronts

The visible front was checked for sphericity, using the measurements of flame radii. Mean radii, r, and rms values for these, r', were found for each flame front. This was done for a range of explosions. Shown here are results from two laminar explosions with 27 flame fronts in each. Also shown are results from three turbulent explosions, with 17, 11 and 9 flame fronts in each. The rms flame front radii, normalized by the mean radius, for twin imploding laminar flames, are plotted against the mean normalized radius in Fig. 4.5. The data are for a stoichiometric iso-octane – air mixture, at initial conditions of 1.0 MPa and 358 K. Also shown in Fig. 4.6 are similar plots for stoichmetric methane – air laminar flames, initially at 0.1 MPa and 298 K. The values cover the full range of measured radii of the two kernels. The normalized rms values are consistently low, giving support to the assumption of spherical flame fronts.

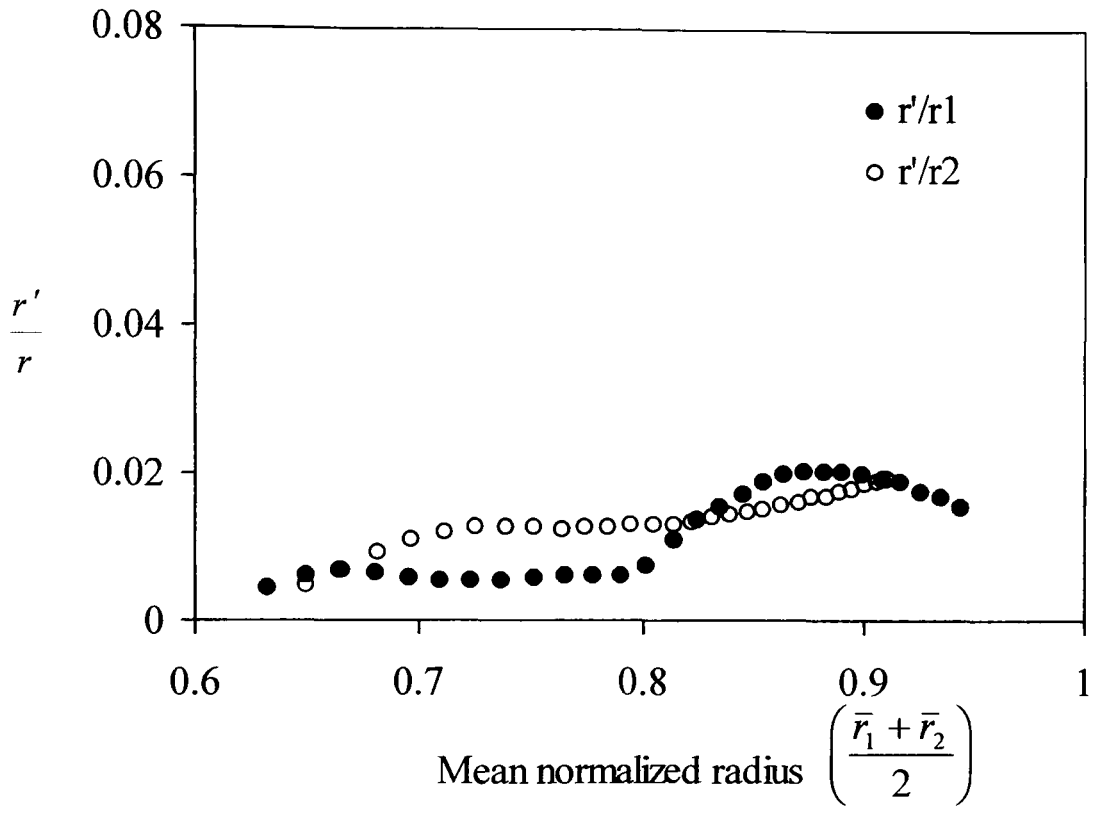

Fig. 4.5. Normalized rms flame front radii for twin imploding laminar flames, for iso-octane – air mixture, $\phi = 1$, $p_o = 1$ MPa, $T_o = 358$ K.

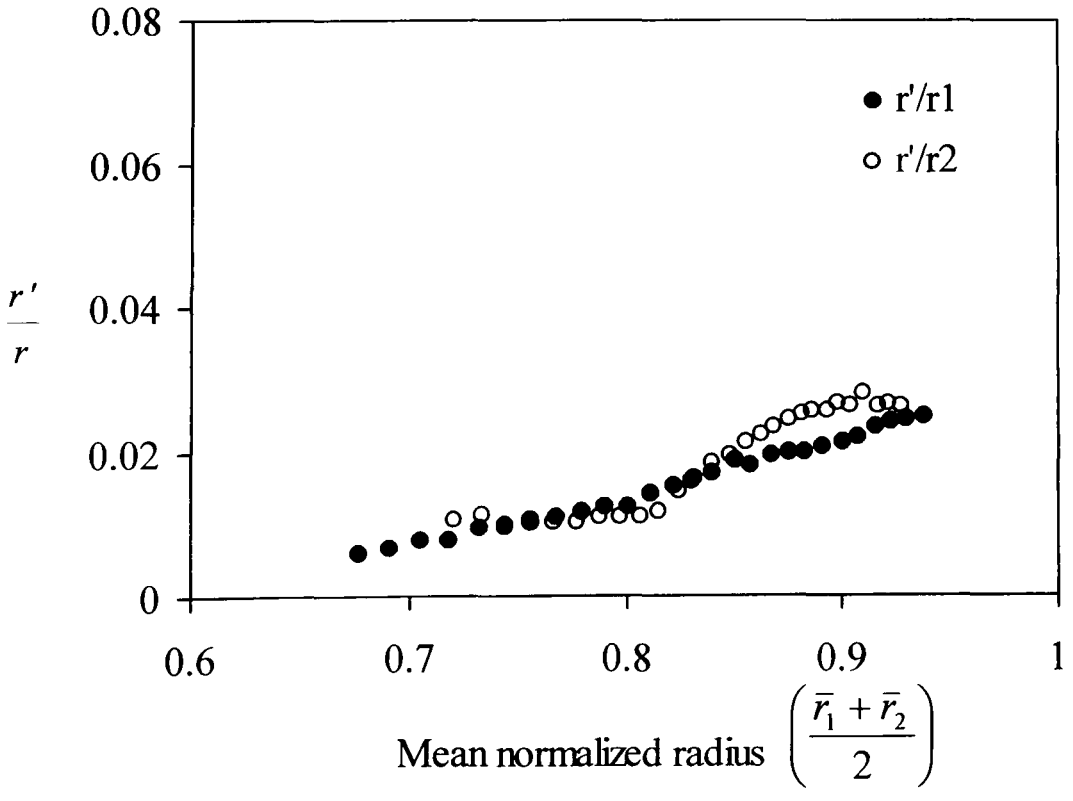

Fig. 4.6. Normalized rms flame front radii for twin imploding laminar flames, for methane – air mixture, $\phi = 1$, $p_o = 0.1$ MPa, $T_o = 298$ K.

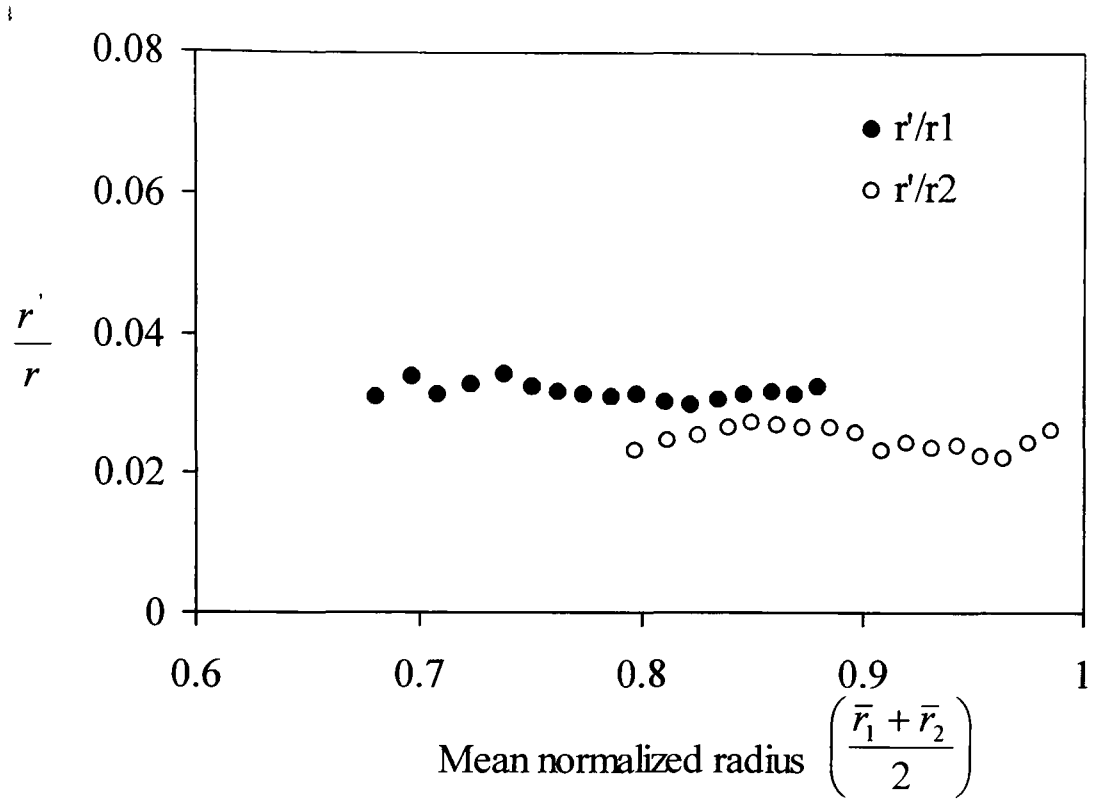

Fig. 4.7. Normalized rms flame front radii for twin imploding turbulent flames, for iso-octane – mixture, $\phi = 1.4$, $p_o = 0.5$ MPa, $T_o = 358$ K, $u' = 0.25$ m/s.

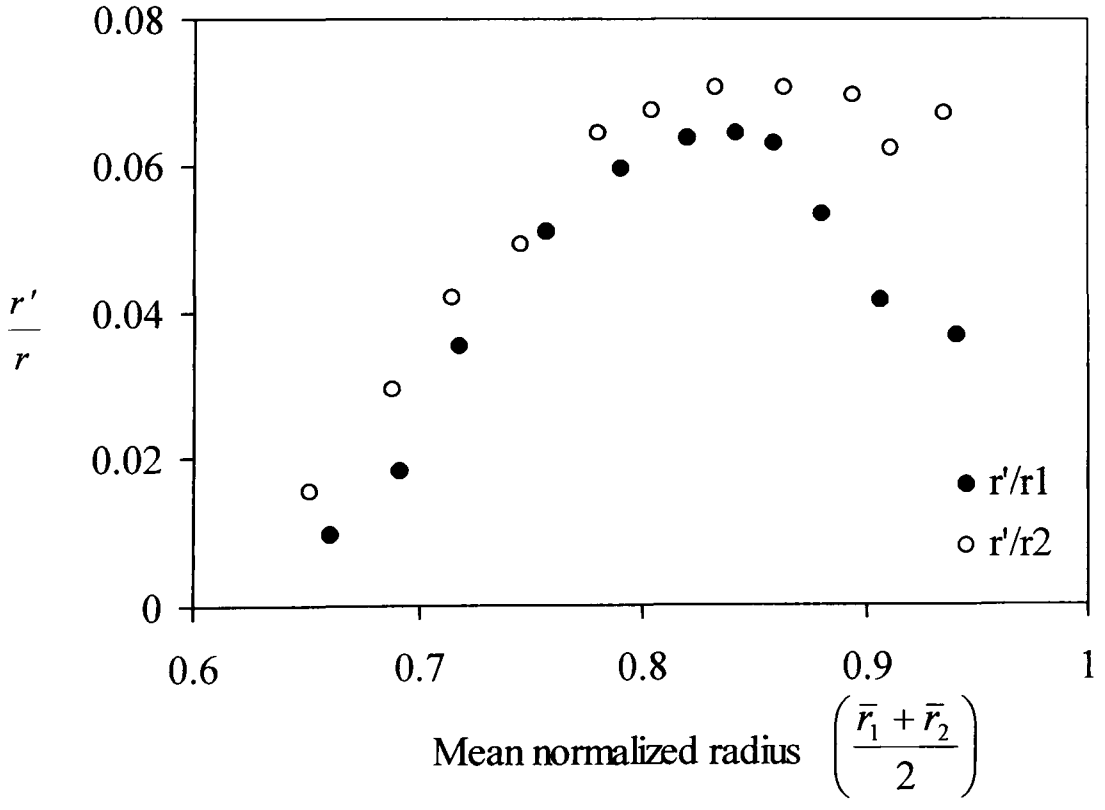

Fig. 4.8. Normalized rms flame front radii for twin imploding turbulent flames for iso-octane – mixture, $\phi = 1.4$, $p_o = 0.5$MPa, $T_o = 358$ K, $u' = 1$ m/s.

Shown in Figs. 4.7 - 4.9, in ascending order of u', are values of r'/r for turbulent flames. Not surprisingly, this ratio is greater than that with laminar flames and it increases with u'.

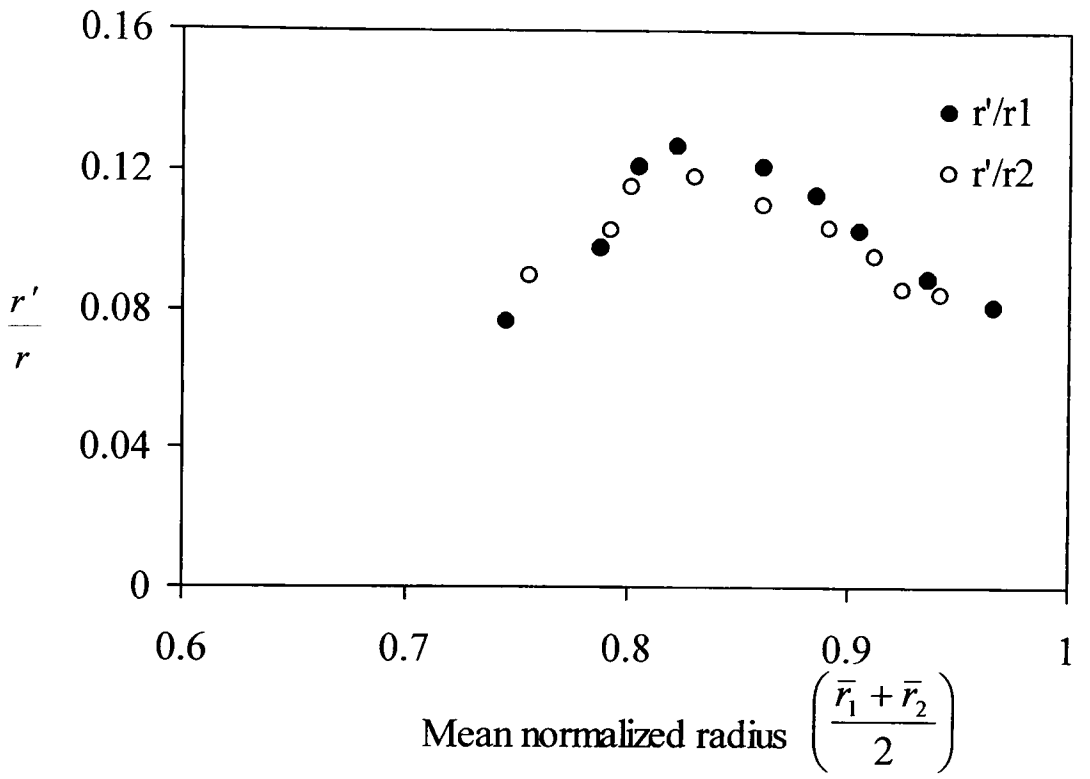

Fig. 4.9. Normalized rms flame front radii for twin imploding turbulent flames for iso-octane – air mixture, $\phi = 1.4$, $p_o = 0.5$ MPa, $T_o = 358$ K, $u' = 3$ m/s.

4.5.2 Effects of V_r for Laminar Flames

The residual volume of unburned gas, V_r, is given by Eq. 4.18. As explained in Section 4.3, this volume, which changes with time, is that residing in recesses of windows and behind the apparent, photographed, flame front minus the volume occupied by parts of the fans inside the apparent volume of unburned gas. With $R_o = 192.78$ mm and $R = 190$ mm, the normalized values $\bar{V}_r = V_r/4/3\pi R^3$ given by Eq. 4.18 are shown in Fig. 4.10 plotted against the mean normalized radius for laminar flames in different mixtures, at different pressures.

The general slow decrease in $\bar{V}_r$ with increasing radius is due to the burning of gas in the windows recesses. At a given mean radius the volume of parts of the fans inside the apparent volume of unburned gas is likely to be the same. The decrease in $\bar{V}_r$ with pressure is most possibly due to the associated decrease in flame thickness.

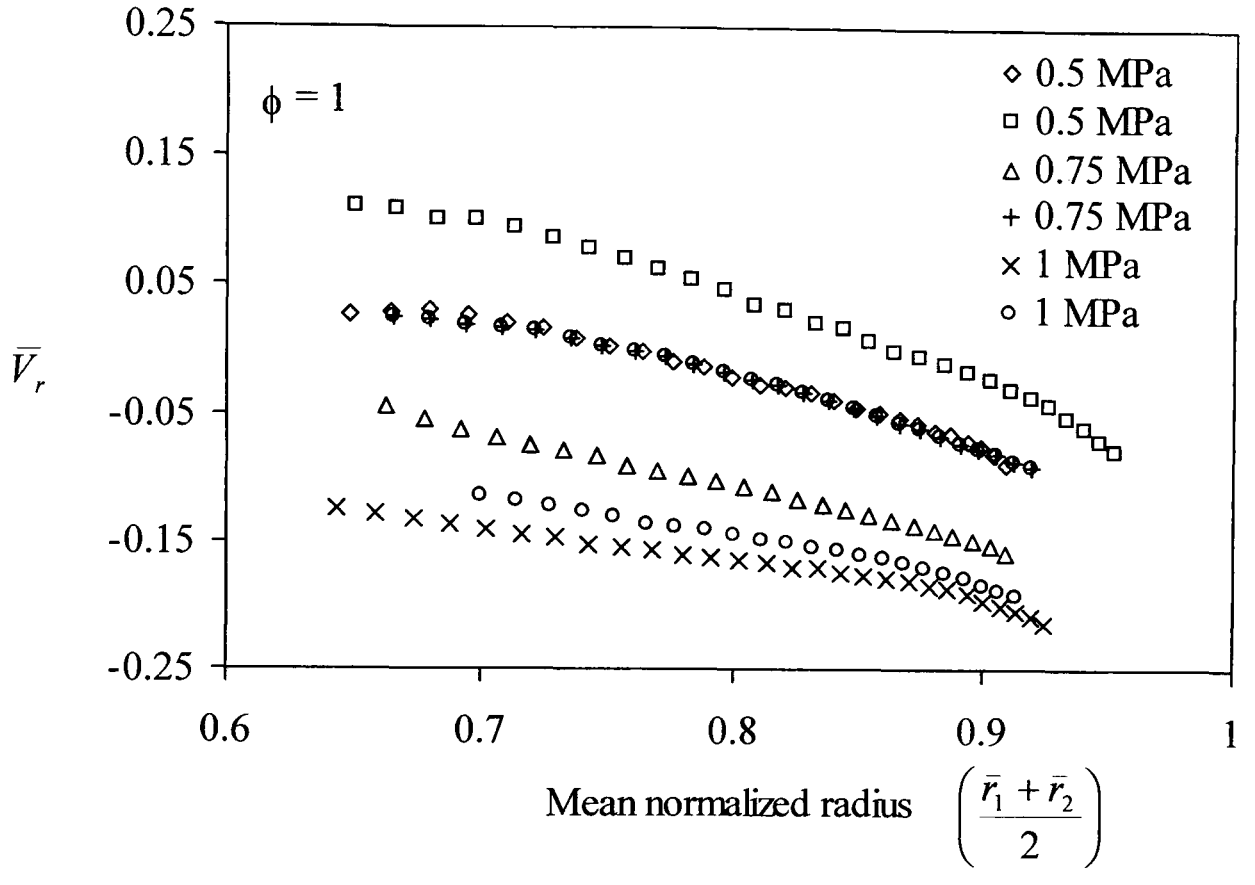

Fig. 4.10. Variation of $\bar{V}_r$ with mean normalized radius for initially laminar flames of stoichiometric iso-octane – air, at different initial pressures and an initial temperature of 358 K.

4.5.3 Comparison of Laminar Burning Velocity Obtained by the Two Expressions

Values of laminar burning velocity obtained from the expressions, Eqs. (4.14) and (4.19) are shown, plotted against time from ignition, in Fig 4.11. Both of the full lines show values allowing for $\bar{V}_r$. The broken lines show values when the effect of V_r is neglected. It can be seen that it is important to allow for this effect. When this was done there was reasonable agreement between the two expressions for burning velocity and this was found to be generally so in all explosions. There was evidence of a relatively low frequency flame oscillation and this also appeared in many explosions.

In the early stages, when the flame radii are relatively small, there is a greater difference in the two values of u_n. This would appear to be associated with greater error in the measurement of flame radii when they first come into view through the windows.

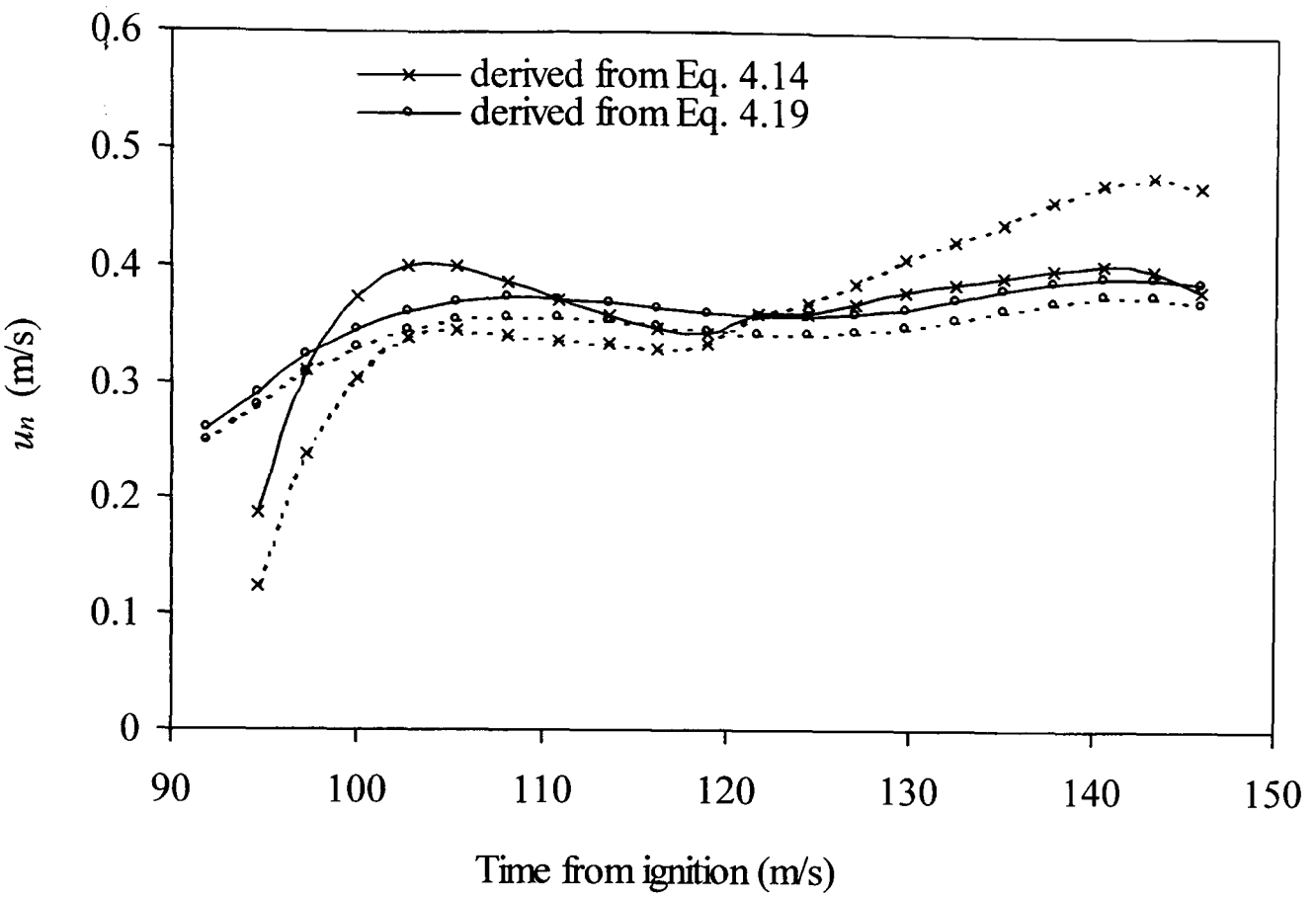

Fig. 4.11. Variations of burning velocity with time from ignition for iso-octane mixture, ϕ = 0.8, p_o = 0.5 MPa, T_o = 358 K, using Eqs. (4.14) and (4.19). Broken curves: no allowance for V_r.

4.5.4 Effects of V_r for Turbulent Flames

The V_r values for turbulent flames were deduced in such a way that sectors of circles were fitted to the observed flame-fronts and virtual centers were deduced. Results for the turbulent flames are shown in Fig. 4.12. Here there is a *decrease* in $\overline{V_r}$ as u' is increased. The values of $\overline{V_r}$ became significantly less than those observed in laminar explosions. The extent of this represents a decrease in the volume of unburned gas, beyond that due to the volume of parts of the fans. This can only be attributed to a greater volume of burned gas than is suggested by the flame radii. Whereas laminar flames tend to propagate from a point source, turbulent flames initiated close to the wall would spread along the wall of the bomb. As a result, the assumed spherical surface as the flames developed would be centered outside the vessel wall. It can be seen from Fig. 4.13 that this would result in the deduced increase in the volume of burned gas and decrease in the volume of unburned gas.

With turbulent flames the definition of a flame radius is much more difficult than with laminar flames. Measurements of flame radii, centered beyond the vessel wall were compatible with the

observed flame front. However, because of the wrinkled nature of flames, measurements of burned gas volume from flame radii were less reliable than they were with laminar flames. Hence, recourse to the pressure measurement method became more important to find the amount of gas burned. This is fully explained in the next Section.

For a given mean radius the value of V_r was noted for the comparable laminar explosion. The difference between this and the smaller value of $\overline{V}_r$ in the turbulent explosion gave the additional volume of gas burned in the latter.

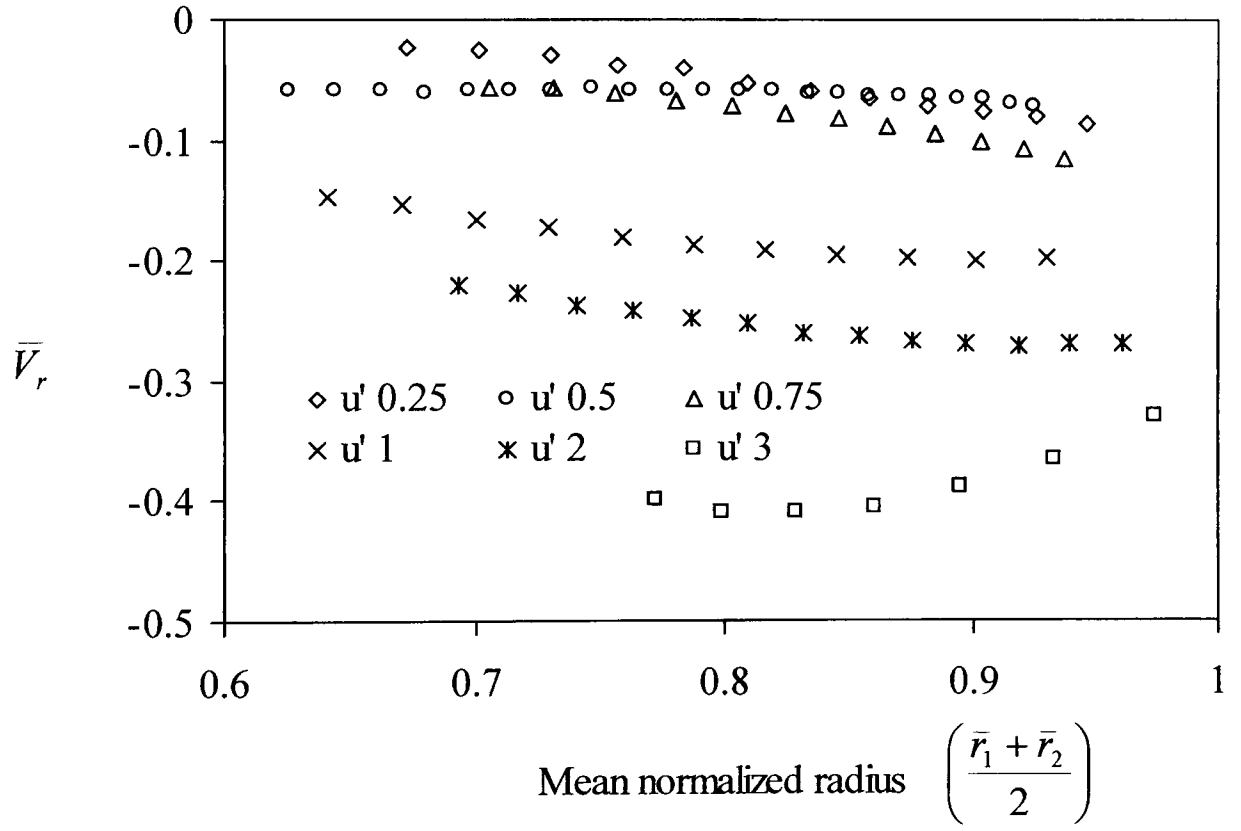

Fig. 4.12. Variation of $\overline{V}_r$ with mean radius in turbulent flames for different values of u' (m/s), p_o = 0.75 MPa, T_o = 358 K.

4.5.5 Burned Gas Volume and Flame Area Correction for Turbulent Conditions

Here the burned gas volume and flame area are derived for flame radii centered *outside* the inner wall of the spherical vessel. This condition arises when the burned gas volume exceeds that which is possible when the radii are centered at the wall. The geometry is shown in Fig. 4.13. The flame radius is now r_v, while the r is the radius if it were centered at the wall. This is shown by the broken curve. The new centre for the radius of

the burned cusp is a distance kR along the axis of symmetry from the centre of the spherical bomb. It can be seen that the new radius, r_v, decreases the volume of unburned gas. The angles α' and θ' are defined on the figure. Clearly,

$$r_v - r = kR - R \tag{4.20}$$

$$r_v \cos\alpha' + R\cos\theta' = k\,R \tag{4.21}$$

$$R\sin\theta' = r_v \sin\alpha' \tag{4.22}$$

from the initial expression for a and b in Section 4.2

$$a' = \left(\pi R^3/3\right)\left[2 - \cos\theta'\left(3 - \cos^2\theta'\right)\right] \tag{4.23}$$

$$b' = \left(\pi R^3 \bar{r}_v/3\right)\left[2 - \cos\alpha'\left(3 - \cos^2\alpha'\right)\right] \tag{4.24}$$

where $\bar{r}_v = r_v / R$.

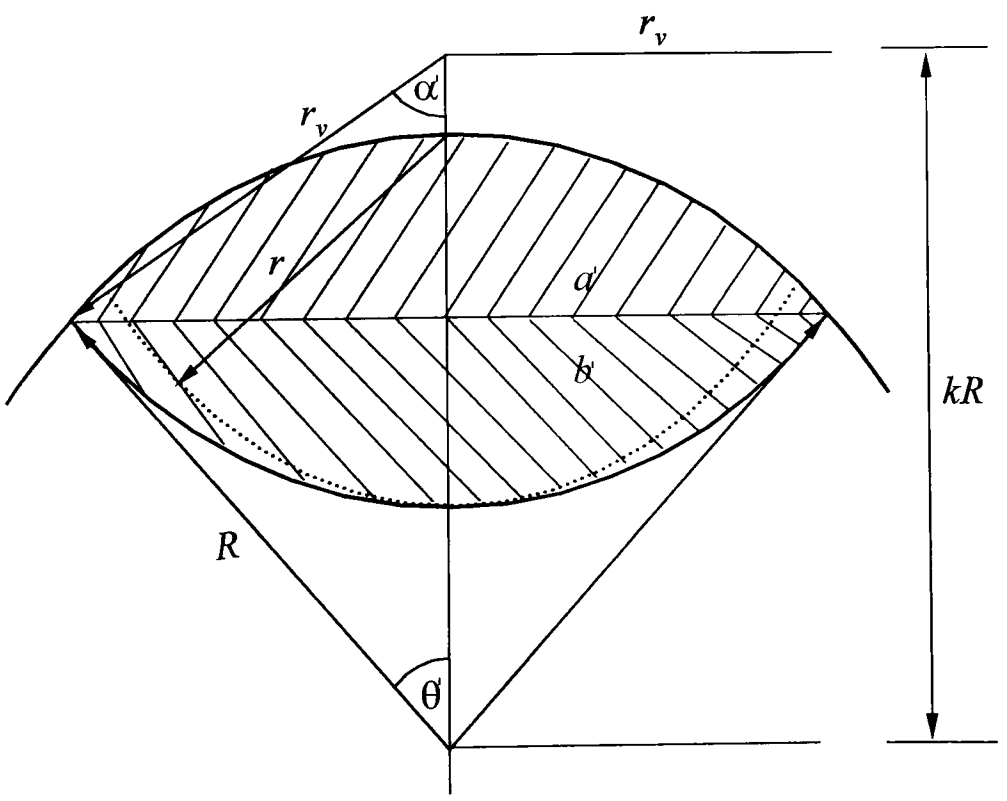

Fig. 4.13. Flame front correction for turbulent conditions.

From Eq. (4.22) $\quad 1 - \cos^2\theta' = \bar{r}_v^2\left(1 - \cos^2\alpha'\right)$ (4.25)

From Eq. (4.21) $\quad \cos\alpha' = \left(k - \cos\theta'\right)/\bar{r}_v$ (4.26)

From Eqs. (4.25) and (4.26)

$$1 - \cos^2\theta' = \bar{r}_v^2\left[1 - \left(k - \cos\theta'\right)^2/\bar{r}_v\right]$$

$$= \bar{r}_v^2 - k^2 - \cos^2\theta' + 2k\cos\theta'$$

Hence $\cos\theta' = \left(1-\bar{r}_v^2+k^2\right)/2k$ (4.27)

From Eq. (4.20) $\bar{r}_v = \bar{r}+(k-1)$ (4.28)

Equation (4.26) and (4.27) give

$\cos\alpha' = \left(2k^2-1+\bar{r}_v^2-k^2\right)/2k\bar{r}_v$ (4.29)

$\cos\alpha' = \left(k^2-1+\bar{r}_v^2\right)/2k\bar{r}_v$ (4.30)

From Eq. (4.8), with r centered in the vessel wall

$(a+b)\left(\pi R^3/3\right)^{-1} = 2\bar{r}^3-3\bar{r}^4/4$ (4.31)

$= 2\left(\bar{r}_v+1-k\right)^3-3\left(\bar{r}_v+1-k\right)^4/4$ (4.32)

invoking Eq. (4.28).

From Eqs. (4.23) and (4.27)

$$a'\left(\pi R^3/3\right)^{-1} = 2-\left(\frac{1-\bar{r}_v^2+k^2}{2k}\right)\left[3-\left(\frac{1-\bar{r}_v^2+k^2}{2k}\right)^2\right] \quad (4.33)$$

From Eq. (4.24) and (4.29)

$$b'\left(\pi R^3/3\right)^{-1} = \bar{r}_v^3\left[2-\left(\frac{k^2-1+\bar{r}_v^2}{2k\bar{r}}\right)\right]\left[3-\left(\frac{k^2-1+\bar{r}_v^2}{2k\bar{r}_v}\right)^2\right] \quad (4.34)$$

For a given value of r let $V_{r\ell}$ be the net volume of 'residual' unburned gas in a laminar explosion. This is in excess of that in the equivalent turbulent explosion at the same distance, r, on the centre line in Fig. 4.13: namely a volume of 'residual' gas indicated by V_{rt}. Let $V_{u\ell}$ be the volume of unburned gas in a laminar explosion and V_{ut} that in a turbulent explosion for the same volume of r. (In the case of the turbulent explosion this is not a true cusp radius, only the distance from the point of ignition to the intersection of the cusp with the centre line in Fig. 4.13). If Eq. 4.11 is divided by ρ_u, then

$$V_{u\ell} = 4\pi R^3/3+V_{r\ell}-\sum(a+b). \quad (4.35)$$

For the turbulent implosion if it is assumed the flame radii are given by r, and not r_v,

$$V_{ut} = 4\pi R^3/3+V_{rt}-\sum(a+b). \quad (4.36)$$

The decrease in volume of unburned gas in a turbulent implosion, as compared with a laminar implosion, is

$$V_{ut}-V_{u\ell} = V_{rt}-V_{r\ell} \quad (4.37)$$

Both V_{rt} and $V_{r\ell}$ were found from Eq. (4.18). The greater volume of burned gas in the turbulent implosion has been derived from the radius, r_v, centred outside the vessel and the volume $\sum (a' + b')$. Hence

$$V_{ut} = 4\pi R^3/3 + V'_{rt} - \sum(a' + b'). \tag{4.38}$$

The residual voume V'_{rt} now no longer expresses an enhanced volume of burned gas in the turbulent implosion: this is now accounted for within the $\sum (a' + b')$ term. Instead V'_{rt} reverts to expressing the recessed volumes of unburned gas at the windows minus any volume of unburned gas occupied by the fans. If the assumption is made for the same value of r in the two types of implosion that $V_{r\ell} = V'_{rt}$ then from Eqs. (4.36), (4.37) and (4.38)

$$V_{ut} - V_{u\ell} = \sum(a + b) - \sum(a' + b') = V_{rt} - V_{r\ell}. \tag{4.39}$$

The enhanced volume of burned gas in the turbulent explosion is found from the experimental results and is

$$\sum(a' + b') - \sum(a + b) = V_{r\ell} - V_{rt}. \tag{4.40}$$

It is conveniently normalized by the volume of burned gas, $\Sigma\ (a+b)$, for comparable values of r to give an enhancement burned volume factor, B. This factor was found experimentally for each radius during the explosion. The factor can also be derived analytically. For convenience it is assumed that the radii of the two kernels are the same. This assumption is not restrictive for present purposes. Hence

$$B = \frac{2(a'+b') - 2(a+b)}{2(a+b)}$$

$$\frac{2 - \left(\dfrac{1-\bar{r}_v^2+k^2}{2k}\right)\left[3 - \left(\dfrac{1-\bar{r}_v^2+k^2}{2k}\right)^2\right]}{2(\bar{r}_v+1-k)^3 - 3(\bar{r}_v+1-k)^4/4} +$$

$$\frac{\left\{\bar{r}_v^3\left(2 - \left(\dfrac{k^2-1+\bar{r}_v^2}{2k\bar{r}_v}\right)\left[3 - \left(\dfrac{k^2-1+\bar{r}_v^2}{2k\bar{r}_v}\right)^2\right]\right)\right\}}{2(\bar{r}_v+1-k)^3 - 3(\bar{r}_v+1-k)^4/4} - 1 = \frac{V_{r\ell} - V_{rt}}{2(a+b)} \tag{4.41}$$

4.5.6 Correction to Turbulent Burning Velocities Measured with Radii Centred at the Wall

From Eq. (4.10), with a flame of radius, r, the area of the flame front, A, is given by

$$A/2\pi R^2 = \bar{r}^2\left(1-\bar{r}/2\right) \tag{4.42}$$

$$=\left(\bar{r}_v-(k-1)\right)^2\left(1+k-\bar{r}_v\right)/2 \quad \text{, from Eq. (4.28).} \tag{4.43}$$

Similarly, with the flame radius, r_v, the area of the flame front, A', is given by

$$A'/2\pi R^2 = \bar{r}_v^2\left(1-\cos\alpha'\right)=\bar{r}_v^2\left(1-\left|k^2-1+\bar{r}_v^2\right|/2k\bar{r}_v\right). \tag{4.44}$$

Again, assuming the radii of the two kernels are the same

$$\frac{A'}{A}=\frac{\bar{r}_v^2\left(1-\left(k^2-1+\bar{r}_v^2\right)/2k\bar{r}_v\right)}{\left(\bar{r}_v-(k-1)\right)^2\left(1+k-\bar{r}_v\right)/2}. \tag{4.45}$$

Equations (4.41) and (4.45) enable A'/A to be plotted against B for different values of k and $\bar{r}_v$. This is done in Fig. 4.14. The broken lines are for values of k equal to 1, 1.2, 1.3, 1.4, 1.6, 1.8 and 2.0. The lines are for values of $\bar{r}$ (= 1- k + $\bar{r}_v$).

Because $A' > A$, when the area of the flame front was taken to be A the value of u_t was overestimated. It should correspond to the area A' and be reduced by dividing A'/A to give a more accurate value. The procedure adopted was to evaluate $B = (V_{r\ell} - V_{rt}) / \Sigma (a+b)$ at different values of $\bar{r}$ from the experimental values of V_r for the turbulent explosion and a laminar explosion. From the known values of B and $\bar{r}$, the flame area correction factor A'/A was readily obtained from Fig. 4.14.

Values of turbulent burning velocity based on the flame radius being centered at the wall of the vessel are given in Chapter 7.2. These are indicated by the symbol u'_t. When these values are corrected using the measured values of V_r they are indicated by the symbol u_t.

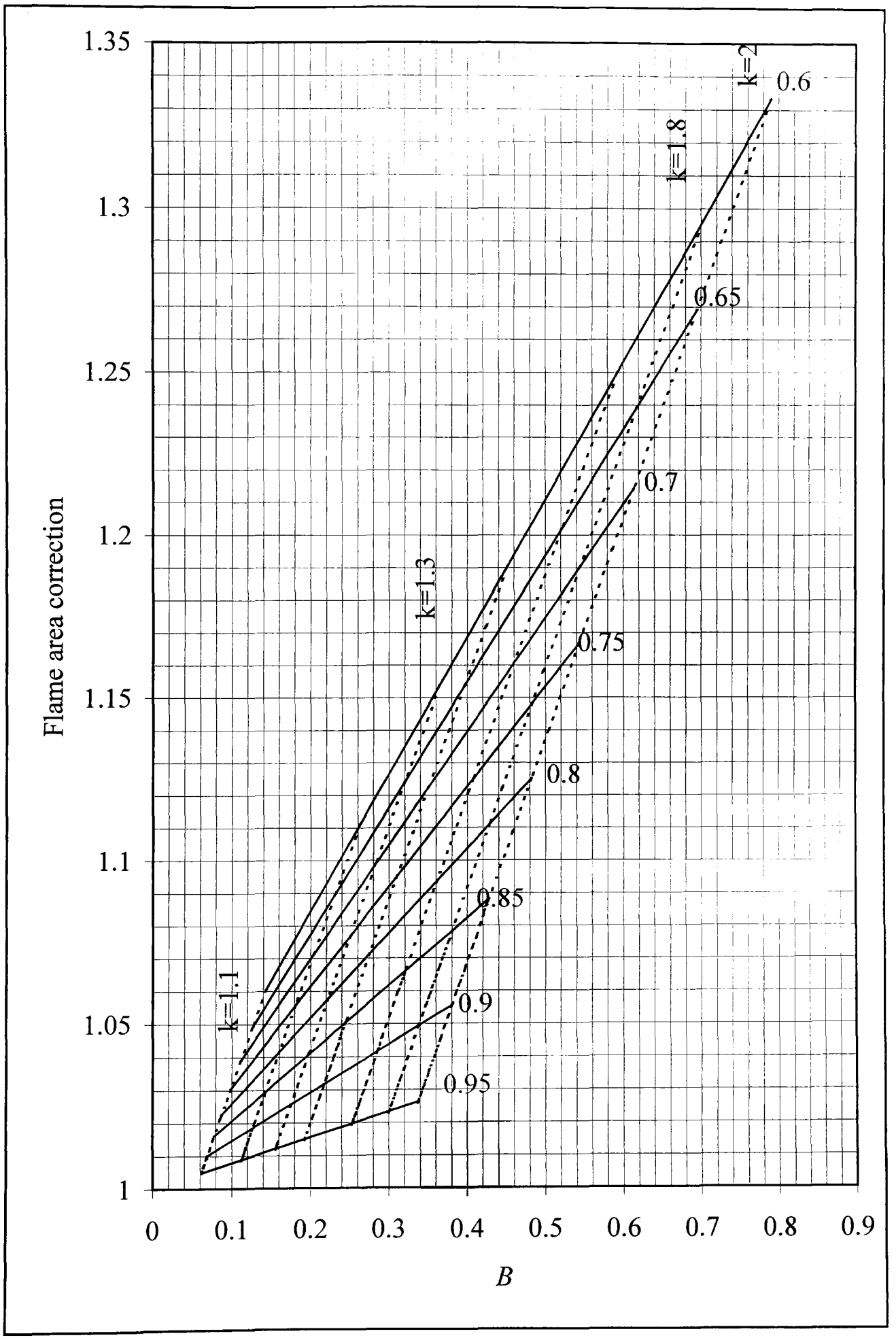

Fig. 4.14. Flame area correction chart for turbulent conditions, Full lines give $\bar{r}$.

Chapter 5

Development of Laminar Flame Instabilities and their Effect on Burning Velocities

5.1 Causes of Instabilities

The study of the phenomena of flame instability goes back many years. Darrieus (1938), Landau (1944) and Landau & Lifshitz (1987), showed that the propagation at a constant speed of a wave of density discontinuity creates a hydrodynamic instability. A flame advancing into unburned gas comprises such a surface. In the models of these researchers, the structure of the flame was neglected and, consequently, thermo-diffusive effects were also neglected. The instability was explained by considering the gas motion relative to the wave. When cold reactants (unburned gas) move into the crest of a flame front they diverge and this locally increases the pressure. Conversely, when the oncoming cold gases approach the trough of the flame front they converge and this motion locally decreases the pressure. These localized pressure changes deform the flame surface and, as a consequence, the overall burning velocity is increased. This type of instability, known as a Darrieus-Landau instability, results from the interaction of the flame with the hydrodynamic disturbances. This mechanism was thought to be responsible for the wrinkled, or cellular, flames structures that have been observed by several experimentalists (Lind *et al.*, 1977, Ivashchenko *et al.*, 1978).

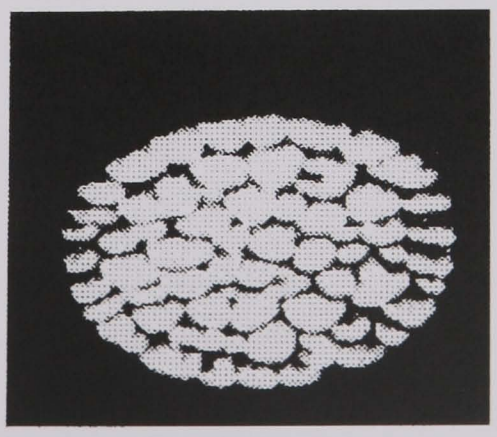

Fig. 5.1. Photographic image of a cellular rich propane/air/nitrogen flame, (Markstein, 1964).

Cellular flames have been studied in both plane flames (Markstein, 1951, Mitani *et al.*, 1980), and spherical flames (Manton *et al.*, 1952, Troshin *et al.*, 1955, and Palm-Leis *et al.*, 1969). Cells were observed to form with rich mixtures of heavy hydrocarbons, and lean mixtures of lighter methane and hydrogen. As the understanding of flame structure increased, it began to be recognised that thermo-diffusive phenomena must be important. These involve the competing effects of heat conduction from, and reactant diffusion towards, the reaction zone. In unstable spherical explosion flames, a wave-like deformation develops at the leading edge. A coherent cellular structure within a stationary flame on a burner is shown in Fig. 5.1.

The thermo-diffusive mechanism for such cellularity is indicated in Fig. 5.2. With a wavy flame front, there is a diverging conductive heat flux away from the flame surface into the cold unburned gas (reactant) ahead of it and a converging diffusive flux of the deficient reactant into the flame surface. The relationship between the conductive heat flux and diffusive flux in terms of magnitudes plays a main role in characterizing the flame as either stable or unstable, depending on which one dominates. Clearly, the Lewis number, $Le = \alpha / D$, the ratio of thermal to mass diffusivity, plays an important role. When the mass diffusivity of the deficient reactant is sufficiently greater than the thermal diffusivity, $Le < 1$, the flame front is more likely to be unstable. Conversely if $Le > 1$ the flame tends to be stable.

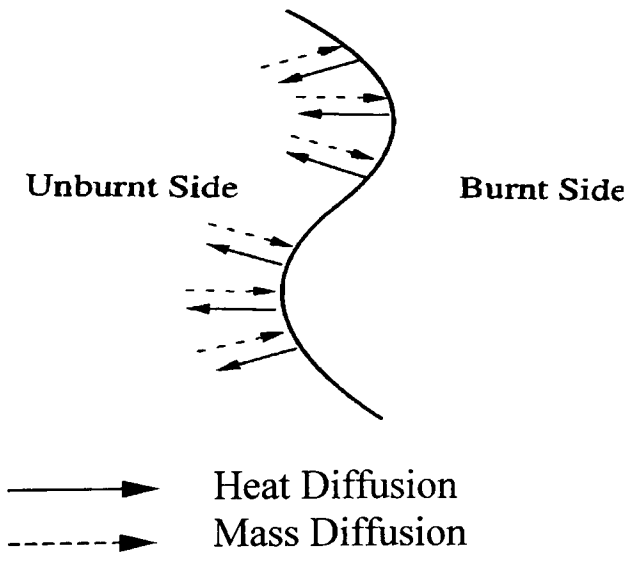

Fig. 5.2. Schematic mechanism of diffusional–thermal cellular instability, (Law *et al.*, 2000).

Gostintsev *et al.* (1988) have studied large hemispherical flames, and concluded that at high values of Peclet number (flame radius normalized by flame thickness) there was a transition to a very unstable cellular flame at a critical Peclet number. After the transition, they expressed the flame radius, r, as a function of time by the following relationship:

$$r = r_o + At^{1.5} \tag{5.1}$$

Here r_o is an arbitrary flame radius at a time $t = 0$ and A is a constant that depends upon the mixture (Bradley, 1999). This temporal dependency might be expected from flame surface area fractal considerations.

Below the critical Peclet number the exponent of t was less than 1.5. Experimental studies (Bradley *et al.*, 1998 and Bradley, 2002), have shown that a sharp transition to a fully developed cellular flame, with associated flame acceleration, occurs at a significantly lower critical value of Pe than suggested by Gostinstev *et al.*

5.2 More Recent Fundamental Studies of Explosion Flame Instabilities

In addition to the experimental studies, theoretical studies have also been conducted by (Sivashinsky, 1977, 1983), and these have given a satisfactory general explanation of the experimental observations. Sivashinsky's equations have focused on the evolution of the flame surface. Filyand *et al.* (1994) gave a qualitative description of the flame wrinkling and demonstrated the dependence of the flame speed upon $t^{1/2}$. Generally such approaches underestimate the flame speed. Cambray *et al.* (1996) suggested that, with regards to the causes of cell splitting, the theoretical understanding of this phenomenon deteriorates as Pe exceeds the critical value. Ashurst (1997) used a potential flow assumption combined with two-dimensional Lagrangian simulations to derive an expression for flame propagation that again confirmed the flame speed dependency upon $t^{1/2}$.

In experimental studies of lean propane–air closed vessel explosions Groff (1983) observed that the onset of a cellular flame structure occurred somewhat later than was theoretically predicted. This was also found to be so by Bradley and Harper (1994), while Gu *et.al.* (2000), in their studies of bomb explosions, proposed a correlation

between the Markstein number of the mixture and the critical Peclet number, Pe_{cl}, for the onset of flame cellularity.

Of particular relevance to the present studies, Bechtold and Matalon, (1987) have presented a comprehensive linear instability theory for spherical explosion flames. The Markstein number was not explicit in this theory, but it was derived from the other employed parameters by Bradley and Harper, (1994). It is possible to derive a theoretical explosion peninsula, within which flames are unstable, of wave number plotted against Peclet number for different positive values of, Ma_{sr} and particular values of density ratio, ρ_u / ρ_b. Bradley (1999) and Bradley *et al.* (2000a) have derived such peninsulas in terms of the wave numbers, n_l and n_s of upper and lower unstable wavelengths, as shown in Fig. 5.3. Within the peninsula the amplitude of the flame disturbance is amplified. At the boundary wave numbers, there is neither amplification nor attenuation of the disturbance. Outside the peninsula the flame is stable. It can be seen that the range of unstable wave numbers increases with an increase in Peclet number, Pe, and a decrease in the strain rate Markstein number, Ma_{sr}.

Large values of Pe can arise in large atmospheric explosions. They also can arise at higher pressures, such as occur in engines, due to the smaller values of δ_ℓ. A higher pressure also decreases Ma_{sr} (Bradley *et al.*, 1998, Gu *et al.*, 2000, Bradley *et al.*, 1996, and Aung *et al.*, 2002). Of particular relevance to the present thesis, the associated instabilities create a continually increasing burning velocity. Tentative estimates of the magnitudes of this, due to increases in both flame radius and pressure are given in Bradley (2000). The Bechtold and Matalon theory shows that only when a critical value of Pe, indicated by Pe_{cr}, wave number n_{cr}, has been attained can instabilities develop (Bradley, 2000). It can be seen from Fig. 5.3 that Pe_{cr} decreases with Ma_{sr}.

Unfortunately, the experimental data from large scale and laboratory bomb explosions are not in complete quantitative agreement with the theory. The experiments show that a cellular structure only develops fully, through fissioning of a few larger into smaller cells, at a second critical value of Pe_{cl}, that is greater than Pe_{cr} (Bradley, 1999 and Bradley *et al.*, 1998). This also implies that instabilities only develop below a critical

value of the Karlovitz stretch factor. In general, an increase in flame stretch rate stabilises a flame with a particular value of Ma_{sr}.

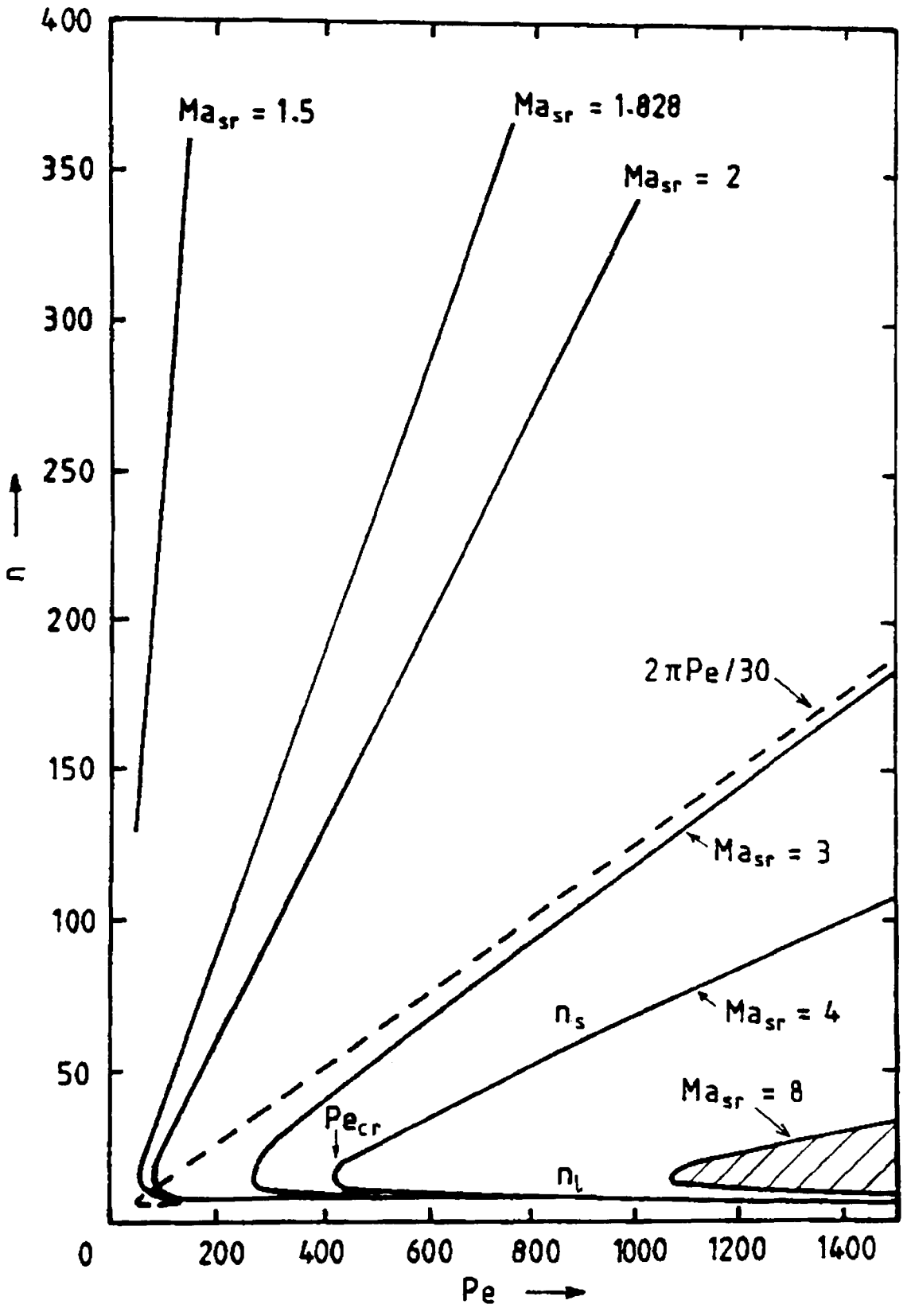

Fig. 5.3. Theoretical wave number, n, at limits of stability for different Ma_{sr}, as a function of Peclet number, (Bradley *et al.*, 2000a).

5.3 Prediction of Burning Velocities of Initially Laminar Unstable Flames

The approach adopted in the present work was to combine flame instability theory with the assumption of fractal wrinkling of the flame surface to obtain a burning velocity. It was first necessary to find the range of flame unstable wavelengths. Unstable spherical explosion flames at constant pressure first begin to show cracks propagating across their surfaces at critical Peclet numbers that are close to the theoretically predicted values for the onset of flame instability, Pe_{cr} (Bradley and Harper, 1994). However, full cellularity and an associated increase in flame speed only occur at the higher critical Peclet number, Pe_{cl}, (Bradley *et al.*, 2000a, and Gu *et al.*, 2000). It is as if, in practice, there is a lag in the full development of the instability. In particular, the theoretical wave number, n_s, of the

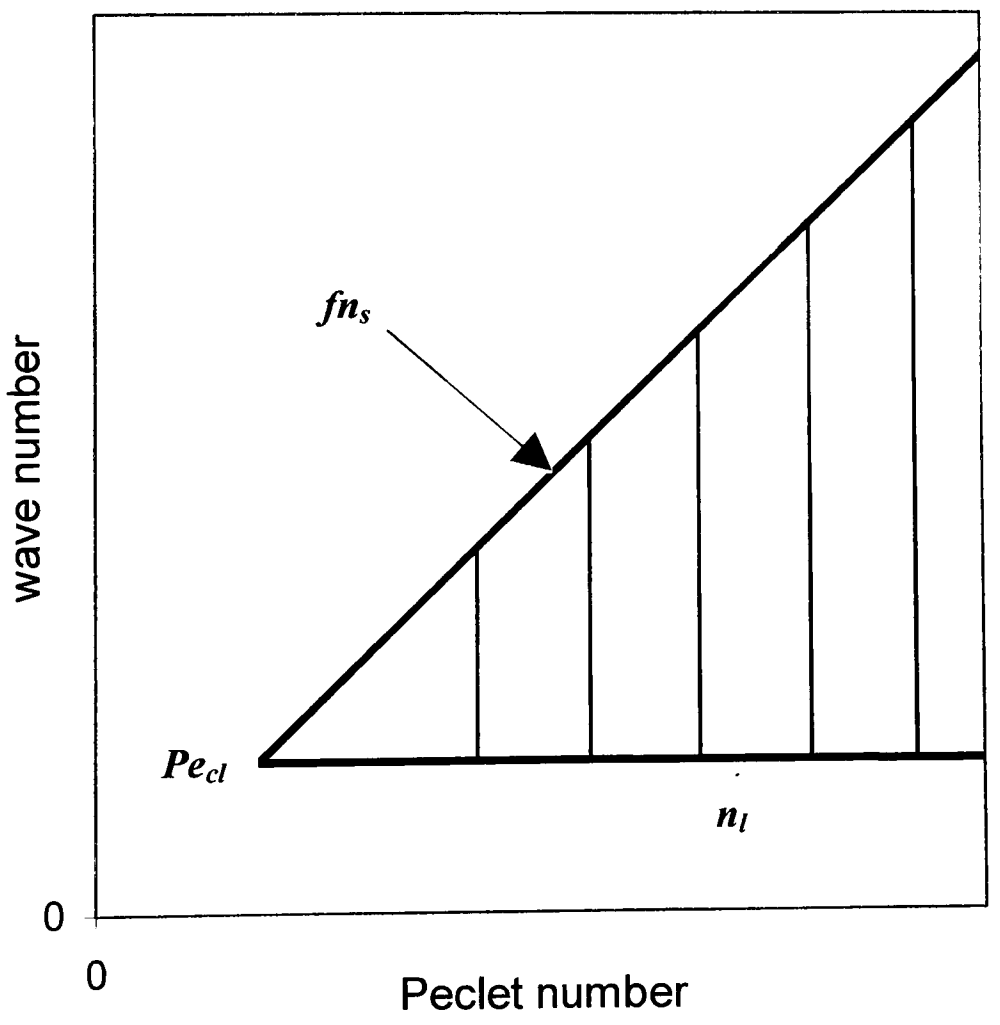

Fig. 5.4. Instability peninsula, with limiting wave numbers fn_s and n_l. The critical, cellular, Peclet number, Pe_{cl} is at the tip of the peninsula.

smallest unstable wavelength or inner cut-off, given by Bechtold and Matalon (1987). is reduced. There is no comparable change in the wave number, n_l, of the longest unstable wavelength, which changes much less with Pe. Wave numbers are related to wavelengths by

$$n = 2\pi Pe / \Lambda \tag{5.2}$$

Where Λ is the wave length associated with any wave number n, normalised by δ_t.

To allow for the lag effect, Bradley (1999) proposed, that the theoretical wave number, n_s, assumes a value of fn_s, where f is a numerical constant less than one. The range of unstable wavelengths that contribute to the flame wrinkling only exists beyond the tip of the instability peninsula where $Pe \geq Pe_{cl}$. The value of Pe_{cl} is obtained experimentally by observing when full cellularity has developed and the flame speed begins to increase. An idealised and simplified instability peninsula for particular values of Ma_{sr} and ρ_u/ρ_b is shown in Fig. 5.4. This contrasts with the theoretical peninsula in Fig. 5.3. The tip condition enables f to be evaluated, because at Pe_{cl}, $(fn_s)_{cl}$ is equal to the wave number of the largest unstable wavelength, n_l, also, like n_s, given by the Bechtold – Matalon theory.

Throughout the present study this theory is, of necessity, supplemented by experimental findings, particularly at negative values of Ma_{sr}. Experimental values of Pe_{cl} have been correlated in terms of Ma_{sr} by Gu *et al.* (2000):

$$Pe_{cl} = 177 Ma_{sr} + 2177 \tag{5.3}$$

although this relationship is less reliable for negative values of Ma_{sr}. For these increasingly unstable flames, measurement of Pe_{cl} is easier than of Ma_{sr}.

For $Pe \geq Pe_{cl}$, because the theoretical relationship of n_s increases close to linearly with Pe, the largest unstable wave number at Pe is given by (Bradley, 1999)

$$(fn_s)_{Pe} = (fn_s)_{cl} + (Pe - Pe_{cl})\left(\frac{dfn_s}{dPe}\right)_{Pe} \tag{5.4}$$

The full theory of Bechtold and Matalon, (1987) is only valid for $\Lambda_s \geq 30$, which generally implies $Ma_{sr} \geq 3$. Within this regime the theory enabled $(df n_s/dPe)_{Pe}$ to be evaluated for the appropriate values of Ma_{sr} and ratio of unburned to burned gas density, ρ_u/ρ_b. The rate of increase (or decrease) of the amplitude of any flame instability was obtained for different values of n at a particular value of Pe. The highest wave number at which the rate became zero was n_s. The lowest wave number at which it became zero was n_l. Other such pairs of points were identified at different values of Pe.

For $Ma_{sr} < 3$ recourse was made to experimental findings concerning the cellular structures of unstable flames. In Bradley *et al.* (2000) these structures appeared to be in dynamic equilibrium. Small cells increased in size as a flame kernel grew. This decreased the localised flame stretch rate at a cell surface and, consequently, the cell became unstable. It re-stabilised by fissioning into smaller cells, with higher, stabilising, local stretch rates. Just prior to fissioning it was found that the wavelength of a localised cell, Λ_s, was close to that of the original flame kernel at the cellular Peclet number, Pe_{cl}. From Eq. 5.2, this consideration gives

$$\Lambda_s = 2\pi Pe_{cl}/(n_l)_{cl}, \tag{5.5}$$

With $n = fn_s$ and $\Lambda = \Lambda_s$ Eq. 5.2 gives

$$\left(\frac{dfn_s}{dPe}\right)_{Pe} = \frac{2\pi}{\Lambda_s} \tag{5.6}$$

from Eqs. 5.5 and 5.6

$$\left(\frac{dfn_s}{dPe}\right)_{Pe} = \frac{(n_l)_{cl}}{Pe_{cl}} \tag{5.7}$$

this expression was used for $Ma_{sr} \leq 3$.

Clearly, there must be a lower physico-chemical limit to the value of the wavelength of a localised cell, Λ_s, below which a wrinkled flame sheet cannot be maintained. It might be surmised that this occurs at the order of the flame thickness and the diagnostic

studies in Bradley *et al.* (2000) suggested an inner cut-off, given by the wavelength of the smallest cells, of $\Lambda_s \approx 50$. With this inner cut-off, the maximum limiting value of $(dfn_s/dPe)_{Pe}$ at highly negative values of Ma_{sr}, from Eq. 5.6, is given by:

$$\left(\frac{dfn_s}{dPe}\right)_{Pe} = \frac{2\pi}{50} \tag{5.8}$$

The pressure remains constant in the theory of Bechtold and Matalon, (1987) and Bradley, (1999). This does not cover confined explosions, in which the pressure and unburned gas temperature are increasing, accompanied by associated decreases in δ_t and Ma_{sr}. Unburned gas temperatures were found from the measured pressures on the assumption of isentropic compression and in some instances Ma_{sr} could be found from previous measurement of it. Together with ρ_u/ρ_b, this enabled $(dfn_s/dPe)_{Pe}$ to be found from the theory of Bechtold and Matalon (1987) and Bradley (1999), at the different values of Pe for $Ma_{sr} \geq 3$. During an explosion $(dfn_s/dPe)_{Pe}$ increased due to the decrease in Ma_{sr}. At lower values of Ma_{sr} either Eq. 5.7 or Eq. 5.8 was employed.

When $(dfn_s/dPe)_{Pe}$ was changing during a confined explosion, the highest unstable wave number $(fn_s)_{pe}$ at a given Pe was found from a quasi-steady state modification of Eq. 5.4:

$$(fn_s)_{Pe} = (fn_s)_{cl} + \int_{Pe_{cl}}^{Pe} \left(\frac{dfn_s}{dPe}\right)_{Pe} dPe \tag{5.9}$$

Pe was evaluated for the mean radius of the two kernels with $\delta_\ell = \nu/u_\ell$, where ν was the kinematic viscosity of the mixture. The value of u_ℓ was either known *a priori* or was evaluated by iteration.

The ratio of the limiting values of the unstable wave numbers is inversely proportional to that of the wavelengths. Fractal considerations previously employed by other workers and in Bradley (1999) gave the ratio of the fractal surface area with a resolution of the inner cut-off to that with a resolution of the outer cut-off off as $(fn_s/n_l)^{D-2}$, where D is the fractal dimension. A value of D = 7/3 has been employed for turbulent surface wrinkling (Bradley, 1992). The ratio of burning velocities with and without instabilities

is equal to that of the surface areas, provided flame stretch effects on localised burning velocities can be neglected. Hence, at Pe

$$F = \left(\frac{u_n}{u_\ell}\right)_{Pe} = \left(\frac{fn_s}{n_l}\right)_{Pe}^{1/3} \tag{5.10}$$

where F is a burning velocity enhancement factor that expresses the ratio of the burning velocity enhanced by instabilities to the laminar burning velocity at any instant. Theoretical values of n_l were found for appropriate values of Ma_{sr} and ρ_u/ρ_b and Pe. Equation 5.10 enabled values of u_ℓ to be derived from experimental measurements of u_n.

Chapter 6

Experimental Results From Initially Laminar Imploding Flames

6.1 Introduction

The present Chapter reports on the measurements of burning velocities, u_n, using the twin kernel technique described earlier, in the spherical bomb. The flames were initially laminar and the expressions for u_n are presented in Chapter 4. It is first necessary to obtain an expression for the amount of burned gas. Two approaches were employed for this, one based on geometrical considerations, the other on the fractional pressure rise. A knowledge of the flame area then enabled two expressions to give values of the burning velocity, u_n. The detailed procedure for deriving the laminar burning velocity, u_ℓ, from u_n allowing for instabilities, is described in Section 6.3. This procedure rests on the theoretical approaches of Chapter Five.

6.2 Measurements of Burning Velocity Using Imploding Method

Table 6.1 summarizes all these explosions, in terms of the fuel, equivalence ratio, initial pressure and temperature. The experimental results, presented in Figs. 6.1 to 6.25, appear at the end of the Chapter. All follow the same format. Each figure shows, plotted against time from ignition, (a) measured temporal variations of pressure and temperature, (b) radii of the two flame kernels, (c) flame speeds, $\partial r/\partial t$, and (d) values of u_n derived from both Eqs. (4.14) and (4.19), for the appropriate initial conditions. Equation (4.14) is based on the flame speeds and the unburned gas volume, while Eq. (4.19) is based on the unburned gas volume deduced from the pressure rise. The unburned gas temperatures during the explosions were obtained from the measured pressures, using the GASEQ codes (Morley, 2001) on the assumption of isentropic compression from the initial temperature and pressure of the reactants at ignition. In all cases V_r was found from Eq. (4.18) and the burning velocities obtained by the two methods were in close agreement. After the leading edges of the two kernels began to flatten, indicated by 'flat' on some of the figures, the method was no longer applicable.

Thereafter, values of u_n were obtained directly by the double kernel method. This gave the limiting burning velocity as the two kernels merged together. The filled triangles in the bottom right hand quadrant (d) indicates the burning velocity measured by this technique. The values often showed a continuation of the trends observed with the other two methods. All experiments were repeated at least once to check repeatability, which was generally good. Results from only one explosion are presented in this chapter. Those all repeated experiments are shown in Appendix B.

Fig. No	C_8H_{18} ϕ	p_o (MPa)	T_o (K)	Fig. No	C_8H_{18} ϕ	p_o (MPa)	T_o (K)
6.1	0.8	0.5	358	6.2	0.8	1	358
6.3	0.9	0.5	358	6.4	0.9	1	358
6.5	1.0	0.5	358	6.6	1.0	1	358
6.7	1.1	0.5	358	6.8	1.1	1	358
6.9	1.2	0.5	358	6.10	1.2	1	358
6.11	1.3	0.5	358	6.12	1.3	1	358
6.13	1.4	0.5	358	6.14	1.4	1	358
6.15	1.5	0.5	358	6.16	1.5	1	358
6.17	1.6	0.5	358	6.18	1.6	1	358
6.19	1	0.75	358	6.20	1.4	0.75	358
	CH_4						
6.21	1	0.1	298				
6.22	1	0.5	358				
	H_2						
6.23	0.3	0.5	358				
6.24	0.4	0.5	358				
6.25	0.5	0.5	358				

Table 6.1. Schedules of all laminar explosions during which measurements were made.

Having established the general consistency of the twin kernel implosion technique, it was first necessary to assess the reliability of deriving values of u_ℓ in this way. To do this, mixtures were exploded for which the values of u_ℓ, Ma_{sr} and Pe_{cl} were already known. Three mixtures were chosen for this purpose and the details of them are given below in Table 6.2.

Mixture	ϕ	p_o (MPa)	T_o (K)	Data for u_ℓ and Ma_{sr}
CH_4 - air	1.0	0.1	298	Gu *et al.*, (2000)
i-C_8H_{18} - air	1.0	0.5	358	Bradley *et al.*, (1998)
i-C_8H_{18} - air	0.8	0.5	358	Bradley *et al.*, (1998)

Table 6.2. Chosen mixtures to assess the reliability of deriving values of u_ℓ.

6.3 Derivation of Laminar Burning Velocity, u_ℓ, from u_n

The aim was to estimate the enhancement in the measured burning velocity u_n above u_ℓ that is a consequence of flame instabilities. This was done using the modified Bechtold and Matalon approach described in Chapter 5. This enabled values of laminar burning velocity, u_ℓ, to be obtained at the different temperatures and pressures during an explosion.

The methodology was first checked using the CH_4-air mixture, ϕ = 1.0, initial pressure 0.1 MPa and temperature 298 K, for which u_ℓ and Ma_{sr} had been well characterised over the full range of pressures by Gu *et al.* (2000). The various measured experimental values for two explosions of methane –air mixture are given in Fig. 6.21, plotted against time from ignition. Schlieren images of the two kernels at an instance close to their making contact are given in Fig 6.26. The two sets of values of u_n, shown by different symbols in Fig. 6.27, are in reasonable agreement, giving some confirmation of the validity of the twin kernel analysis. Importantly, they are significantly greater than the values of laminar burning velocity measured by Gu *et al.* (2000), with central ignition

for the corresponding pressures and temperatures and shown by the dotted curves in Fig. 6.27. This confirmed that, once the critical Peclet number had been exceeded, the continually developing burning velocity, u_n, increasingly exceeded the value of u_ℓ at the same temperature and pressure.

This aspect was studied using Eqs. 5.2 to 5.10 and the instability theory. This theory was used to predict the unstable burning velocity, u_n, from the laminar burning velocity. Part of the processing spread sheet, for increasing values of pressure, p, in a single implosion is reproduced in Table 6.3. The procedure adopted was to find the isentropic temperature, column C6, of the unburned mixture at the measured pressure, p, given in column C3. GASEQ was used to find this temperature and also the kinematic viscosity, ν, from which the mean Peclet number, column C5, could be found from the measured mean radius and $\delta_\ell = \nu/u_\ell$. Values of u_ℓ, C4, were given by Gu *et al.* (2000) and those for Ma_{sr}, C2, also were obtained from this source. From the data in Gu *et al.* (2000) and the theoretical data in Bradley *et al.* (1996) these depended upon p and T, and are shown in column C2.

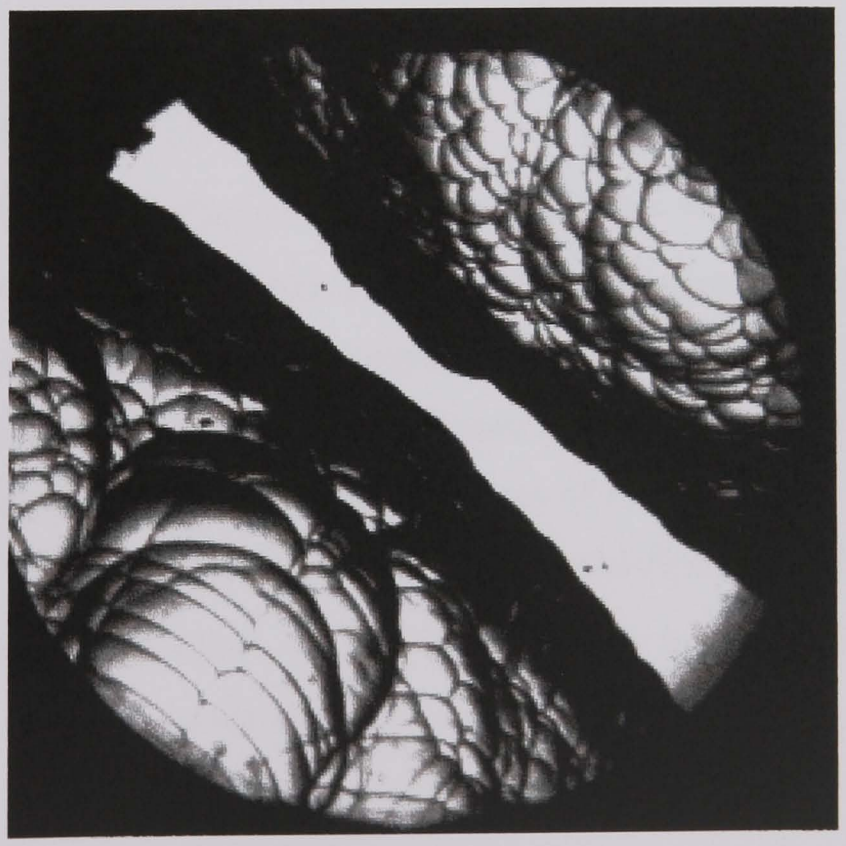

Fig. 6.26. Schlieren images of the two kernels close to making contact of stoichiometric CH_4-air initially at 0.1 MPa and 298 K, (p = 0.37 MPa, T = 430 K, t = 104.86 ms).

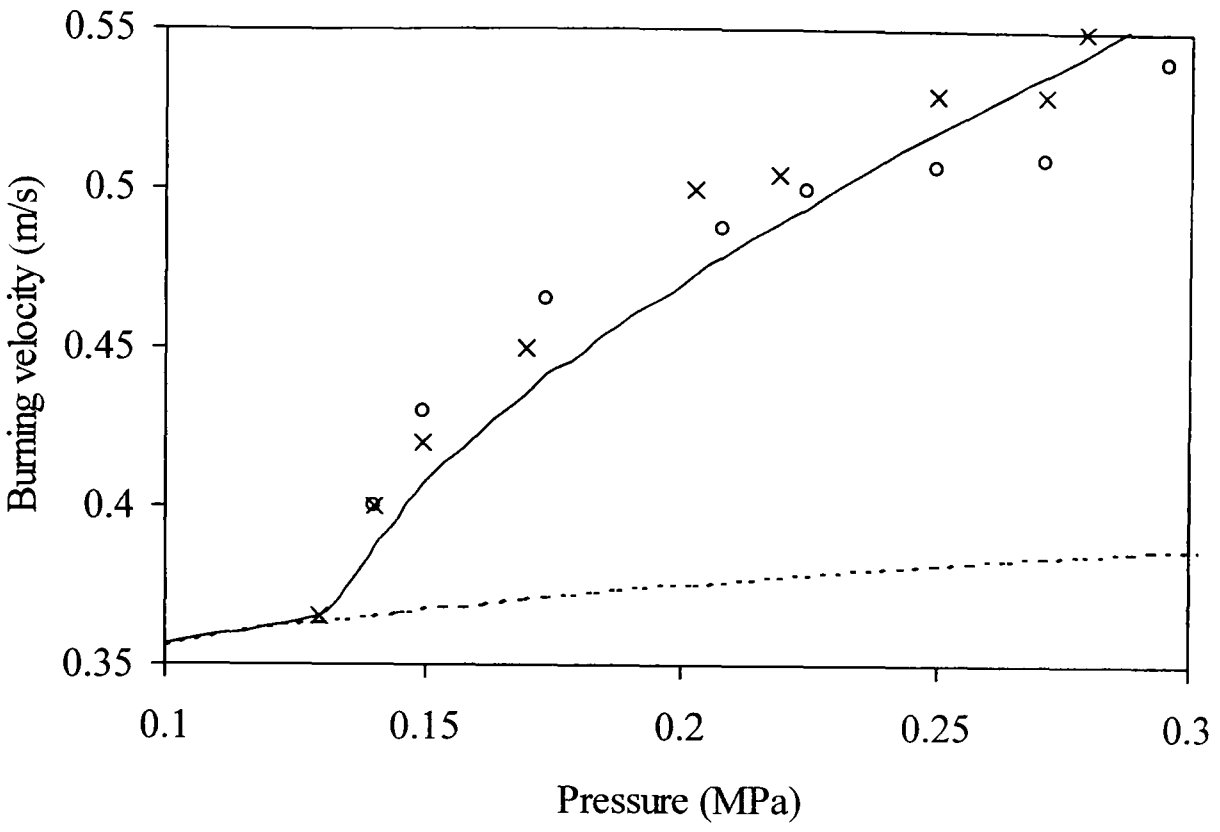

Fig. 6.27. Symbols: experimental values of u_n from two explosions of stoichiometric CH_4-air initially at 0.1 MPa and 298 K. Broken curve, values of u_ℓ from Gu *et al.* (2000), full line curve, predicted unstable burning velocities, u_n.

The Bechtold - Matalon, (1987) theory then was employed for the known values of ρ_u/ρ_b and Ma_{sr}. The value Pe_{cl} was found for each value of Ma_{sr} from Eq. 5.3 and $(n_\ell)_{cl}$ and $(n_s)_{cl}$ were evaluated as described in Chapter 5.3. Computations of $n_{s,}$ using the Bechtold - Matalon, theory over the appropriate range of Pe gave dfn_s/dPe. Shown in C7 is fn_s, evaluated from Eq 5.9 for the different values of Pe. From these, also utilising the theoretical values of n_l at the particular values of Pe in Eq. 5.10, the values of F, the burning velocity enhancement factor due to the instabilities, could be found from Eq. 5.10, see C8. The final column, C9, the product of u_ℓ in column C4 and F gives the theoretical value of the unstable burning velocity, $u_{n,}$ for each value of p and Pe. These predicted values are shown by the upper full line curve in Fig. 6.27 and are in good agreement with the experimental values measured in the two explosions and indicated by the symbols.

C1	C2	C3	C4	C5	C6	C7	C8	C9
dfn_s/dPe	Ma_{sr}	p (MPa)	u_l	Pe	T (K)	fn_s	F factor	u_n theory
	4	0.100	0.356	800	298	0.000	1.000	0.356
	4	0.120	0.362	2885	314	0.000	1.000	0.362
0.00245	4	0.130	0.364	2920	321	6.816	1.004	0.365
0.00246		0.135	0.364	3100	324	7.259	1.027	0.374
0.00247		0.141	0.366	3384.73	327.774	7.962	1.059	0.387
0.00247		0.144	0.366	3515.28	329.848	8.284	1.074	0.393
0.00247		0.145	0.367	3617.01	330.808	8.536	1.085	0.398
0.00247		0.147	0.367	3689.98	331.698	8.716	1.094	0.401
0.00248	3.5	0.150	0.368	3823.48	333.835	9.047	1.109	0.407
0.00248	3.5	0.154	0.368	3960	336.121	9.385	1.123	0.414
0.00248	3.5	0.158	0.369	4066.91	338.488	9.651	1.135	0.419
0.00249		0.162	0.370	4207.35	340.813	10.000	1.149	0.425
0.0025		0.165	0.370	4314.7	342.982	10.269	1.160	0.429
0.00251		0.170	0.371	4459.88	345.516	10.633	1.174	0.436
0.00252	3	0.174	0.372	4607.33	347.836	11.005	1.188	0.442
0.00252	3	0.179	0.373	4719.11	350.556	11.286	1.198	0.446
0.00252	3	0.183	0.373	4871.34	352.954	11.670	1.212	0.452
0.00252	3	0.188	0.374	4983.49	355.416	11.953	1.222	0.457
0.00252	3	0.193	0.375	5141.2	357.992	12.350	1.236	0.463
0.00252	3	0.198	0.375	5256.06	360.776	12.639	1.246	0.468
0.00253		0.203	0.376	5417.91	363.106	13.049	1.260	0.474
0.00255		0.208	0.377	5534.52	365.939	13.346	1.270	0.479
0.00257		0.214	0.378	5703.13	368.573	13.780	1.283	0.485
0.0026		0.219	0.378	5819.71	371.017	14.083	1.293	0.489
0.00263		0.225	0.379	5937.55	373.746	14.393	1.303	0.494
0.00266	1.25	0.230	0.380	6114.17	376.472	14.862	1.319	0.501
0.00269		0.237	0.381	6233.93	379.237	15.185	1.330	0.506
0.00271		0.243	0.381	6417.42	382.039	15.682	1.345	0.513
0.00273		0.250	0.382	6546.83	385.049	16.035	1.356	0.518
0.00275		0.257	0.383	6697.17	388.042	16.449	1.368	0.524
0.00281		0.264	0.384	6857.03	391.143	16.898	1.381	0.530
0.00288		0.271	0.385	7003.87	394.101	17.321	1.394	0.536
0.00296		0.279	0.386	7160.96	397.281	17.786	1.407	0.543
0.00305		0.288	0.387	7369.13	400.632	18.421	1.425	0.551
0.0031		0.296	0.387	7490.02	403.683	18.795	1.435	N/A
0.00313	-1.5	0.350	0.391	8000	422	20.392	1.475	N/A

Table 6.3. Data for predication of unstable burning velocity, u_n, from laminar burning velocity u_ℓ, using instability theory. CH_4 – air, $\phi = 1.0$, initial pressure and temperature, 0.1 MPa and 298 K.

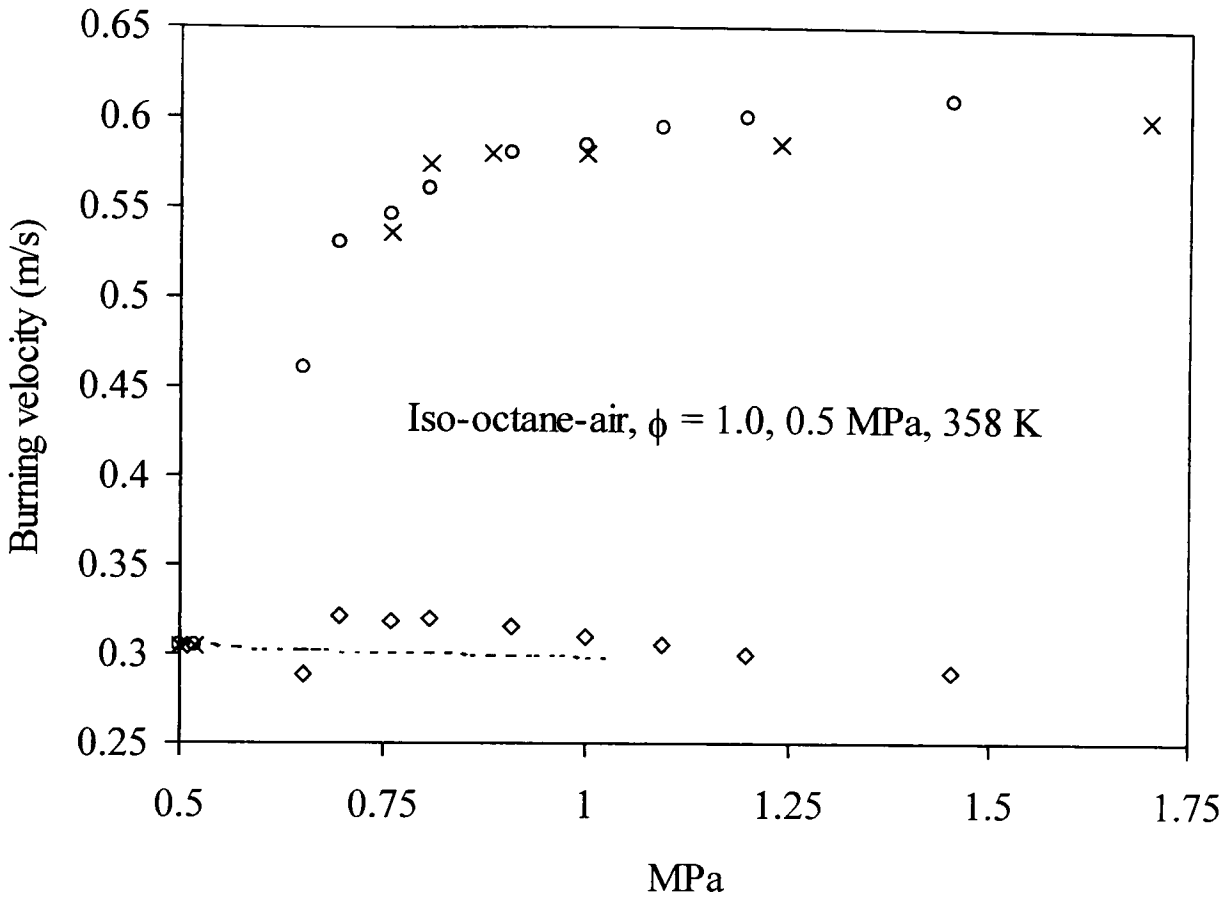

Fig. 6.28. Symbols: experimental values of u_n from two implosions of stoichiometric iso-octane-air initially at 0.5 MPa and 358 K, (upper symbols). Lower symbols show values of u_ℓ predicted from these compared with values from Bradley *et al.* (1998) (broken curve).

The second well-characterised mixture was iso-octane-air, ϕ = 1.0, initially at 0.5 MPa and 358 K. Values of u_ℓ and Ma_{sr} for the appropriate pressures and temperatures were known from the experimental measurements of Bradley *et al.* (1998). The upper symbols in Fig. 6.28 are the experimental values of u_n, while the symbols below indicate the derived values of u_ℓ, obtained from a value of F, derived as just described. These derived values compare well with those measured by Bradley *et al.* (1998), at up to 1 MPa, for different temperatures and shown by the broken curve in Fig. 6. 28.

The third test condition was for the iso-octane mixture, ϕ = 0.8, listed in Table 6.2. Results for this mixture are given in Fig. 6.29. As with the stoichiometric iso-octane – air mixture, values of u_ℓ were obtained from the modified Bechtold – Matalon theory and are shown by the lower symbols in the figure. As before, these compare well with the values shown by the broken line, again measured in central ignition explosions.

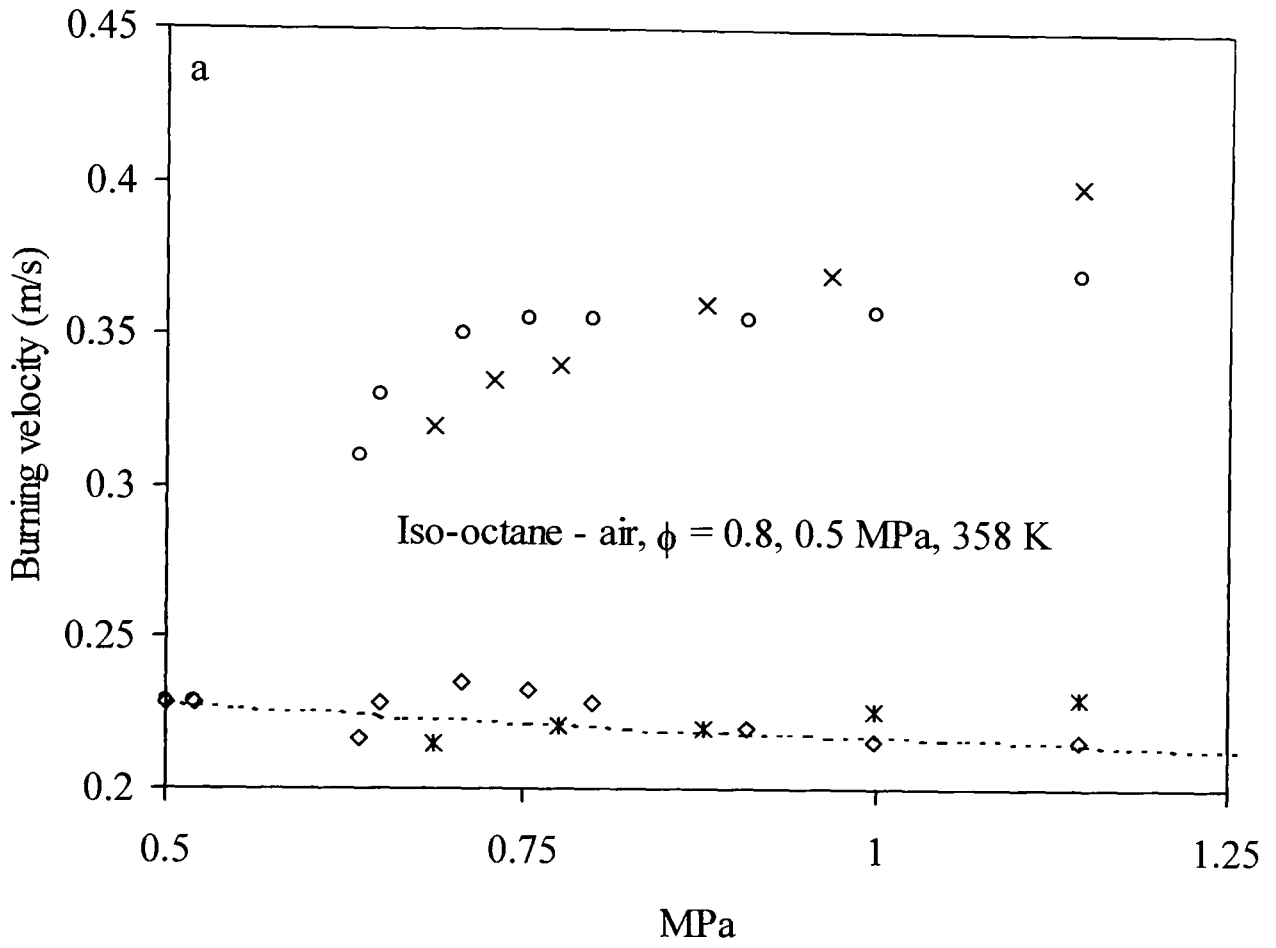

Fig. 6.29. Symbols: experimental values of u_n from two implosions of of lean ($\phi = 0.8$) iso-octane-air initially at 0.5 MPa and 358 K, (upper symbols). Lower symbols show values of u_ℓ predicted from these, compared with values from Bradley *et al.* (1998) (broken curve).

Because of these satisfactory predictions in Figs. 6.27 to 6.29, it was decided to extend this approach to process a wide range of measurements, covering equivalence ratios, from $\phi = 0.8$ up to 1.4 for iso-octane – air mixtures and $\phi = 0.3$ to 0.5 for hydrogen – air mixtures to yield values of u_ℓ. shown at the end of the Chapter, in Figs. 6.30 – 6.35. These figures show, plotted against pressure, upper experimental values of u_n and lower derived u_ℓ. Initial conditions for the mixtures presented in this way are summarised in Table 6.4. These covered two different initial pressures for iso-octane mixtures, (p_o = 0.5 MPa and 1.0 MPa) and one initial pressure (p_o = 0.5 MPa), for hydrogen mixtures. All explosions were at an initial temperature of 358 K.

Fig. No	C_8H_{18} ϕ	p_o (MPa)	T_o (K)	Fig. No	C_8H_{18} ϕ	p_o (MPa)	T_o (K)
6.30 a	0.8	1	358	6.30 b	1.0	1	358
6.31 a	0.9	0.5	358	6.31 b	0.9	1	358
6.32 a	1.1	0.5	358	6.32 b	1.1	1	358
6.33 a	1.2	0.5	358	6.33 b	1.2	1	358
6.34 a	1.3	0.5	358	6.34 b	1.3	1	358
6.35 a	1.4	0.5	358	6.35 b	1.4	1	358
				8.8	1.5	1	358
	H_2						
8.7 a	0.3	0.5	358				
8.7 b	0.4	0.5	358				
8.7 c	0.5	0.5	358				

Table 6.4. Schedule of all laminar implosions for which values of u_ℓ were obtained from the measured values of u_n, using the modified Bechtold – Matalon theory.

As the pressure increased there was an increased early pressure range in the explosions during which no values of u_n could be measured because the two kernels were out of view. This was ameliorated by, where possible, using measured values of u_ℓ in explosions with central ignition at the initial pressure, before instabilities had developed (Bradley *et al.*, 1998).

Another problem at high pressures was that the values of Ma_{sr} may not have been measured. Experimental measurements of Ma_{sr} require a stable flame to exist for sufficient time to measure the gradient of a plot of burning velocity against flame stretch rate. This became impossible with very unstable flames. The alternative of measuring Pe_{cl}, discussed in Chapter 5, was then adopted, except that in the case of very unstable flames, particularly those in lean hydrogen mixtures, even this approach was difficult. For these mixtures, all values of Pe_{cl} were taken to be 100 for ϕ = 0.3, 0.4 and 0.5 respectively. All these mixtures were assumed to have a "saturated" inner cut-off with Λ_s = 50 in Eq. 5.8.

For iso-octane mixtures, necessary values of Ma_{sr} for the derivation of u_ℓ were obtained, or estimated, from the data in Bradley *et al.* (1998), where this was possible. These were supplemented by experimental measurements of Pe_{cl}. The theoretical treatment described in Chapter 5.3 for $Ma_{sr} > 3$ could be used for ϕ up to 0.9 (0.5 MPa) and 1.0 (0.5 MPa partially). That involving Eq. 5.7 was used for values of ϕ from 0.9 (1.0 MPa) and 1.0 (0.5 MPa partially) up to $\phi = 1.3$ (1.0 MPa partially), while the limit inner cut–off of $\Lambda_s = 50$, with the use of Eq. 5.8, was reached for $\phi \geq 1.3$ (1.0 MPa partially).

Another problem was that it was necessary to know the Peclet numbers of the kernels in order to derive the values of u_ℓ from those of u_n using instability theory. Because $\delta_\ell = \nu / u_\ell$, this necessitated assuming an initial vale of u_ℓ. A revised value then emerged from Eq. 5.10. This enabled an updated value of Pe to be employed. Solution for u_ℓ converged well, usually within four iterations. The derived values of u_ℓ for the hydrogen – air mixtures are compared with computed values in Chapter 8.4. The enhanced instabilities of the iso-octane – air mixtures, $\phi = 1.5$ and 1.6, are discussed in detail in Chapter 8.5.

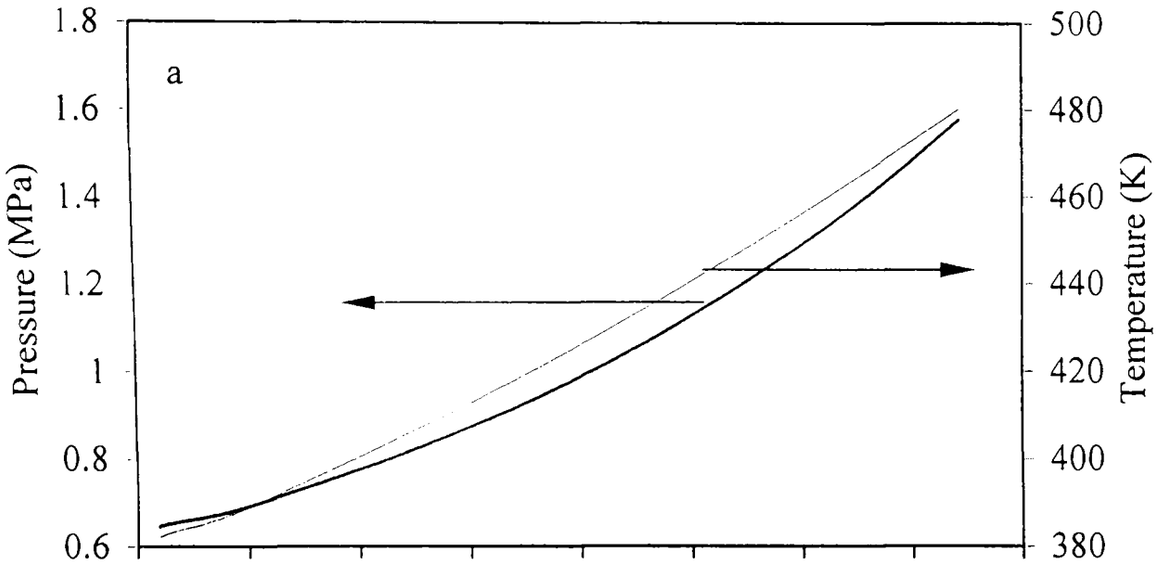

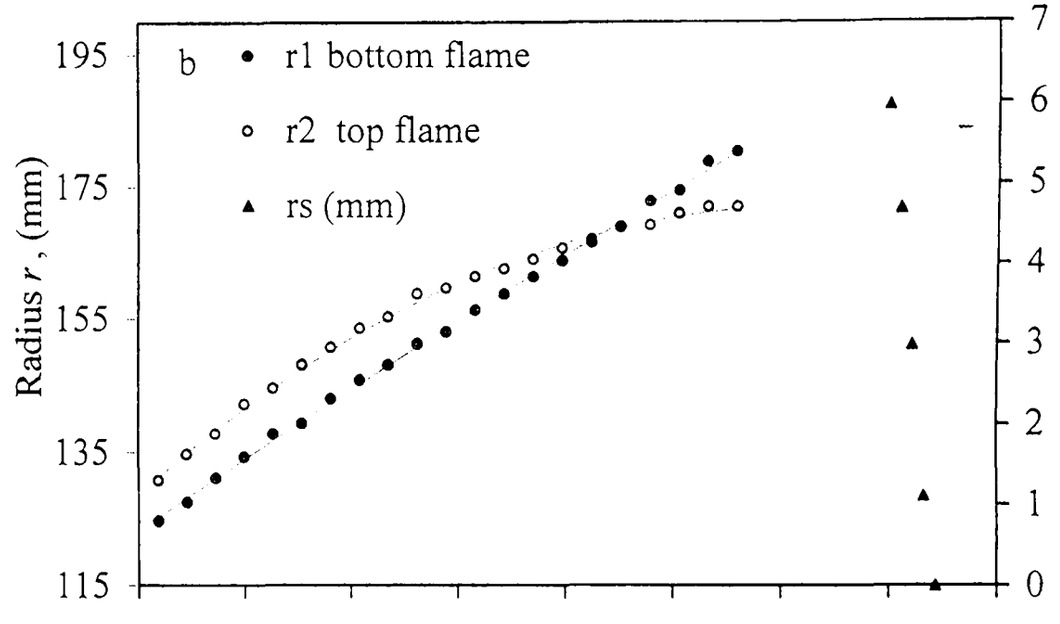

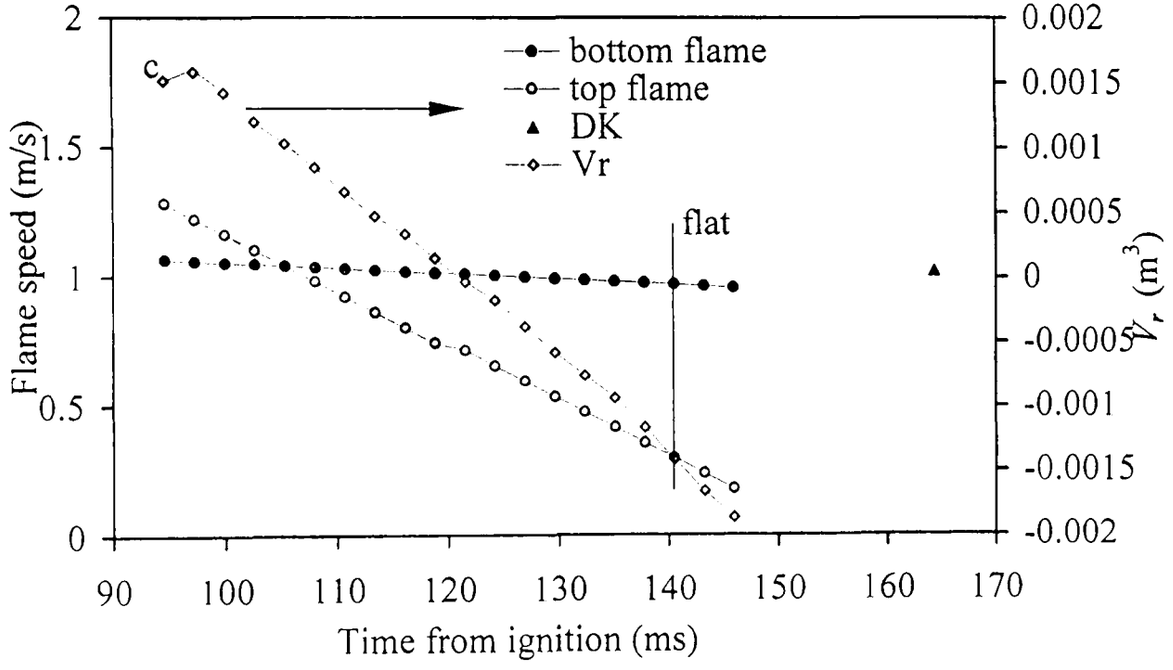

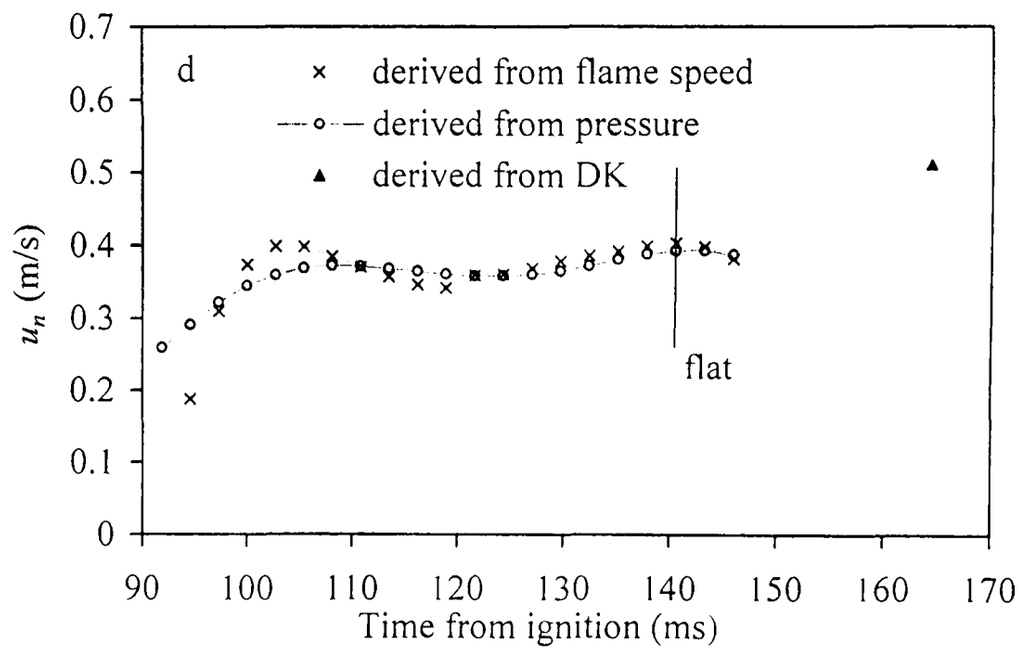

Fig. 6.1 Iso-octane - air implosion, ϕ = 0.8, p_o = 0.5 MPa, T_o = 358 K

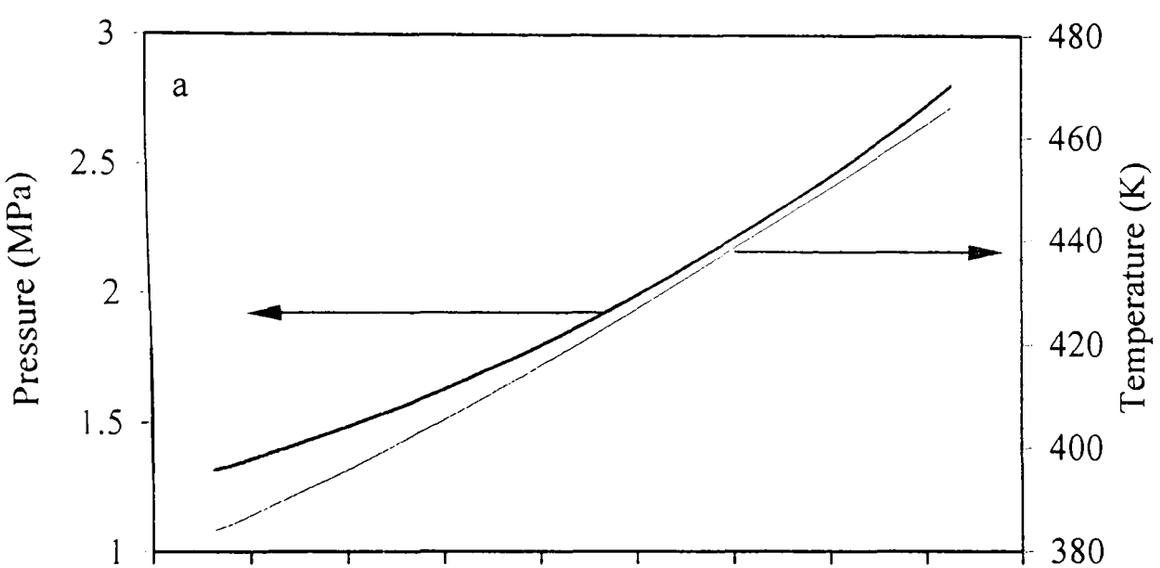

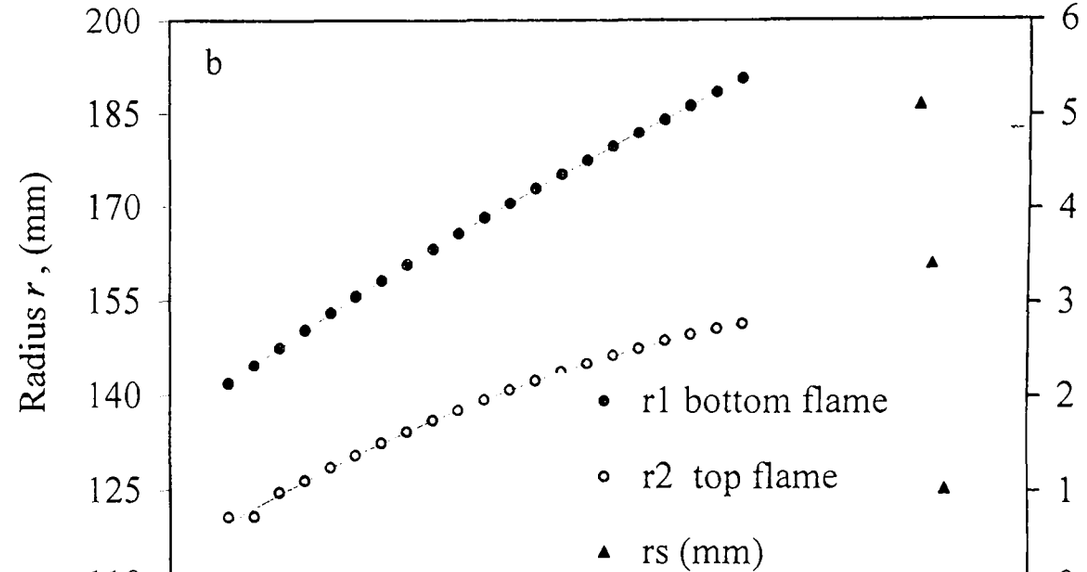

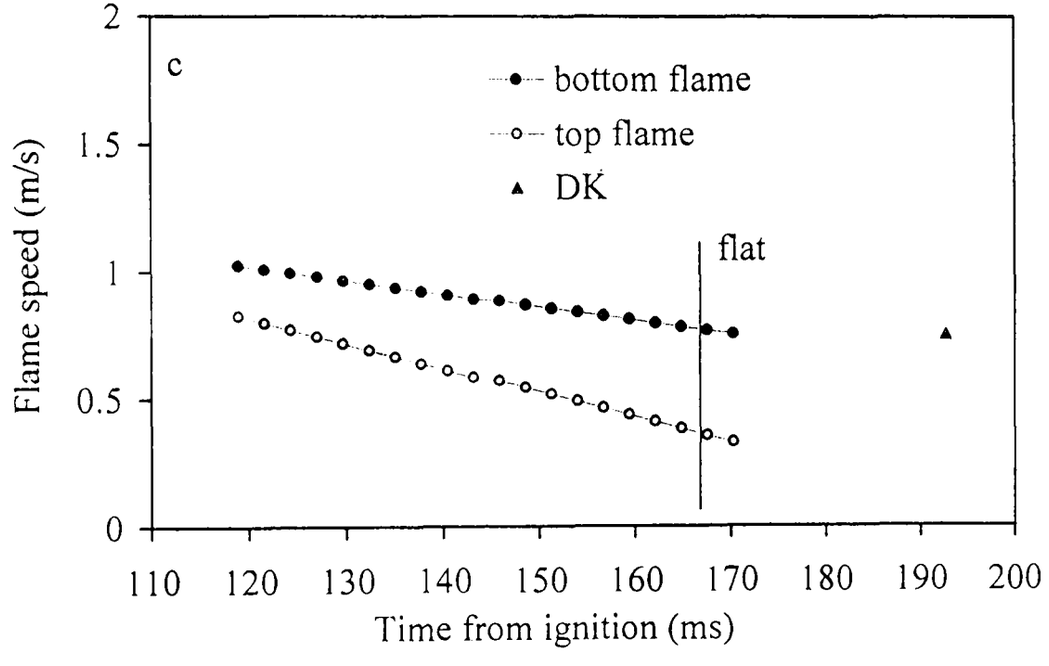

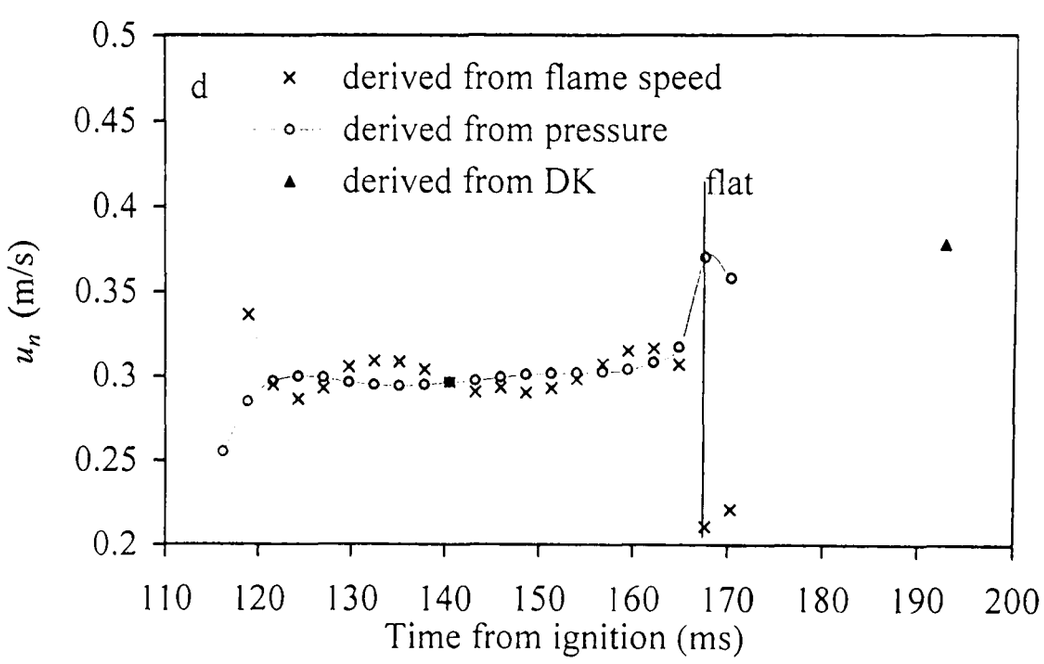

Fig. 6.2. Iso-octane - air implosion, $\phi = 0.8, p_o = 1\text{MPa}, T_o = 358\ \text{K}$

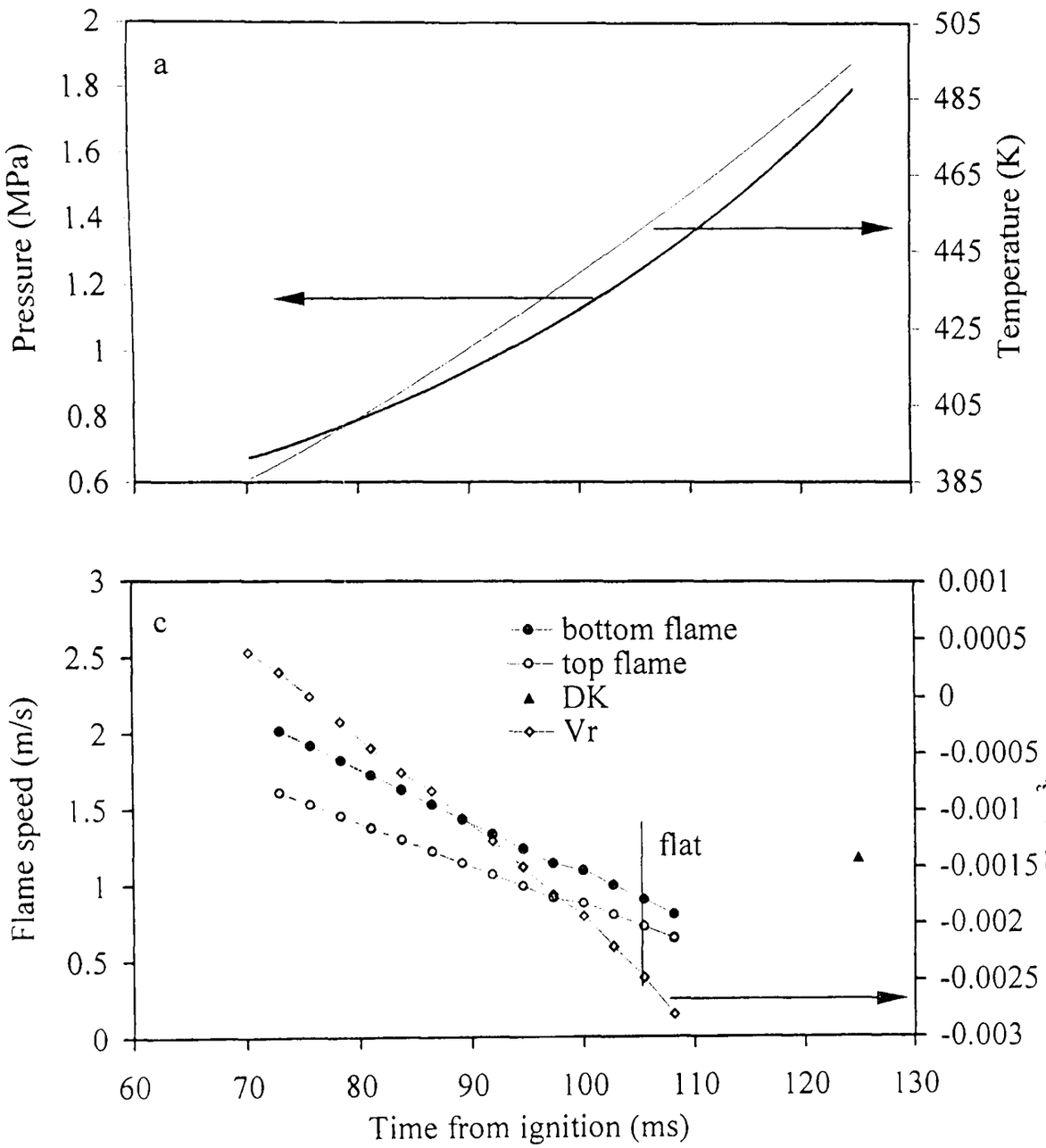

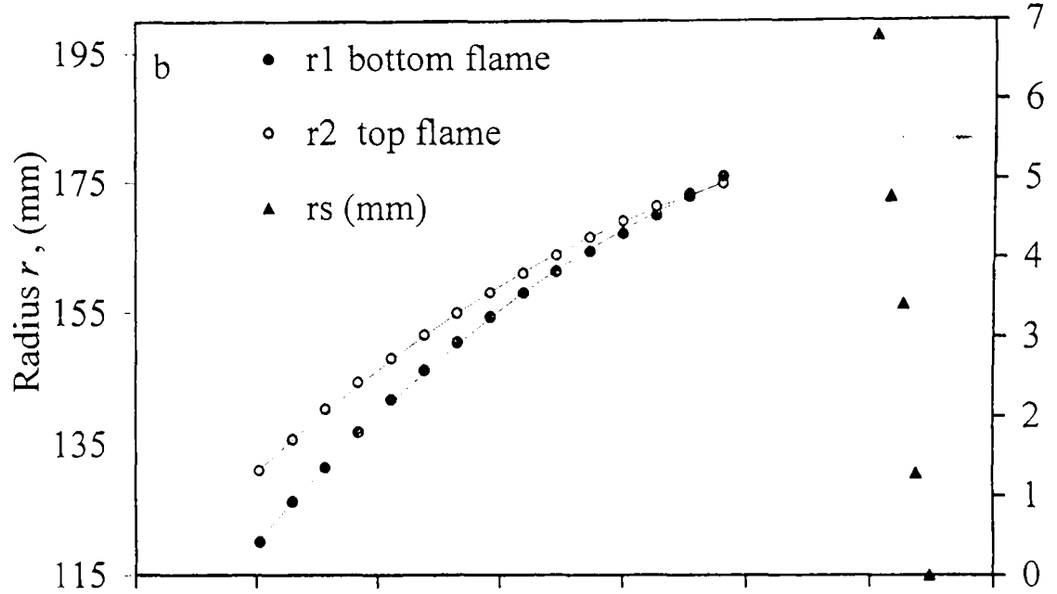

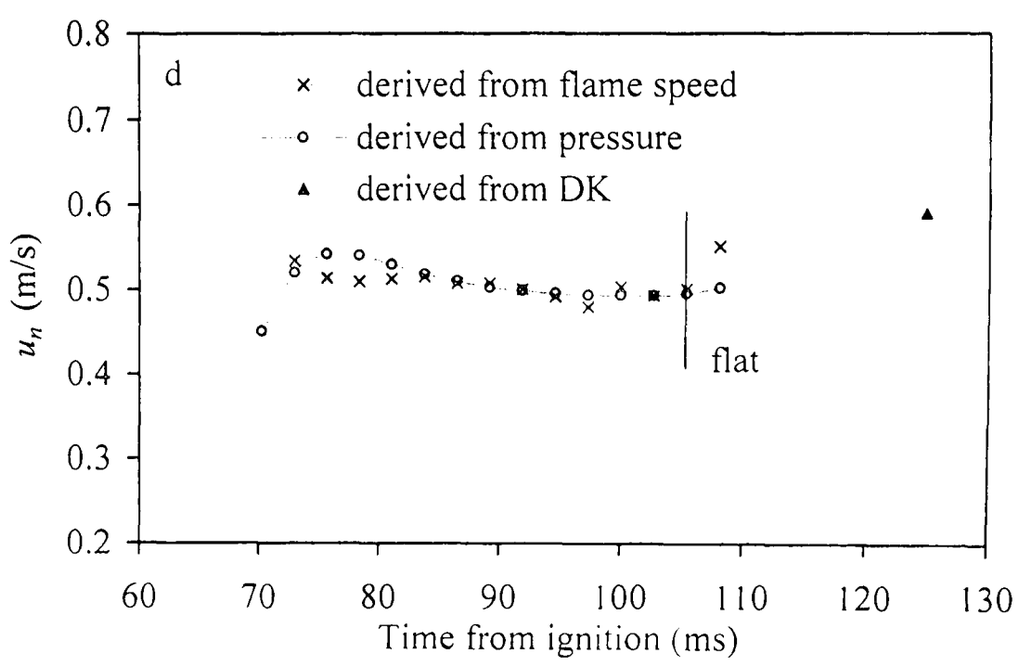

Fig. 6.3. Iso-octane - air implosion, ϕ = 0.9, p_o = 0.5 MPa, T_o = 358 K

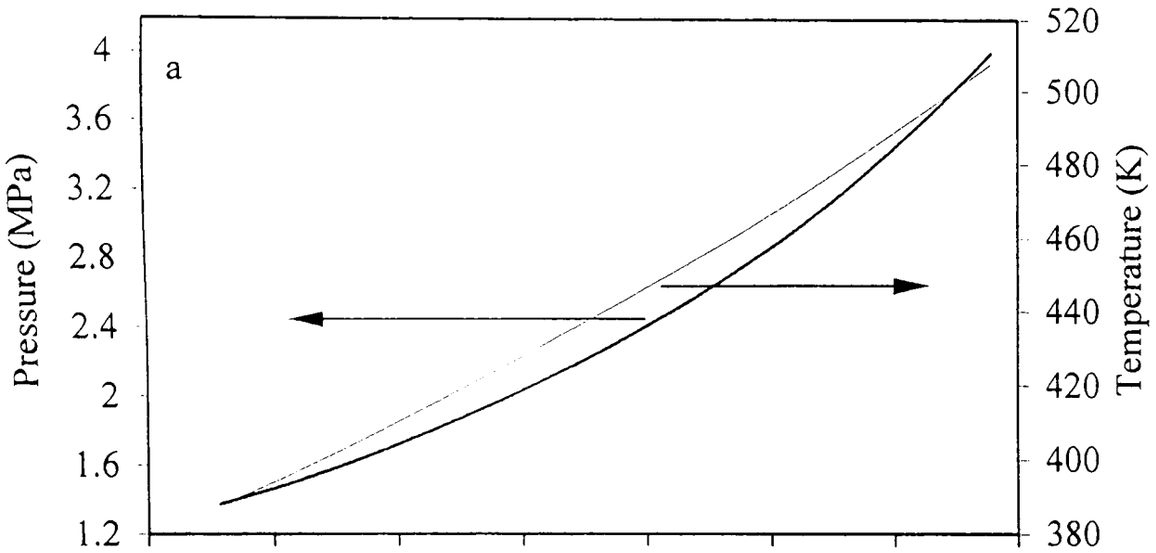

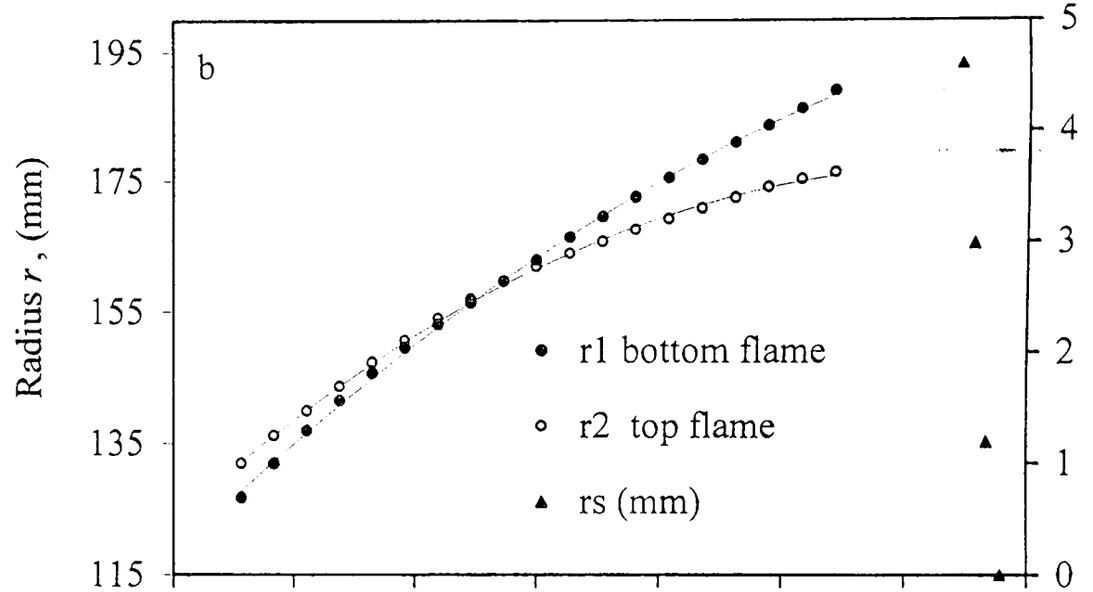

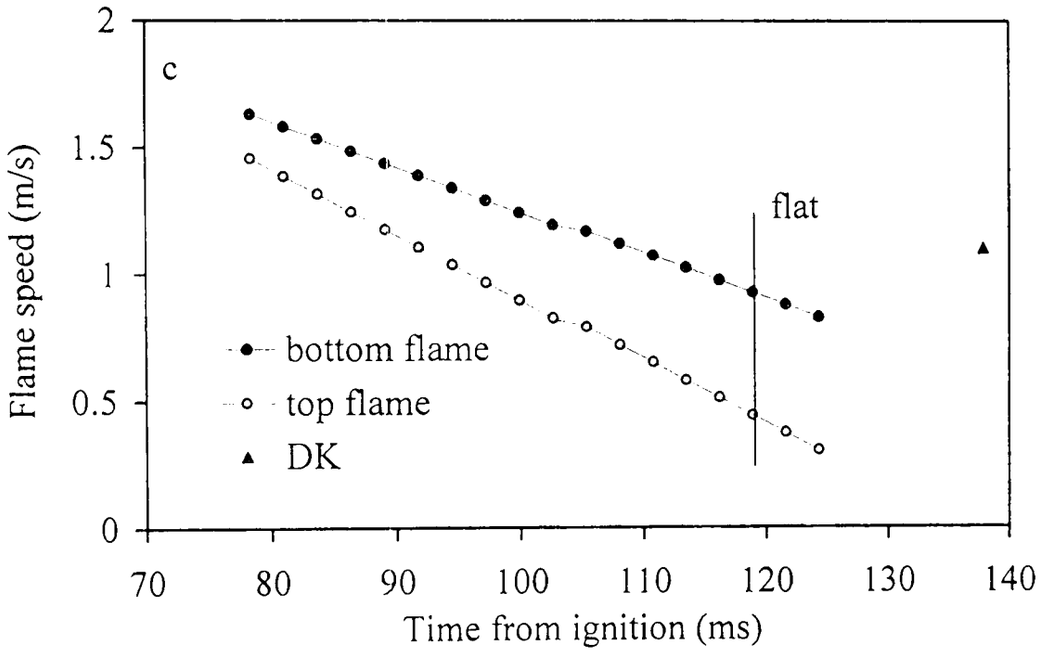

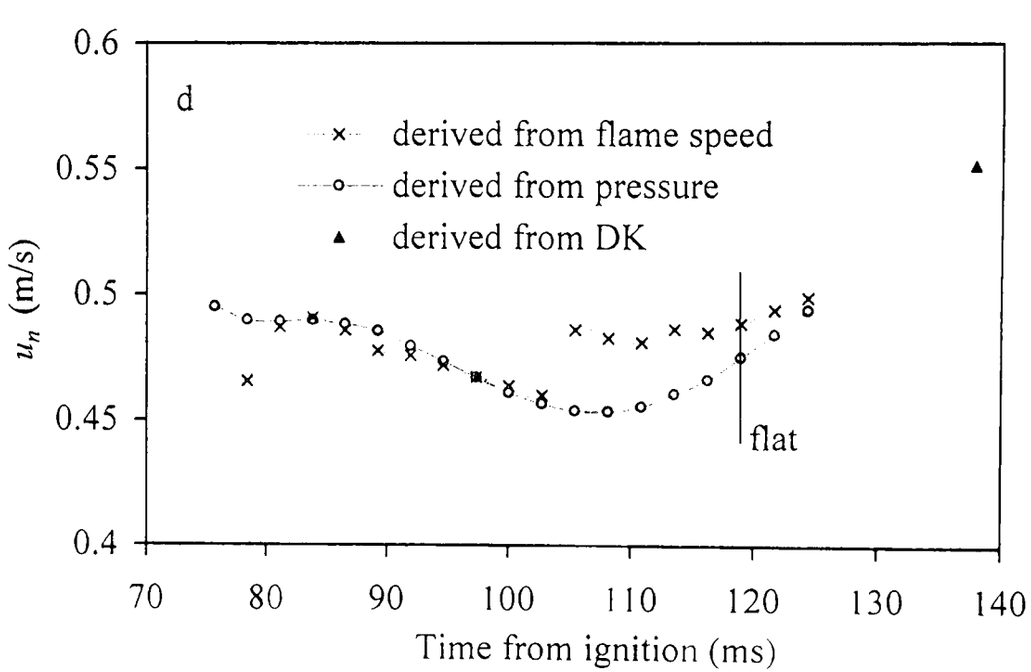

Fig. 6.4. Iso-octane - air implosion, $\phi = 0.9$, $p_o = 1$MPa, $T_o = 358$ K

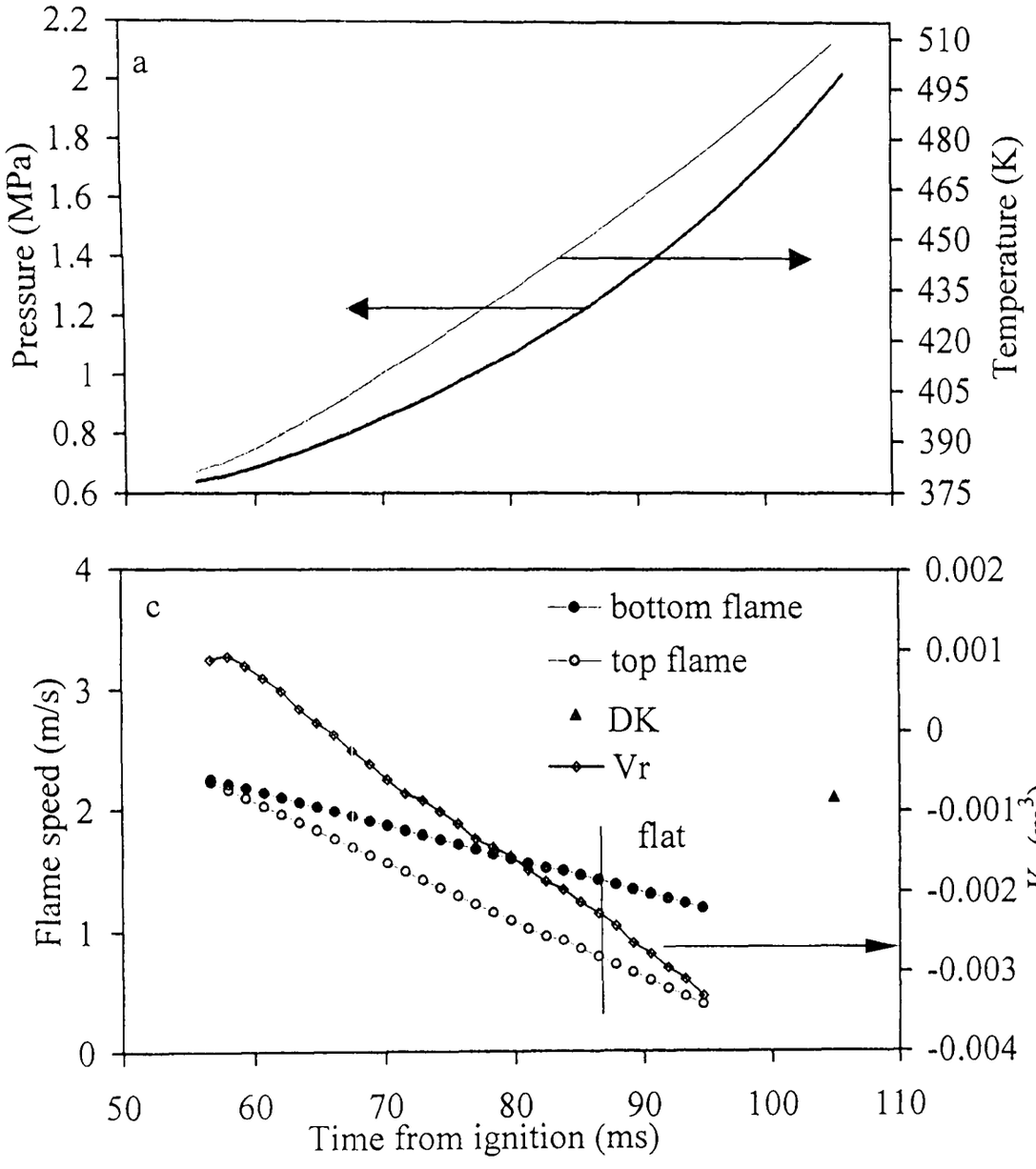

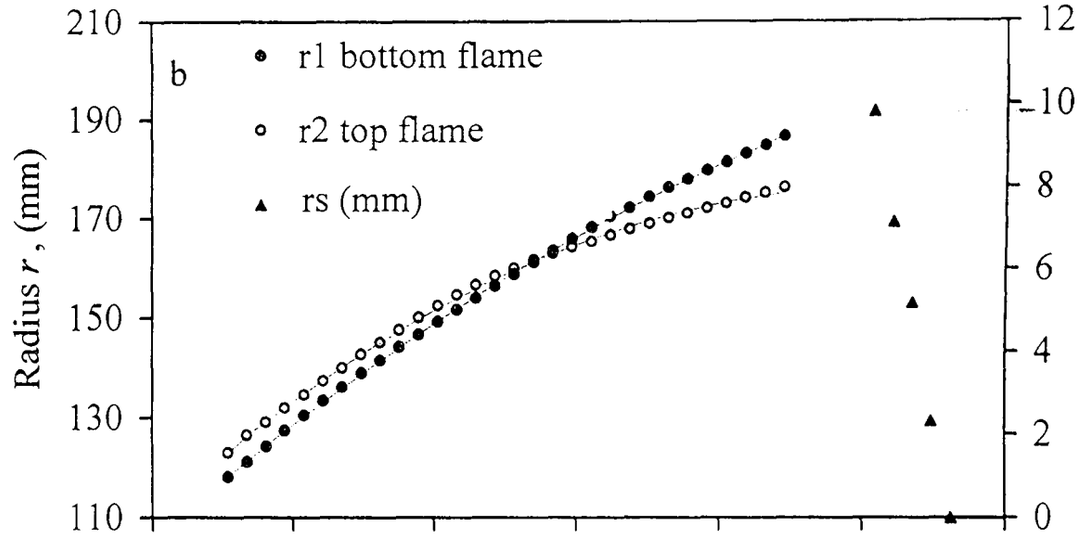

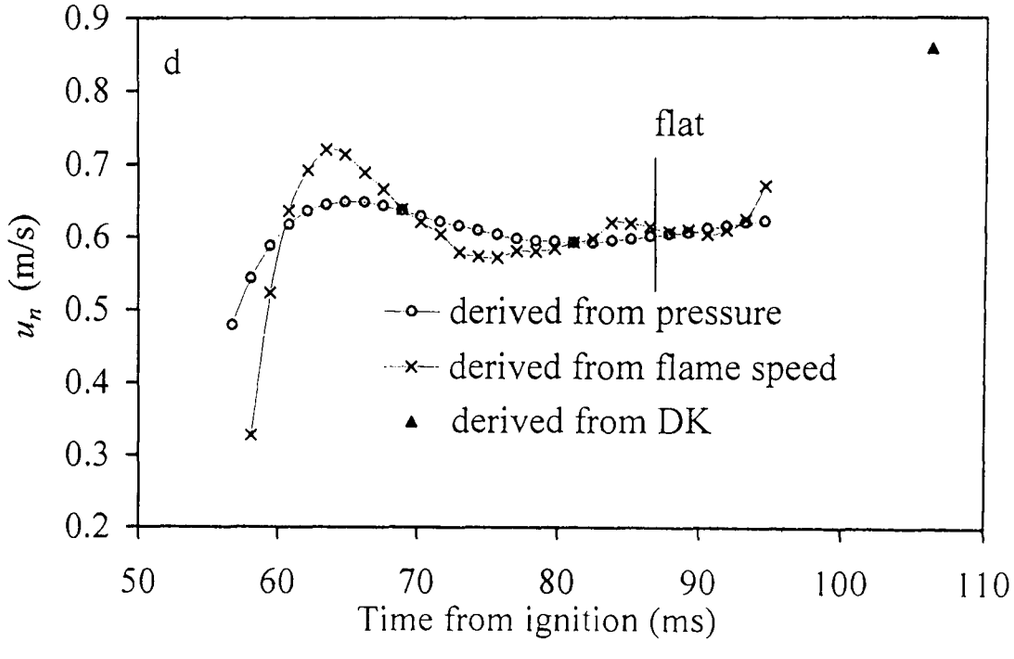

Fig. 6.5. Iso-octane - air implosion, $\phi = 1, p_o = 0.5$ MPa, $T_o = 358$ K

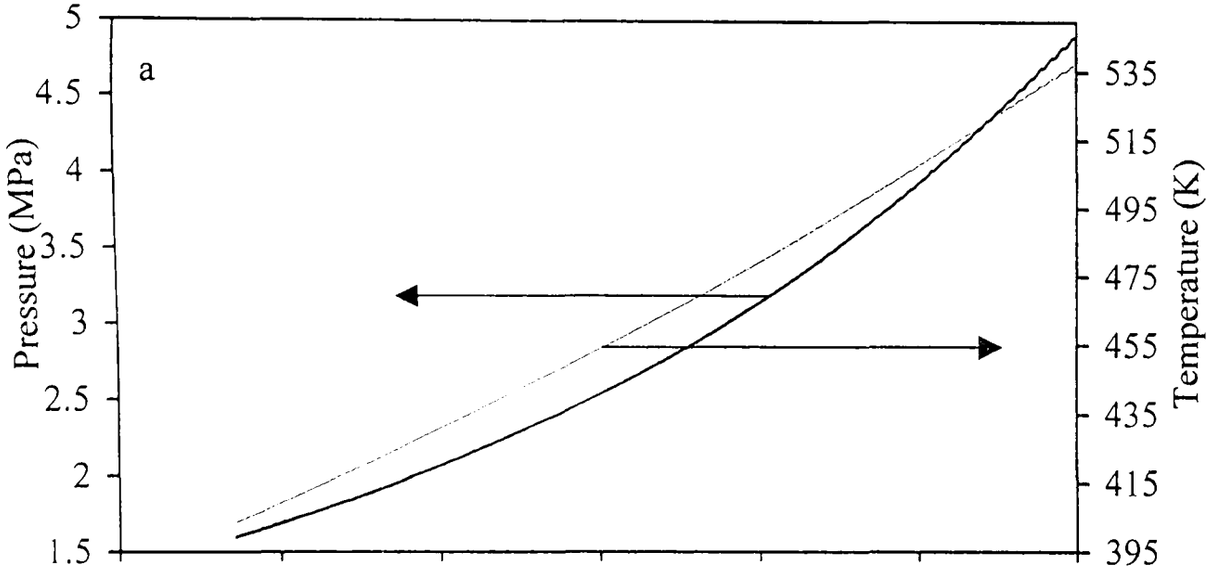

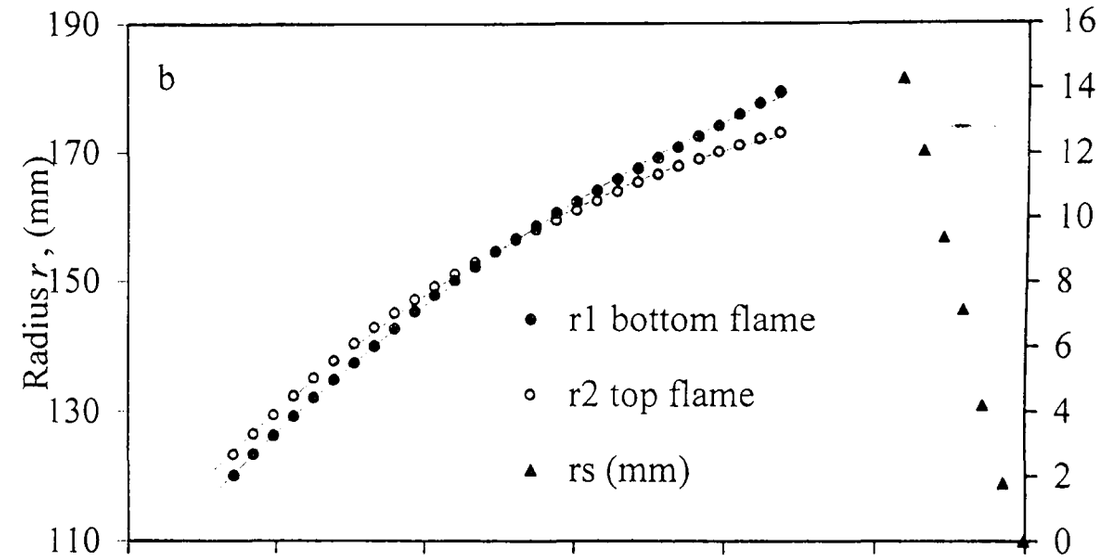

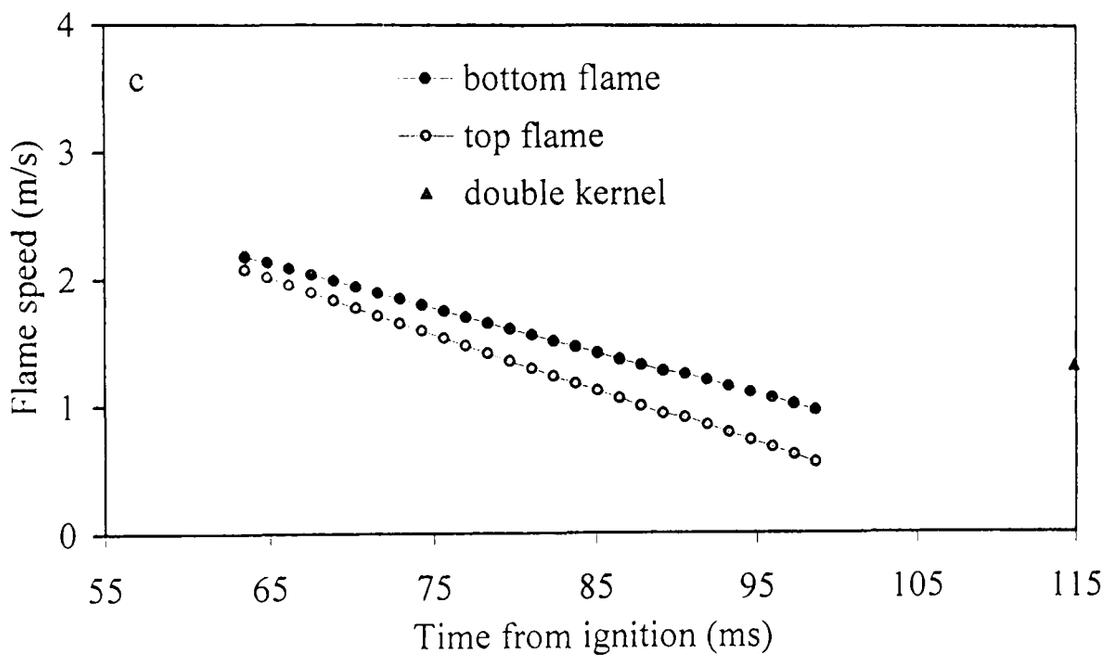

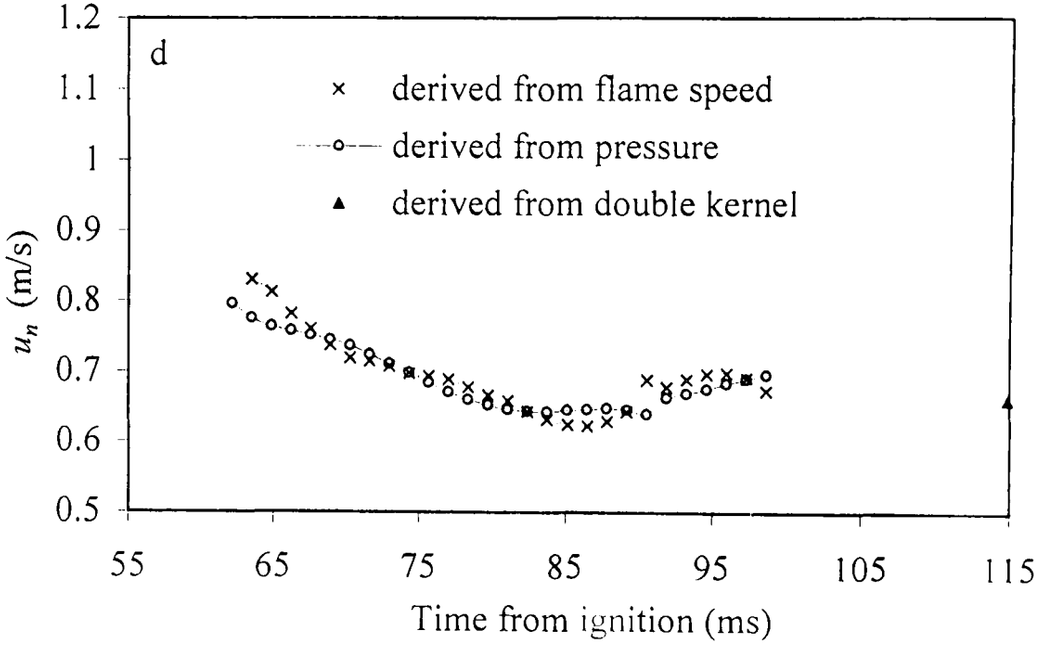

Fig. 6.6. Iso-octane - air implosion, ϕ = 1, p_o = 1MPa, T_o = 358 K

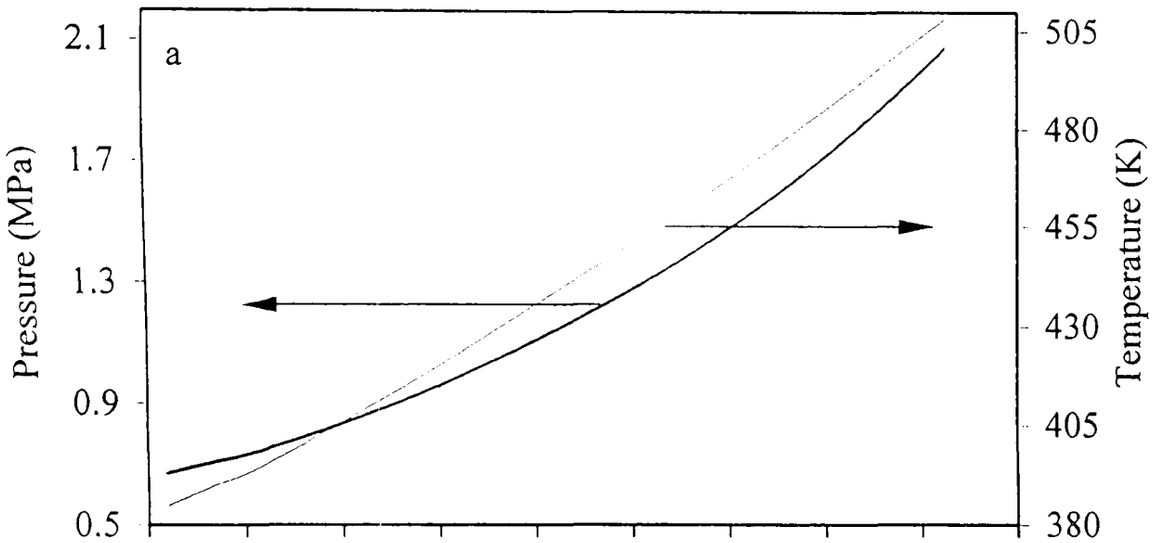

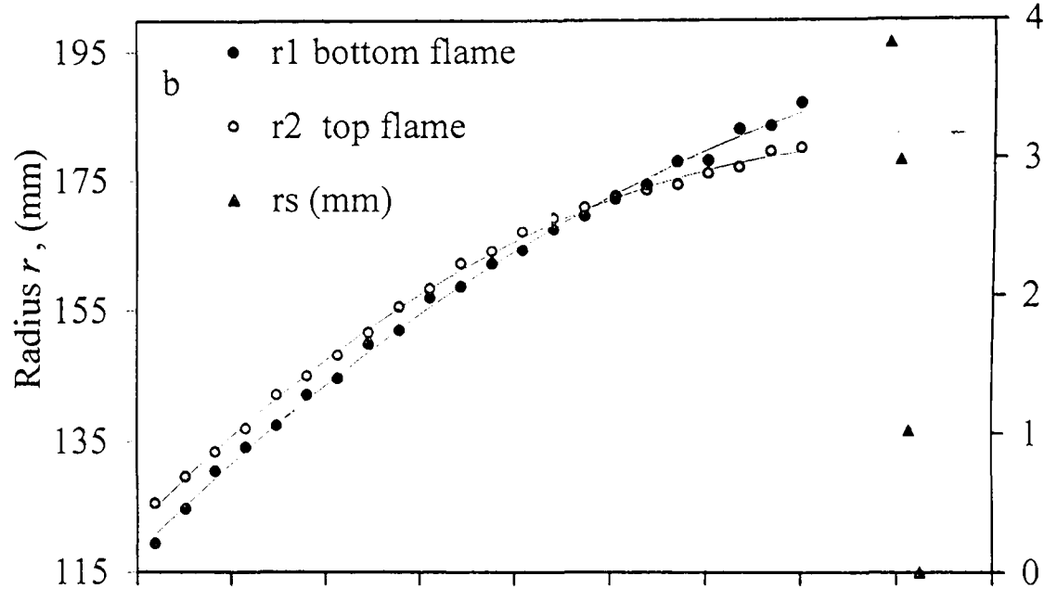

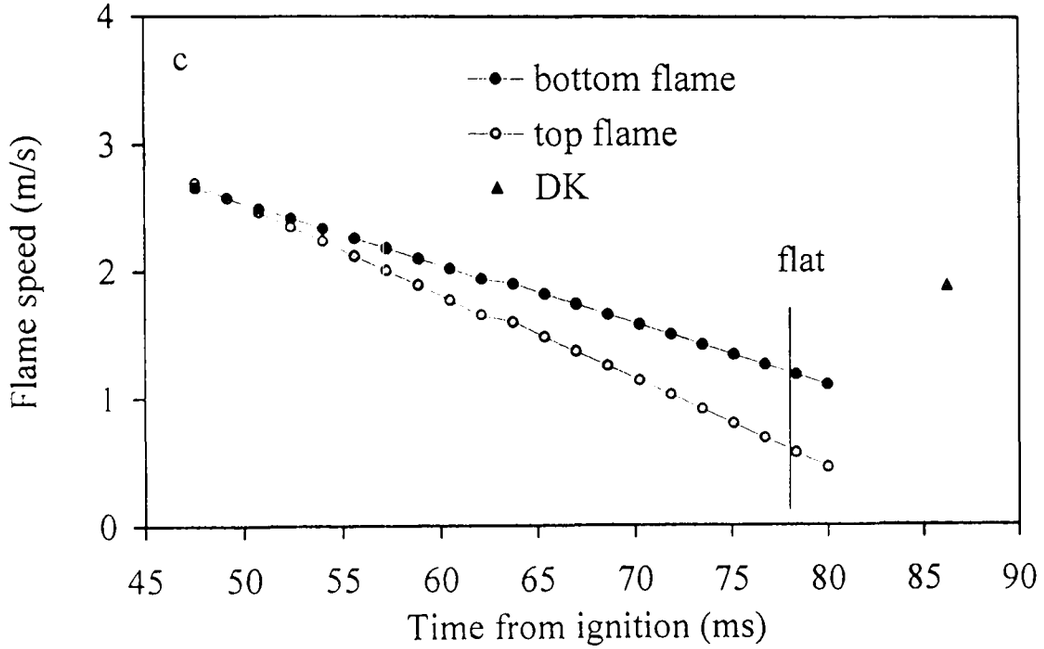

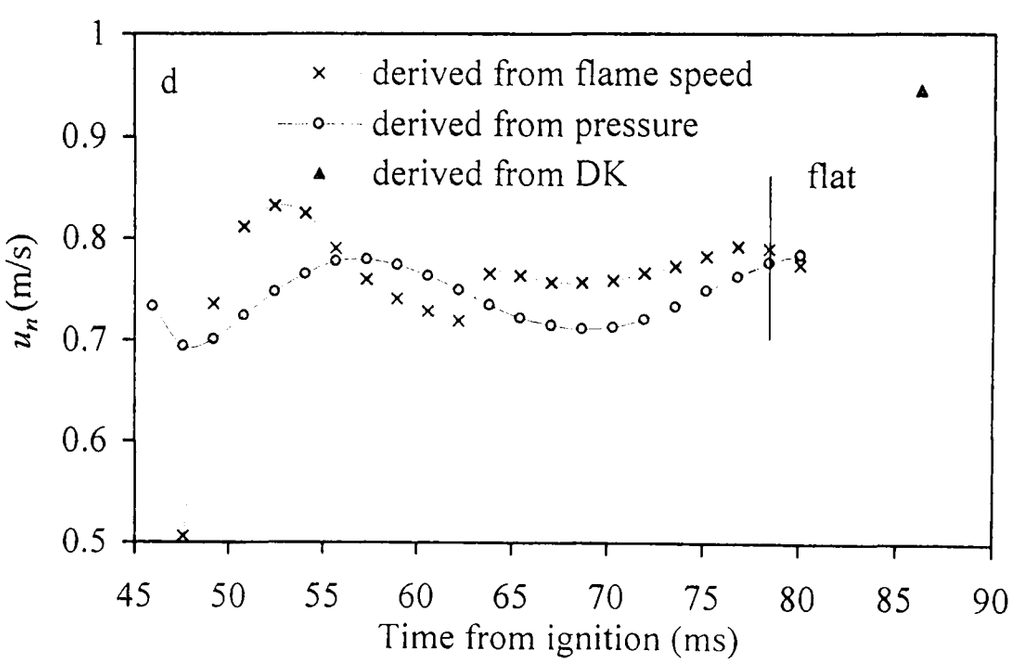

Fig. 6.7. Iso-octane - air implosion, ϕ = 1.1, p_o = 0.5 MPa, T_o = 358 K

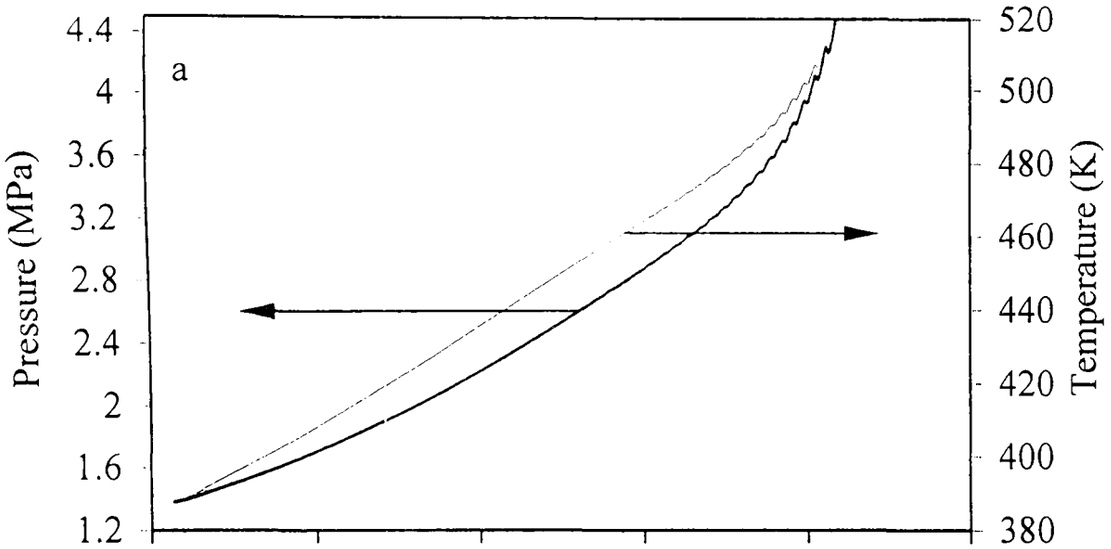

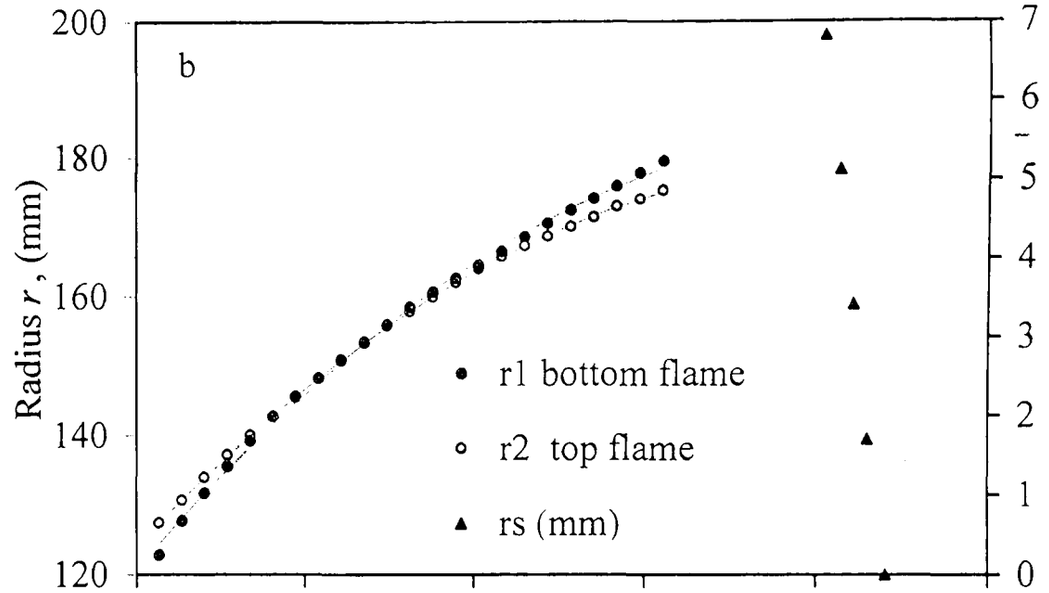

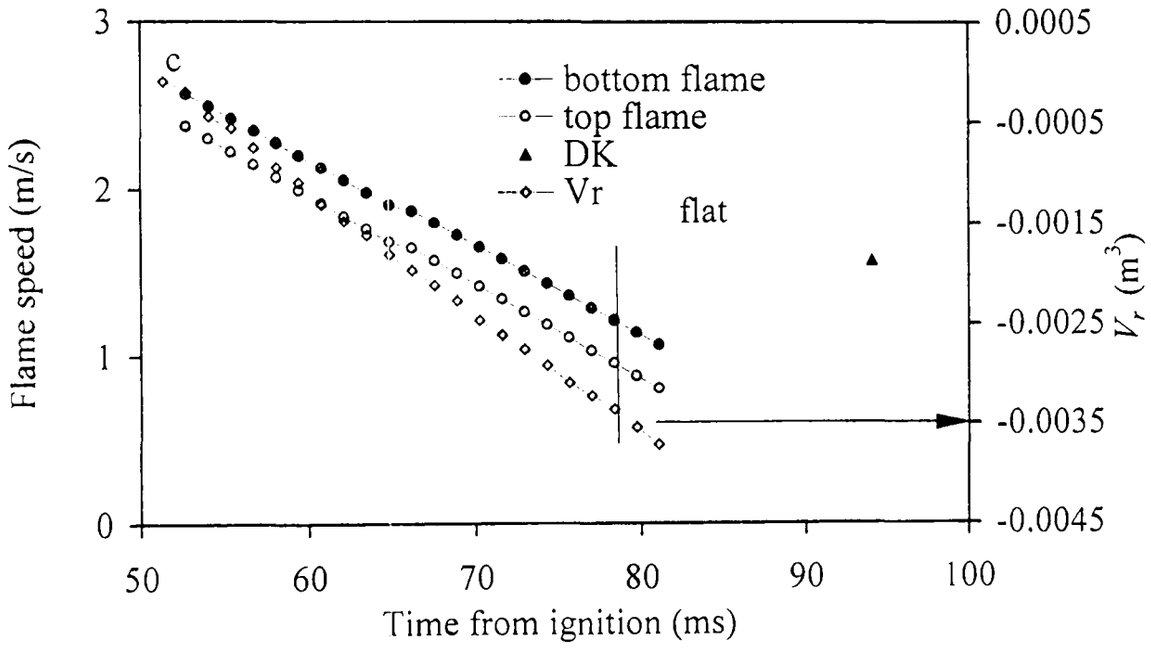

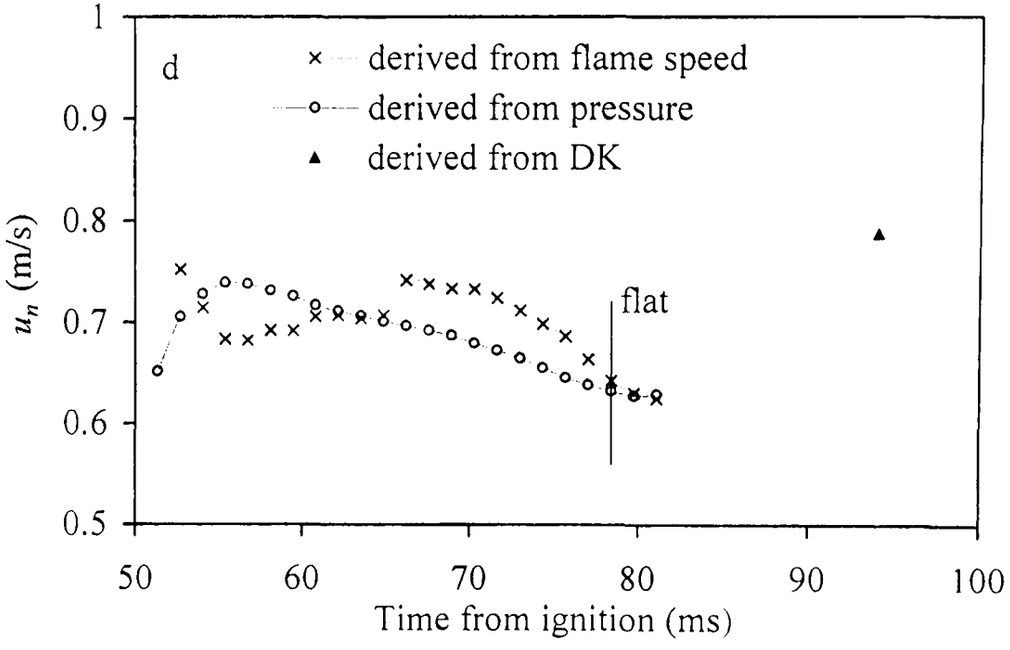

Fig. 6.8. Iso-octane - air implosion, ϕ = 1.1, p_o = 1MPa, T_o = 358 K

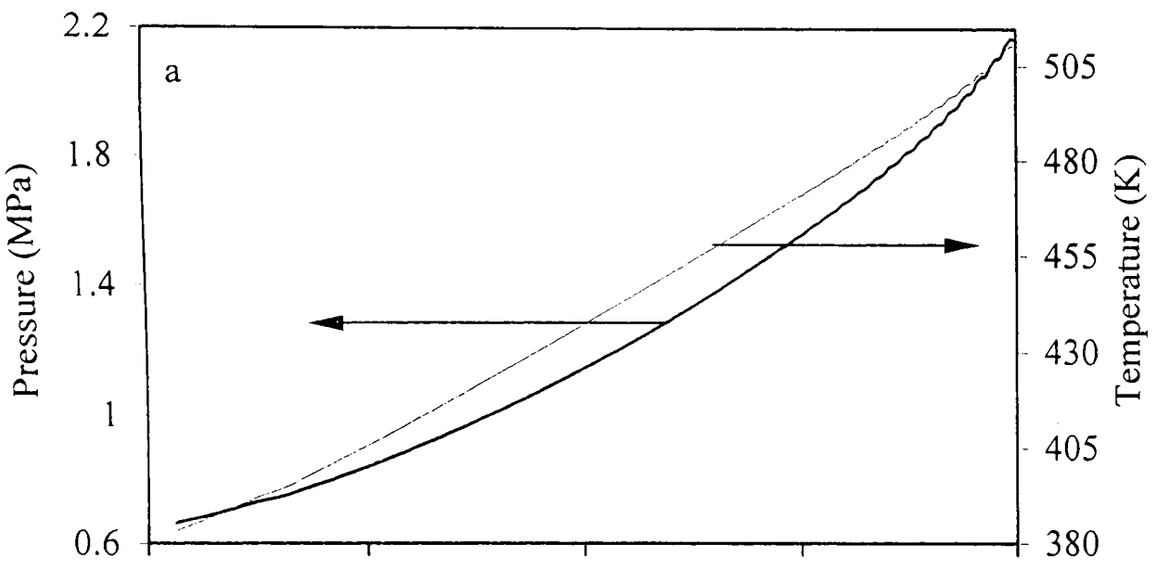

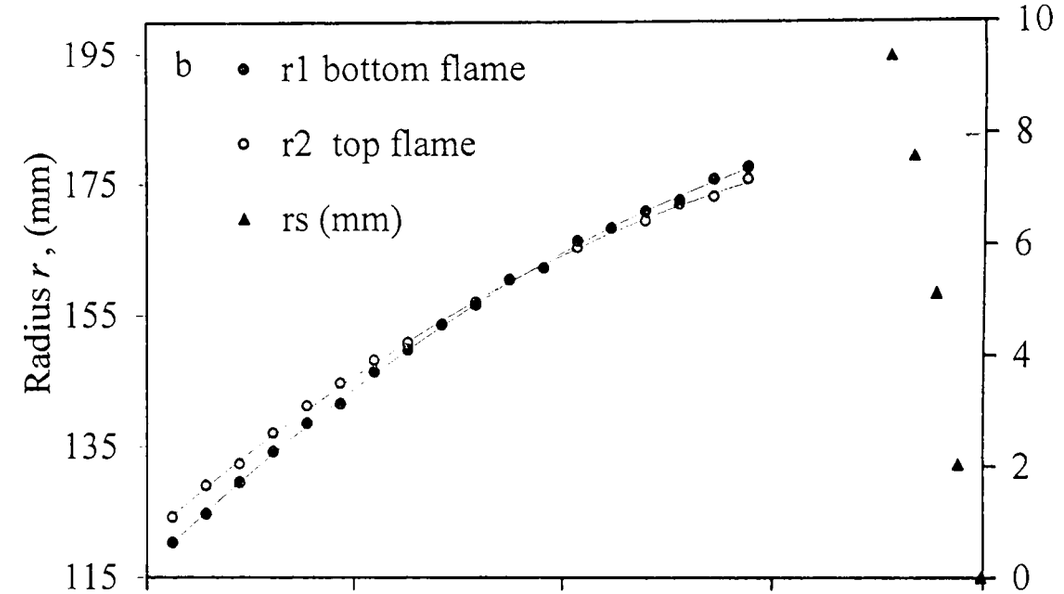

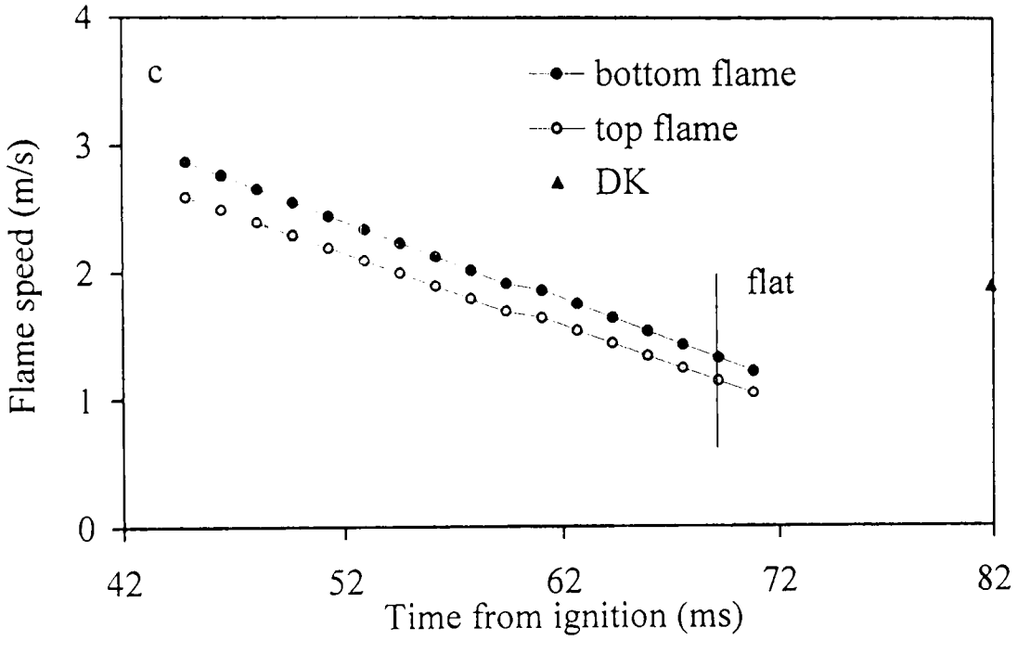

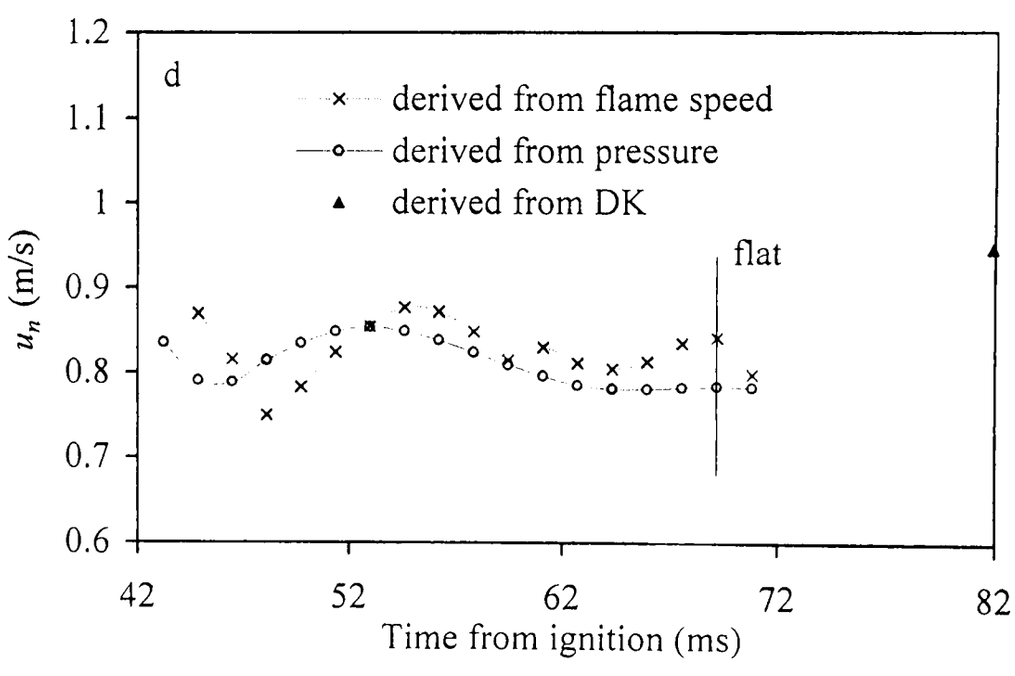

Fig. 6.9. Iso-octane - air implosion, ϕ = 1.2, p_o = 0.5 MPa, T_o = 358 K

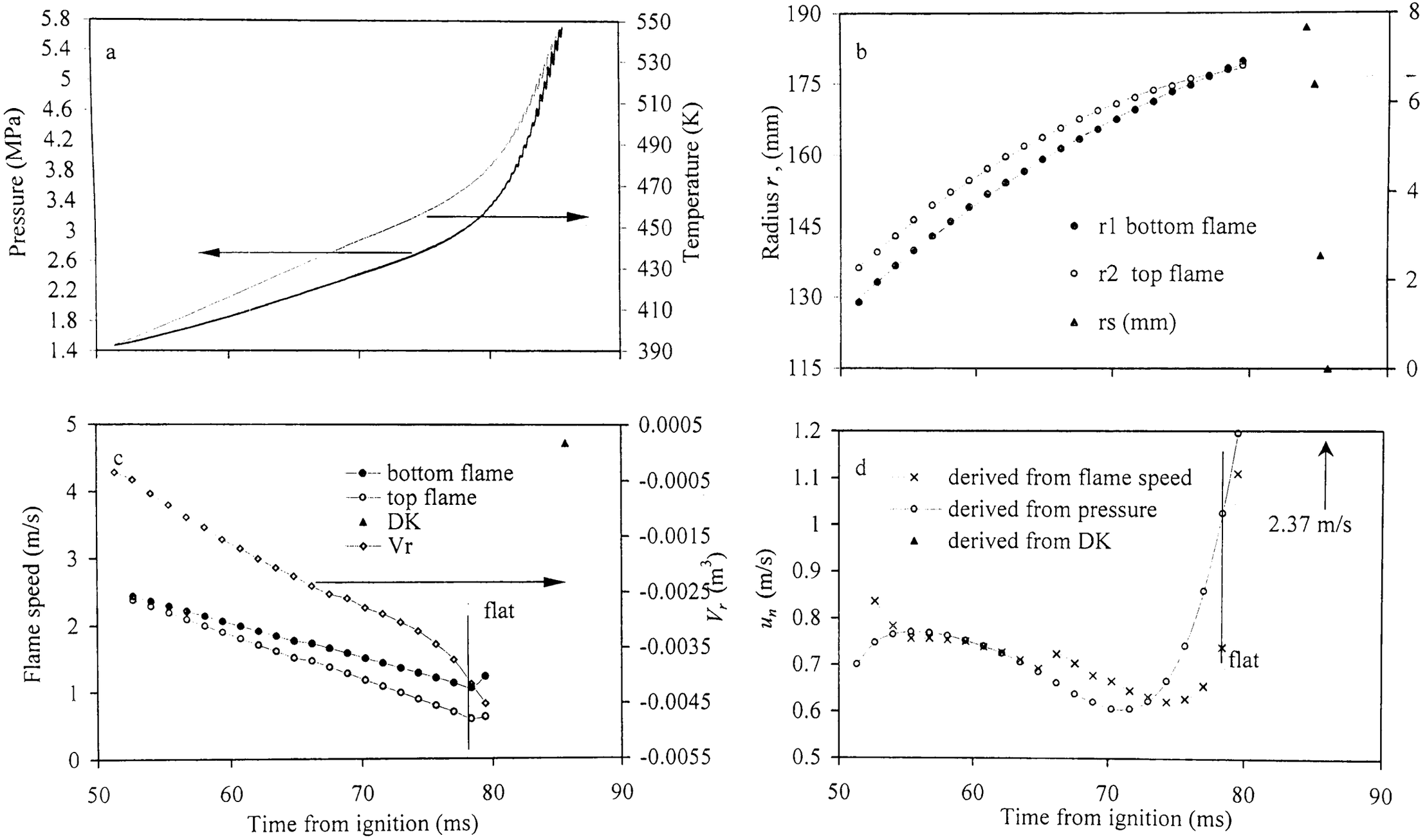

Fig. 6.10. Iso-octane - air implosion, ϕ = 1.2, p_o = 1 MPa, T_o = 358 K

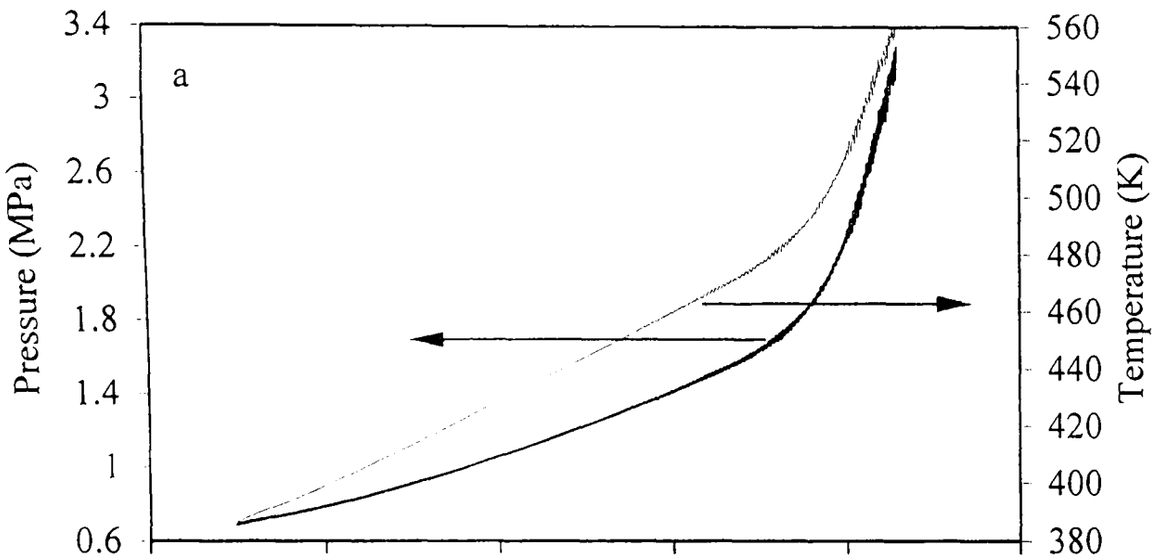

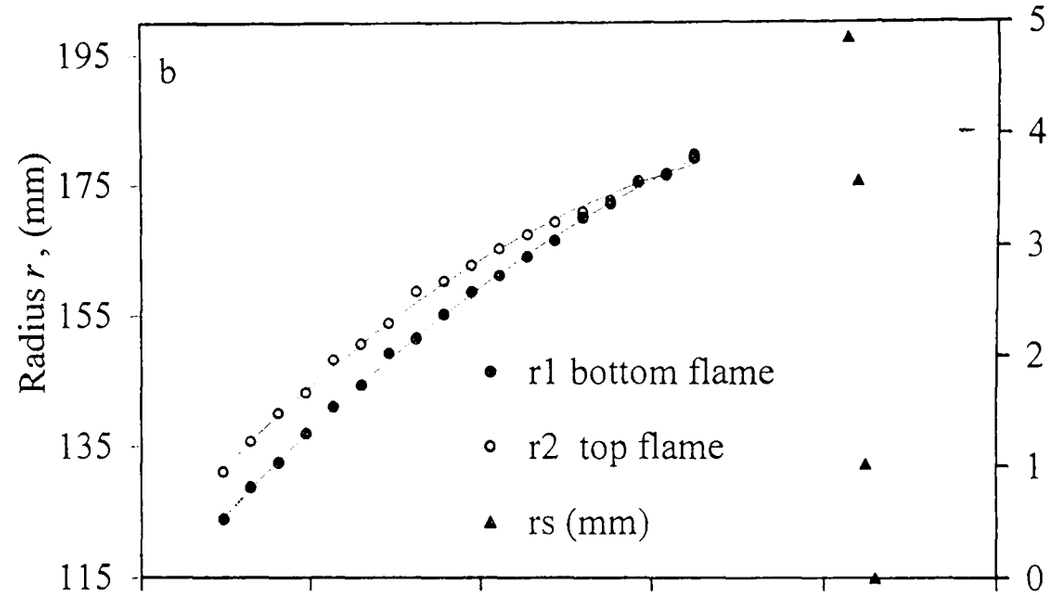

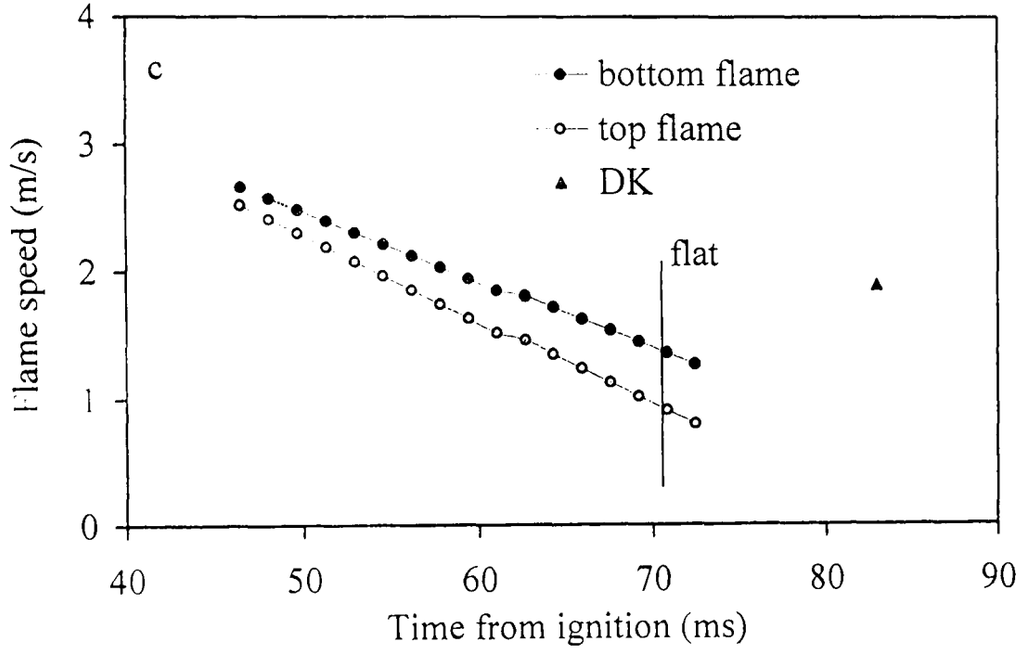

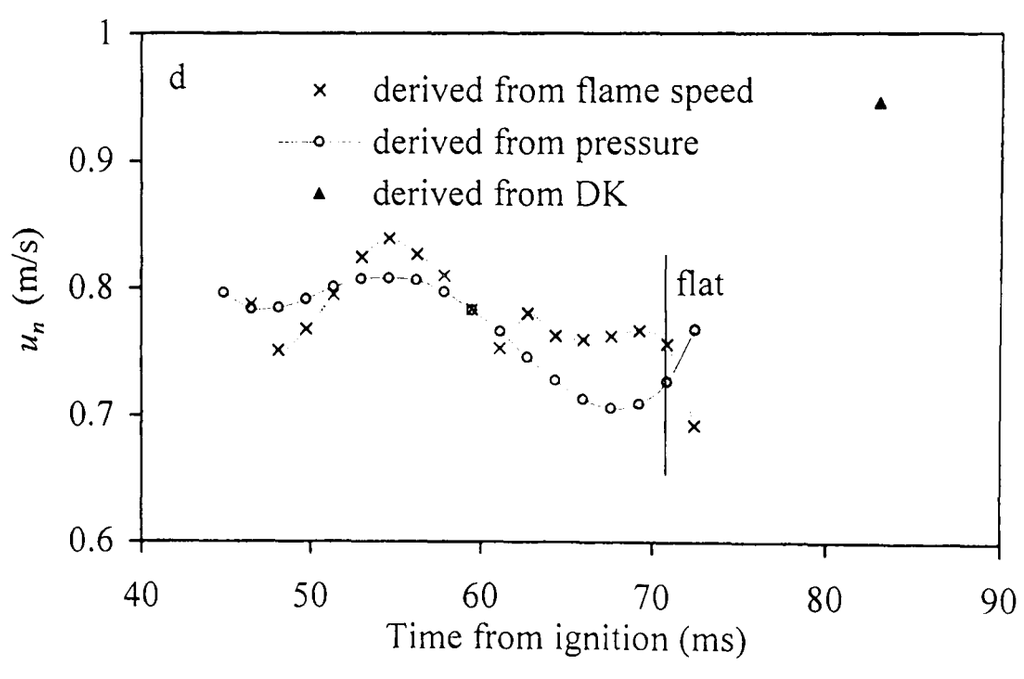

Fig. 6.11. Iso-octane - air implosion, ϕ = 1.3, p_o = 0.5 MPa, T_o = 358 K

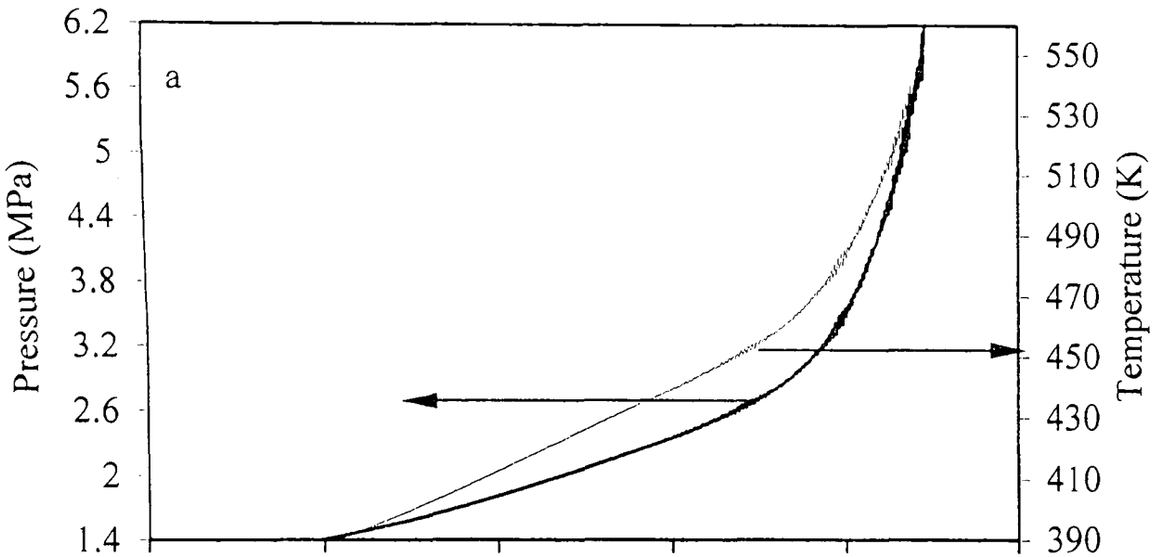

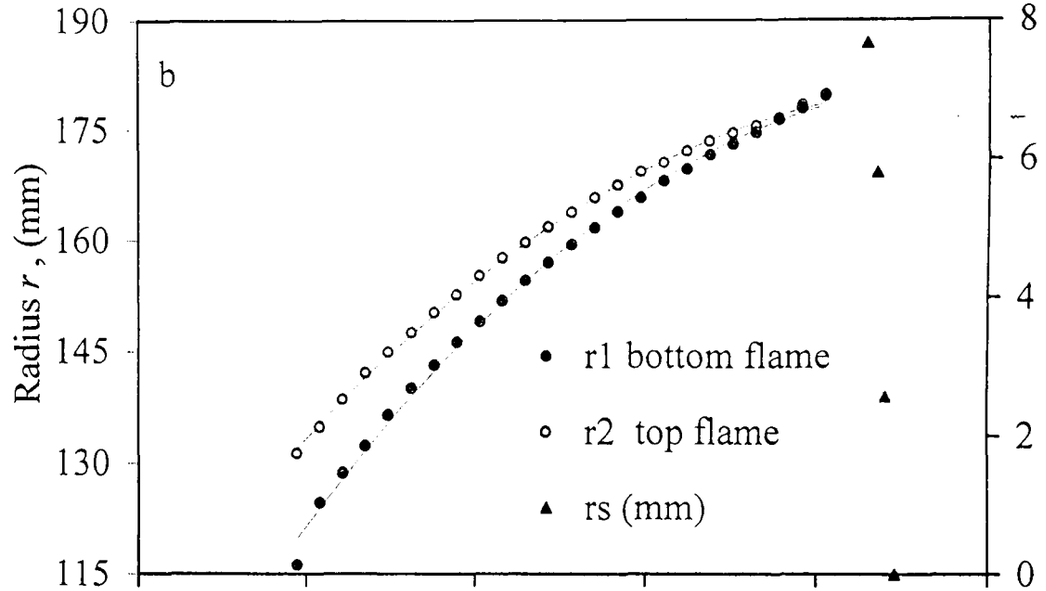

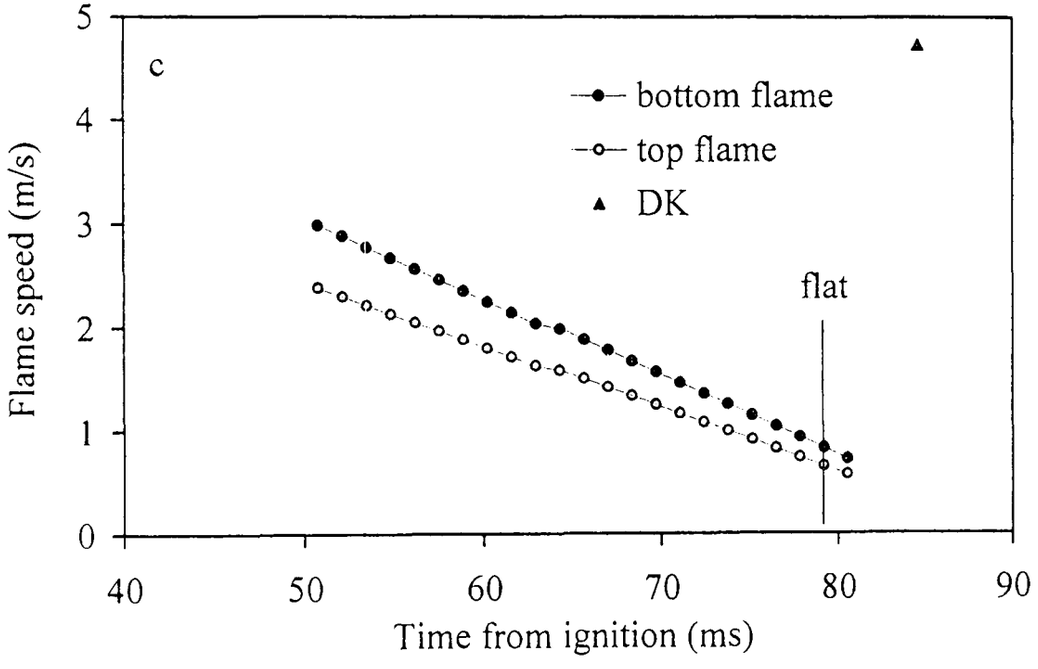

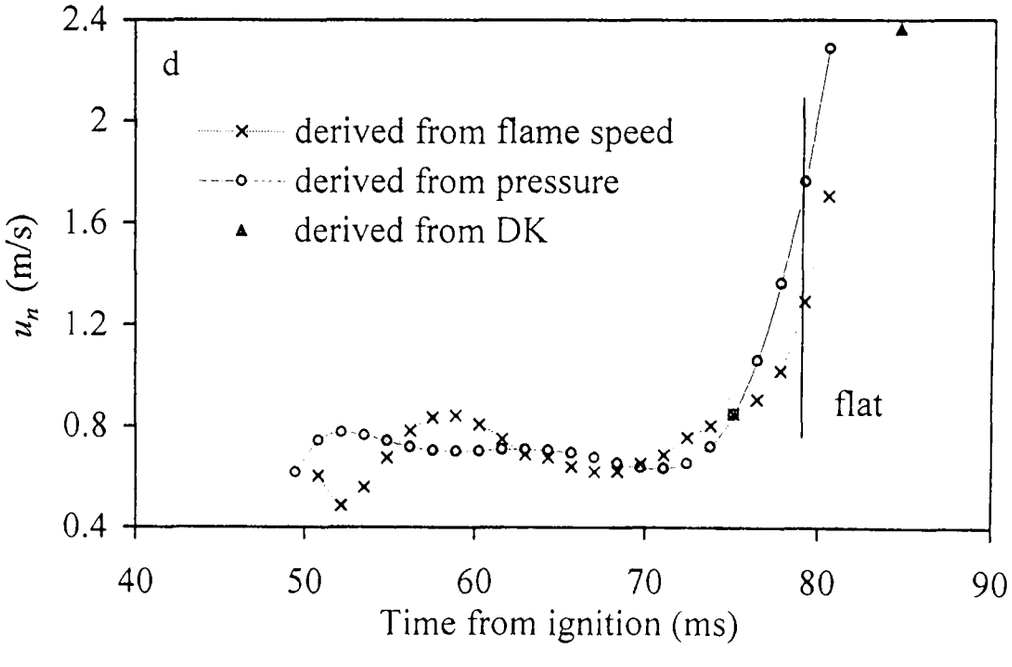

Fig. 6.12. Iso-octane - air implosion, ϕ = 1.3, P_o = 1 MPa, T_o = 358 K

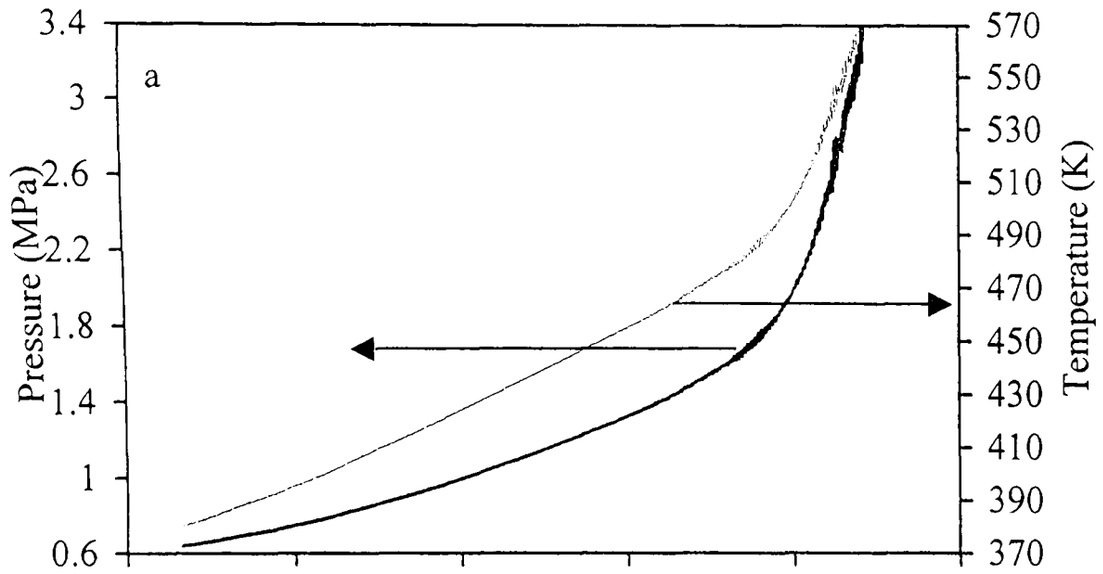

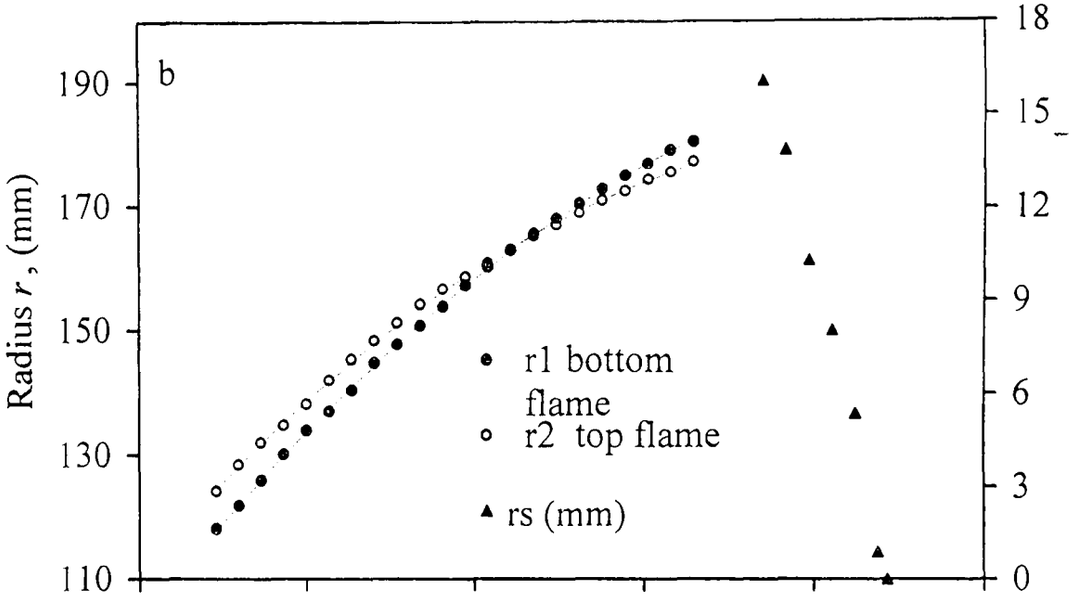

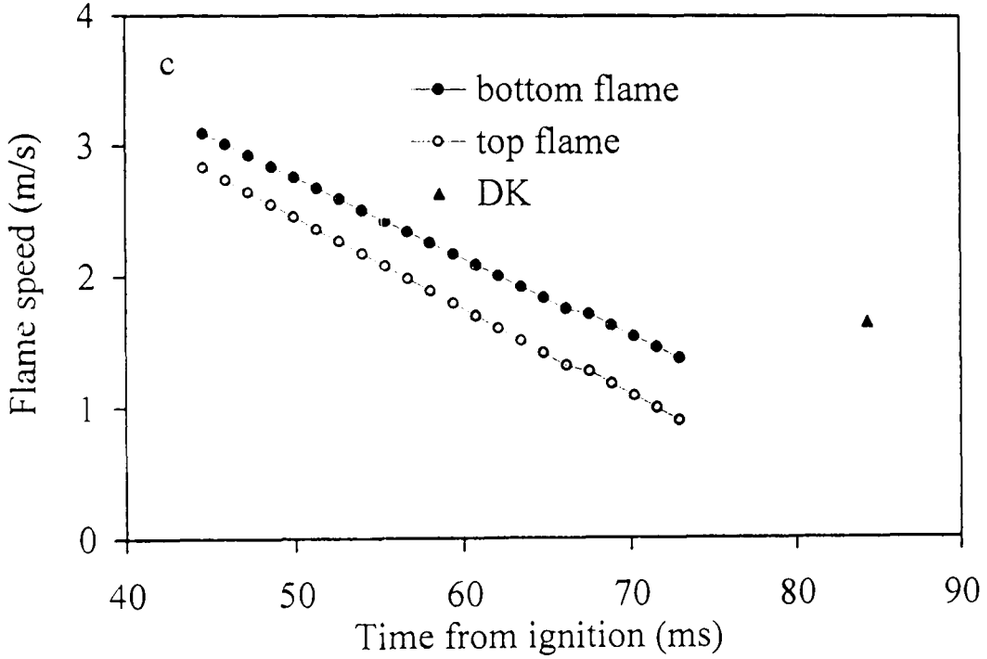

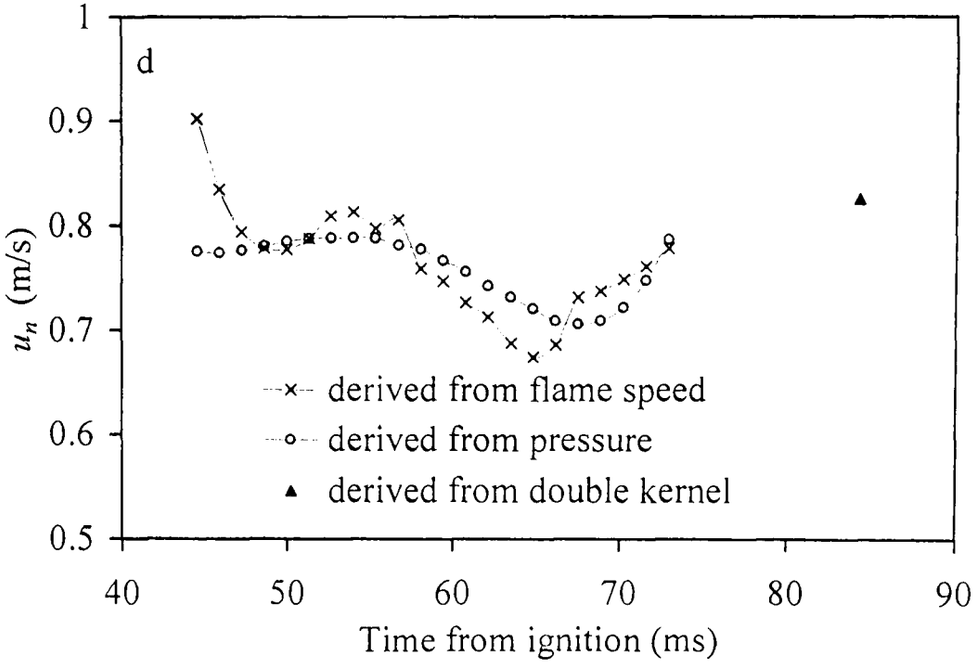

Fig. 6.13. Iso-octane - air implosion, ϕ = 1.4, p_o = 0.5 MPa, T_o = 358 K

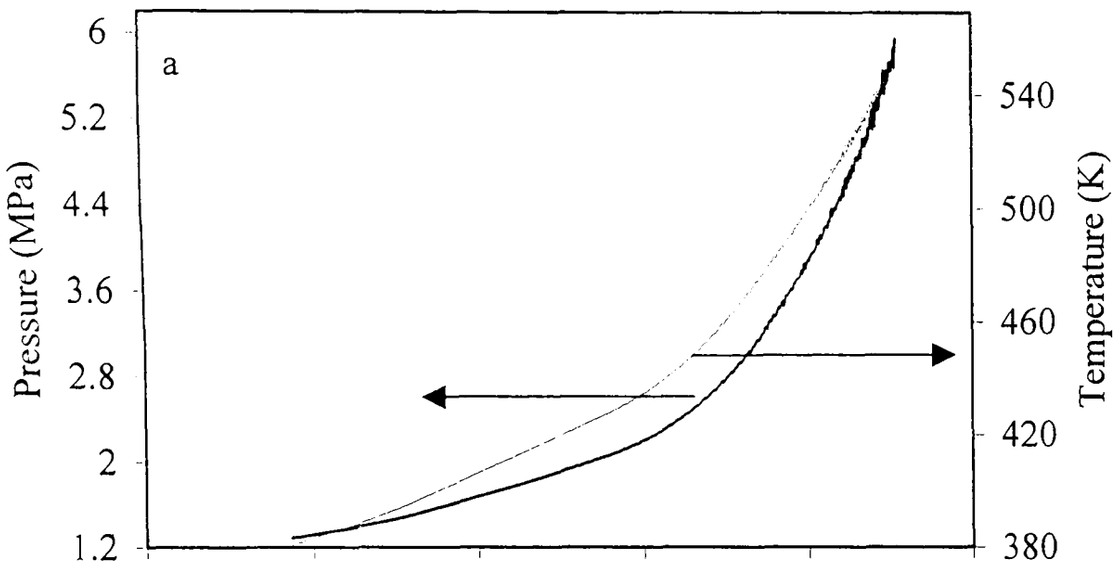

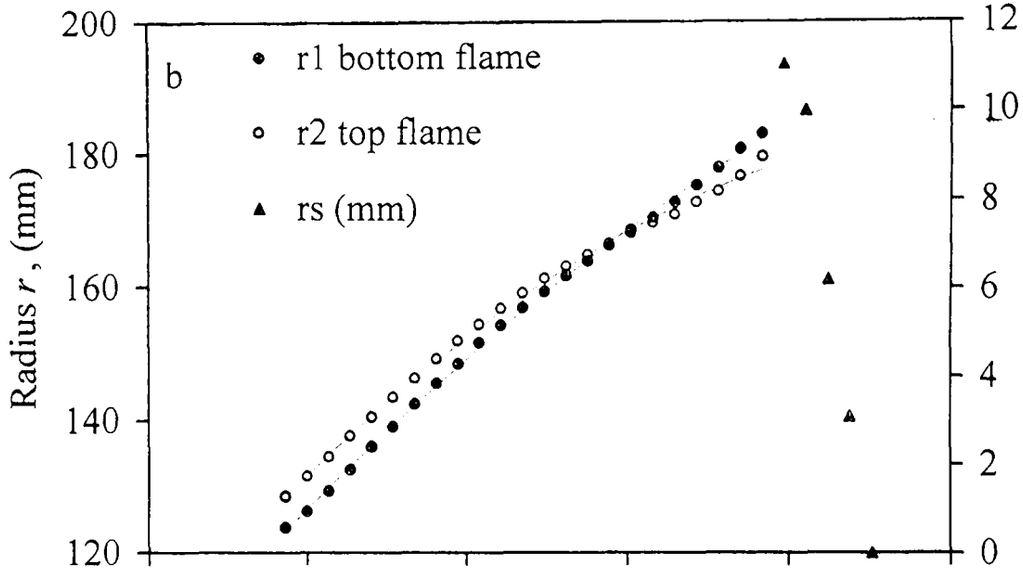

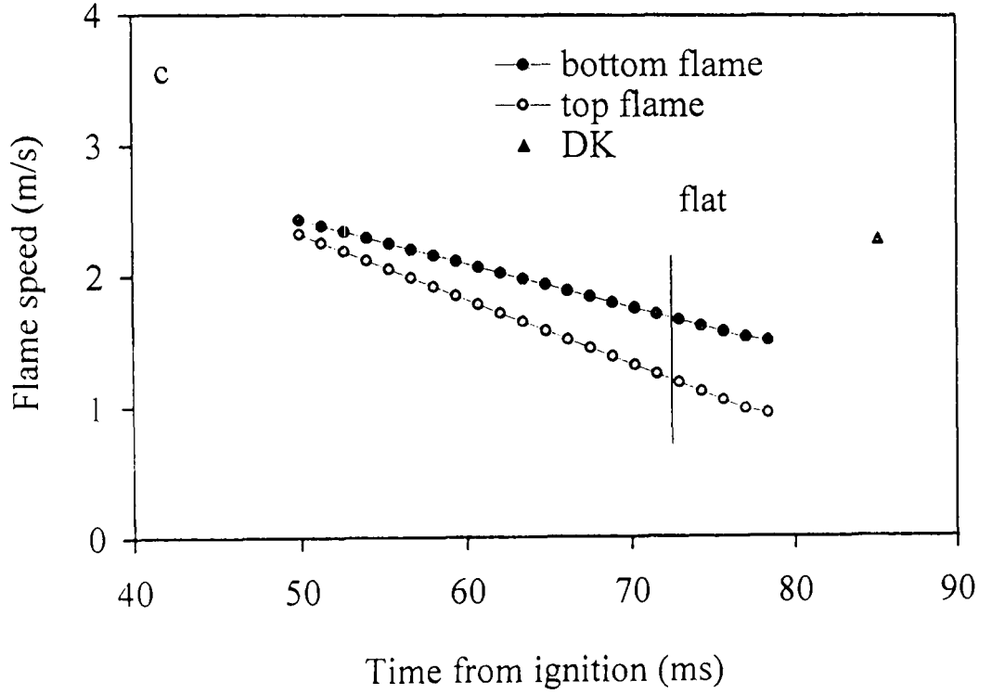

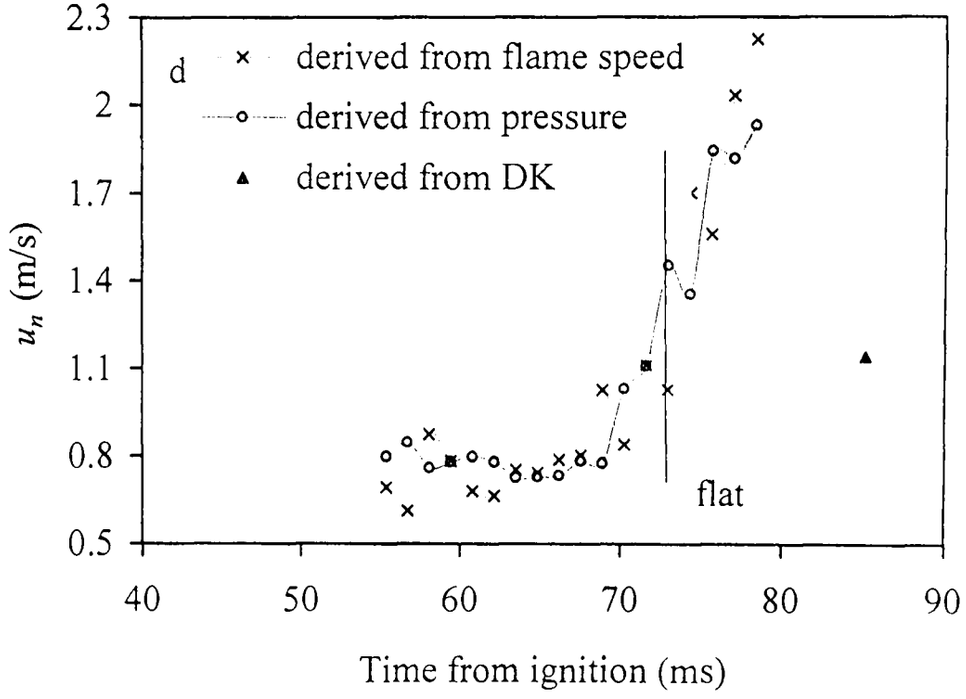

Fig. 6.14. Iso-octane - air implosion, ϕ = 1.4, p_o = 1 MPa, T_o = 358 K

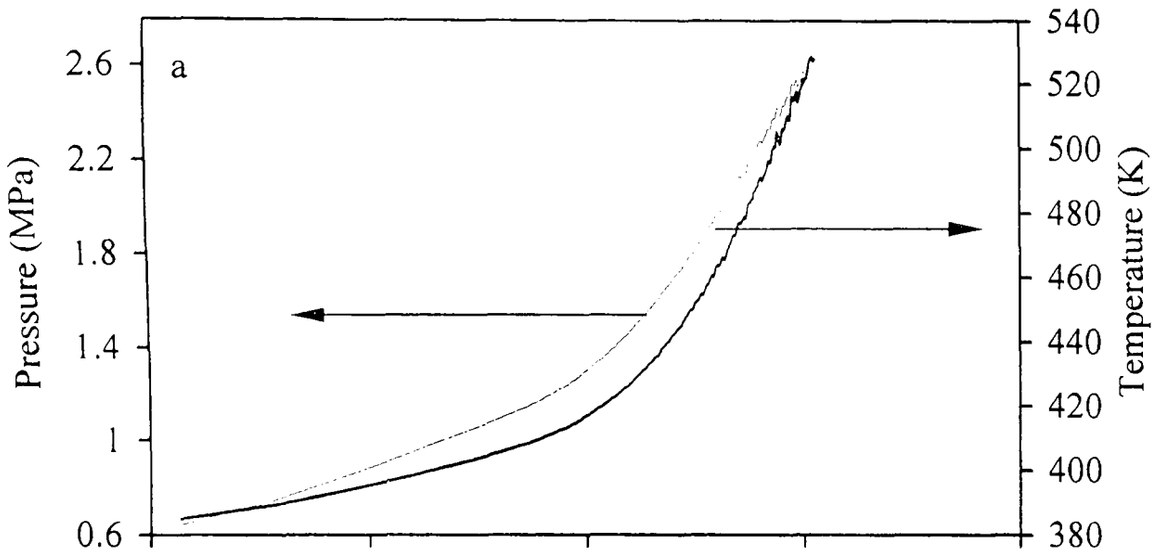

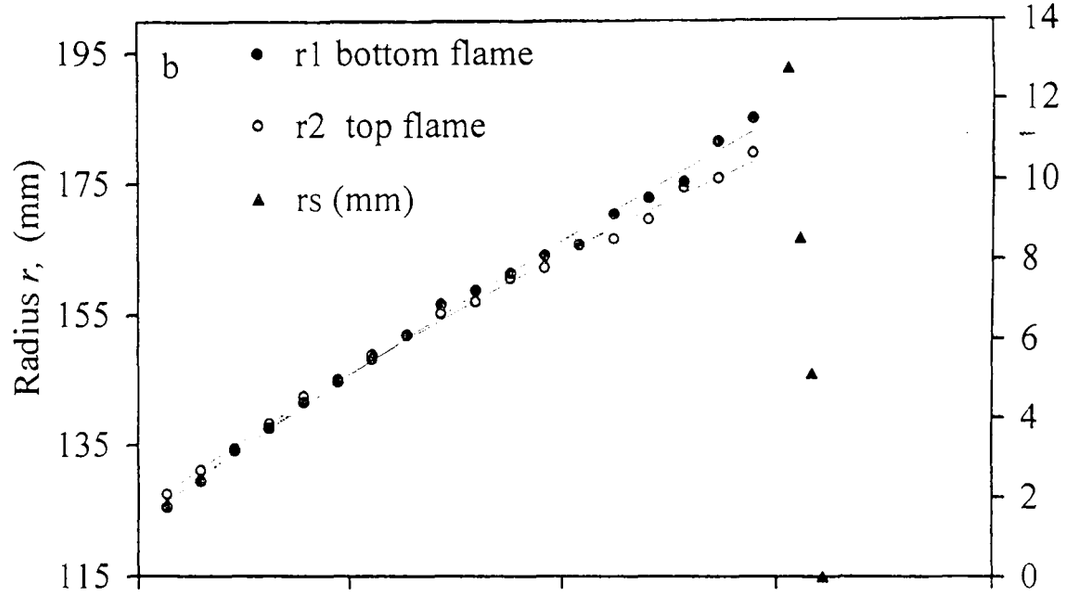

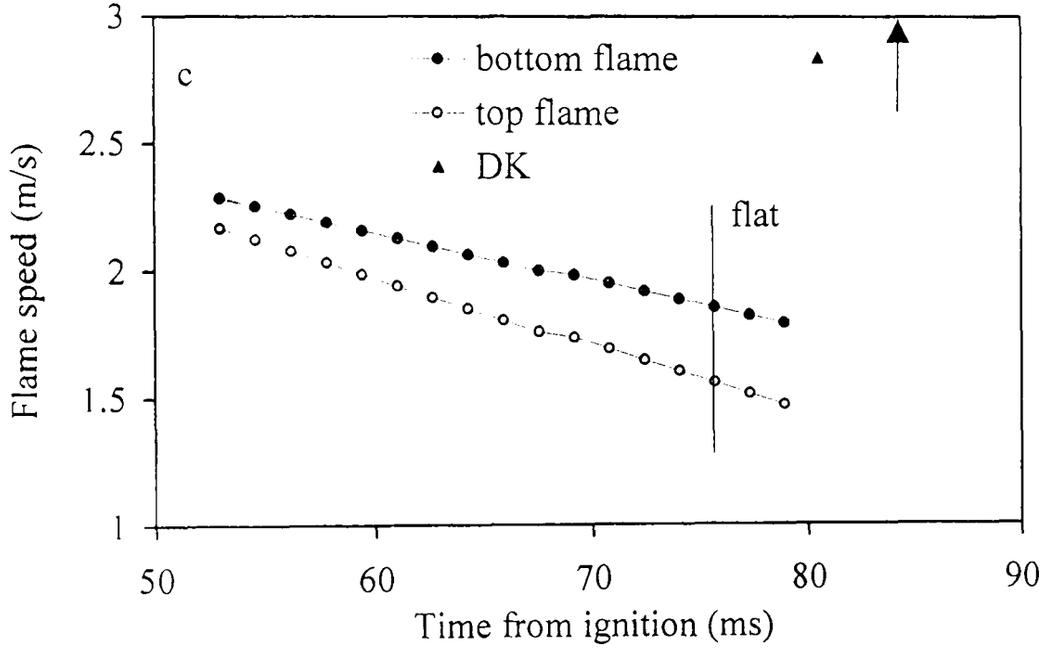

Fig. 6.15. Iso-octane - air implosion, ϕ = 1.5, p_o = 0.5 MPa, T_o = 358 K

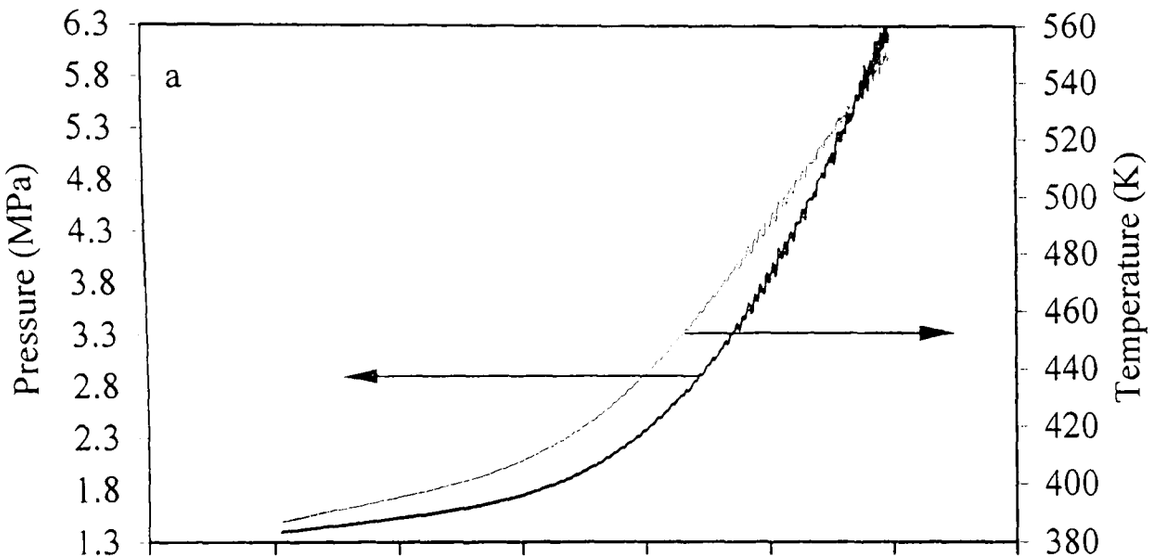

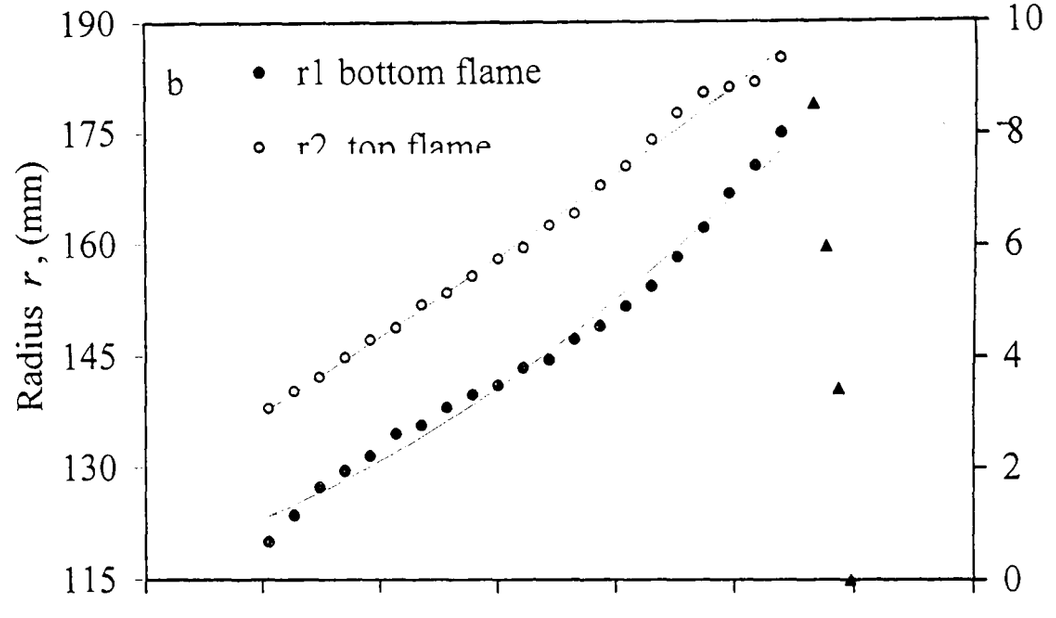

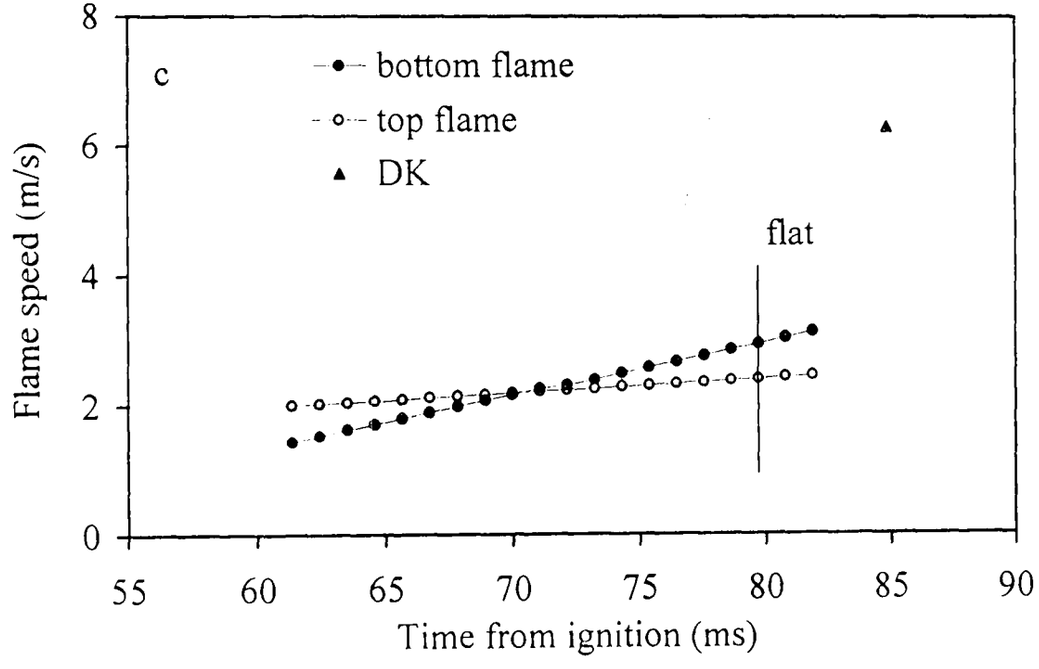

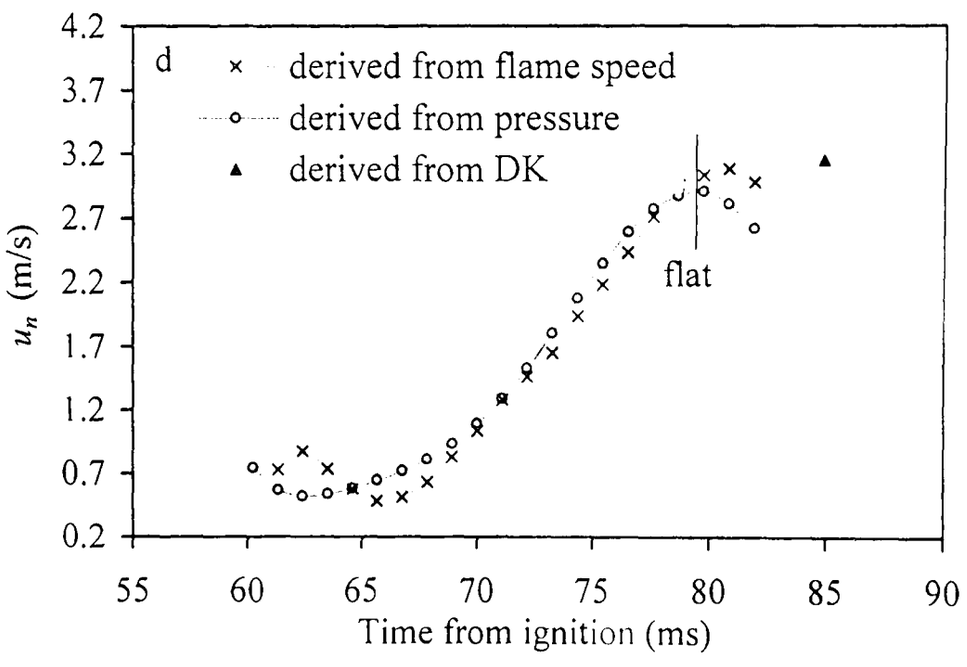

Fig. 6.16. Iso-octane - air implosion, ϕ = 1.5, p_o = 1MPa, T_o = 358 K

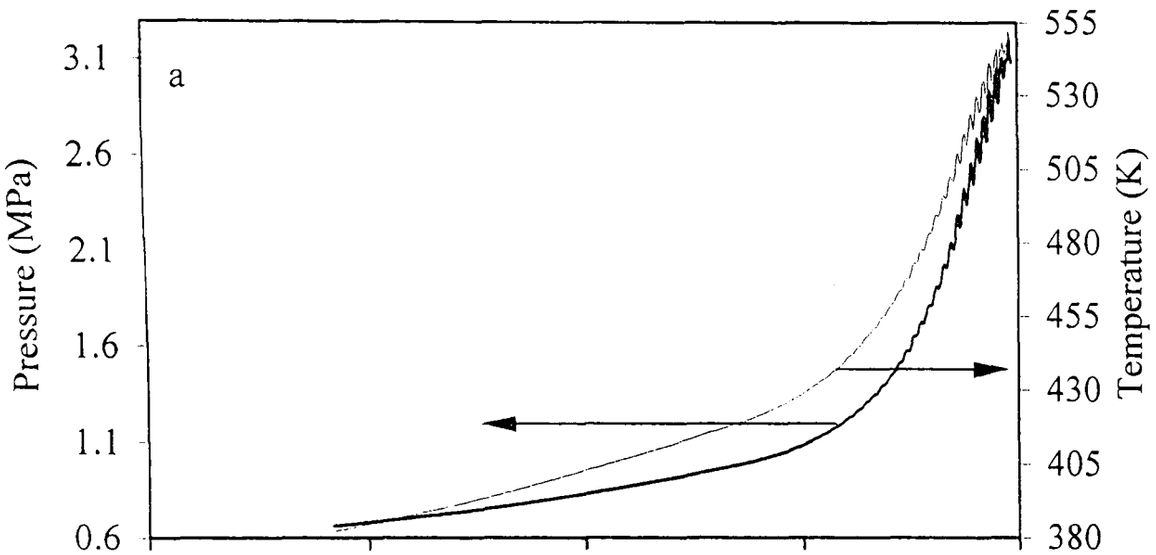

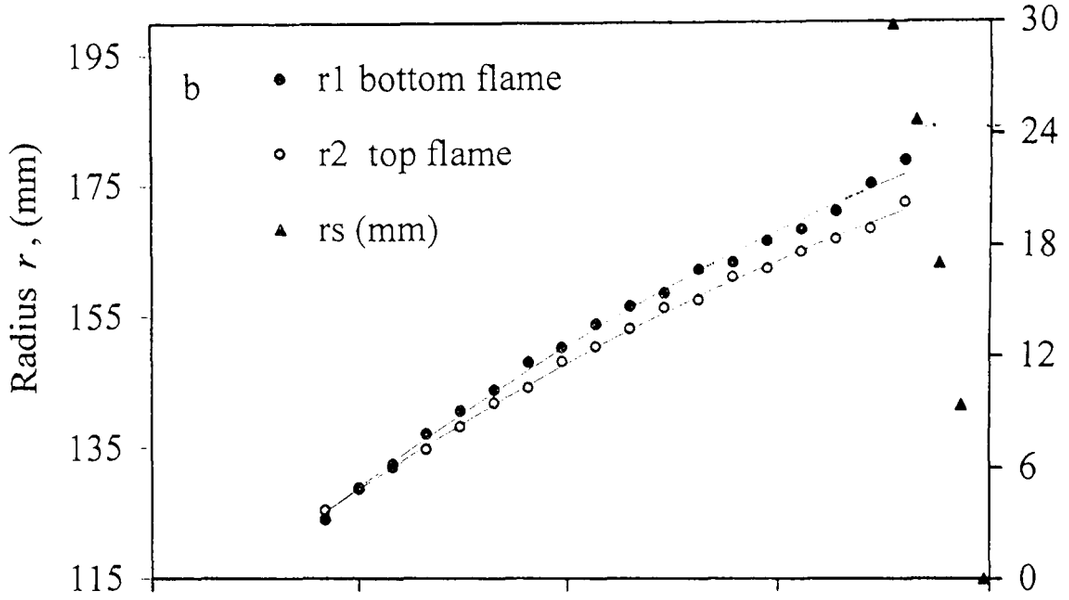

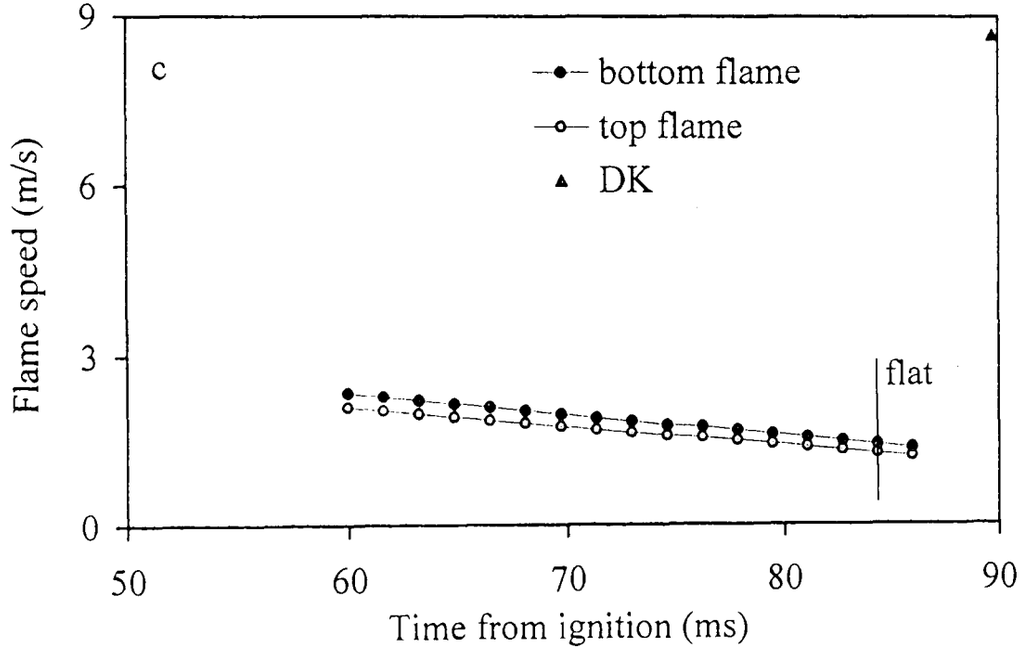

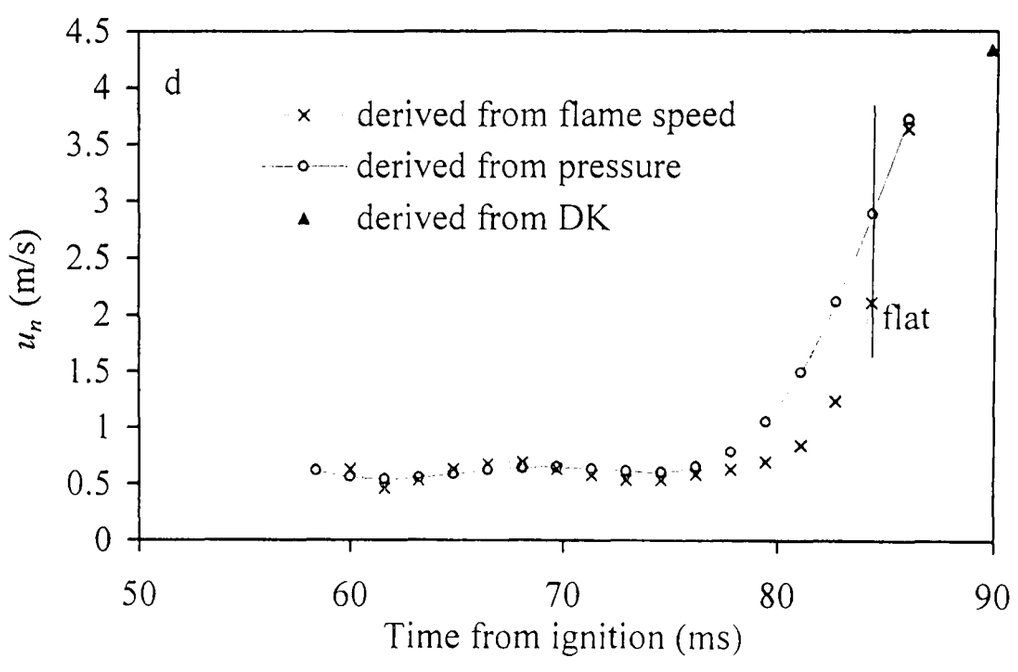

Fig. 6.17. Iso-octane - air implosion, ϕ = 1.6, P_o = 0.5 MPa, T_o = 358 K

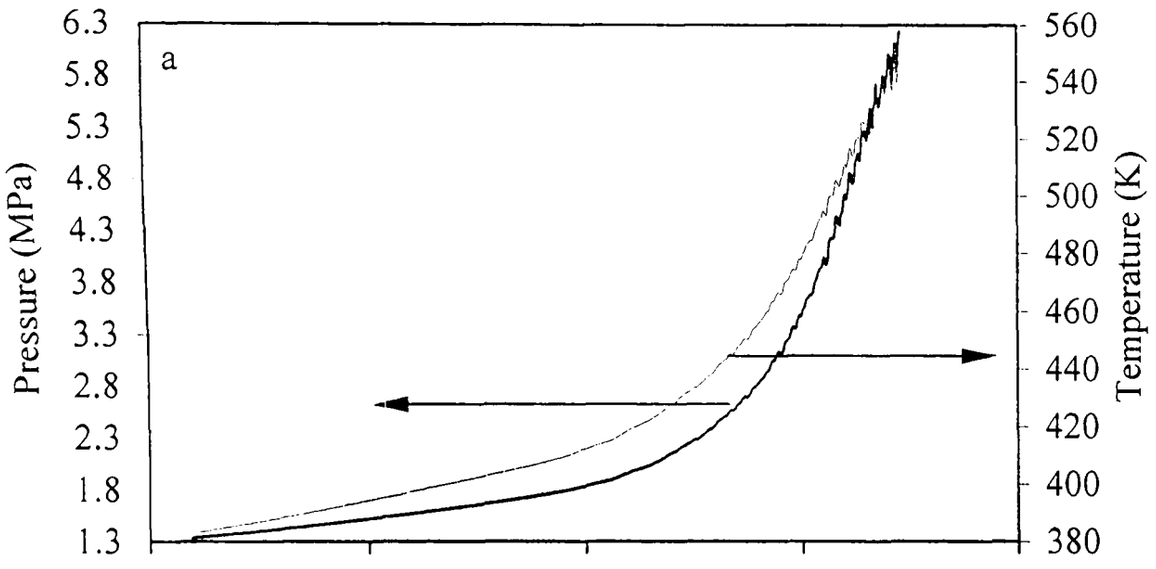

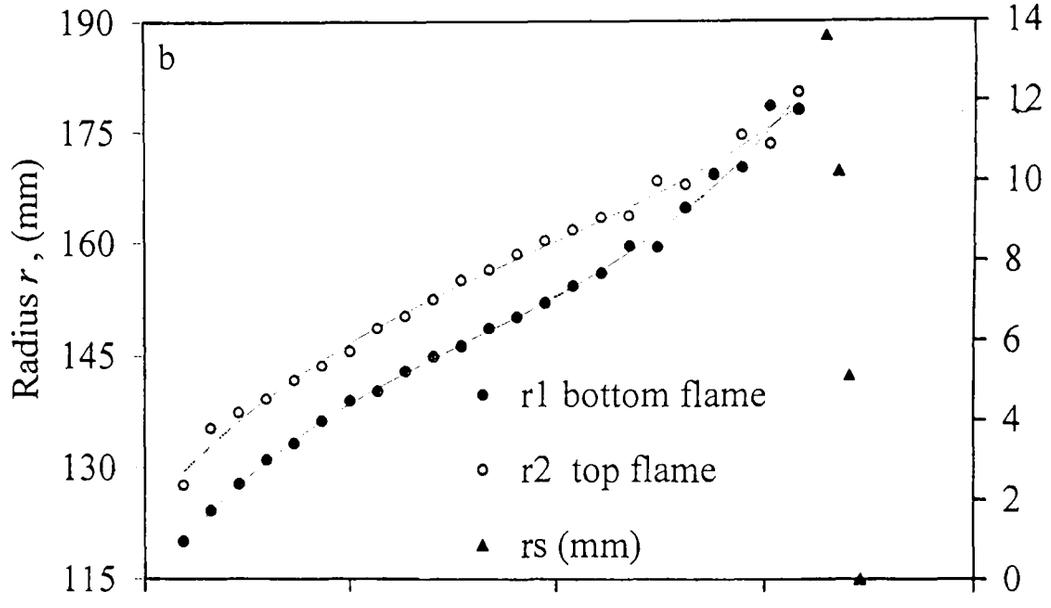

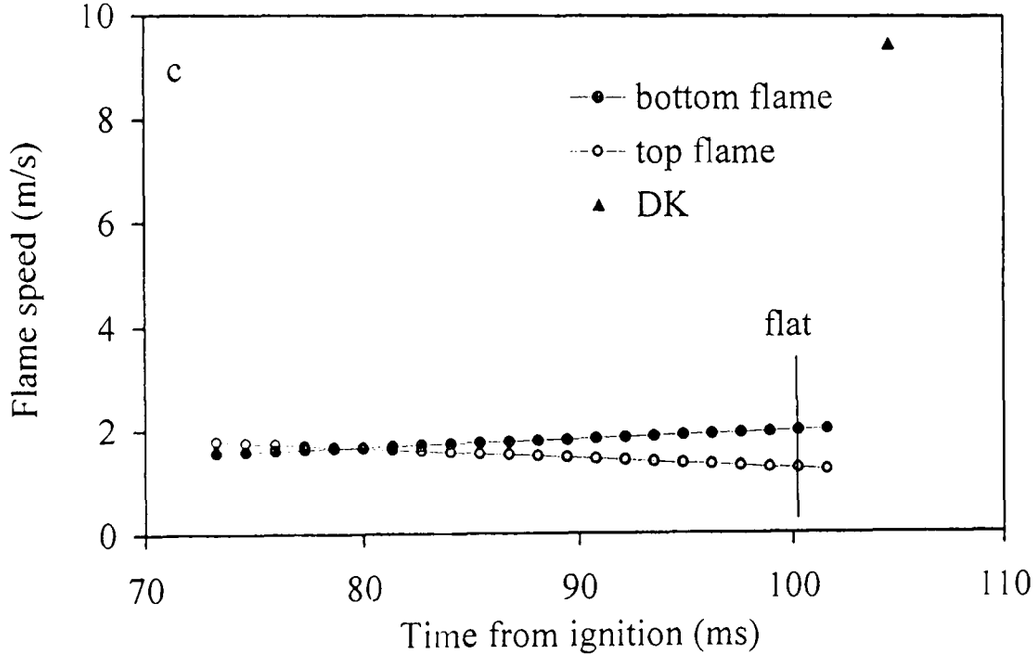

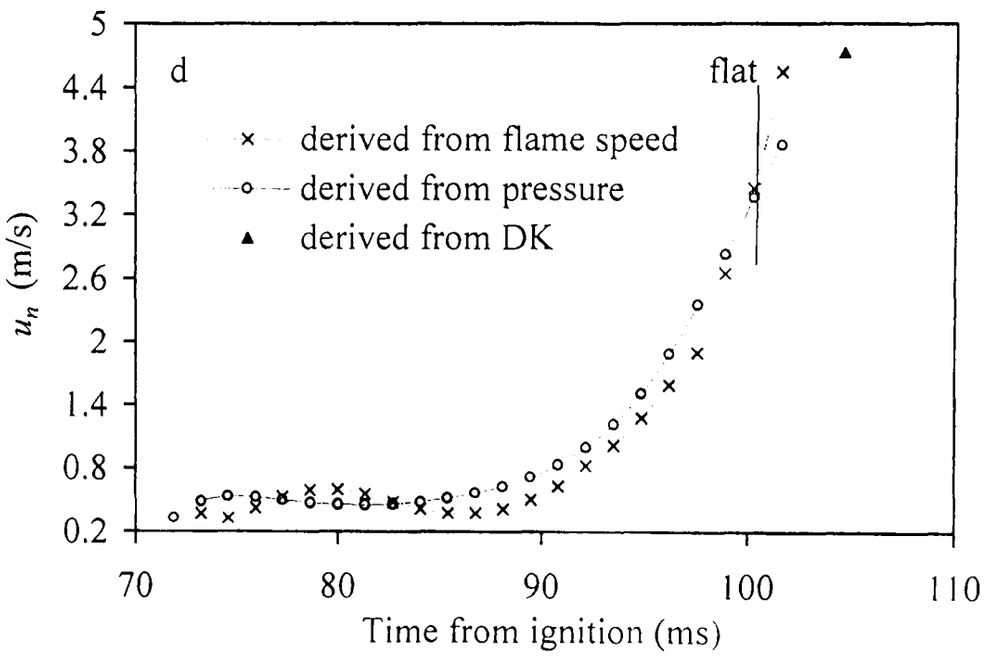

Fig. 6.18. Iso-octane - air implosion, ϕ = 1.6, p_o = 1MPa, T_o = 358 K

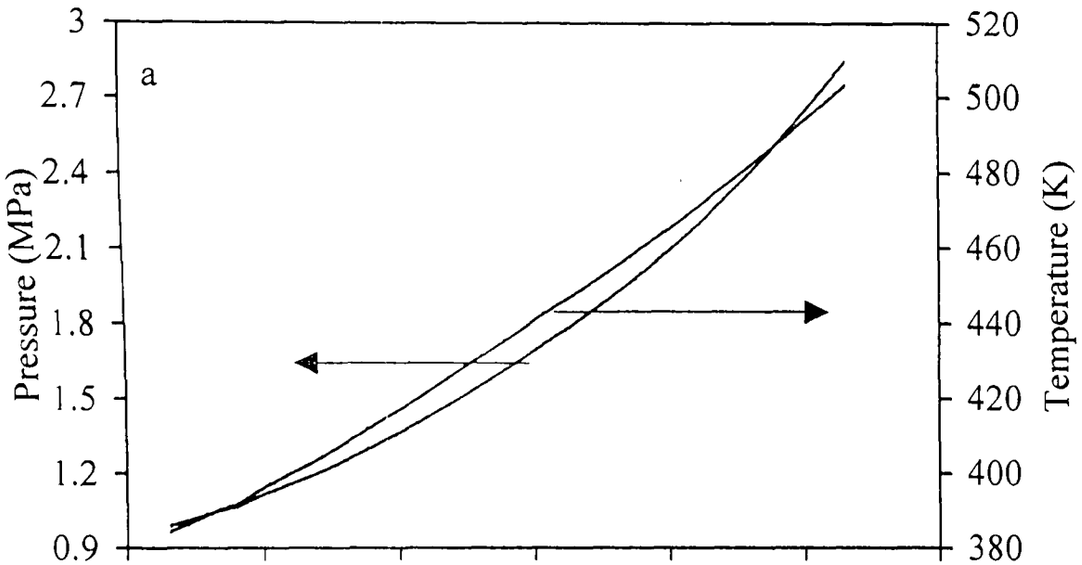

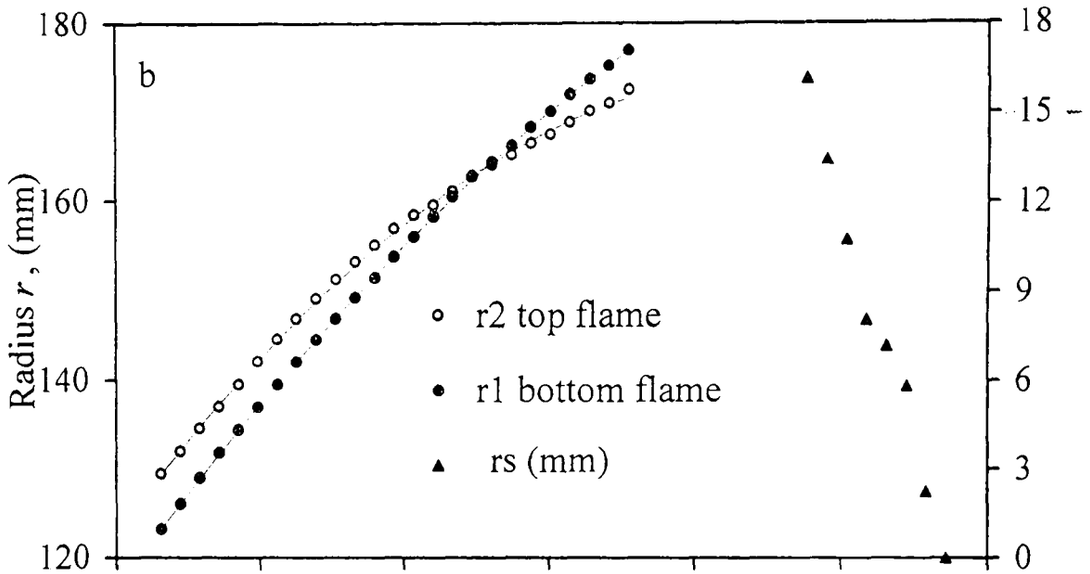

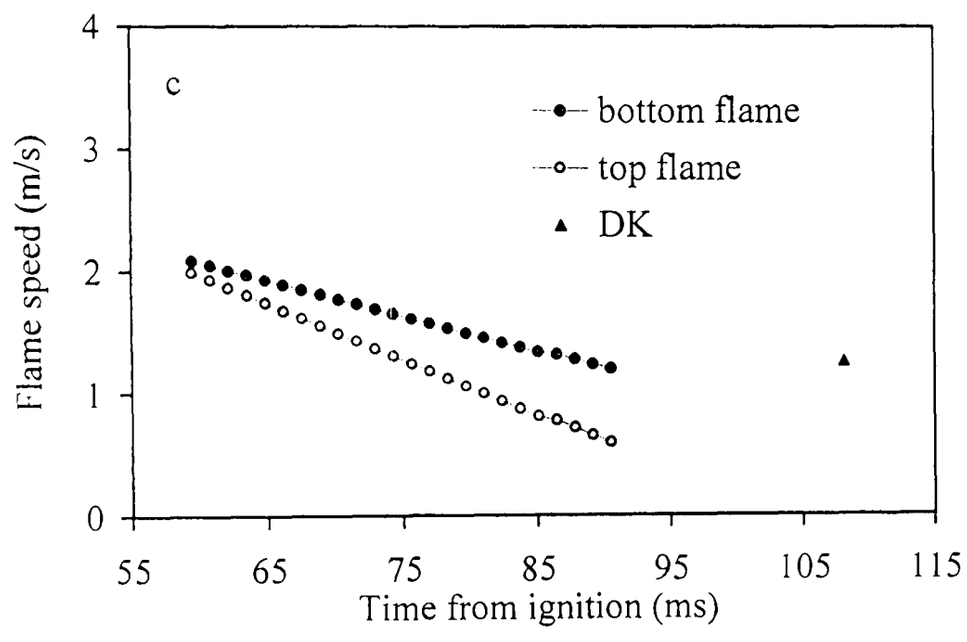

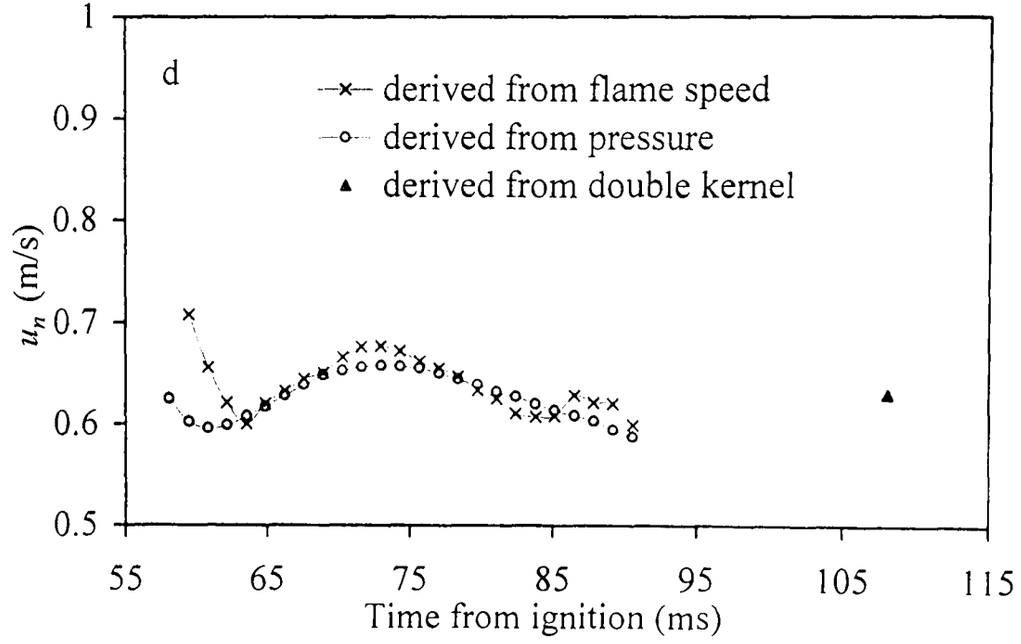

Fig. 6.19. Iso-octane - air implosion, $\phi = 1, p_o = 0.75$ MPa, $T_o = 358$ K

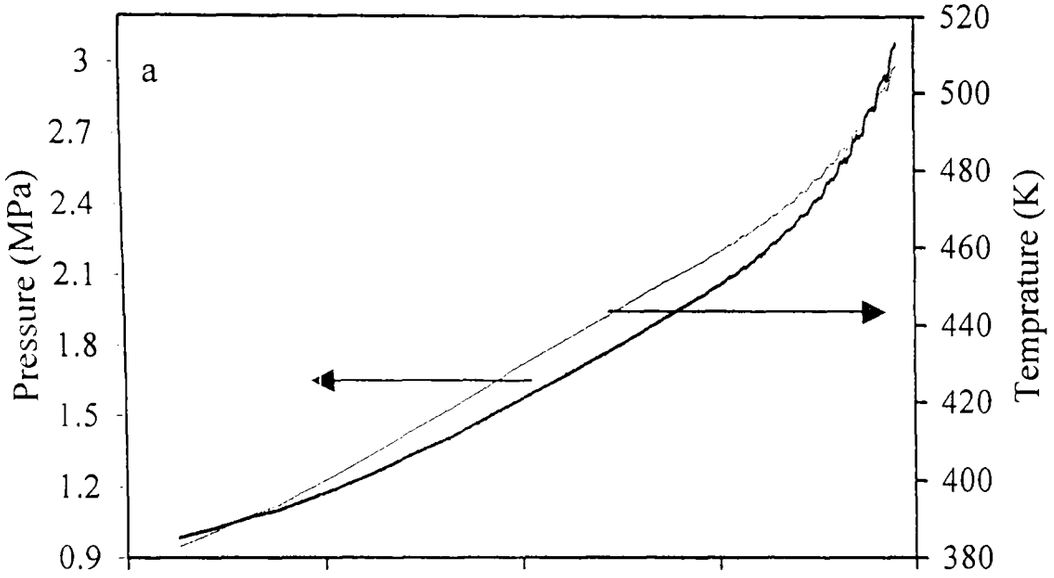

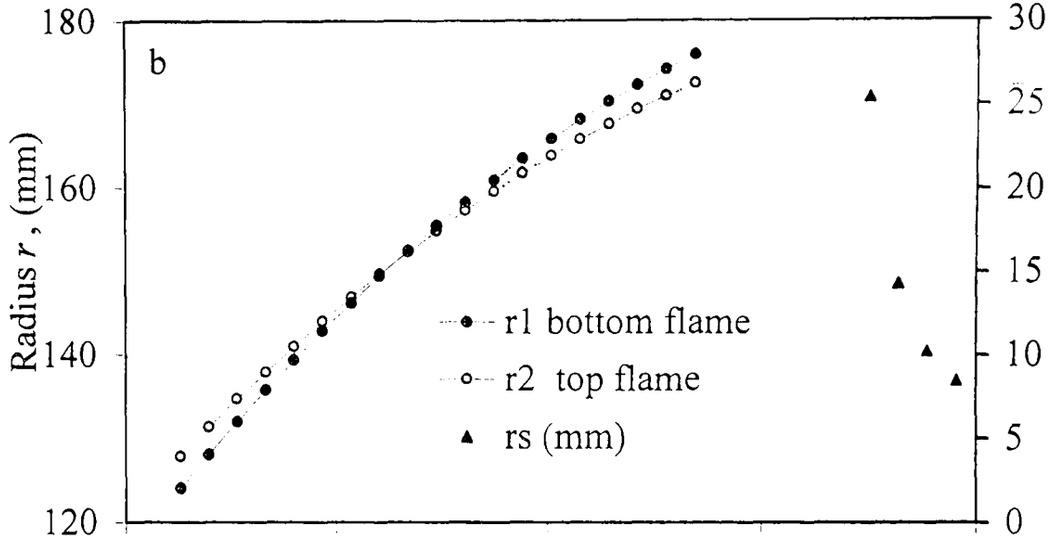

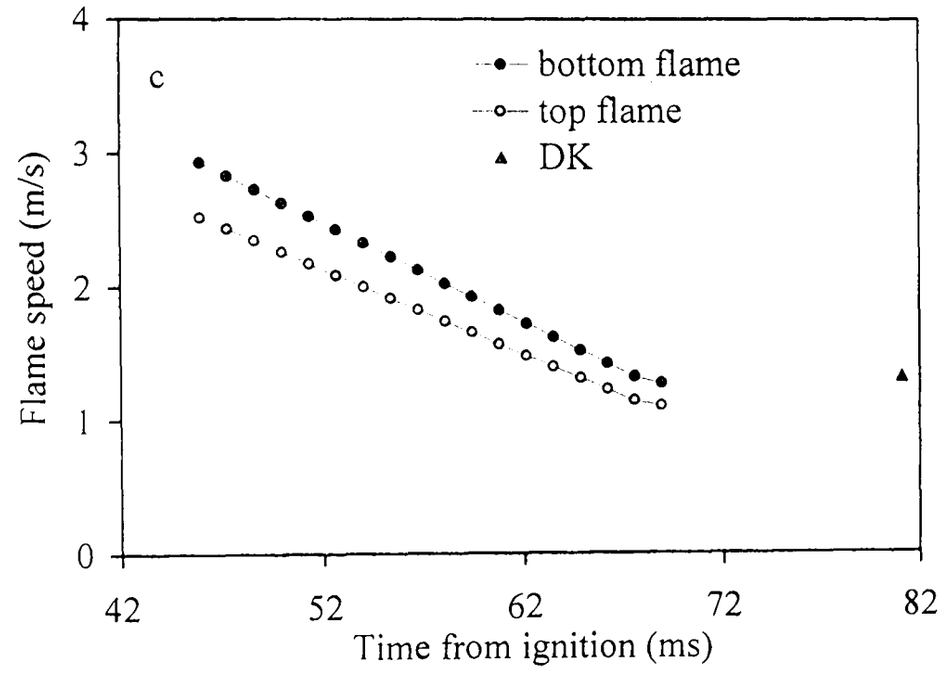

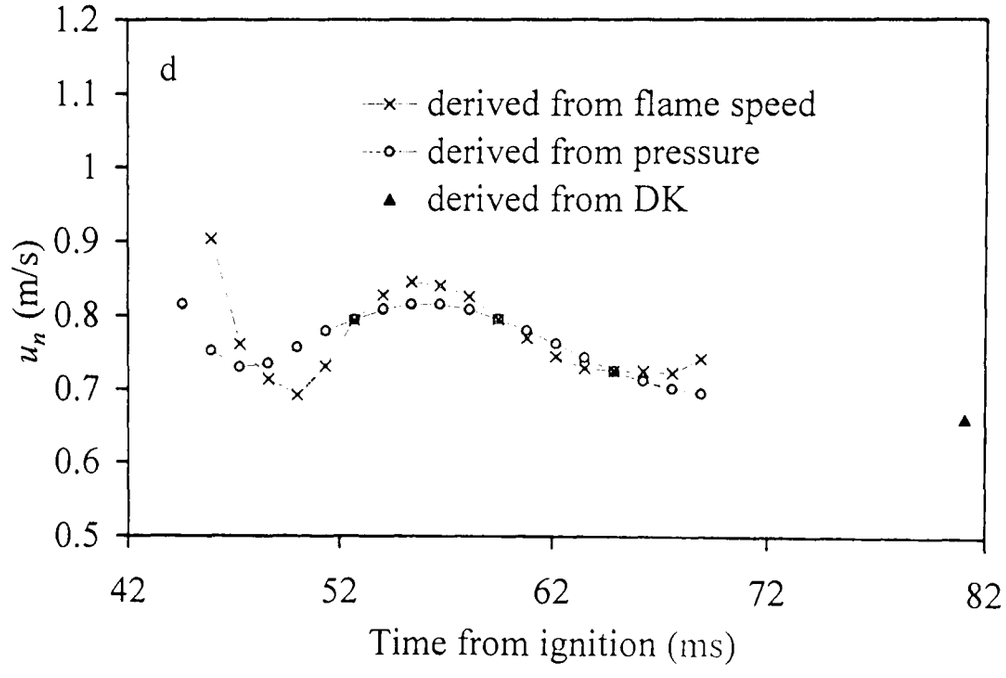

Fig. 6.20. Iso-octane - air implosion, ϕ = 1.4, p_o = 0.75 MPa, T_o = 358 K

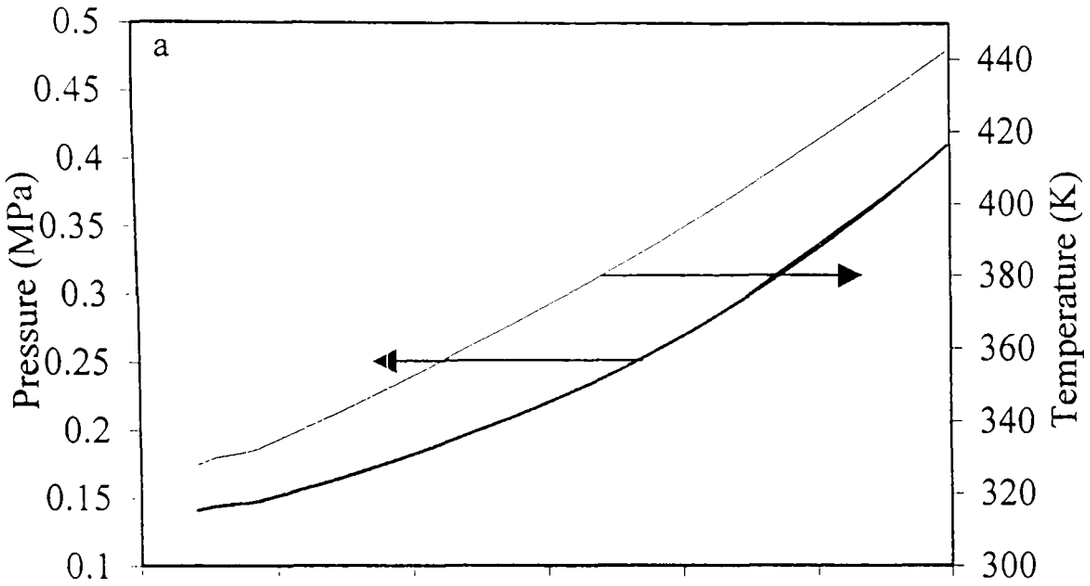

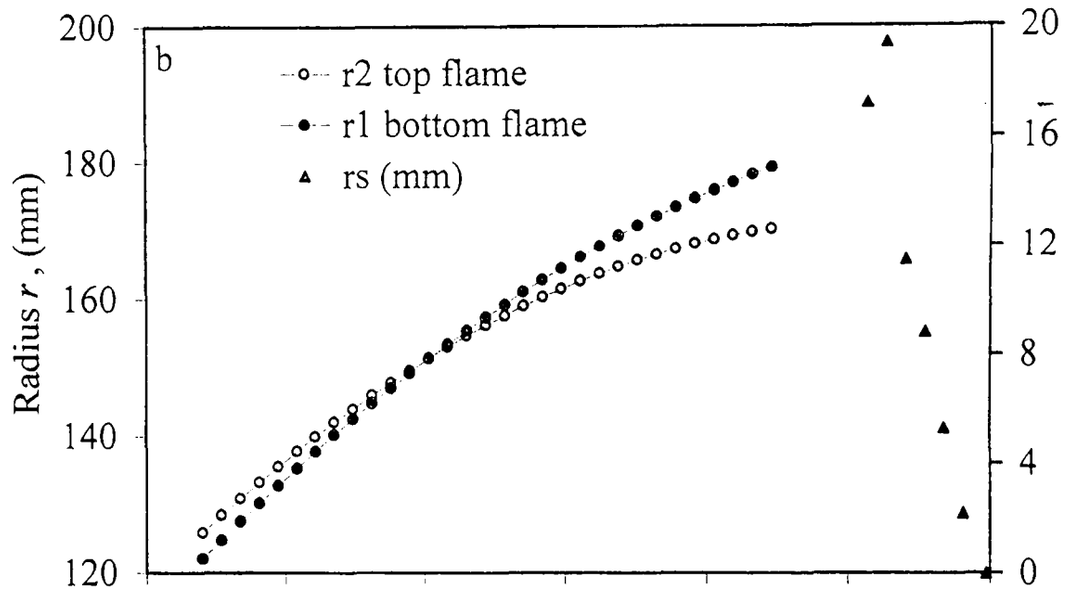

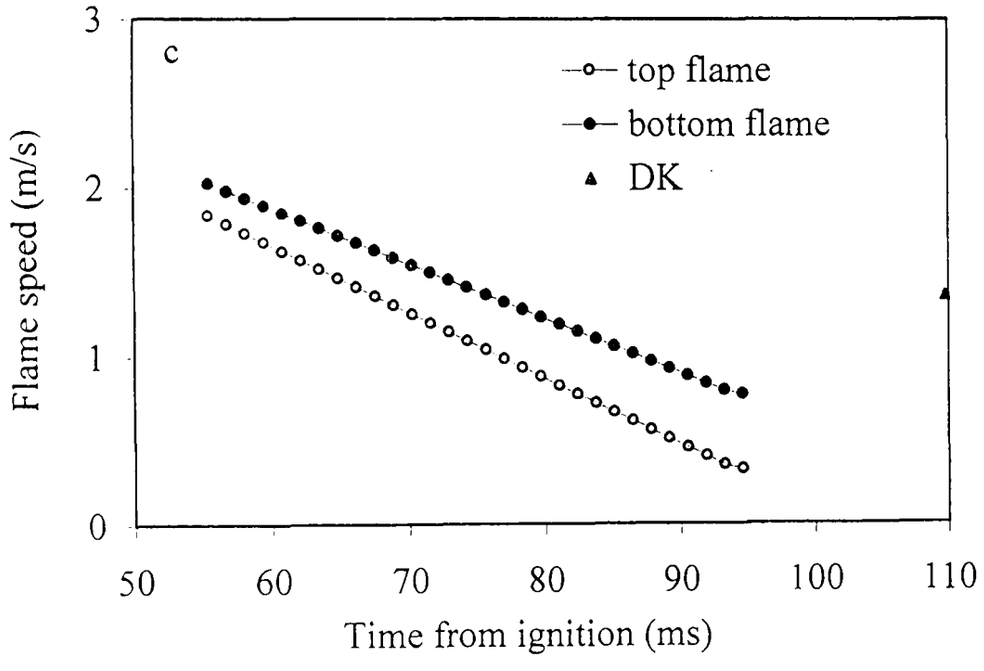

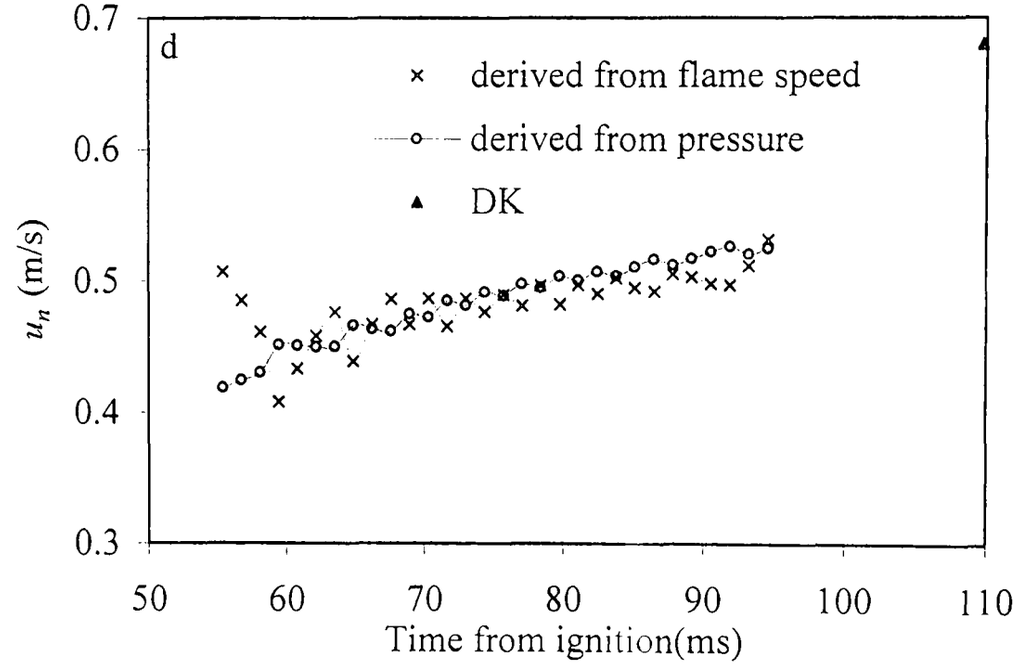

Fig. 6.21. Methane - air implosion, $\phi = 1, p_o = 0.1$ MPa, $T_o = 298$ K

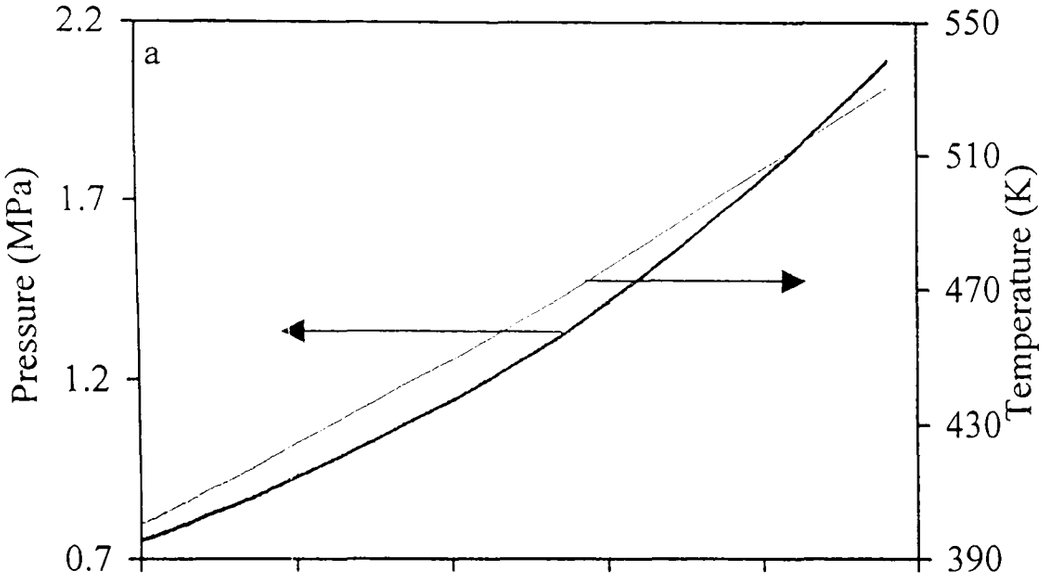

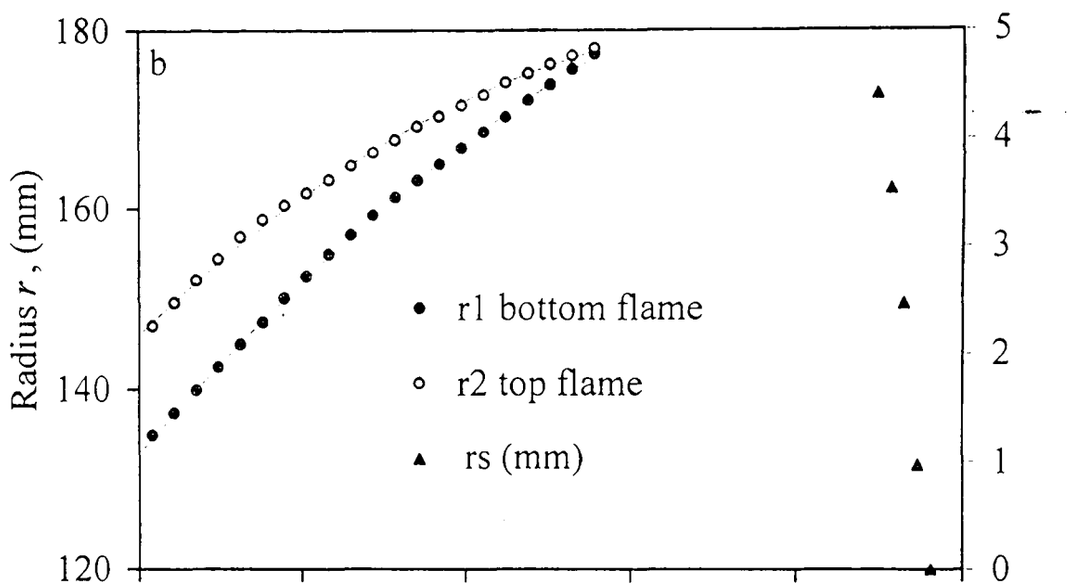

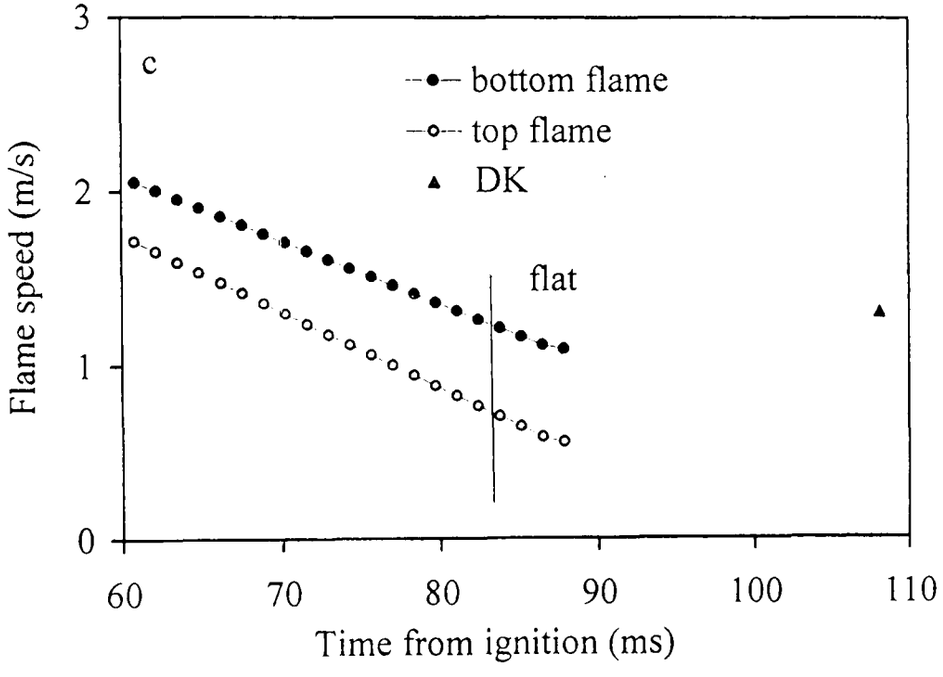

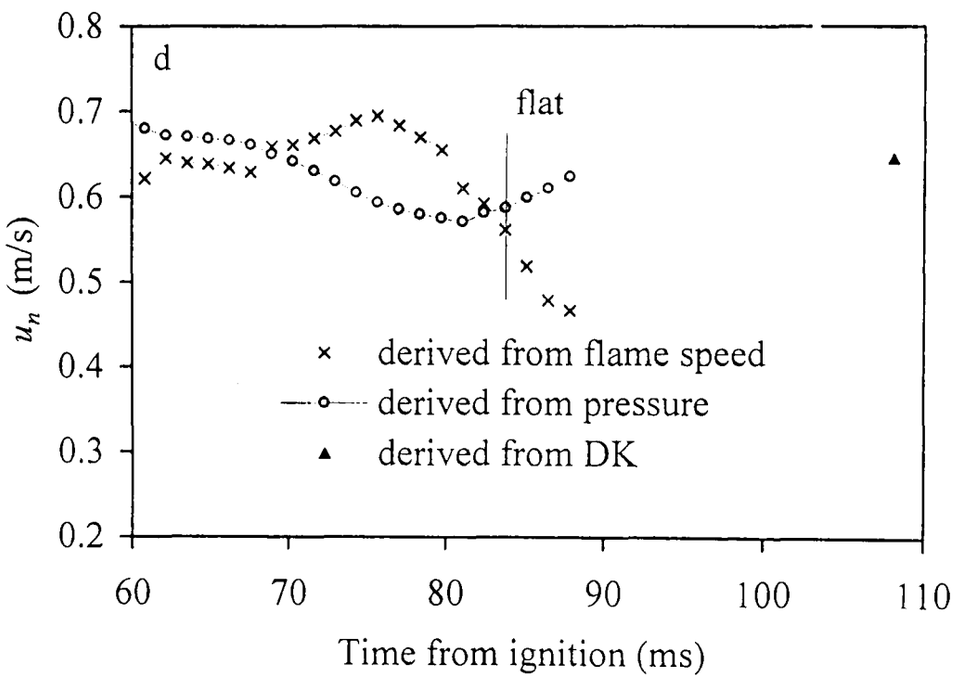

Fig. 6.22. Methane - air implosion, $\phi = 1$, $P_o = 0.5$ MPa, $T_o = 358$ K

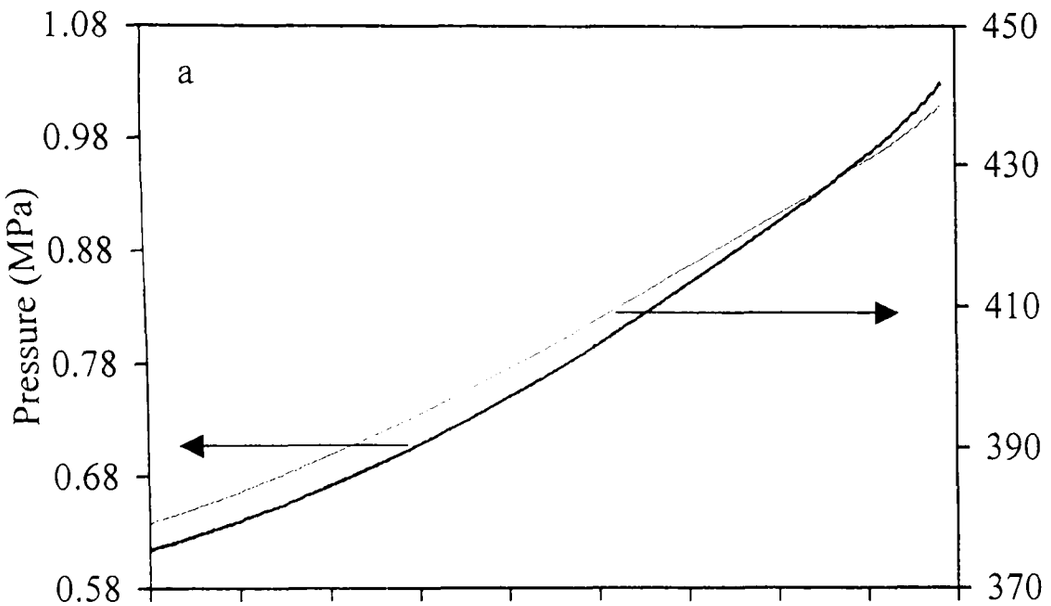

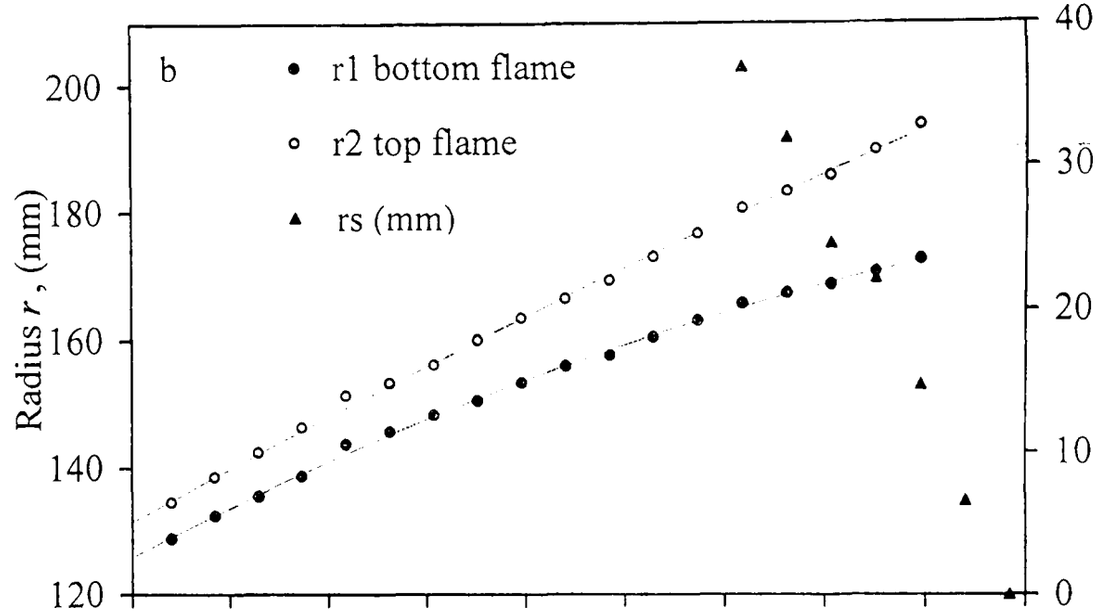

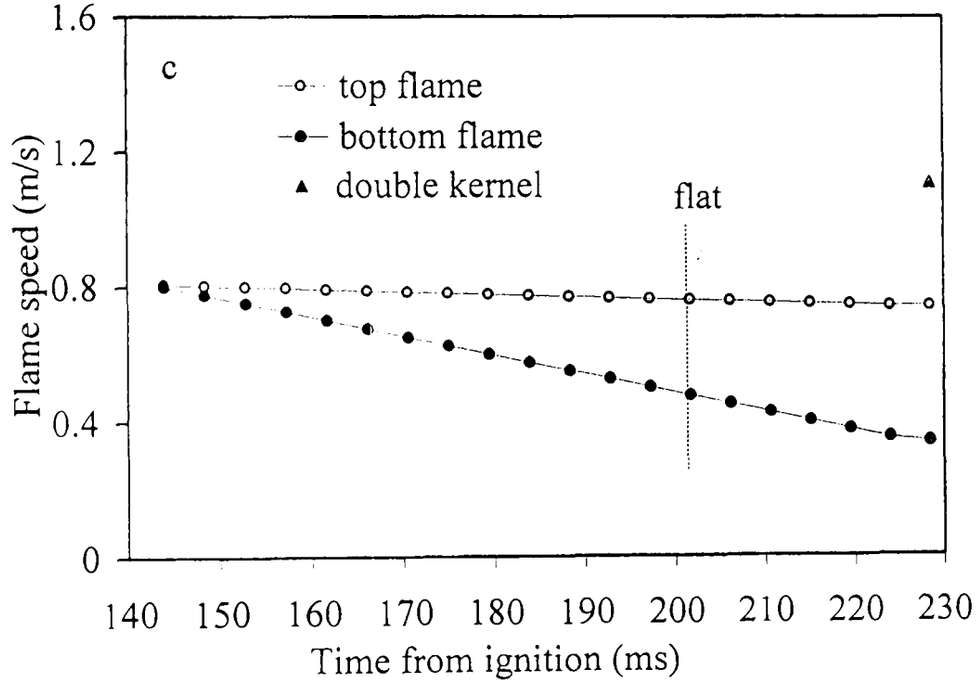

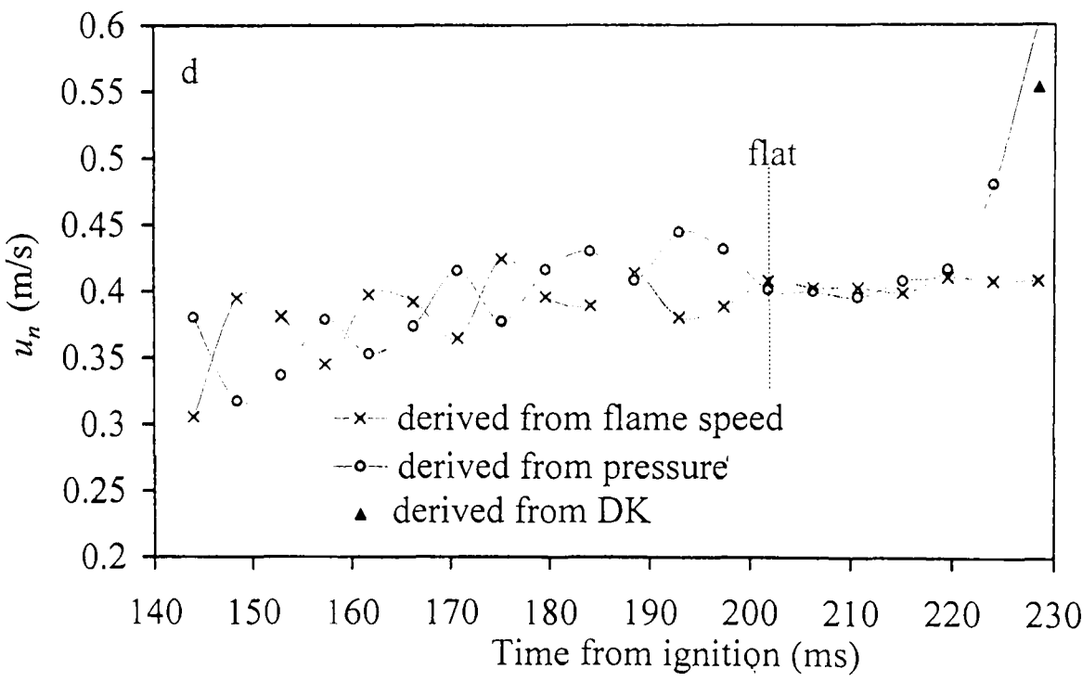

Fig. 6.23. Hydrogen - air implosion, $\phi = 0.3$, $p_o = 0.5$ MPa, $T_o = 358$ K

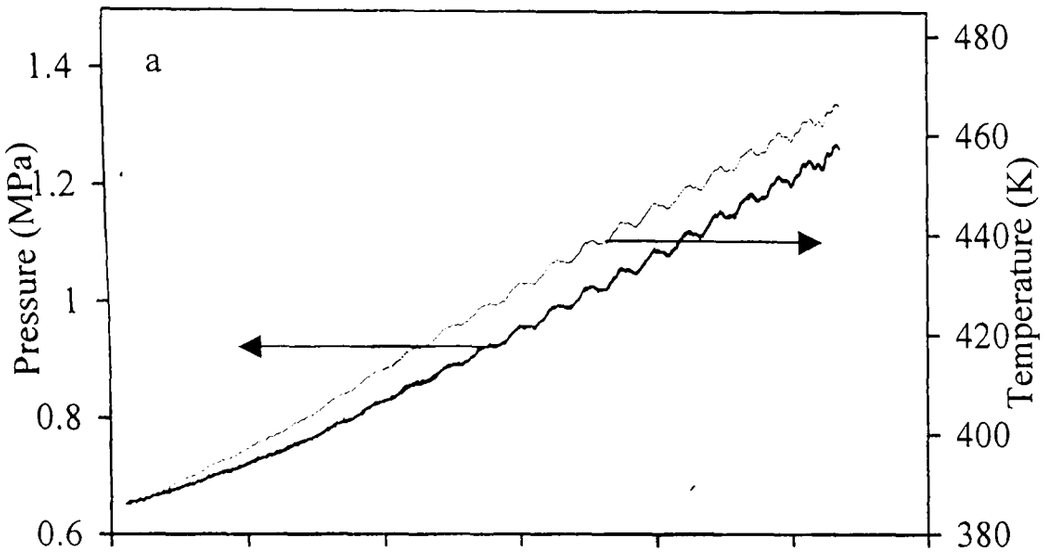

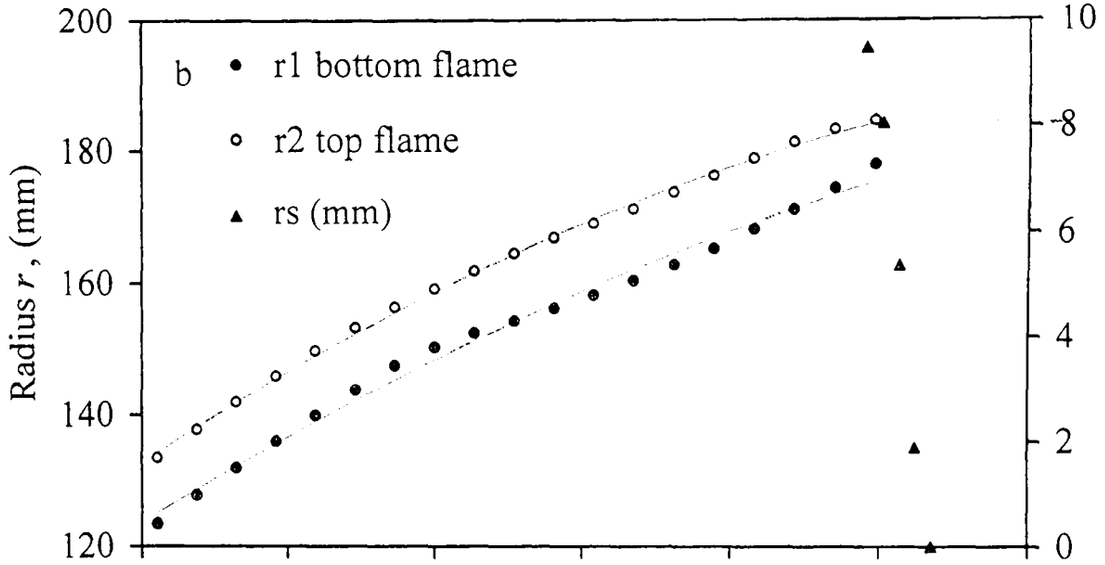

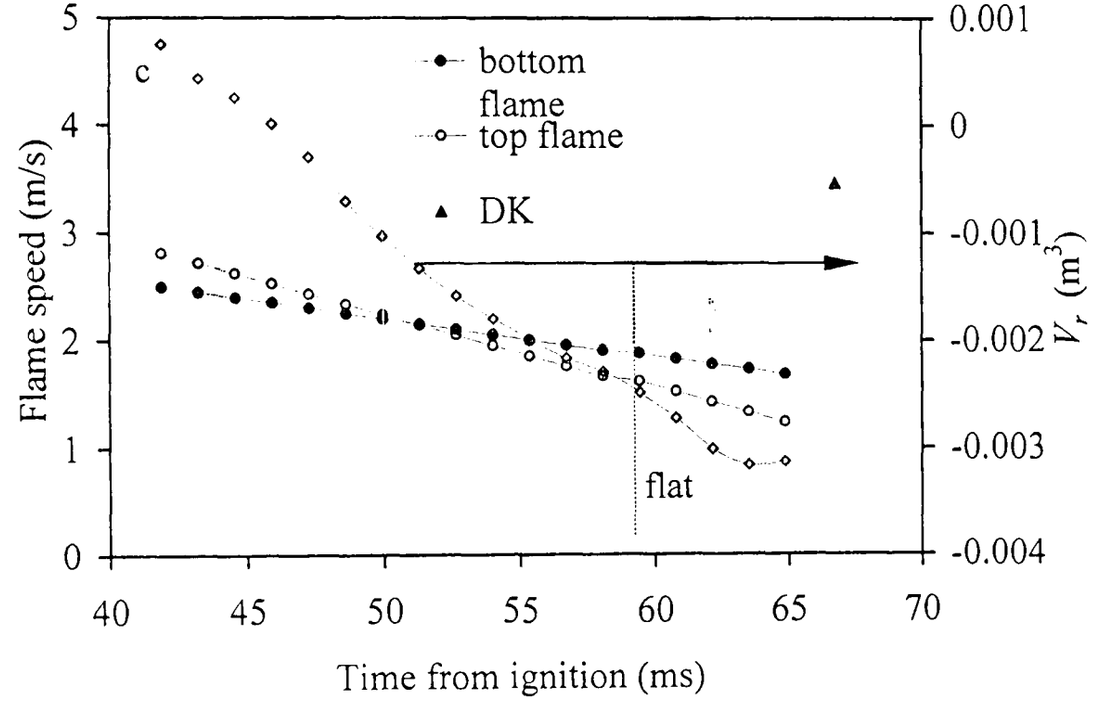

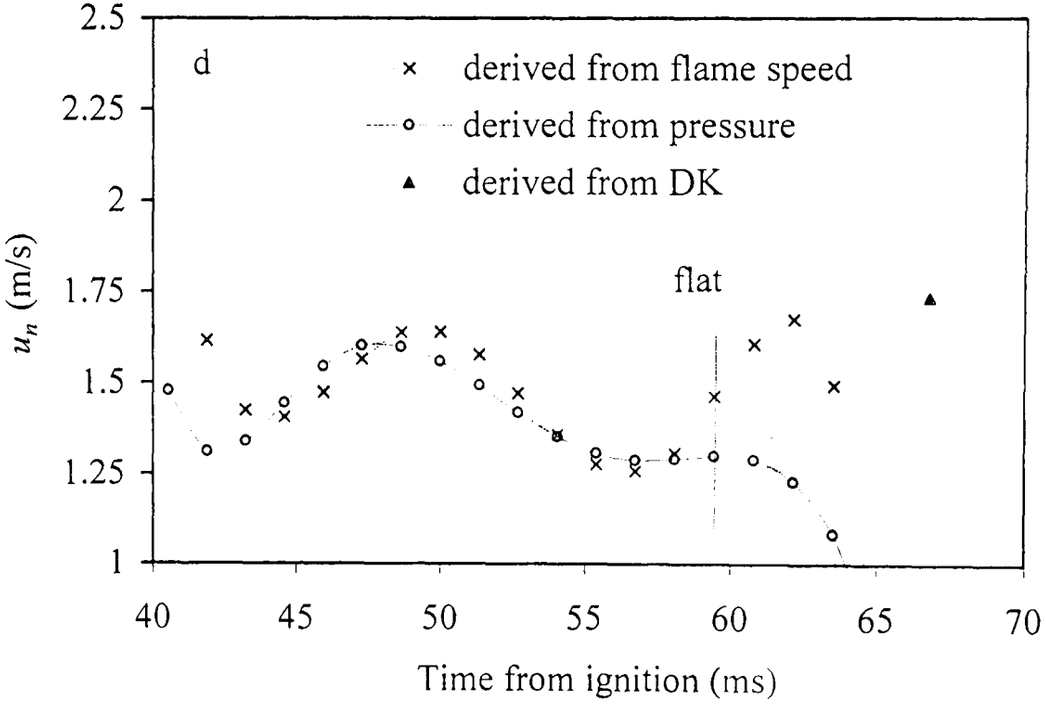

Fig. 6.24. Hydrogen - air implosion, ϕ = 0.4, p_o = 0.5 MPa, T_o = 358 K

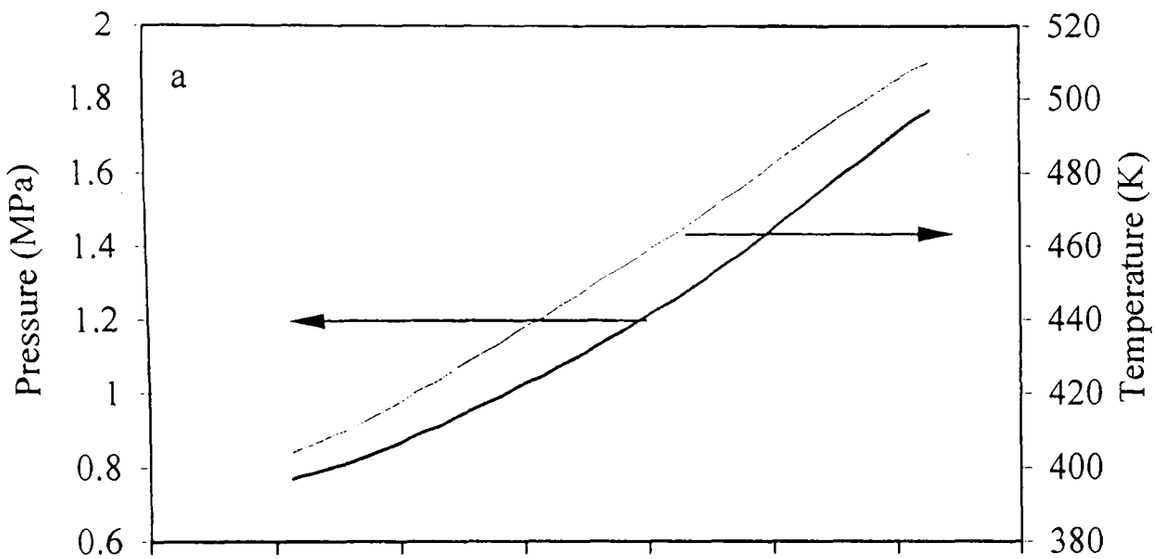

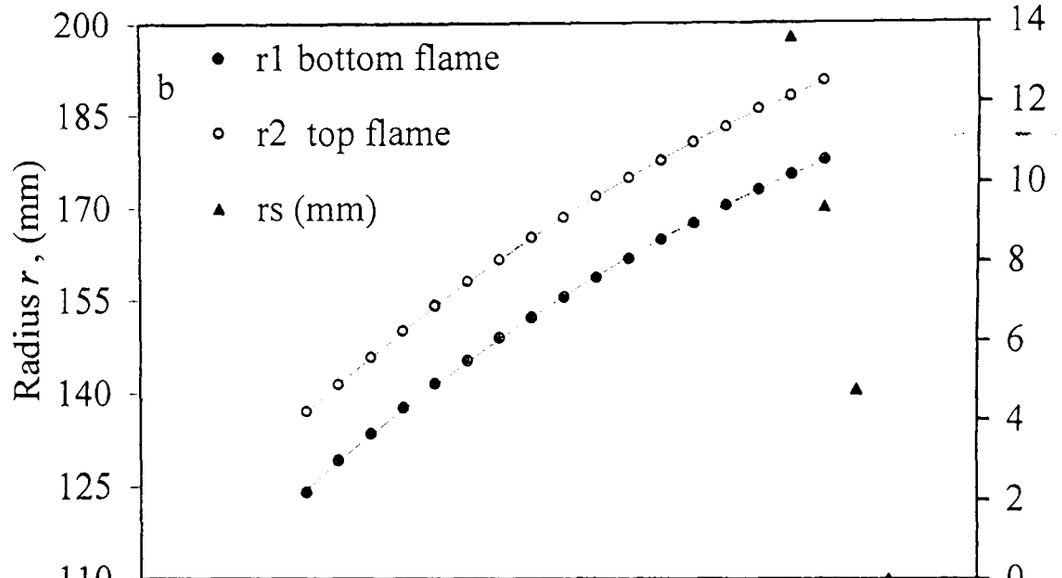

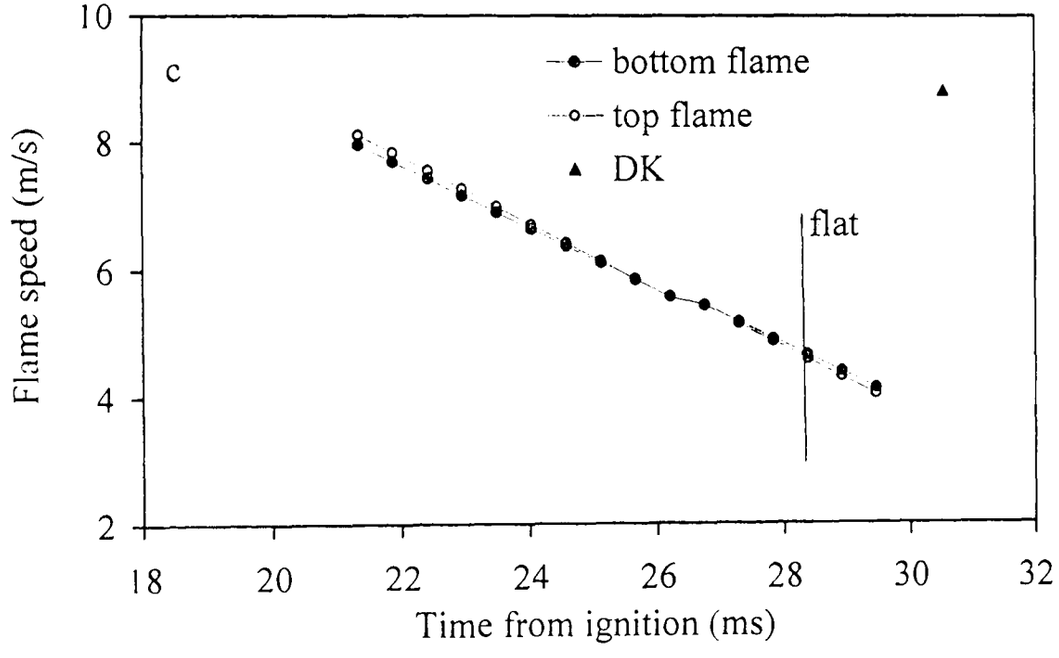

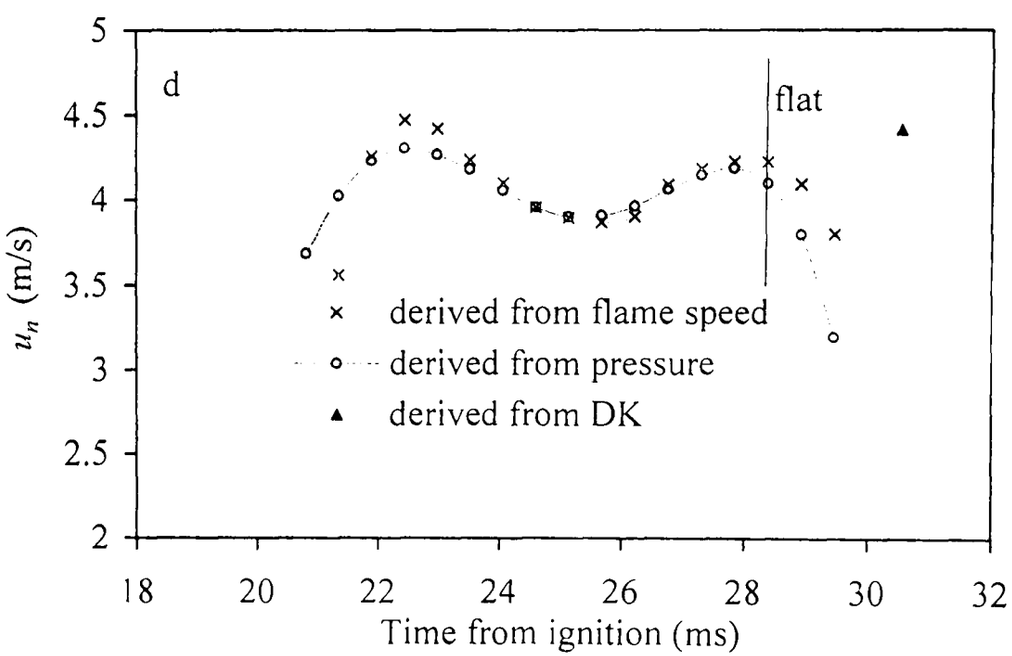

Fig. 6.25. Hydrogen - air implosion, ϕ = 0.5, p_o = 0.5 MPa, T_o = 358 K

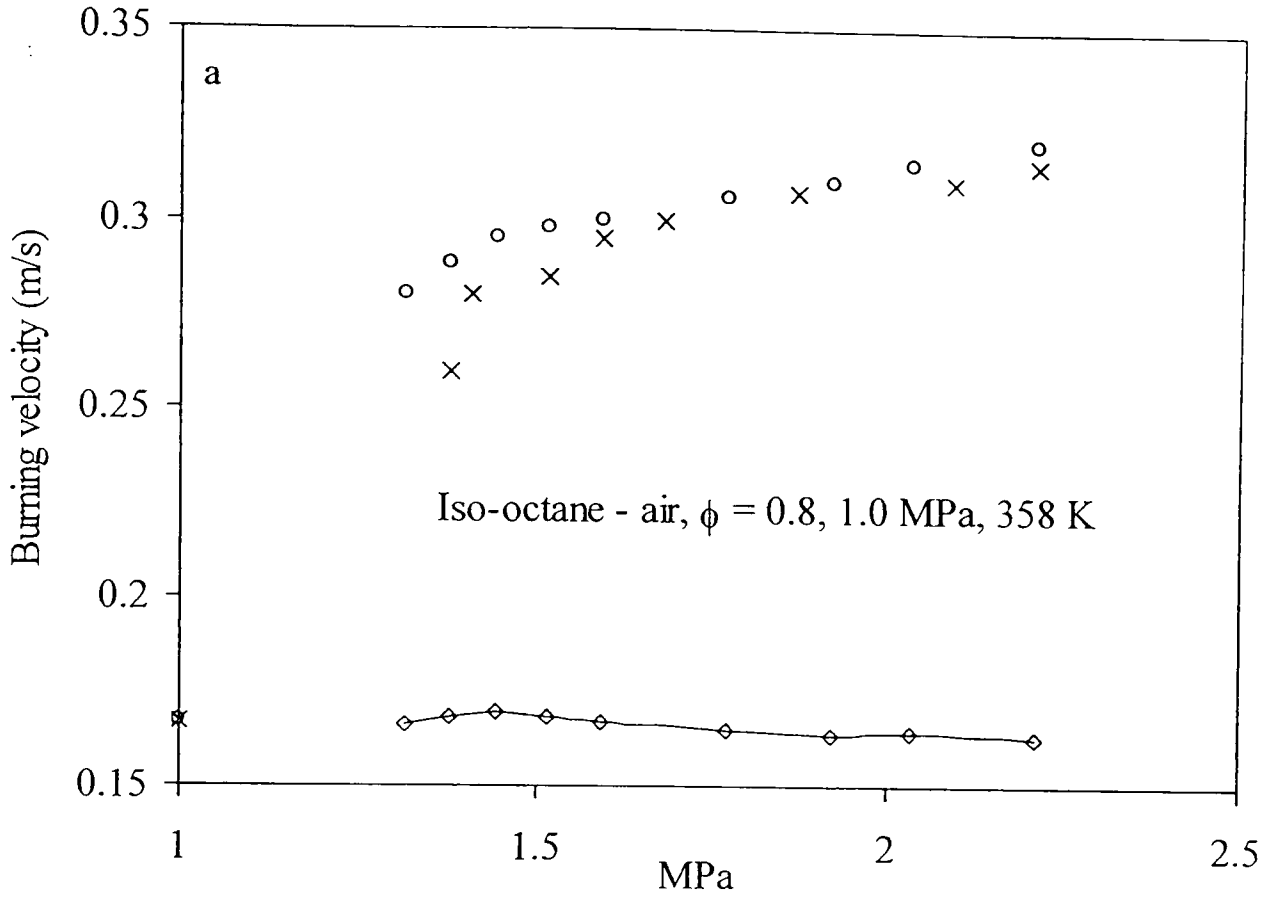

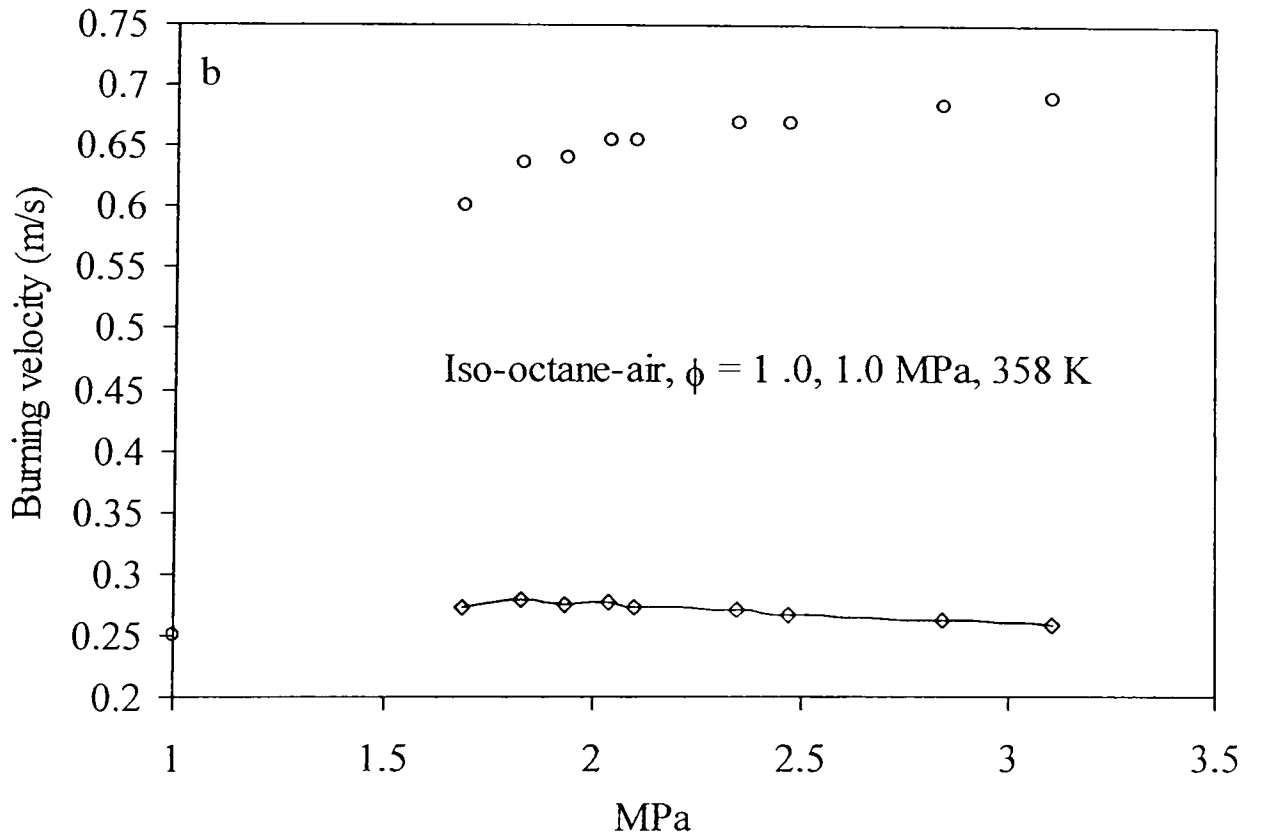

Fig. 6.30. Experimental values of u_n from two implosions of (a) lean (ϕ = 0.8) iso-octane-air initially at 1.0 MPa, (b) for stoichiometric iso-octane initially 1.0 MPa, both at initial temperature of 358 K (upper symbols). Lower symbols show values of u_l predicted from these.

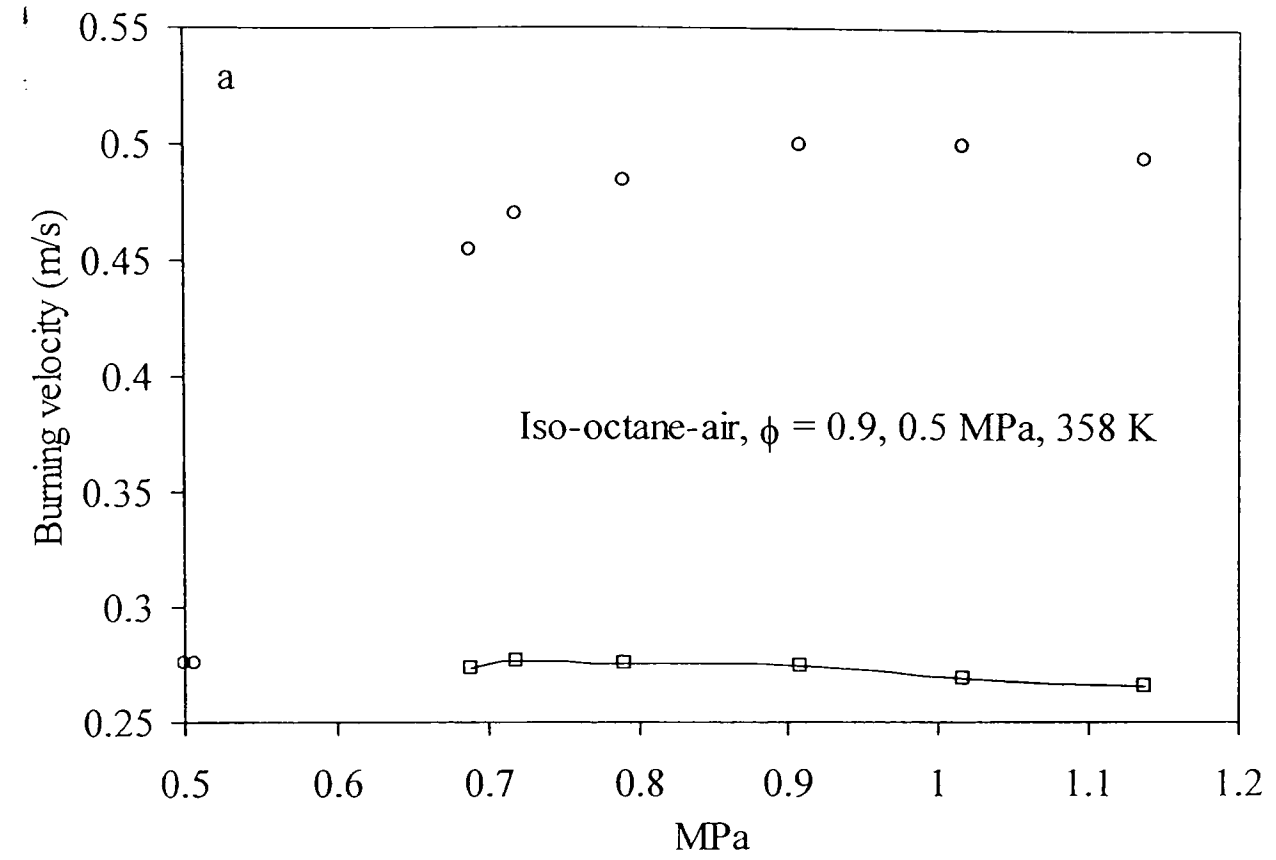

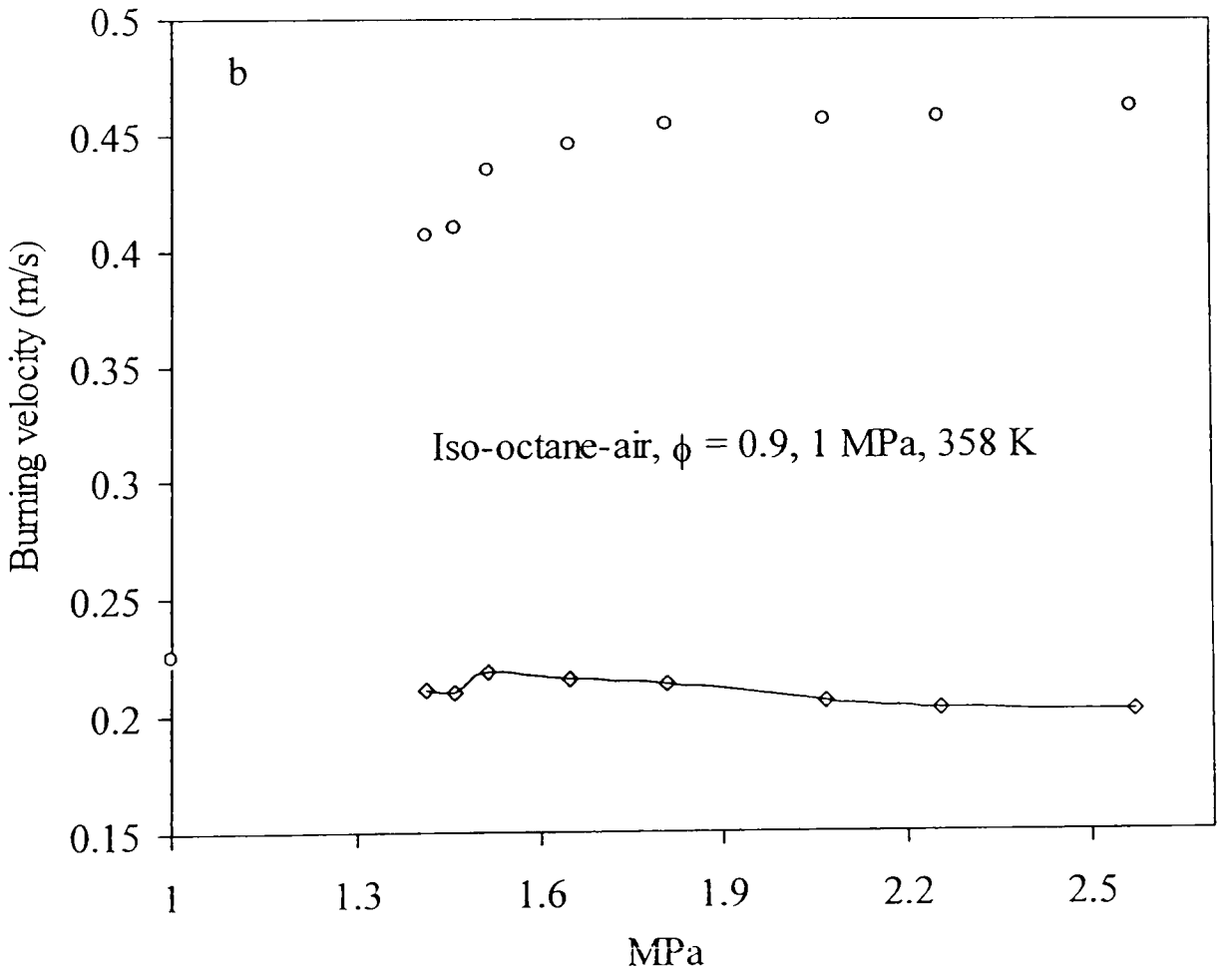

Fig. 6.31. Experimental values of u_n from two implosions of lean (ϕ = 0.9) iso-octane-air initially at (a) 0.5 MPa, (b) 1 MPa and 358 K (upper symbols). Lower symbols show values of u_ℓ predicted from these.

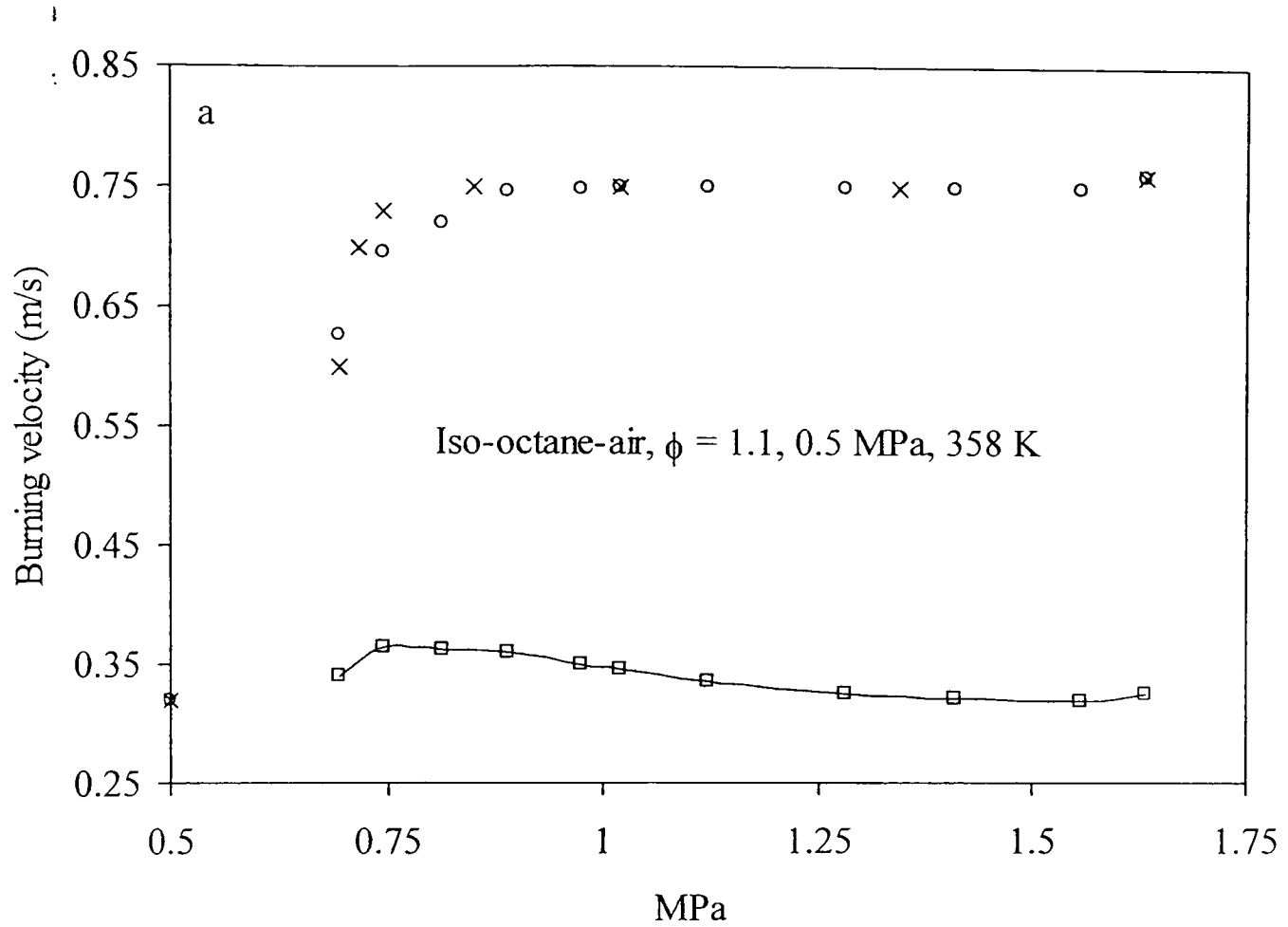

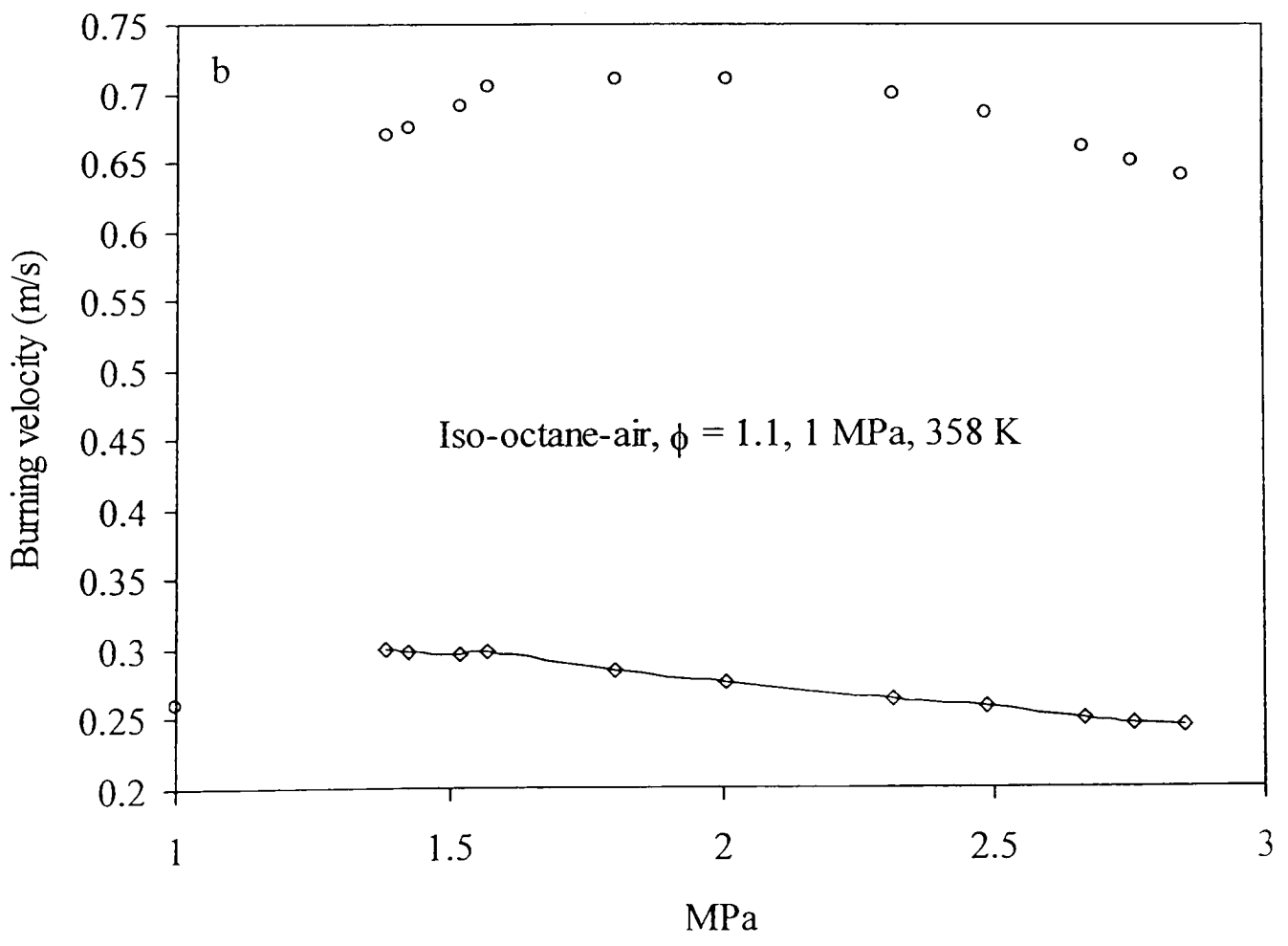

Fig. 6.32. Experimental values of u_n from two implosions of rich (ϕ = 1.1) iso-octane-air initially at (a) 0.5 MPa, (b) 1 MPa and 358 K (upper symbols). Lower symbols show values of u_f predicted from these.

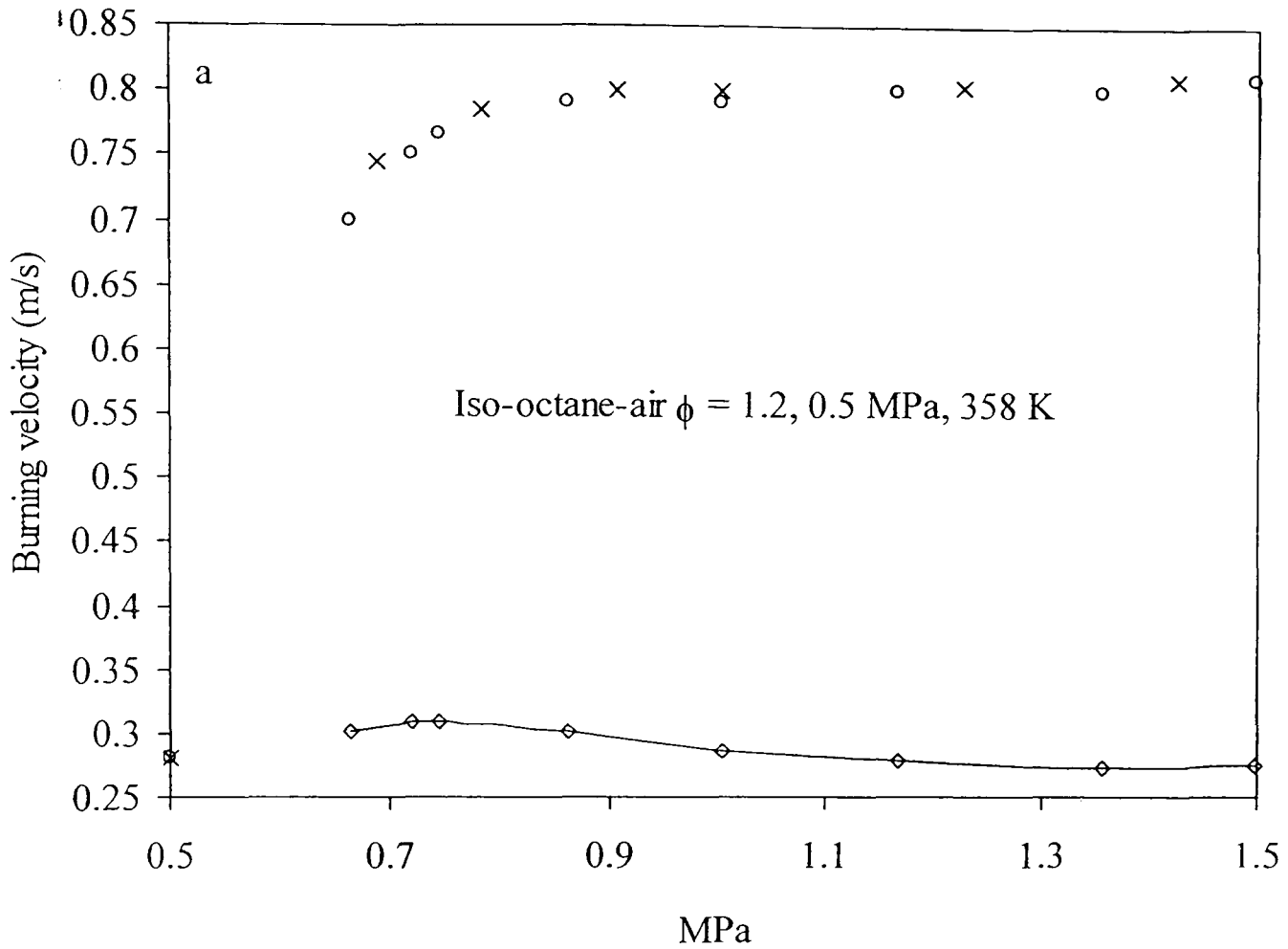

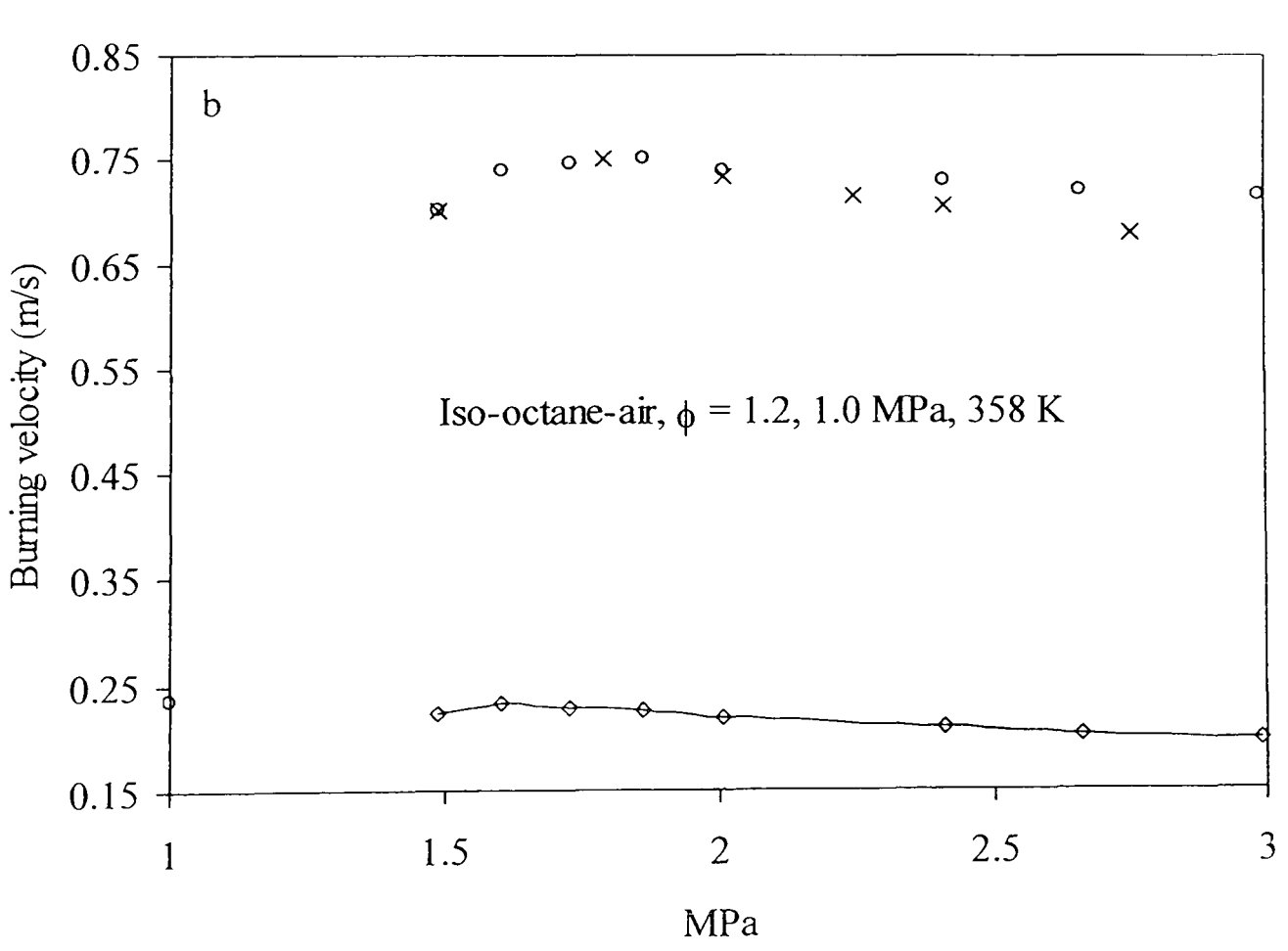

Fig. 6.33. Experimental values of u_n from two implosions of rich ($\phi = 1.2$) iso-octane-air initially at (a) 0.5 MPa, (b) 1 MPa and 358 K (upper symbols). Lower symbols show values of u_ℓ predicted from these.

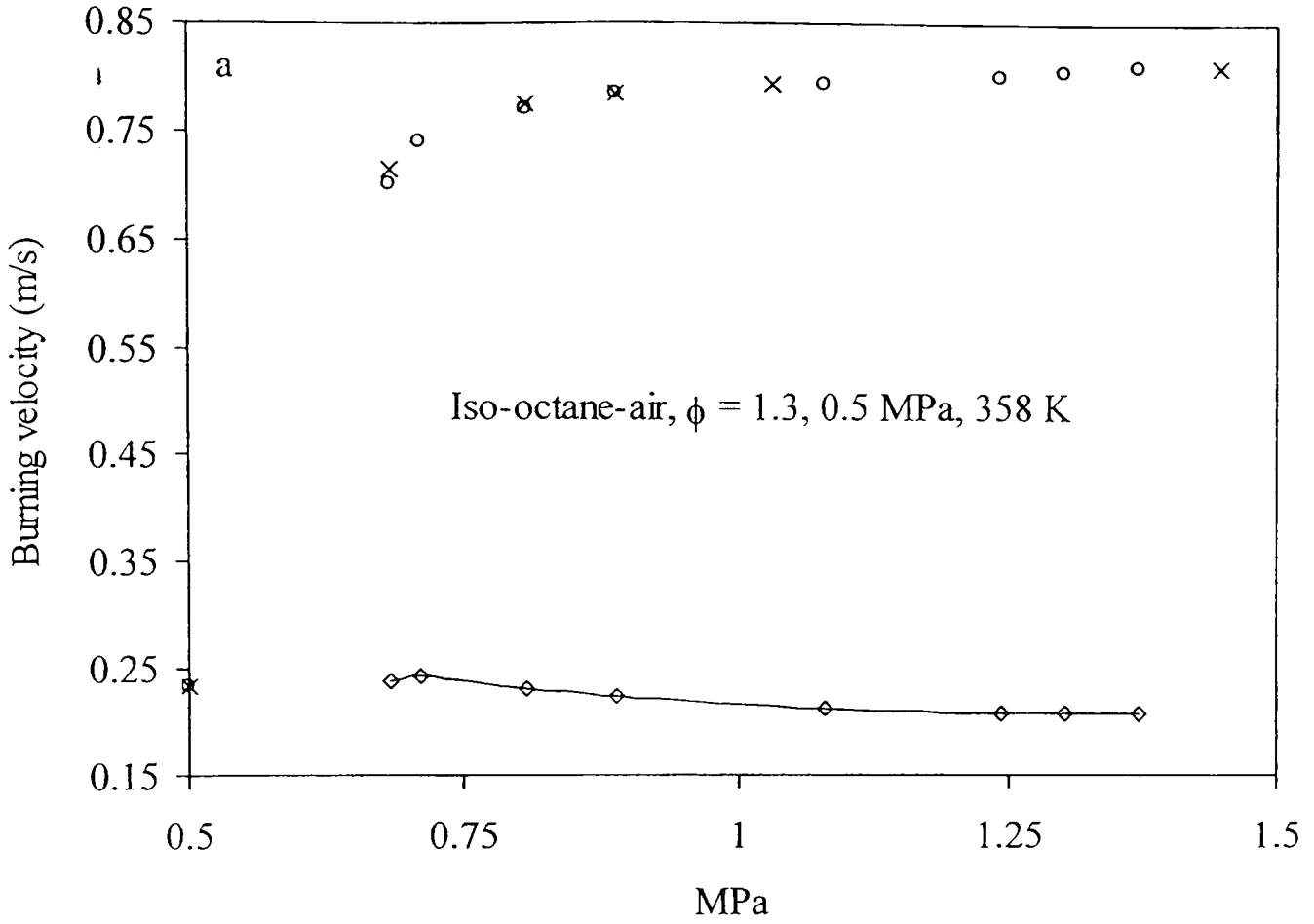

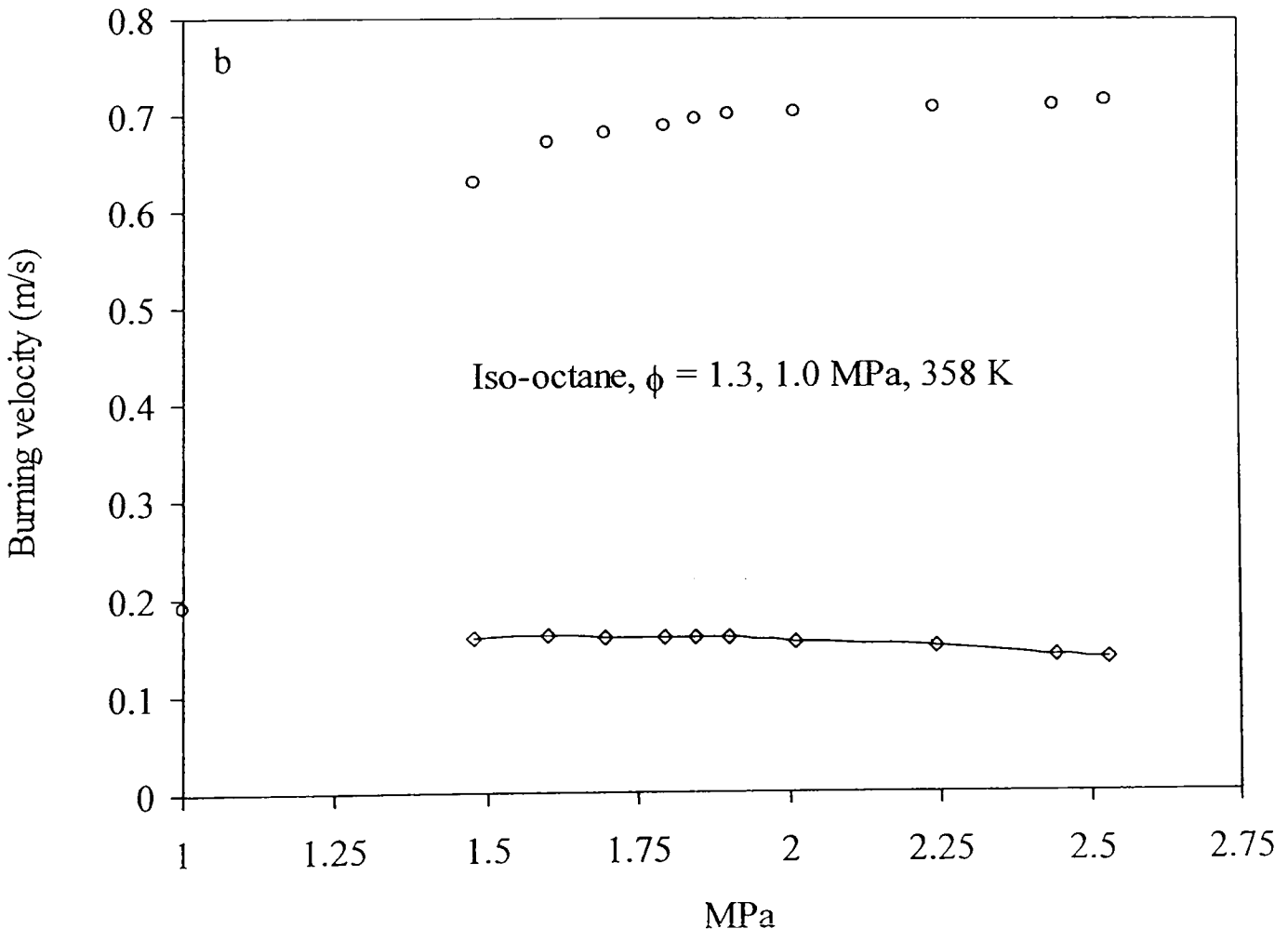

Fig. 6.34. Experimental values of u_n from two implosions of rich ($\phi = 1.3$) iso-octane-air initially at (a) 0.5 MPa, (b) 1 MPa and 358 K (upper symbols). Lower symbols show values of u_ℓ predicted from these.

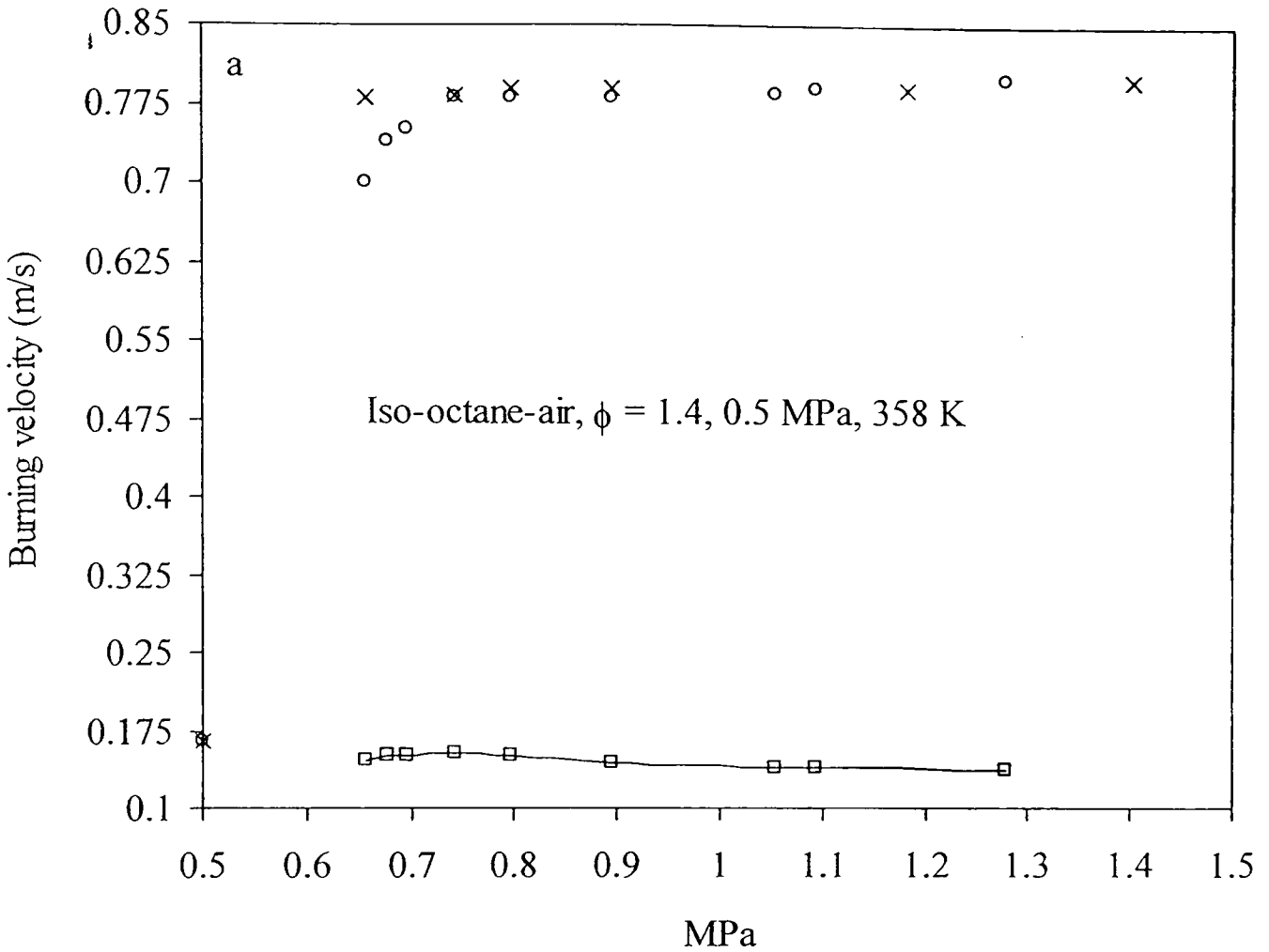

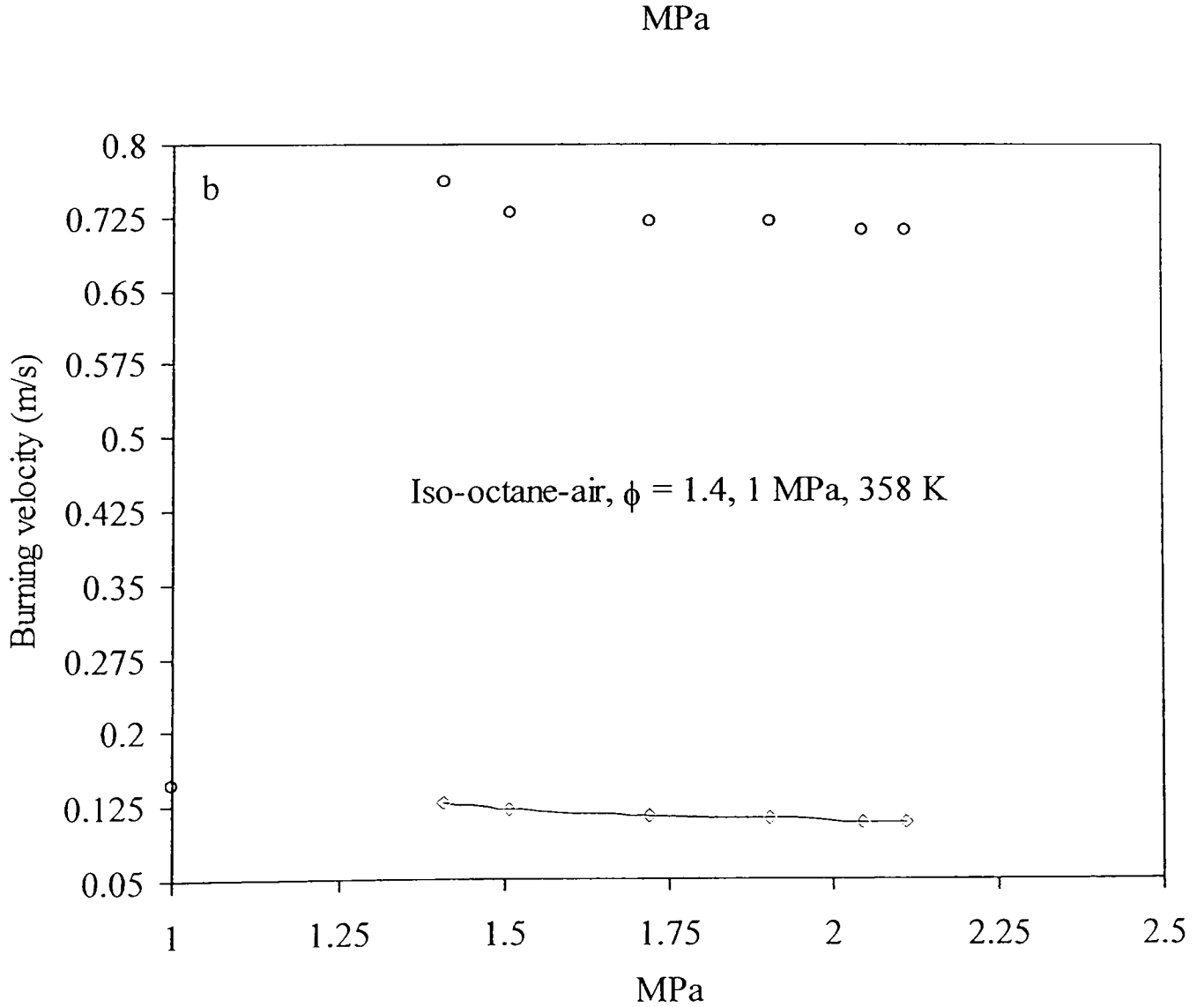

Fig. 6.35. Experimental values of u_n from two implosions of rich ($\phi = 1.4$) iso-octane-air initially at (a) 0.5 MPa, (b) 1 MPa and 358 K (upper symbols). Lower symbols show values of u_ℓ predicted from these.

Chapter 7

Experimental Results From Turbulent Imploding Flames

7.1 Introduction

The present chapter reports measured values of turbulent burning velocities, u_t, using the twin kernel technique as described previously for turbulent conditions in Chapter 4. This technique has the advantage of yielding data at higher pressures and, in addition, the larger kernel diameters give a greater degree of flame surface development into the longer wavelengths of the turbulent spectrum (Abdel-Gayed *et al.*, 1987), an advantage also enjoyed by well-designed burners (Bédat and Cheng, 1995).

All of the turbulent results from this technique are summarised in Section 7.2. The effective value of rms turbulent velocity, u'_k, affecting flame wrinkling is derived in Section 7.3. Stoichiometric and rich iso-octane-air flames, ϕ = 1.4, were selected for study in order to provide a contrast between a mixture that under atmospheric conditions gave a reasonably stable laminar flame and one that gave an unstable one. Mixtures were ignited at initial pressures of 0.5 and 1.0 MPa. This enabled burning velocities to be measured up to 6 MPa. Values of u' ranged from 0.25 to 3 m/s and the integral length scale, L, for turbulence was 20 mm.

7.2 Measurements of Turbulent Burning Velocity Using the Twin Kernel Method

At least two explosions for each gaseous mixture condition were exploded in the spherical bomb. Tables 7.1 and 7.2 summarise all explosions during which measurements were made. Figure numbers indicate where the experimental data, including u'_t, can be found and the figures covering each explosion are given at the end of the chapter. Data from additional explosions are given in Appendix C. Values of u'_t (m/s) were based on the assumption that a spherical flame front was centred at the vessel wall and these were found from Eqs. (4. 14) and (4. 19). Corrected values, u_t, based on V_r and obtained as described in Section 4.5, are presented in Figs. 7.50 - 52 in Section 7.4.

A wide range of conditions was investigated at different rms turbulent velocities, u'. Pressure measurements coupled with high-speed flame photography during the explosions, allied to the appropriate geometrical considerations, yielded values of u'_t. For iso-octane-air mixtures these covered $\phi = 1.0$ and 1.4 over the pressure range 0.73 to 6 MPa. For hydrogen – air mixtures, these covered $\phi = 0.3$ and 0.4 over the pressure range 0.63 to 1.65 MPa. The unburned gas was assumed to be compressed isentropically and the temperature was obtained, using the GASEQ code, from the measured pressure.

Iso-octane		$\phi = 1$				$\phi = 1.4$	
Fig. No	u' (m/s)	p_o (MPa)	T_o (K)	Fig. No	u' (m/s)	p_o (MPa)	T_o (K)
7.1	0.25	0.5	358	7.7	0.25	0.5	358
7.2	0.5	0.5	358	7.8	0.5	0.5	358
7.3	075	0.5	358	7.9	075	0.5	358
7.4	1	0.5	358	7.10	1	0.5	358
7.5	2	0.5	358	7.11	2	0.5	358
7.6	3	0.5	358	7.12	3	0.5	358
7.13	0.25	0.75	358	7.19	0.25	0.75	358
7.14	0.5	0.75	358	7.20	0.5	0.75	358
7.15	075	0.75	358	7.21	075	0.75	358
7.16	1	0.75	358	7.22	1	0.75	358
7.17	2	0.75	358	7.23	2	0.75	358
7.18	3	0.75	358	7.24	3	0.75	358
7.25	0.25	1	358	7.31	0.25	1	358
7.26	0.5	1	358	7.32	0.5	1	358
7.27	075	1	358	7.33	075	1	358
7.28	1	1	358	7.34	1	1	358
7.29	2	1	358	7.35	2	1	358
7.30	3	1	358	7.36	3	1	358

Table 7.1 Summary of conditions for different values of u' for all turbulent explosions during which measurements were made for iso-octane – air mixtures. p_o and T_o are initial pressures and temperatures.

Hydrogen	$\phi = 0.3$				$\phi = 0.4$		
Fig. No	u' (m/s)	p_o (MPa)	T_o (K)	Fig. No	u' (m/s)	p_o (MPa)	T_o (K)
7.37	0.25	0.5	358	7.42	0.25	0.5	358
7.38	0.50	0.5	358	7.43	0.50	0.5	358
7.39	0.75	0.5	358	7.44	0.75	0.5	358
7.40	1	0.5	358	7.45	1	0.5	358
7.41	2	0.5	358	7.46	2	0.5	358

Table 7.2 Summary of all turbulent explosions during which measurements were made for hydrogen – air mixtures, $\phi = 0.3$ and $\phi = 0.4$. p_o and T_o are initial pressures and temperatures.

The presentation of the experimental results is similar to that adopted for the laminar explosions. Figures 7.1 to 7.46 give plots against time from ignition of (a) measured temporal variations of pressure and temperature, (b) radii of the two flame kernels, (c) flame speeds, $\partial r/\partial t$, and (d) values of u'_t, for the appropriate conditions. After the leading edges of the two kernels began to flatten the method was no longer applicable and again the double kernel method was applied in the limit as the two kernels merged together, to yield the burning velocity. The filled triangle in the bottom right hand graphs at the end of the explosions always indicates the burning velocity measured by this technique.

A typical schlieren image of the two kernels is given in Fig. 7.47 for a hydrogen – air mixture, $\phi = 0.3$, at an rms turbulent velocity of 1 m/s. In general, the flame kernels had different radii and the surface of turbulent flame was represented by a smoothed spherical surface, such that on the 2D schlieren image the area of unburned gas outside the surface was equal to that within it, as in Bradley *et al.* (2003).

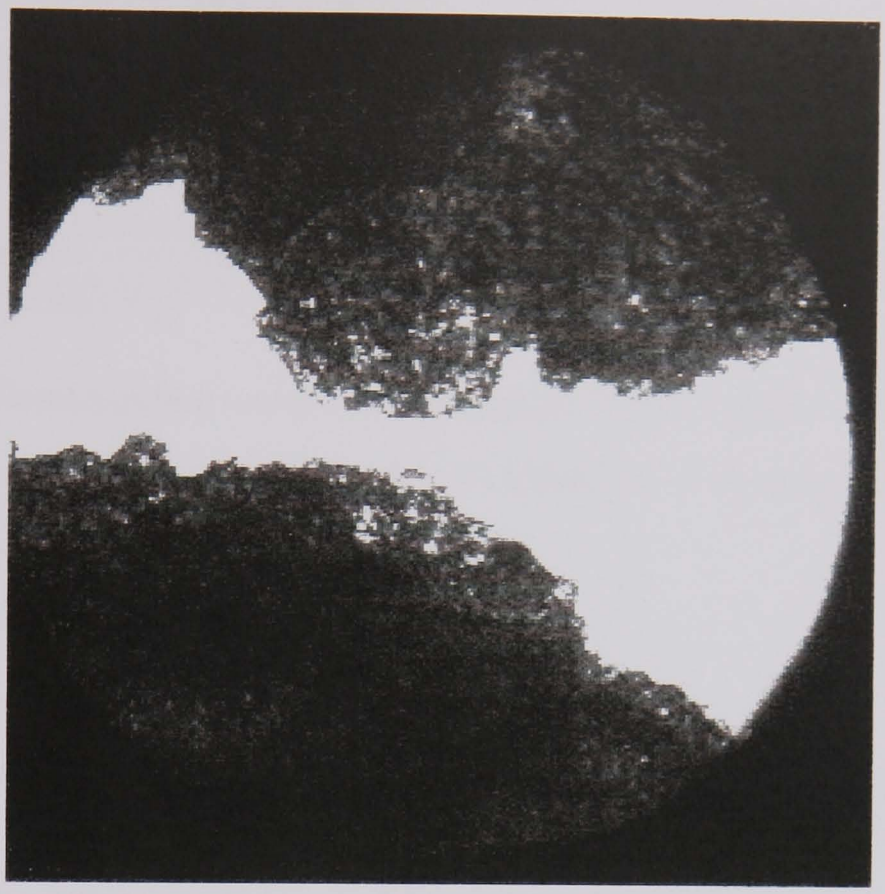

Fig. 7.47. Schlieren image of the two kernels close to making contact of lean ($\phi = 0.3$) H_2-air initially at 0.5 MPa and 358 K, $u' = 1$ m/s.

7.3 Derivation of Effective rms Turbulent Velocity, u'_k, Acting on the Flame Kernel

When a flame kernel grows from a point source, initially only the smaller wavelengths from the full spectrum of turbulence wavelengths can wrinkle the kernel. The longer wavelengths contribute a velocity that convects the kernel. As the kernel propagates, an increasing part of the spectrum, starting with the smallest wavelengths, will wrinkle the flame front (Abdel-Gayed *et al.*, 1987). Following Abdel-Gayed *et al.* (1987) and Scott (1992), the effective rms turbulent velocity, u'_k, is given by:

$$\frac{u'_k}{u'} = \left[\frac{15^{0.5}}{R_\lambda} \int_{\bar{k}_{\eta k}}^{\infty} \bar{S}\left(\bar{k}_\eta\right) d\bar{k}_\eta \right]^{1/2} \tag{7.1}$$

here $\bar{S}\left(\bar{k}_\eta\right)$ is the non - dimensional power spectral density based on the Kolmogorov scale, η.

An earlier expression for $\bar{S}(\bar{k}_\eta)$ employed by Abdel - Gayed *et al.* (1987) and based on the integral length scale was replaced by a more accurate one by Scott (1992), given by :

$$\bar{S}(\bar{k}_\eta)=\frac{0.01668R_\lambda^{2.5}+3.74R_\lambda^{0.9}-70R_\lambda^{-0.1}}{1+\left(0.127R_\lambda^{1.5}\bar{k}_\eta\right)^{5/3}+\left(1.15R_\lambda^{0.622}\bar{k}_\eta\right)^4+\left(1.27R_\lambda^{0.357}\bar{k}_\eta\right)^7} \tag{7.2}$$

here, $\bar{k}_\eta$ is a dimensionless wave number and $R_\lambda = u'\lambda/\nu$ is the Taylor scale Reynolds number based on the Taylor microscale of turbulence, λ. This is related to the integral length scale by: $\lambda / L = A / R_\lambda$ (7.3)

here, A is a numerical constant = 16.

Haq (1998) derived the largest effective wavelength of the turbulence at a given time in the explosion by multiplying the mean cold gas speed by the elapsed time from initiation. This might be valid for small time intervals, but is less so for longer times and larger kernel sizes, such as those in the present study. The alternative approach was adopted of using the kernel diameter directly at any instant as the largest effective wavelength for flame wrinkling. As a result, the associated smallest effective wave number in the integral in Eq. (7.1) is

$$k_k=\frac{2\pi}{2r}=\frac{\pi}{Pe\delta_\ell} \tag{7.4}$$

where r is the kernel radius, Pe the Peclet number and δ_ℓ the flame thickness. Normalized by the Kolmogorov scale, η, it gives $\bar{k}_{\eta\kappa}$

$$\bar{k}_{\eta k}=k_k\eta=\frac{\pi}{Pe\delta_\ell}\left(\frac{\lambda}{15^{0.25}R_\lambda^{0.5}}\right) \tag{7.5}$$

where the term in the bracket expresses η.

With $\delta_\ell=\nu/u_\ell$ (7.6)

$$\bar{k}_{\eta k}=\frac{\pi}{Pe\delta_\ell}\left(\frac{\lambda}{15^{0.25}}\left(\frac{\delta_\ell u_\ell}{u'\lambda}\right)^{0.5}\right)=\frac{\pi}{Pe15^{0.25}}\left(\frac{\lambda u_\ell}{u'\delta_\ell}\right)^{0.5} \tag{7.7}$$

The turbulent Karlovitz stretch factor $K = (u'/\lambda)\,(\delta_\ell/u_\ell)$. (7.8)

Hence:

$$\bar{k}_{\eta k}^{-1}=0.6264PeK^{0.5}. \tag{7.9}$$

From Eq. (7.3), with A = 16,

$R_\lambda = 4R_l^{0.5}$ where $R_l = u'L/\nu$. (7.10)

Equation (7.10) enabled $\bar{S}\left(\bar{k}_\eta\right)$ to be evaluated for different values of $\bar{k}_\eta$. The integral expression, Eq (7.1), could then be evaluated to give u'_k/u' by integrating between the limits $\bar{k}_{\eta k} = \infty$ and $\bar{k}_{\eta k}^{-1}$ given by Eq. 7.9.

Values of the integral were found from different values of $\bar{k}_{\eta k}^{-1}$ using the software implemented by Haq (1998). Values of ν were obtained from the GASEQ code. Figure 7.48 shows the values of u'_k/u' plotted against $\bar{k}_{\eta k}^{-1}$ for different values of R_λ using this software. Over the full range of values in the present work values of u'_k/u' ranged between 0.644 and 0.932. Typical ways in which u'_k/u' developed during the present explosions are shown in Fig. 7.49. This covers two different mixtures and different values of u'. There is a rapid development of u'_k/u' even before the flames appear within the windows. However, it is of an importance to mention here that u'_k were related to u' which was measured in the central (isotropic) region of the bomb and that u' in the outer regions near the walls may not necessarily have the same value.

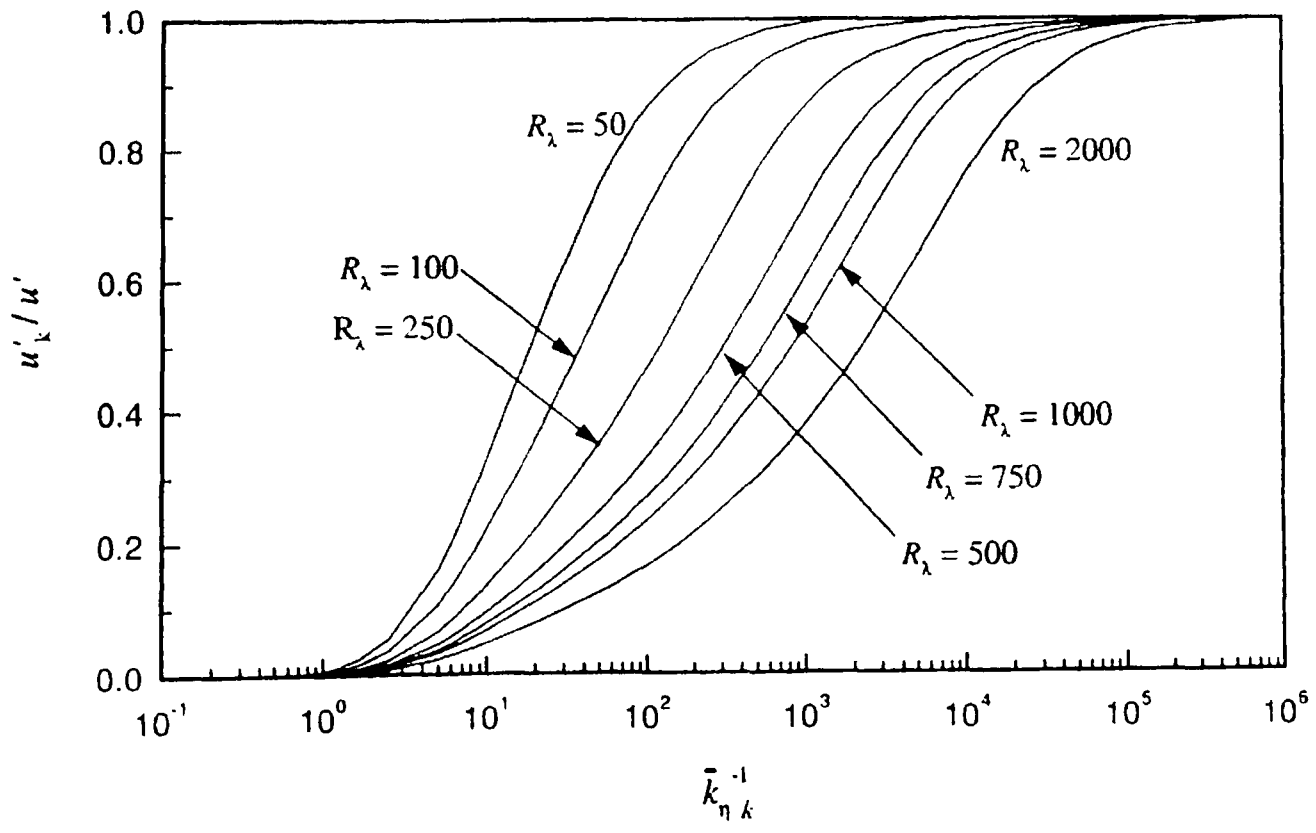

Fig. 7.48. Development of effective rms turbulent velocity (Haq, 1998).

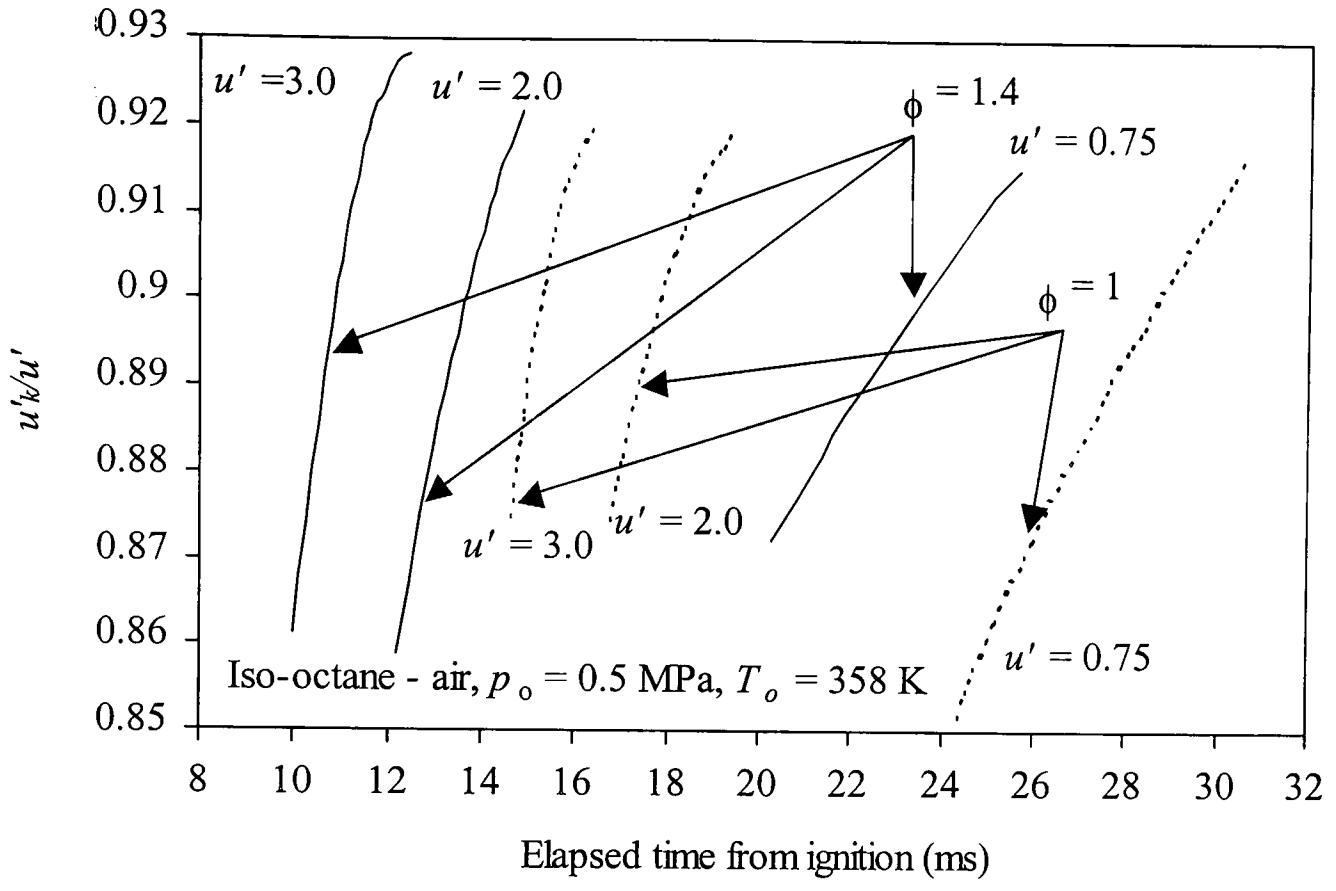

Fig. 7.49. Temporal development of u'_k/u', in iso-octane –air mixture, $\phi = 1.0$ and $\phi = 1.4$.

7.4 Corrected Values of u_t and Effects of High p and T

Values of turbulent burning velocity, u_t, corrected as explained in Section 4.5.6 at different pressures and temperatures are shown plotted against the effective rms turbulent velocity, u'_k in Figs. 7.50 and 7.51. These cover iso-octane - air mixtures, (a) with ϕ=1.0 and (b) with ϕ= 1.4, at initial pressure of 0.5 MPa and 1.0 MPa, respectively. All initial temperatures were 358 K. Particular values of p were selected and as many data points as possible were obtained from the different explosions. Shown in Fig. 7.52 are the corrected values of u_t, for hydrogen - air mixtures, (a) with $\phi = 0.3$ and (b) with $\phi = 0.4$, at an initial pressure of 0.5 MPa and initial temperature of 358 K.

All the results show what appears to be a linear increase in u_t with u'_k at constant pressure and temperature. There also appears to be a general tendency for u_t to increase with pressure at a given value of u'_k at the lower pressures, but this trend levels out at the higher pressures. These results and how they might be correlated are discussed in the next chapter, after discussion of those for quiescent mixtures and the appropriate values of u_ℓ.

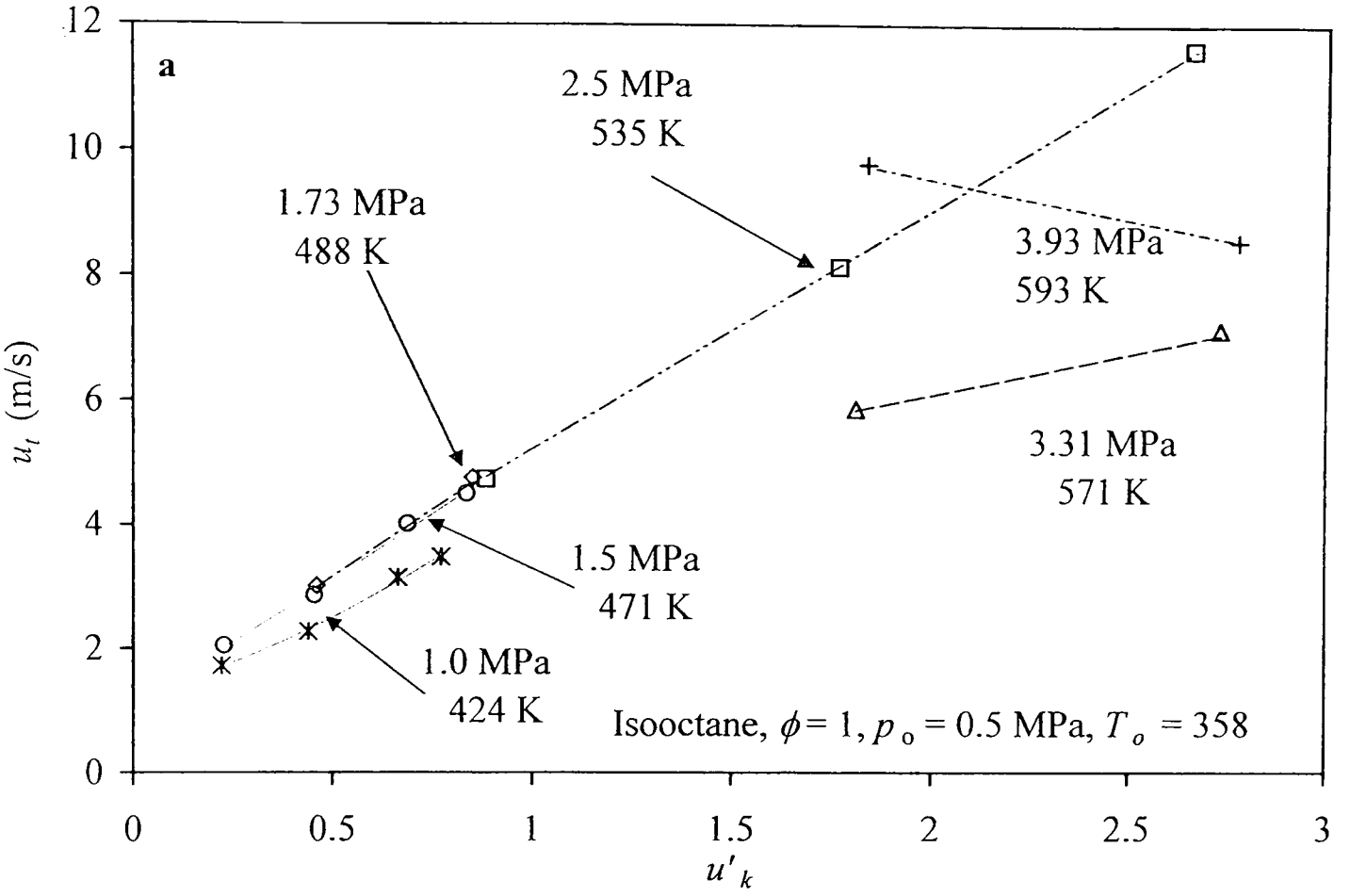

Fig. 7.50. Corrected values of u_t for iso-octane - air implosions, (a) ϕ = 1, (b) ϕ = 1.4, at p_o = 0.5 MPa, T_o = 358 K

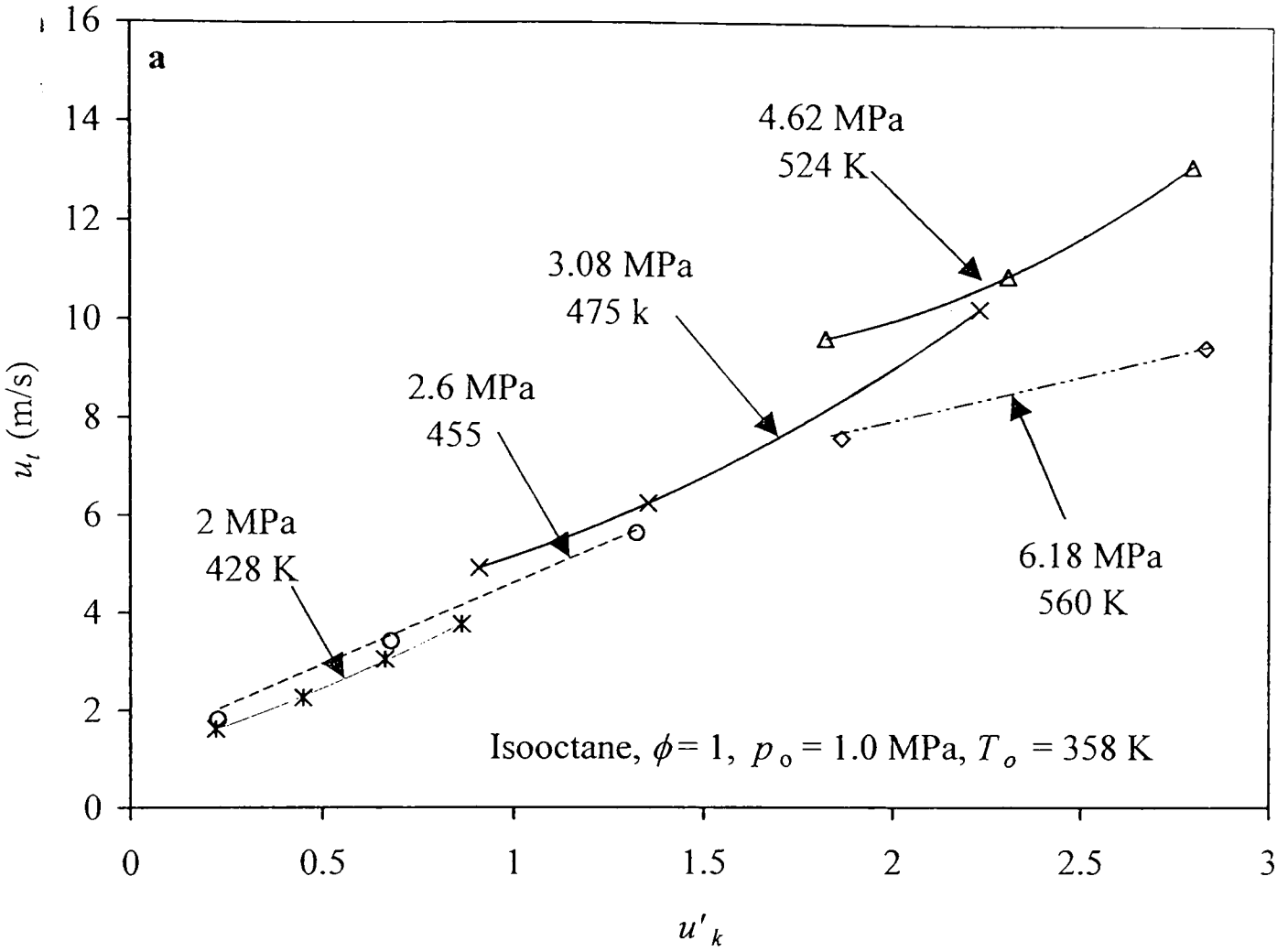

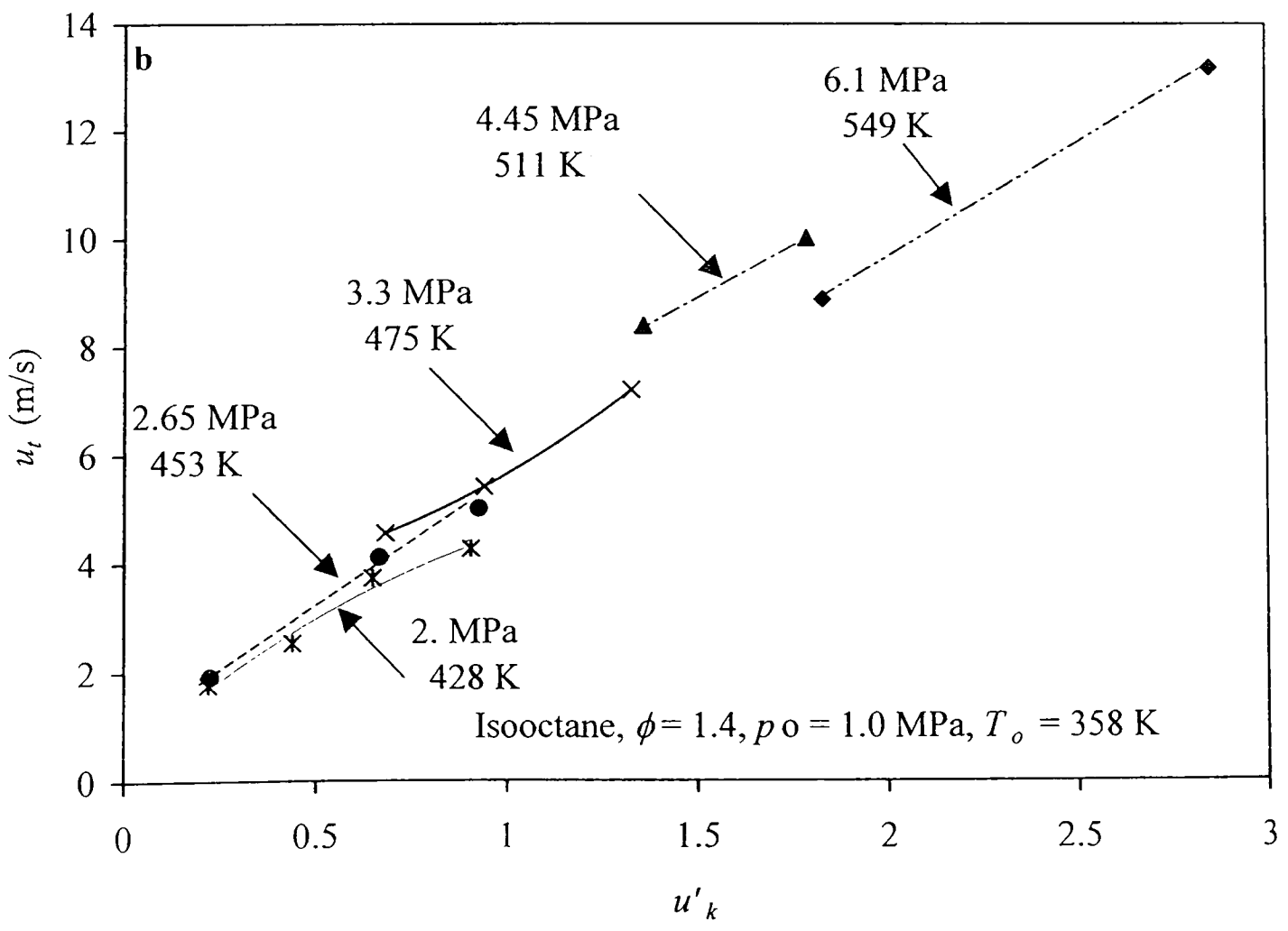

Fig. 7.51. Corrected values of u_t for iso-octane - air implosions, (a) ϕ = 1, (b) ϕ = 1.4, at p_o = 1.0 MPa, T_o = 358 K

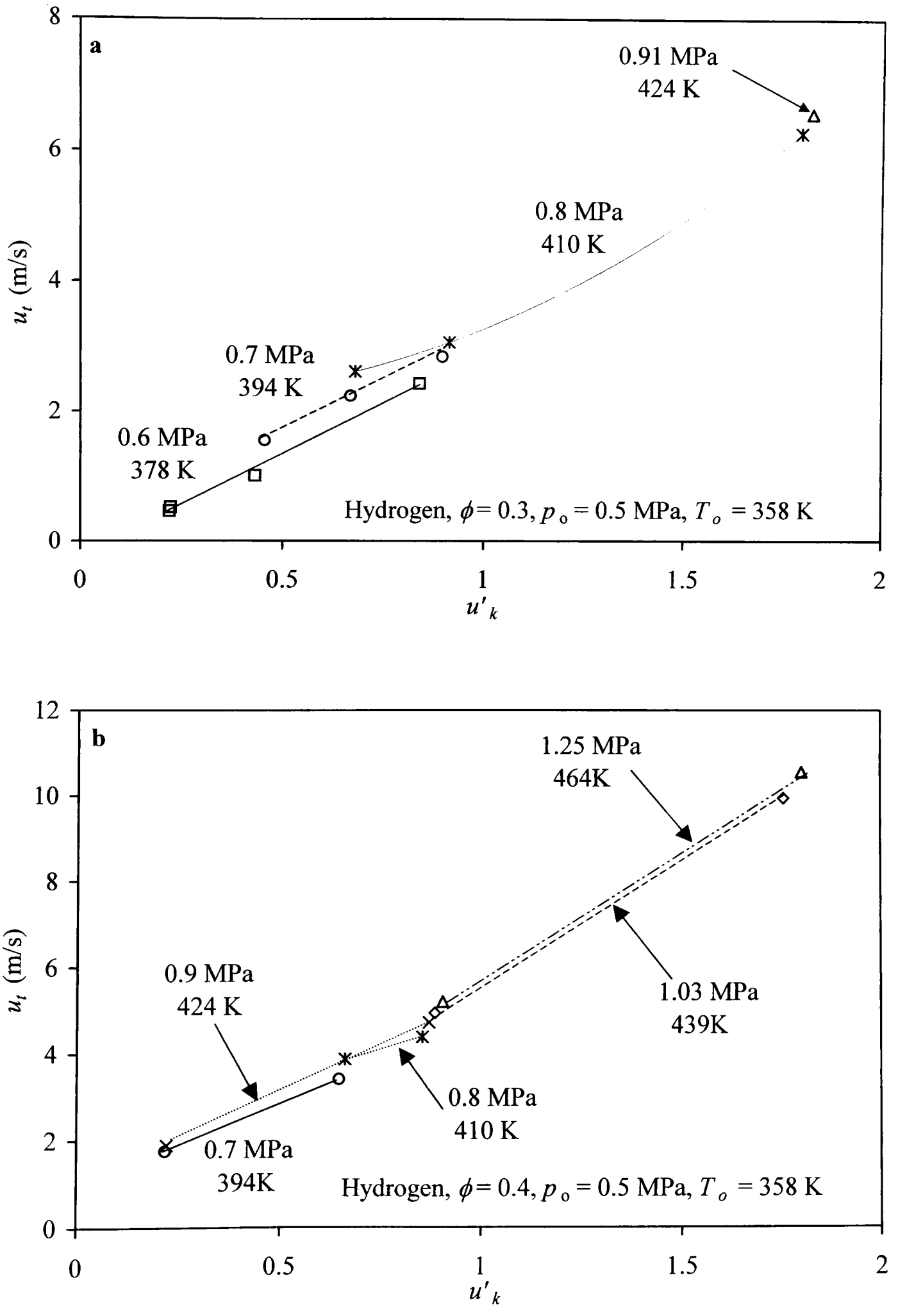

Fig. 7.52. Corrected values of u_t for Hydrogen - air implosions, (a) ϕ = 0.3, (b) ϕ = 0.4, at p_o = 0.5 MPa, T_o = 358 K

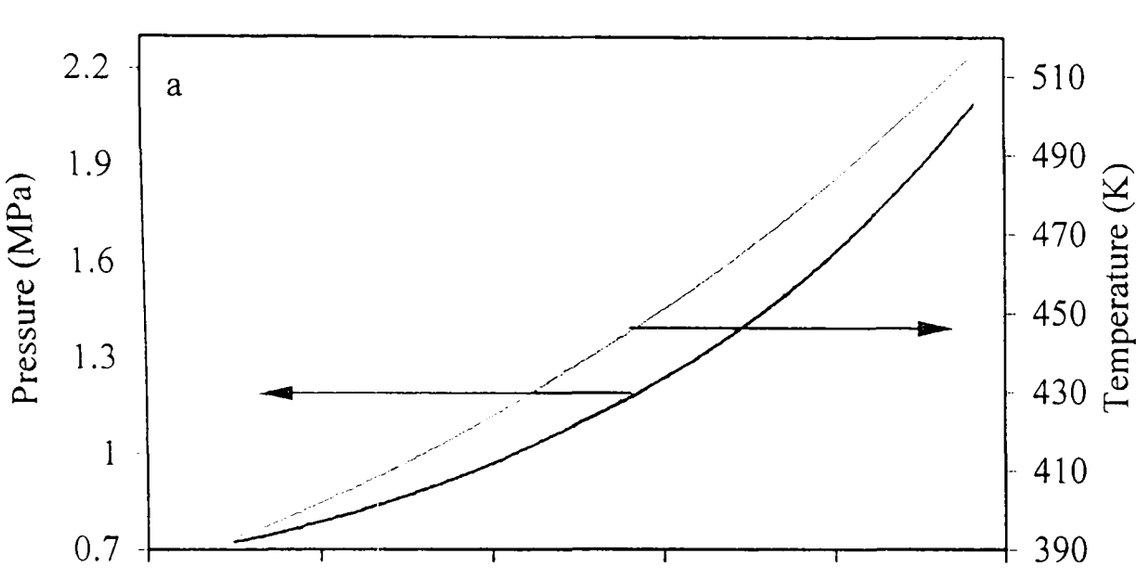

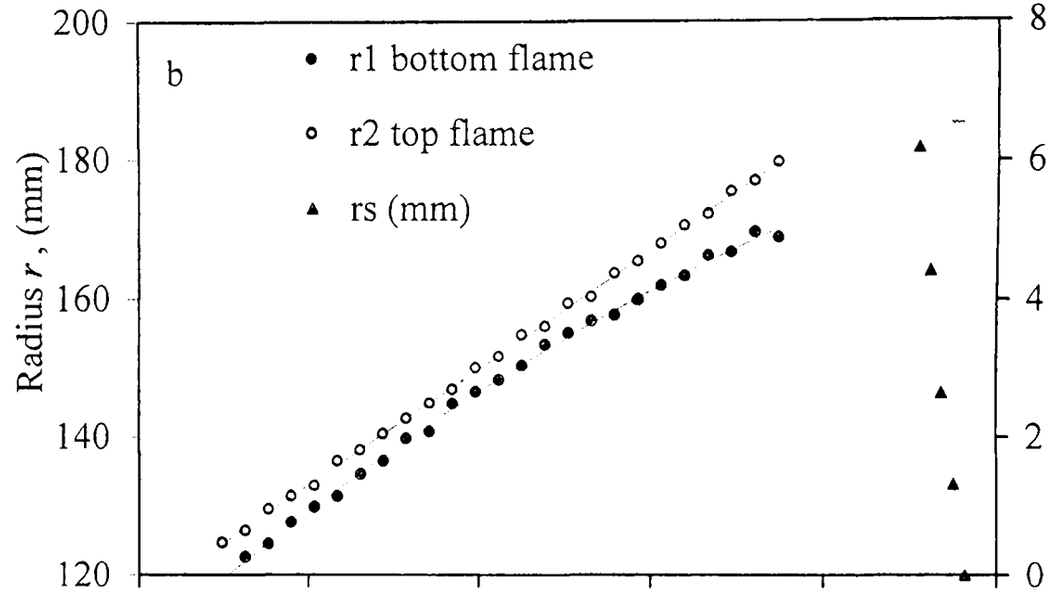

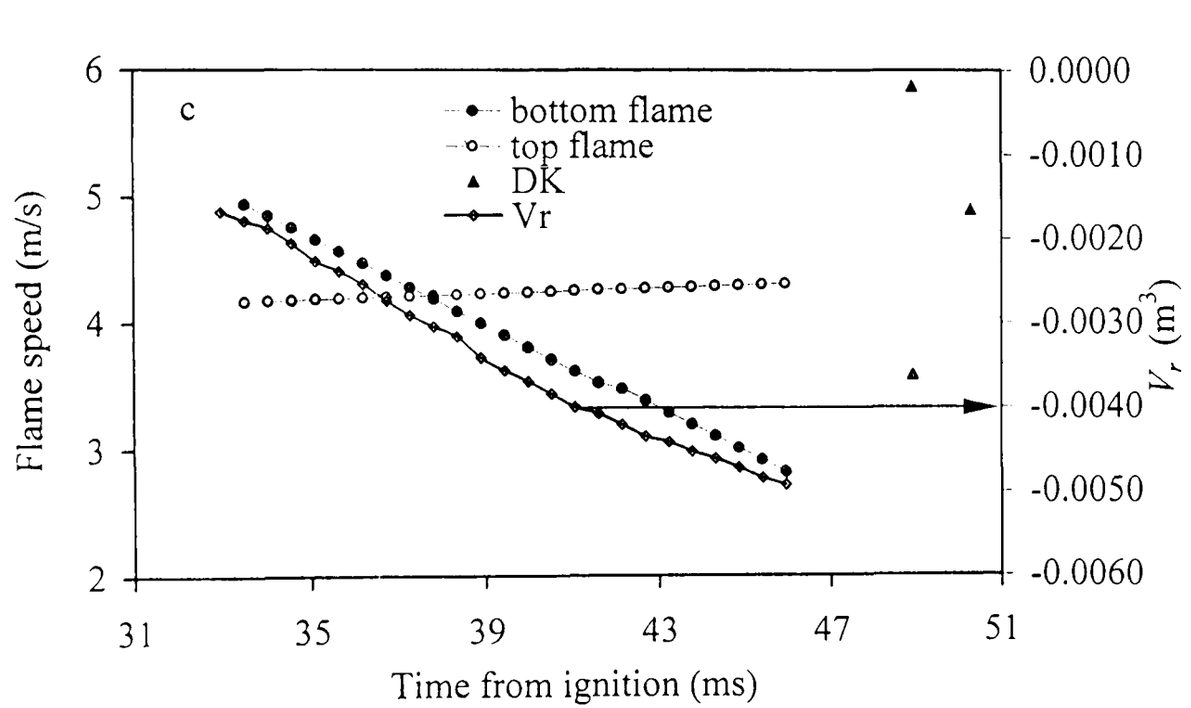

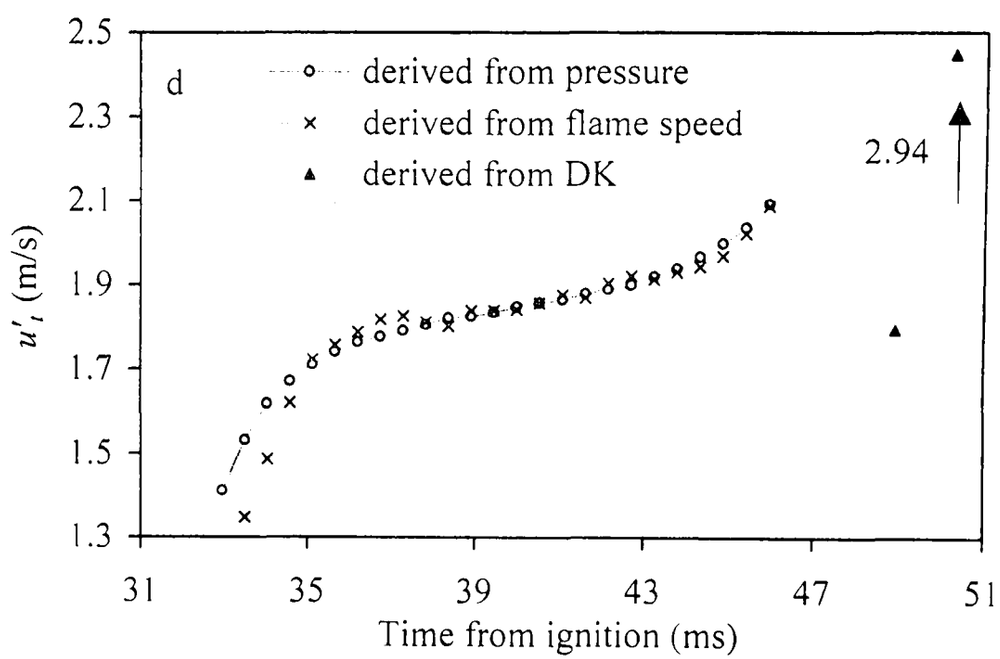

Fig. 7.1. Iso-octane - air implosion, $\phi = 1$, $p_o = 0.5$ MPa, $T_o = 358$ K, $u' = 0.25$

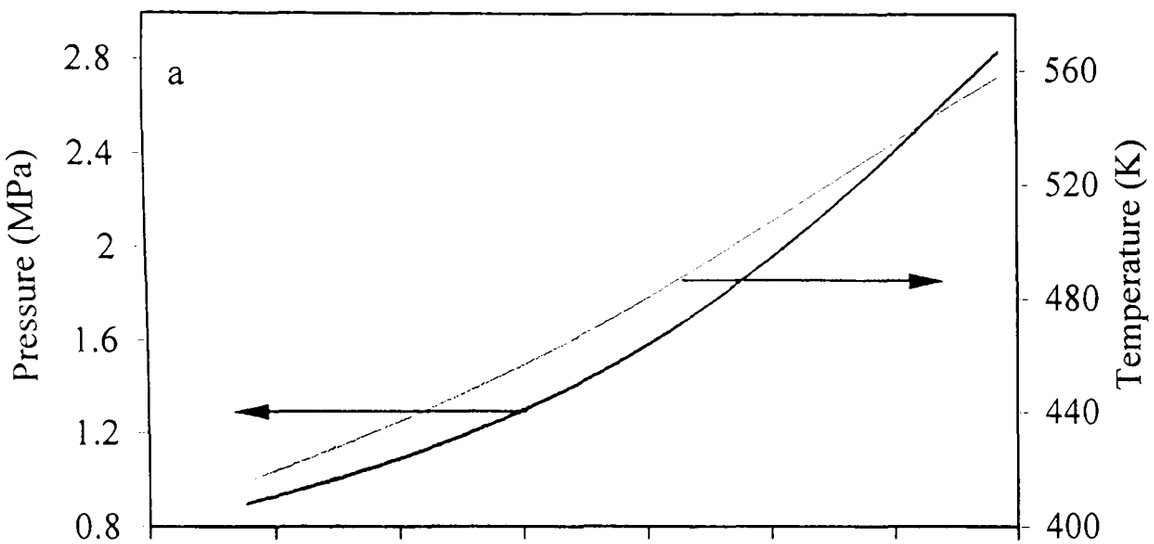

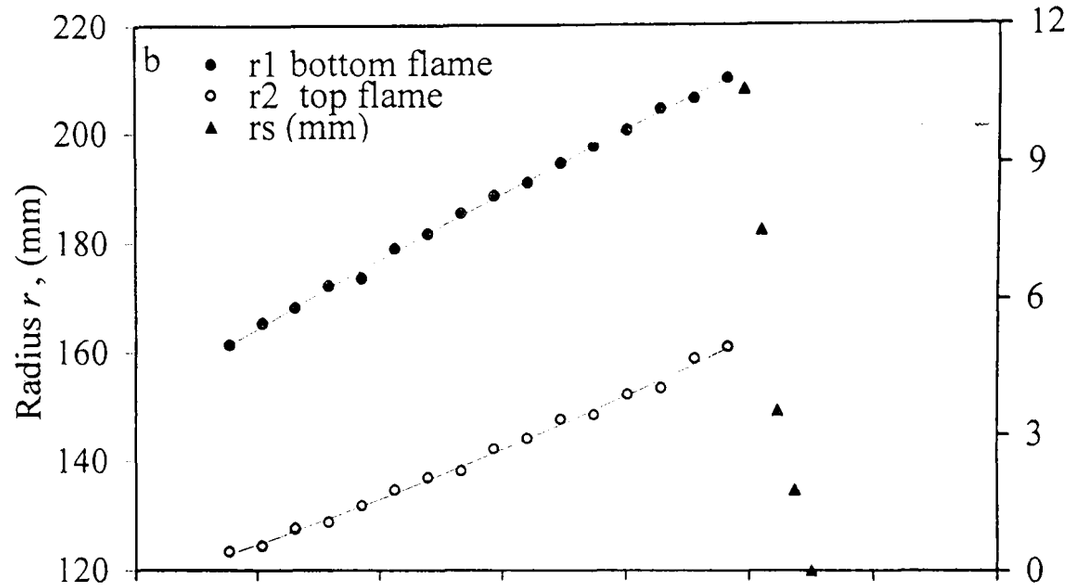

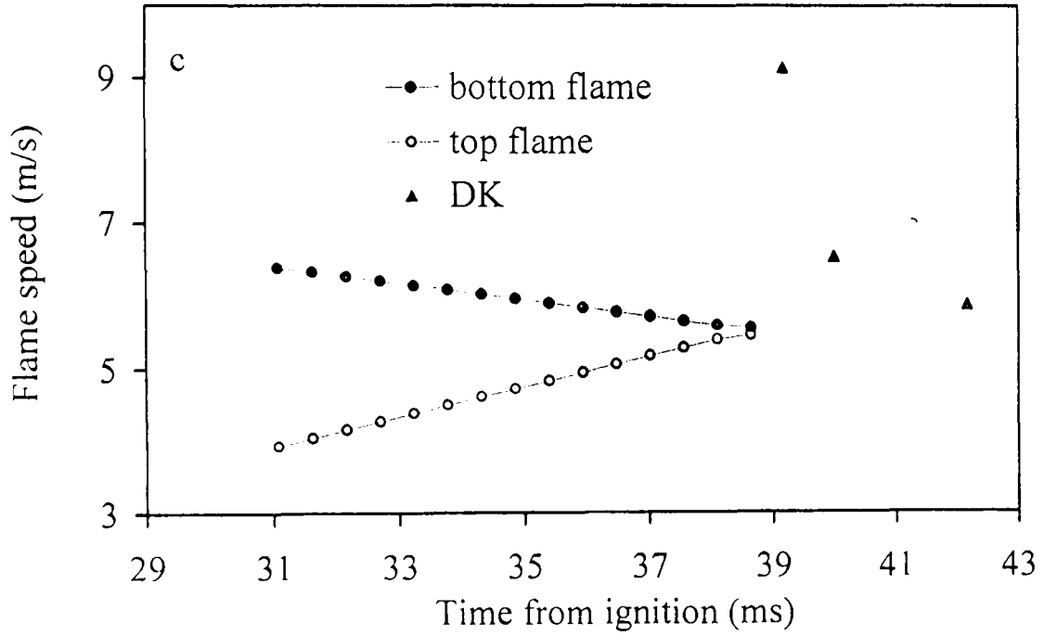

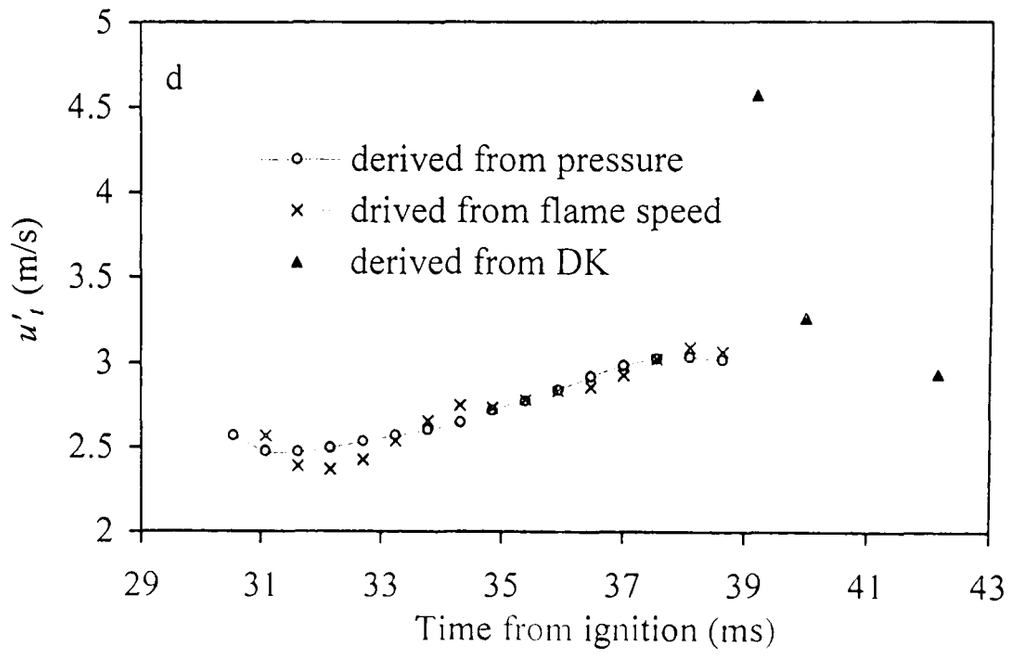

Fig. 7.2. Iso-octane - air implosion, $\phi = 1, p_o = 0.5$ MPa, $T_o = 358$ K, $u' = 0.5$

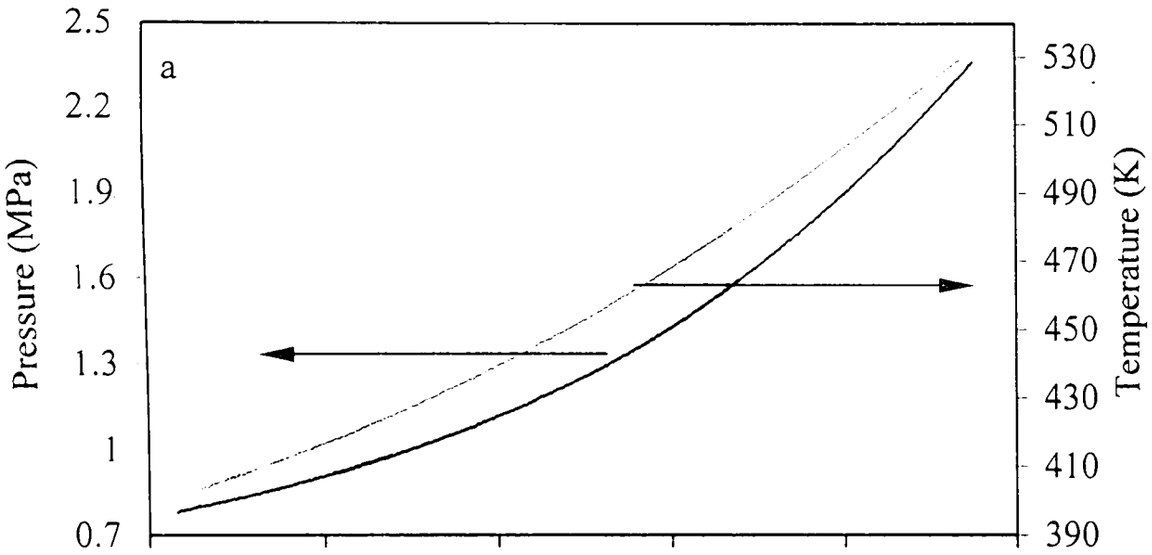

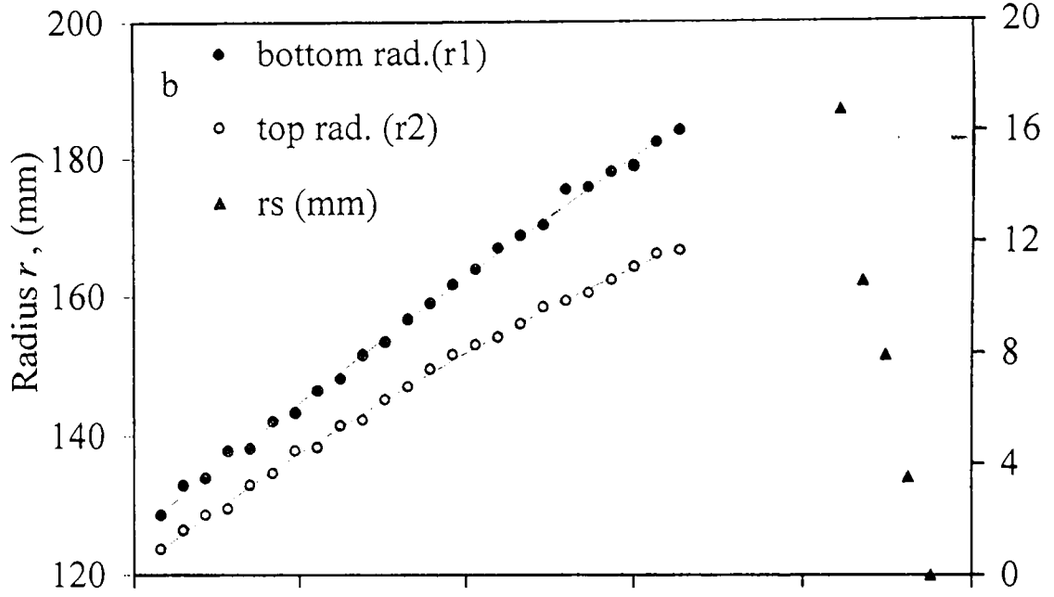

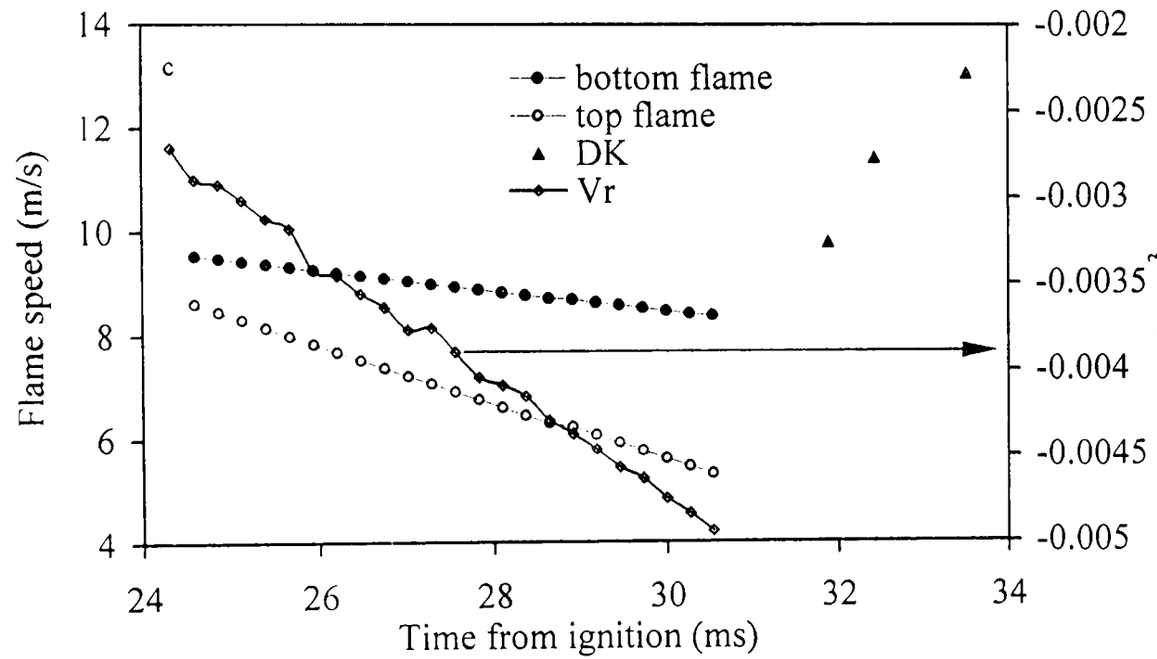

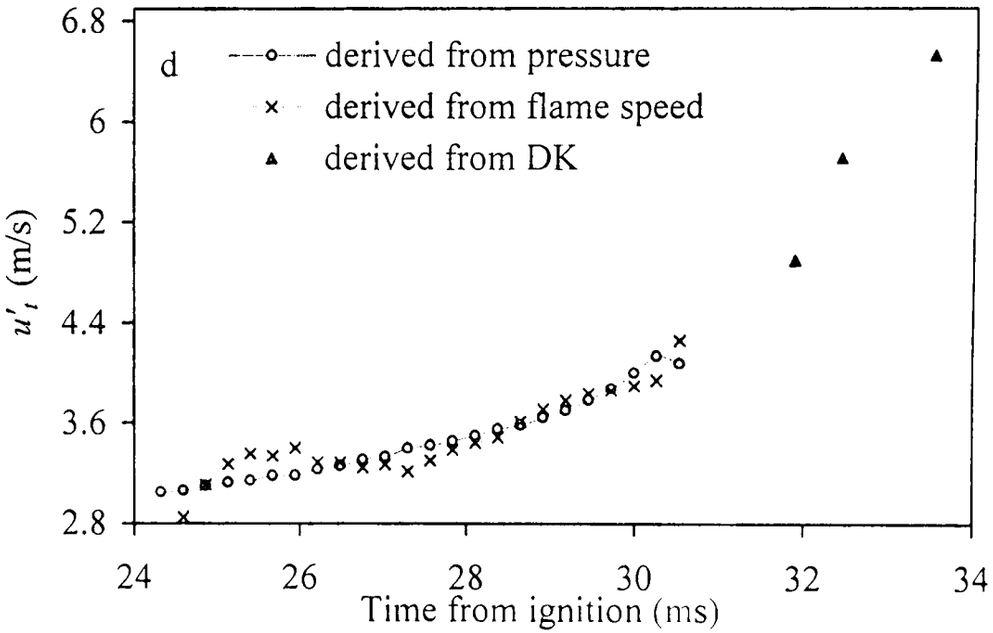

Fig. 7.3. Iso-octane - air implosion, ϕ = 1, p_o = 0.5 MPa, T_o = 358 K, u' = 0.75

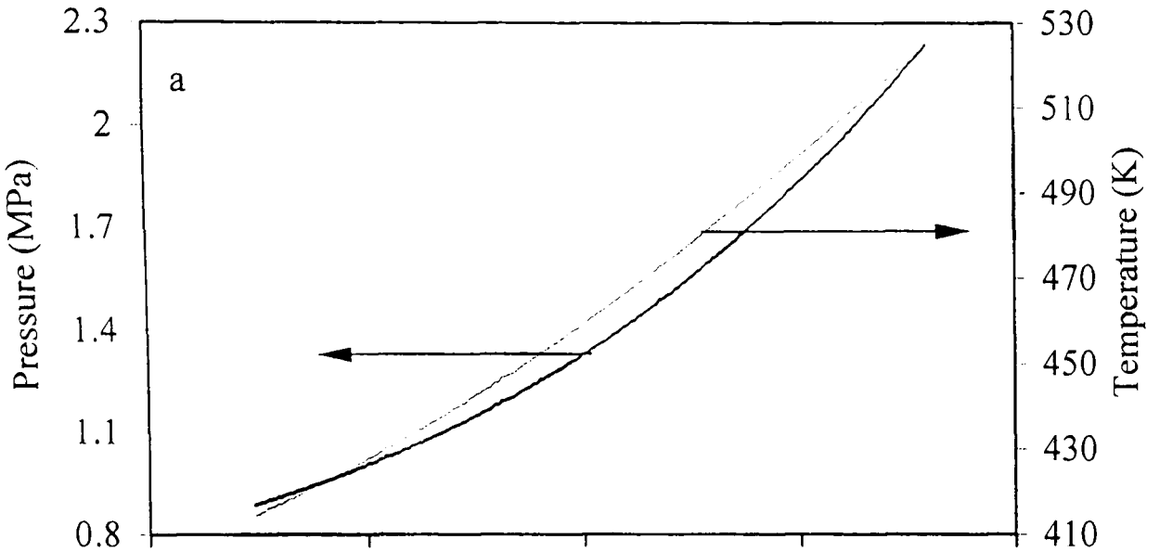

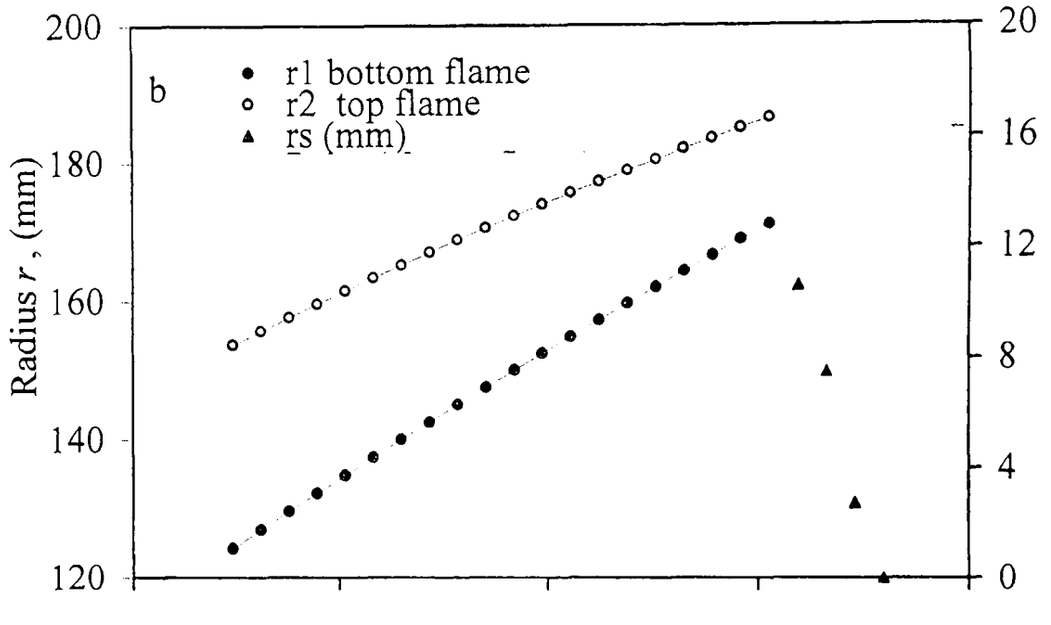

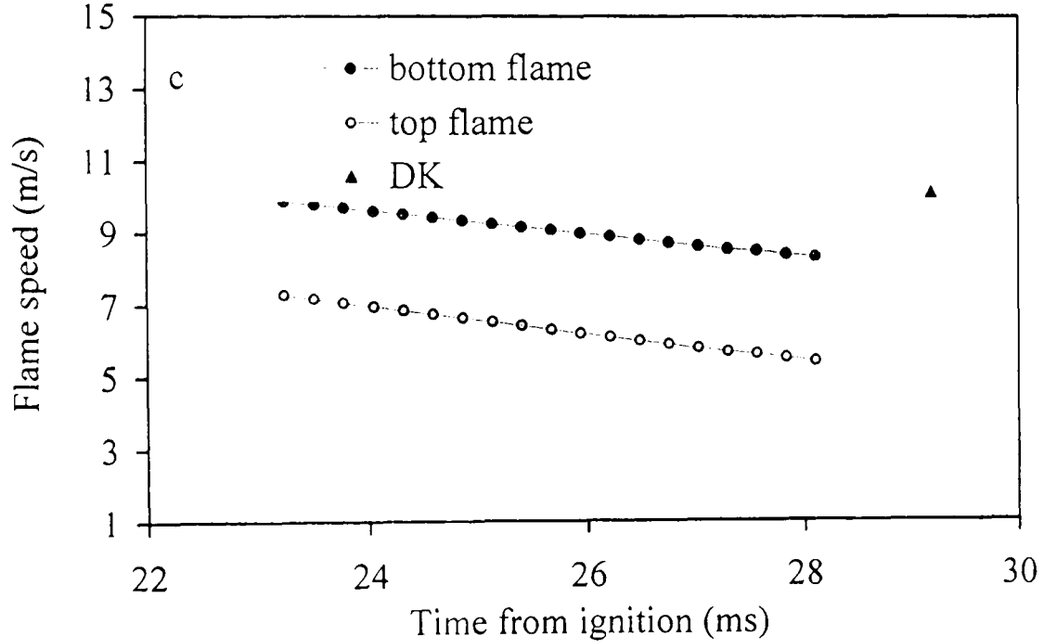

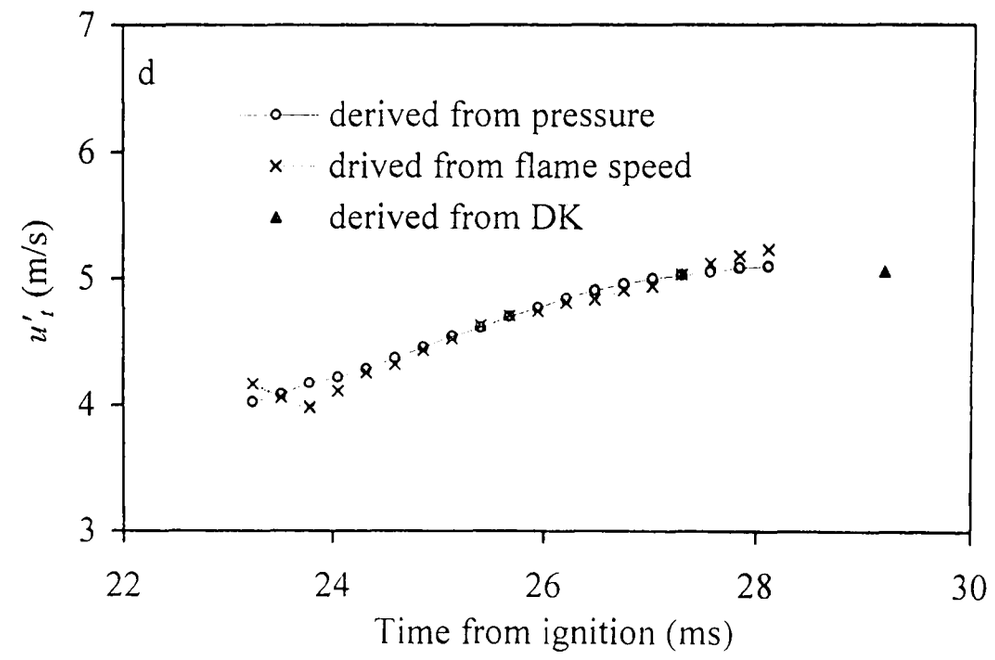

Fig. 7.4. Iso-octane - air implosion, $\phi = 1, p_o = 0.5$ MPa, $T_o = 358$ K, $u' = 1$

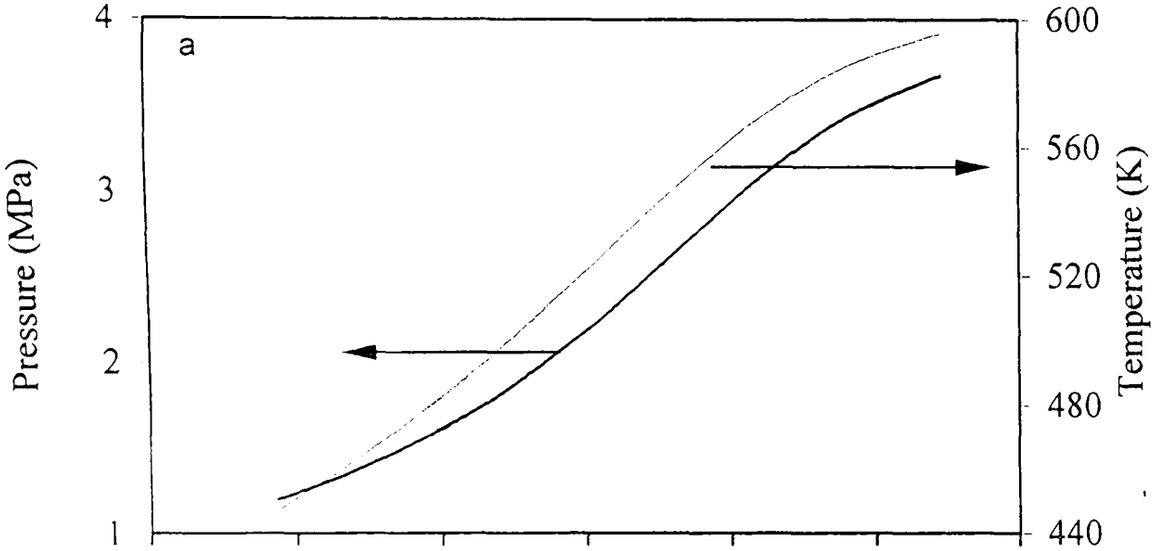

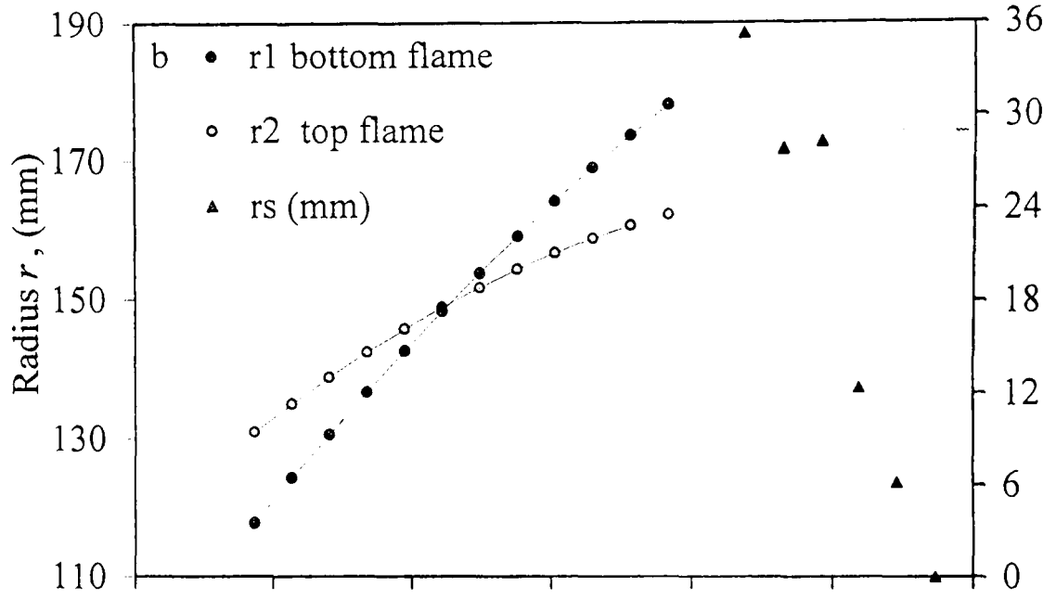

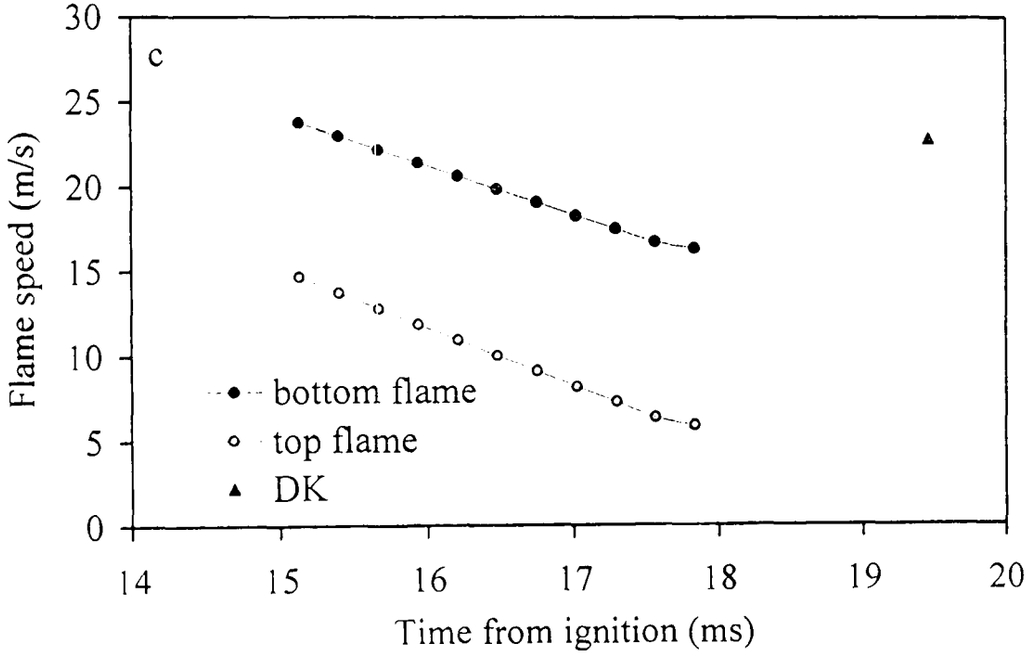

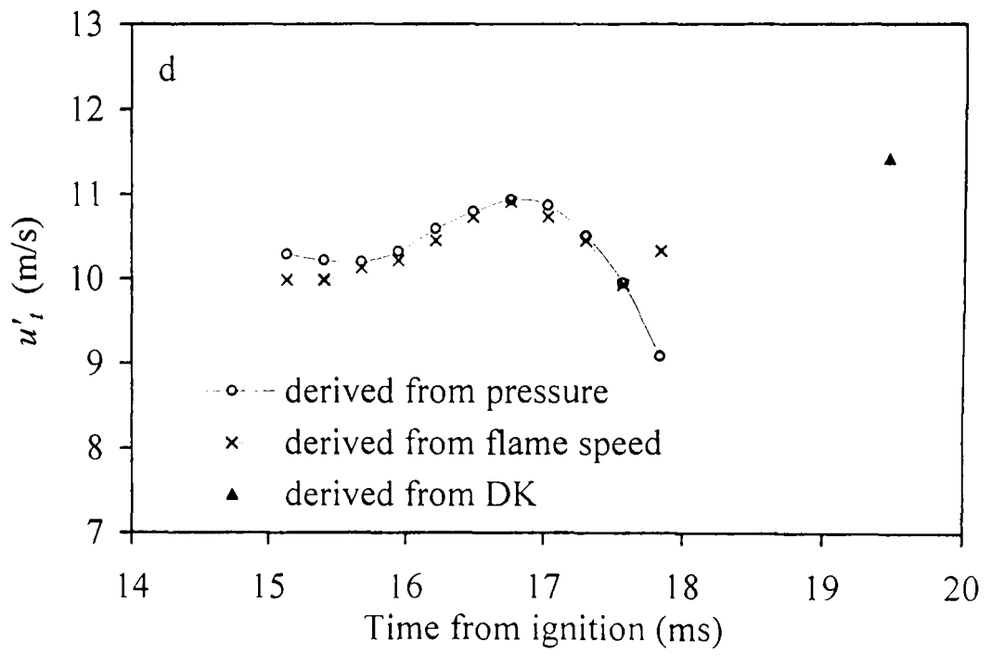

Fig. 7.5. Iso-octane - air implosion, $\phi = 1$, $p_o = 0.5$ MPa, $T_o = 358$ K, $u' = 2$

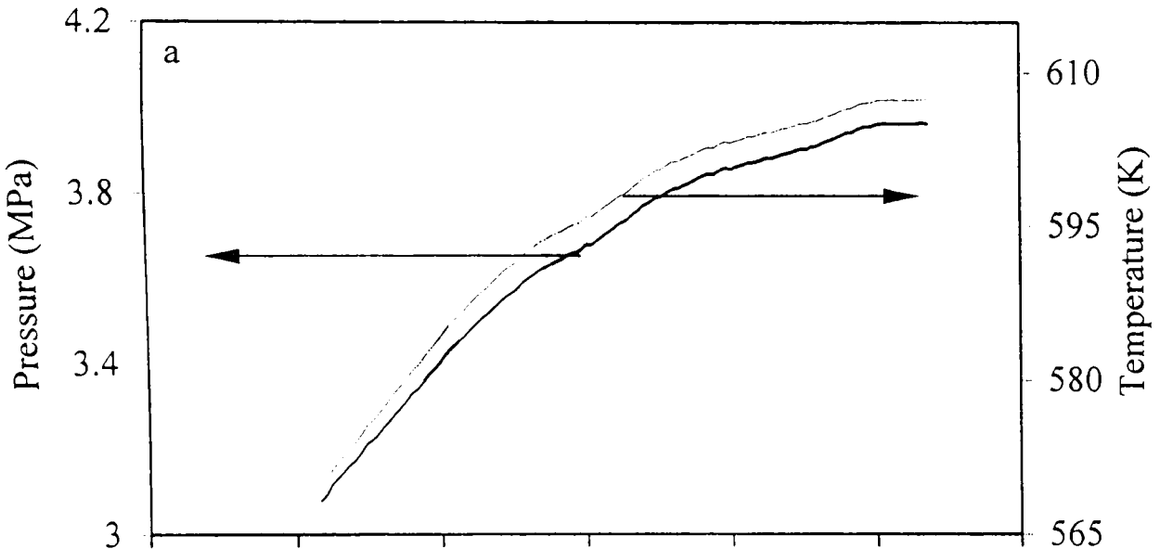

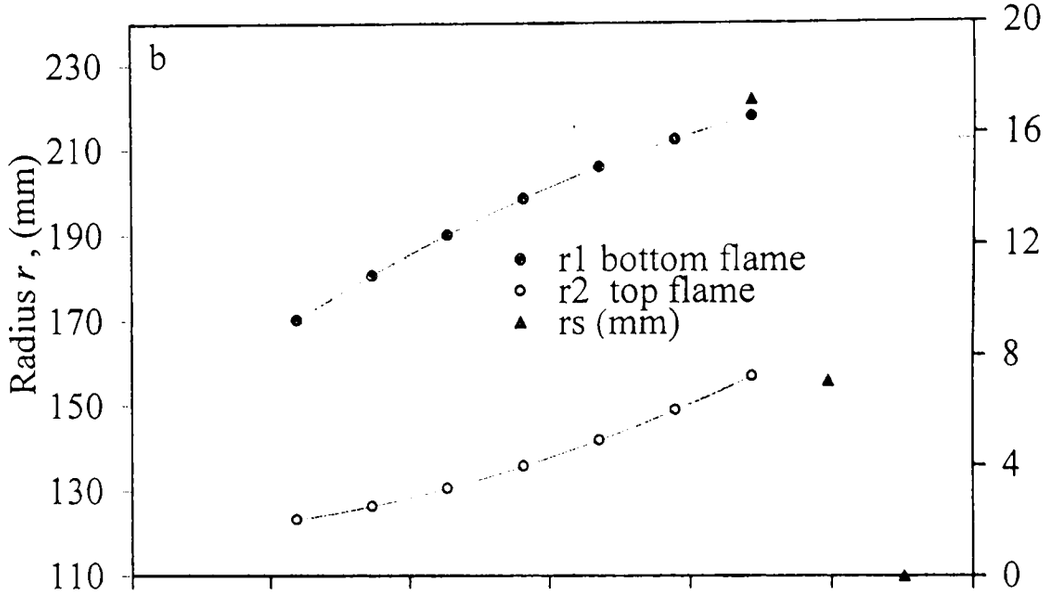

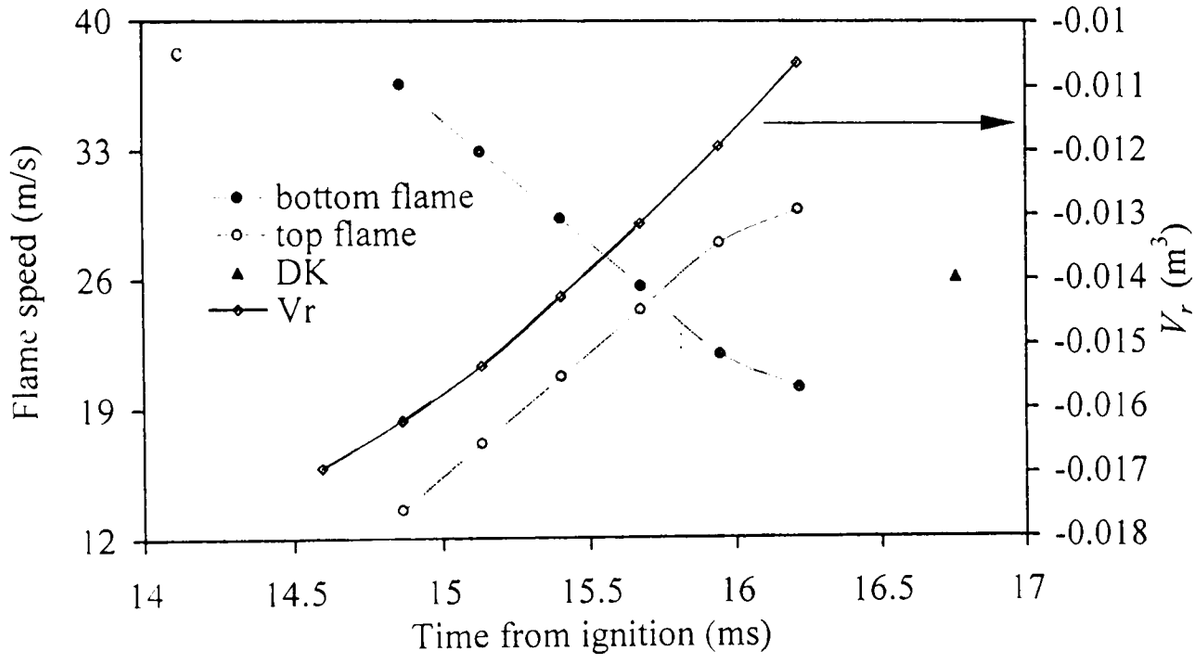

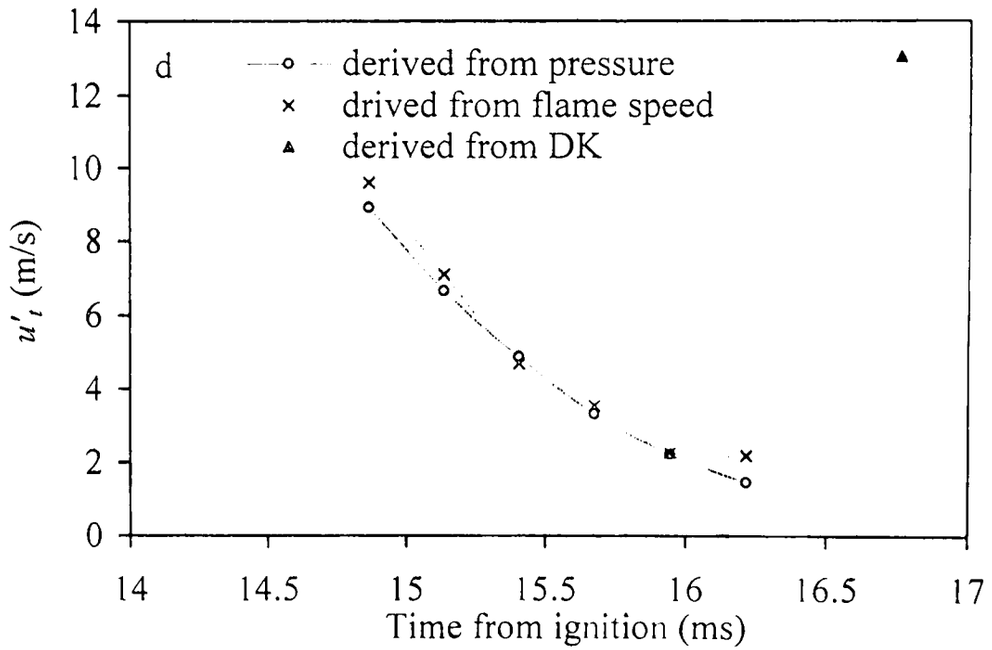

Fig. 7.6. Iso-octane - air implosion, $\phi = 1, p_o = 0.5$ MPa, $T_o = 358$ K, $u' = 3$

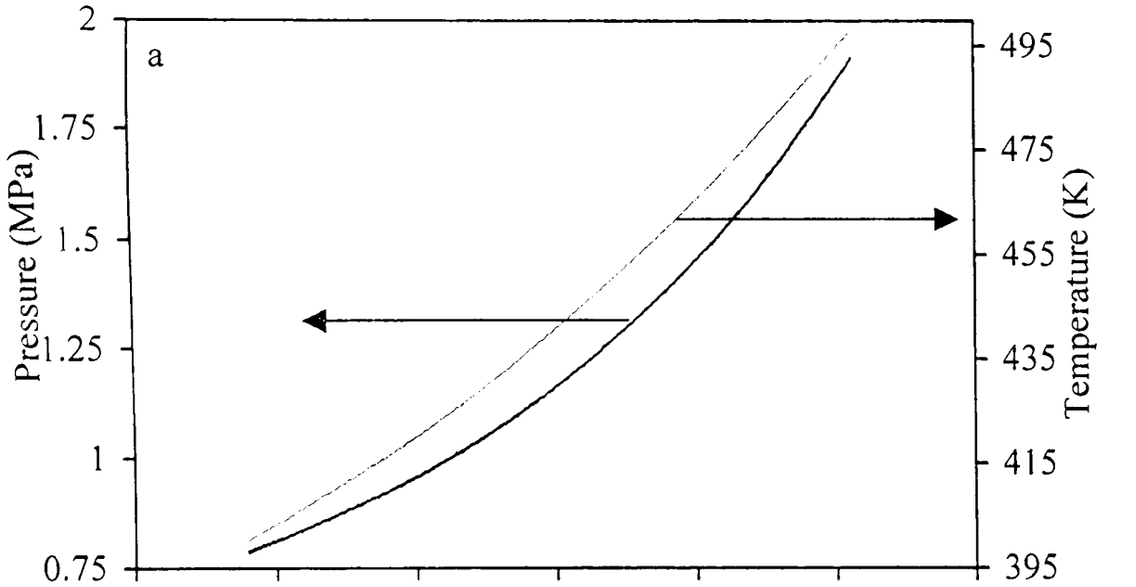

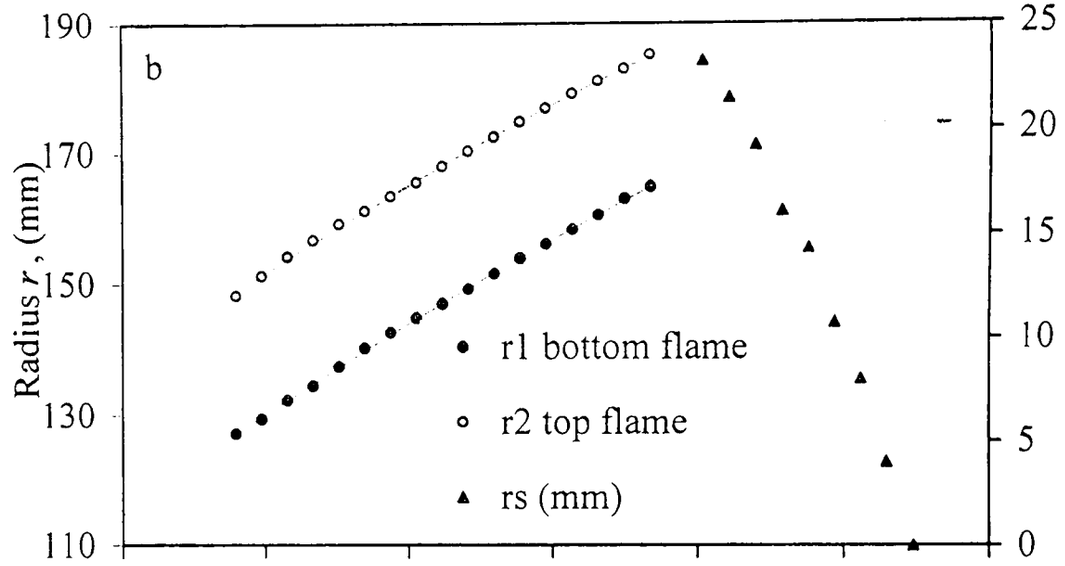

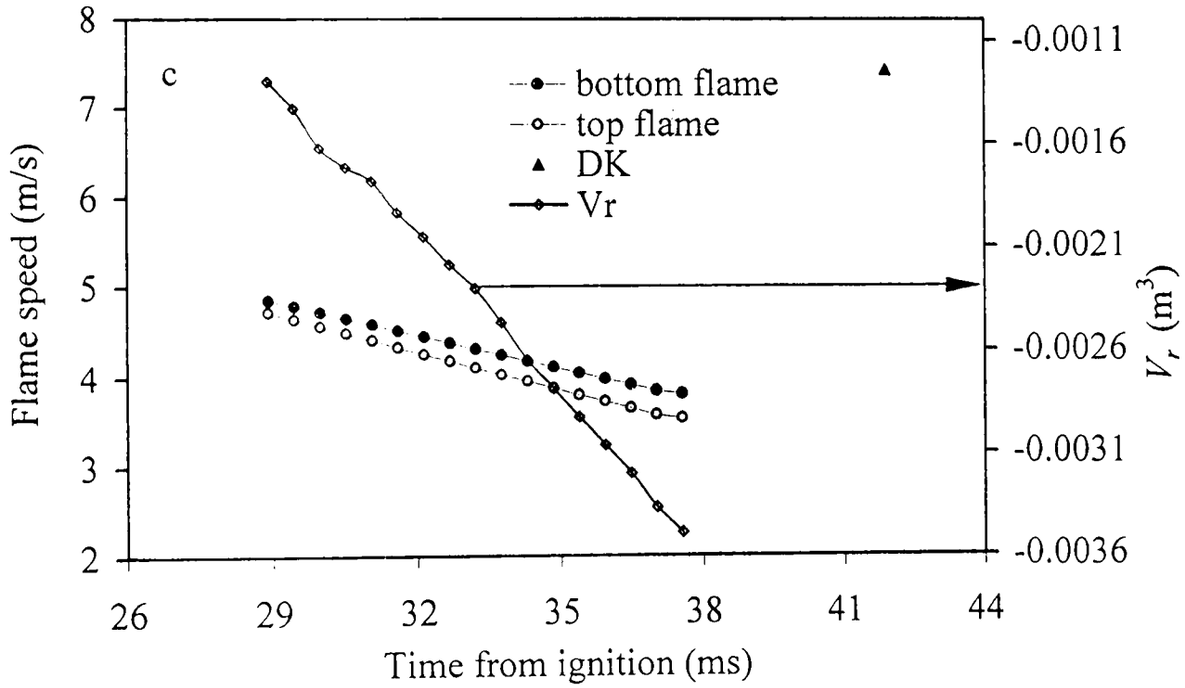

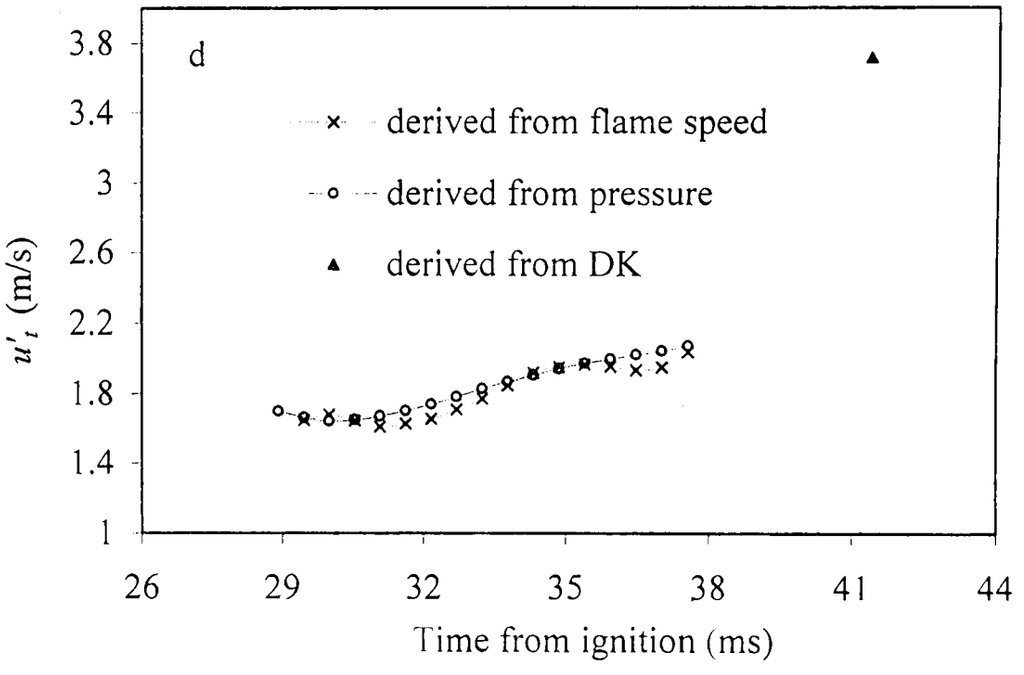

Fig. 7.7. Iso-octane - air implosion, ϕ = 1.4, p_o = 0.5 MPa, T_o = 358 K, u' = 0.25

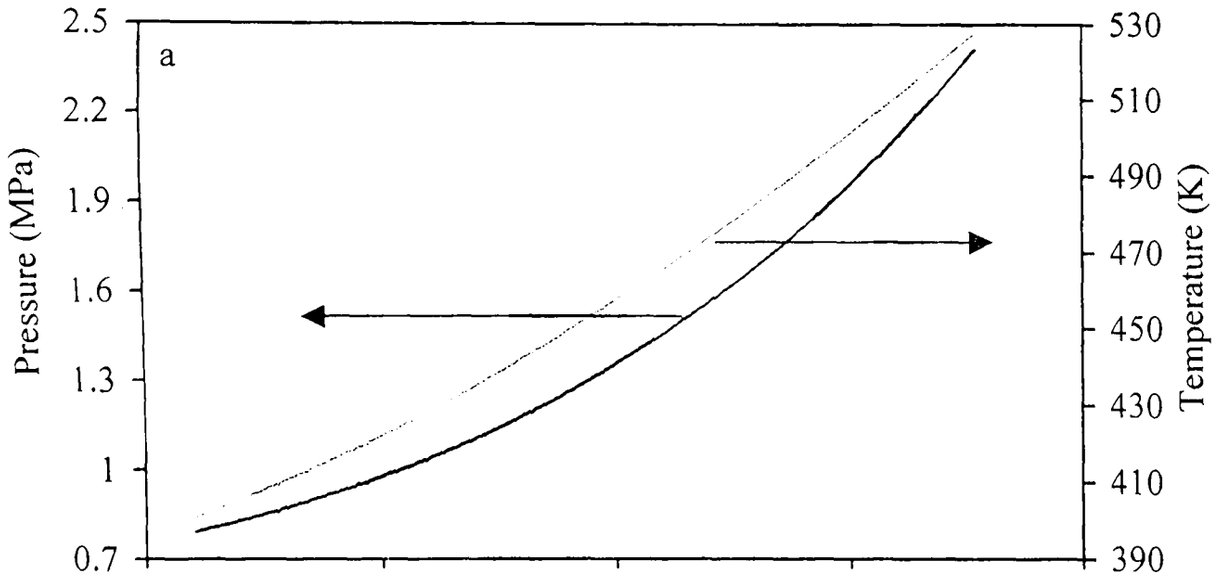

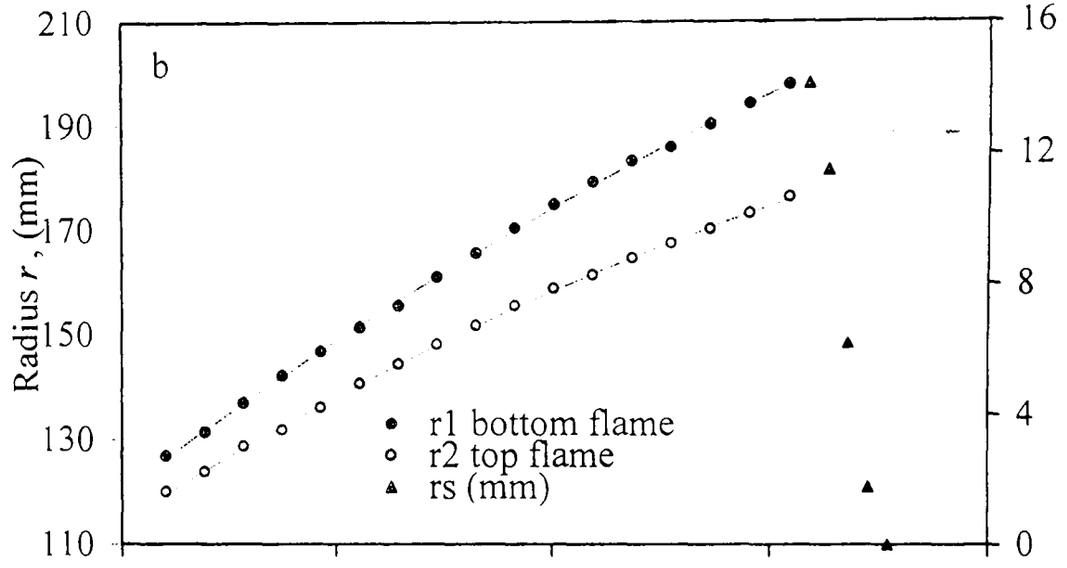

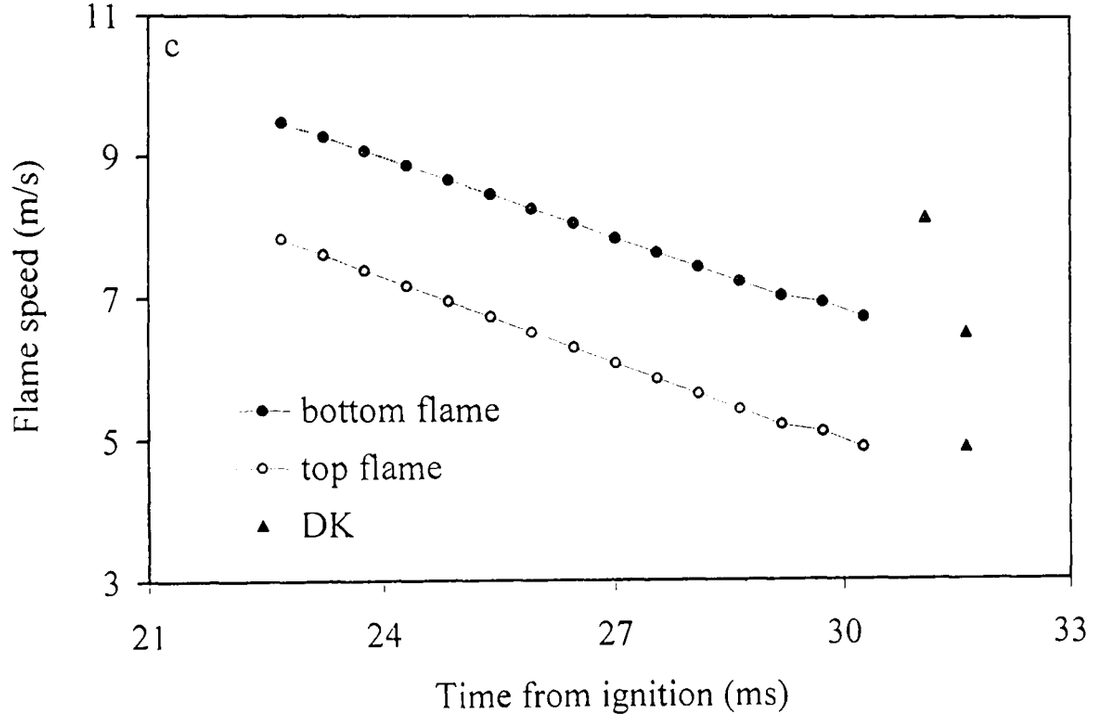

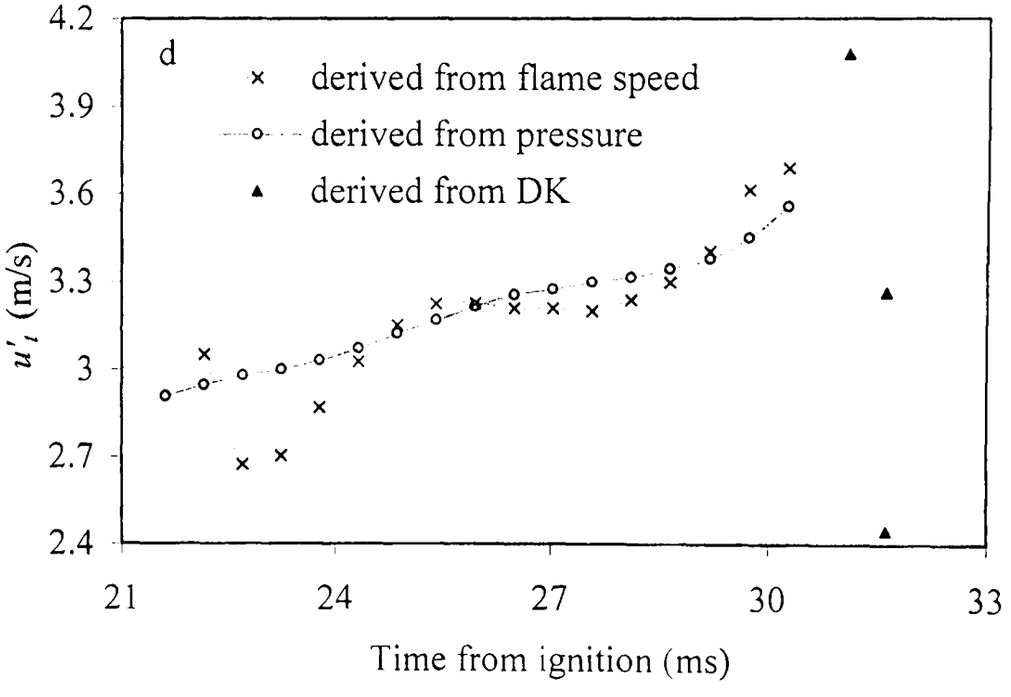

Fig. 7.8. Iso-octane - air implosion, ϕ = 1.4, p_o = 0.5 MPa, T_o = 358 K, u' = 0.5

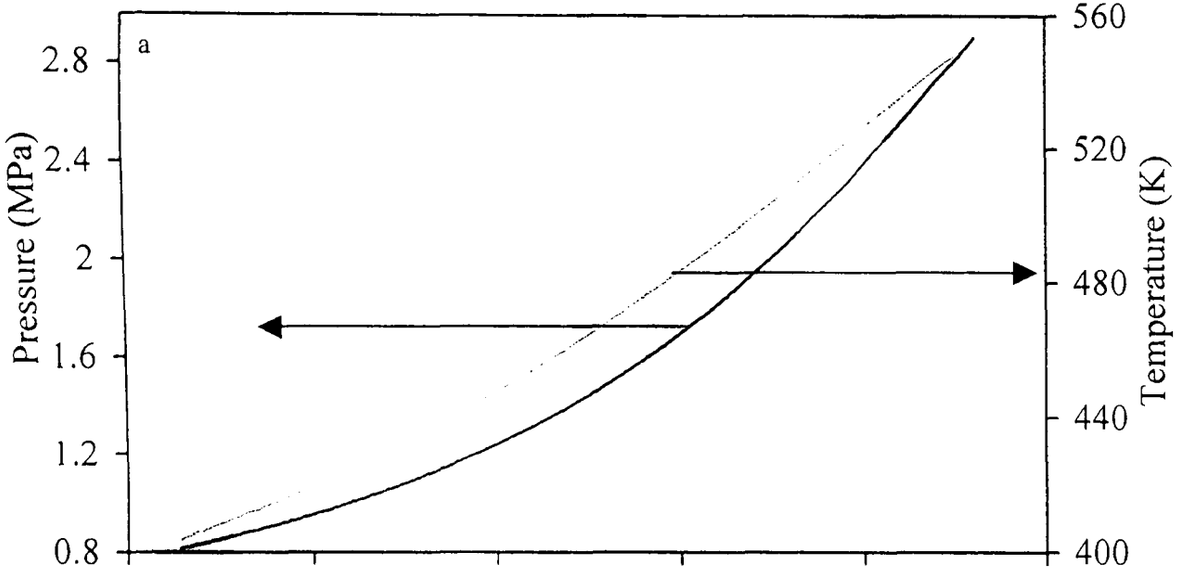

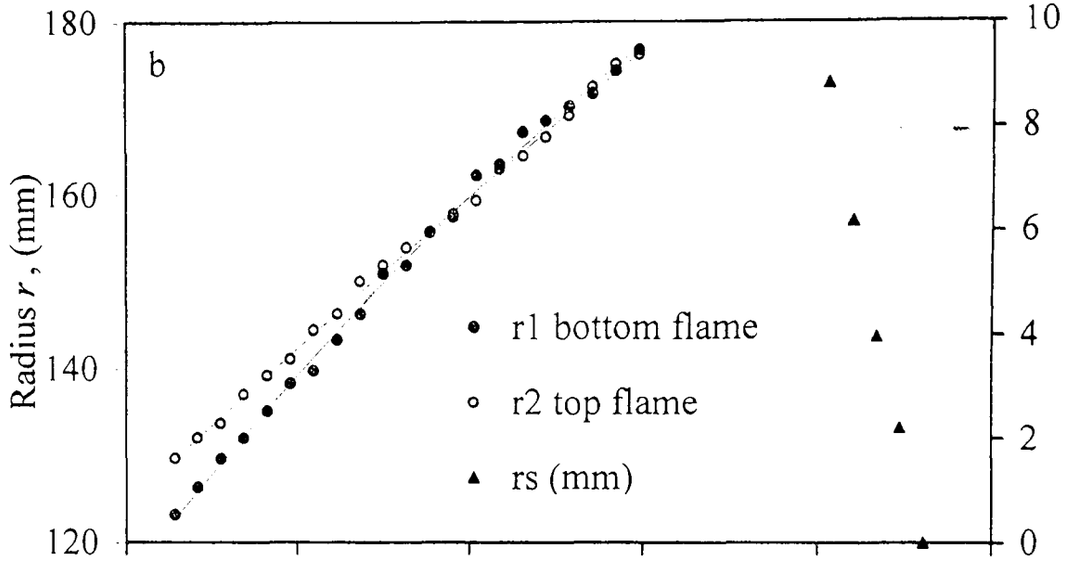

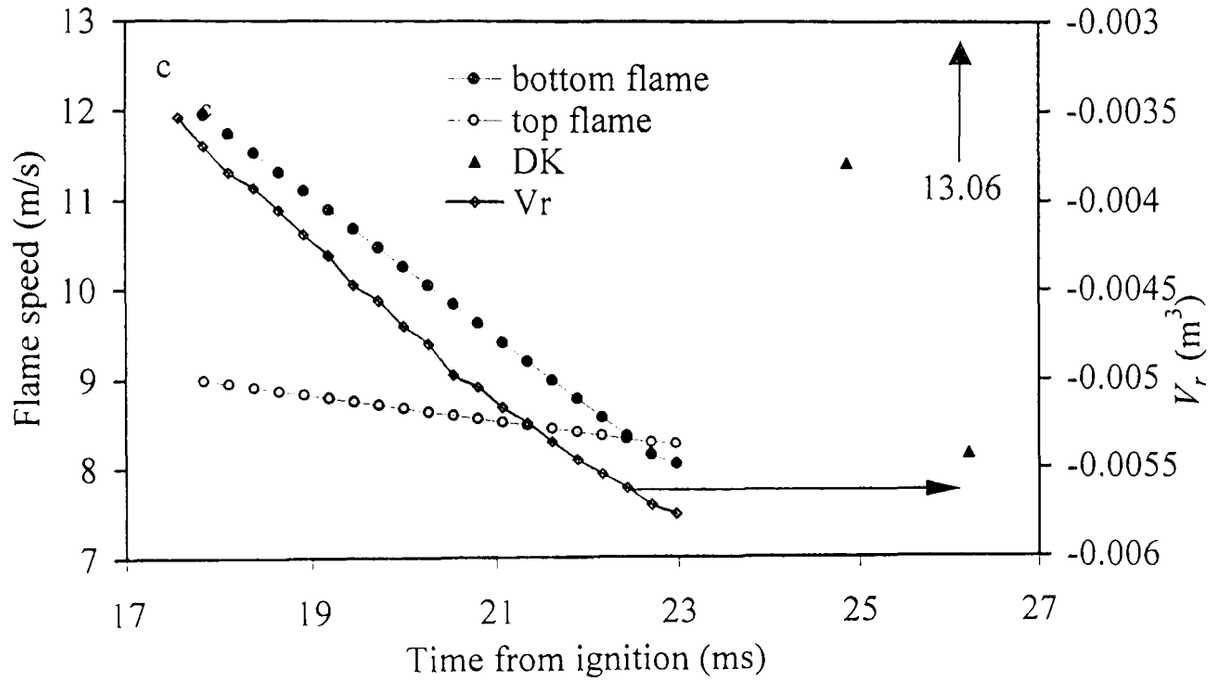

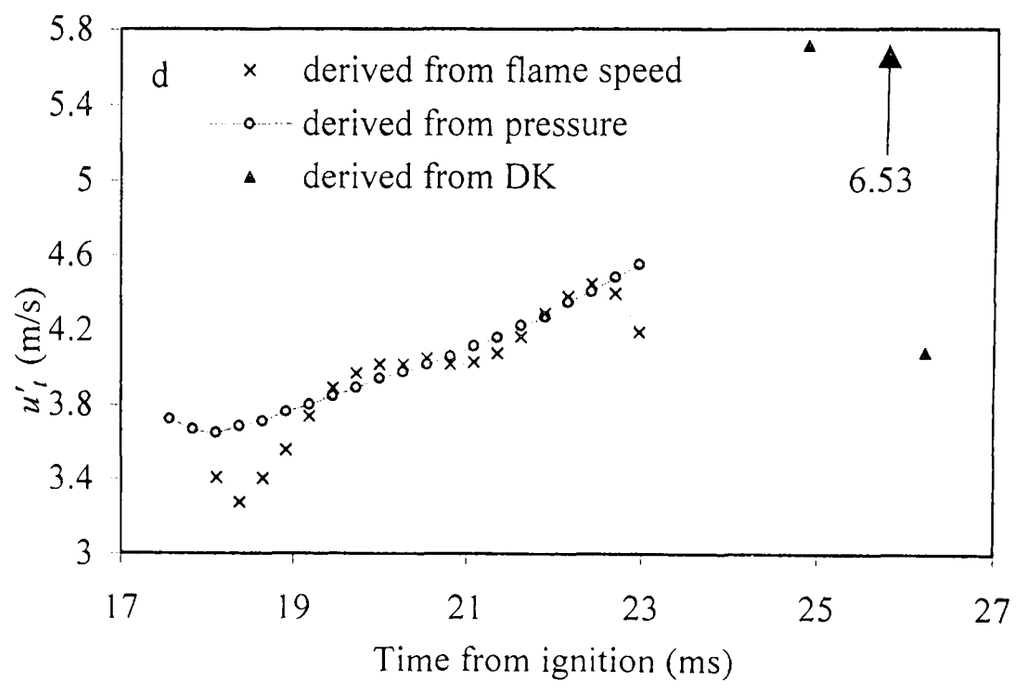

Fig. 7.9. Iso-octane - air implosion, ϕ = 1.4, p_o = 0.5 MPa, T_o = 358 K, u' = 0.75

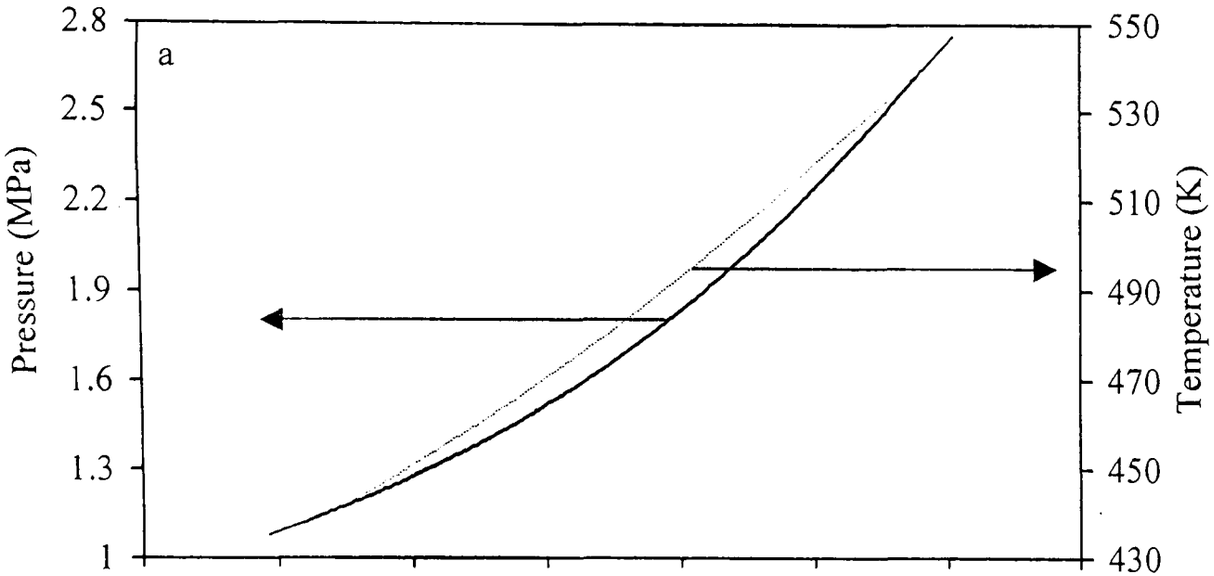

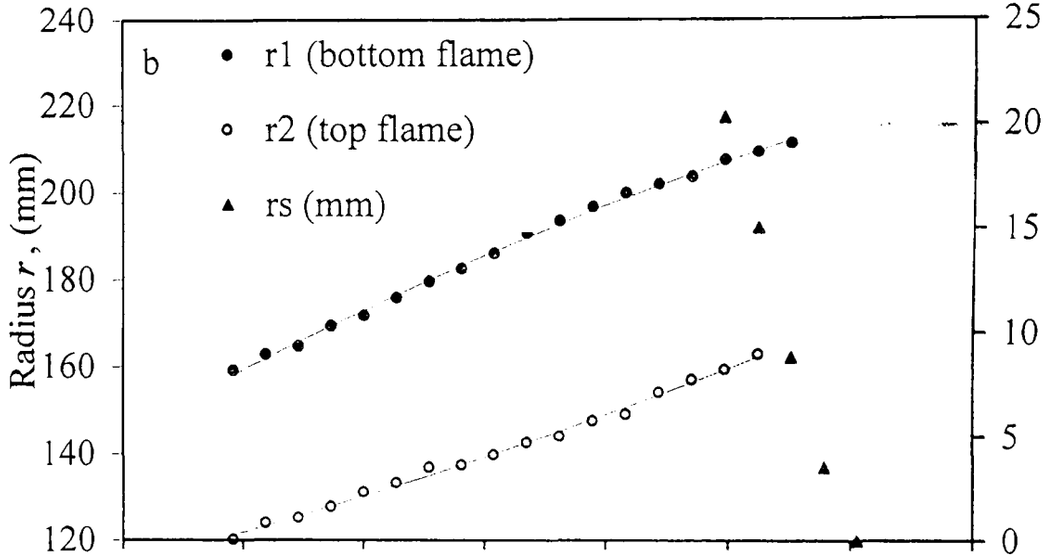

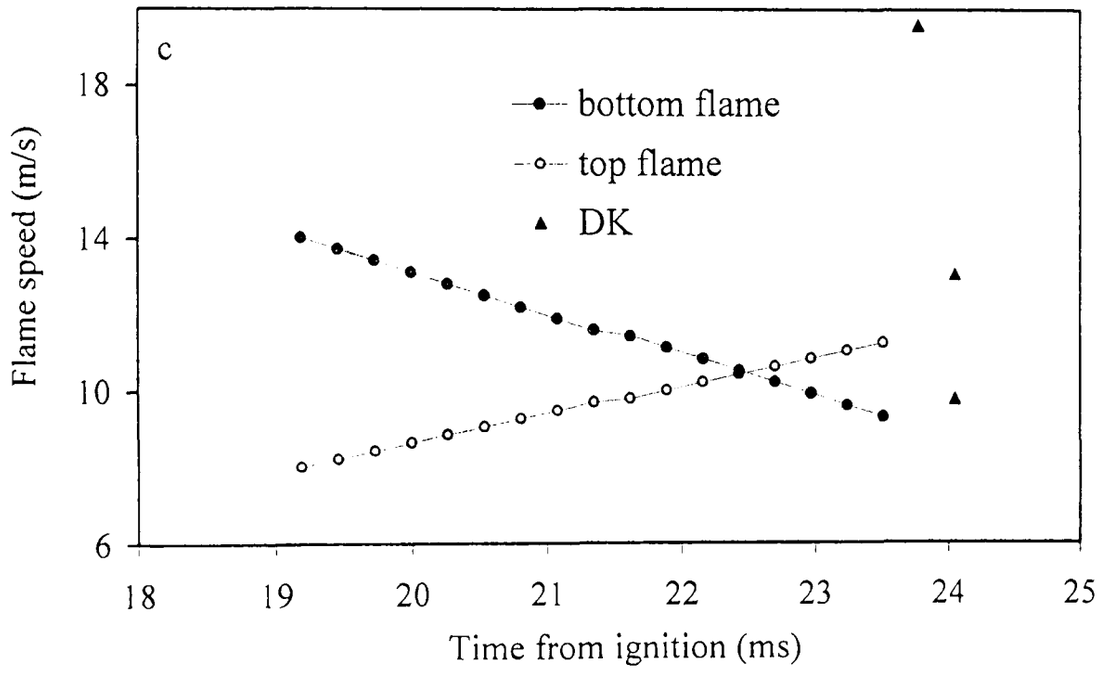

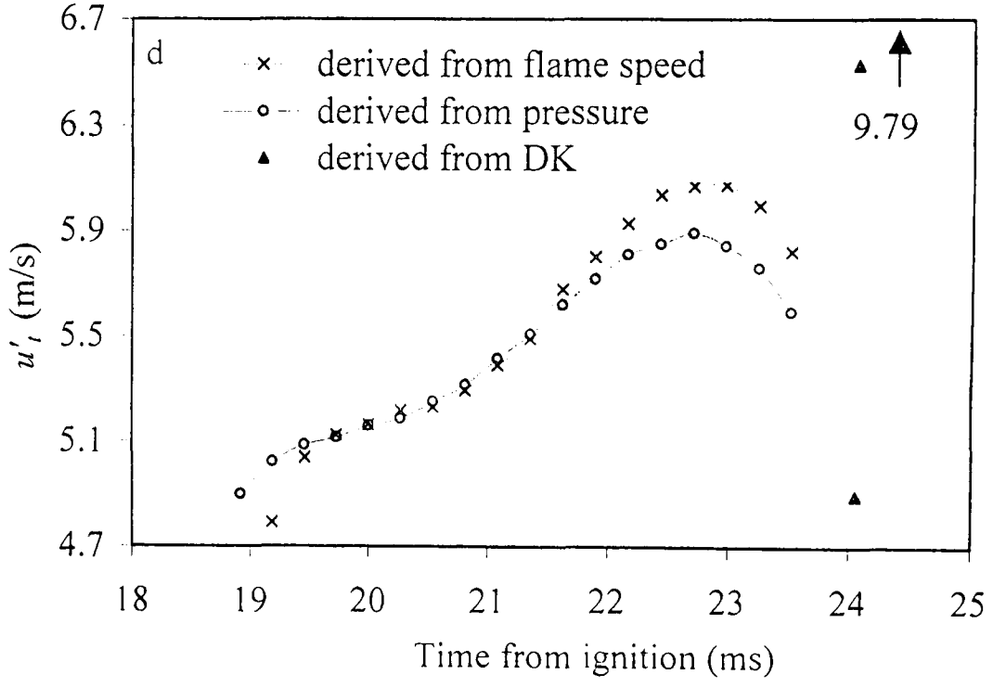

Fig. 7.10. Iso-octane - air implosion, ϕ = 1.4, p_o = 0.5 MPa, T_o = 358 K, u' = 1

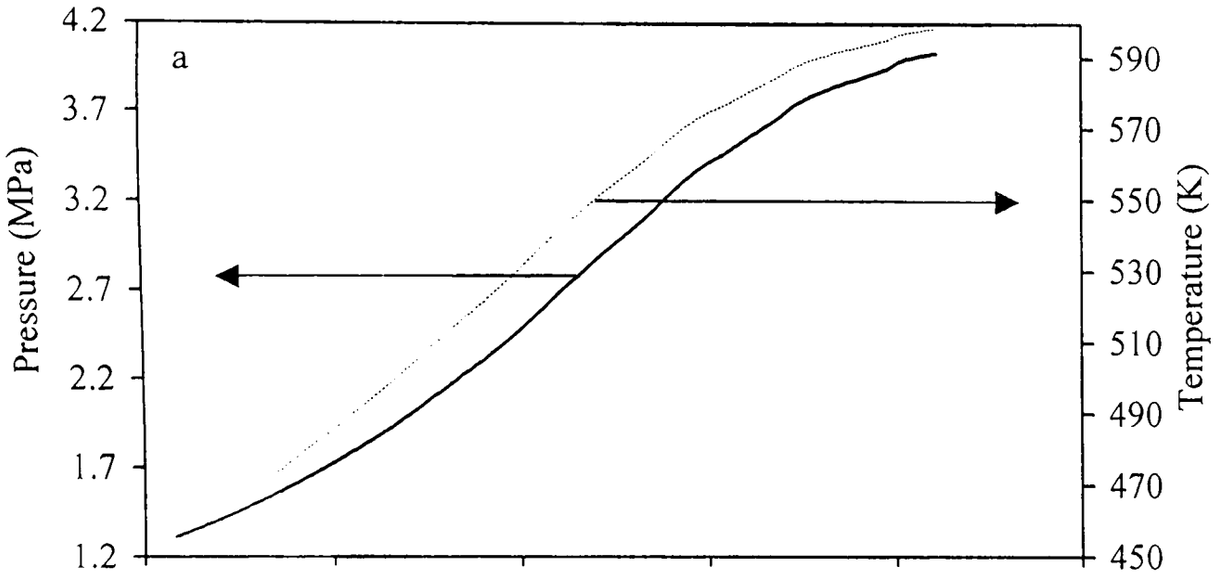

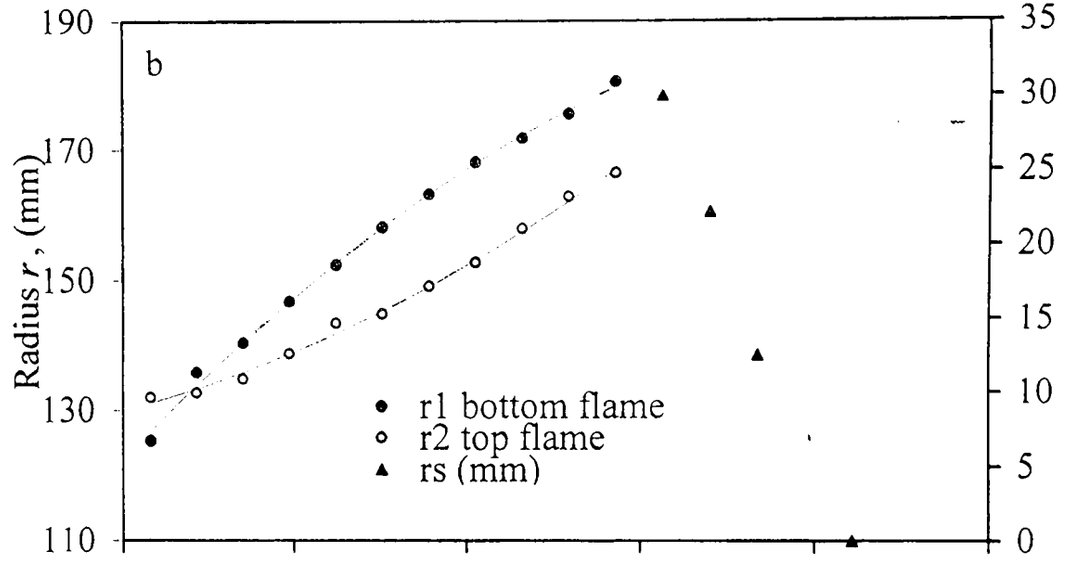

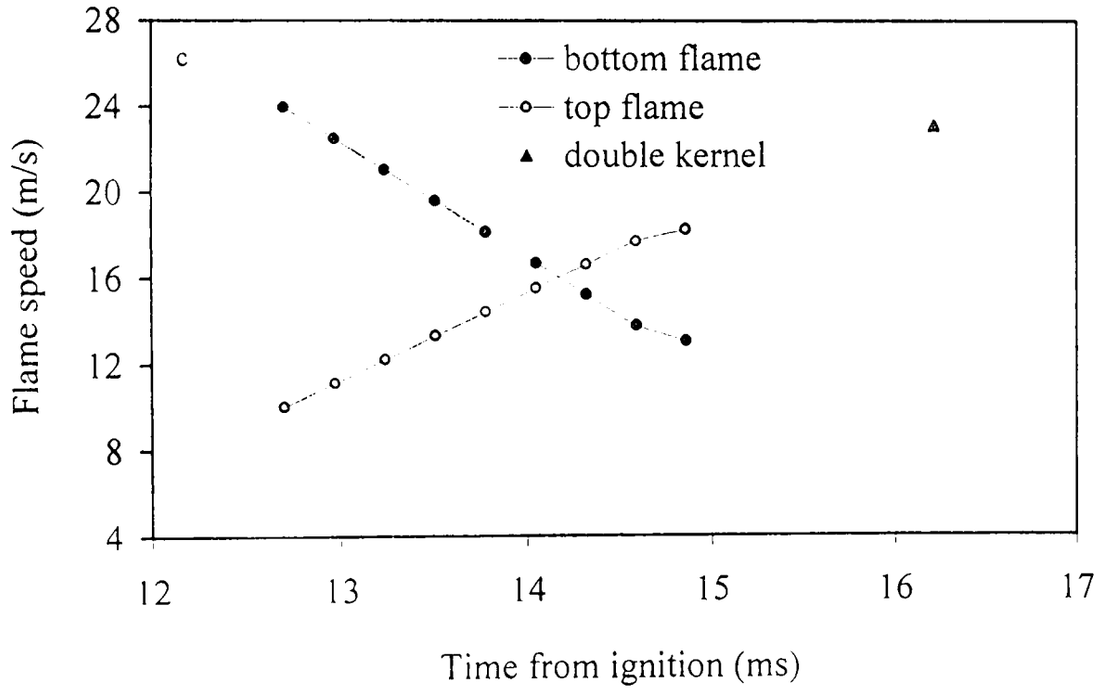

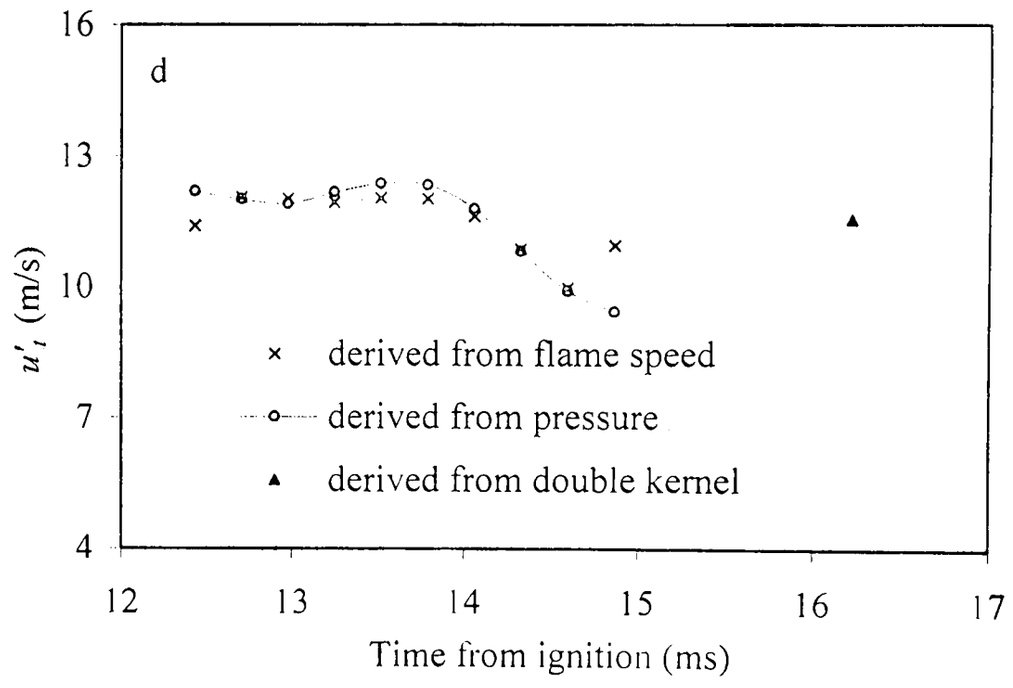

Fig. 7.11. Iso-octane - air implosion, ϕ = 1.4, p_o = 0.5 MPa, T_o = 358 K, u' = 2

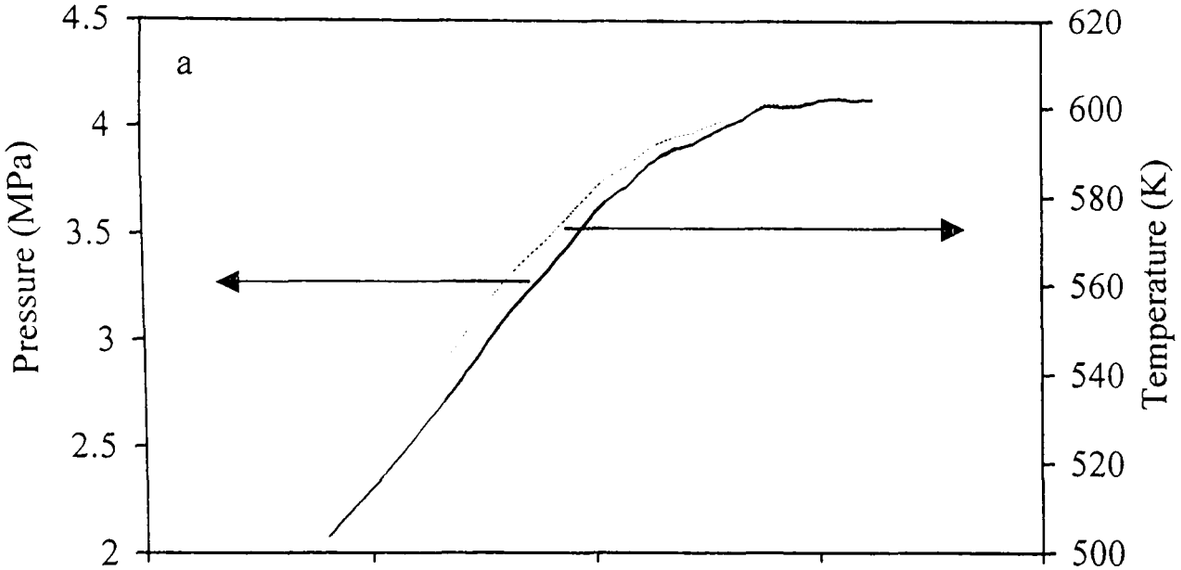

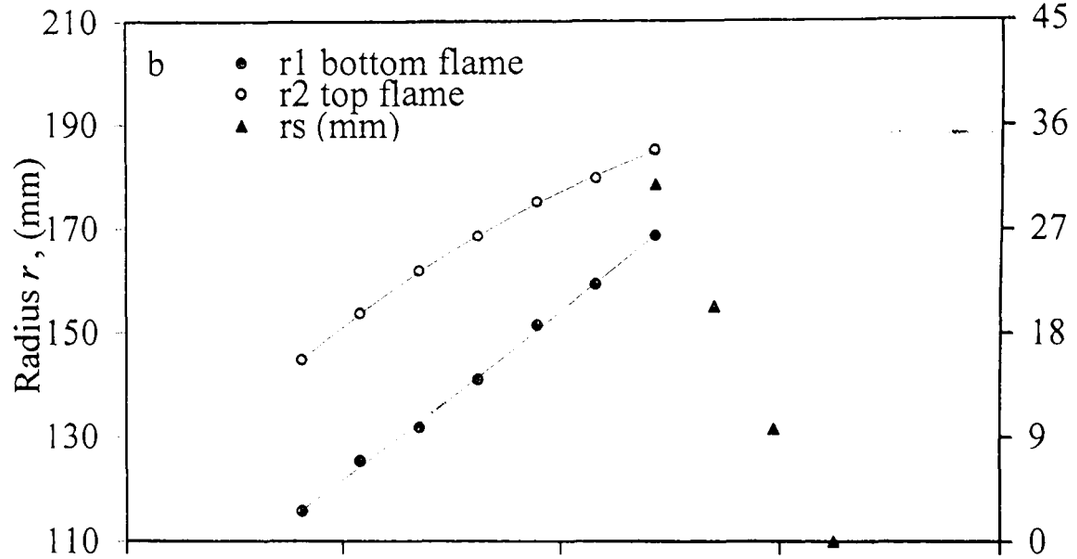

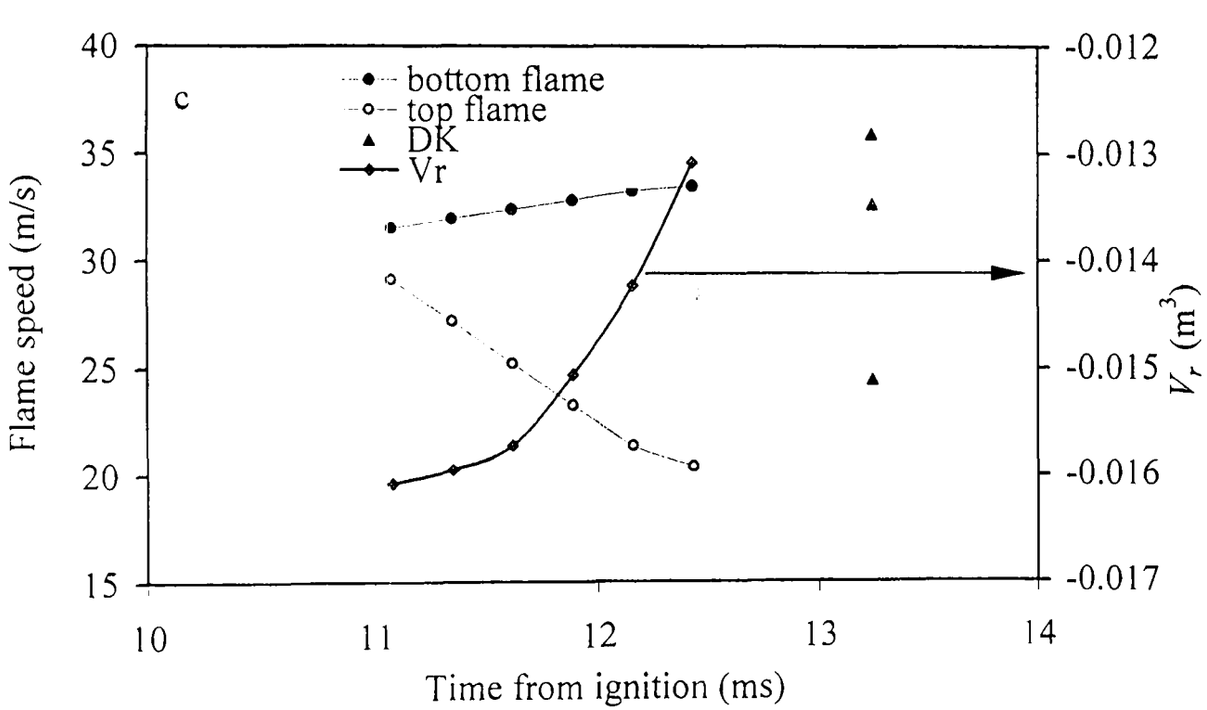

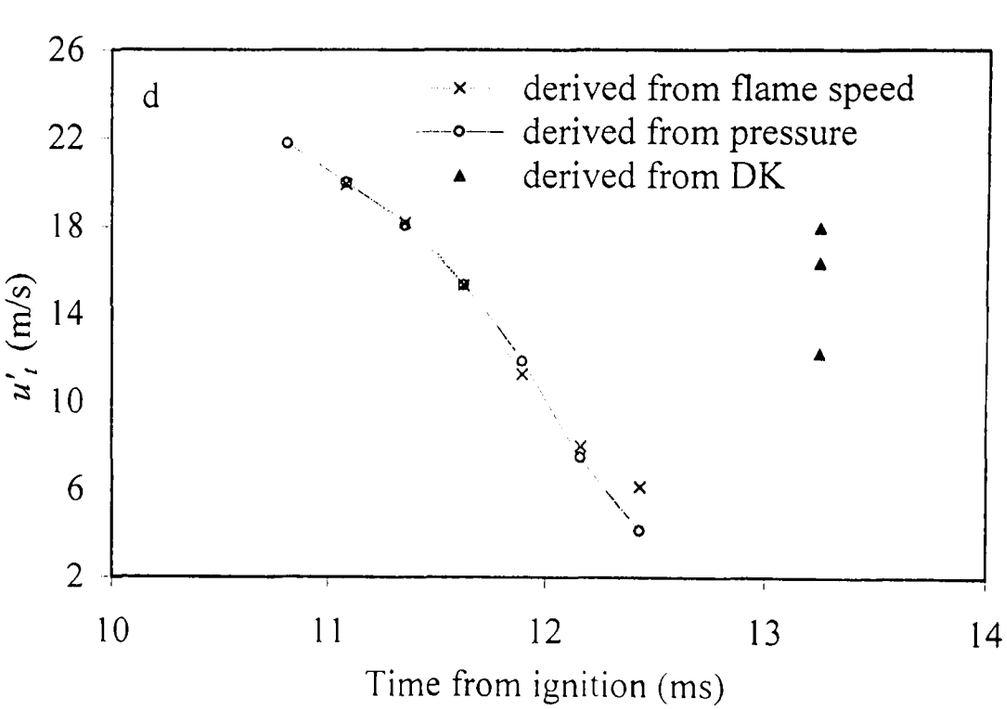

Fig. 7.12. Iso-octane - air implosion, ϕ = 1.4, p_o = 0.5 MPa, T_o = 358 K, u' = 3

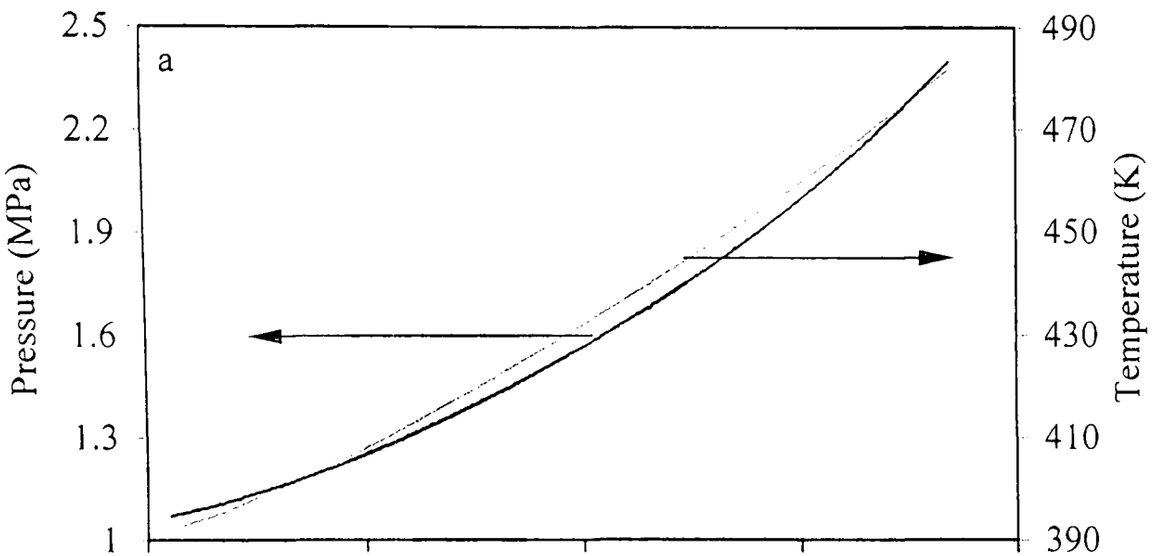

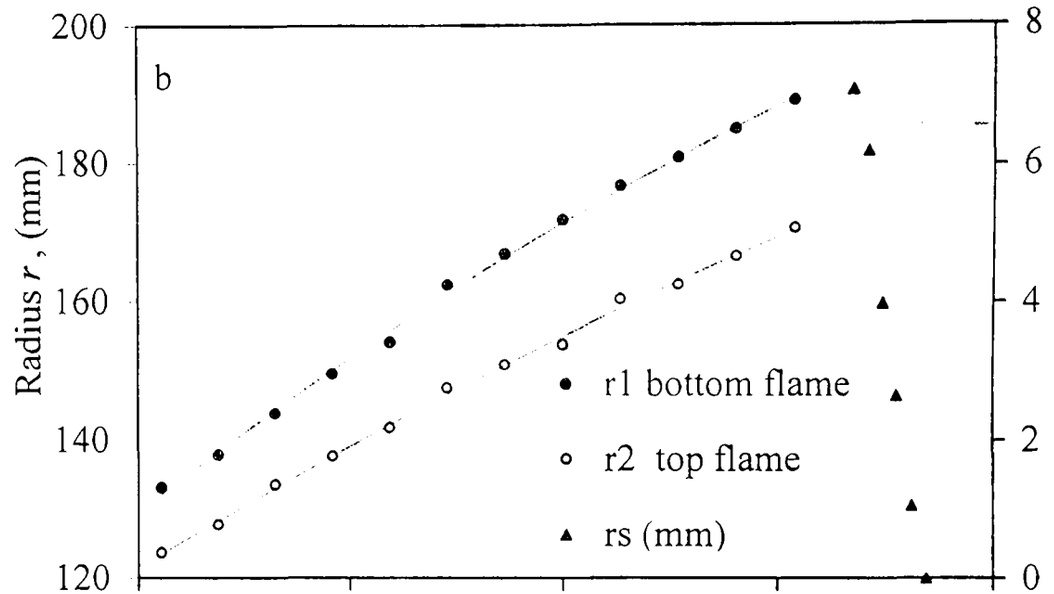

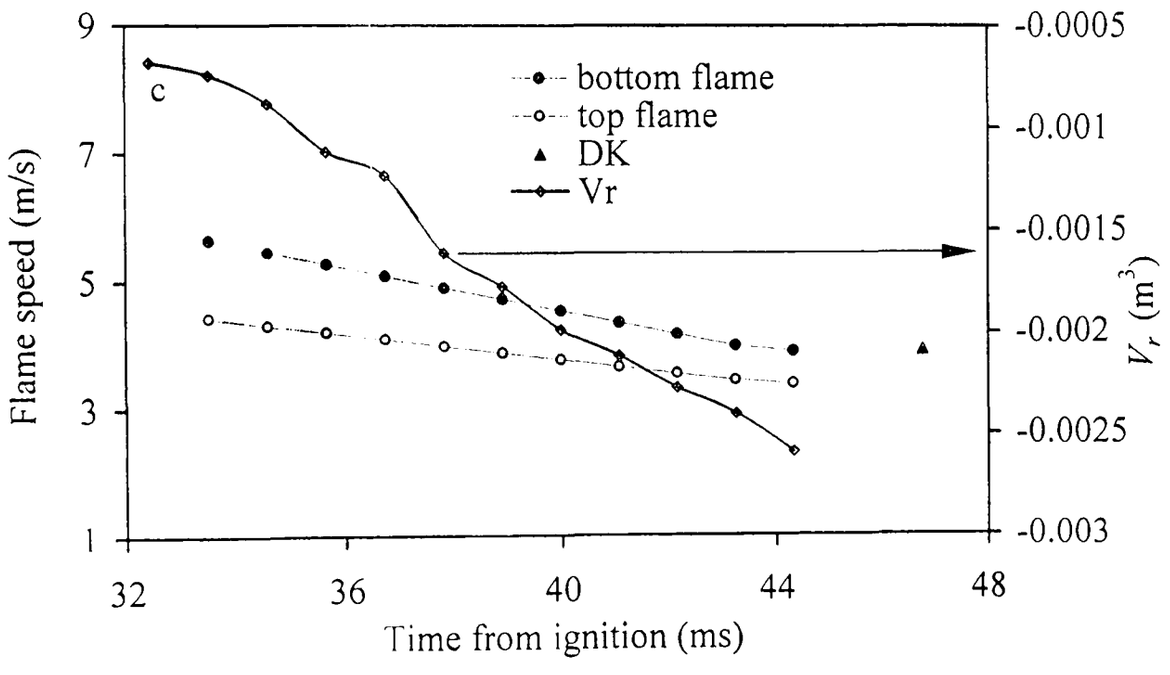

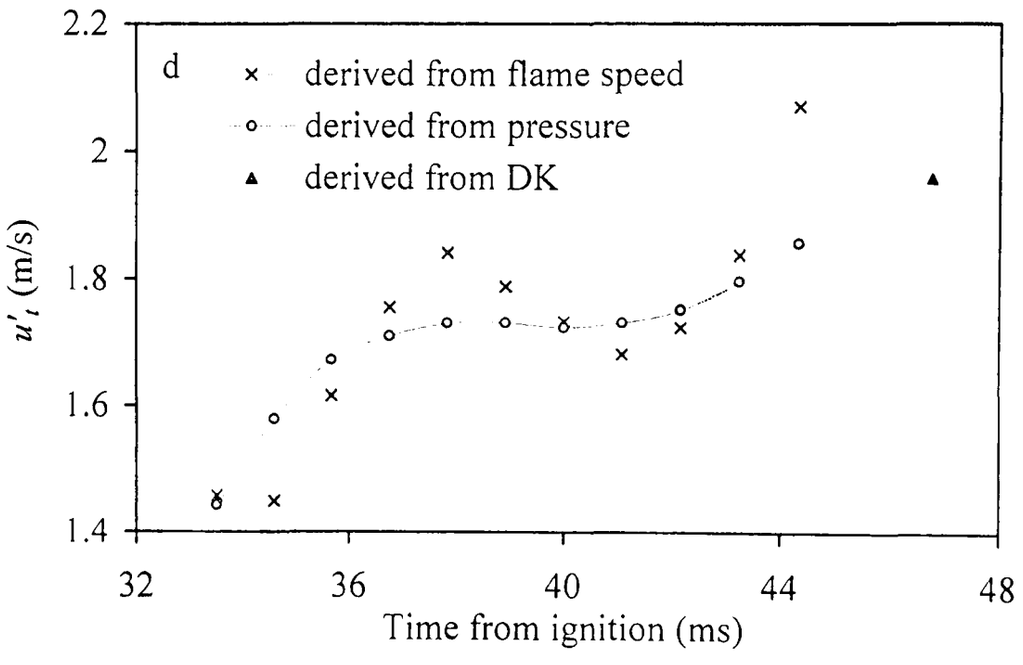

Fig. 7.13. Iso-octane - air implosion, $\phi = 1, p_o = 0.75$ MPa, $T_o = 358$ K, $u' = 0.25$

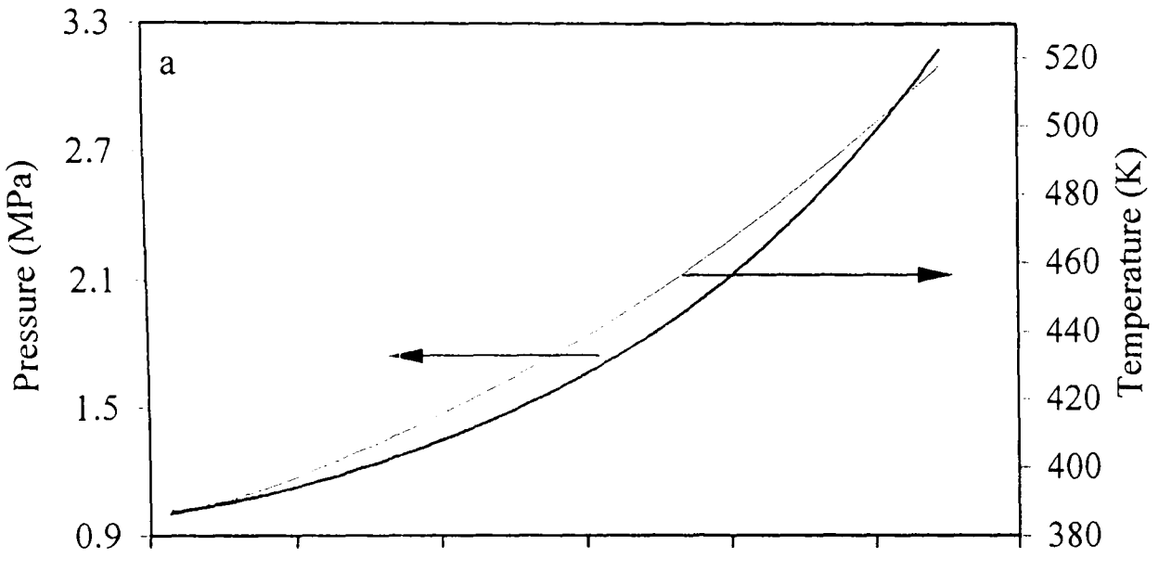

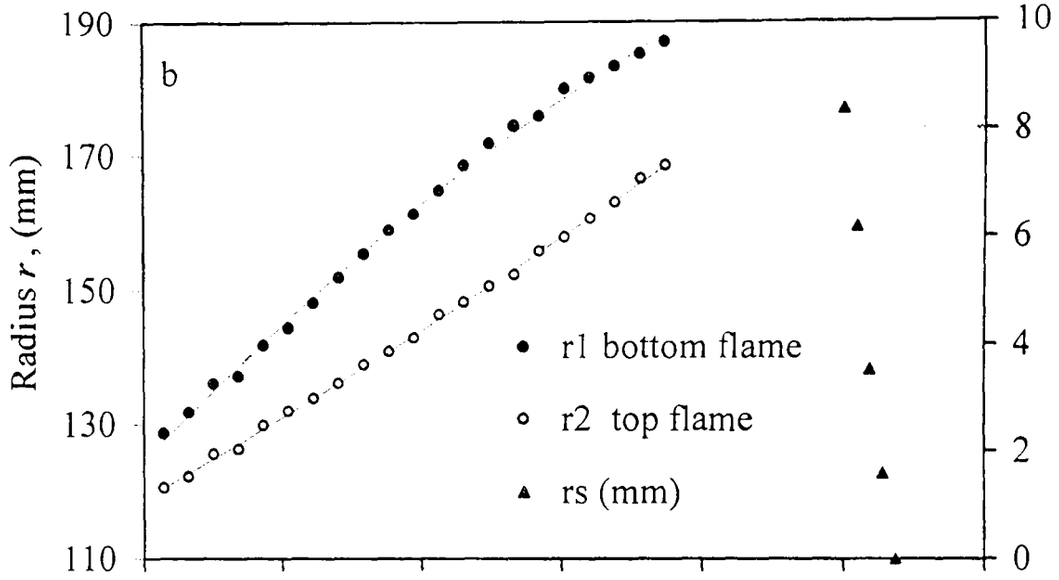

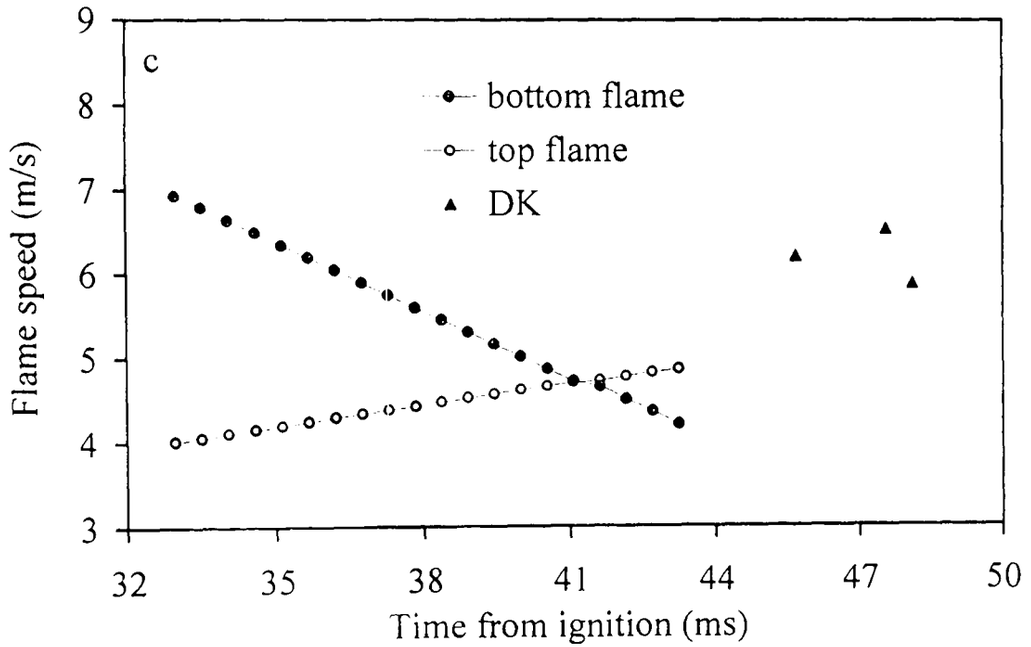

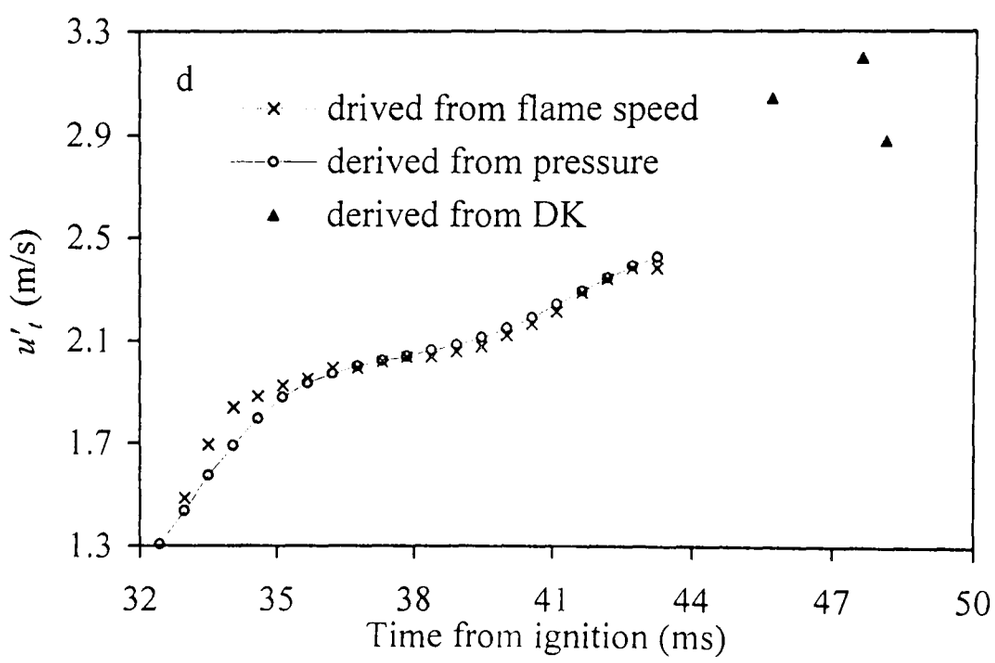

Fig. 7.14. Iso-octane - air implosion, $\phi = 1, p_o = 0.75$ MPa, $T_o = 358$ K, $u' = 0.5$

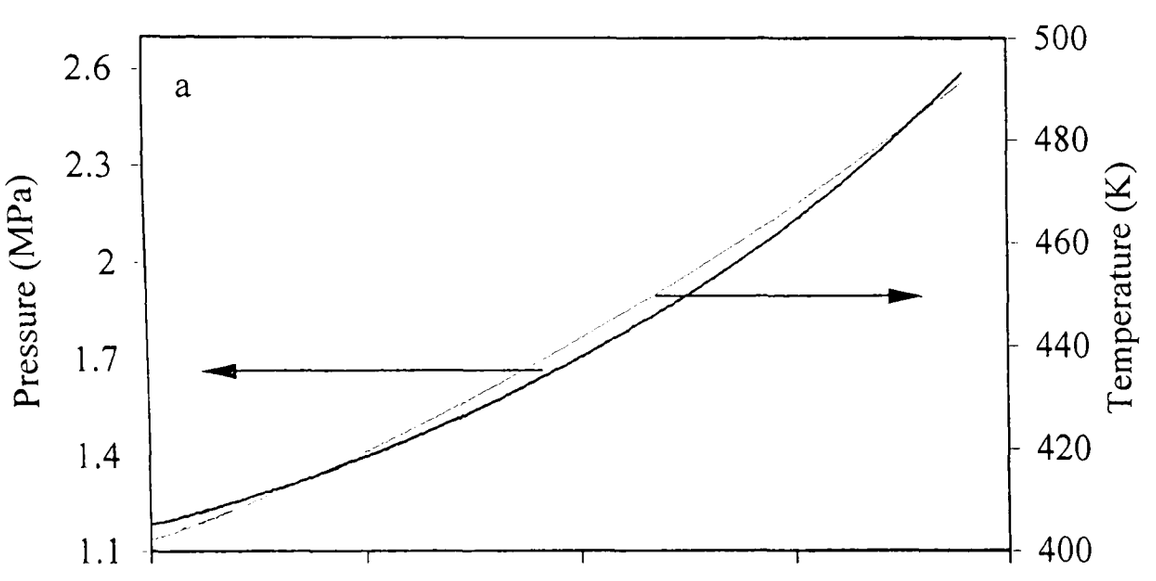

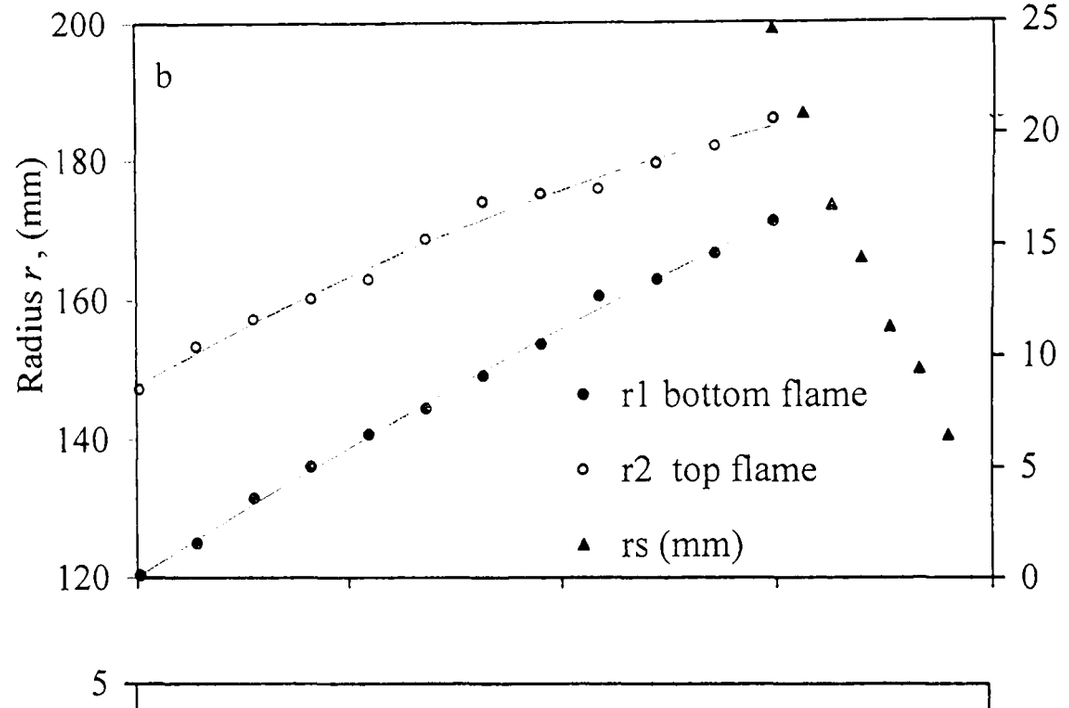

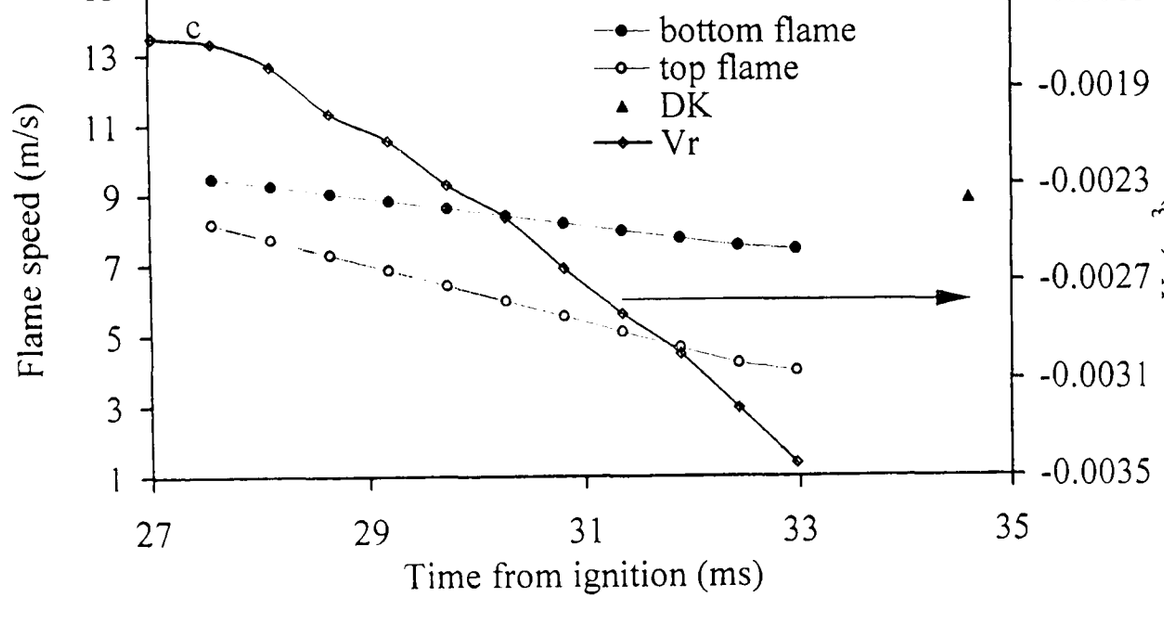

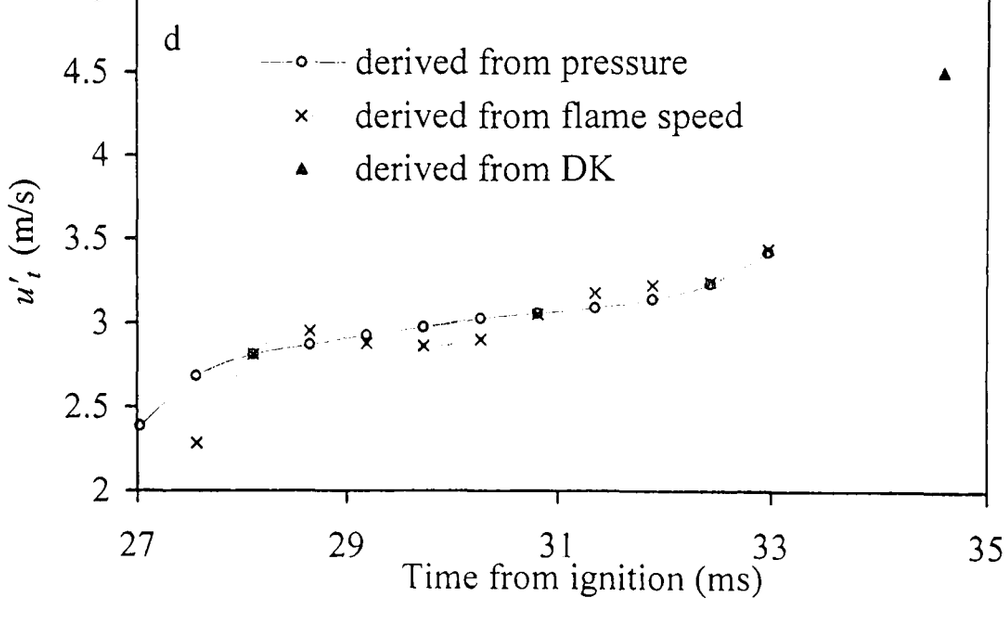

Fig. 7.15. Iso-octane - air implosion, $\phi = 1, p_o = 0.75$ MPa, $T_o = 358$ K, $u' = 0.75$

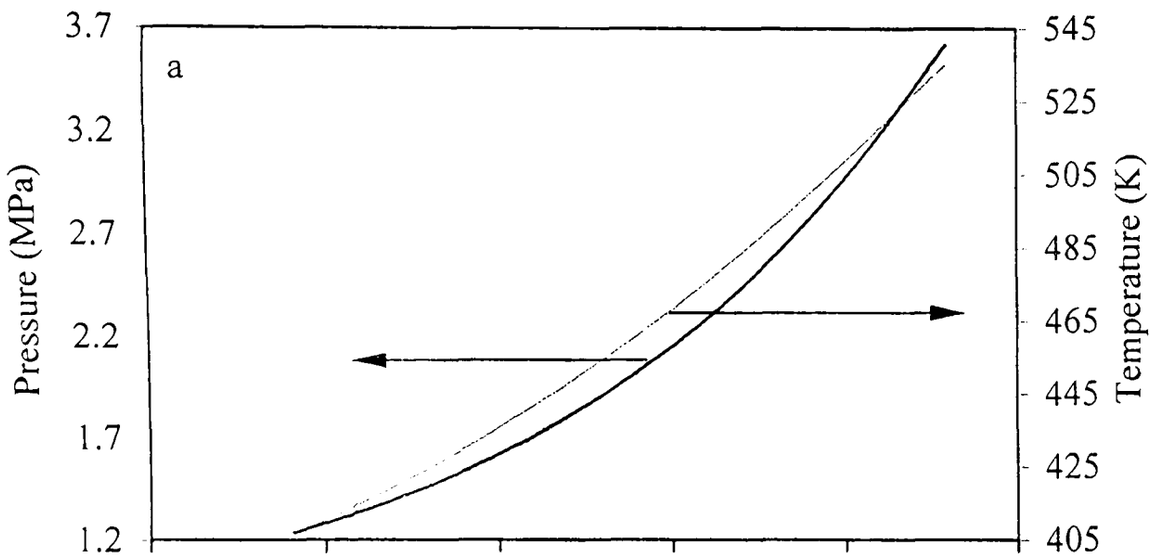

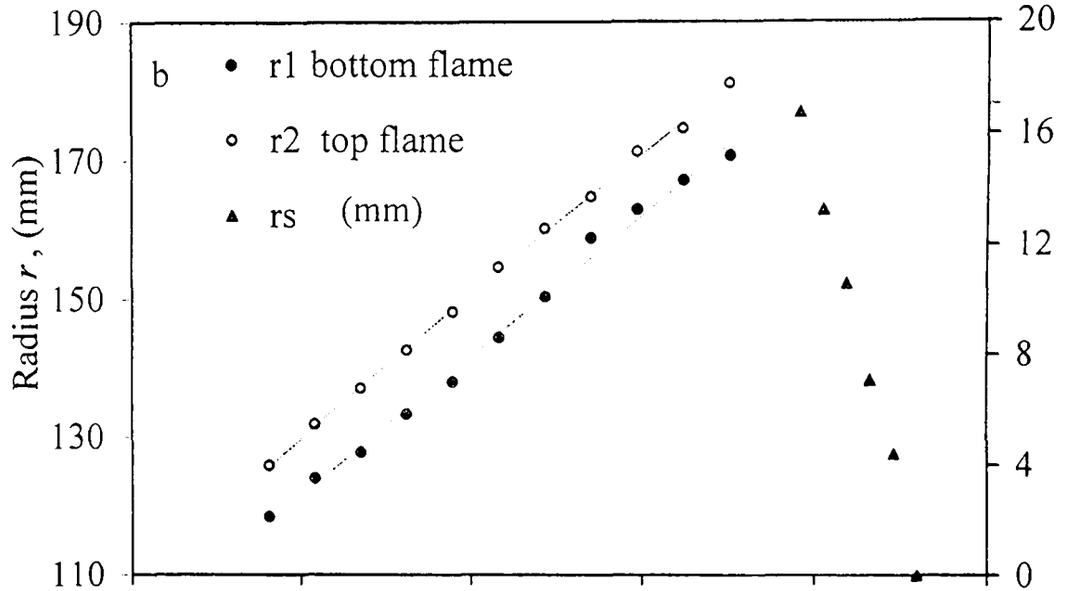

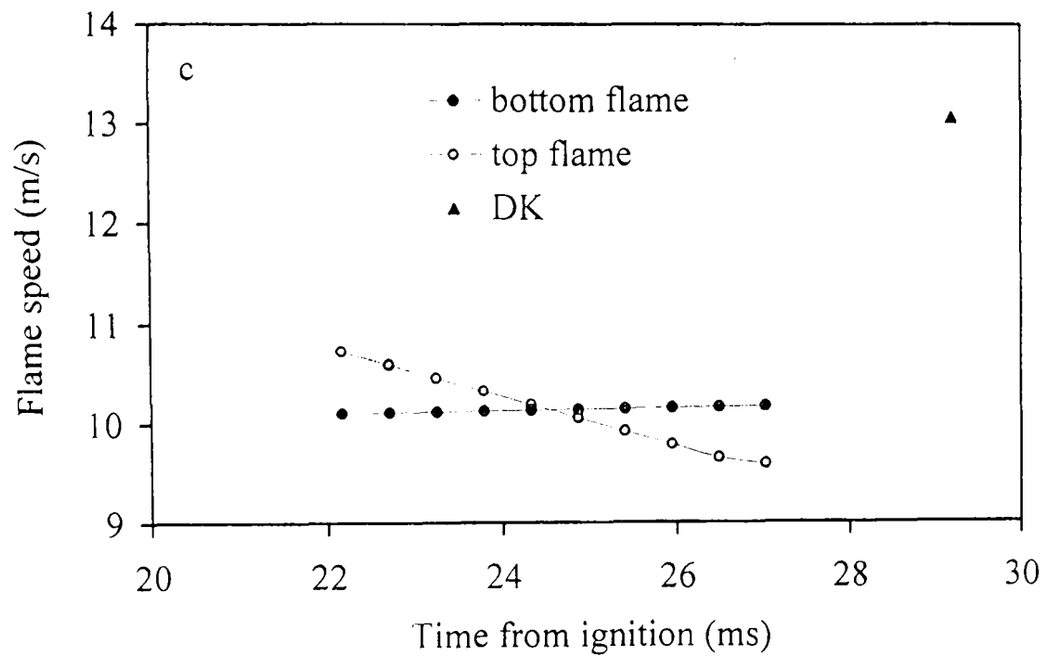

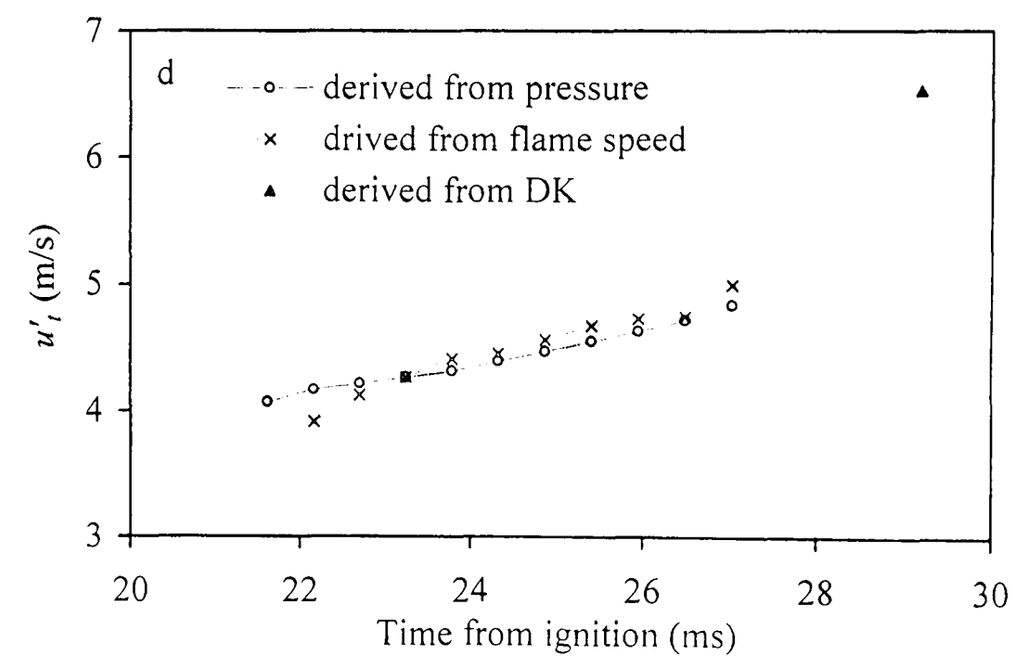

Fig. 7.16. Iso-octane - air implosion, $\phi = 1, p_o = 0.75$ MPa, $T_o = 358$ K, $u' = 1$

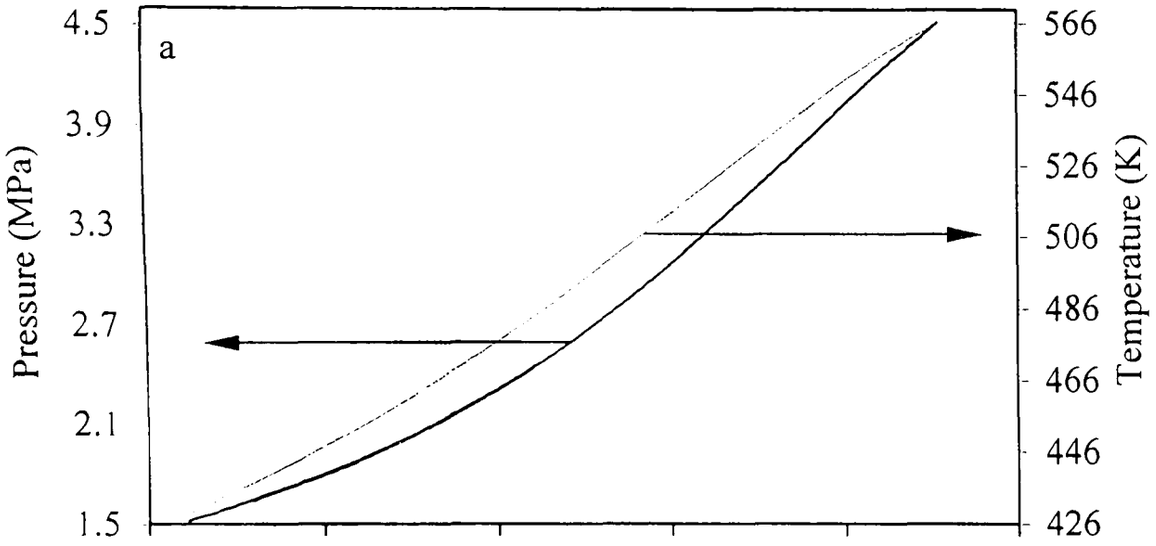

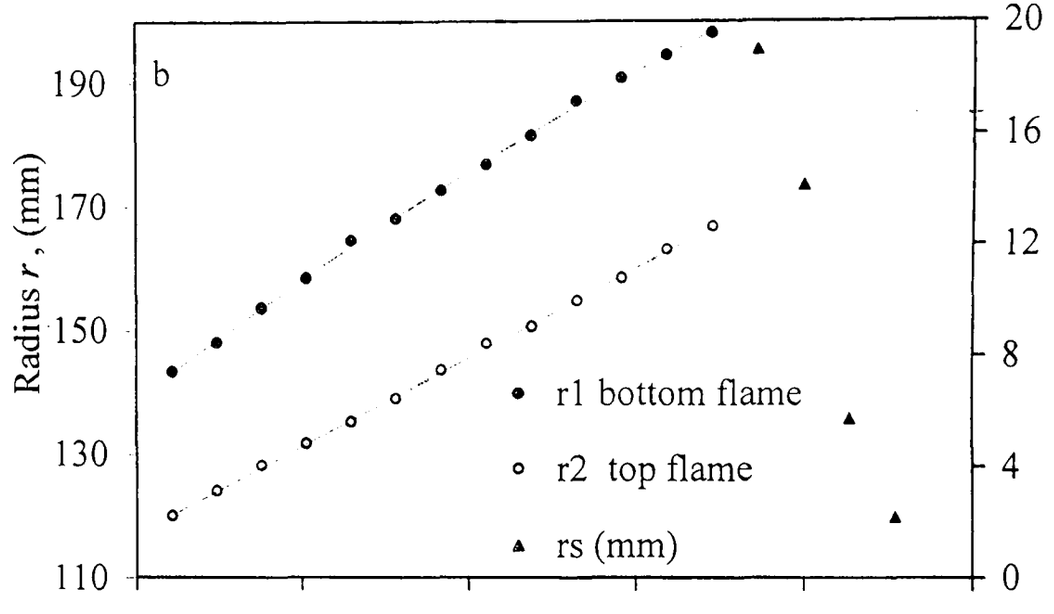

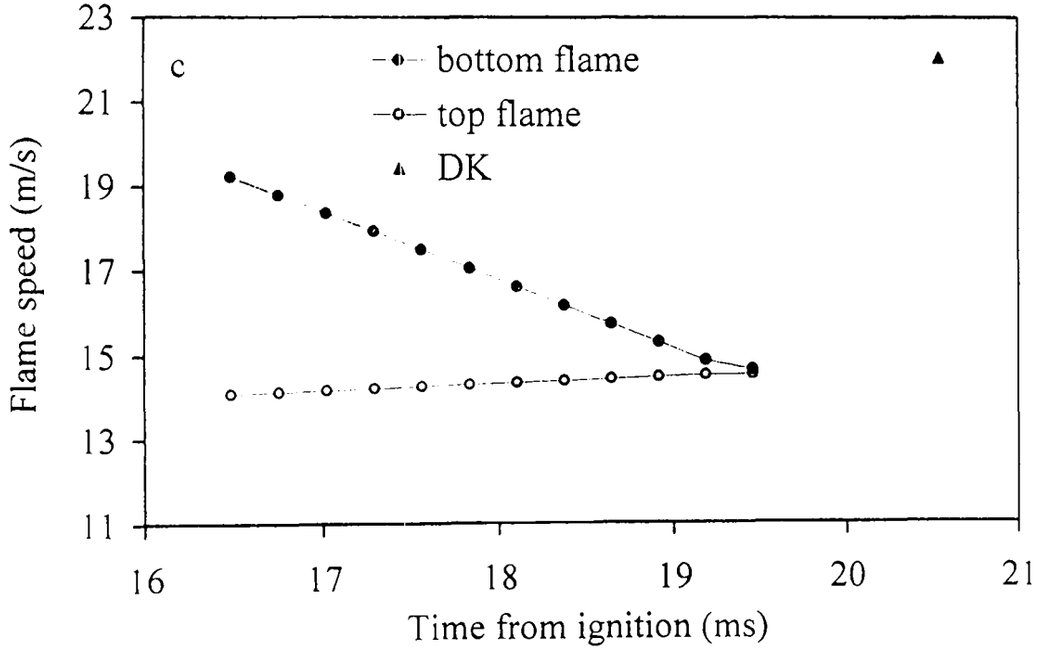

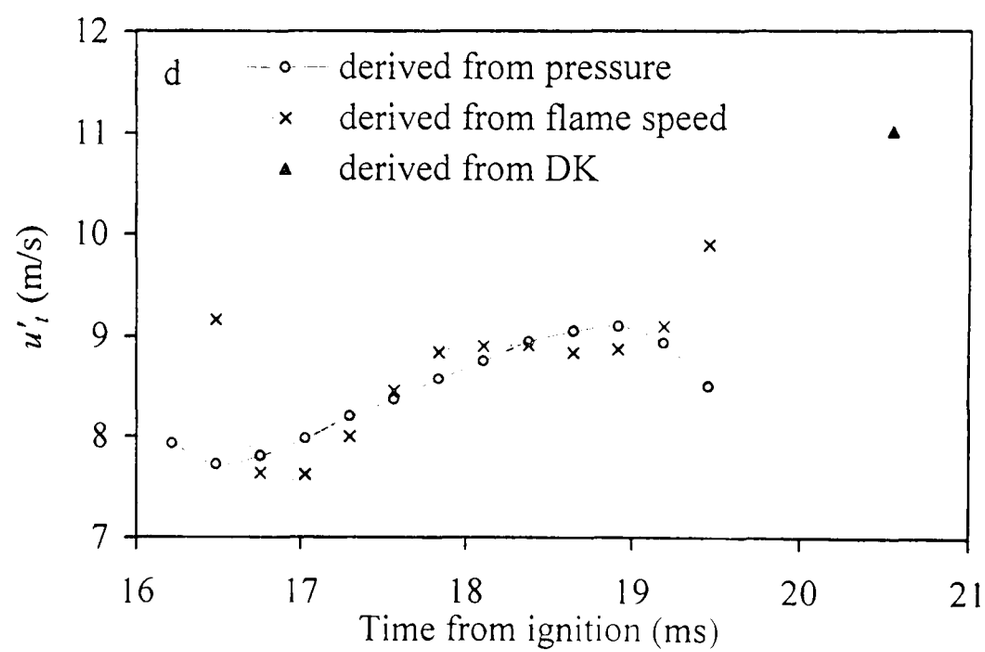

Fig. 7.17. Iso-octane - air implosion, $\phi = 1, p_o = 0.75$ MPa, $T_o = 358$ K, $u' = 2$

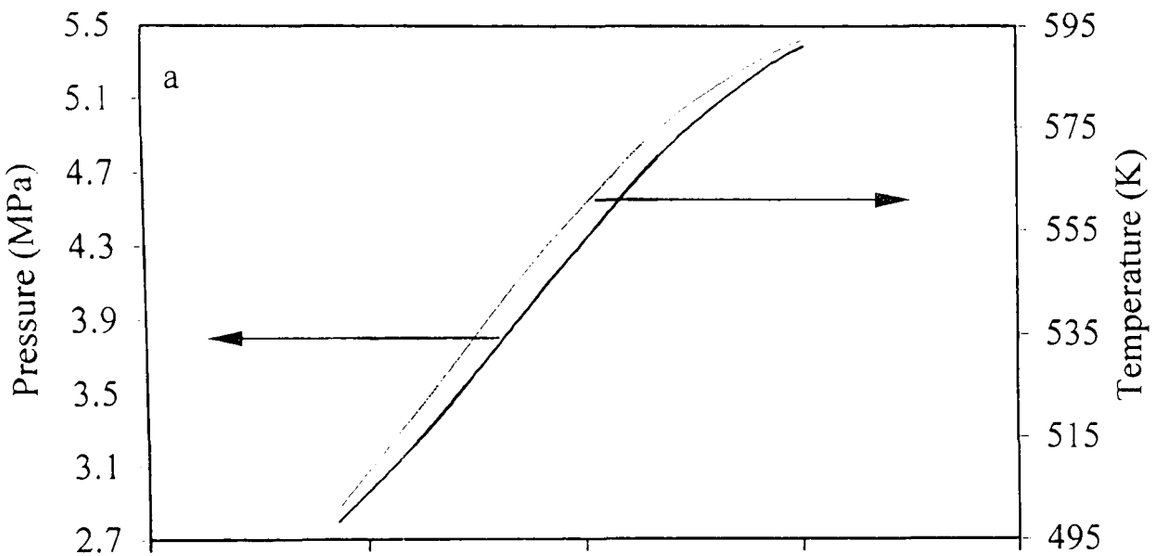

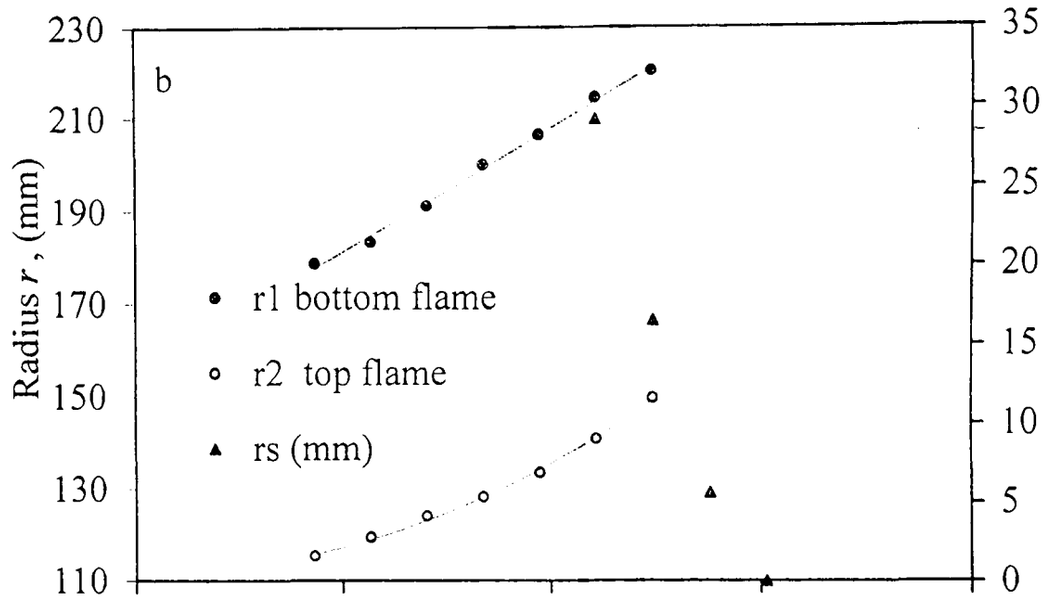

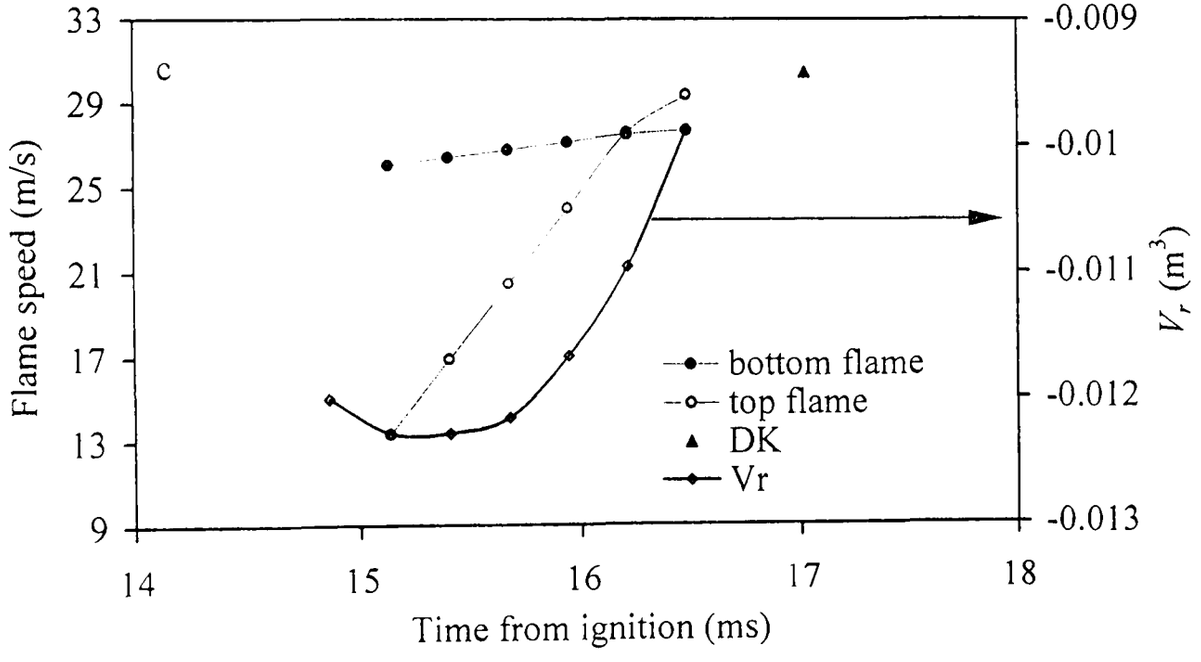

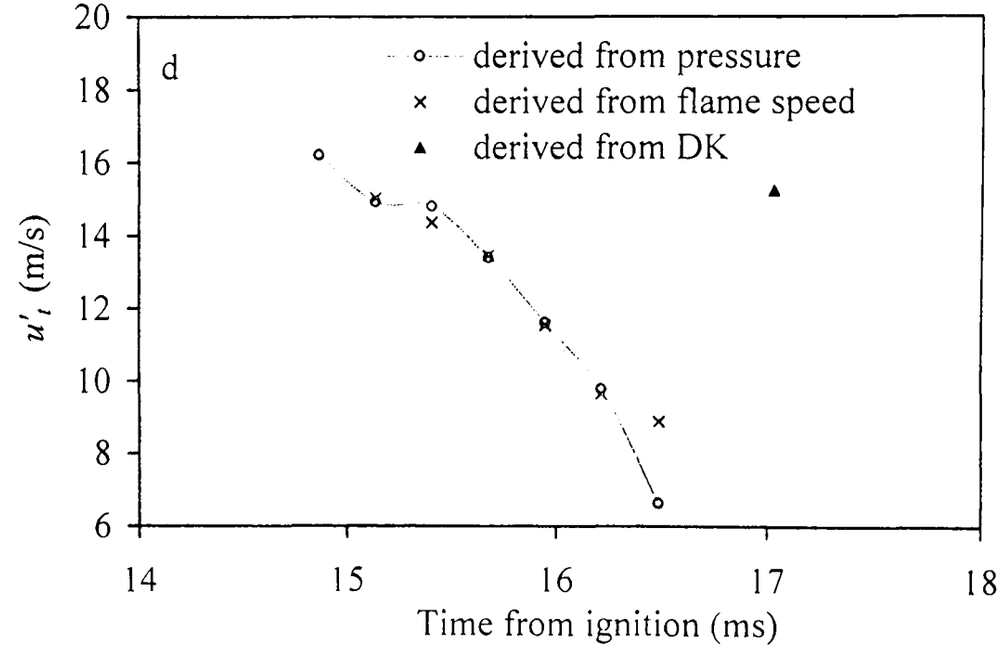

Fig. 7.18. Iso-octane - air implosion, $\phi = 1, p_o = 0.75$ MPa, $T_o = 358$ K, $u' = 3$

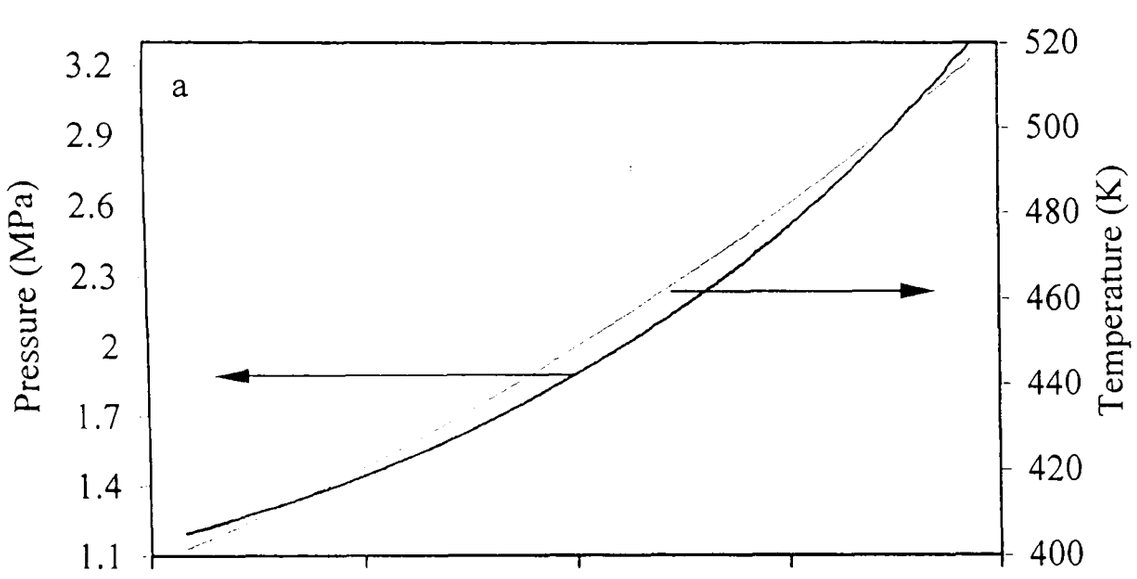

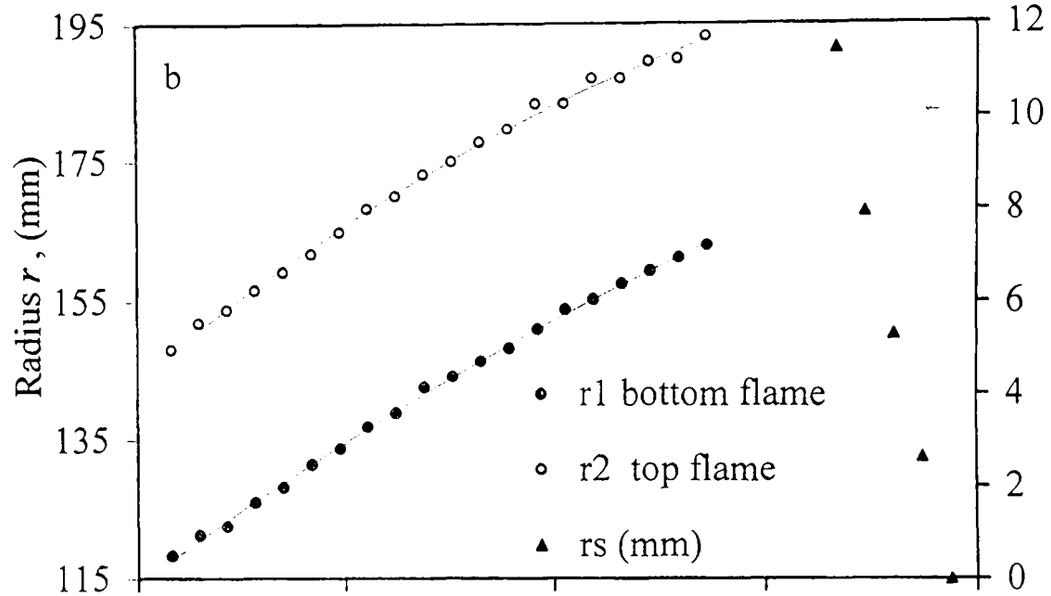

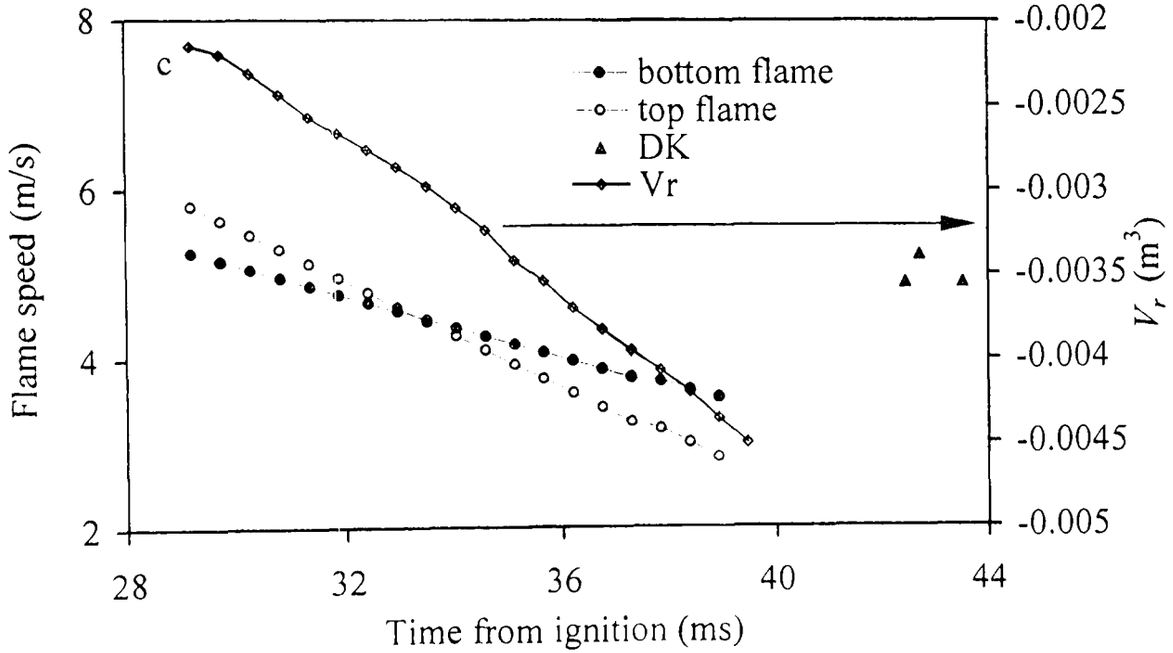

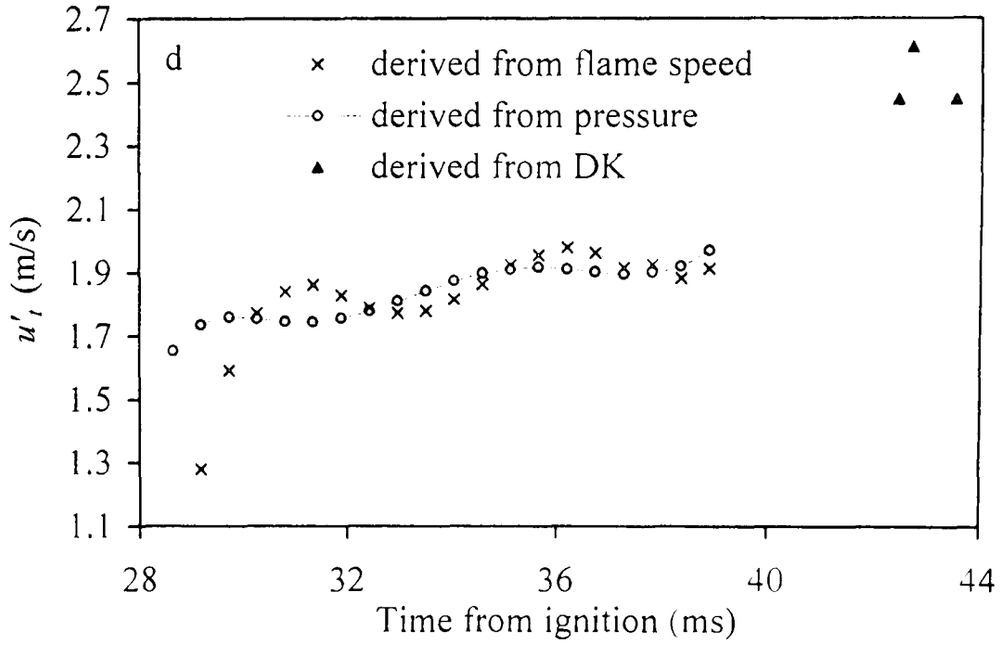

Fig. 7.19. Iso-octane - air implosion, ϕ = 1.4, p_o = 0.75 MPa, T_o = 358 K, u' = 0.25

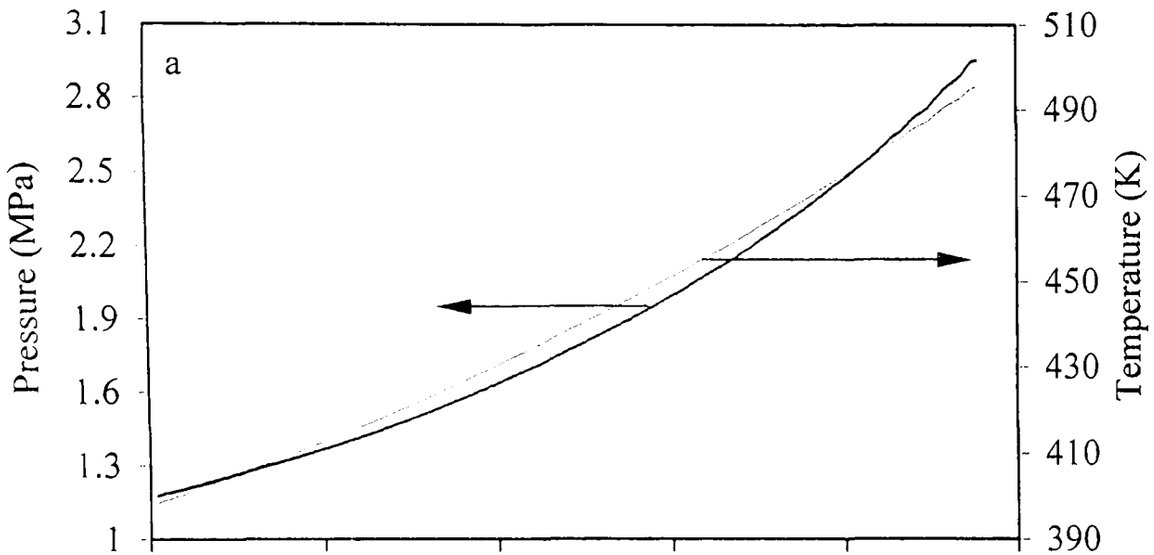

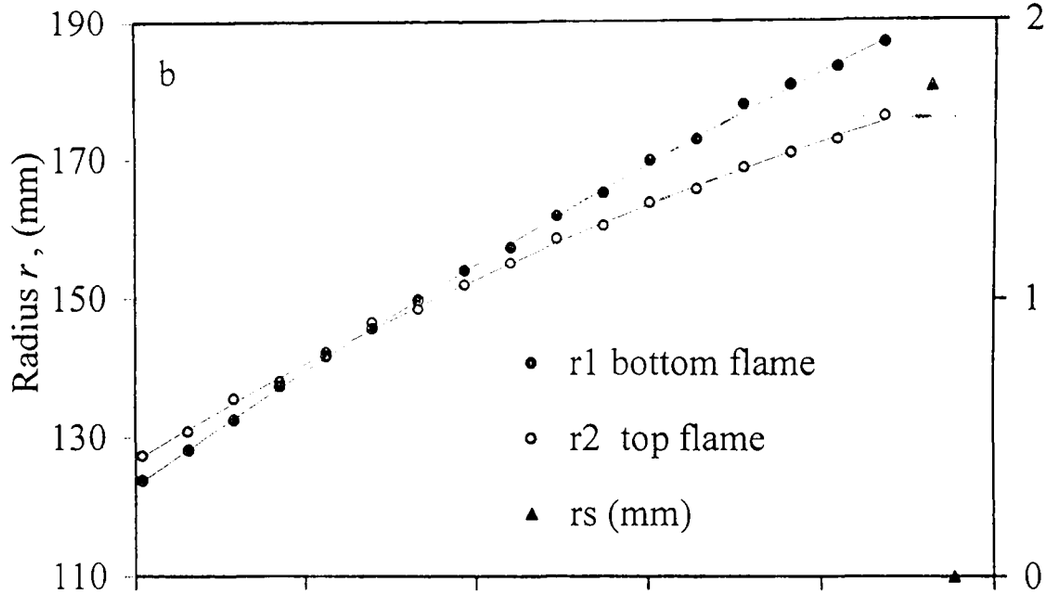

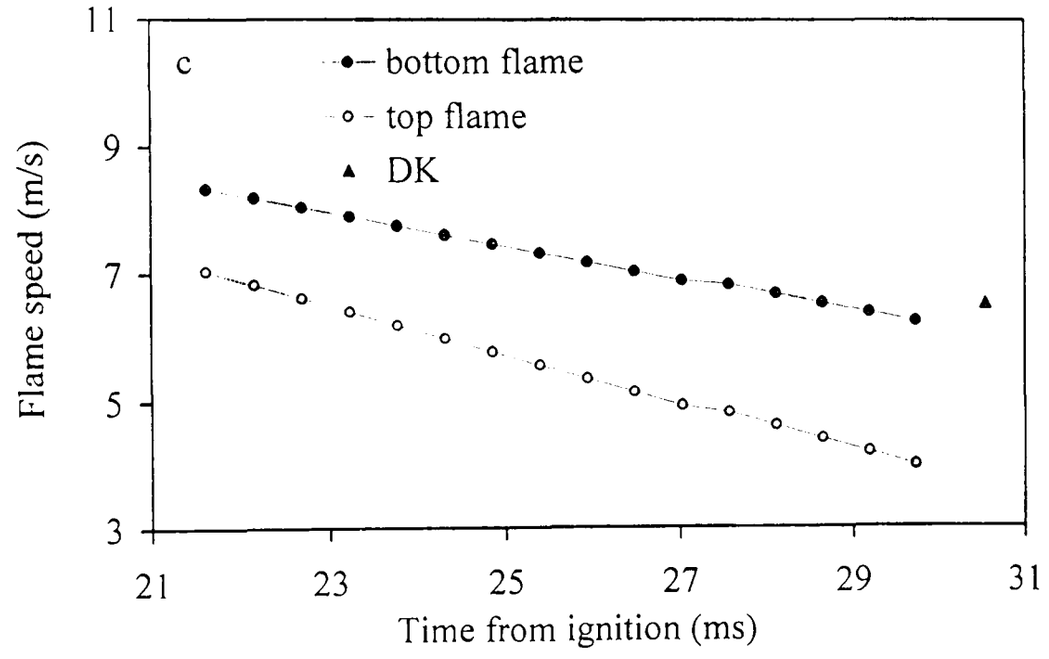

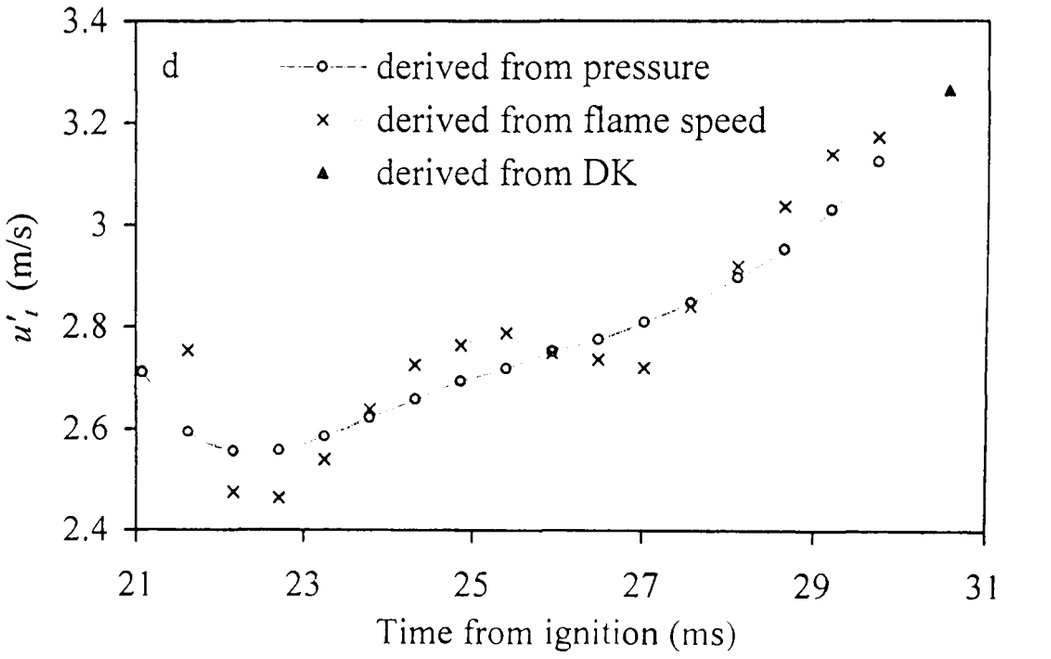

Fig. 7.20. Iso-octane - air implosion, ϕ = 1.4, p_o = 0.75 MPa, T_o = 358 K, u' = 0.5

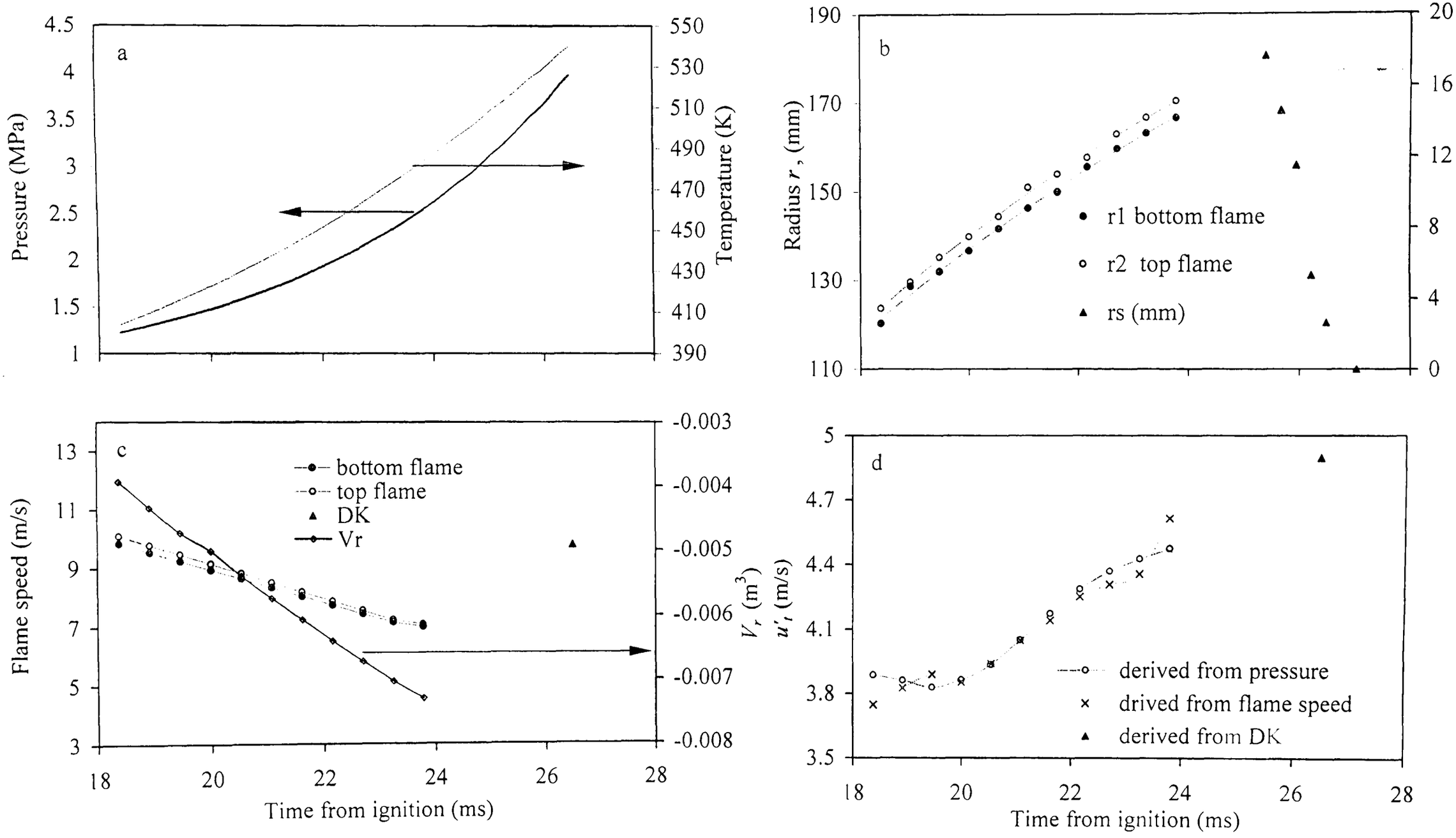

Fig. 7.21. Iso-octane - air implosion, $\phi = 1.4$, $p_o = 0.75$ MPa, $T_o = 358$ K, $u' = 0.75$

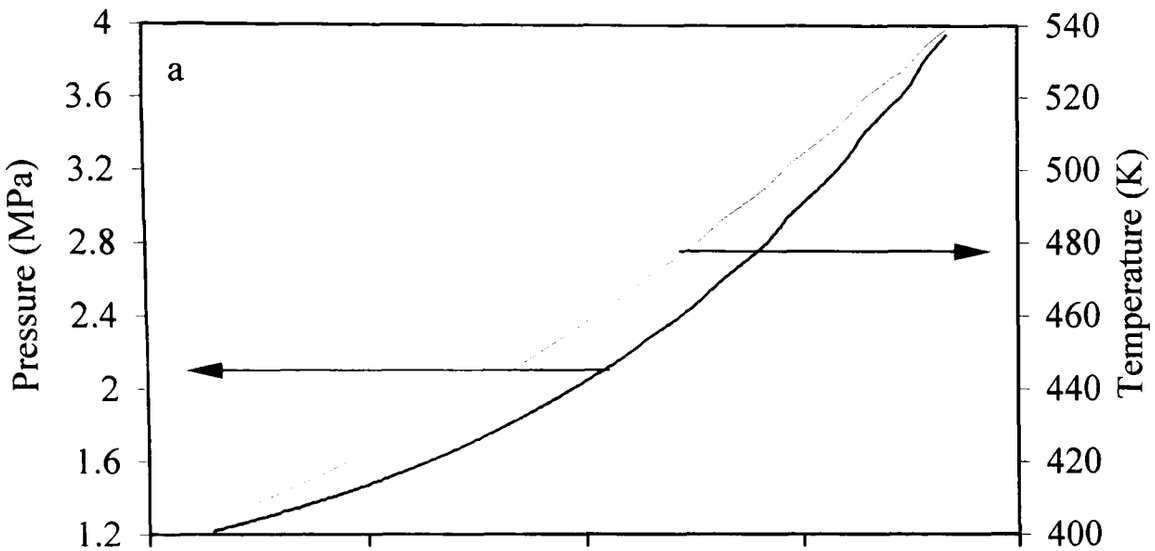

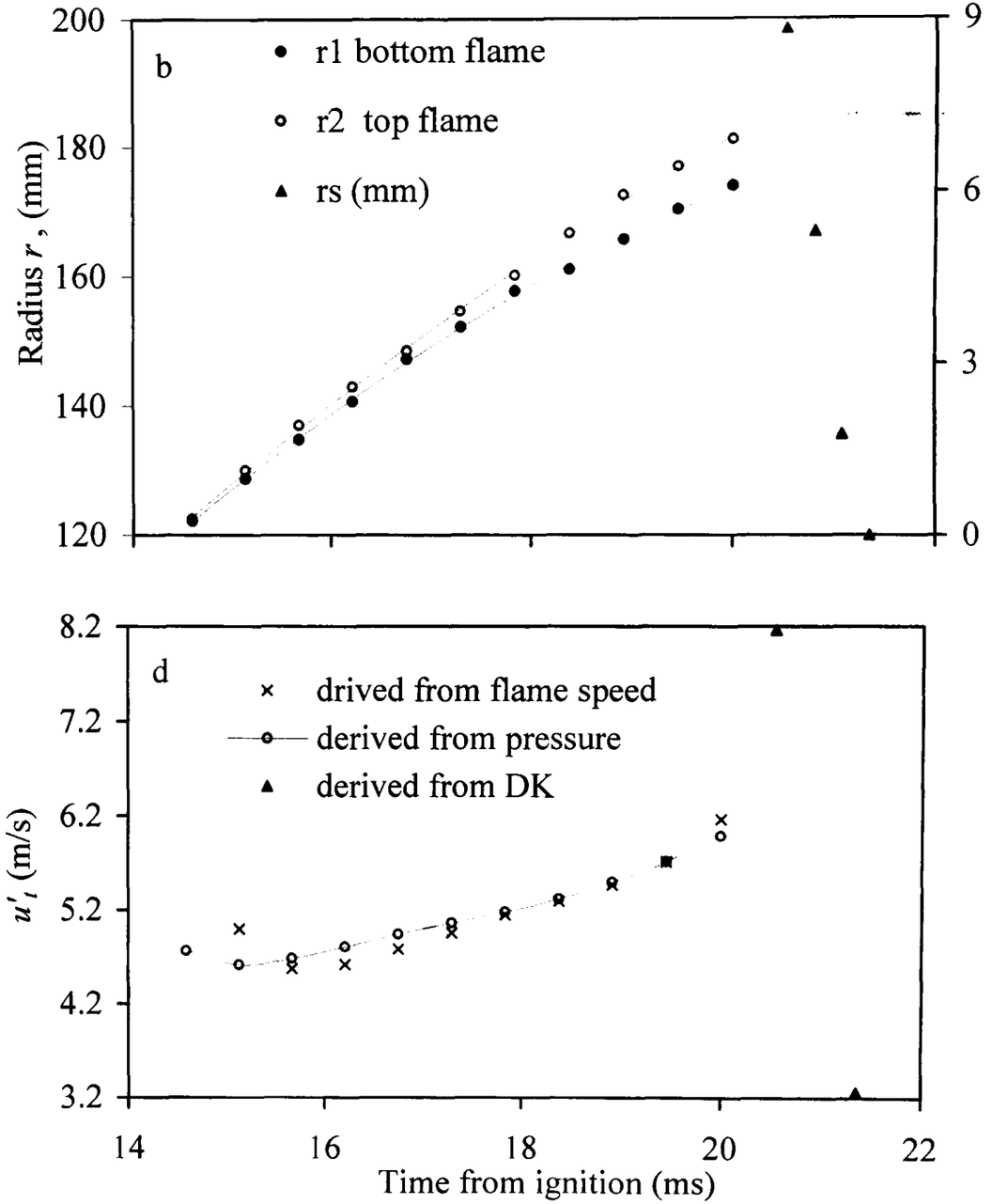

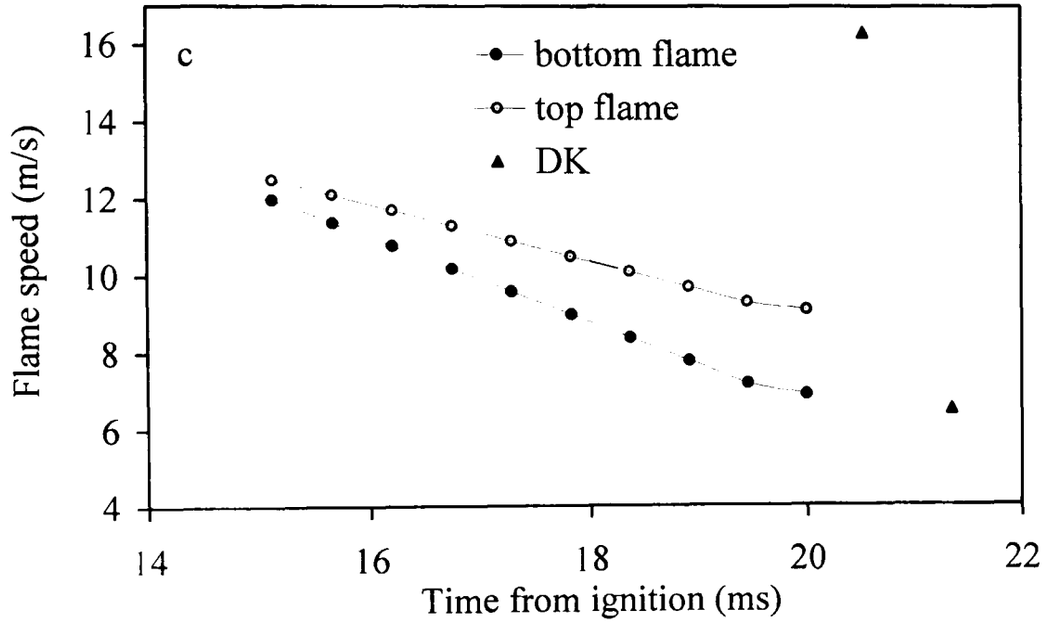

Fig. 7.22. Iso-octane - air implosion, $\phi = 1.4, p_o = 0.75$ MPa, $T_o = 358$ K, $u' = 1$

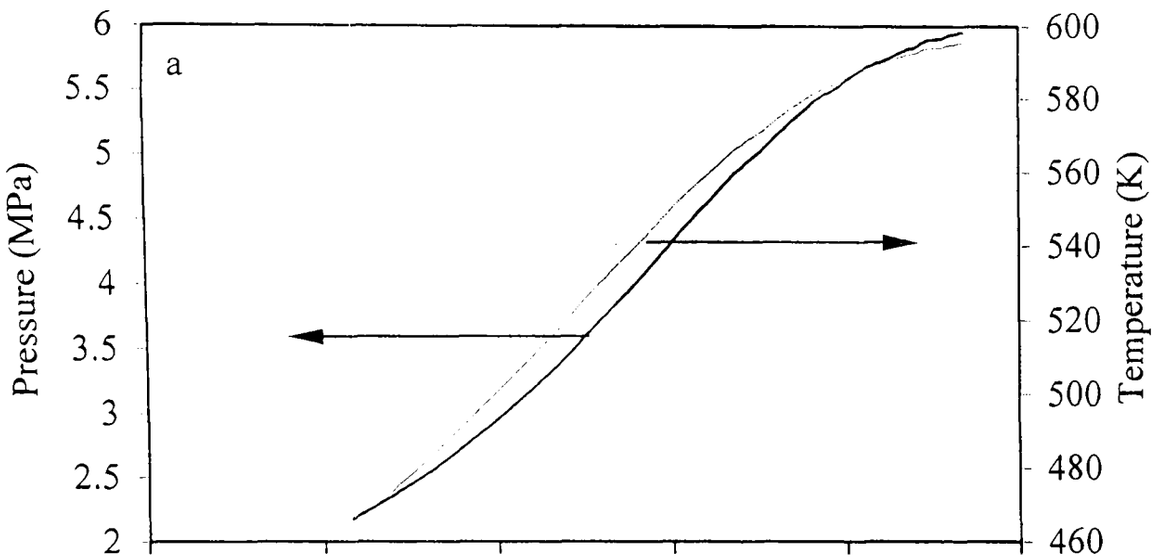

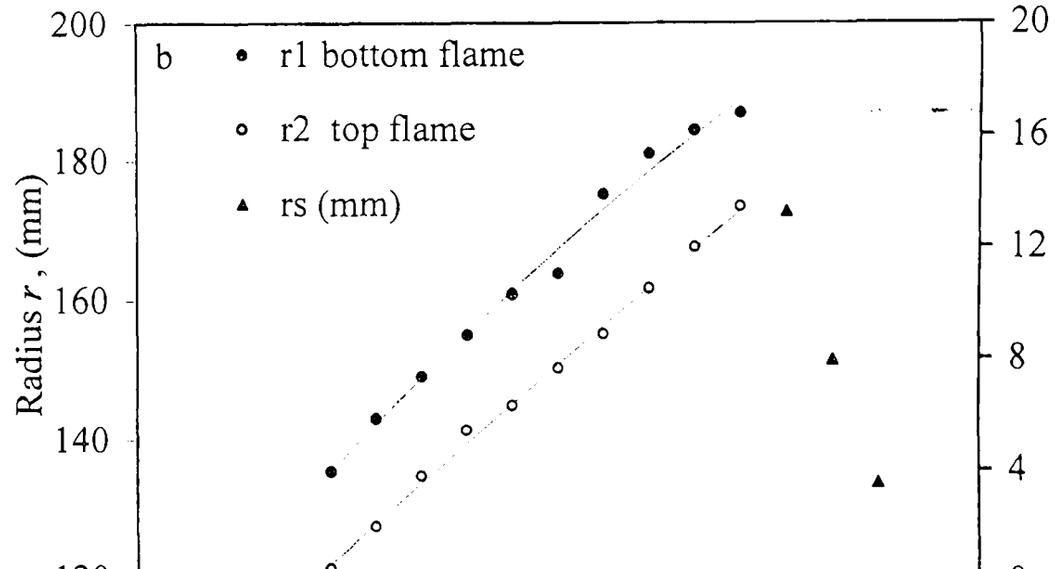

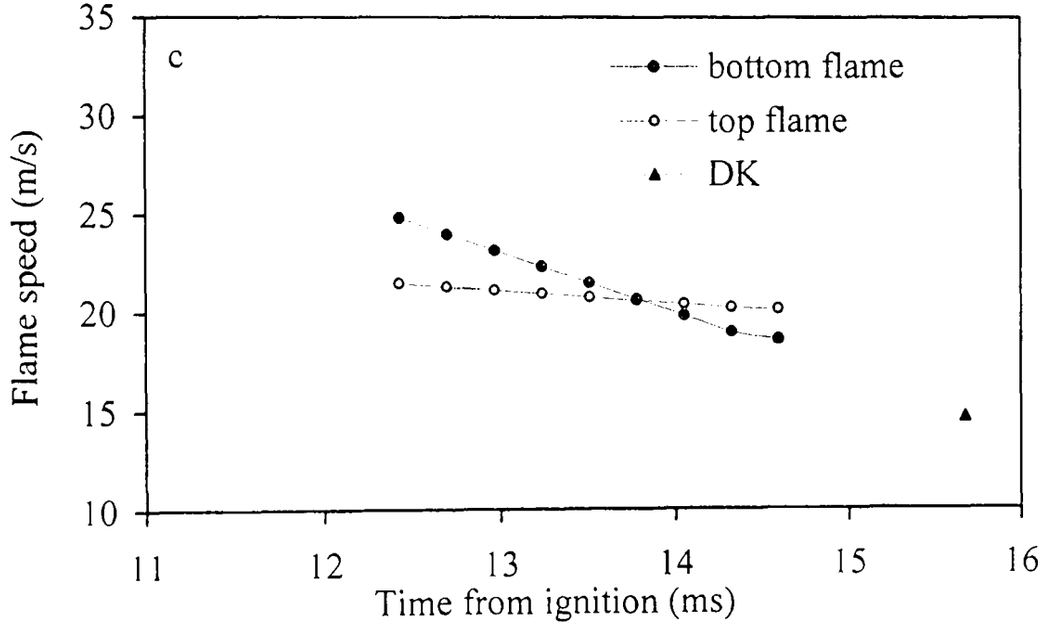

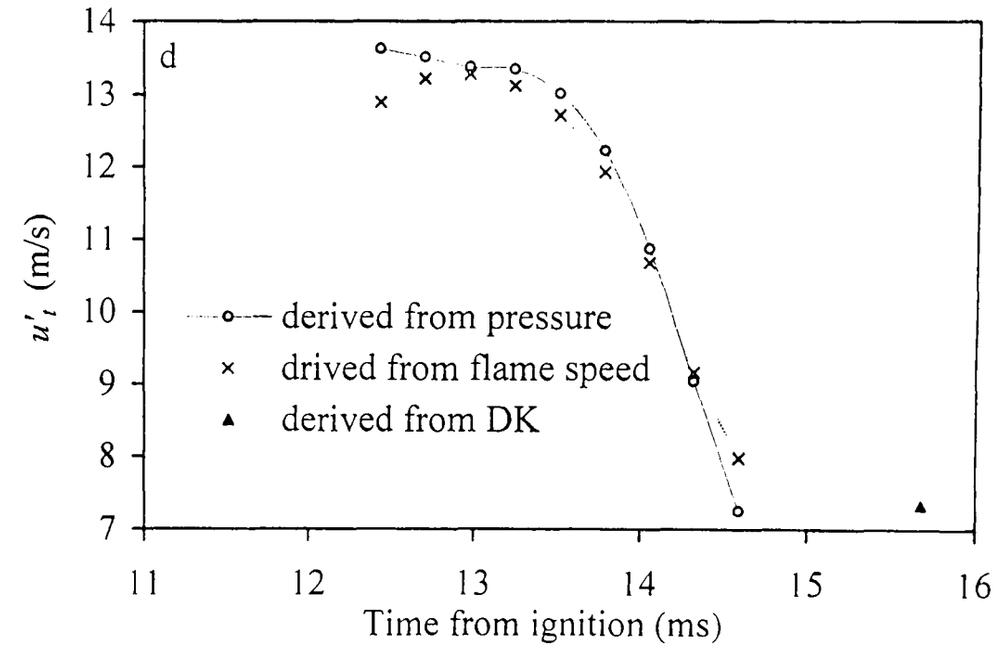

Fig. 7.23. Iso-octane - air implosion, ϕ = 1.4, p_o = 0.75 MPa, T_o = 358 K, u' = 2

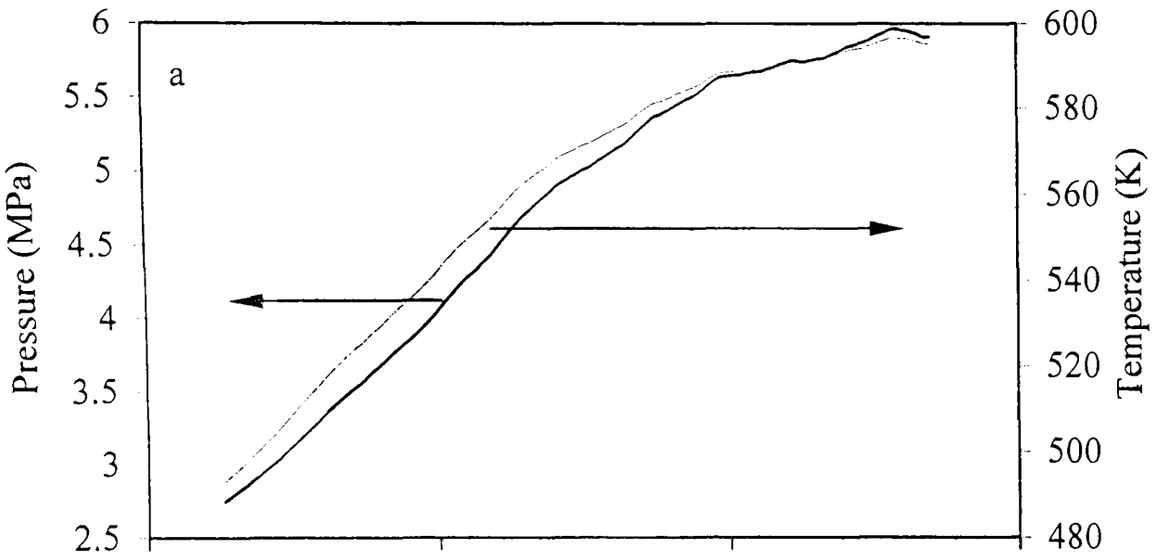

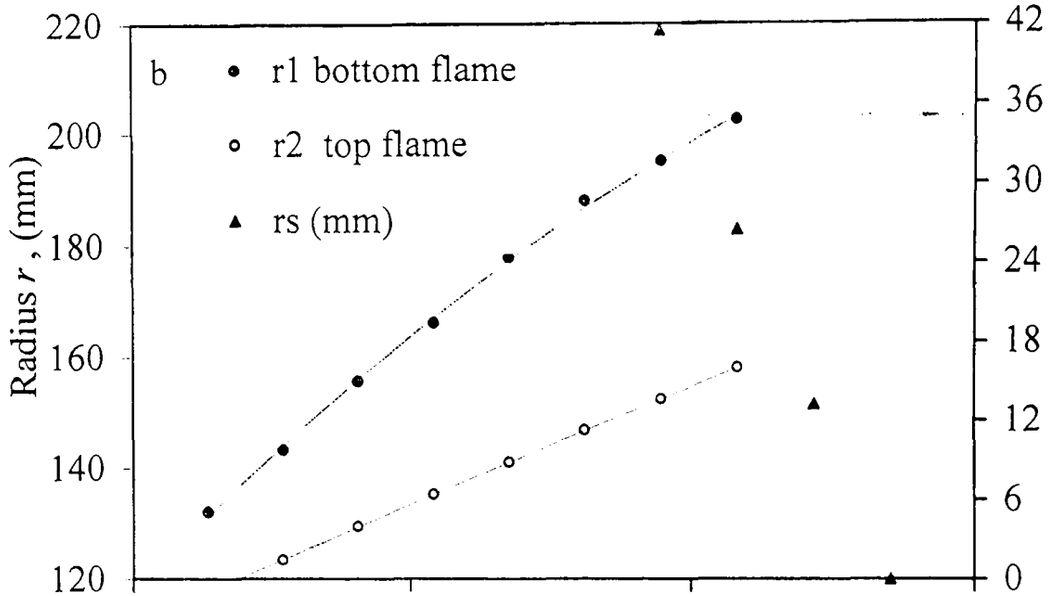

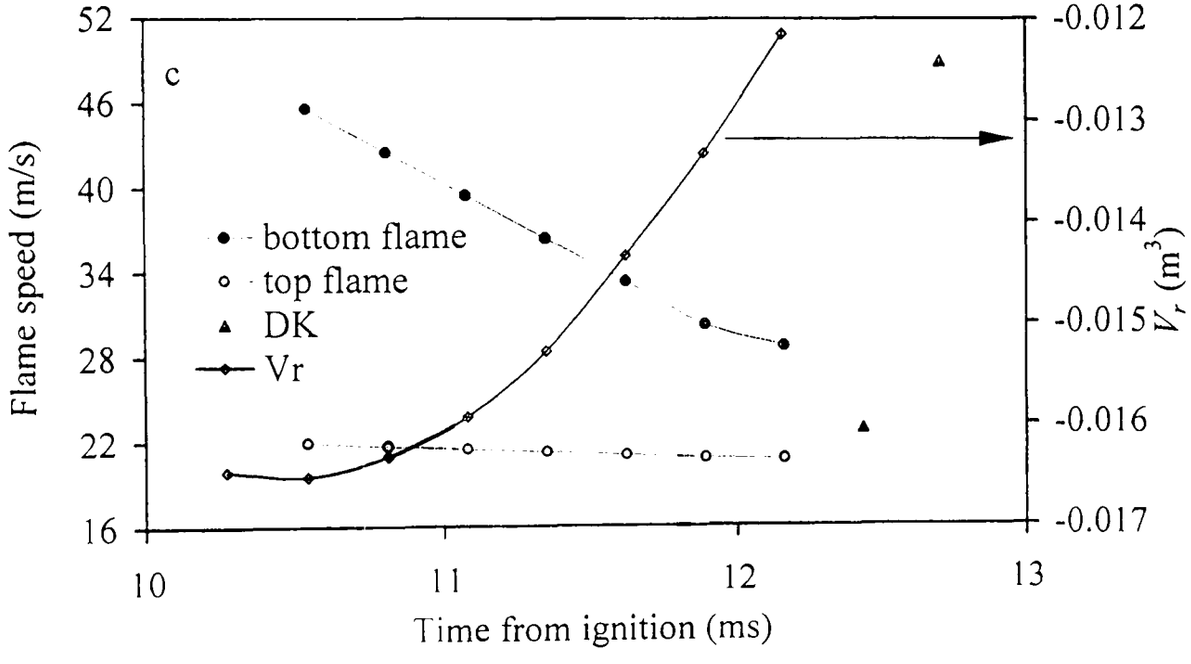

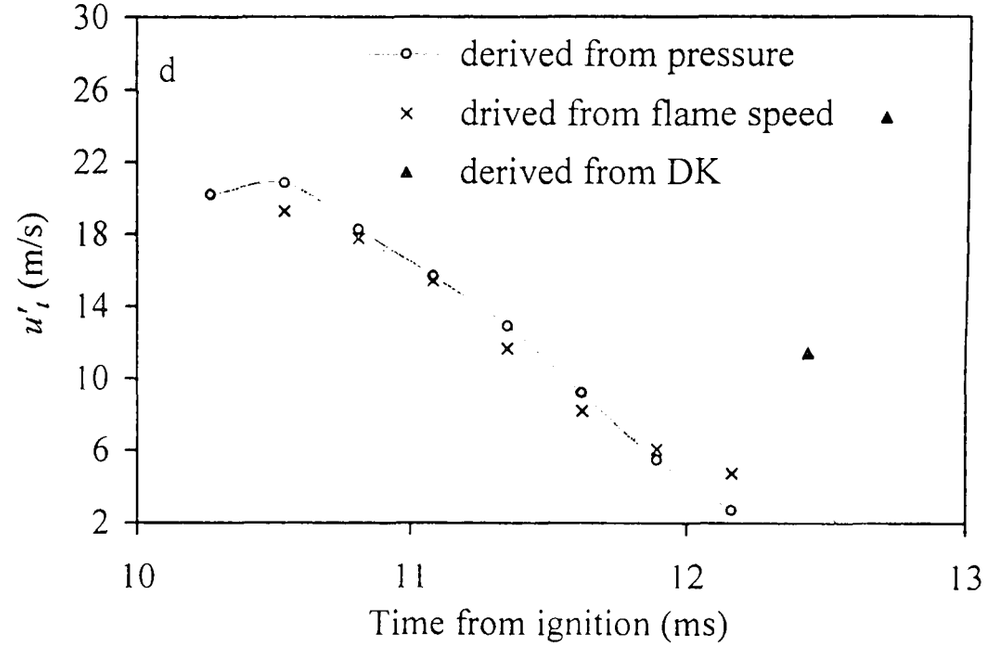

Fig. 7.24. Iso-octane - air implosion, ϕ = 1.4, p_o = 0.75 MPa, T_o = 358 K, u' = 3

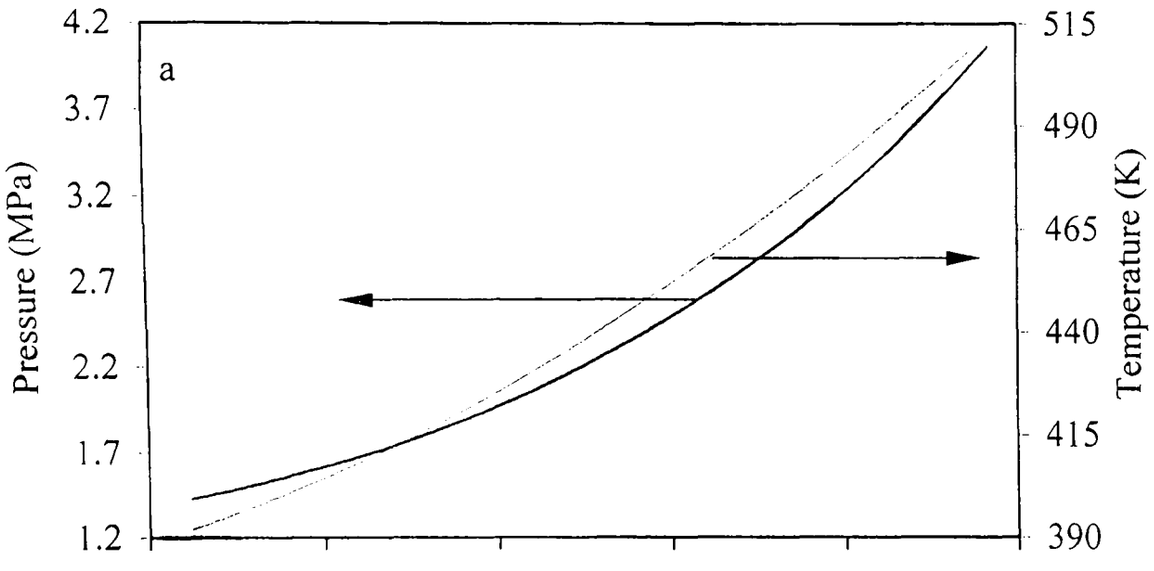

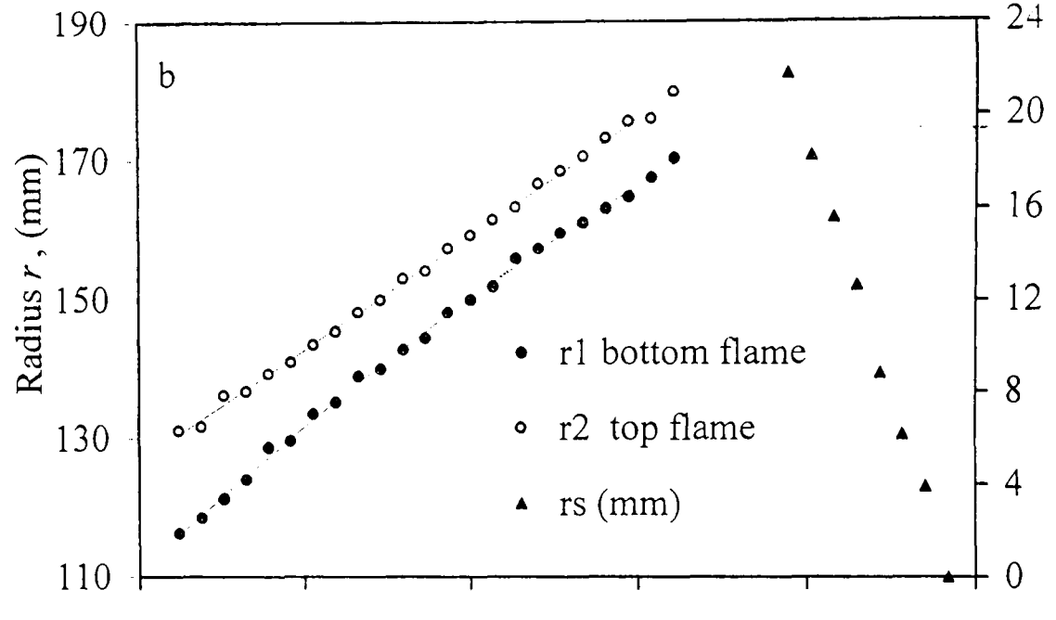

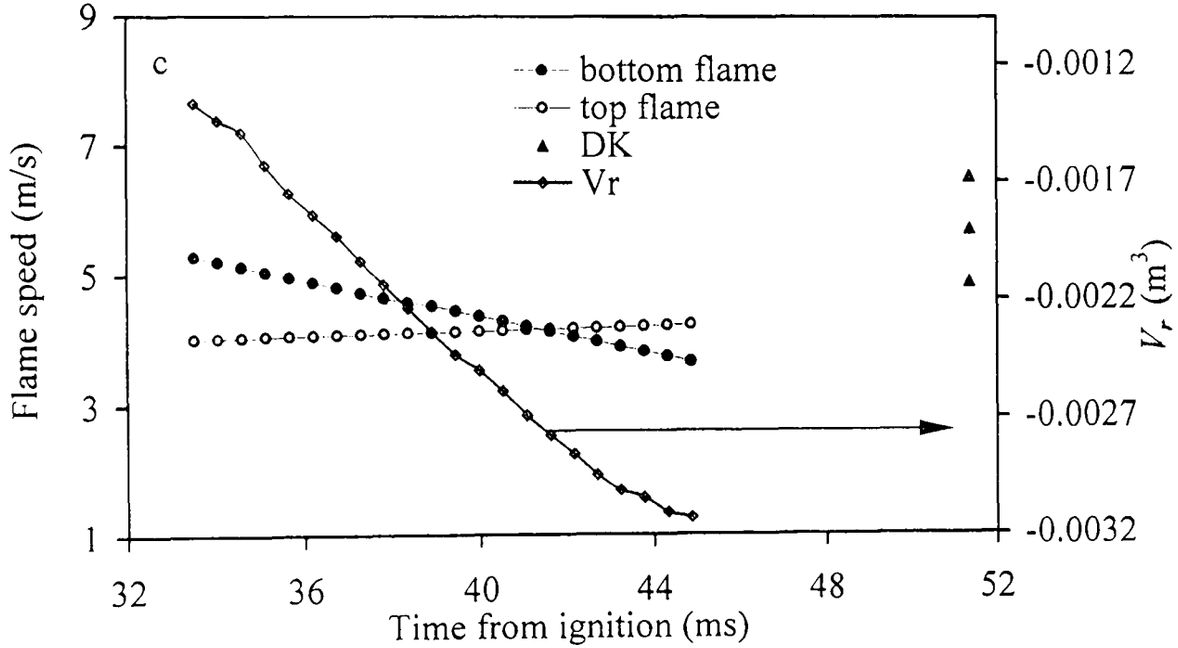

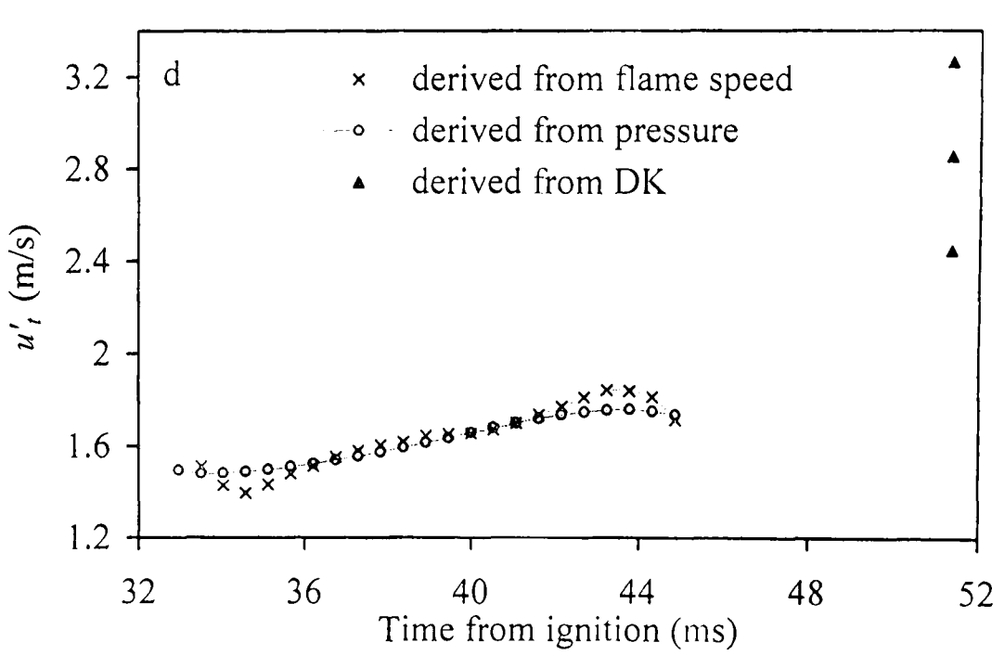

Fig. 7.25. Iso-octane - air implosion, $\phi = 1, p_o = 1$ MPa, $T_o = 358$ K, $u' = 0.25$

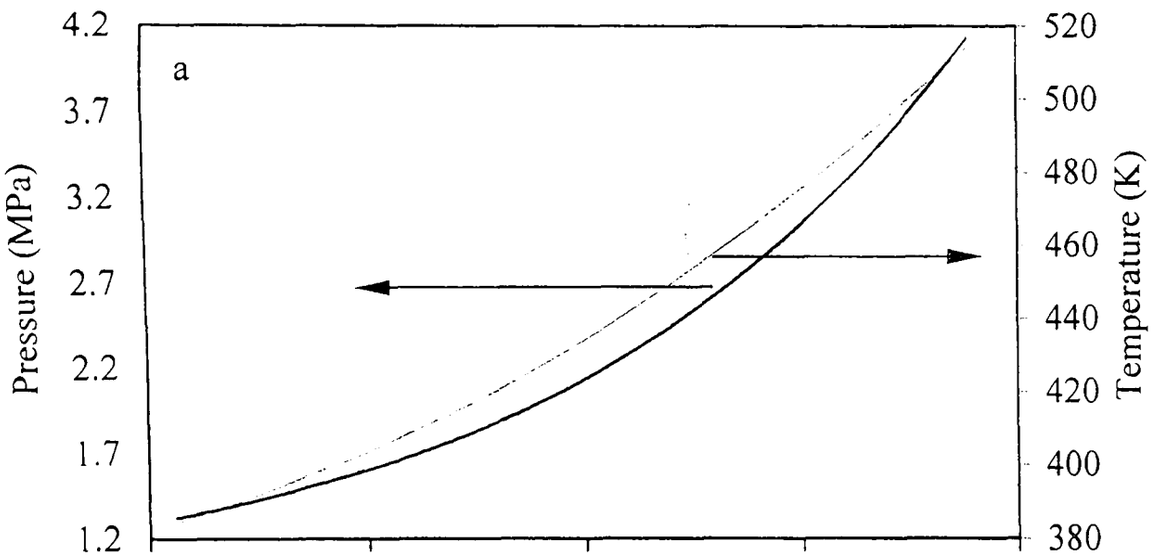

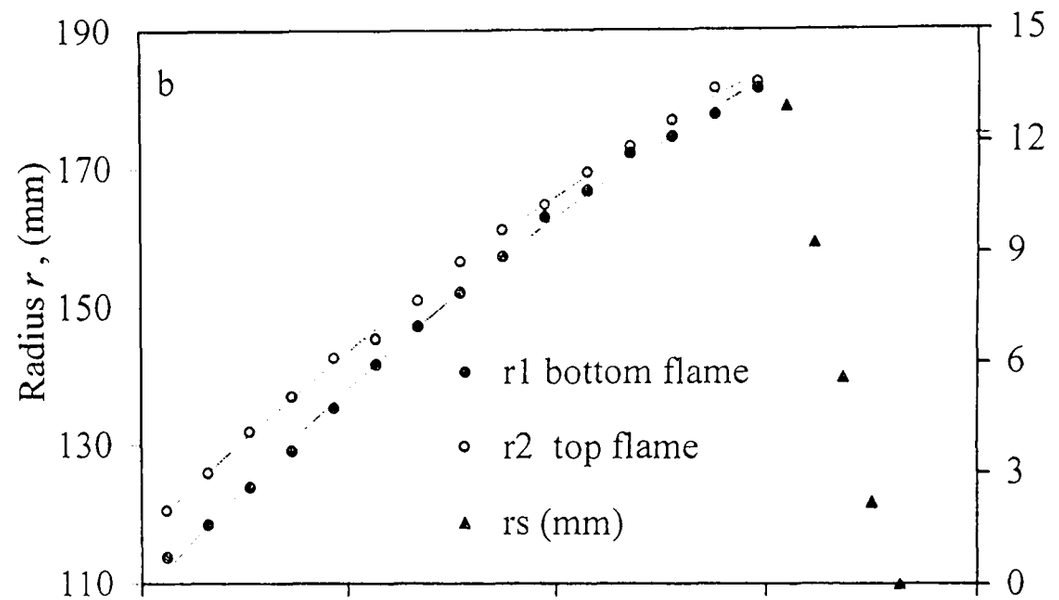

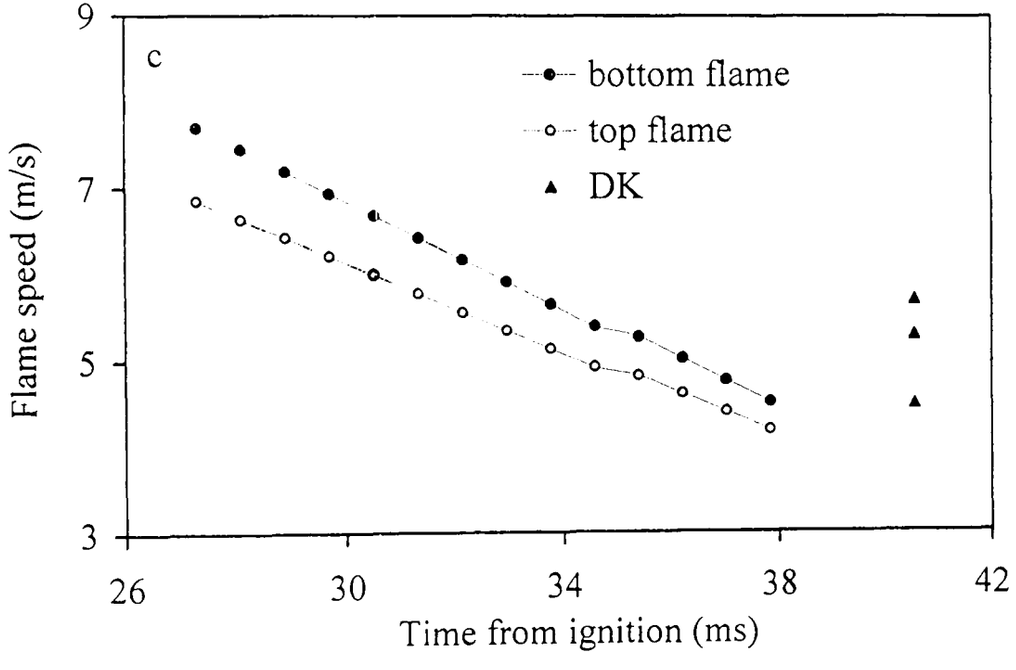

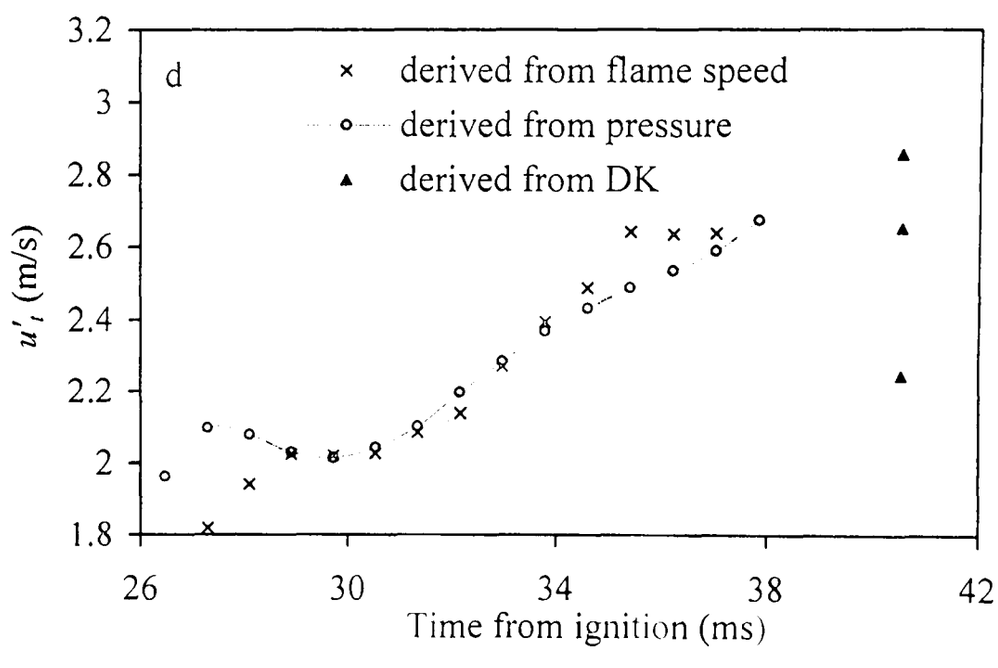

Fig. 7.26. Iso-octane - air implosion, $\phi = 1, p_o = 1$ MPa, $T_o = 358$ K, $u' = 0.5$

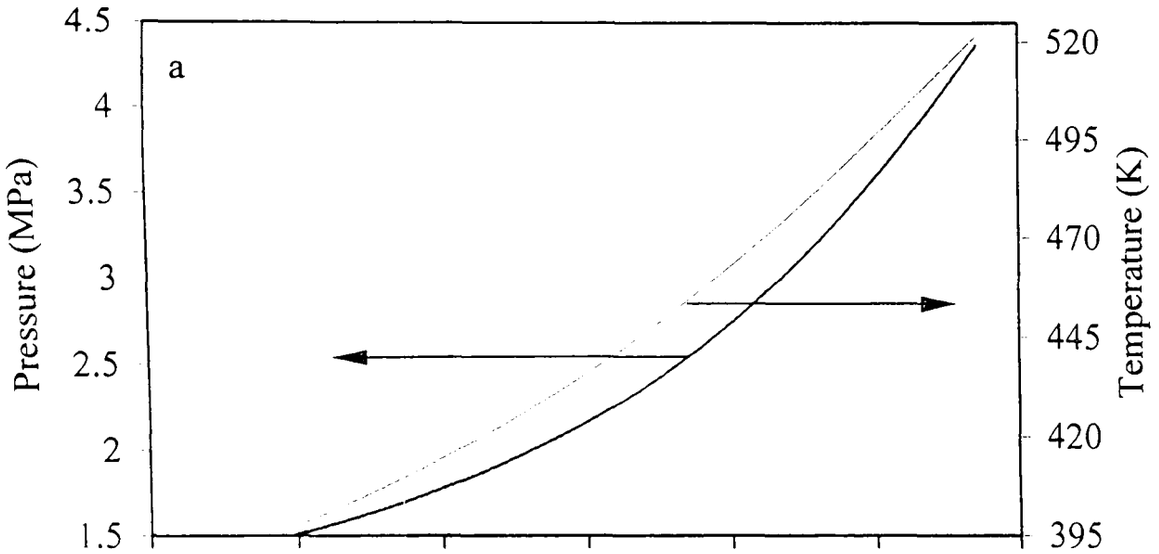

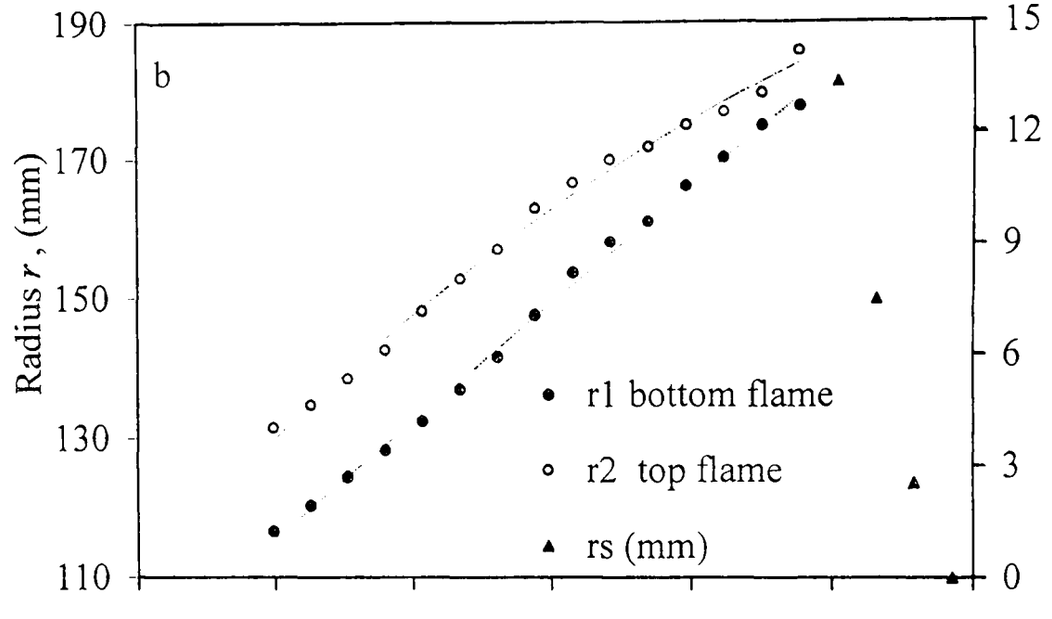

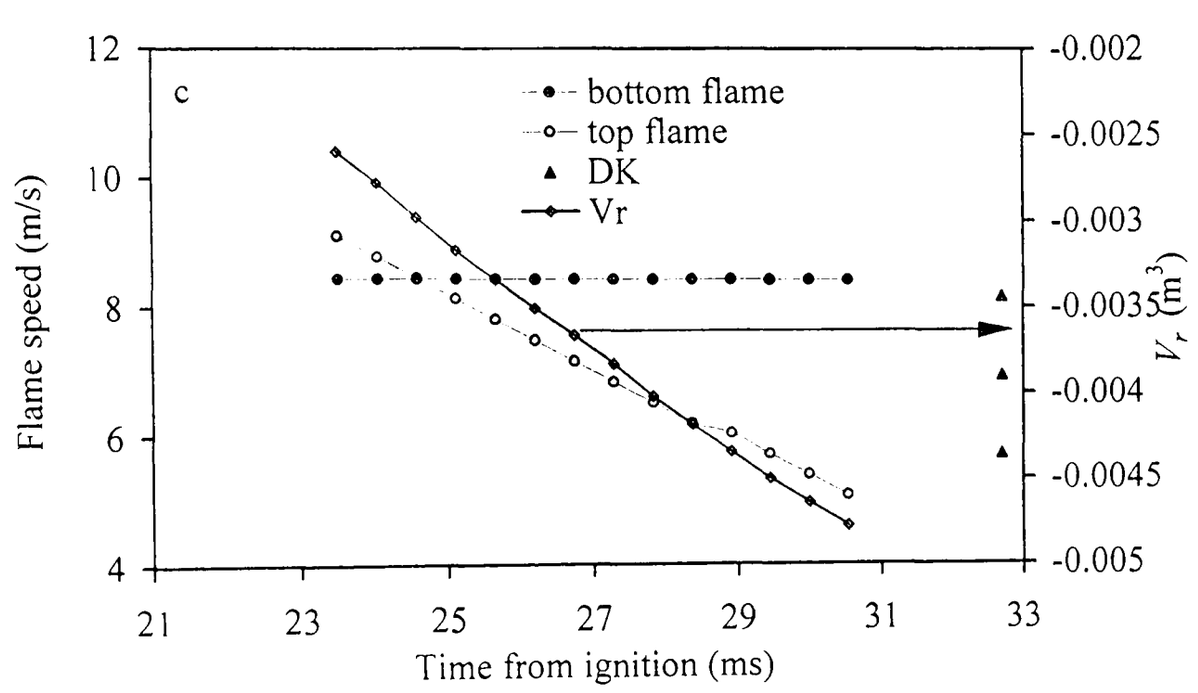

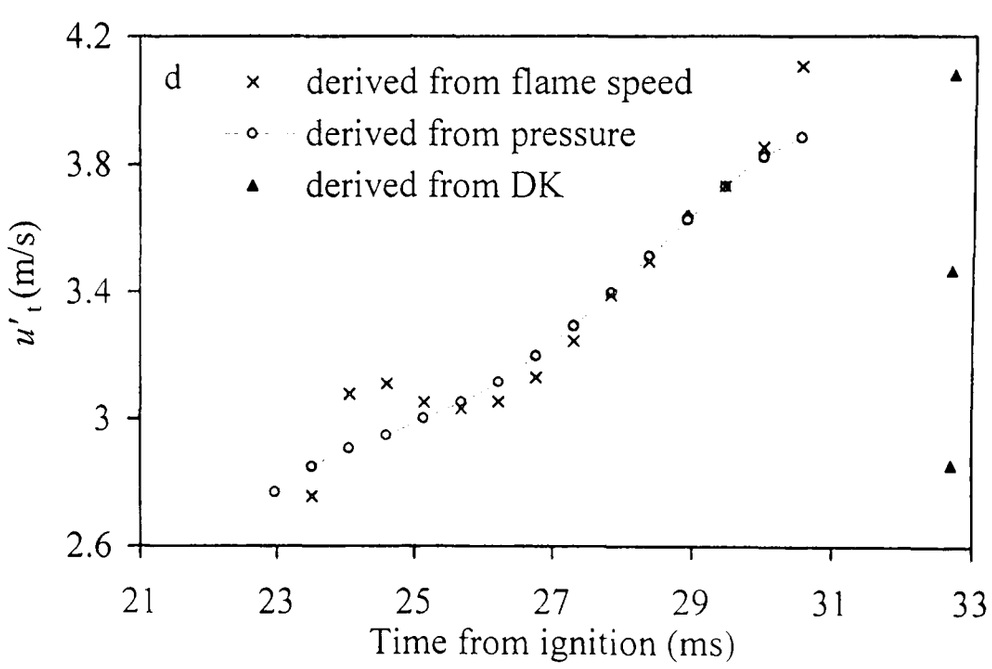

Fig. 7.27. Iso-octane - air implosion, $\phi = 1, p_o = 1$ MPa, $T_o = 358$ K, $u' = 0.75$

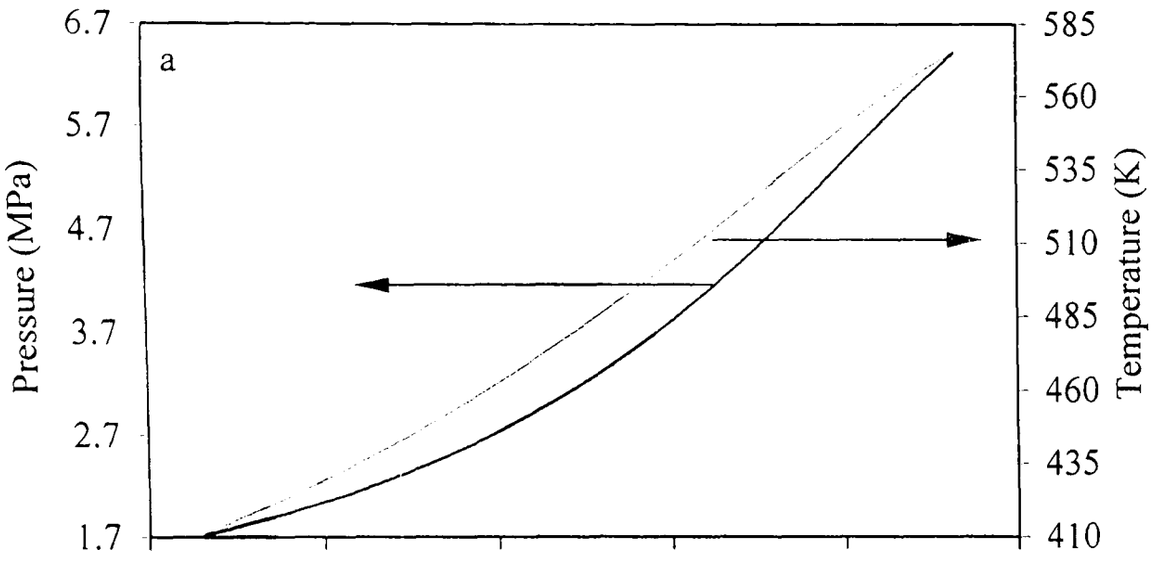

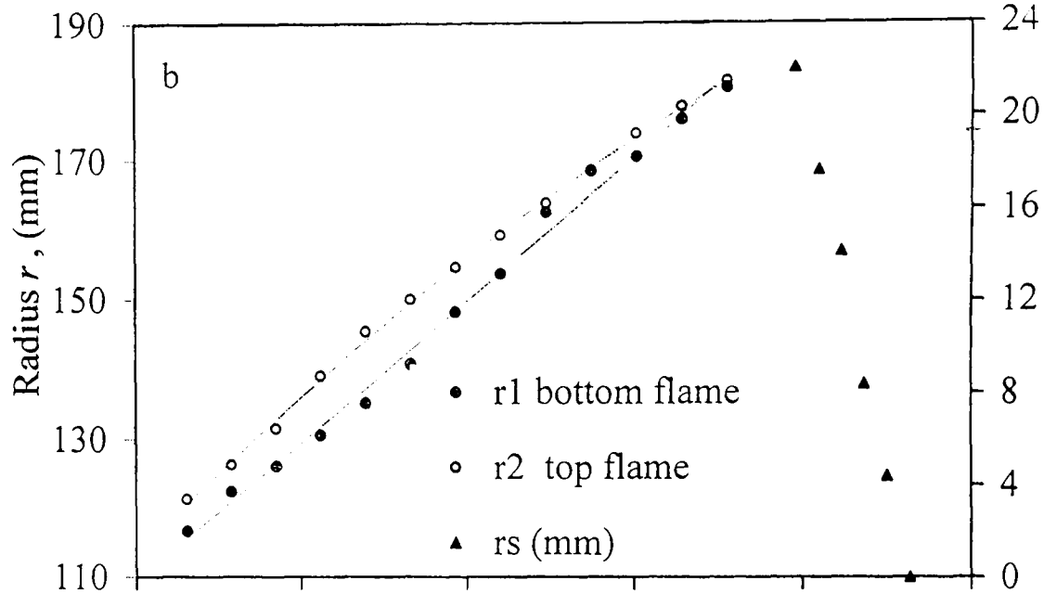

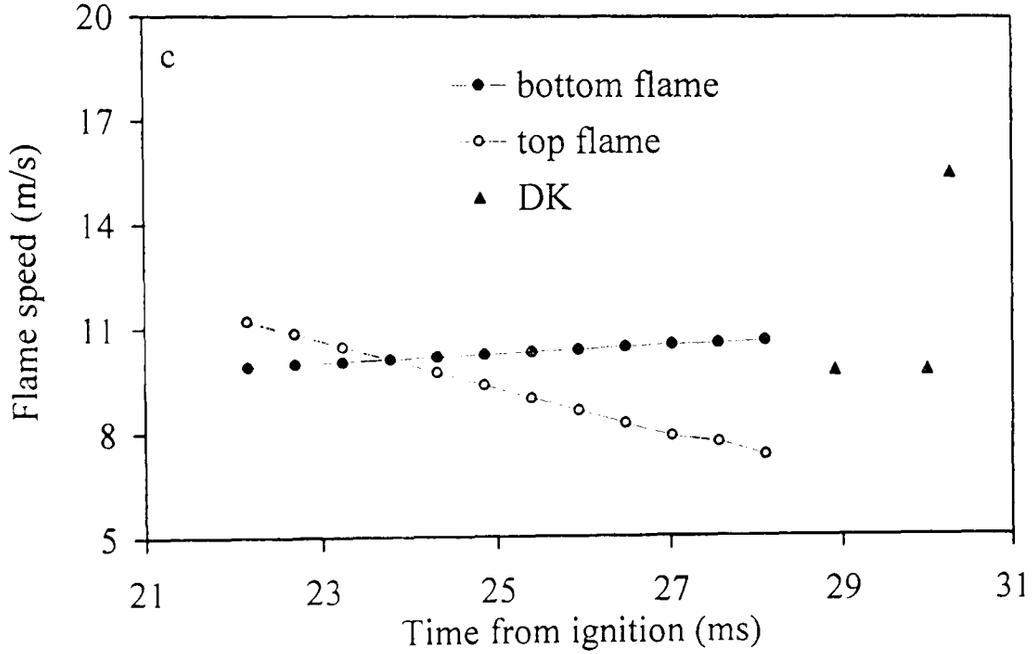

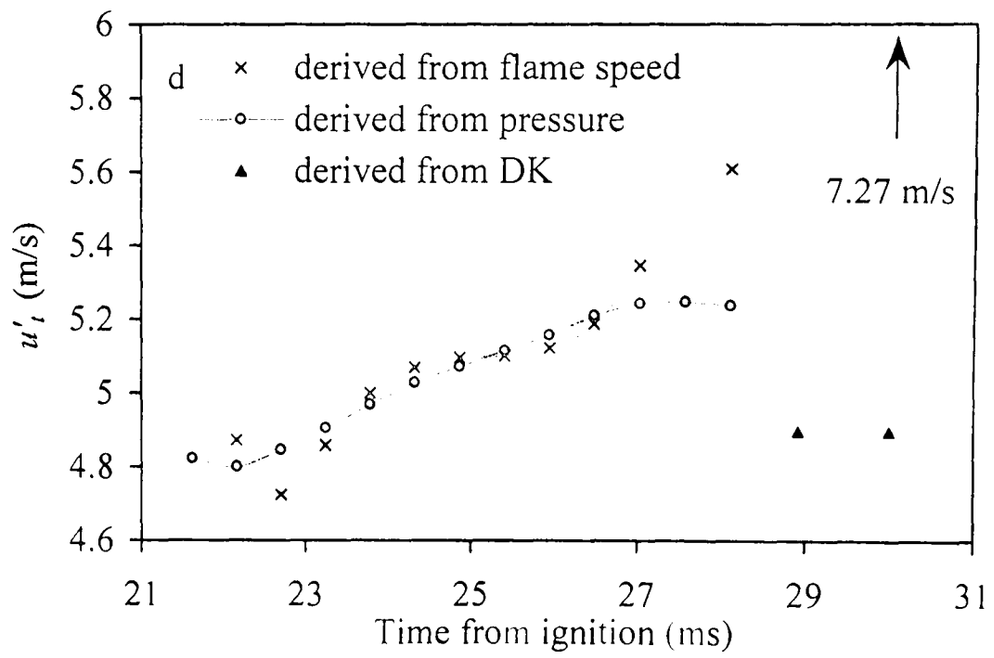

Fig. 7.28. Iso-octane - air implosion, $\phi = 1, p_o = 1$ MPa, $T_o = 358$ K, $u' = 1$

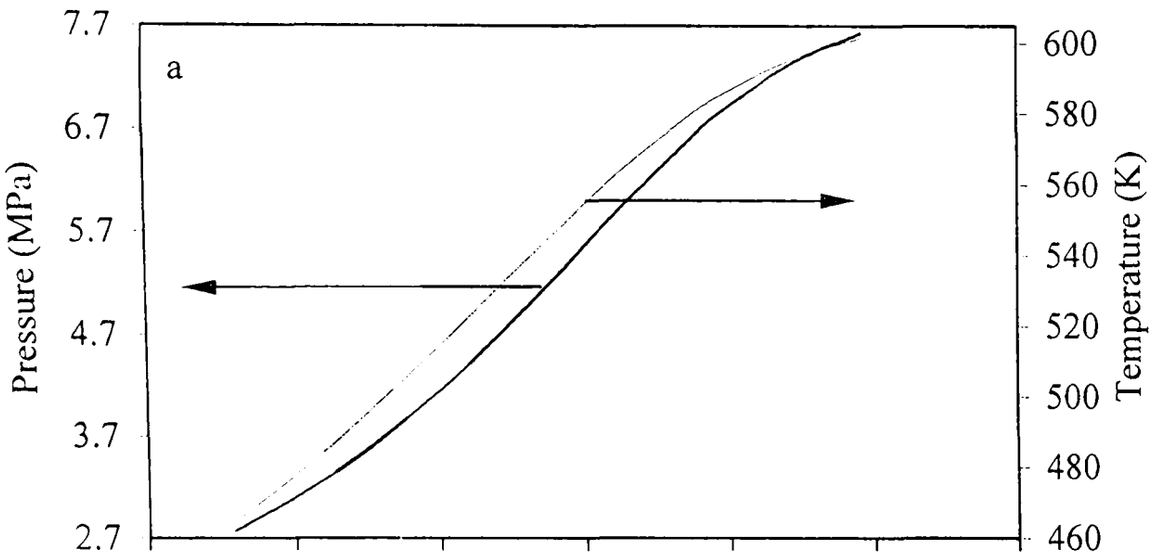

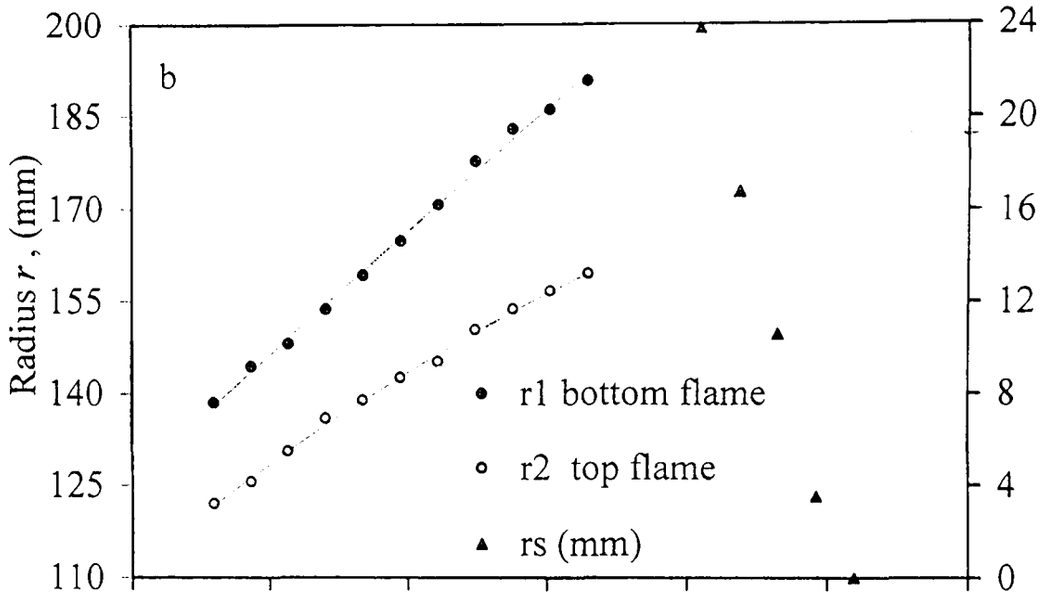

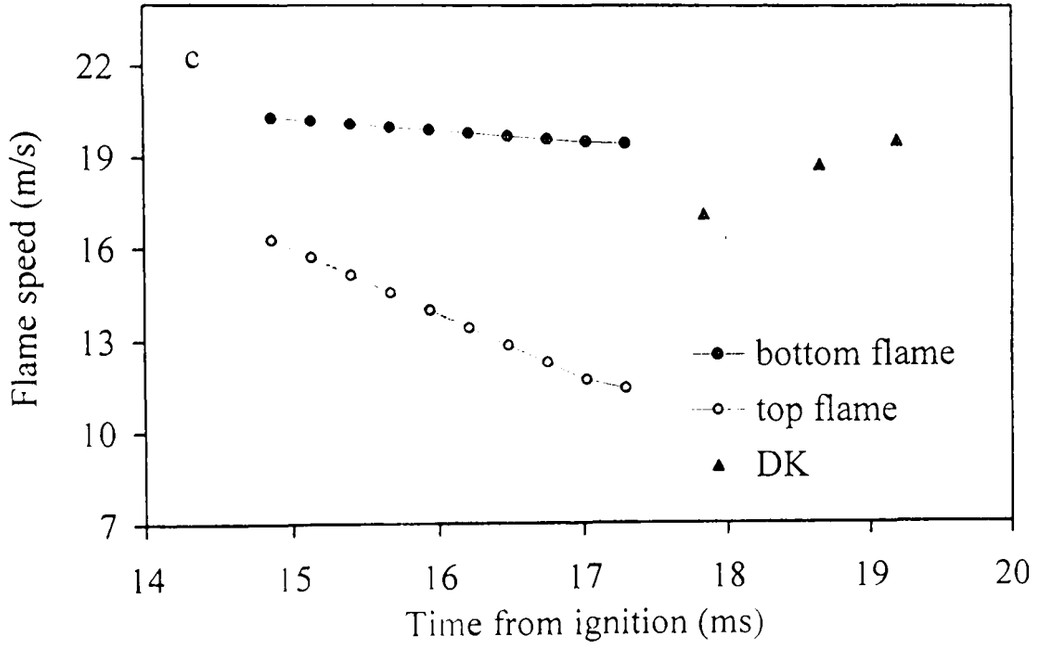

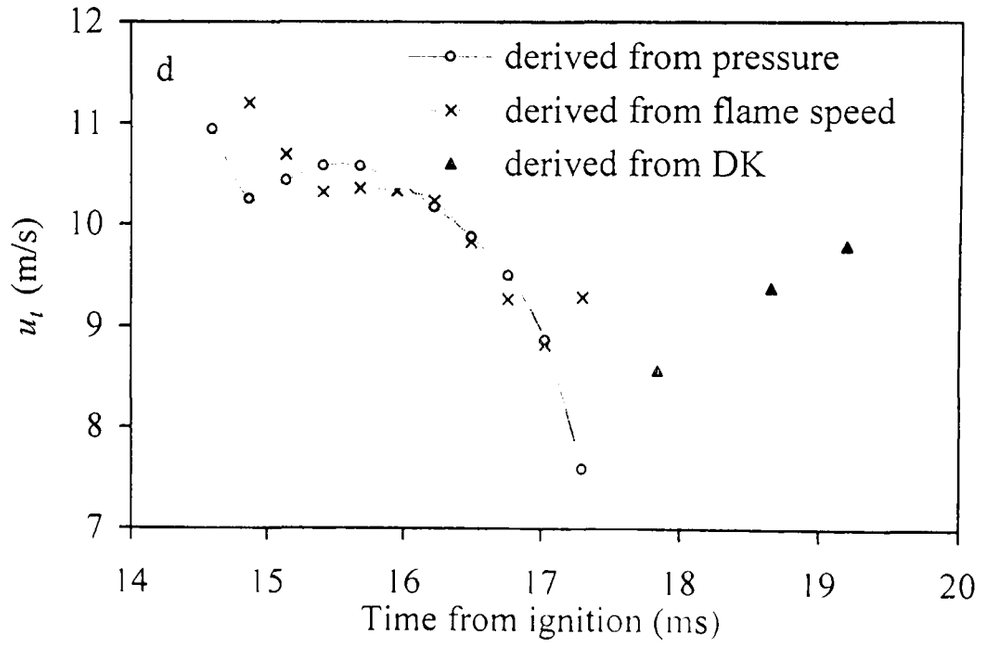

Fig. 7.29. Iso-octane - air implosion, $\phi = 1, p_o = 1$ MPa, $T_o = 358$ K, $u' = 2$

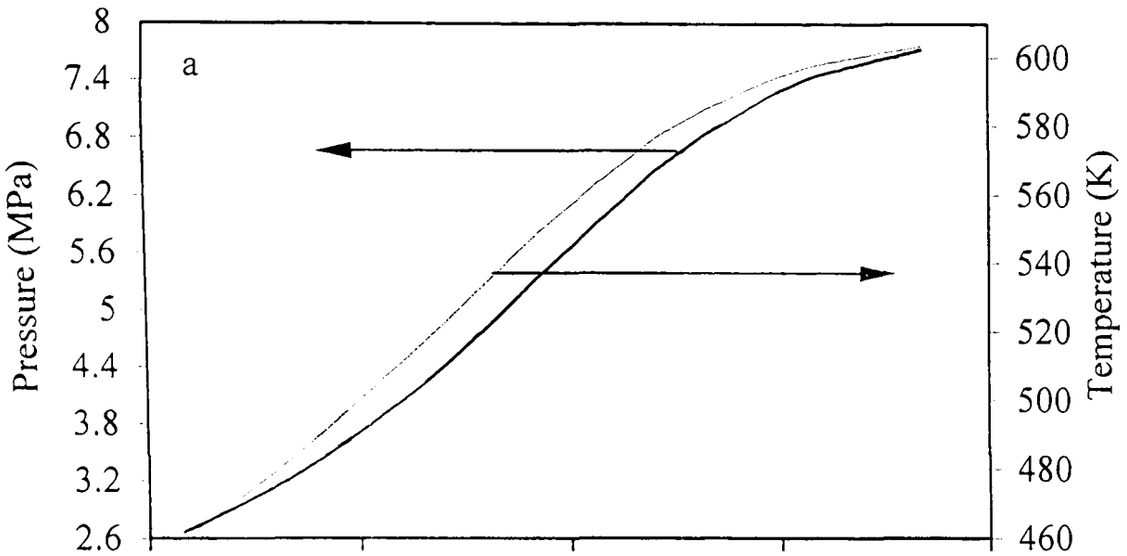

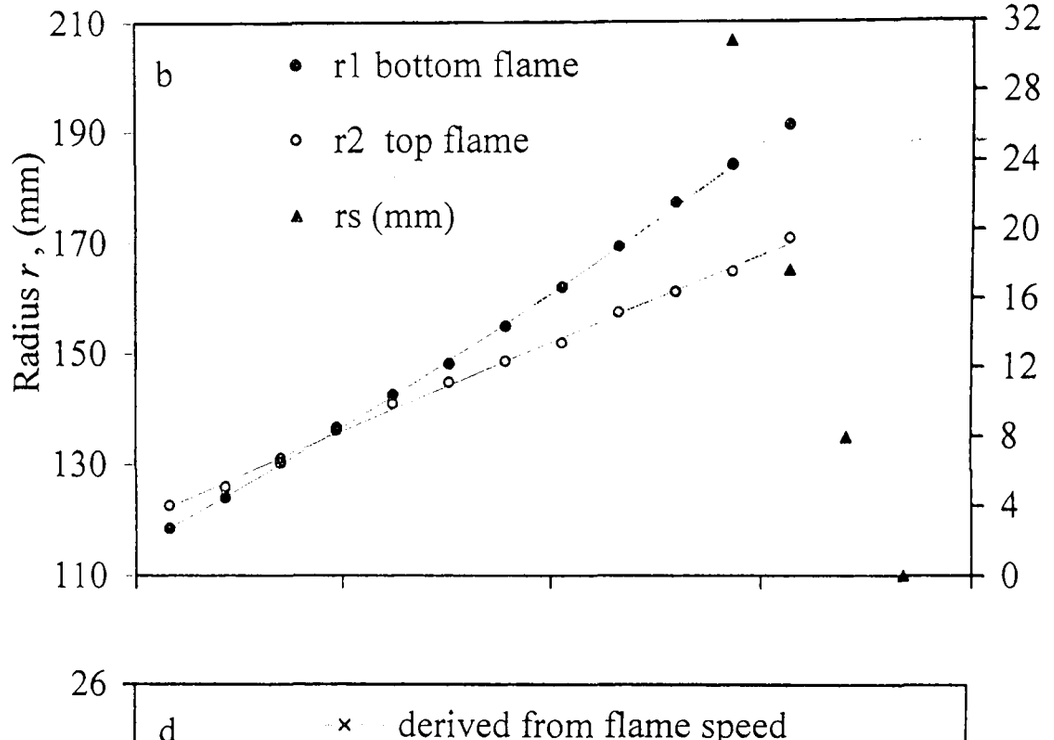

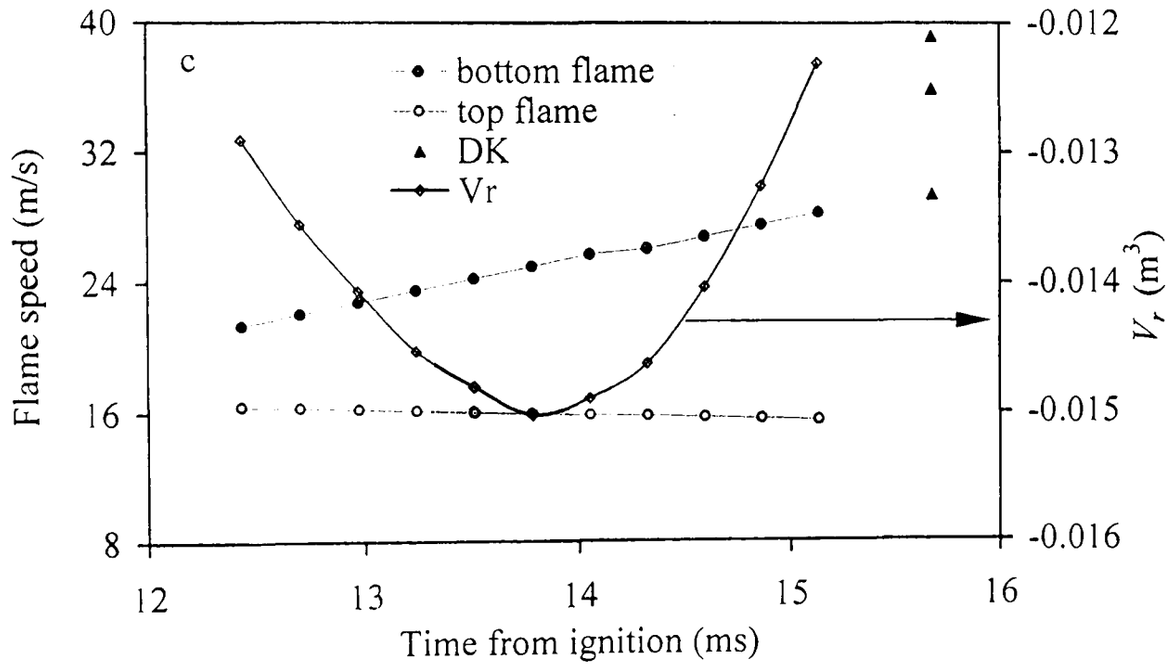

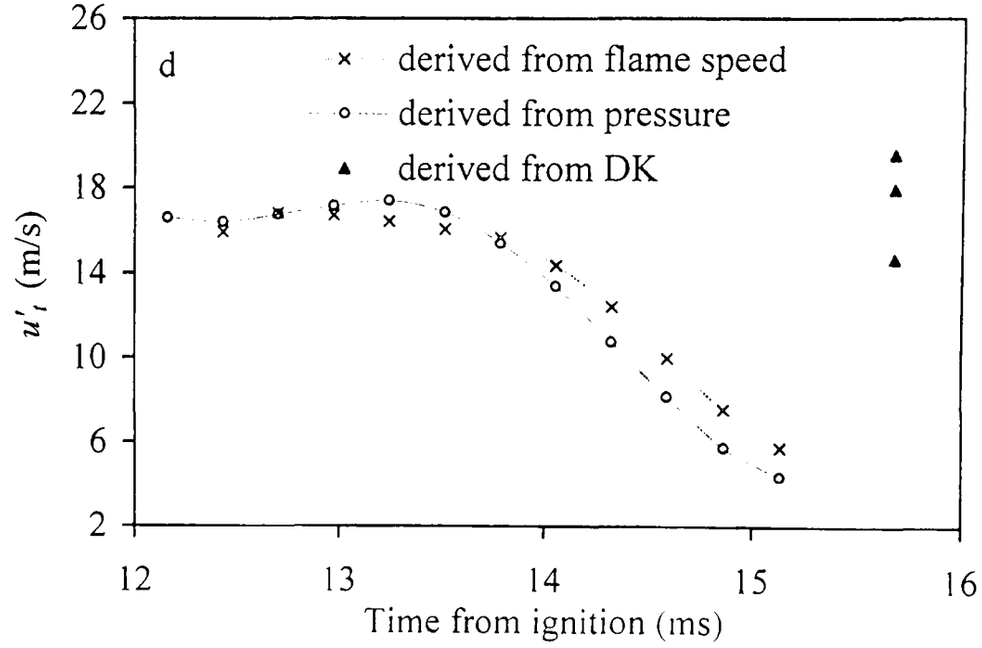

Fig. 7.30. Iso-octane - air implosion, ϕ = 1, p_o = 1 MPa, T_o = 358 K, u' = 3

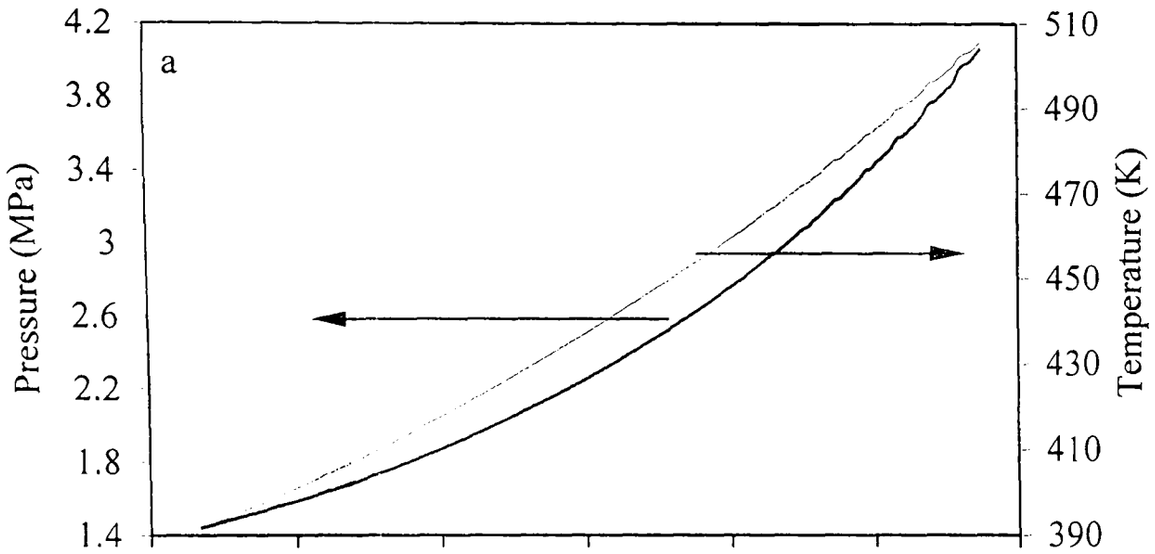

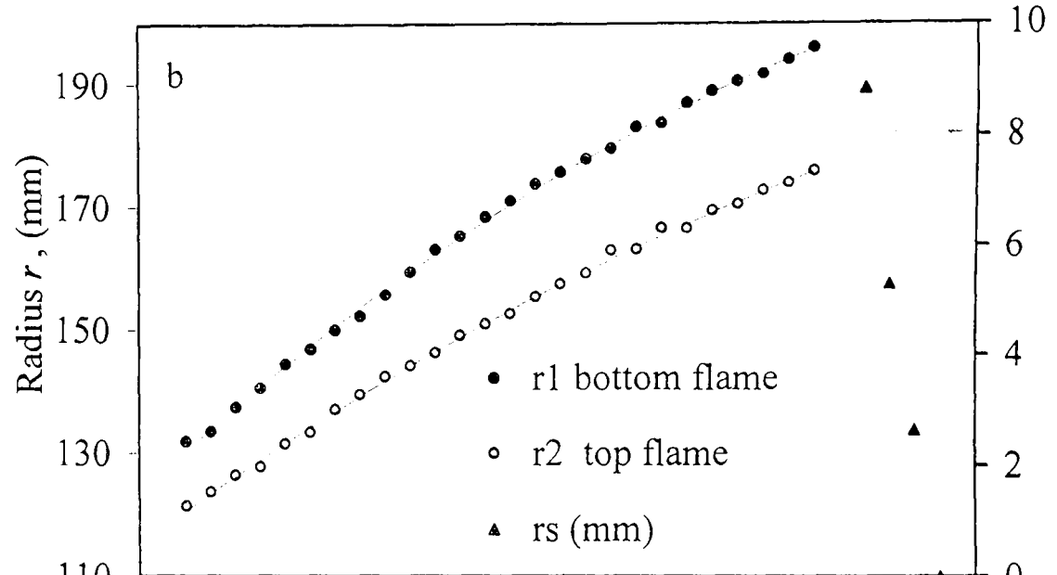

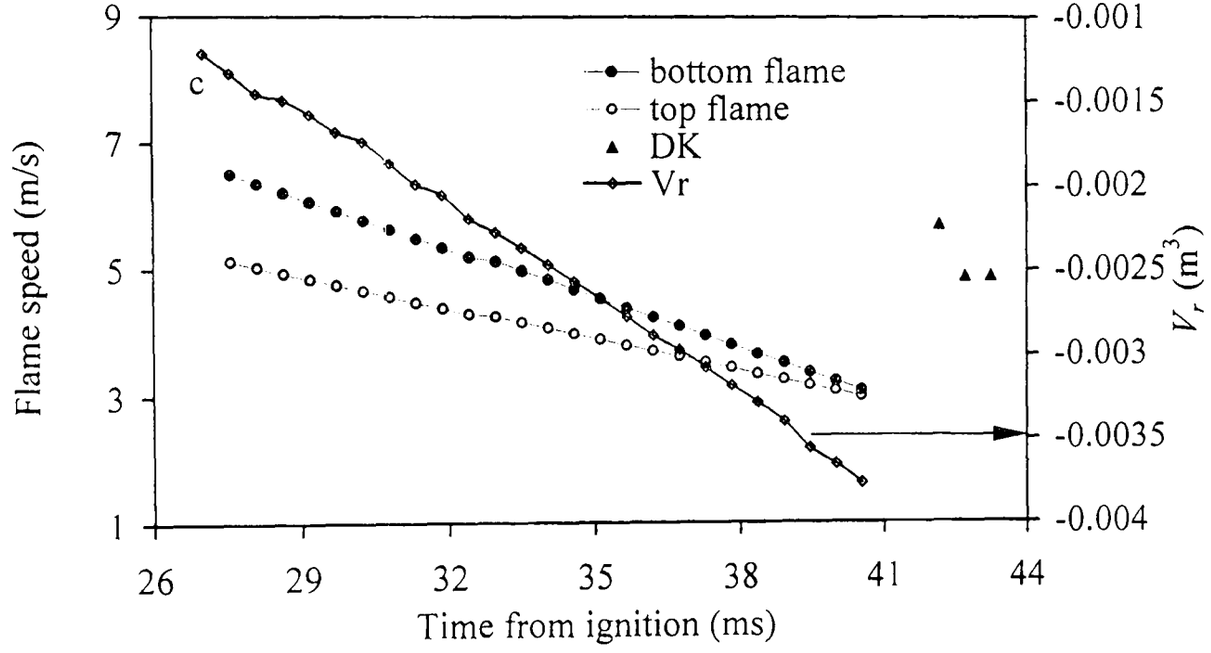

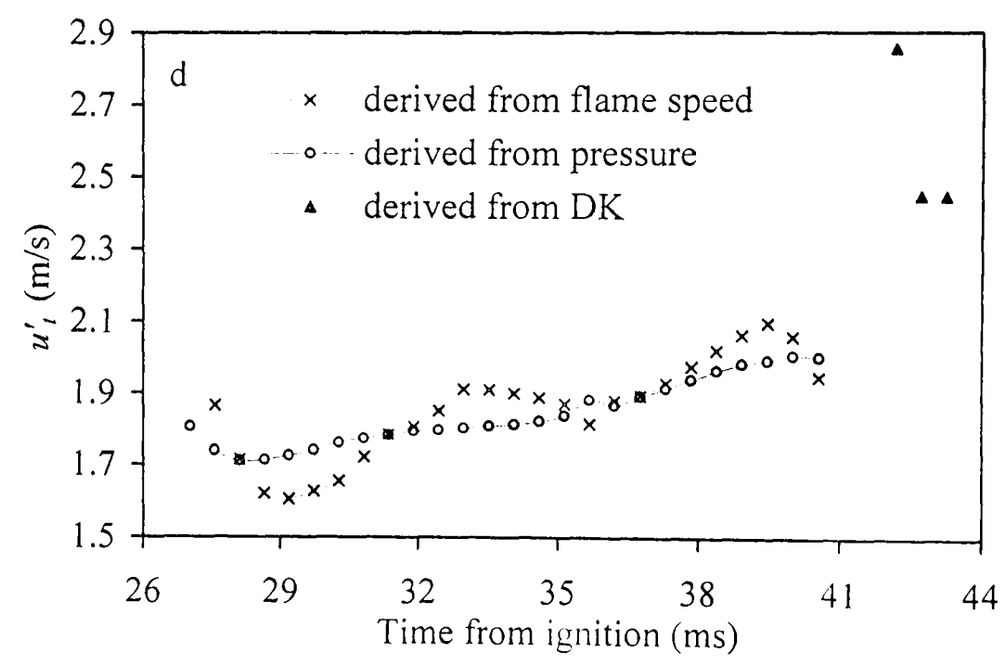

Fig. 7.31. Iso-octane - air implosion, ϕ = 1.4, p_o = 1 MPa, T_o = 358 K, u' = 0.25

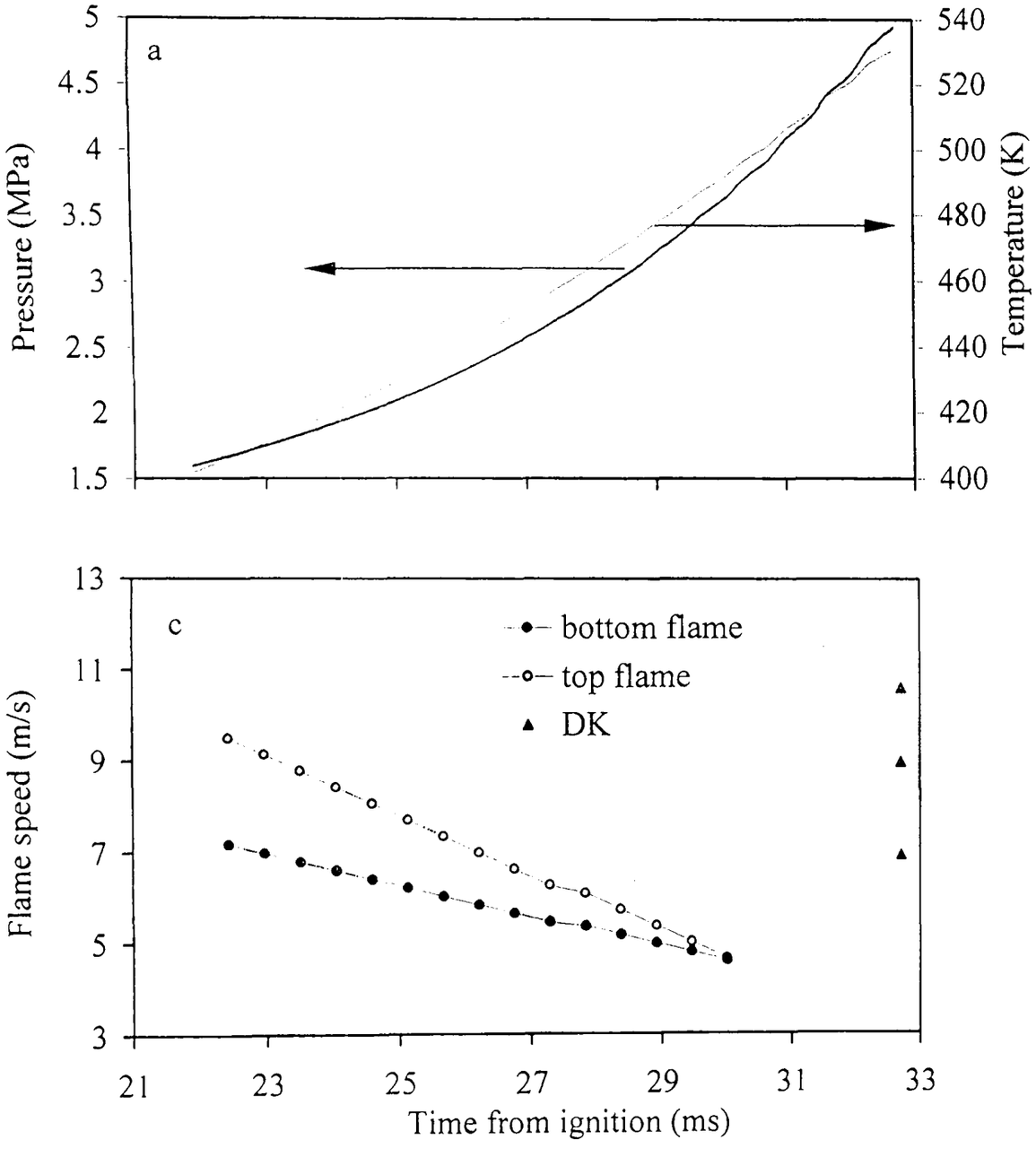

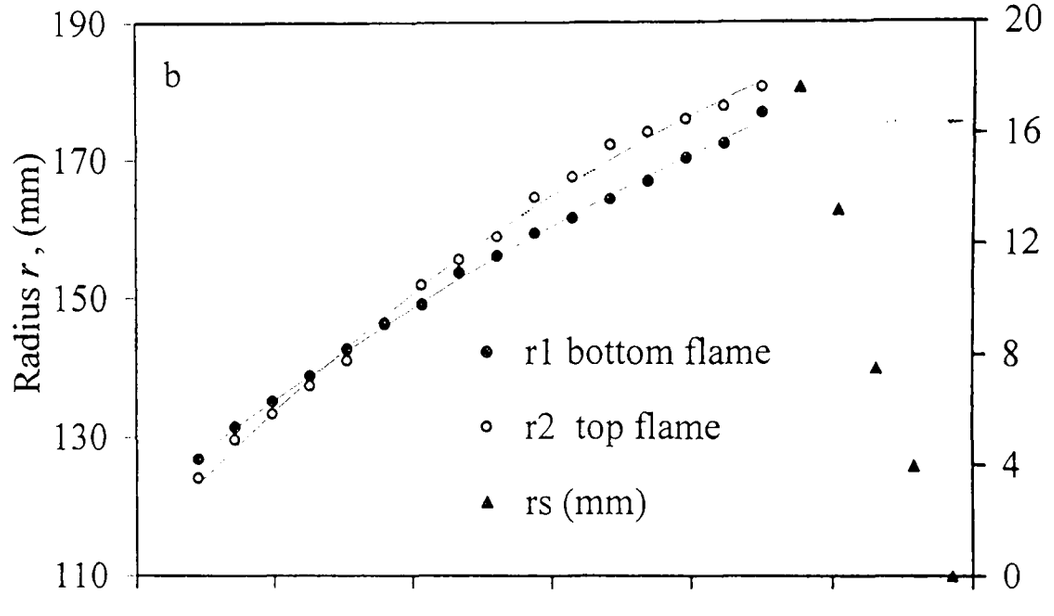

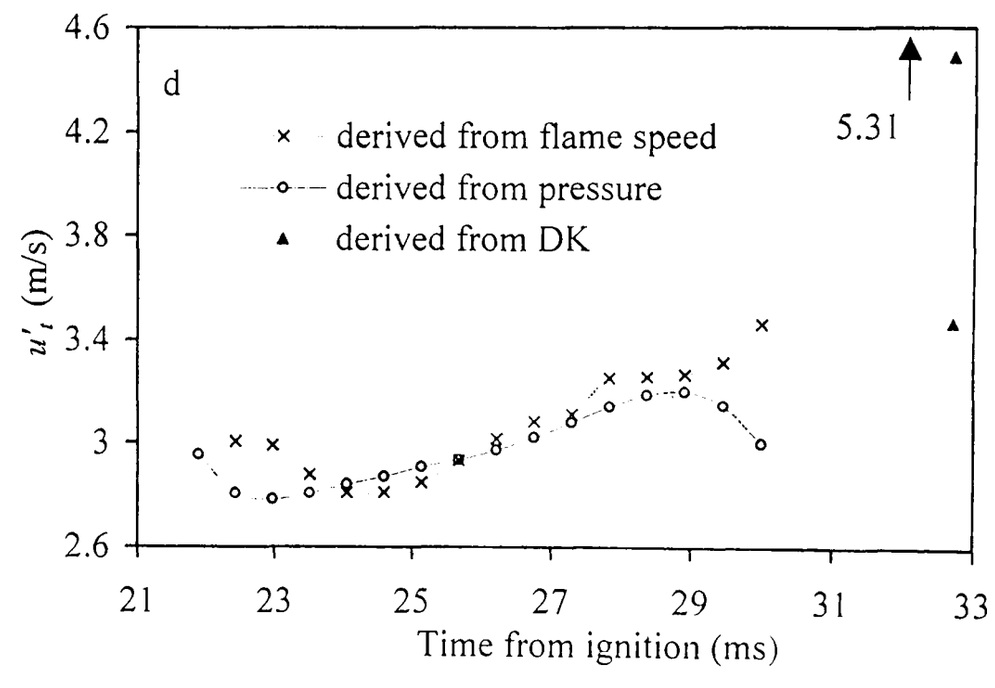

Fig. 7.32. Iso-octane - air implosion, ϕ = 1.4, p_o = 1 MPa, T_o = 358 K, u' = 0.5

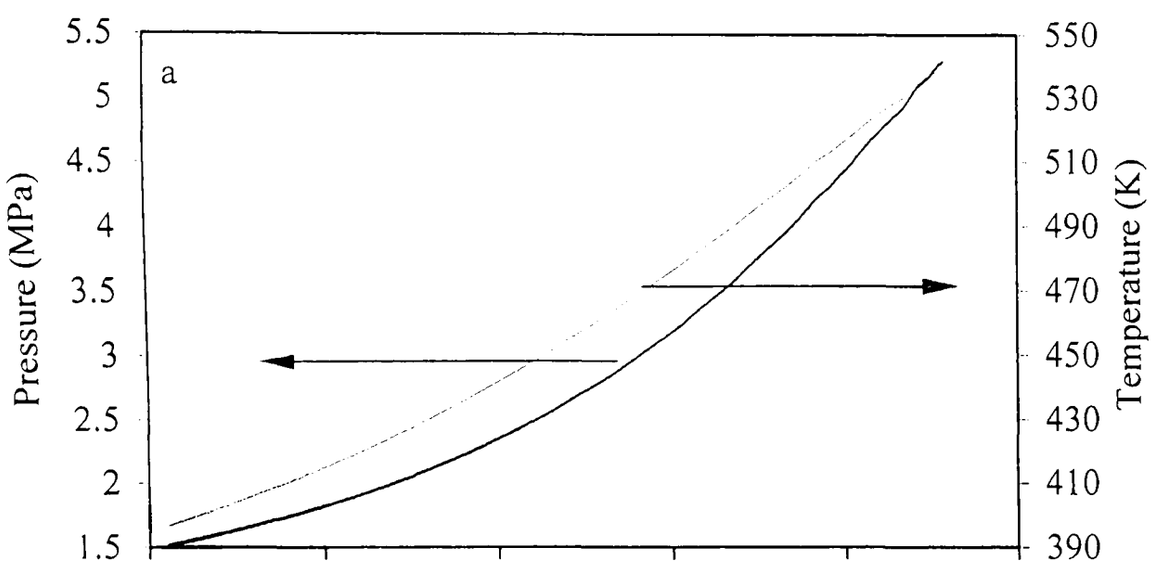

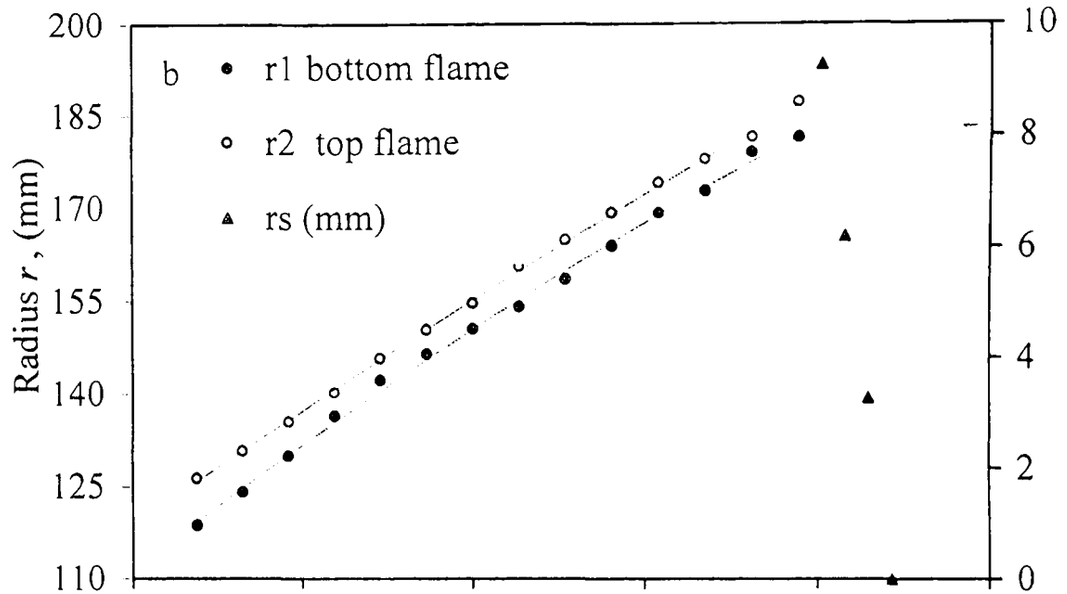

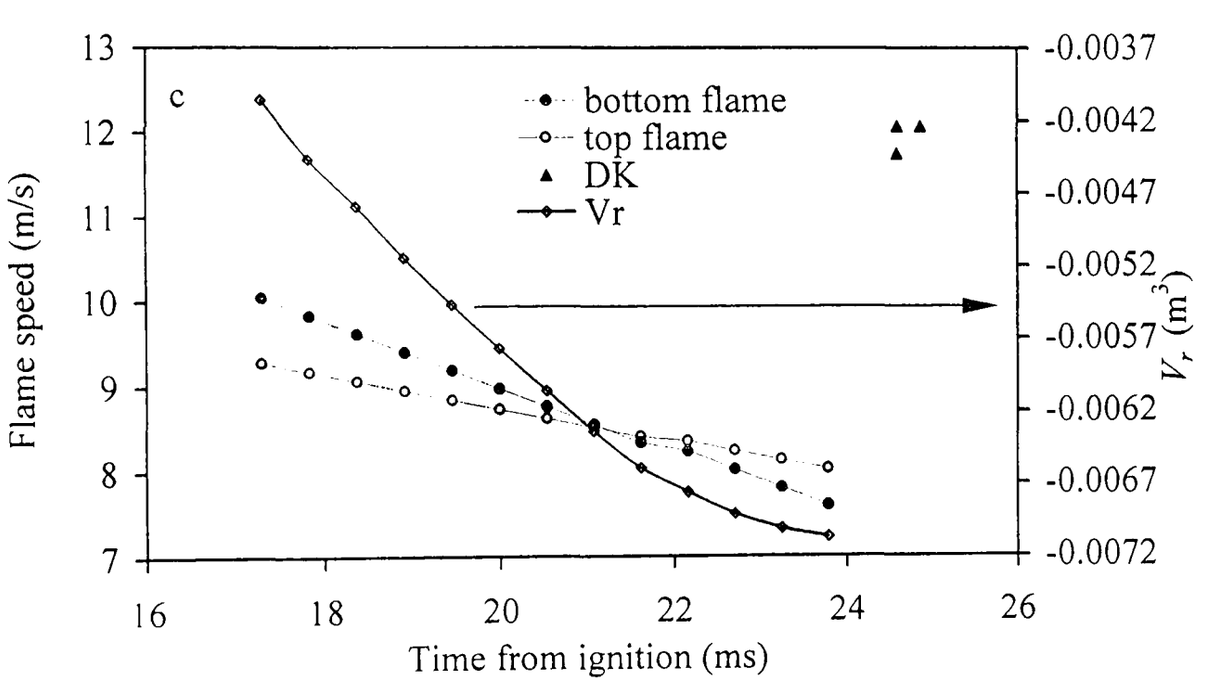

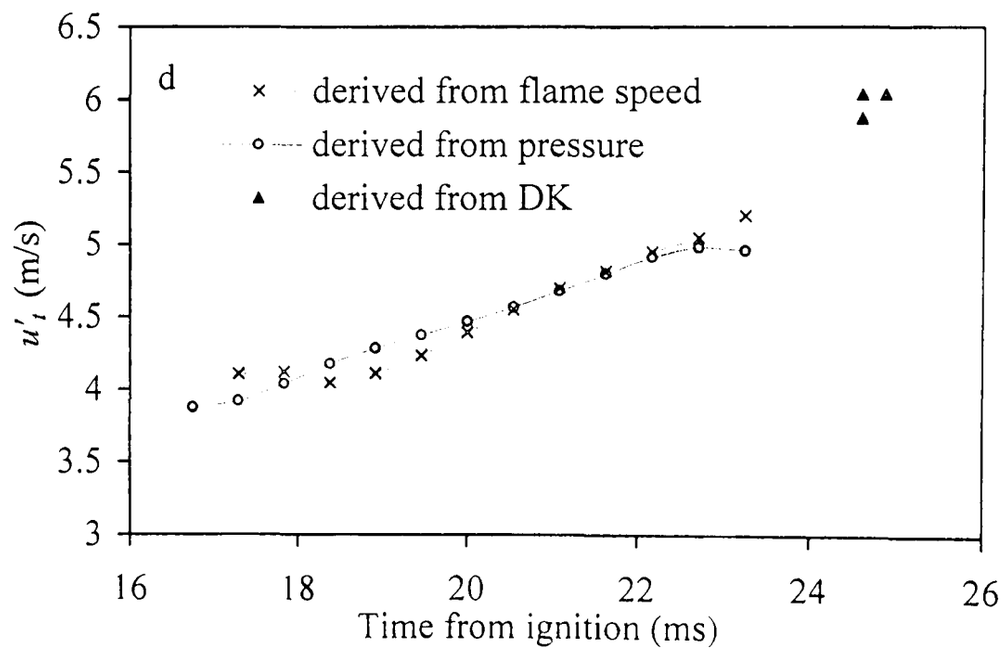

Fig. 7.33. Iso-octane - air implosion, ϕ = 1.4, p_o = 1 MPa, T_o = 358 K, u' = 0.75

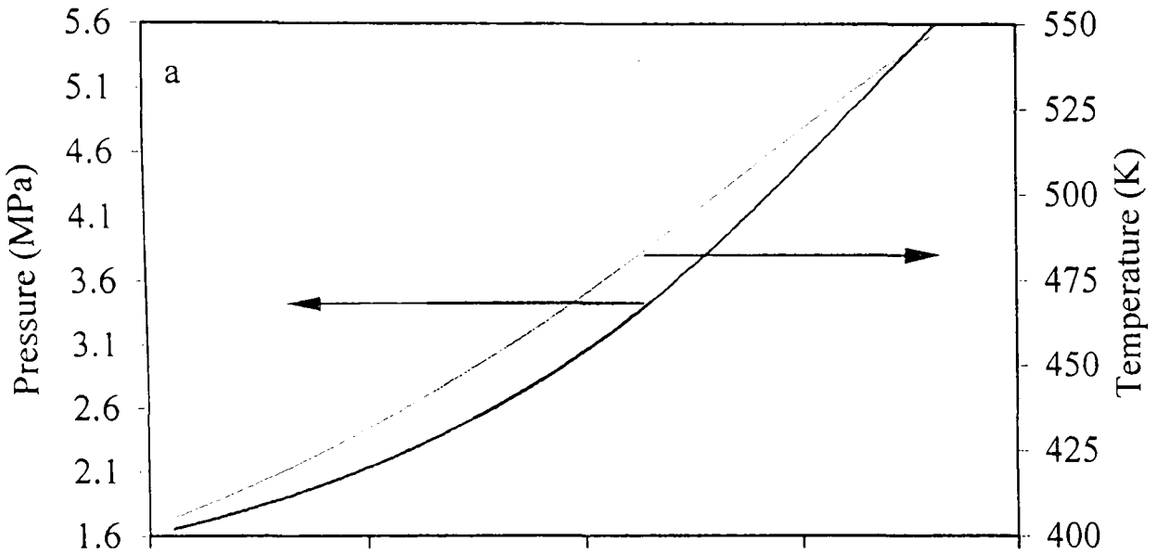

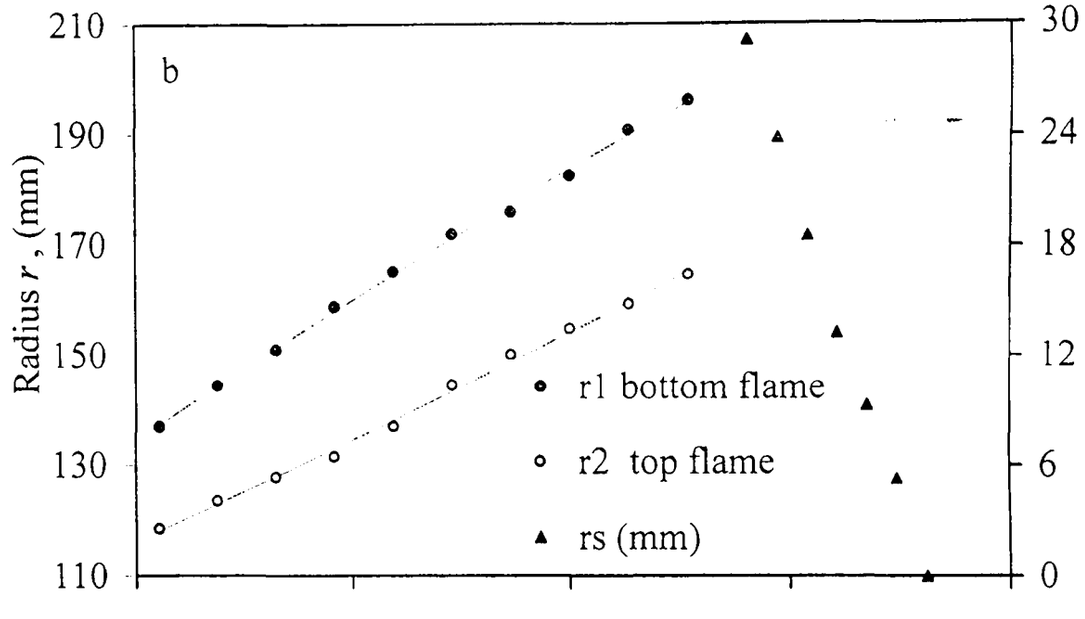

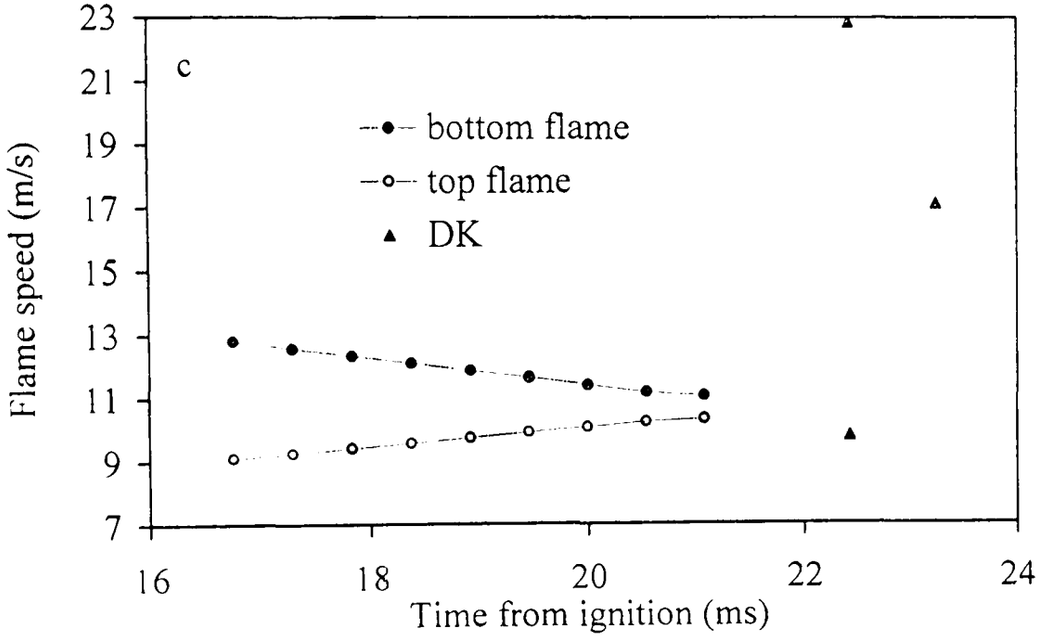

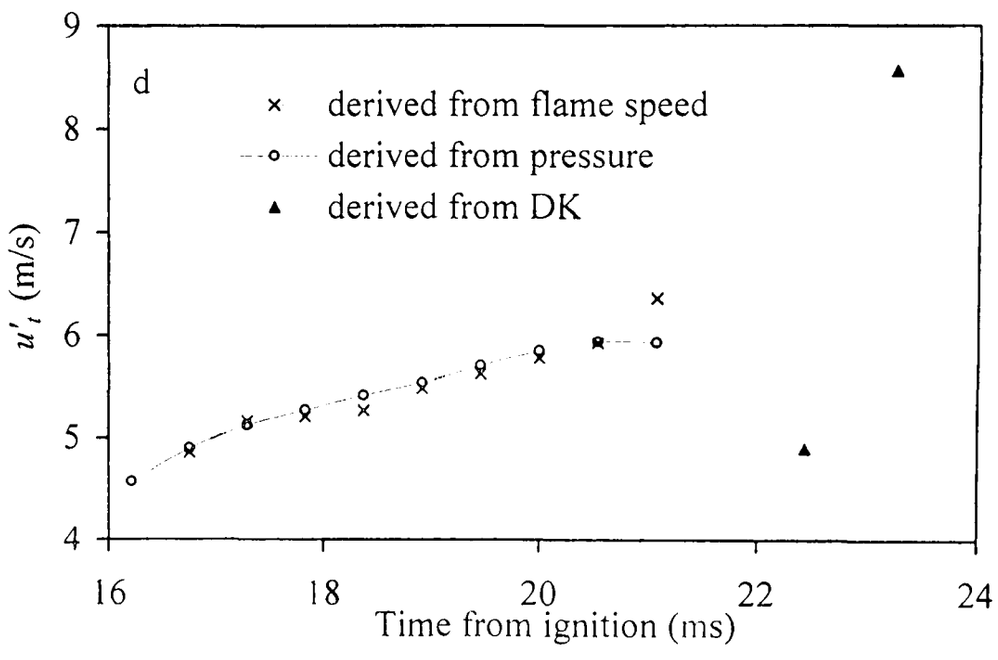

Fig. 7.34. Iso-octane - air implosion, ϕ = 1.4, p_o = 1 MPa, T_o = 358 K, u' = 1

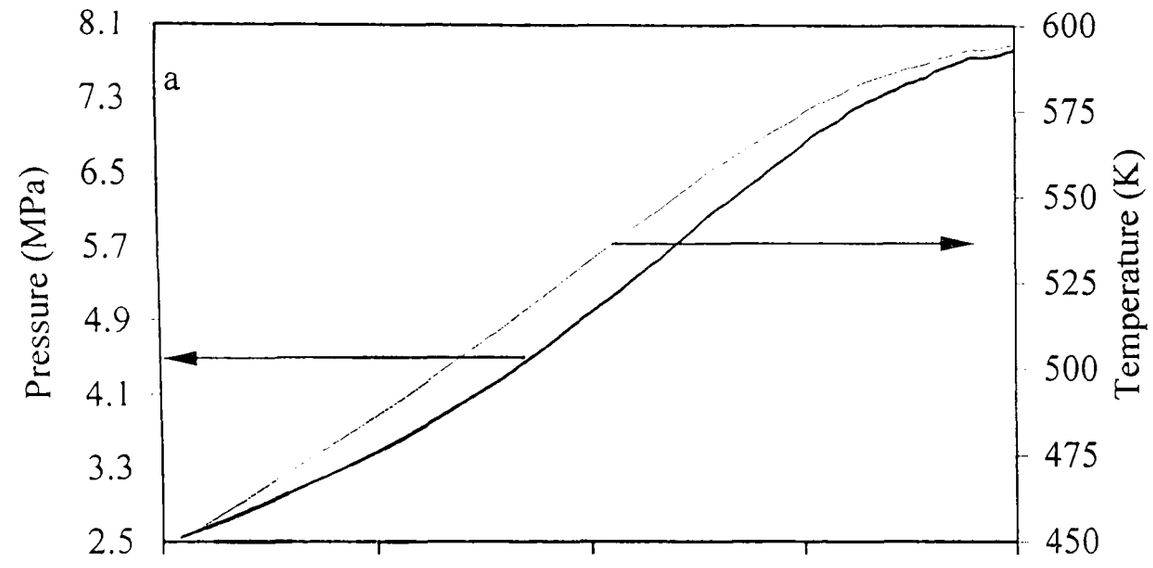

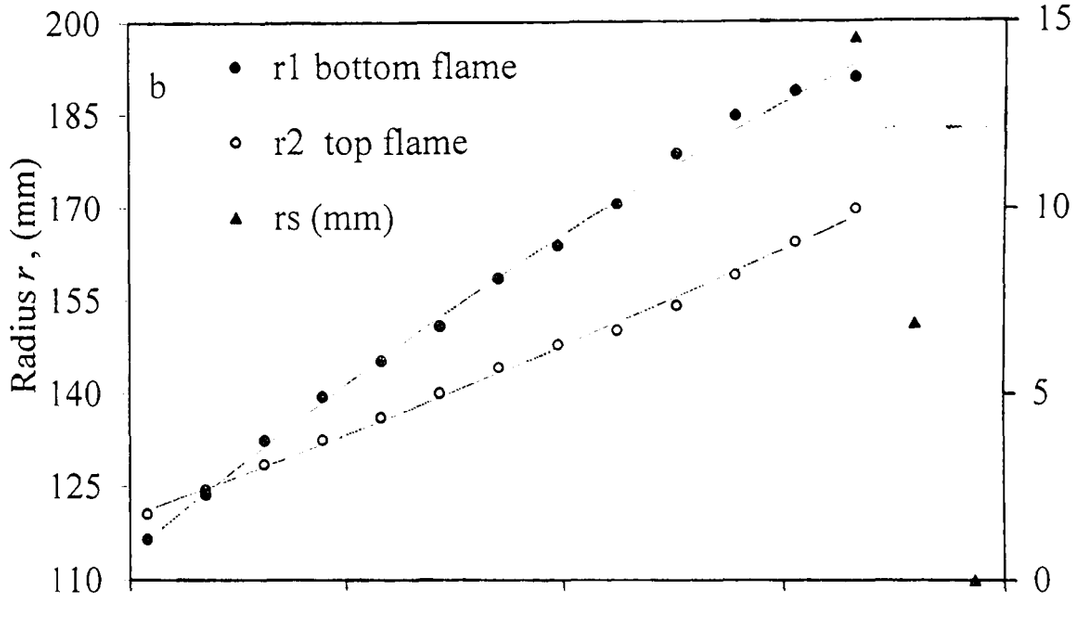

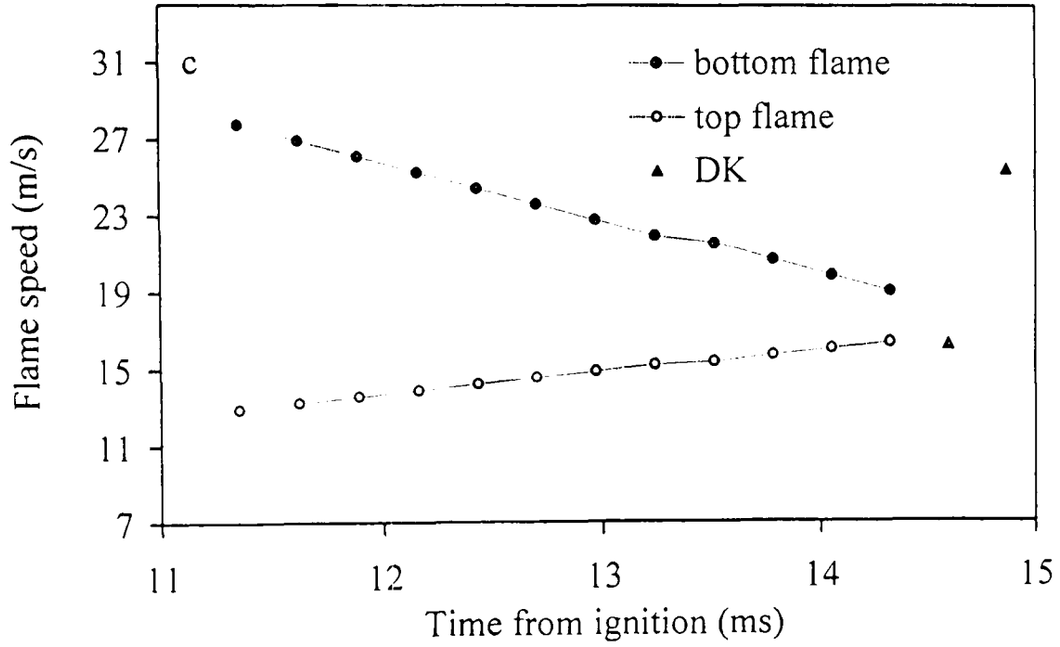

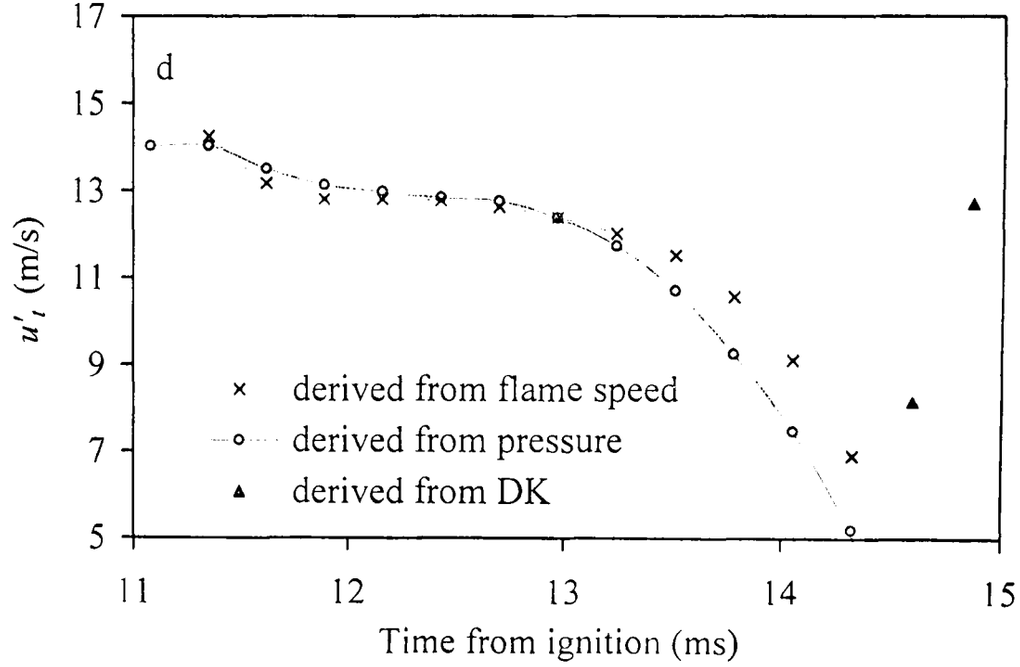

Fig. 7.35. Iso-octane - air implosion, $\phi = 1.4$, $p_o = 1$ MPa, $T_o = 358$ K, $u' = 2$

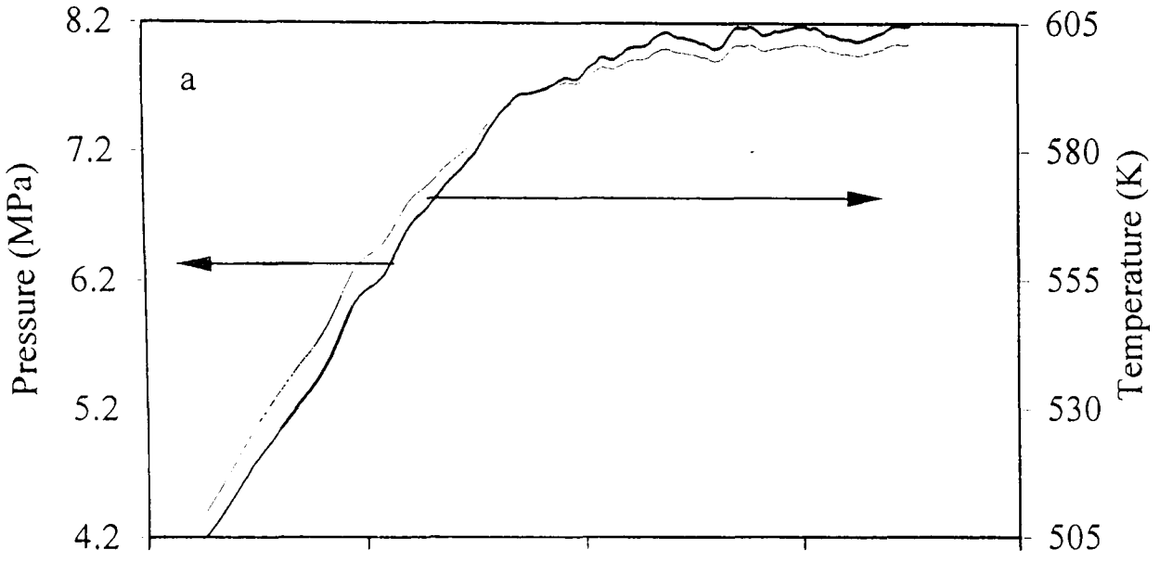

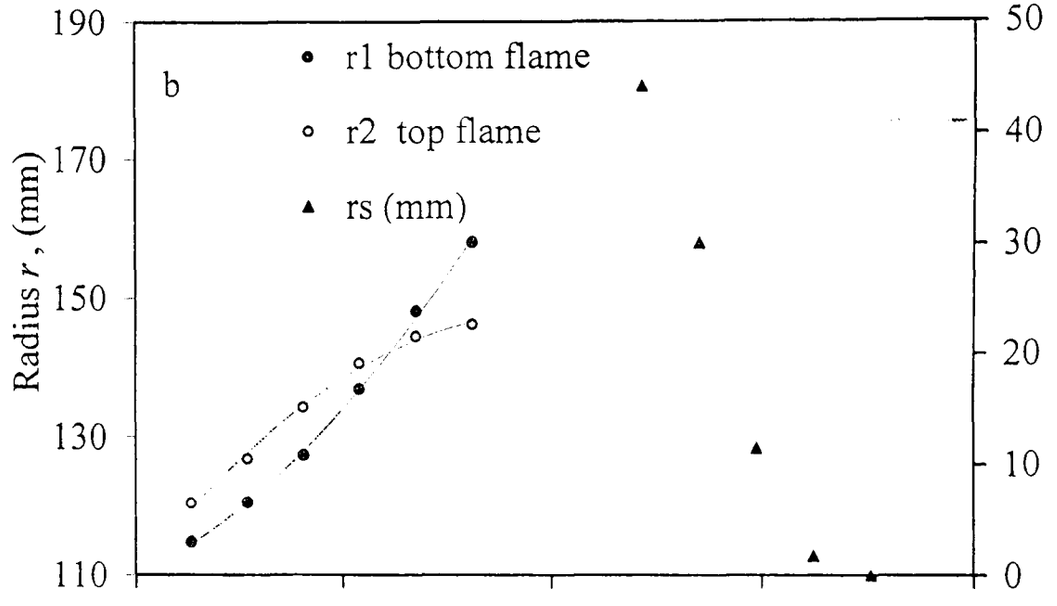

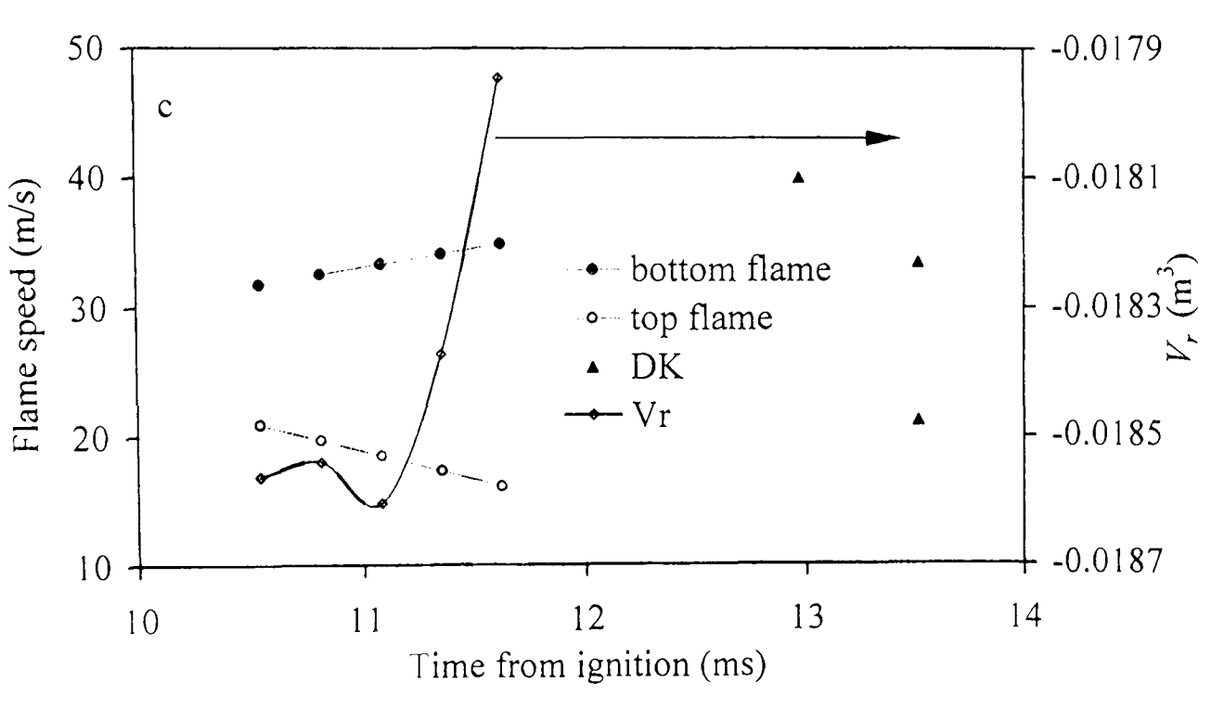

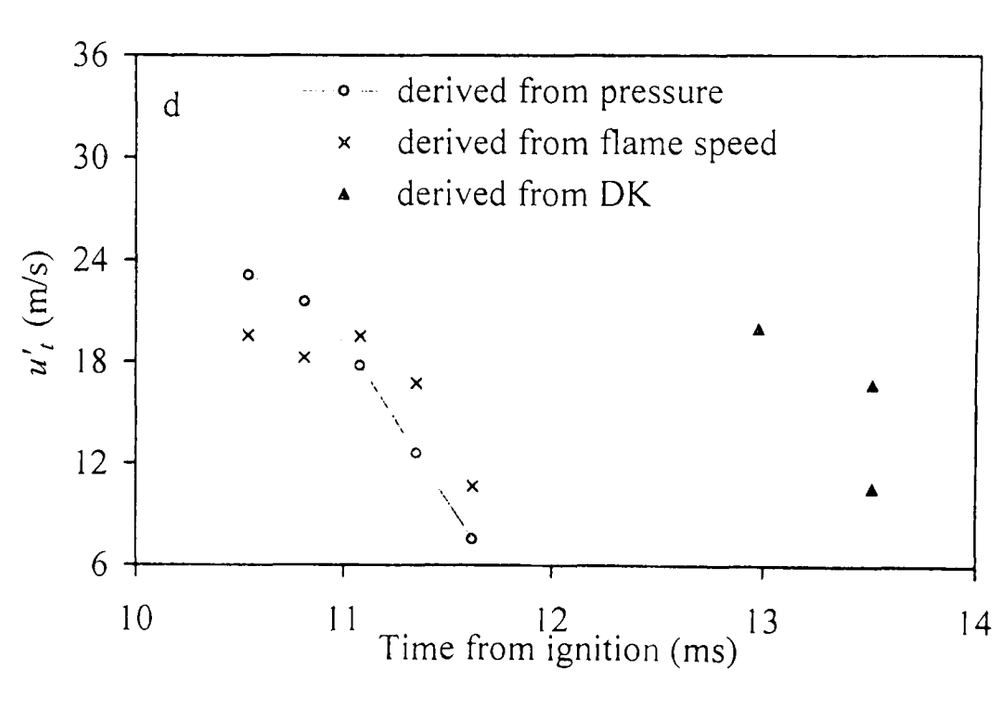

Fig. 7.36. Iso-octane - air implosion, ϕ = 1.4, p_o = 1 MPa, T_o = 358 K, u' = 3

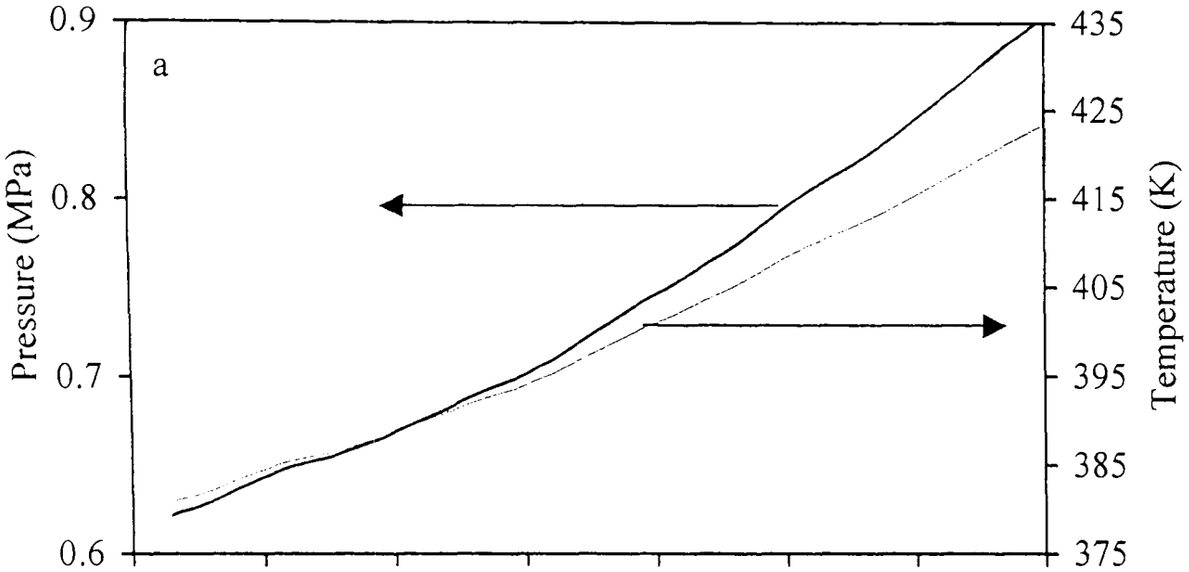

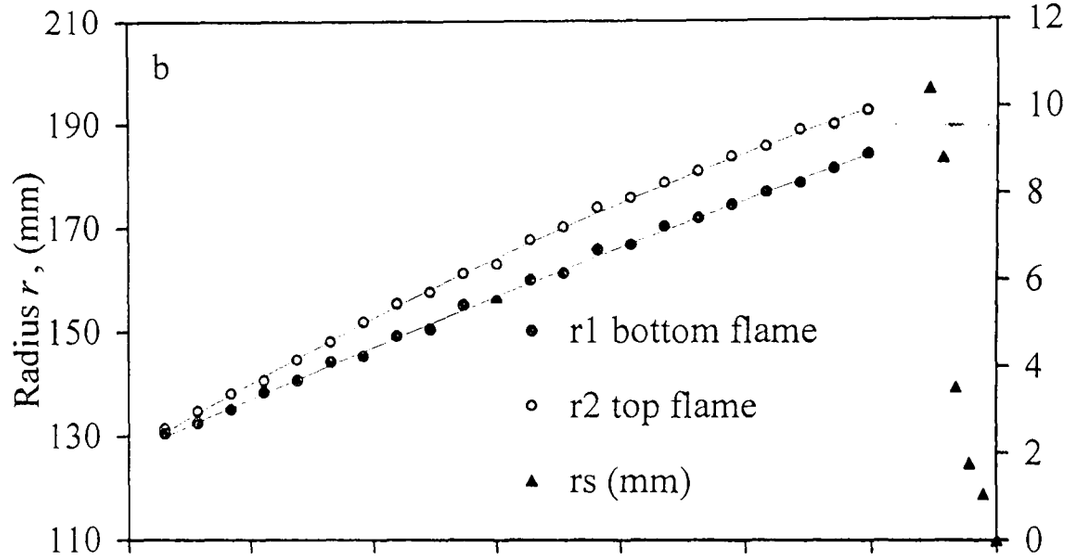

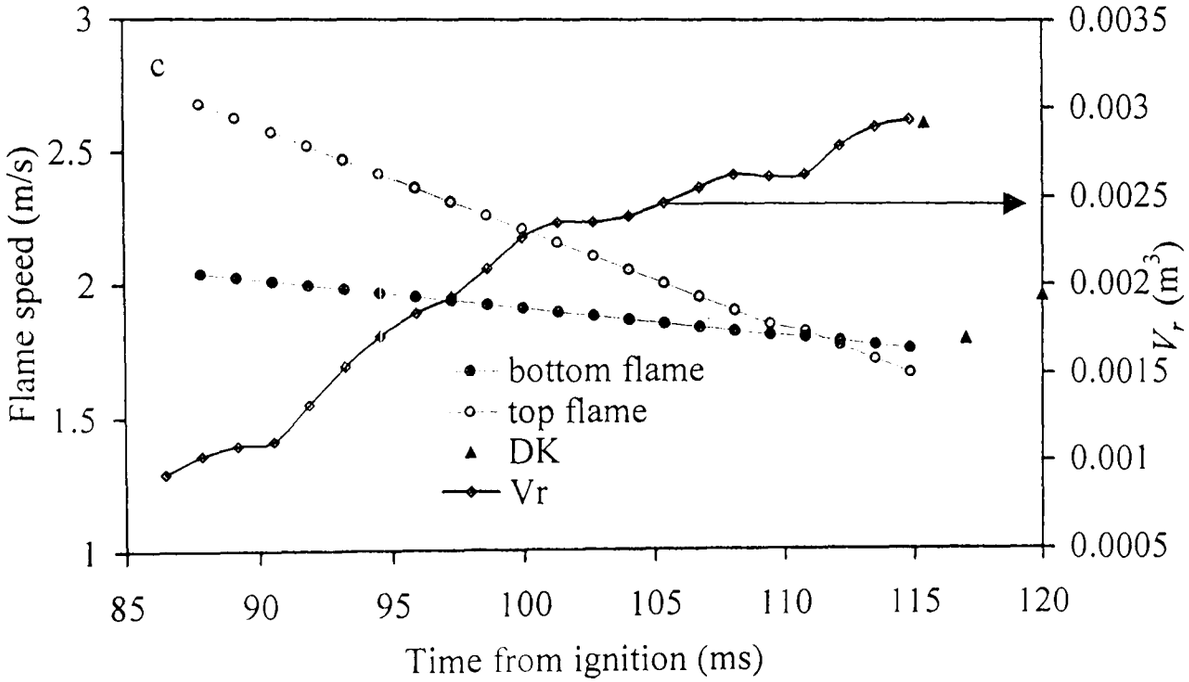

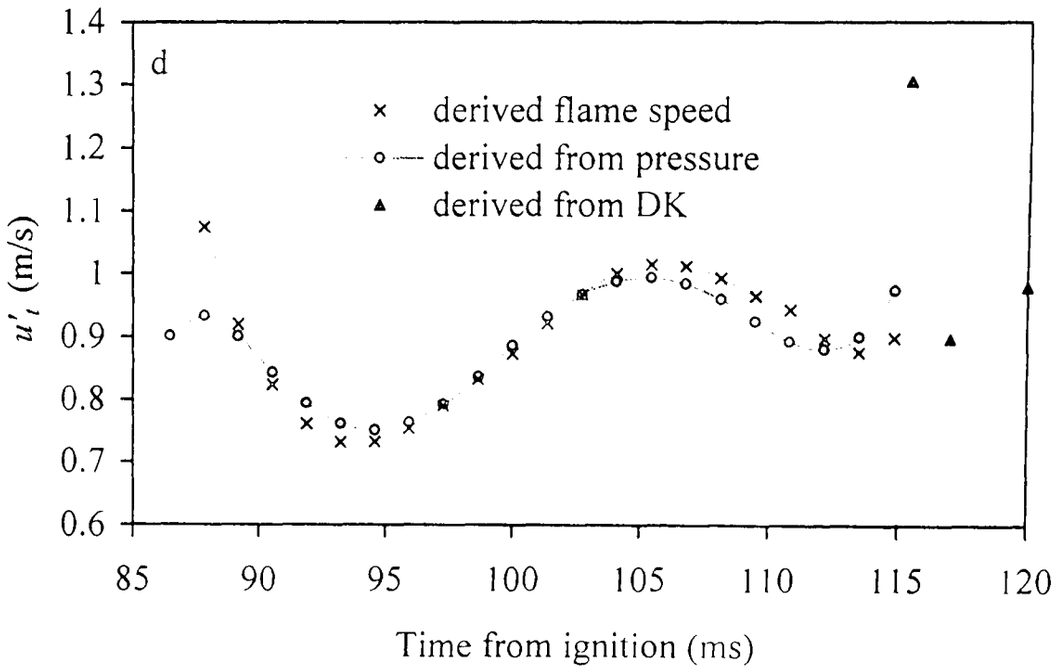

Fig. 7.37. Hydrogen - air implosion, ϕ = 0.3, p_o = 0.5 MPa, T_o = 358 K, u' = 0.25

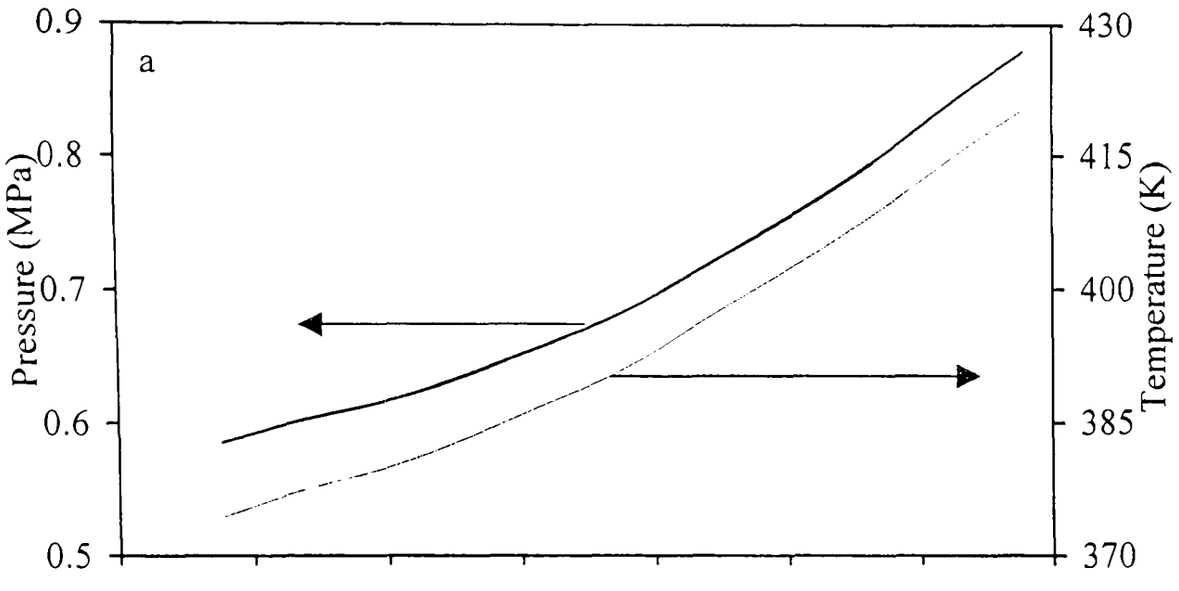

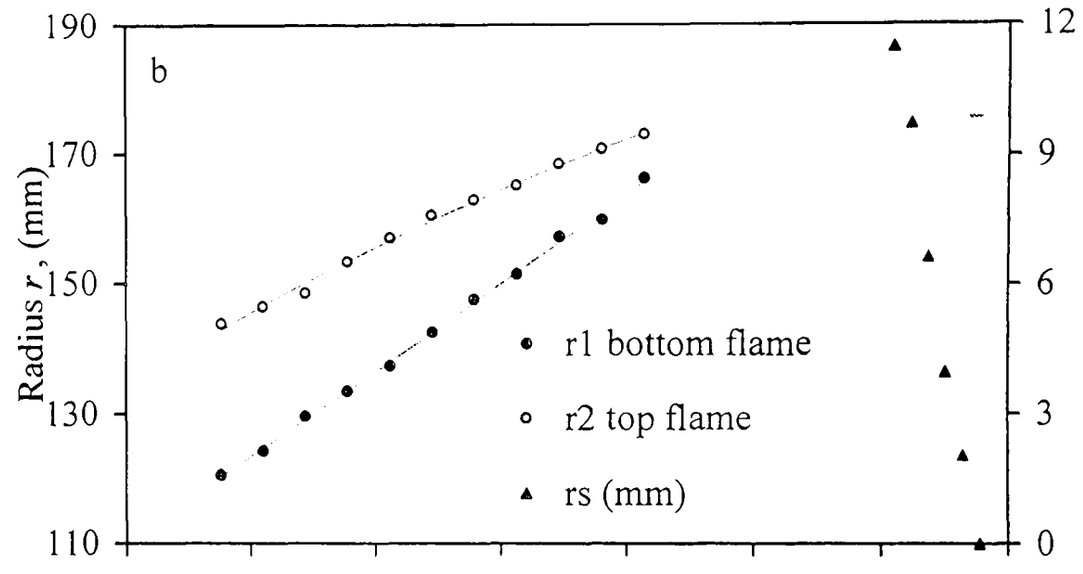

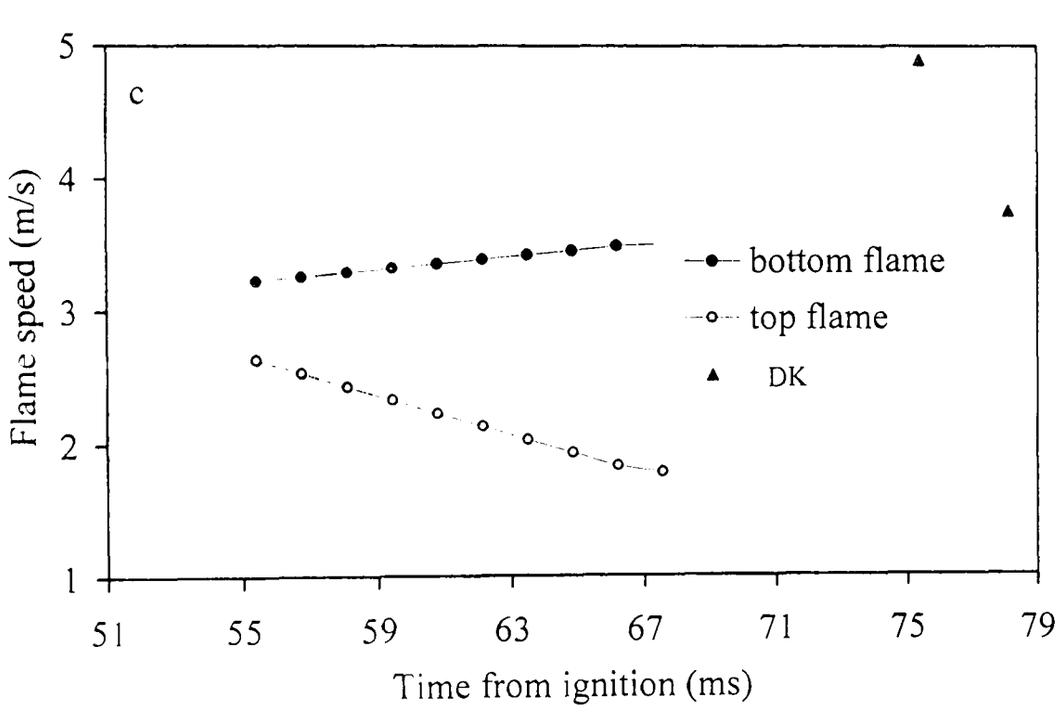

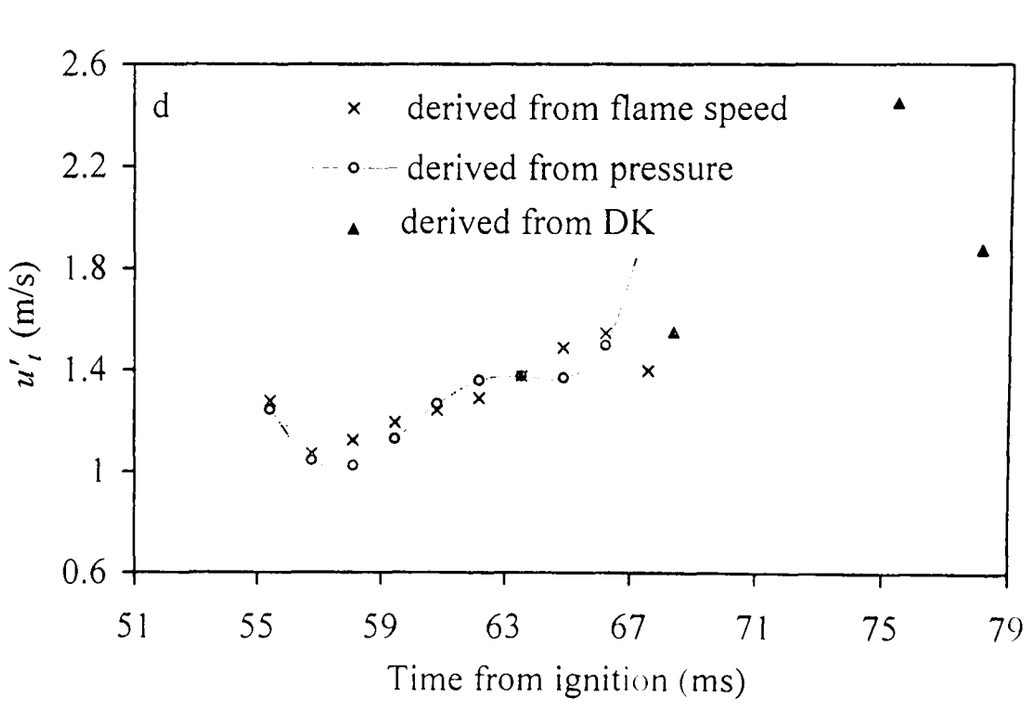

Fig. 7.38. Hydrogen - air implosion, ϕ = 0.3, p_o = 0.5 MPa, T_o = 358 K, u' = 0.5

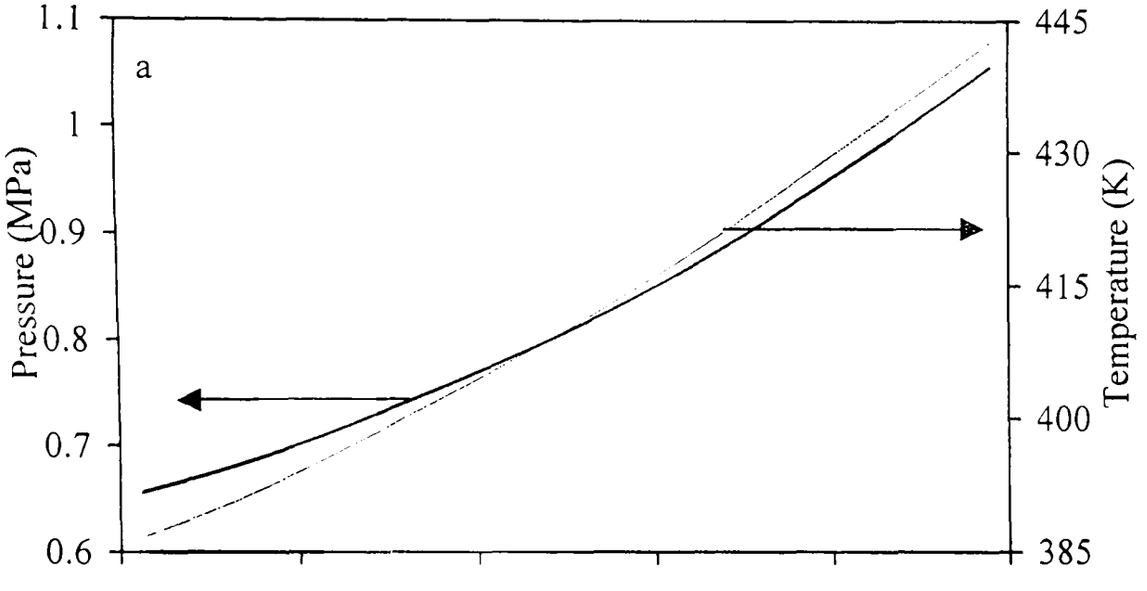

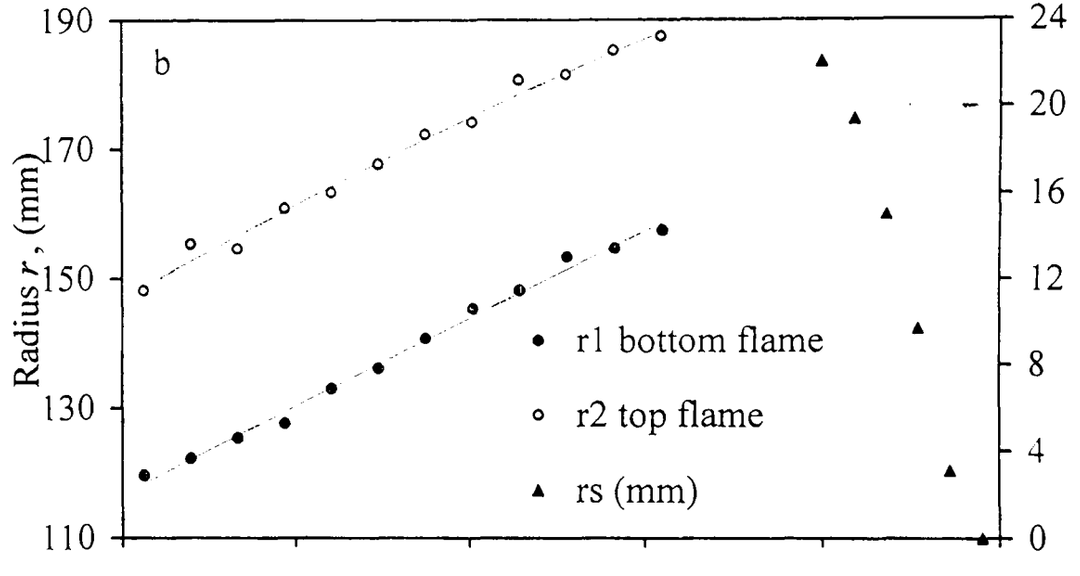

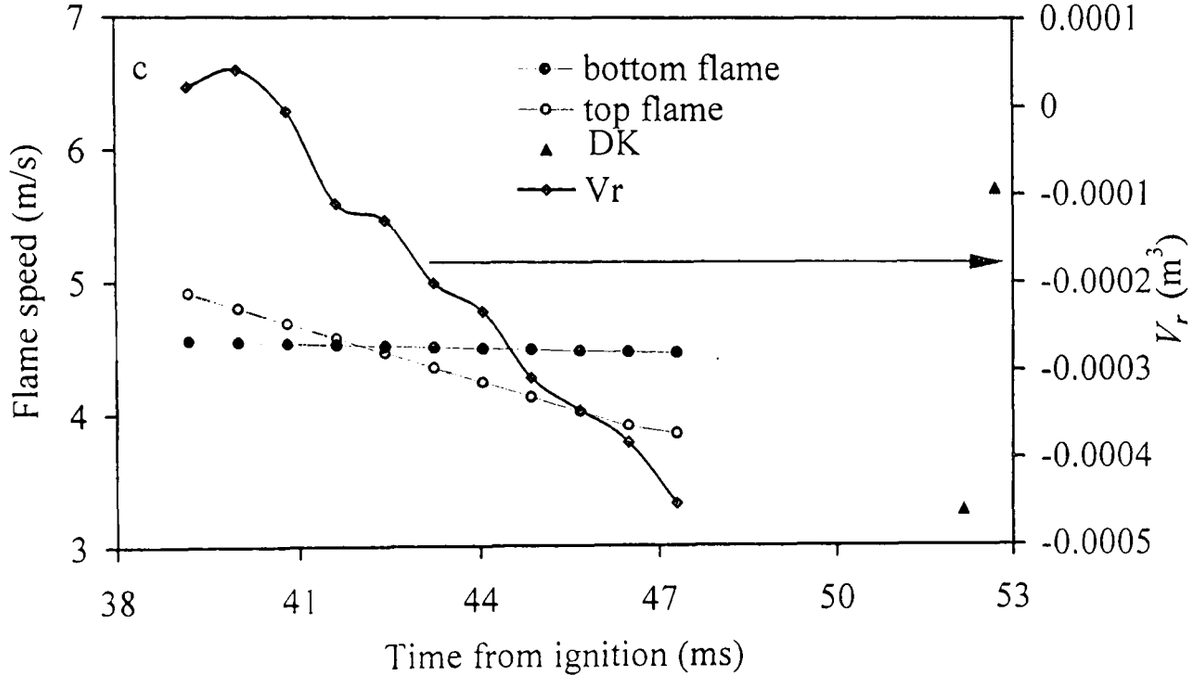

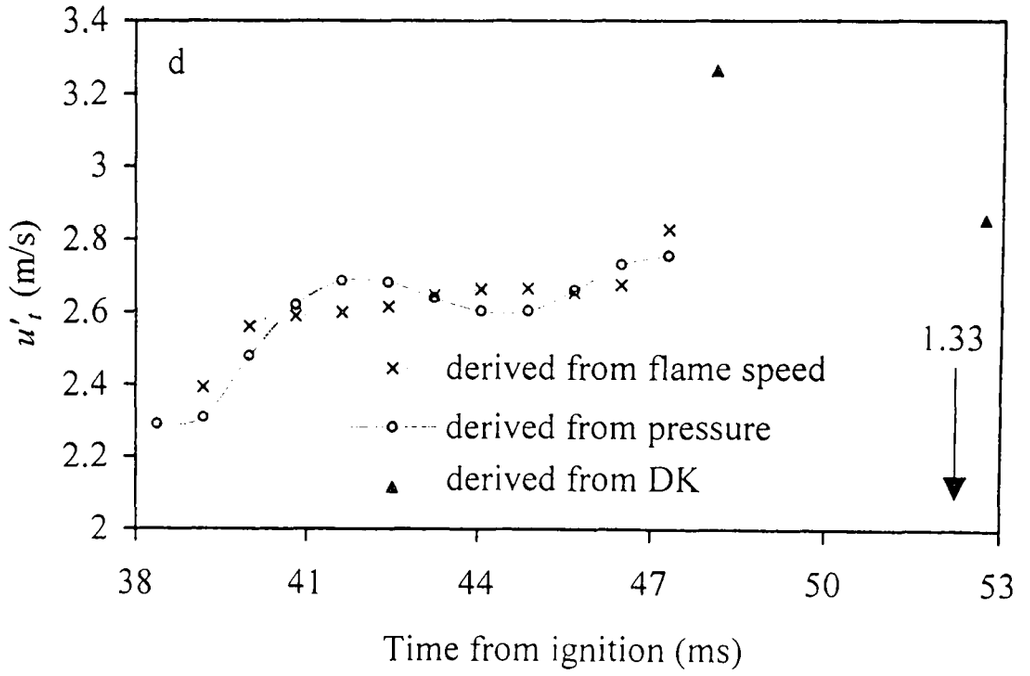

Fig. 7.39. Hydrogen - air implosion, $\phi = 0.3$, $p_o = 0.5$ MPa, $T_o = 358$ K, $u' = 0.75$

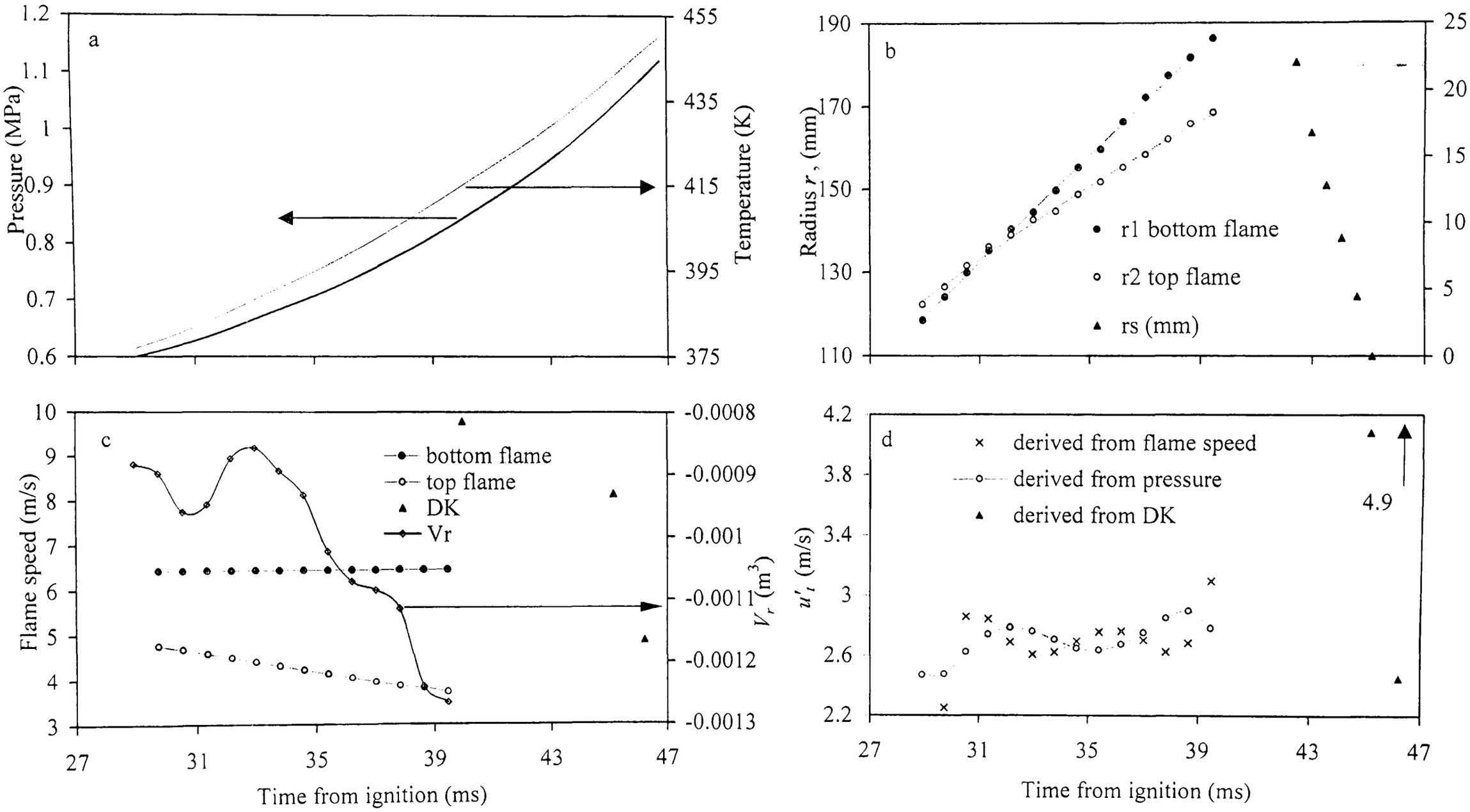

Fig. 7.40. Hydrogen - air implosion, ϕ = 0.3, p_o = 0.5 MPa, T_o = 358 K, u' = 1

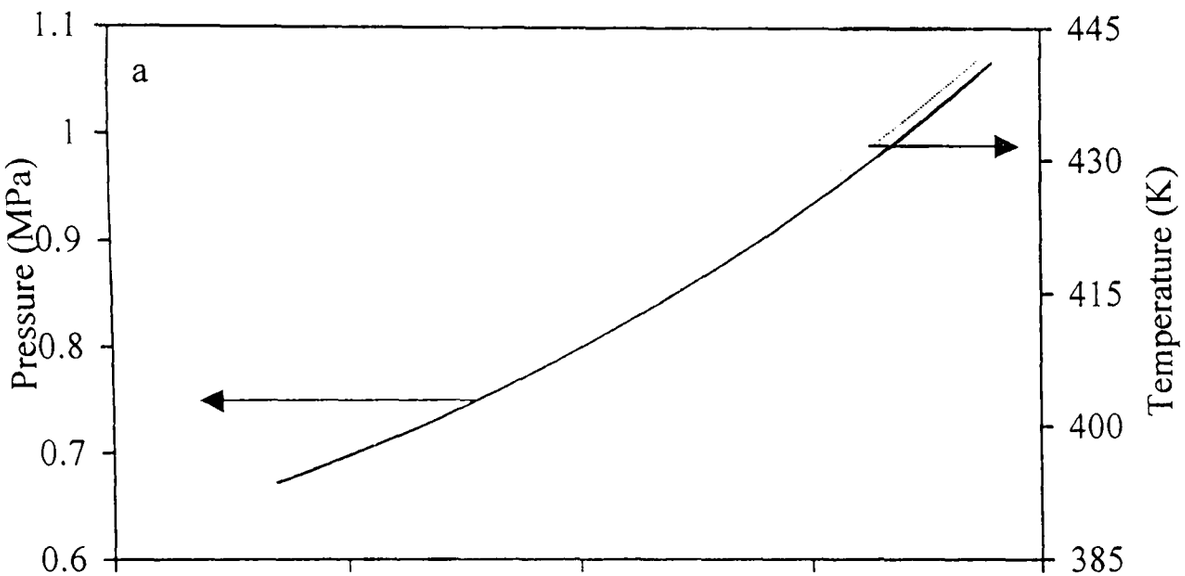

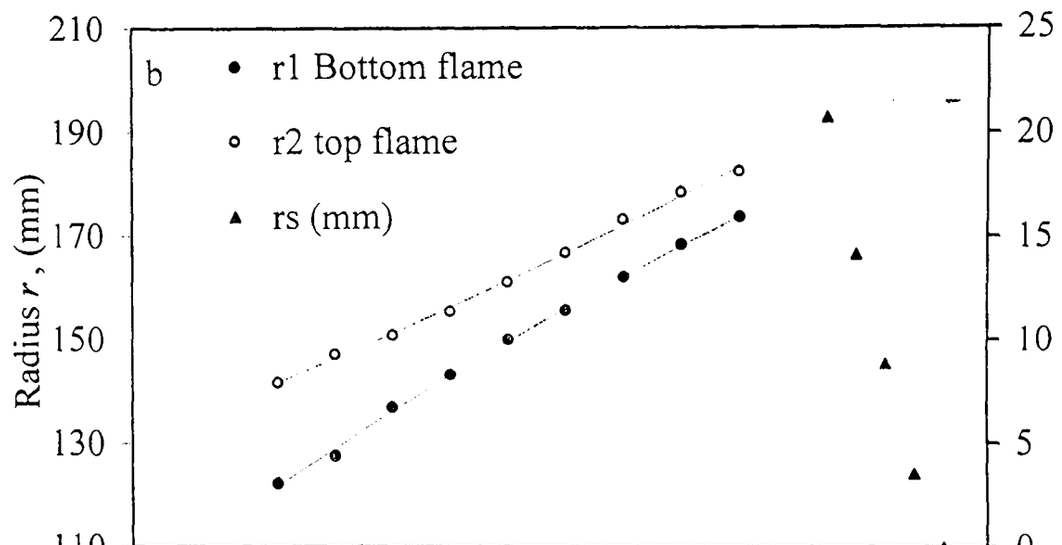

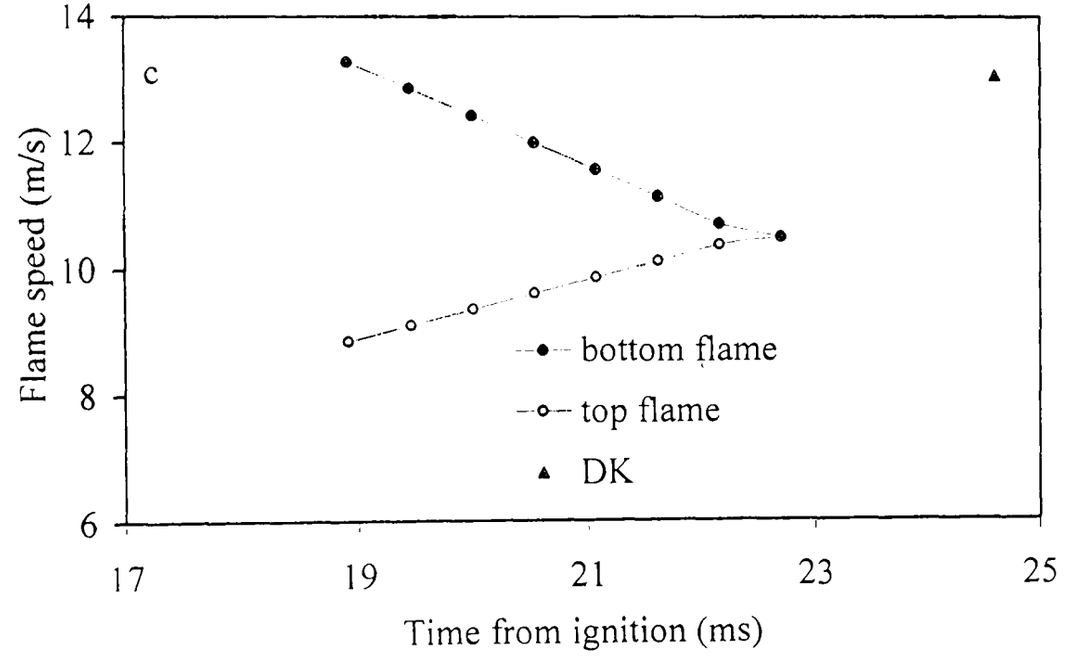

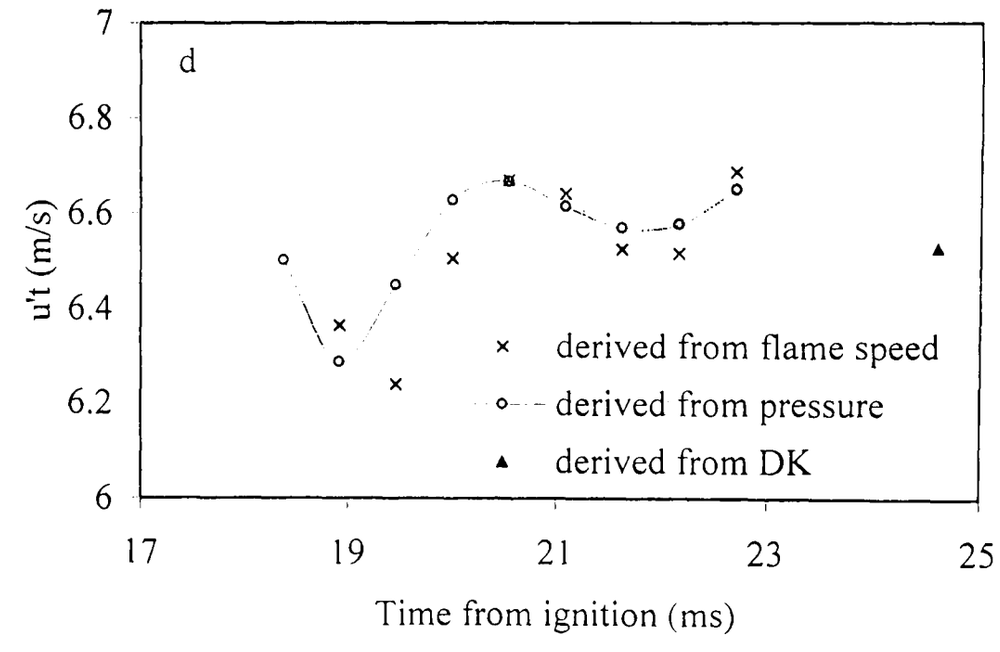

Fig. 7.41. Hydrogen - air implosion, $\phi = 0.3$, $p_o = 0.5$ MPa, $T_o = 358$ K, $u' = 2$

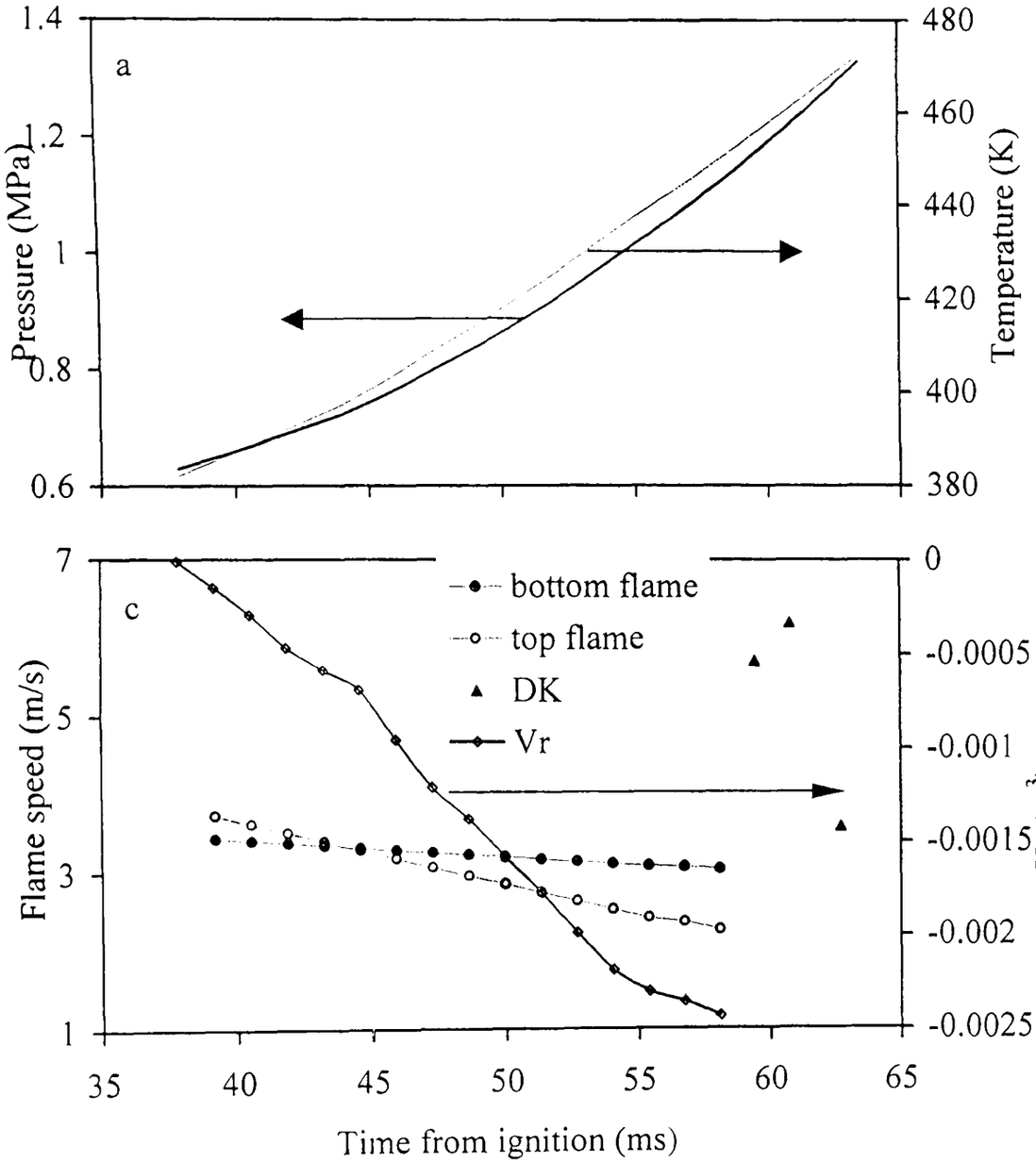

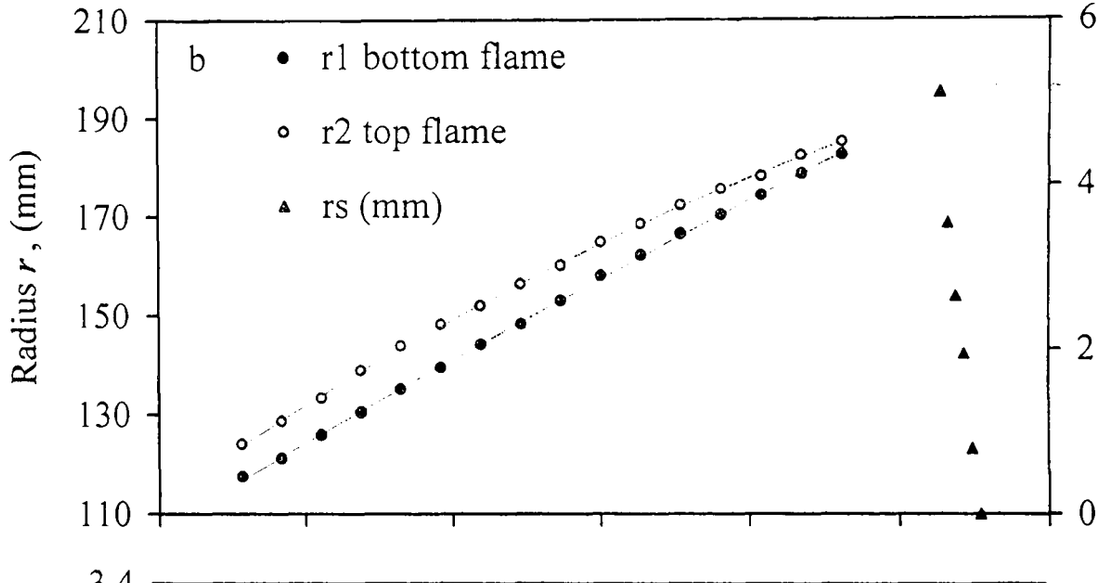

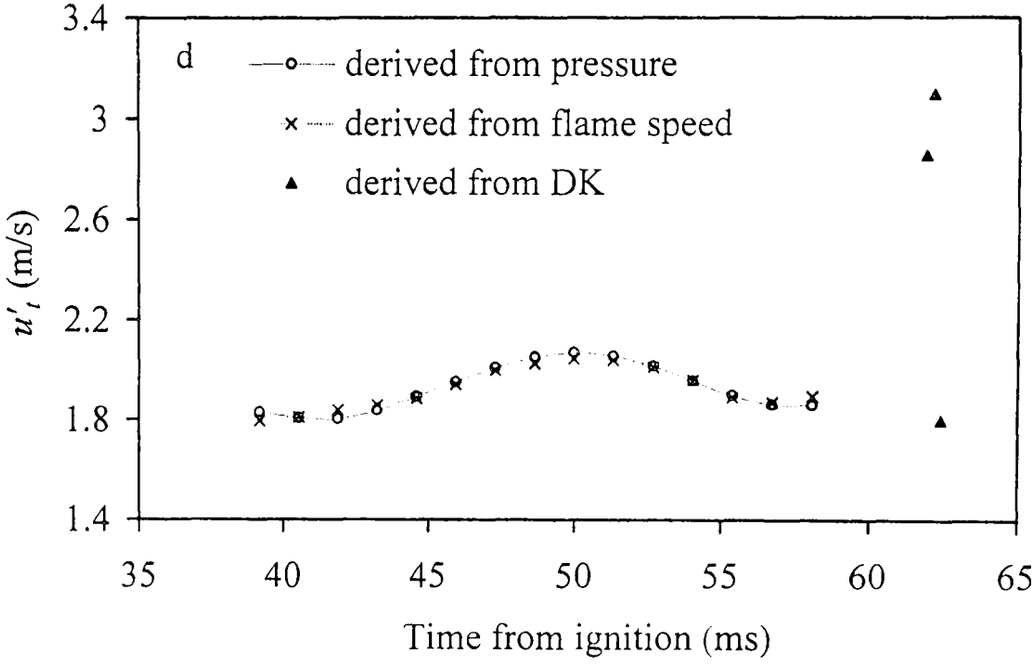

Fig. 7.42. Hydrogen - air implosion, ϕ = 0.4, p_o = 0.5 MPa, T_o = 358 K, u' = 0.25

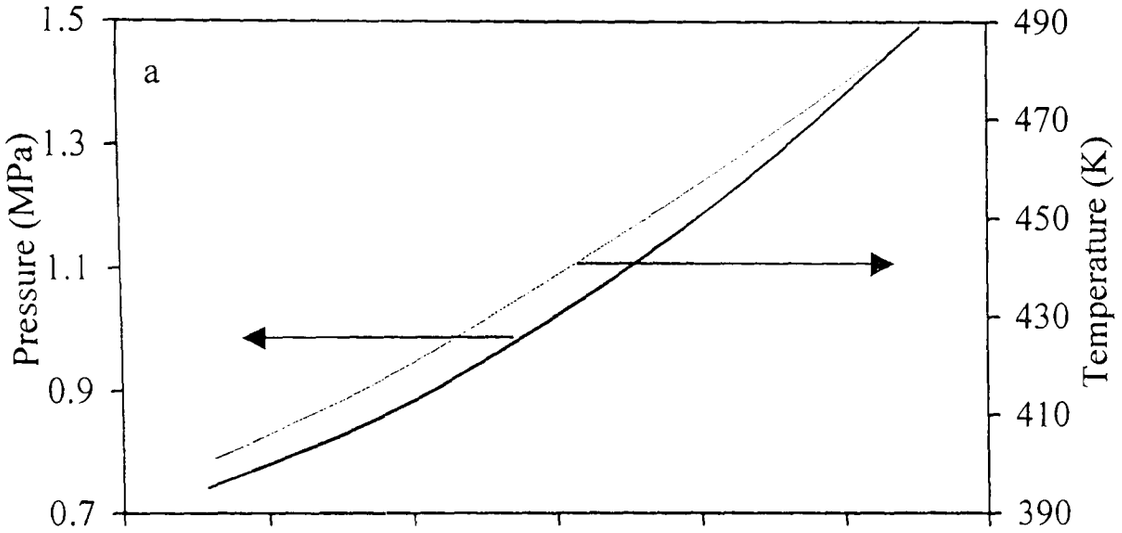

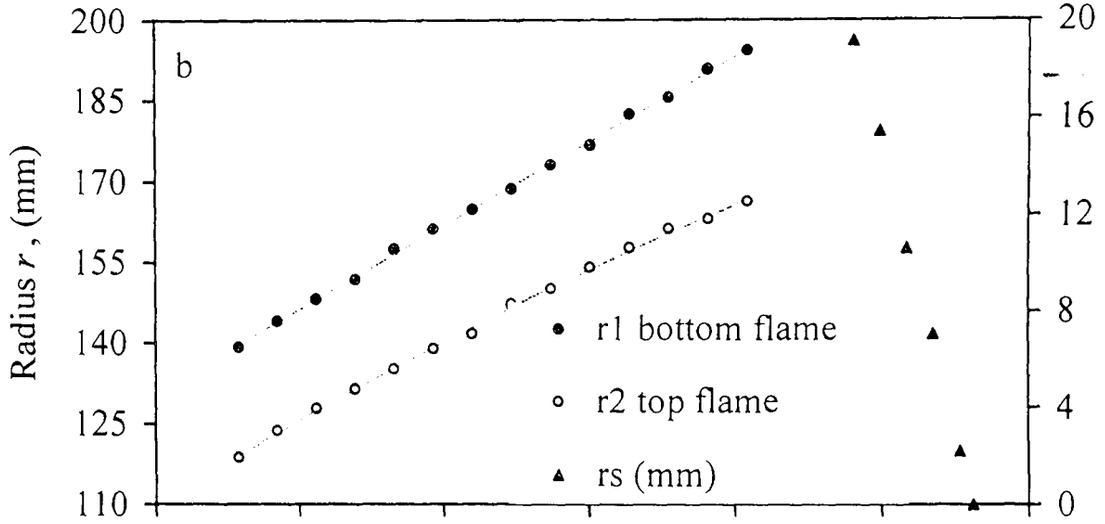

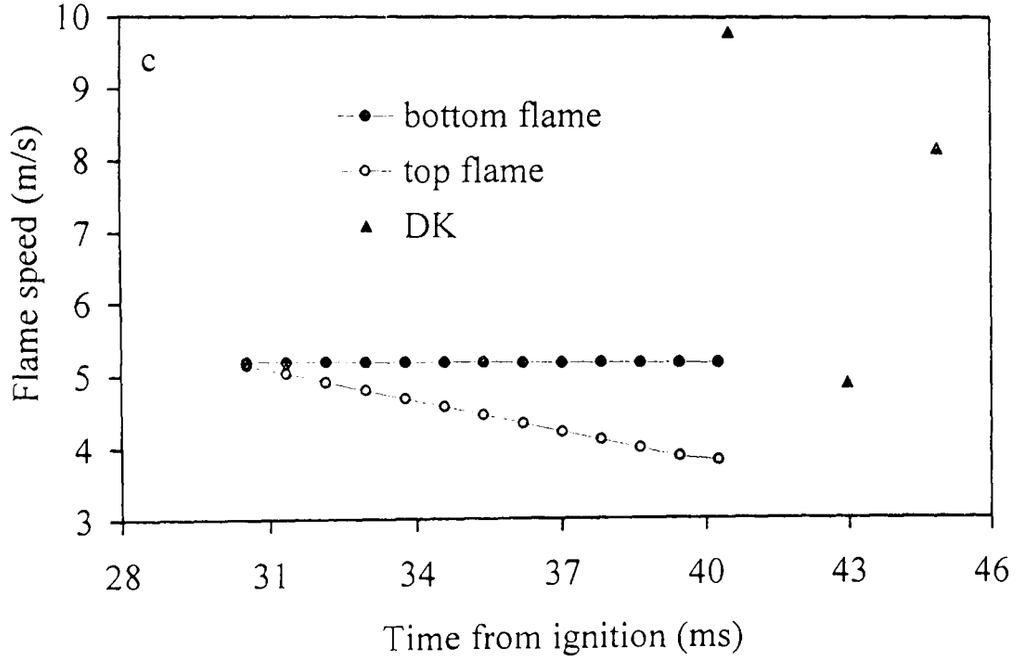

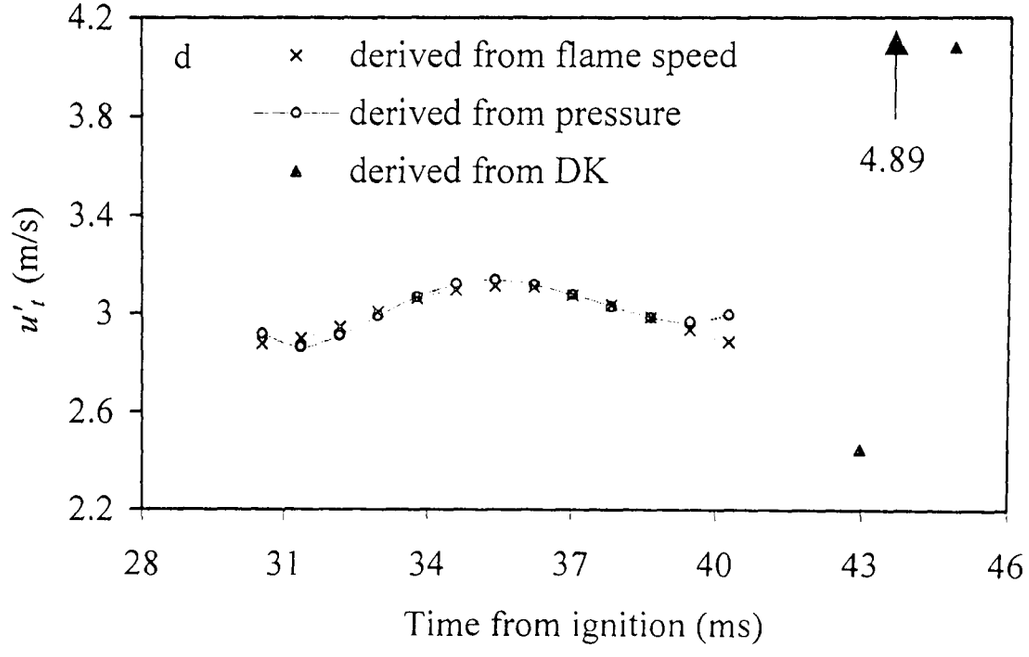

Fig. 7.43. Hydrogen - air implosion, $\phi = 0.4$, $p_o = 0.5$ MPa, $T_o = 358$ K, $u' = 0.5$

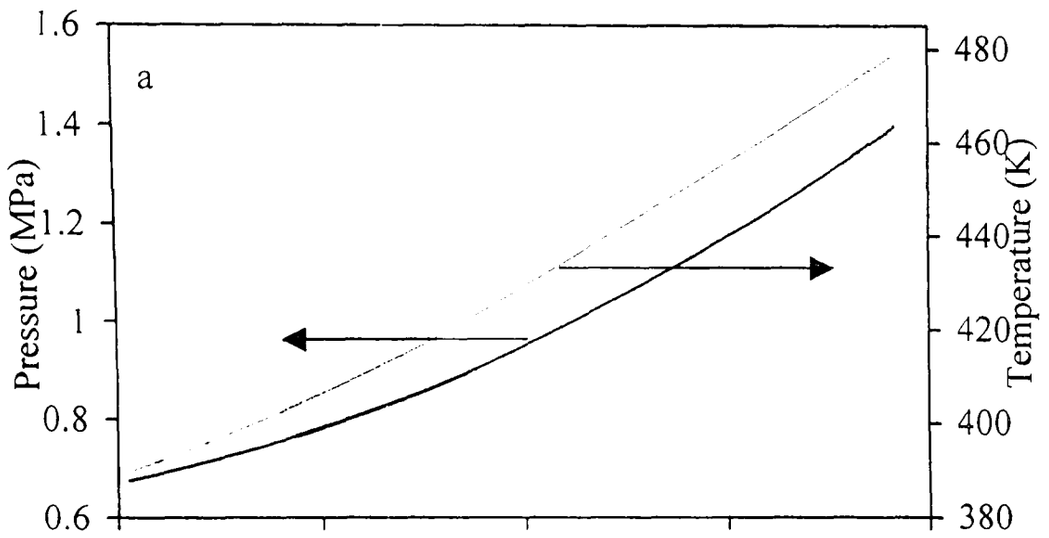

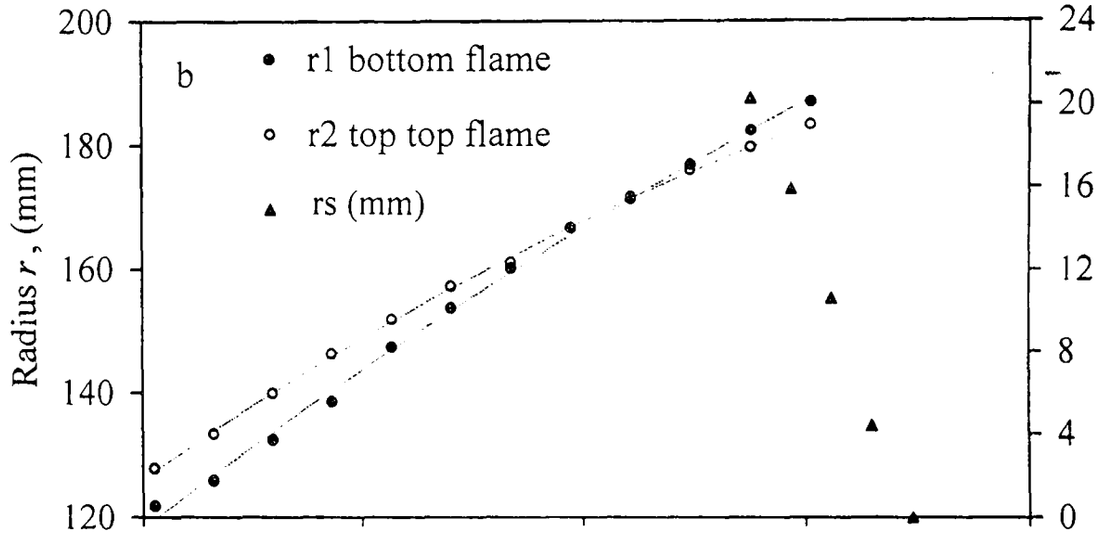

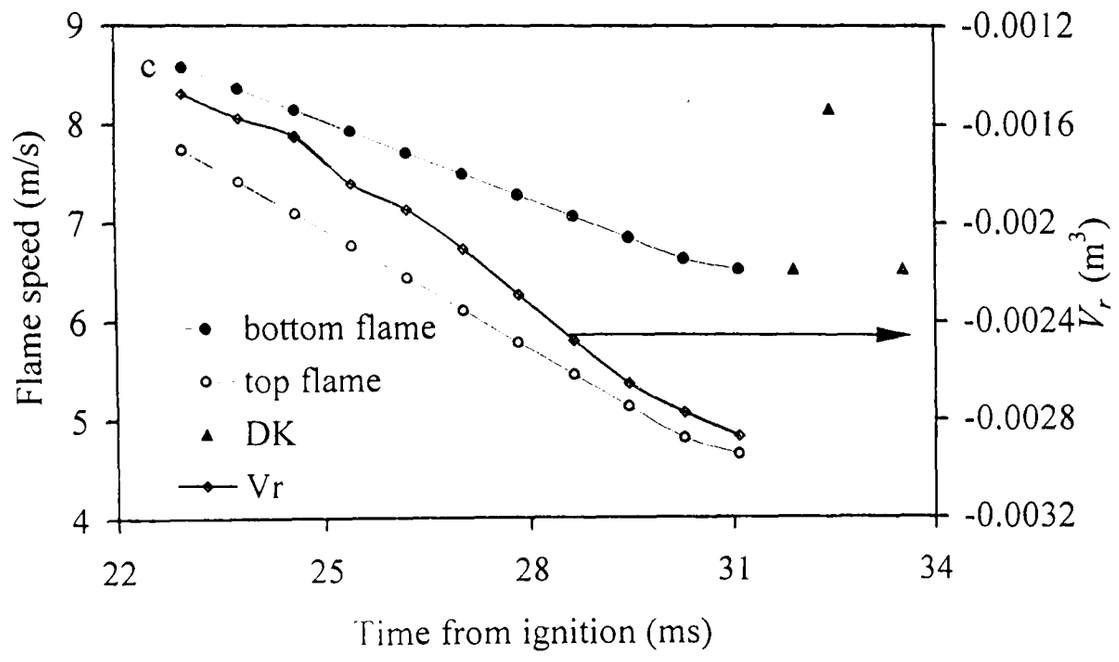

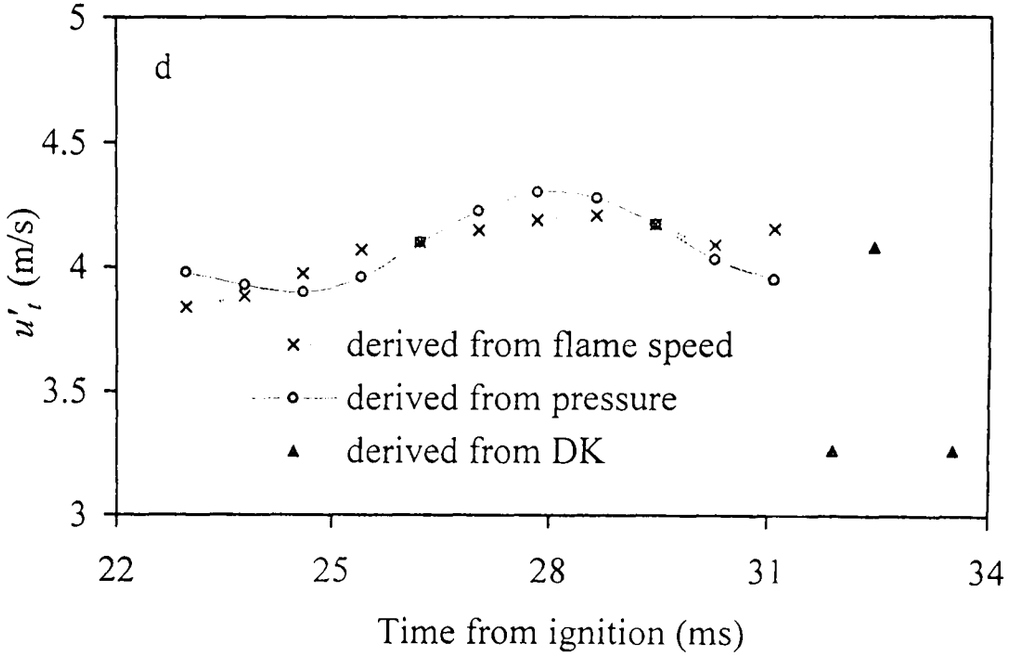

Fig. 7.44. Hydrogen - air implosion, ϕ = 0.4, p_o = 0.5 MPa, T_o = 358 K, u' = 0.75

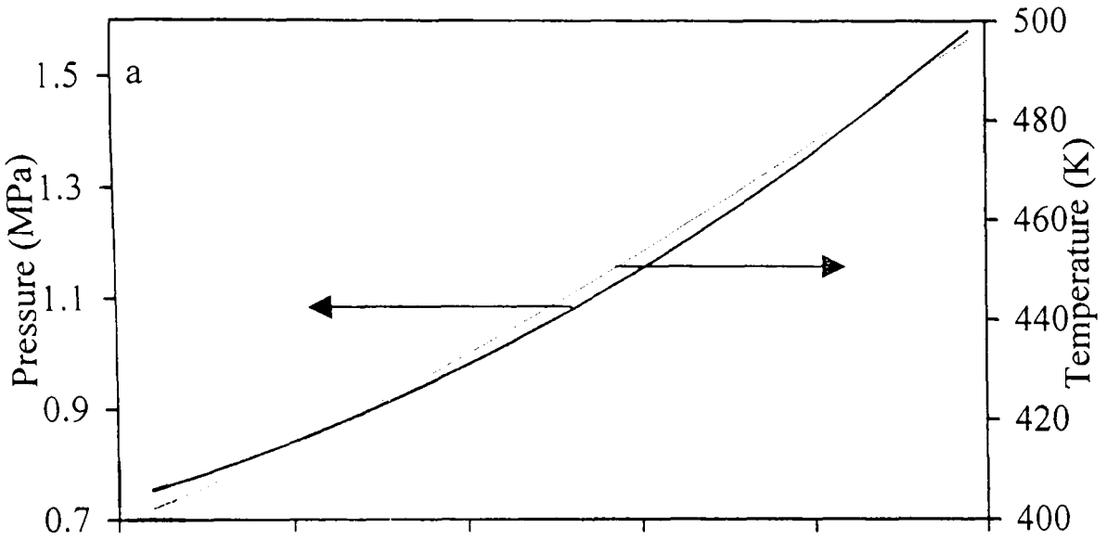

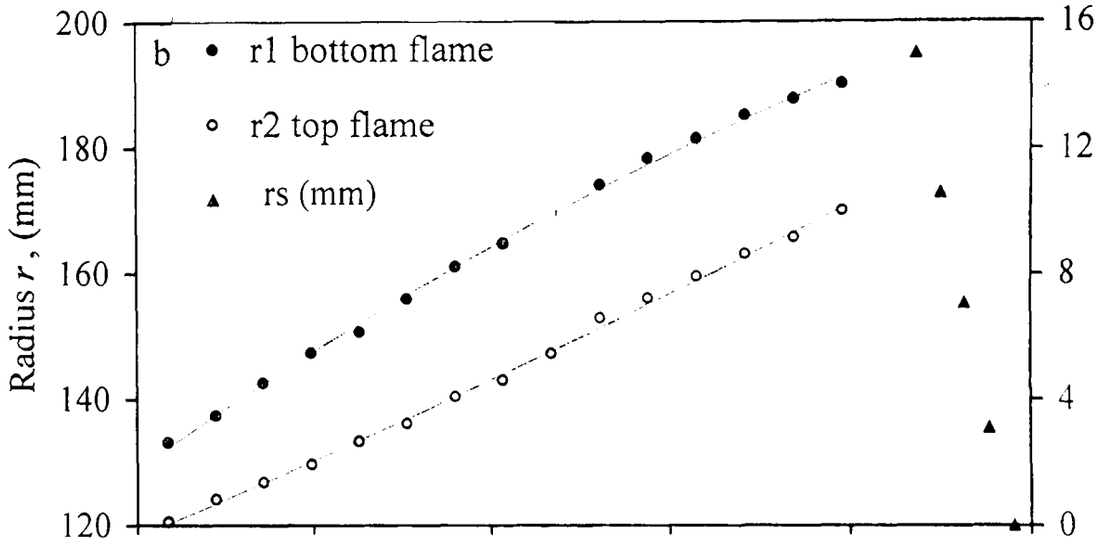

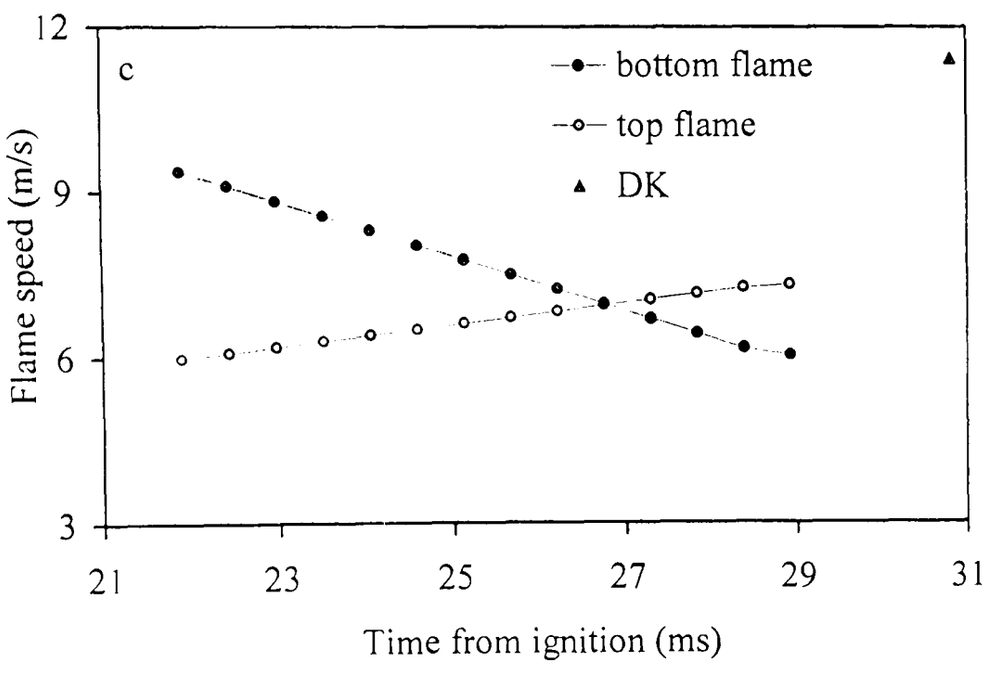

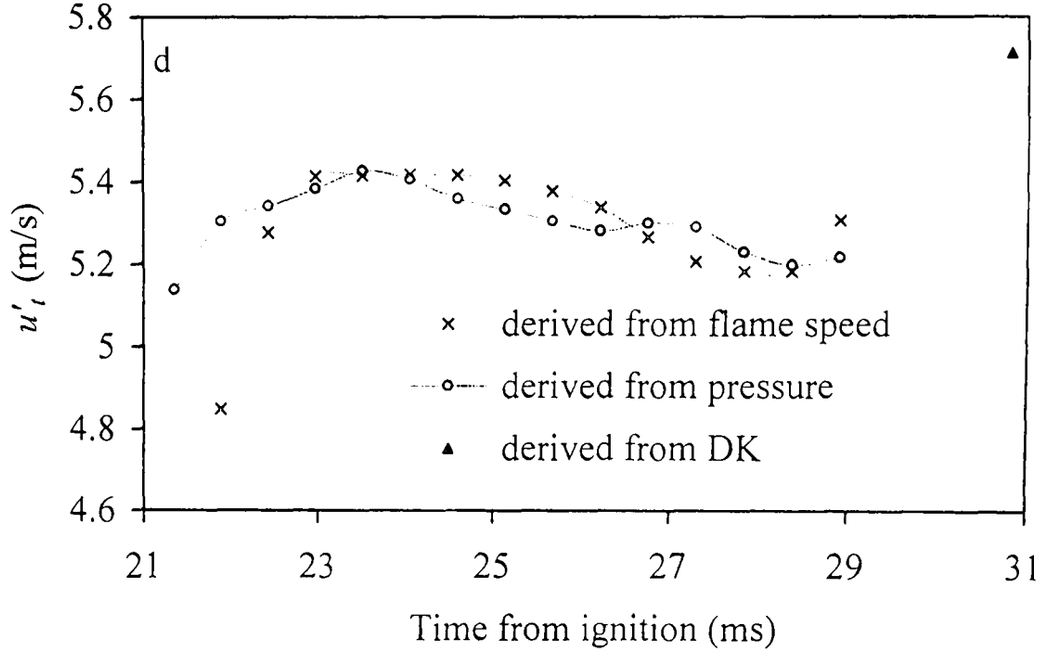

Fig. 7.45. Hydrogen - air implosion, ϕ = 0.4, p_o = 0.5 MPa, T_o = 358 K, u' = 1

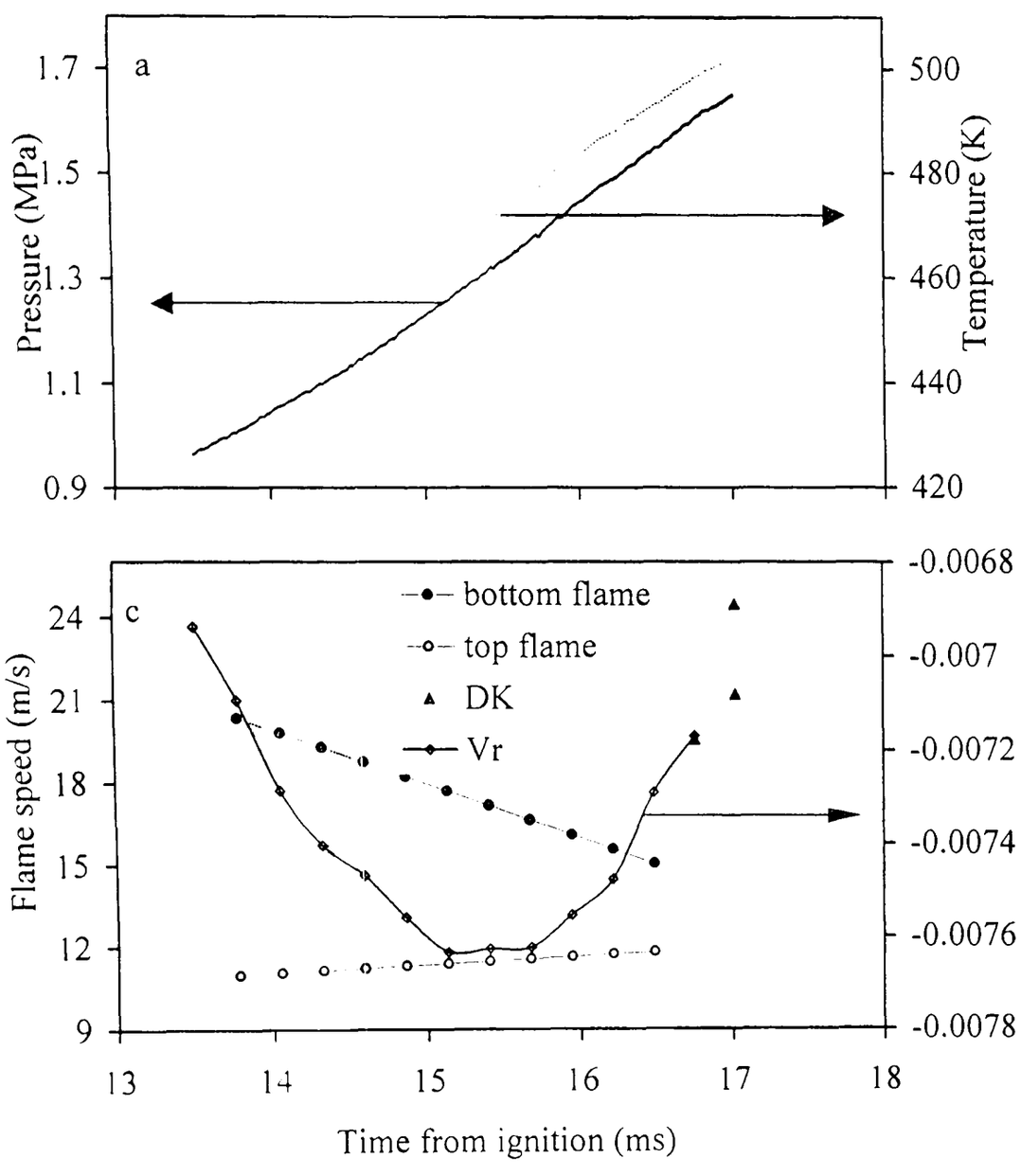

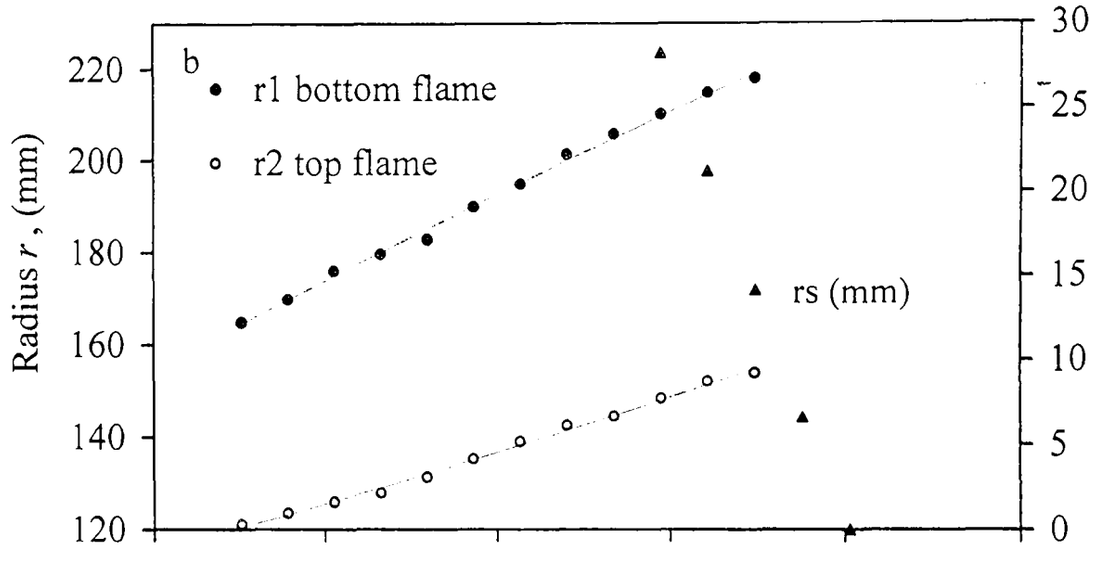

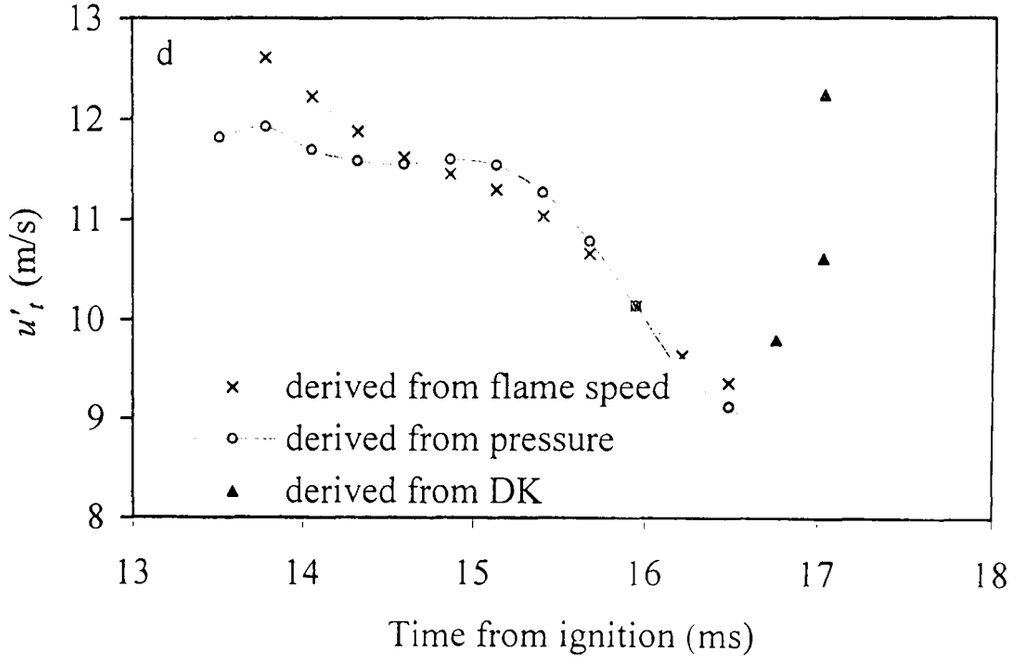

Fig. 7.46. Hydrogen - air implosion, ϕ = 0.4, p_o = 0.5 MPa, T_o = 358 K, u' = 2

Chapter 8

Discussion

8.1 Introduction

This chapter discusses the application of the twin kernel technique, first in the initially laminar flame implosions, then in the turbulent ones. The initially laminar implosions with central ignition demonstrated the importance of flame instabilities and associated increases in burning velocity. These increases are associated with increases in Peclet number, due to the decreasing flame thickness, and the decreasing values of Markstein number with increasing pressure. These effects have been quantified semi-theoretically. In this Chapter they are further discussed and generalized. With regard to turbulent flames, the measured burning velocities are expressed more generally using dimensionless groups. A theoretical approach is applied based on the influence of negative Markstein numbers and instabilities in flamelets.

8.2 Laminar Burning: Central and Twin Ignition

The twin ignition is more difficult to employ than is the central ignition technique, and the processing of the measurements is more time consuming. Its advantage is that it can be employed closer to the maximum operating pressure of the bomb. In terms of measuring burning velocities over a full pressure range, the techniques are complementary.

This is illustrated by reference to explosions of stoichiometric methane – air and iso-octane – air mixtures at initially 0.5 MPa and 358 K. Measurements for these are given in Fig. 3.5 (a) and (b) for central ignition and in Figs. 6.5 and 6.22 for twin ignition. These measured values of u_n are plotted against pressure on Fig. 8.1 and the method of measurement is indicated. Central ignition values, using Eq. (3.8) (optical method) in the initial "pre-pressure" period, are given by the bottom set of symbols. Again with central ignition, but using Eq. (3.22) (pressure method) the pressure rise was measured

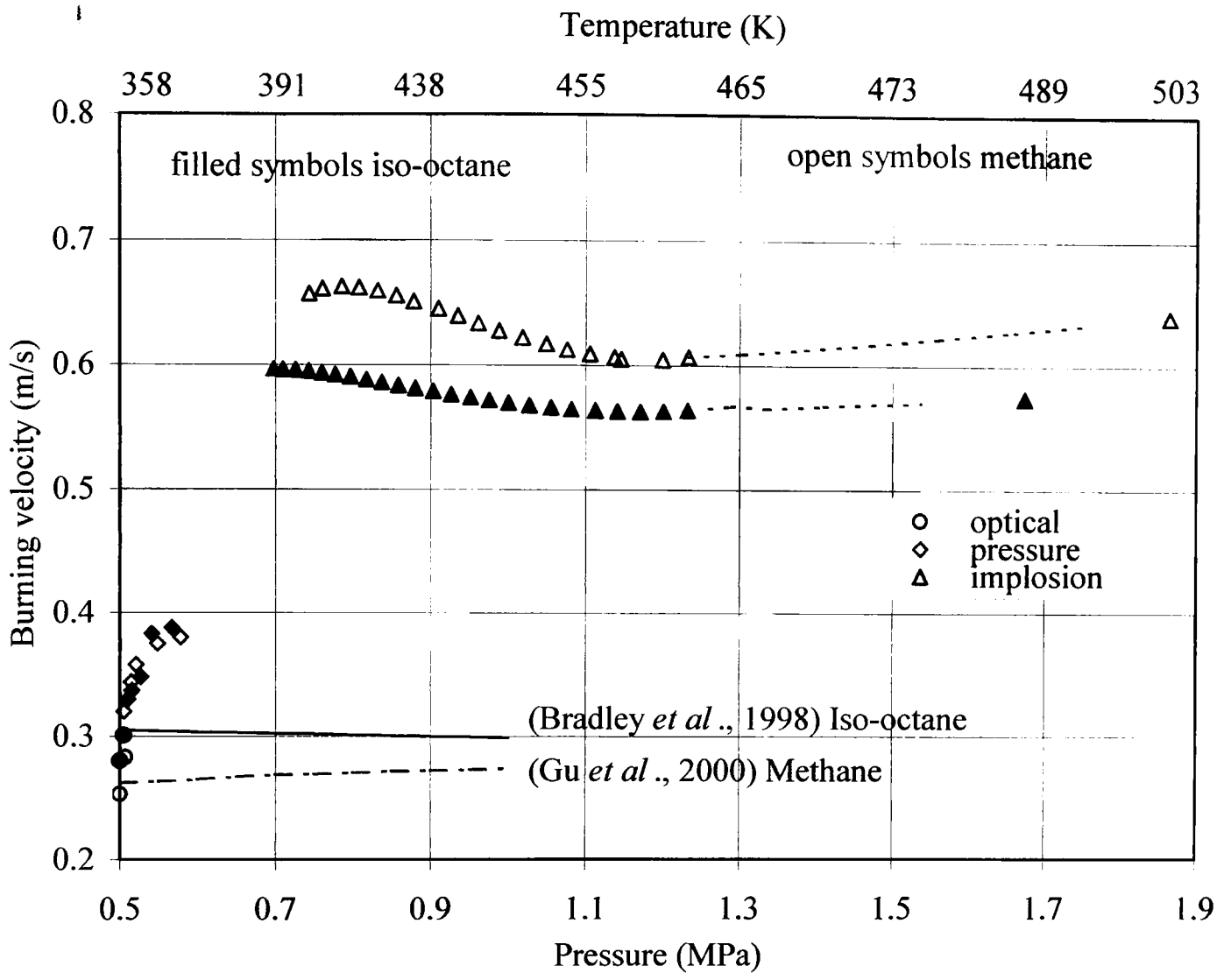

Fig. 8.1. Values of u_n derived from three different methods for stoichiometric iso-octane-air mixture (filled symbols) and methane – air mixture (open symbols), at p_o = 0.5 MPa and T_o = 358 K. Triangle symbols indicate double kernel values.

up to about 0.58 MPa. For twin ignition at the higher pressures (implosion method), Eqs. 4.14 and 4.19 were used. Thereafter, the broken curves are interpolations between these values and those from the double kernel method, indicated by the triangle symbols.

For the Optical Method u_n was plotted against the flame stretch rate during the pre – pressure to give a value of u_ℓ at zero flame stretch rate and the two values are shown for 0.5 MPa. All other values are those of u_n, for flames that soon became unstable and cellular. Shown by the lines at the bottom of the graph are values of u_ℓ originally obtained using the Optical Method. These curves were obtained from previous correlations of the variation of smooth, stable burning velocities with p and T, for iso-octane by Bradley *et al.* (1998), and methane, by Gu *et al.* (2000). In these cases great care was taken to avoid the onset of flame instabilities. The enhancements of u_n above

these values of u_ℓ at the higher pressures have been shown in Chapter 6.2 to be explainable in terms of flame instabilities and wrinkling. Figure 8.1 shows that the early stages of flame propagation from central ignition exhibit some enhancement of burning velocity due to flame instabilities.

8.3 Validity of the Twin Kernel Implosion Technique for Initially Laminar Flames

The agreement between the two different methods of obtaining u_n, described in Section 4.2 for the twin kernel technique, and the general consistency of the results show the technique to be accurate and suitable for obtaining burning velocities at high pressure. The studies also clearly demonstrate the importance of instabilities, even at lower pressures, in enhancing burning velocities.

The other aspect of the twin kernel technique is the application of the modified Bechtold – Matalon theory to obtain values of laminar burning velocity, u_ℓ, from the unstable burning velocity, u_n. For explosions in which u_ℓ and Ma_{sr} are known and the Bechtold – Matalon theory is applicable it has been shown in Section 6.3, by reference to three test explosions, that the approach adopted seems to be valid. Difficulties arise when data on u_ℓ and Ma_{sr} are more sparse and values have to be extrapolated from known values. With regard to the theoretical approach of Bechtold – Matalon, this is only valid for positive values of Ma_{sr}. Otherwise, as described in Chapter 5.3, recourse has to be made to experimental evidence to determine the inner cut–off (lowest wavelength for instability). There is strong evidence that there is a lower limit for this, which in the present study is taken to be $50\delta_\ell$. The limiting value for Ma_{sr} when this value is attained is not clear and more work is required on this question. But perhaps the greatest uncertainty occurs at negative values of Ma_{sr} that are numerically less than those that initially create "saturation" at the lower limit wavelength. Here the instabilities can be so severe initially that even measurements of Pe_{cl} are difficult.

8.4 Values of Laminar Burning Velocity

It follows from the previous Section that more confidence can be placed in some derived values of u_ℓ than others. Shown in summary in Figs. 8.2 and 8.3 are the derived

values of u_ℓ for different values of ϕ for iso-octane-air, at different pressures, p, and temperatures, T. The derived values of u_ℓ appear to be reasonably consistent, with tolerable scatter of the experimental points. Some of the scatter is attributable to the increasingly sparse data on Ma_{sr} and Pe_{cl}, particularly for the richer mixtures at higher pressures, and the inherent difficulty of obtaining these because of flame instabilities. On Fig. 8.3 the curve crossing with ϕ=1.0 and 1.1 is probably anomalous. Resolution of the problem is not helped by the gap in the data between the initial pressure and the next closest higher pressure. Measurements are least accurate with the smaller flame surfaces when these have just come into the field of view. Consequently, the accuracy of the values of u_ℓ was least for these early values.

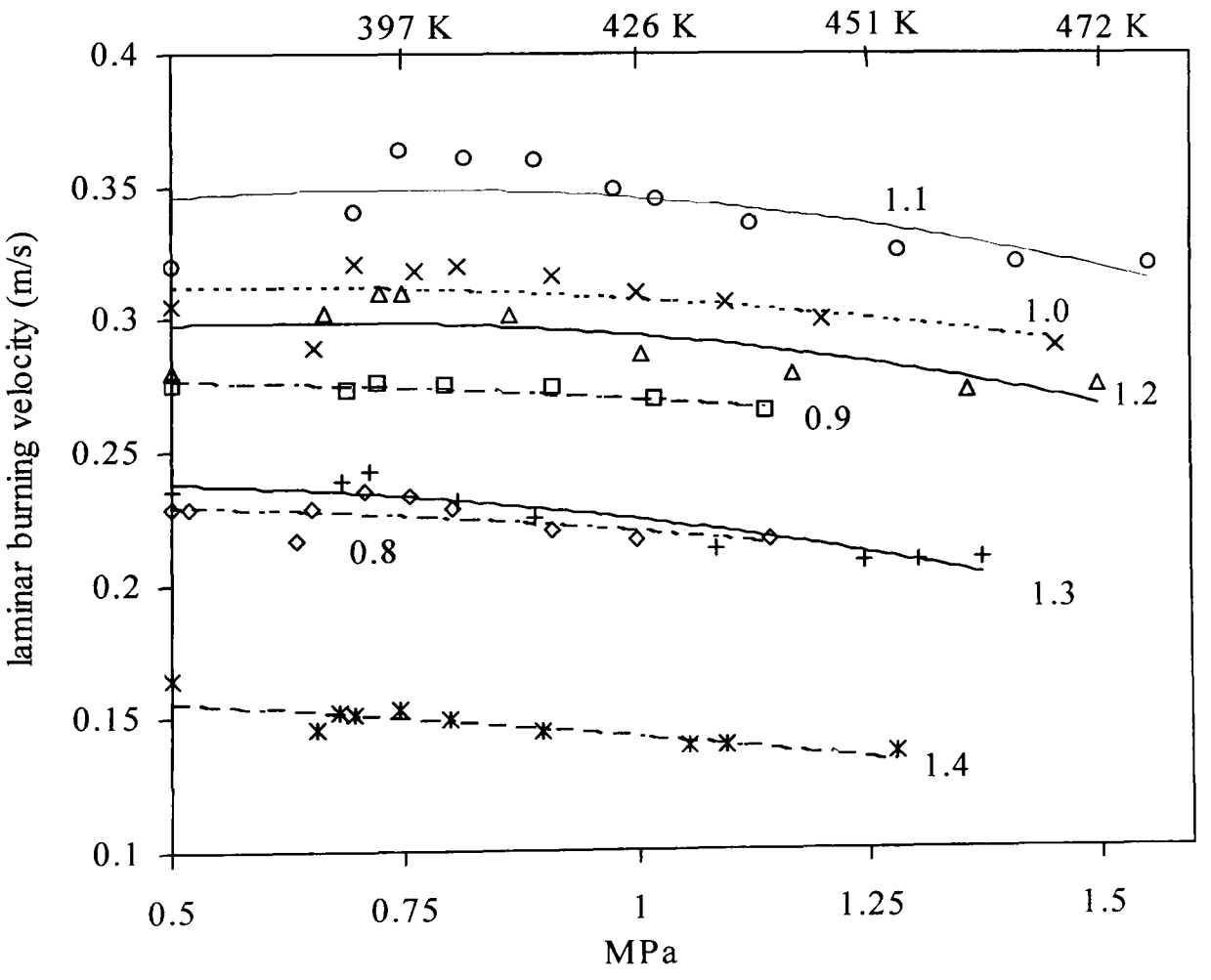

Fig. 8.2. Values of u_ℓ derived from twin kernel measurements for different values of ϕ for iso-octane-air. Initial conditions 0.5 MPa and 358 K.

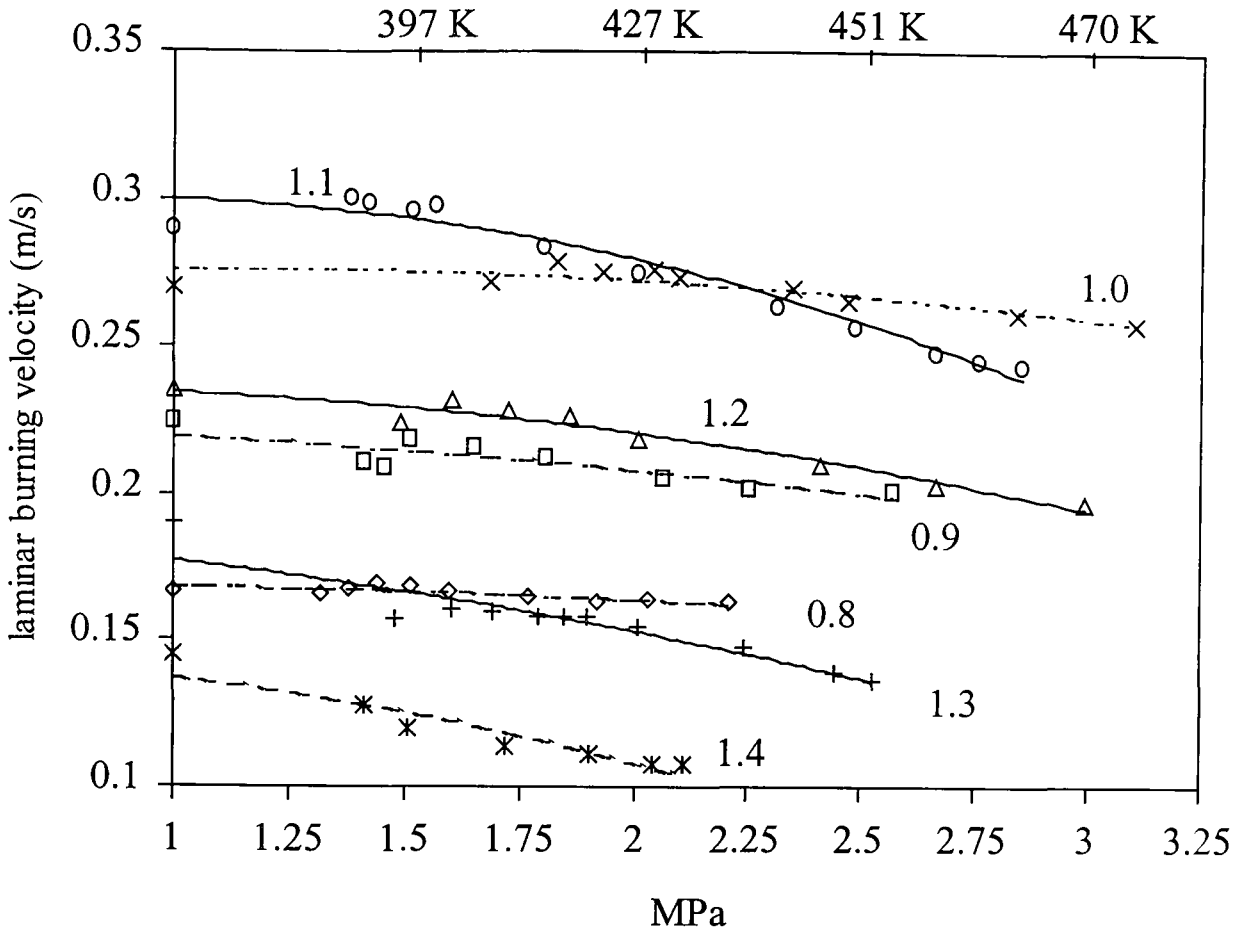

Fig. 8.3. Values of u_ℓ derived from twin kernel measurements for different values of ϕ for iso-octane-air. Initial conditions 1.0 MPa and 358 K.

Figure 8.4 shows the derived variation of u_ℓ at 2.0 MPa and 427 ± 2K for different values of ϕ. Also shown is the variation of the values of the burning velocity, u_n, at this condition. The data on Fig. 6.27, shown in Section 6.3, exhibit a value of enhancement factor, F, of 1.42 at 0.29 MPa, for a mixture that might otherwise have been assumed to be stable. Those on Fig. 8.4 for 2.0 MPa show F (broken curve) attains a value as high as 6.6, due to the increasingly negative values of Ma_{sr} for richer mixtures. Unlike values of u_ℓ, those of u_n are not physicochemical properties, but ones that depend on the history of their development and which would change even if p and T remained constant. The values of F increase continuously with ϕ, due to the decreasing values of Ma_{sr}. These also tend to increase u_n, but with an increase in ϕ for the richer mixtures this is countered by a decrease in u_ℓ and u_n begins to fall.

Derived values of u_ℓ are plotted against ϕ in Figs. 8.5 and 8.6 for different values of pressure and temperature, shown on the Figures. Figure 8.5 is for two different pressures and temperatures in isentropic compression from 0.5 MPa and 358 K. Values

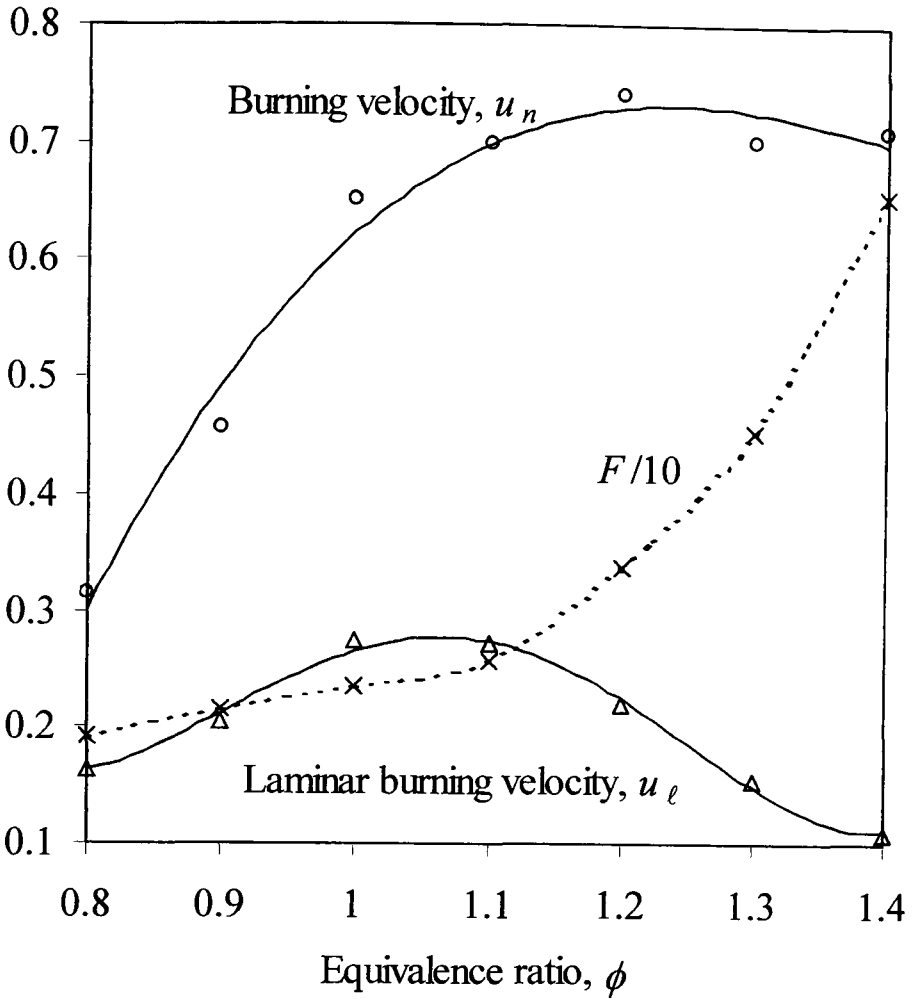

Fig. 8.4. Variations of u_n, F and u_ℓ with equivalence ratio at 2.0 MPa and 427 K. Iso-octane-air, initial conditions 1.0 MPa and 358 K.

of pressures on the figure in MPa are followed by those of temperature. Also shown by the topmost curve, for comparison, are values measured by Davis and Law, (1998) under atmospheric conditions. Shown in Fig. 8.6 are the laminar burning velocities at five different pressures and temperatures in isentropic compression from 1 MPa and 358 K. The lowest curve for 3.0 MPa rests upon only two measured points and the general shape of the other curves.

The present work confirms an earlier study (Bradley *et al.*, 2002) that showed laminar burning velocities of iso-octane-air mixtures tended to decrease slightly with isentropic compression and not increase, as suggested by some previous experimentalists. It also can be seen on Figs. 8.2, 8.3 and Figs. 8.5, 8.6 that u_ℓ tends to decrease more sharply with increasing temperature and pressure during such compressions with rich mixtures than with lean ones. Note, from Fig. 6.27, that CH_4-air mixtures exhibit an opposite trend in that u_ℓ tends to increase with isentropic compression.

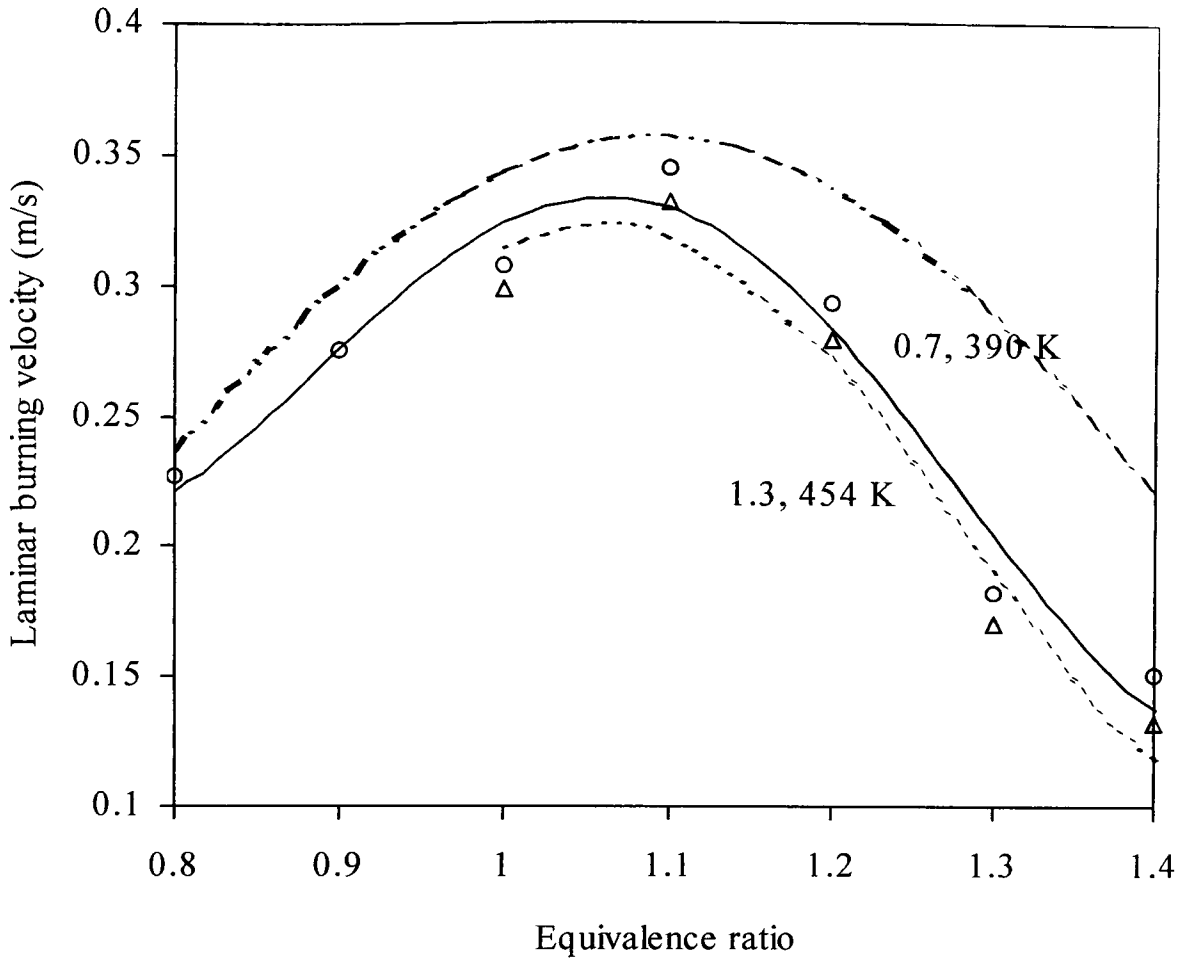

Fig. 8.5. Laminar burning velocity at two different pressures and temperatures in isentropic compression from 0.5 MPa and 358 K. Pressures in MPa followed by temperature. Topmost curve are values from Davis and Law, (1998) under atmospheric conditions.

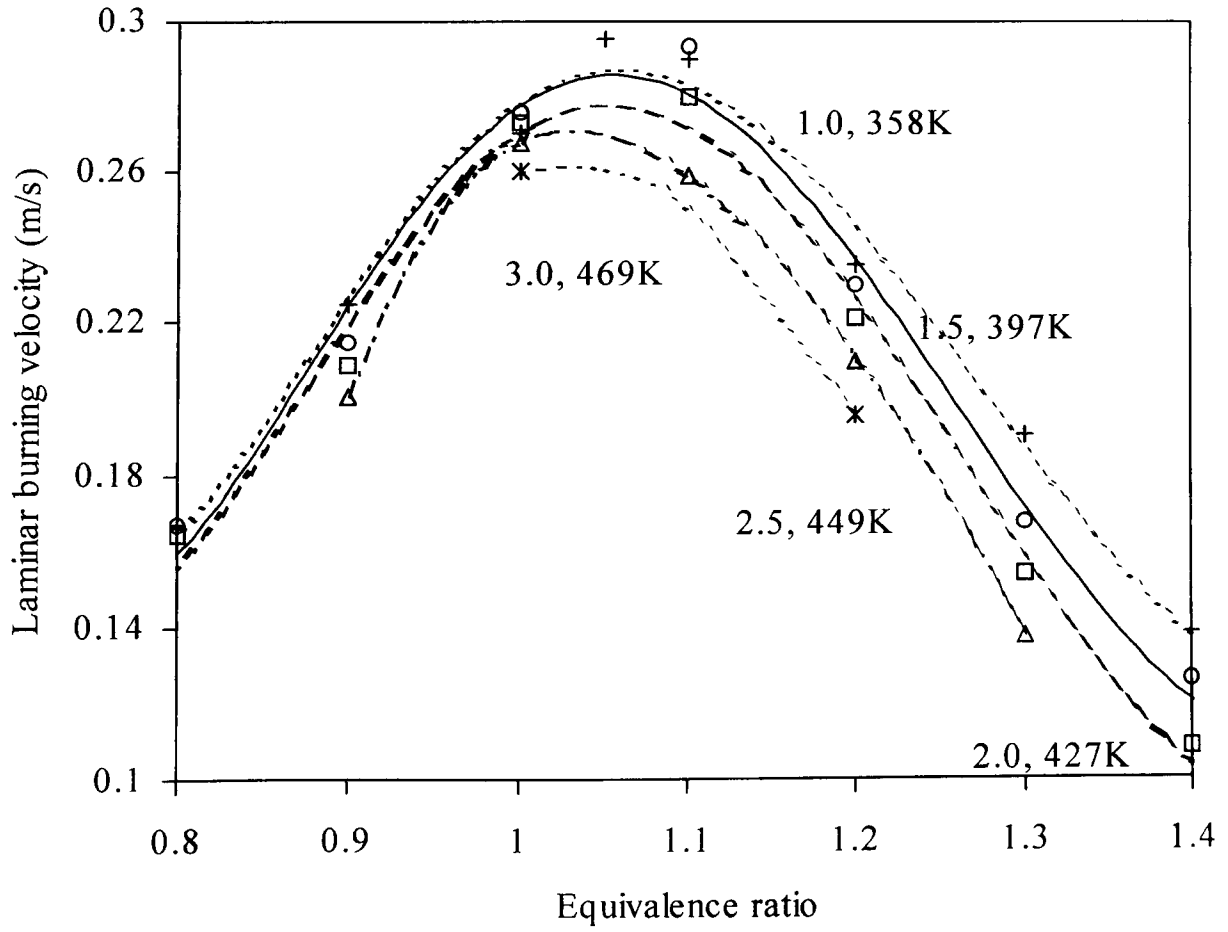

Fig. 8.6. Laminar burning velocity at five different pressures and temperatures in isentropic compression from 1.0 MPa and 358 K. Pressures in MPa followed by temperature.

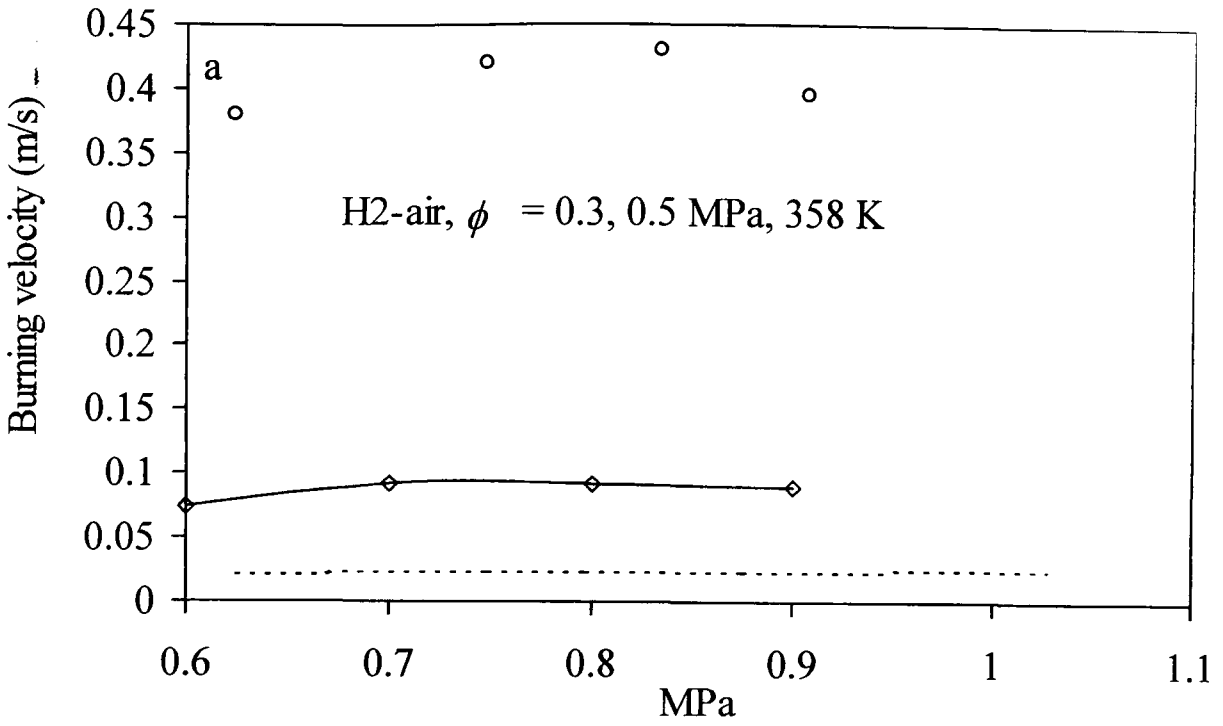

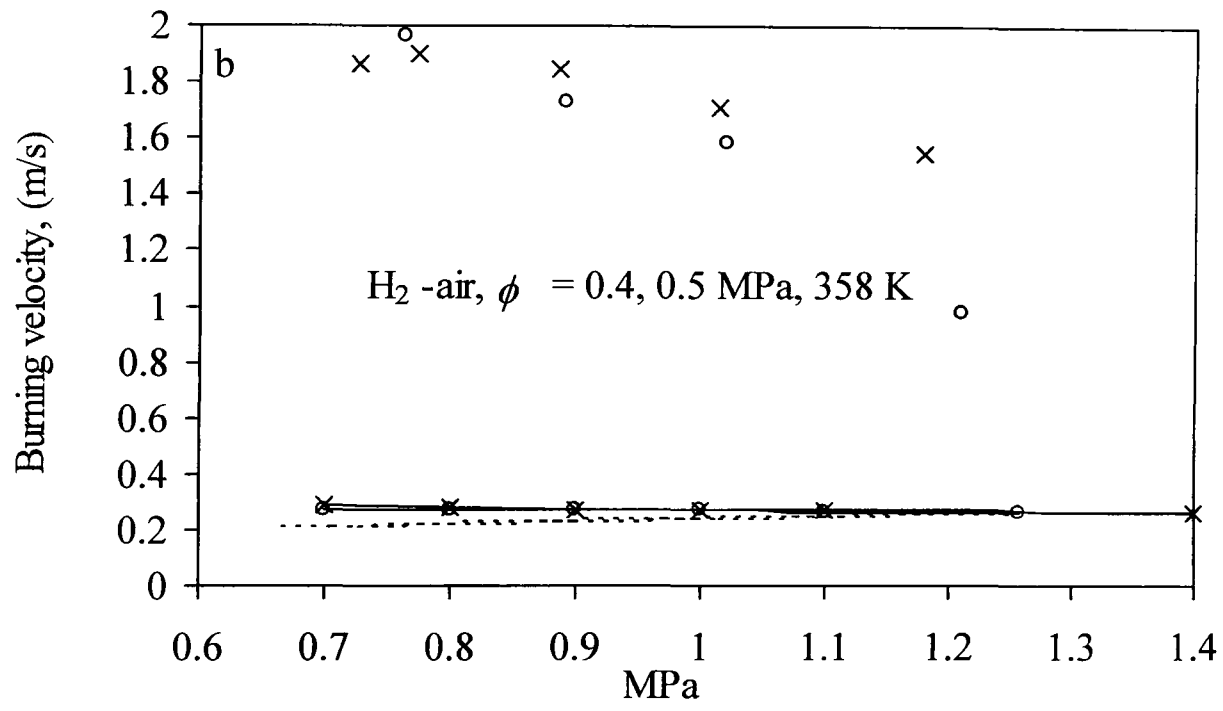

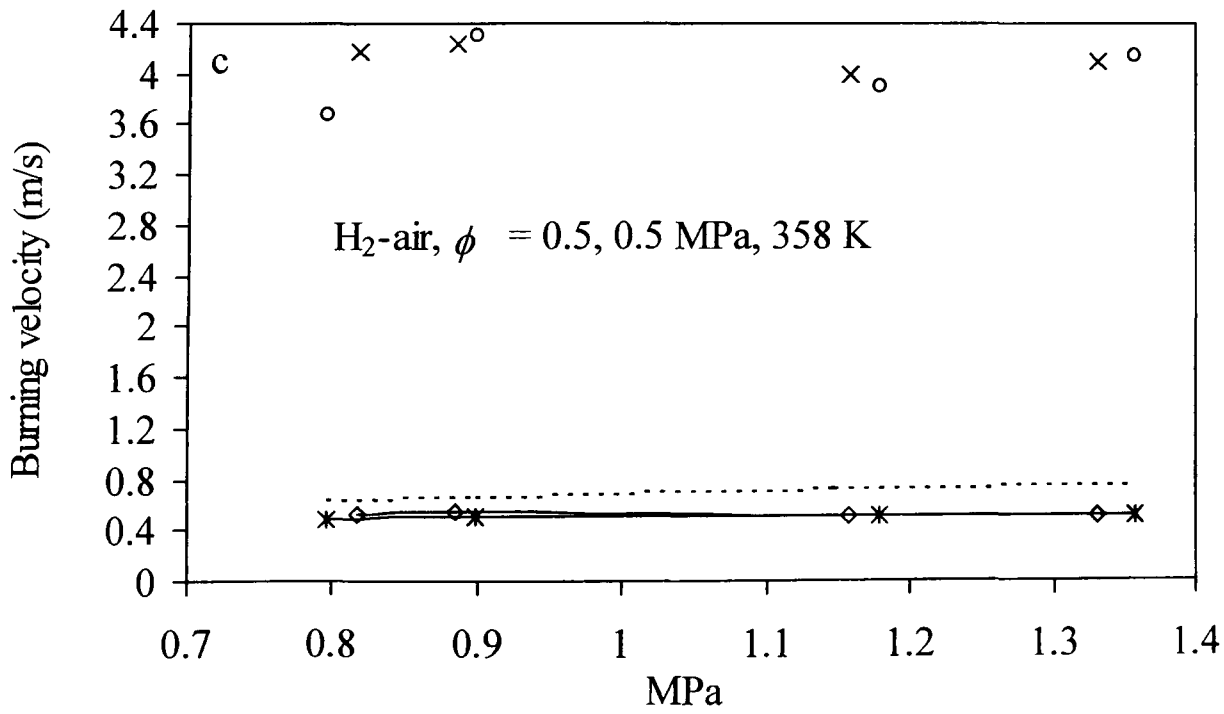

Fig. 8.7. Experimental values of u_n from two implosions of lean hydrogen-air initially at 0.5 MPa and 358 K, (a) $\phi = 0.3$, (b) $\phi = 0.4$ and (c) $\phi = 0.5$ (upper symbols). Lower symbols show values of u_ℓ predicted from these, compared with computed values from Verhelst *et al.*, (2004) (broken curves).

It would appear that earlier reported increases in u_ℓ in such compressions of iso-octane-air, which varied significantly between different researchers at higher pressures, were probably a consequence of flame instabilities. This is not only of practical, but also of theoretical importance, in that laminar burning velocities derived from chemical kinetic, one-dimensional, models can only be validated against experimental measurements in which either there is no inherent instability or the effects of it have been removed.

For the results for hydrogen –air mixtures, shown in Figs. 8.7 (a), (b) and (c) the symbols show derived values of u_ℓ for $\phi = 0.3$, 0.4, and 0.5, plotted against pressure. The broken curves give values of u_ℓ obtained by Verhelst *et al.* (2004), from the CHEM 1D code for these different pressures and temperatures. It can be seen from the figures that u_ℓ tends to increase slightly with isentropic compression. However, the agreement between the two sets of values for the leanest condition, $\phi = 0.3$, is unsatisfactory. The issue was discussed in some detail with Professor G. Dixon-Lewis. He was of the view that the most likely explanation of the disagreement lay in the inadequacies of the species diffusion fluxes at low values of ϕ in the model.

8.5 The Rapid Increase in u_n for Unstable Iso-octane Rich Iso-octane Mixtures

With $\phi > 1.4$ the pressure records for iso-octane – air mixtures, p_o = 1 MPa, $\phi = 1.5$ and 1.6 in Figs. 6.16 and 6.18 reveal the development of strong oscillations at about 2.4 MPa. These are also associated with sharper increases in u_n. Shown in Fig. 8.8 for $\phi =$ 1.5, are measured values of u_n plotted by the circle symbols against pressure and below these, the apparent values of u_ℓ derived from these. These latter values are different from those with $\phi \leq 1.4$ in that u_ℓ is seen to increase with compression. This and the pressure oscillations that can be seen on Fig. 6.16 suggest an additional phenomenon might be affecting the burning rate. One possibility is that autoignitive reactions might be significant ahead of the flame front.

To explore this possibility, the autoignition integral

$$i = \int_{t=0}^{t_i} \frac{dt}{\tau_{(T,p)}} \tag{8.1}$$

was evaluated. Here $\tau_{(T, p)}$ is the ignition delay time at the instantaneous values of T and p, at the elapsed time, t, from the start of the end-gas compression process ($t = 0$), and t_i is the time up to which the integral is evaluated. When the integral attains a value of unity autoignition occurs (Heywood, 1988).

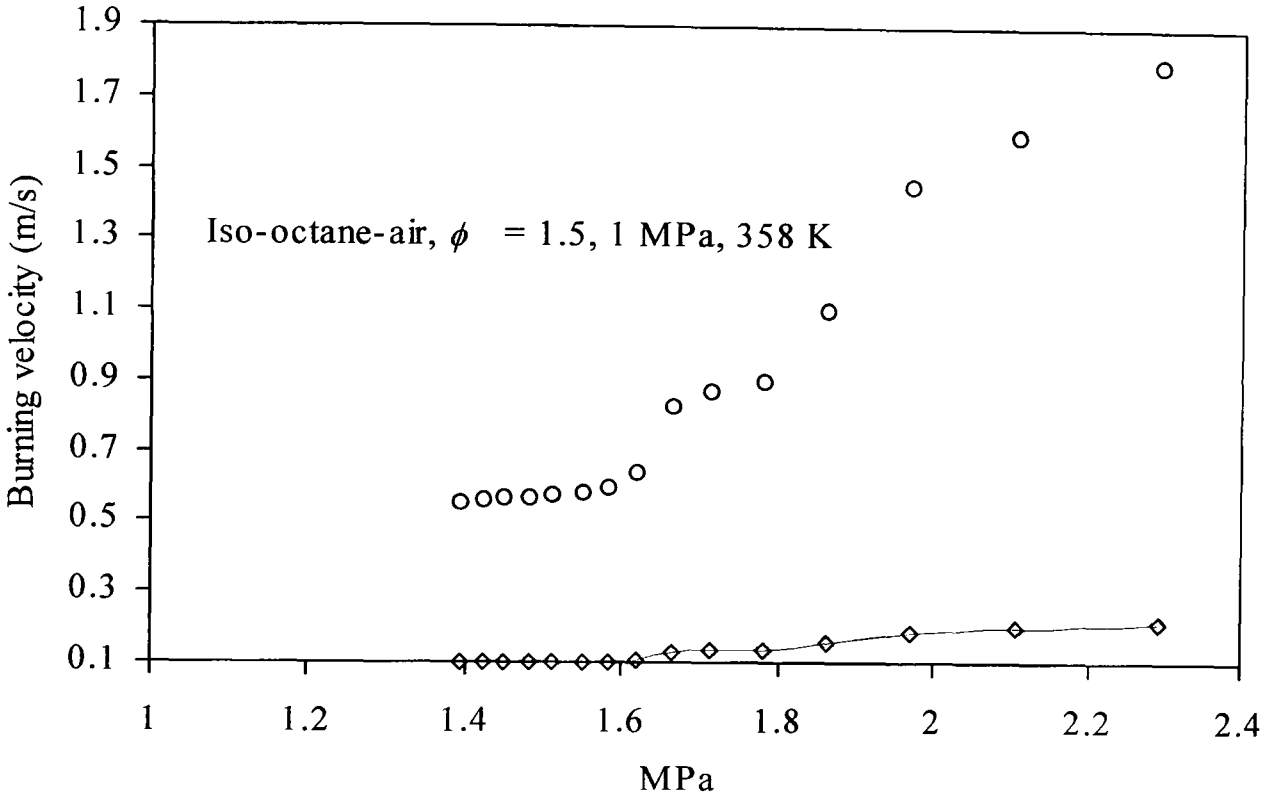

Fig. 8.8. Experimental values of u_n from one implosion of rich ($\phi = 1.5$) iso-octane - air initially at 1 MPa, and 358 K (upper symbols). Lower symbols show apparent values of u_ℓ derived from these.

A worst case condition was chosen for the evaluation of the of the integral: namely, that the values of $\tau_{(T, p)}$ be those computed by Peters *et al.* (2002) for stoichiometric heptane – air and shown in Fig. 8.9. These values are significantly lower than those for iso – octane air. Interpolations had to be made for the appropriate values of p and T corresponding to the explosions at $\phi = 1.5$ and 1.6. The values of the integral, at the different times are given on Figs. 8.10 and 8.11, respectively. For $\phi = 1.5$, i was no higher than 0.021, and at $\phi = 1.6$, i was no higher than 0.031. As a consequence of this analysis, it is legitimate to conclude that autoignition was not a cause of this sudden increase in the burning velocities, u_n for these unstable flames.

Another possible explanation of the enhanced values of u_n and u_ℓ is that they arise from further wrinkling of the flame due to Taylor instabilities (Bradley and Harper, 1994).

The rapid rise in u_n due to flame instabilities might contribute to a further feed-back mechanism through the generation of strong pressure oscillations that contribute to further flame wrinkling.

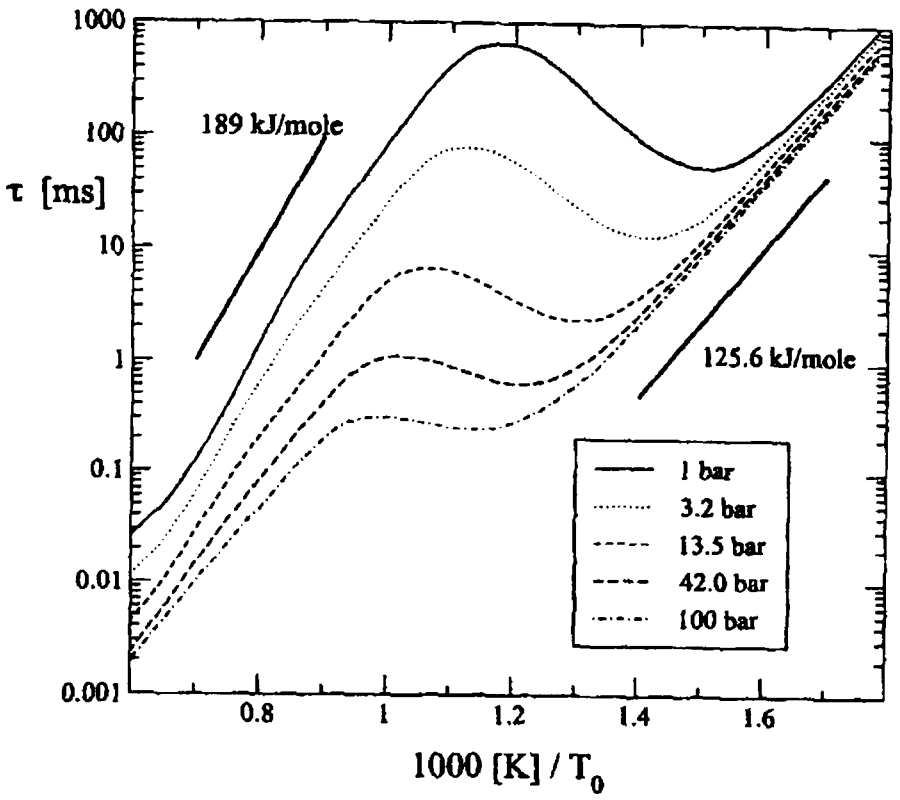

Fig. 8.9. Ignition delay times for stoichiometic n-heptane mixtures at different pressures, Peters *et al.* (2002).

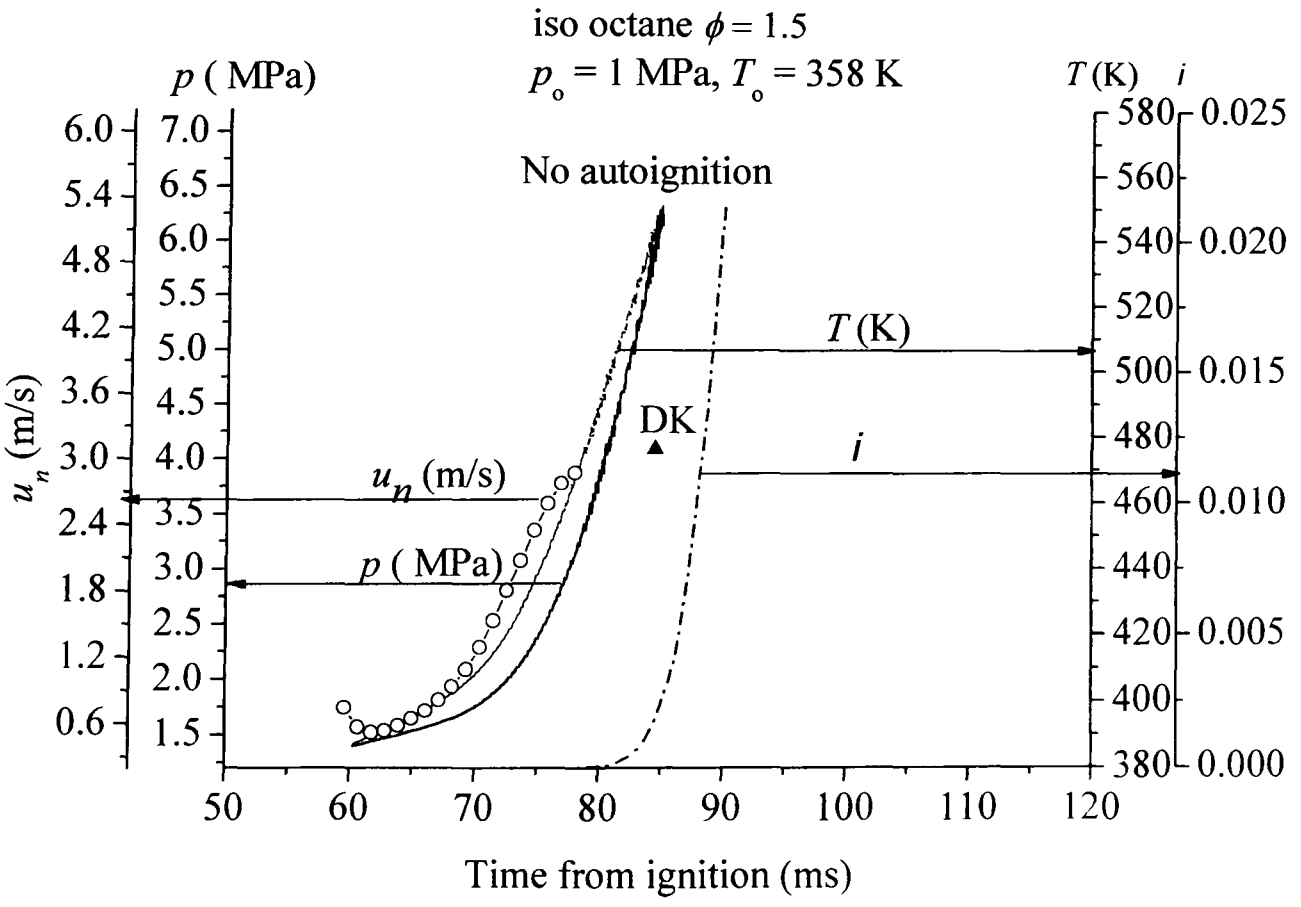

Fig. 8.10. Integral values, i, for laminar iso-octane flame, ϕ = 1.5, p_o = 1 MPa, T_o = 358 K at the appropriate p and T and u_n values for which measurements were made.

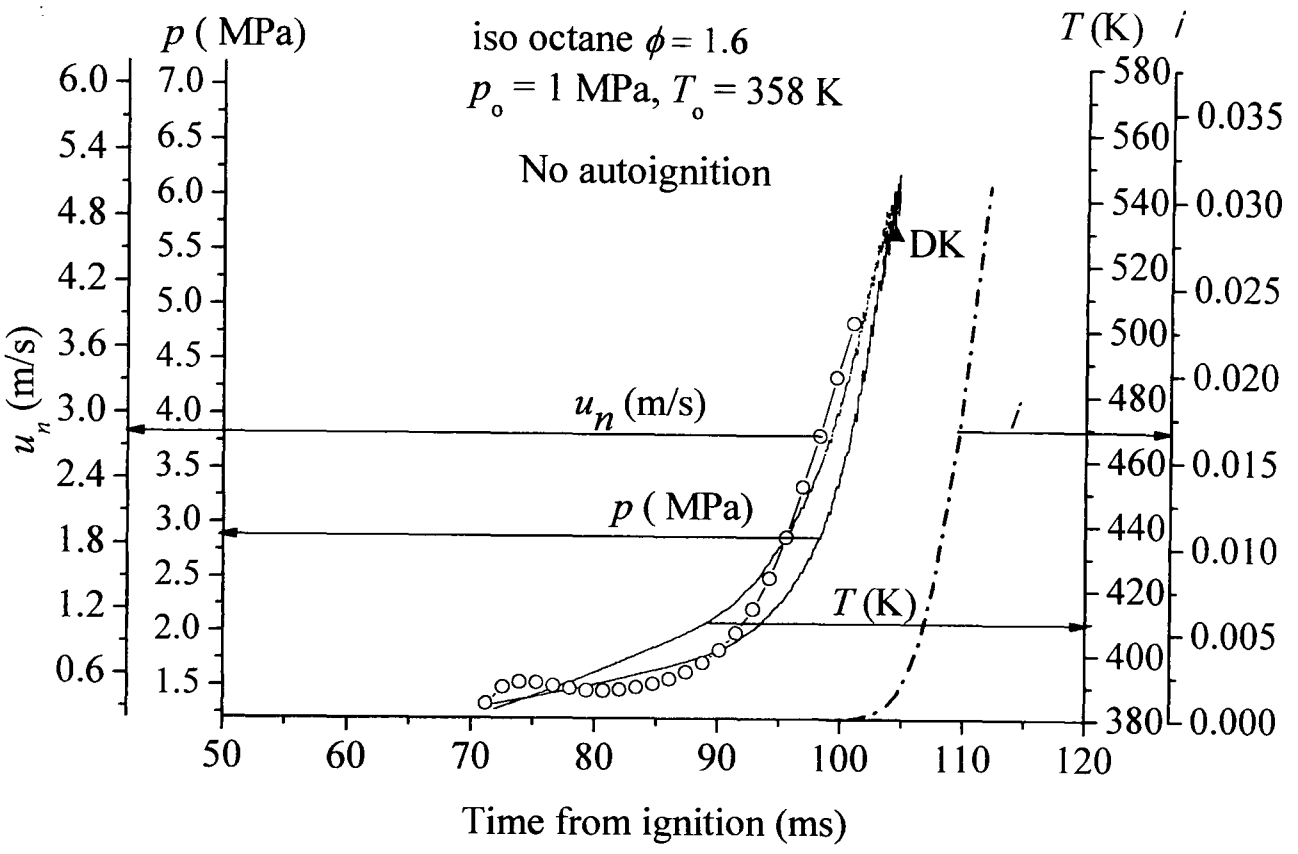

Fig. 8.11. Integral values, *i*, for laminar iso-octane flame, ϕ = 1.6, p_o = 1 MPa, T_o = 358 K at the appropriate *p*, *T* and u_n values for which measurements were made.

8. 6 Correlations of Turbulent Burning Velocity

Correlations of u_t have been expressed in terms of $U_* = u_t/u'_k$, as a function of either the Damköhler number (Peter, 2000), or the turbulent Karlovitz stretch factor, *K*, sometimes with additional influences of *Le* or the Ma_{sr} (Bradley, 2002 and Brutscher *et al.*, 2002). From Equations (7.8), (7.10) and $\delta_\ell = \nu/u_\ell$, it can be shown that $K = 0.25\,(u'/u_\ell)^2\,R_l^{-0.5}$.

At higher pressures and temperatures, for the reasons already discussed, there is a problem in obtaining reliable values of u_ℓ. The derivation of values through detailed chemical kinetic modelling is difficult because of the relatively more frequent three body reactions, the rate constants for which are not accurately known at high pressures. Consequently, the currently measured values of u_t given in Figs. 8.2 to 8.7 were used throughout, supplemented by those in Bradley *et al.* (1998), for the current study.

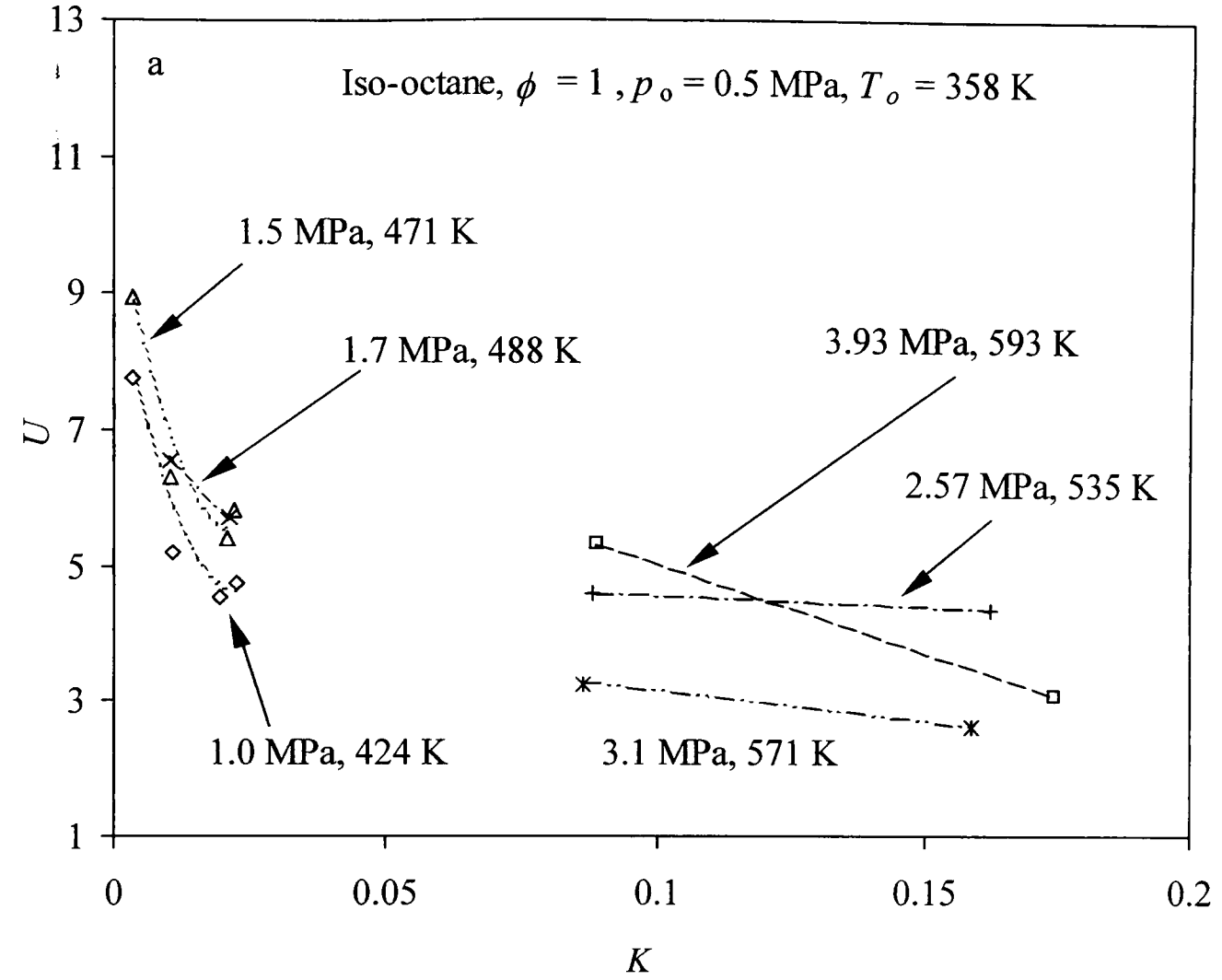

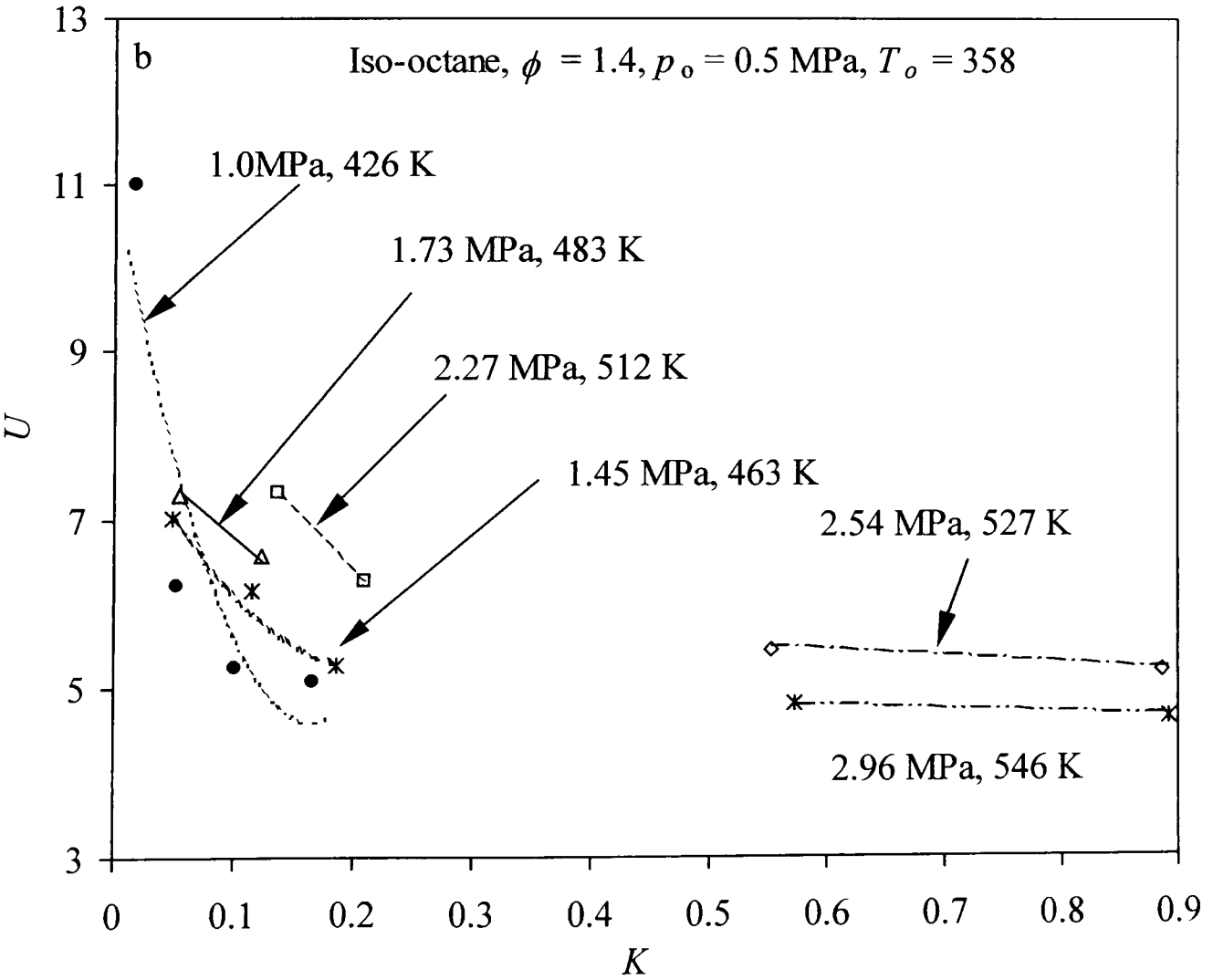

Fig. 8.12. Normalized u_t against K for iso-octane - air mixture at different pressures and temperatures. (a) ϕ = 1.0 , (b) ϕ = 1.4, at p_o = 0.5 MPa, T_o = 358 K.

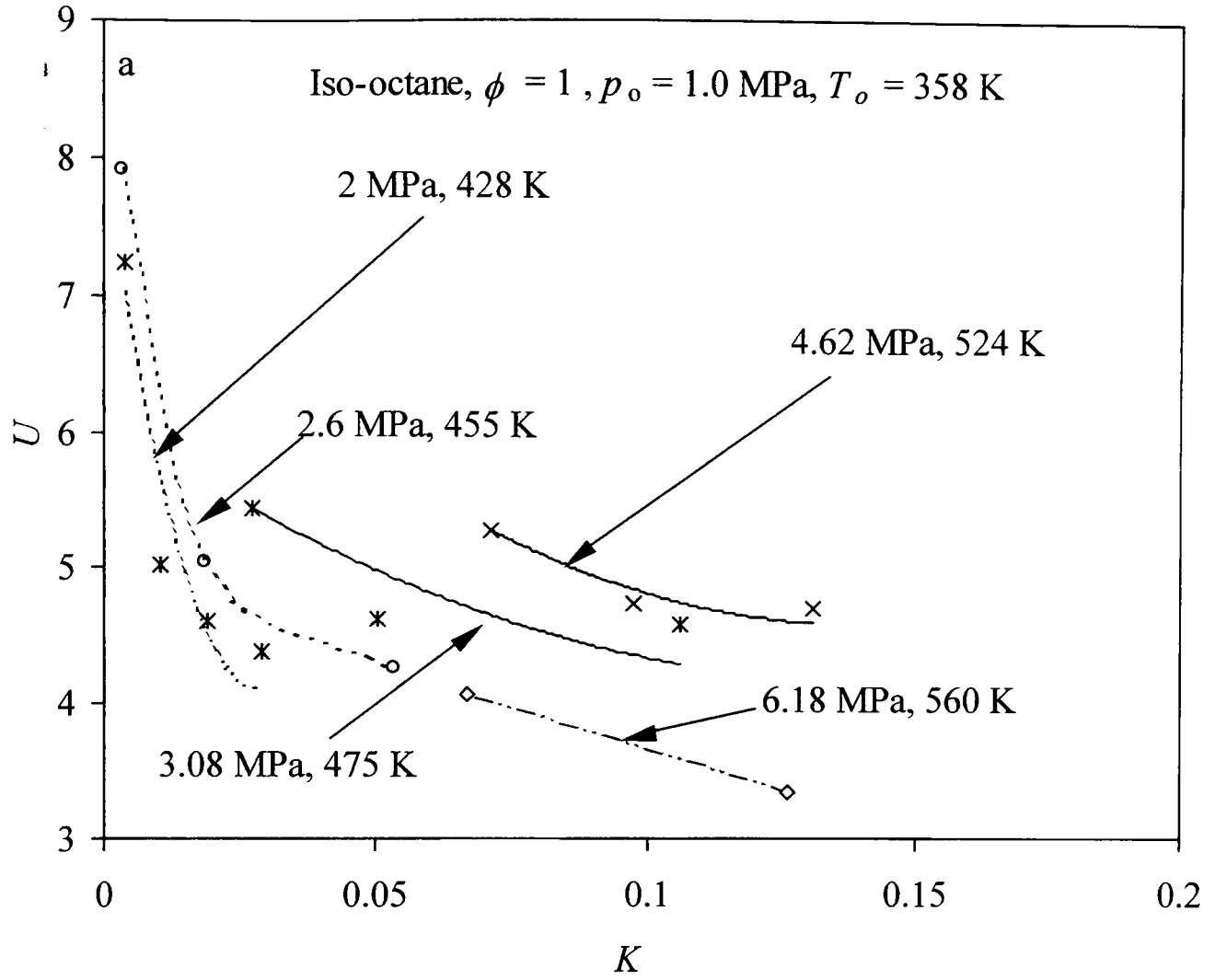

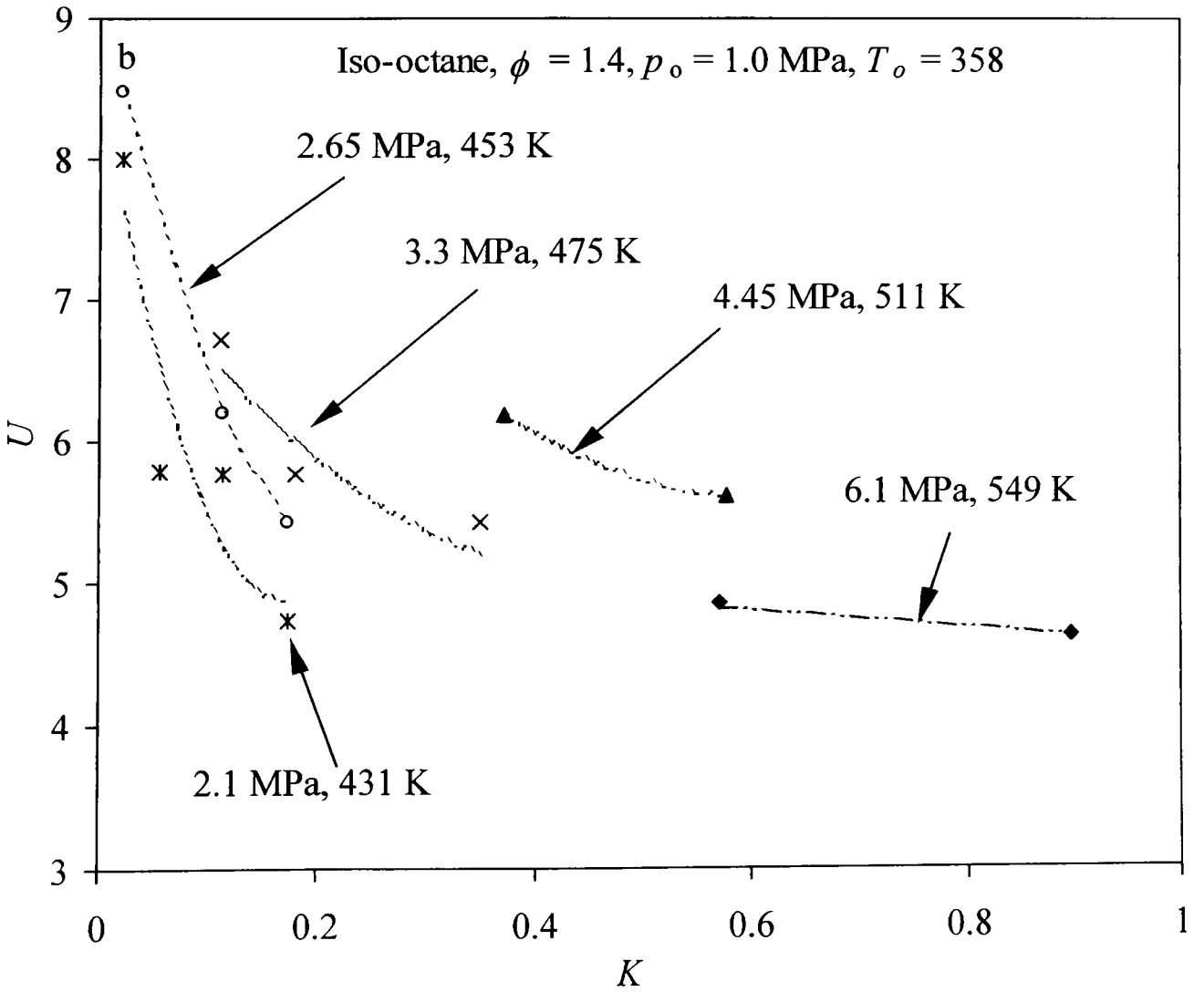

Fig. 8.13. Normalized u_t against K for iso-octane - air mixture at different pressures and temperatures. (a) ϕ = 1.0 , (b) ϕ = 1.4, at p_o = 1.0 MPa, T_o = 358 K.

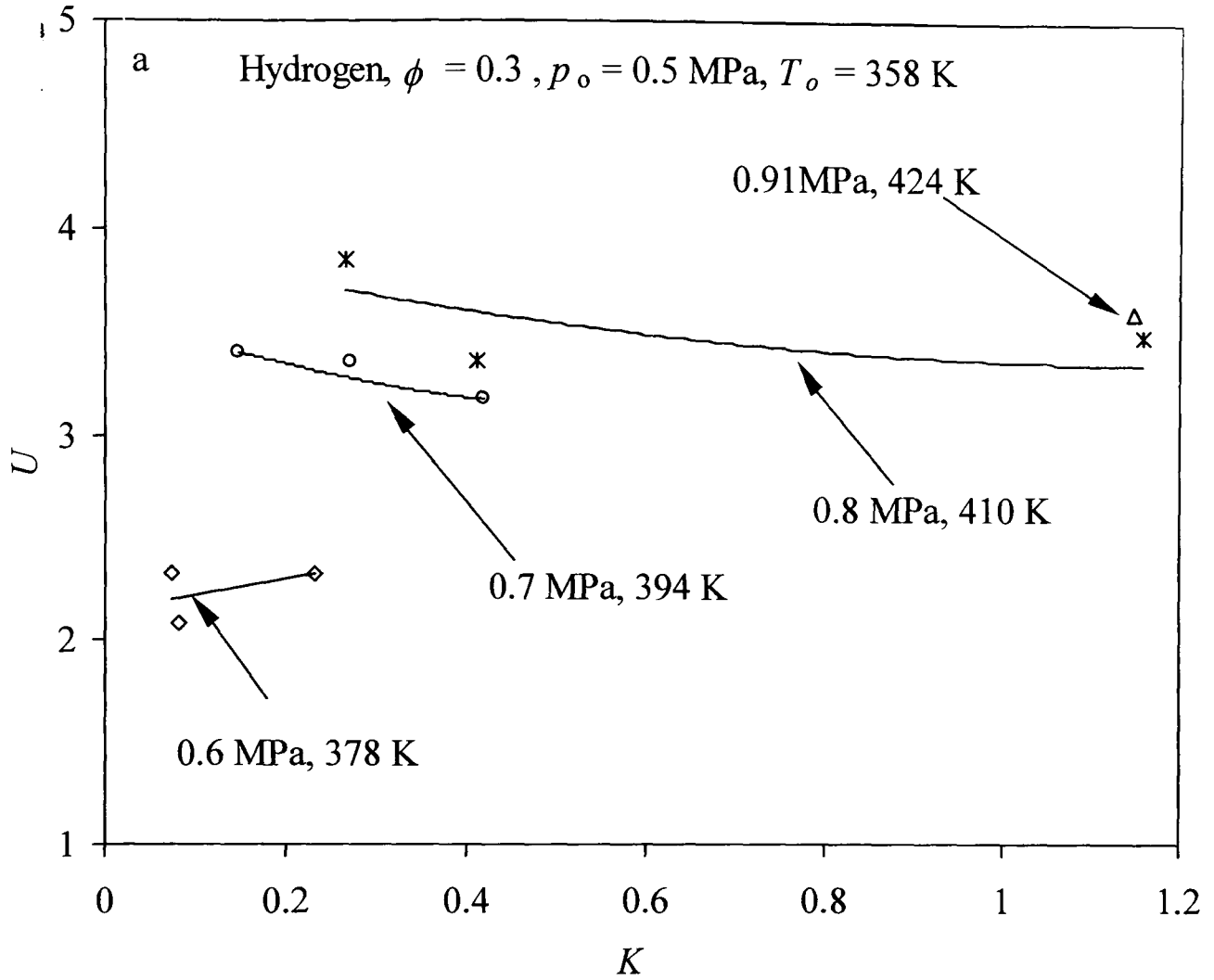

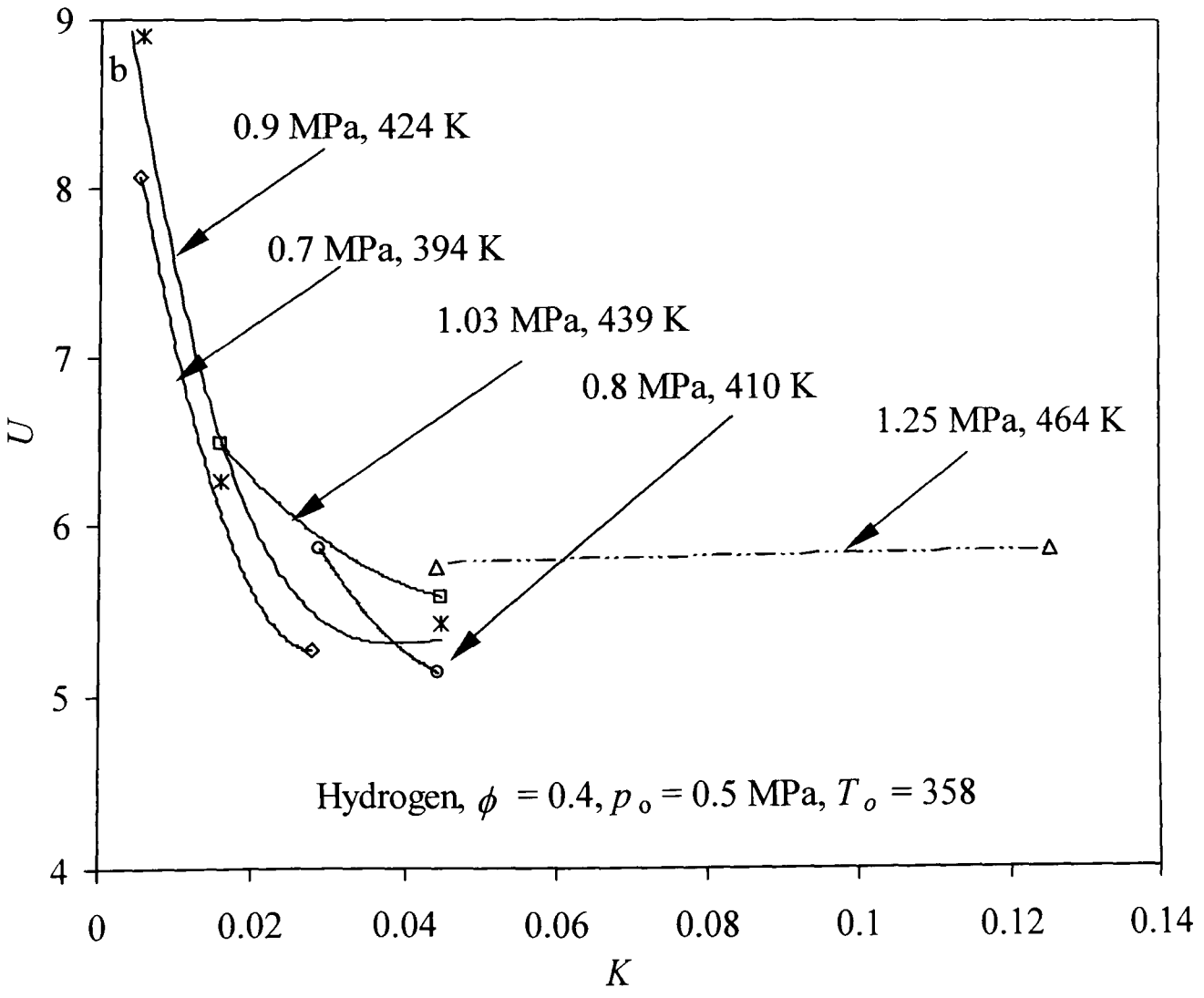

Fig. 8.14. Normalized u_t against K for hydrogen - air mixture at different pressures and temperatures. (a) ϕ = 0.3 , (b) ϕ = 0.4, at p_o = 0.5 MPa, T_o = 358 K.

Shown in Figs 8.12 and 8.13 are the turbulent burning velocities for iso-octane – air normalised by the effective rms turbulent velocity, u_t/u'_k, to give U, plotted against, K. Figure 8.12 (a) shows these parameters for ϕ = 1.0, and Fig. 8.12 (b) shows them for ϕ = 1.4, both at an initial pressure and temperature of 0.5 MPa and 358 K. The data for these figures are drawn from those in Figs. 7.50 (a) and 7.50 (b). Figure 8.13 (a) and (b) shows otherwise the same parameters for these same two mixtures, but with an initial pressure of 1.0 MPa. The data for these figures are drawn from those in Figs. 7.51 (a) and 7.51 (b). The experimental data for hydrogen – air mixtures for ϕ = 0.3 and 0.4 in Figs. 7.52 (a) and (b) appear in plots of U against K in Figs. 8.14 (a) and (b), respectively, both at an initial pressure and temperature of 0.5 MPa and 358 K.There is a general tendency with all mixtures for U to increase with p, particularly at the lower values of K.

All the experimental data used in the plots of U against K are given along with the other relevant parameters in Tables 8.1-8.6 at the end of the chapter. These also contain values of U given by the expressions of Bradley and co-workers (Bradley *et al.*, 1992 and Bradley, 2002), Eq. 1.2 and Gülder (1991), Eq. 1.3. Both of these expressions were predominantly obtained for flames at pressures close to atmospheric. Equation 1.2 included Le in an attempt to allow for thermo-diffusive and flamelet quenching effects. Values of Le were computed for each condition using the in-house software "Properties".

Kobayashi and co-workers (Kobayashi *et al.*, 1998) have measured u_t up to 1.0 MPa for C_2H_4–air (ϕ = 0.5, 0.7 and 0.9) and up to 0.5 MPa for C_3H_8–air (ϕ = 0.9). The results, along with those for lean CH_4–air from (Kobayashi *et al.*, 1996), were correlated by an equation that can be expressed as

$$U = C\left(\frac{p}{p_o}\right)^n \left(\frac{u'_k}{u_\ell}\right)^{n-1}, \qquad (8.1)$$

where (a) for the CH_4–air and C_2H_4–air flames C = 2.9 and n = 0.38, and, (b) for the C_3H_8 - air flames C = 1.9 and n = 0.40. Values of U with these different constants are designated by U a and U b, respectively. The differences in values were attributed to Lewis number effects. Values of U a and U b are also presented in Tables 8.1-8.6. The

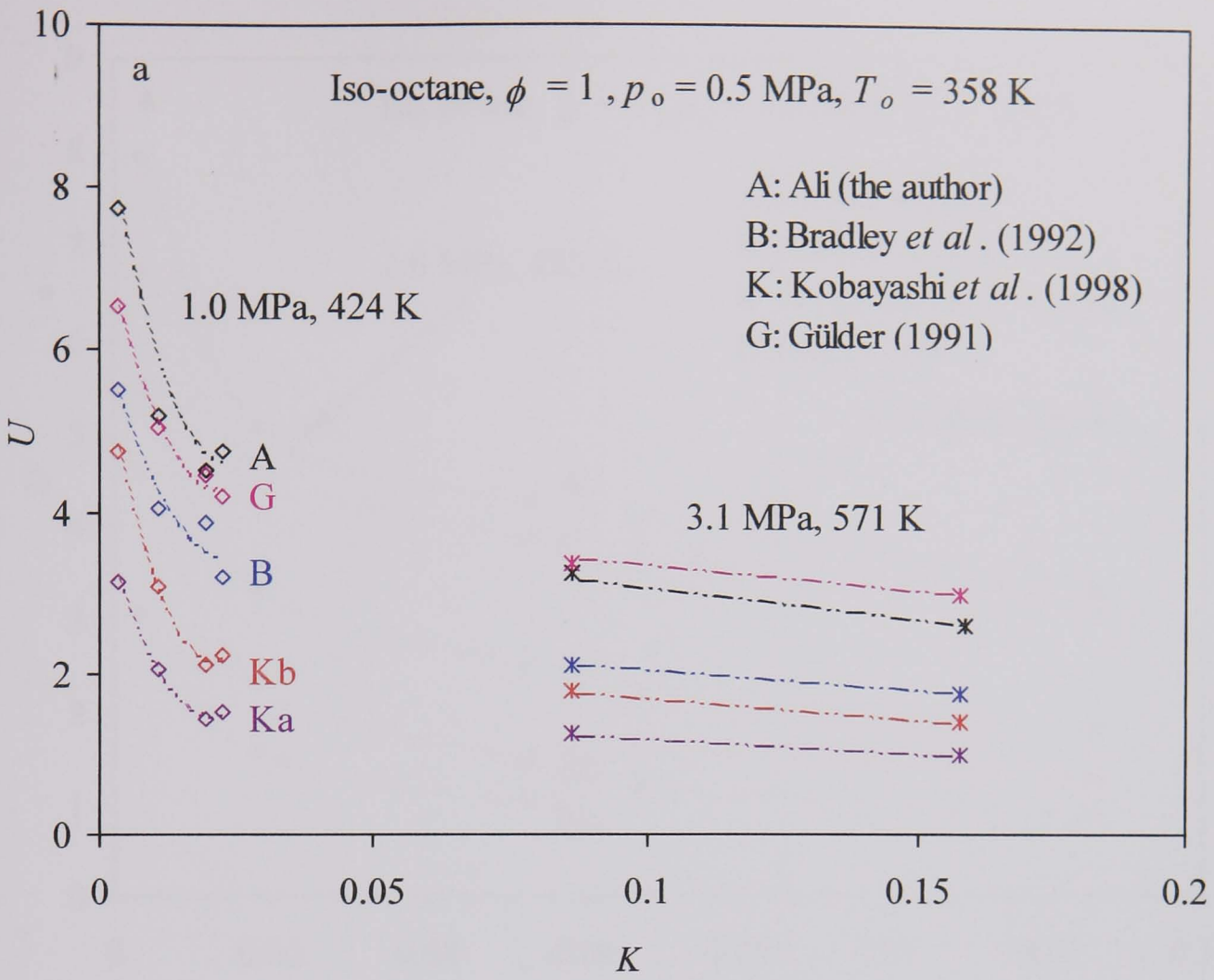

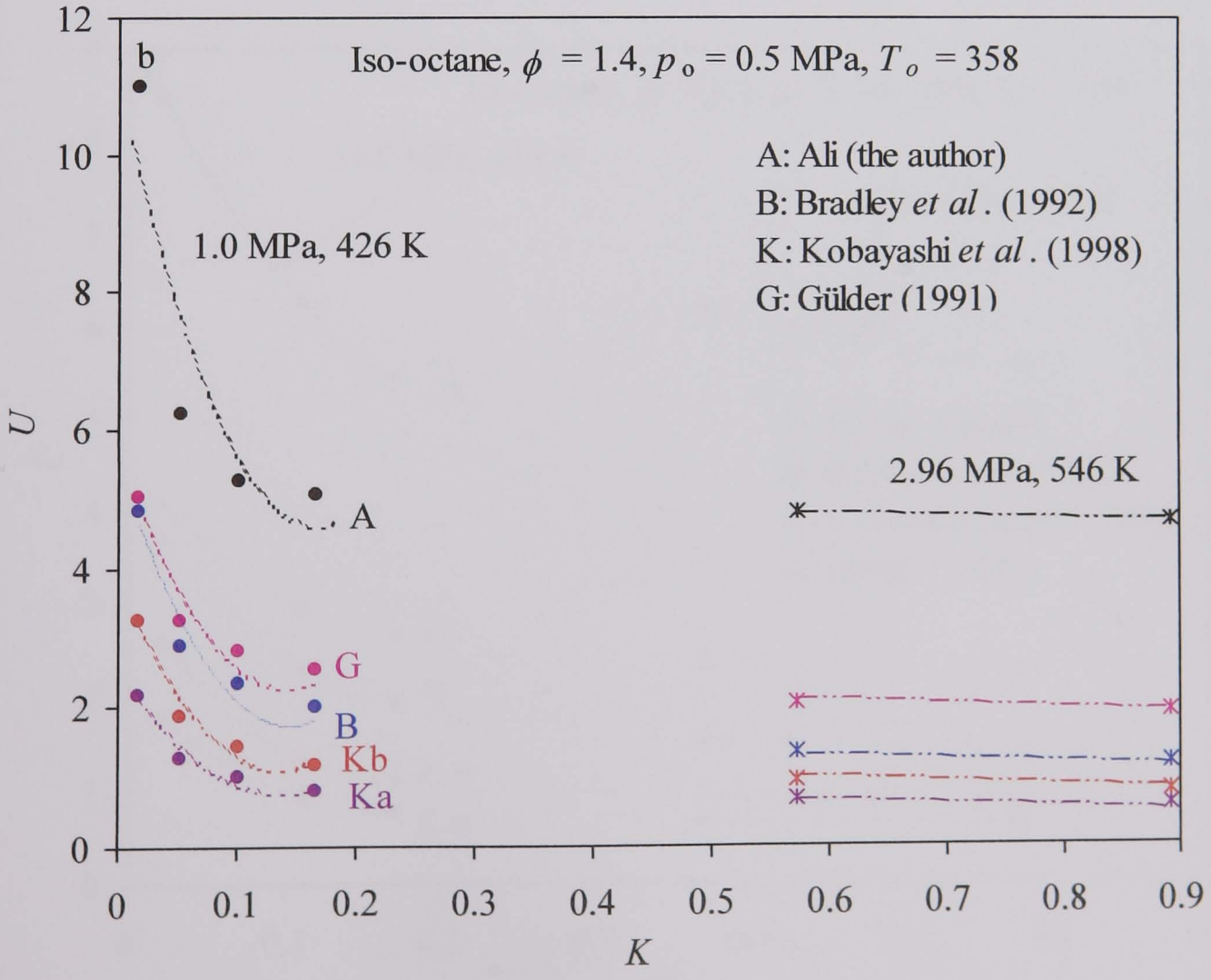

Fig. 8.15. Normalized u_t against K for iso-octane - air mixture at different pressures and temperatures. (a) ϕ = 1.0 , (b) ϕ = 1.4, at p_o = 0.5 MPa, T_o = 358 K.

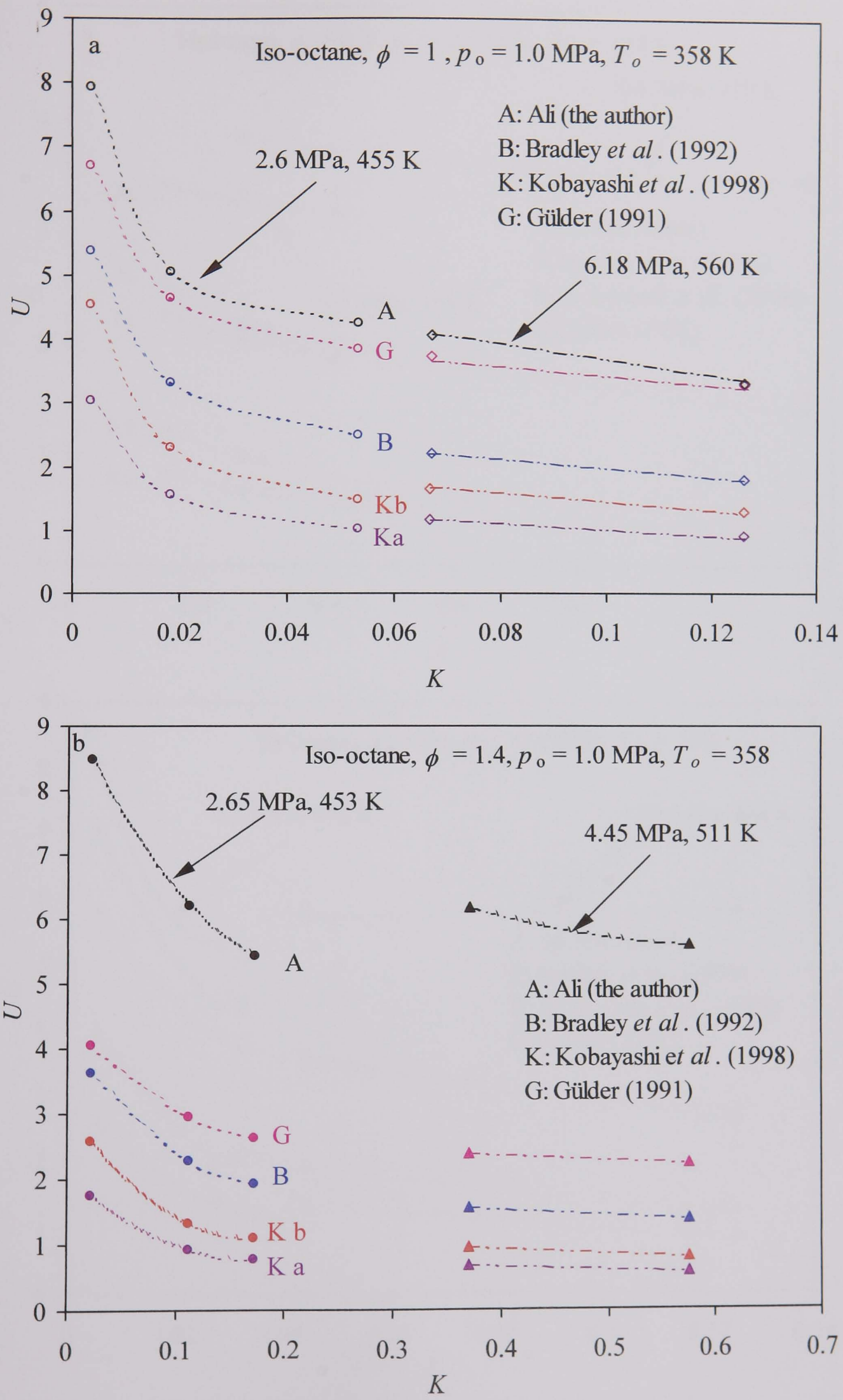

Fig. 8.16. Normalized u_t against K for iso-octane - air mixture at different pressures and temperatures. (a) ϕ = 1.0 , (b) ϕ = 1.4, at p_o = 1.0 MPa, T_o = 358 K.

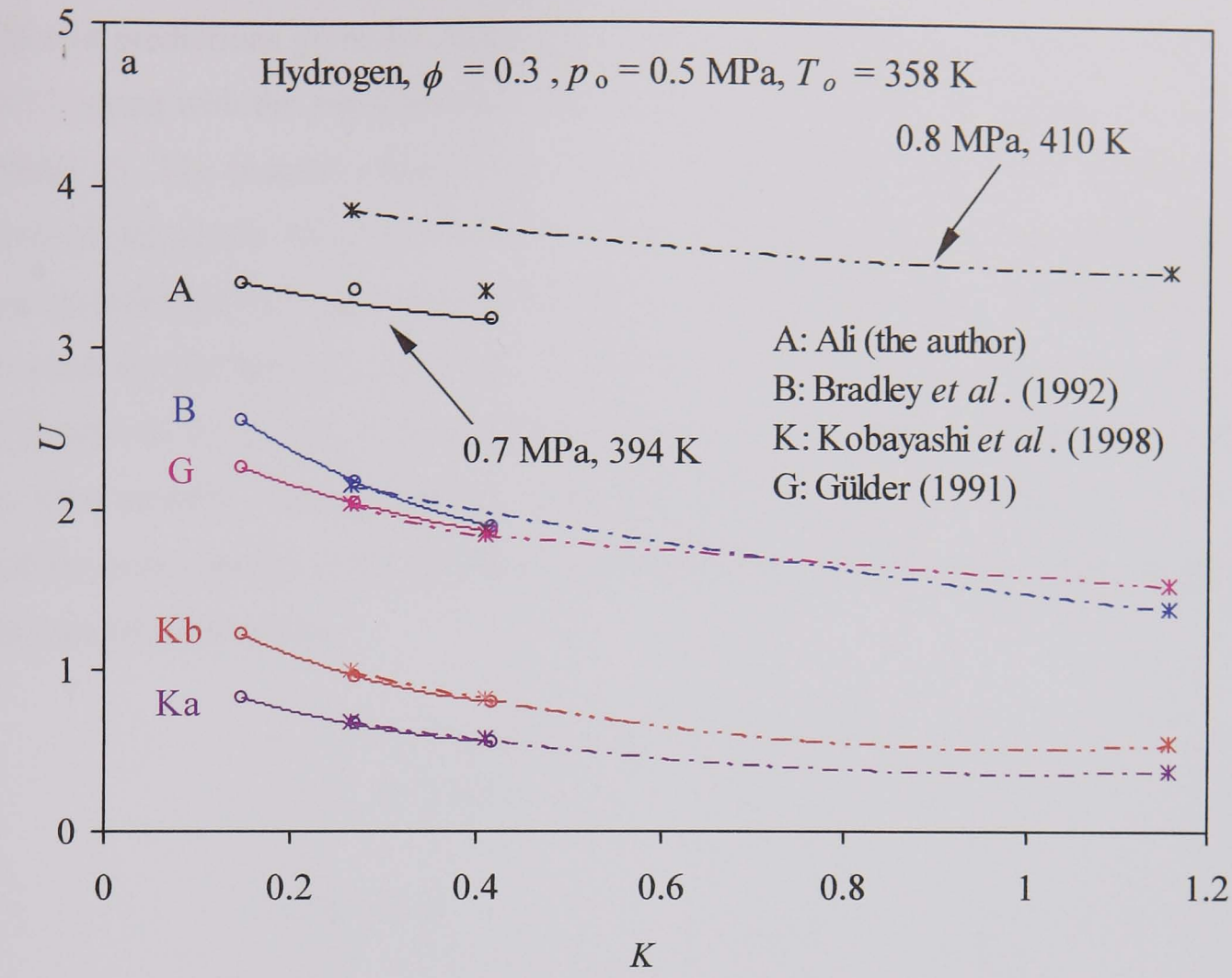

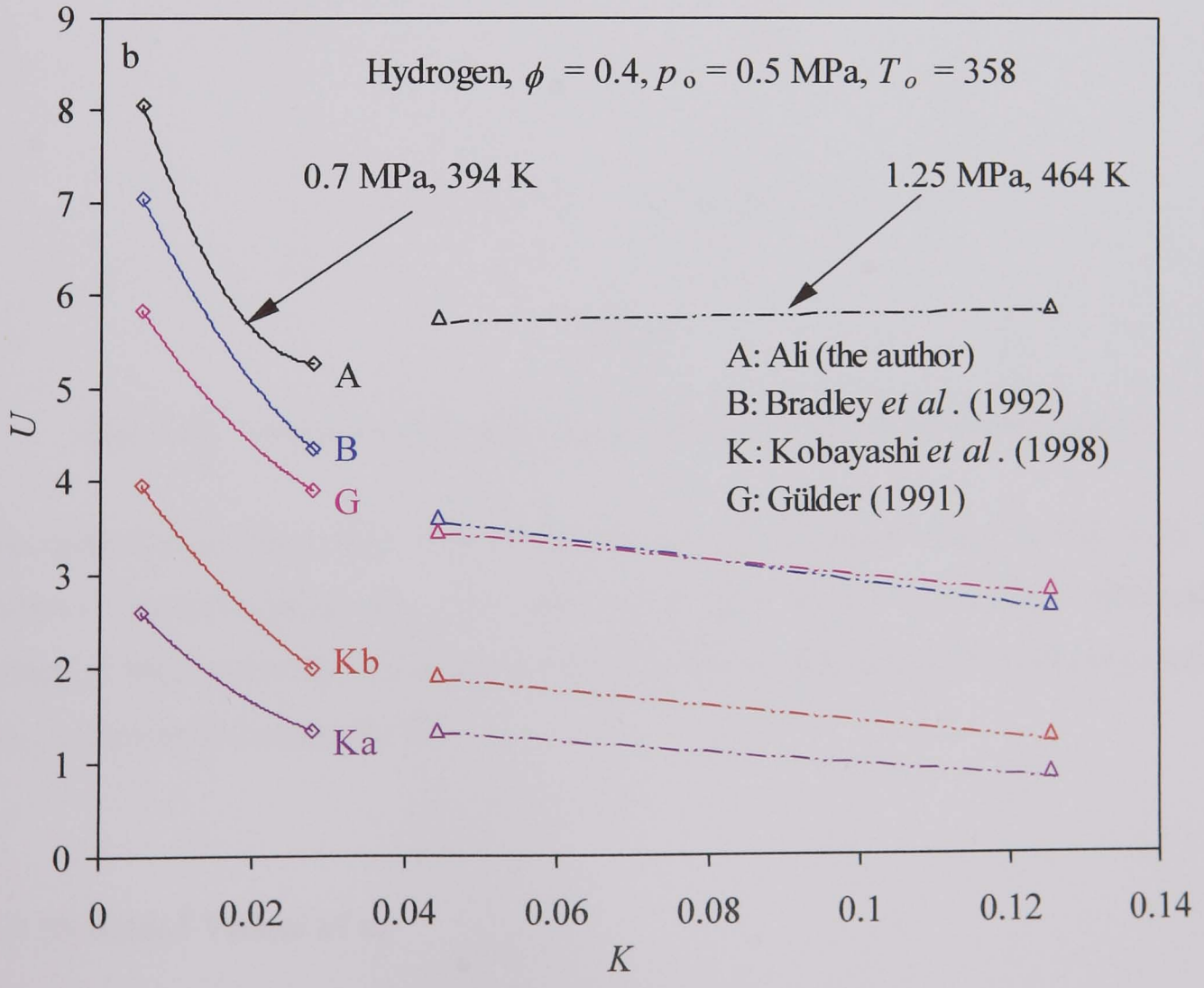

Fig. 8.17. Normalized u_t against K for hydrogen- air mixture at different pressures and temperatures. (a) $\phi = 0.3$, (b) $\phi = 0.4$, at $p_o = 0.5$ MPa, $T_o = 358$ K.

different predictions given by these two equations are given by Ka and Kb in Figs. 8.15 - 8.17, along with the experimental values and the values given by Bradley *et al.*, B. and Gülder, G. The present experimental results are indicated by A. For both iso-octane mixtures the values of U predicted by Gülder's expression are closest to the measured values, followed by values predicted by the expression of Bradley *et al.* This tends to be reversed for the hydrogen mixtures. In all cases the predictions of the two expressions of Kobayashi *et al.* tend to be significantly lower. The iso-octane mixture that produces the most unstable laminar flames is that at an initial pressure of 1 MPa, with $\phi = 1.4$, and for these conditions the values of U given by these expressions are much lower than the experimental values.

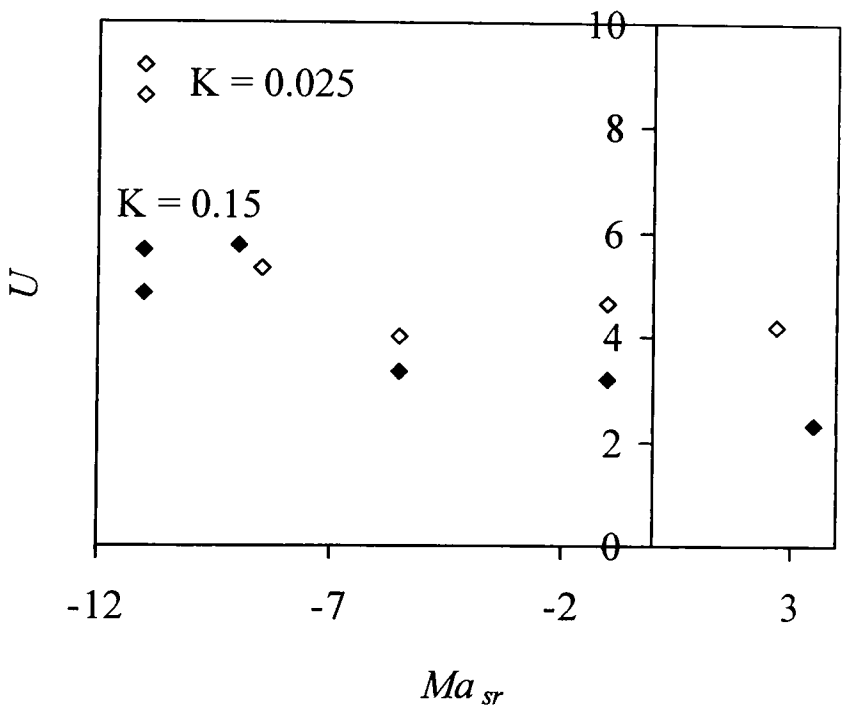

Fig. 8.18. Variation of U with Ma_{sr} for K=0.025 and 0.15 (filled symbol).

The influence of Ma_{sr} upon U at fixed values of K is demonstrated in Fig. 8.18. This shows U plotted against Ma_{sr} for values of K equal to 0.025 and 0.15. Although the values of Ma_{sr} cannot be accurate, the figure demonstrates that a more negative value of Ma_{sr} increases U at constant K.

8. 7 Predicted Values of u_t

The laminar flamelet approach presently being developed by Sedaghat at Leeds attempts to improve the theoretical understanding of negative Markstein number

turbulent flames. It rests on (i) derivation of reliable pdfs of flame stretch rates as a function of K, R_ℓ and Ma_{sr}, (ii) extinction of flames when the stretch rates exceed those at which the laminar flames extinguish (iii) allowance for the effect of Ma_{sr} and stretch rate on the burning rate of flamelets and (iv) allowance for wrinkling of flamelets due to their instabilities at low values of K and Ma_{sr}. This theory was applied by Sedaghat to measurements of u_t at 1 and 2 MPa with the iso-octane–air mixtures, ϕ = 1.0 and 1.4. The results are shown in Fig. 8.19. Figures 8.19 (a) and (b) are for 1 MPa and ϕ =1.0 and 1.4, respectively, in explosions of mixtures initially at 0.5 MPa. Figures 8.19 c and d are for 2 MPa and the same corresponding values of ϕ, but this time for an initial pressure of 1.0 MPa.

The symbols show values interpolated from the present experimental results. The bold full lines curves show values given by the complete theory of Sedaghat (2004), which allows for the instability of some flamelets. The bold broken curves show theoretical values but without any such instability effects, (see iv above). The differences between these two values of U indicate the influence of instabilities. The dotted curves in the figure show the predictions of Eq. (1.2) (Bradley *et al.*, 1992). Equation. (1.3) (Gülder, 1991) gave slightly higher values of U. Although the expression of Bradley *et al.* includes Le in an attempt to allow for thermo-diffusive effects, the predicted values of U are consistently below those measured, particularly at the lowest Markstein number. Perhaps surprisingly, at the positive values of Ma_{sr} they are closer to the measured values than are the present theoretical values. For these conditions the closeness of the continuous and broken bold curves indicates that, with the present theory, there is little influence from flamelet instabilities.

On the other hand, for the two conditions with Ma_{sr} = -2 the theory shows a significant instability contribution that brings theoretical values closer to those measured. For all the negative values of Ma_{sr} the value of the inner cut-off, l_s, was the limiting one of $50\delta_\ell$. In general, as K increases, the instability contribution to U decreases Computations (not shown) for Ma_{sr} =-3 at both 2.5 MPa and 6 MPa showed negligible instability enhancement beyond K=0.30, in accordance with the general predictions of Boughanem and Trouvé (1998). It is, however, interesting to note that an increasingly

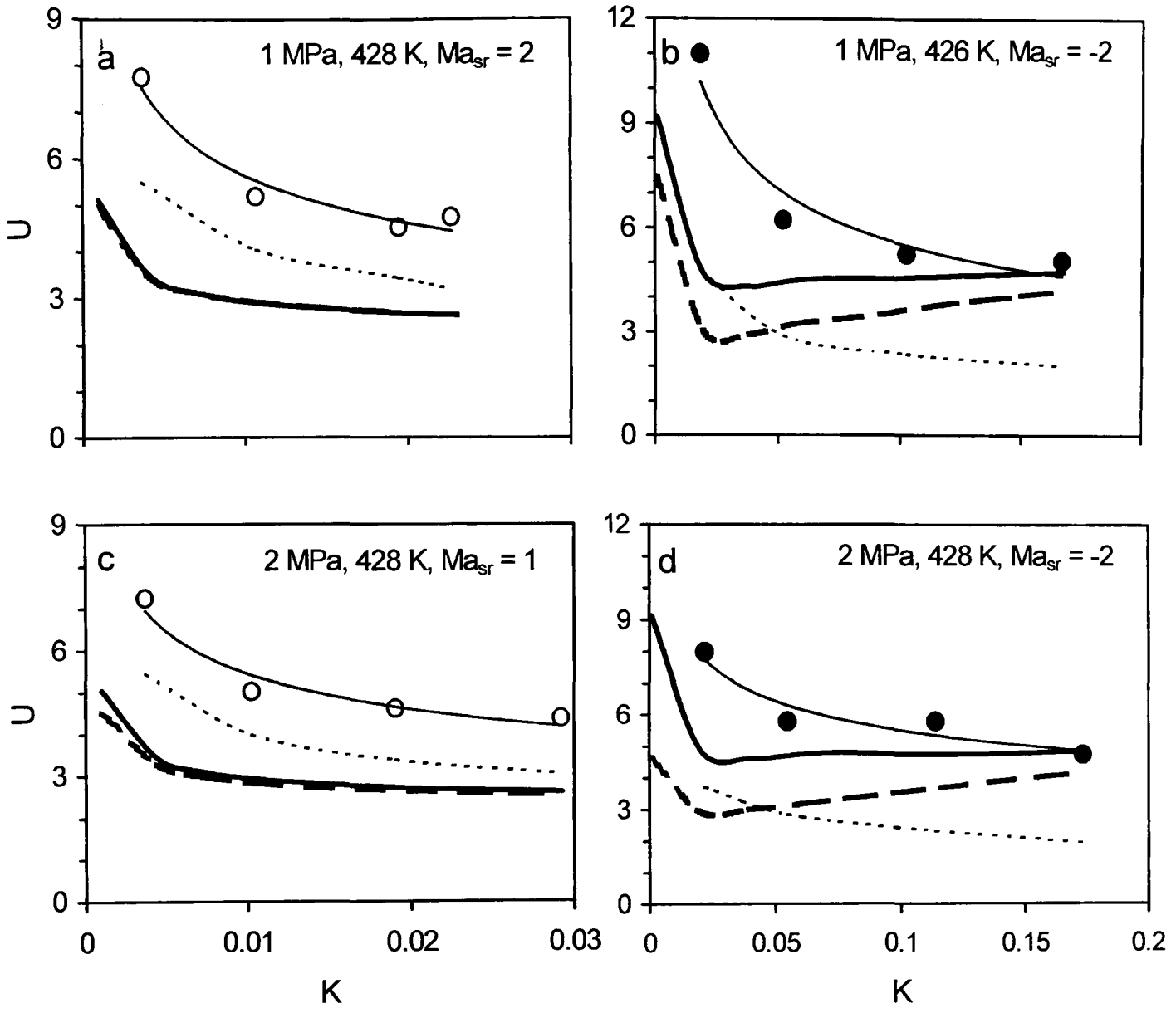

Fig. 8.19. Values of U at 1.0 and 2.0 MPa. a and c, ϕ = 1.0; b and d, ϕ = 1.4. Symbols, measured values from the present work; dotted curve, Bradley *et al.* (1992); bold curves, flamelet instability theory, Sedaghat (2004).

Negative value of Ma_{sr} increases U, even without an instability contribution. However, these predictions at high pressures were hampered by insufficient data on both Markstein numbers and laminar burning velocities.

8. 8 Laminar and Turbulent Instabilities

Measured and theoretical values of U become particularly high at the lowest values of K, as the flame tends towards a laminar flame. It is shown in Section 6.3 that, at high pressures and lower values of Ma_{sr}, laminar flames can exhibit a high enhancement factor, F, the ratio of unstable burning velocity to u_t. At the lowest values of u'_k/u_t and K

the value of U, which can be as high as 8, tends towards that of u_t/u_l, which has similarities to that of F in laminar burning. The maximum value of F measured for the mixture conditions of Fig. 8.19 d for the corresponding unstable, but originally laminar flame was 6.6. Nevertheless, with values of U of 3 or more and with u'_k of, say, 3 m/s, the value of u_t = 9 m/s. This burning velocity is significantly higher than what might be obtained with unstable burning of an initially laminar flame.

In summary, an initially laminar explosion flame with a negative value of Ma_{sr} would soon become unstable and its burning velocity would accelerate. If the flame front were then to propagate into an increasingly turbulent mixture, the turbulence would gradually over-ride the natural instability of the flame. Eventually, flame wrinkling and the consequent value of the turbulent burning velocity would be the result solely of the turbulence of the mixture, with no contribution from laminar flamelet instability and the burning velocity would be higher.

p_o (MPa)	p (MPa)	T (K)	u'_k (m/s)	K	u' (m/s)	R_ℓ	Le	u_ℓ (m/s)	ν m^2/s	U Present work	U Bradley	U Gülder	U a Kobay.	U b Kobay.
0.5	1.00	426	0.22	0.0037	0.25	1786	1.417	0.32	2.80E-06	7.67	5.52	6.55	3.10	4.70
0.5	1.03	429	0.22	0.0037	0.25	1818	1.417	0.32	2.75E-06	7.75	5.51	6.55	3.13	4.74
0.5	1.50	471	0.23	0.0035	0.25	2262	1.417	0.31	2.21E-06	8.93	5.41	6.49	3.51	5.27
0.5	1.02	428	0.44	0.0107	0.50	3610	1.411	0.31	2.77E-06	5.19	4.05	5.04	2.06	3.08
0.5	1.11	438	0.44	0.0107	0.50	3802	1.411	0.31	2.63E-06	5.47	4.02	5.01	2.10	3.14
0.5	1.50	471	0.45	0.0106	0.50	4525	1.411	0.30	2.21E-06	6.30	3.93	4.96	2.28	3.37
0.5	1.77	491	0.46	0.0105	0.50	4975	1.411	0.29	2.01E-06	6.56	3.89	4.95	2.39	3.53
0.5	1.00	427	0.66	0.0227	0.75	5376	1.416	0.29	2.79E-06	4.75	3.21	4.18	1.51	2.24
0.5	1.53	474	0.69	0.0222	0.75	6881	1.416	0.28	2.18E-06	5.40	3.49	4.30	1.72	2.52
0.5	1.03	429	0.77	0.0195	1.00	7273	1.407	0.30	2.75E-06	4.53	3.86	4.45	1.44	2.12
0.5	1.51	472	0.83	0.0209	1.00	9091	1.407	0.29	2.20E-06	5.40	3.49	4.30	1.59	2.32
0.5	1.73	488	0.85	0.0210	1.00	9804	1.407	0.29	2.04E-06	5.71	3.42	4.29	1.65	2.41
0.5	2.52	535	1.77	0.0882	2.00	24540	1.390	0.27	1.63E-06	4.62	2.15	3.18	1.17	1.67
0.5	3.27	569	1.81	0.0865	2.00	28777	1.390	0.26	1.39E-06	3.25	2.11	3.37	1.26	1.78
0.5	3.90	591	1.84	0.0891	2.00	31746	1.390	0.25	1.26E-06	5.32	2.05	3.32	1.30	1.83
0.5	2.55	536	2.66	0.1621	3.00	37037	1.39	0.27	1.62E-06	4.36	1.78	2.83	0.92	1.30
0.5	3.31	571	2.73	0.1579	3.00	43478	1.390	0.26	1.38E-06	2.62	1.75	3.00	1.00	1.40
0.5	3.96	595	2.78	0.1744	3.00	48387	1.390	0.24	1.24E-06	3.08	1.67	2.91	1.01	1.40

Table 8.1 Initial conditions and corresponding turbulence parameters for iso-octane - air mixtures, ϕ = 1.0, p_o = 0.5 MPa, T_o = 358 K.

p_o (MPa)	p (MPa)	T (K)	u'_k (m/s)	K	u' (m/s)	R_ℓ	Le	u_ℓ (m/s)	ν m^2/s	U Present work	U Bradley	U Gülder	U a Kobay.	U b Kobay.
0.5	1.01	425	0.18	0.0186	0.25	1845	0.898	0.14	2.71E-06	11.00	4.81	5.02	2.17	3.25
0.5	1.09	432	0.18	0.0184	0.25	1931	0.898	0.14	2.59E-06	10.84	4.73	4.96	2.20	3.29
0.5	1.01	424	0.44	0.0524	0.25	3704	0.89	0.14	2.70E-06	6.22	2.88	3.24	1.27	1.86
0.5	1.45	462	0.46	0.0495	0.50	4587	0.894	0.14	2.18E-06	7.03	2.83	3.23	1.41	2.06
0.5	1.76	484	0.46	0.0548	0.50	5155	0.894	0.13	1.94E-06	7.30	2.72	3.15	1.45	2.10
0.5	1.06	429	0.66	0.1028	0.75	5703	0.89	0.13	2.63E-06	5.25	2.36	2.81	0.99	1.44
0.5	1.43	461	0.67	0.1163	0.75	6818	0.892	0.12	2.20E-06	6.15	2.23	2.71	1.03	1.49
0.5	1.69	479	0.68	0.1239	0.75	7576	0.892	0.11	1.98E-06	6.57	2.16	2.66	1.06	1.53
0.5	2.24	512	0.69	0.1376	0.75	8929	0.892	0.10	1.68E-06	7.31	2.07	2.60	1.11	1.59
0.5	1.05	428	0.872	0.1669	1.00	7576	0.937	0.13	2.64E-06	5.07	2.02	2.55	0.82	1.19
0.5	1.49	466	0.90	0.1866	1.00	9390	0.937	0.12	2.13E-06	5.28	1.90	2.46	0.87	1.25
0.5	2.29	514	0.92	0.2099	1.00	12121	0.937	0.10	1.65E-06	6.27	1.79	2.40	0.94	1.34
0.5	2.52	526	1.81	0.5537	2.00	25641	0.887	0.11	1.56E-06	5.45	1.38	1.96	0.66	0.92
0.5	3.02	548	1.83	0.5733	2.00	28777	0.887	0.10	1.39E-06	4.79	1.35	2.04	0.69	0.95
0.5	2.56	528	2.72	0.88642	3.00	38961	0.8854	0.11	1.54E-06	5.20	1.20	1.82	0.54	0.75
0.5	2.90	543	2.74	0.8915	3.00	41958	0.885	0.11	1.43E-06	4.64	1.19	1.91	0.56	0.77

Table 8.2 Initial conditions and corresponding turbulence parameters for iso-octane - air mixtures, $\phi = 1.4$, $p_o = 0.5$ MPa, $T_o = 358$ K

p_o (MPa)	p (MPa)	T (K)	u'_k (m/s)	K	u' (m/s)	R_ℓ	Le	u_ℓ (m/s)	v m^2/s	U Present work	U Bradley	U Gülder	U a Kobay.	U b Kobay.
1	1.59	403	0.22	*0.0038*	0.25	3125	1.418	0.27	1.60E-06	6.13	5.60	6.84	2.63	3.99
1	2.09	431	0.22	0.0037	0.25	3676	1.418	0.26	1.36E-06	7.35	5.45	6.72	2.82	4.26
1	2.64	457	0.23	0.0036	0.25	4202	1.418	0.26	1.19E-06	7.92	5.39	6.70	3.02	4.54
1	2.09	431	0.45	0.0102	0.50	7353	1.418	0.27	1.36E-06	4.99	3.99	5.25	1.86	2.77
1	2.00	426	0.66	0.0191	0.75	10714	1.414	0.27	1.40E-06	4.52	3.38	4.67	1.45	2.15
1	2.53	452	0.68	0.0186	0.75	12295	1.414	0.26	1.22E-06	5.04	3.33	4.65	1.55	2.28
1	3.12	476	0.69	0.0181	0.75	13889	1.414	0.26	1.08E-06	5.49	3.30	4.66	1.66	2.42
1	1.99	426	0.86	0.0292	1.00	14286	1.410	0.27	1.40E-06	4.38	3.05	4.38	1.24	1.83
1	2.45	448	1.32	0.0533	1.50	24194	1.409	0.26	1.24E-06	4.27	2.49	3.63	1.03	1.49
1	3.01	472	1.35	0.0504	1.50	27273	1.409	0.26	1.10E-06	4.63	2.48	3.69	1.10	1.59
1	4.44	519	1.82	0.0710	2.00	45506	1.402	0.26	8.79E-07	5.29	2.22	3.71	1.07	1.52
1	6.07	559	1.86	0.0667	2.00	54870	1.402	0.25	7.29E-07	4.08	2.21	3.76	1.18	1.67
1	3.16	477	2.23	0.1061	2.50	46729	1.404	0.26	1.07E-06	5.24	2.01	3.24	0.83	1.19
1	4.79	528	2.30	0.0977	2.50	59595	1.404	0.26	8.39E-07	4.97	1.99	3.34	0.95	1.35
1	6.28	563	2.83	0.1261	3.00	84151	1.398	0.25	6.46E-07	3.35	1.80	3.31	0.92	1.29

Table 8.3 Initial conditions and corresponding turbulence parameters for iso-octane - air mixtures, $\phi = 1.0$, $p_o = 1$ MPa, $T_o = 358$ K.

p_o (MPa)	p (MPa)	T (K)	u'_k (m/s)	K	u' (m/s)	R_ℓ	Le	u_ℓ (m/s)	ν m^2/s	U Present work	U Bradley	U Gülder	U a Kobay.	U b Kobay.
1	2.05	426	0.22	0.0219	0.25	3731	0.896	0.11	1.34E-06	7.95	3.71	4.09	1.65	2.44
1	2.62	452	0.23	0.0221	0.25	4310	0.896	0.10	1.16E-06	8.48	3.63	4.04	1.75	2.58
1	2.01	424	0.44	0.0549	0.50	7407	0.895	0.12	1.35E-06	5.78	2.84	3.40	1.12	1.65
1	2.05	426	0.65	0.1140	0.75	11194	0.892	0.11	1.34E-06	5.39	2.32	2.97	0.86	1.26
1	2.57	449	0.67	0.1127	0.75	12821	0.892	0.11	1.17E-06	6.20	2.27	2.94	0.91	1.32
1	3.31	477	0.68	0.1104	0.75	15000	0.892	0.10	1.00E-06	6.72	2.23	2.94	0.98	1.41
1	2.11	429	0.90	0.1735	1.00	15267	0.89	0.11	1.31E-06	4.73	1.96	2.63	0.72	1.03
1	2.77	457	0.92	0.1730	1.00	17857	0.892	0.10	1.12E-06	5.43	1.92	2.62	0.77	1.10
1	3.28	490	0.93	0.1806	1.00	21575	0.892	0.10	9.21E-07	5.77	1.83	2.57	0.82	1.16
1	3.20	473	1.32	0.3486	1.50	29412	0.887	0.10	1.02E-06	5.43	1.63	2.41	0.63	0.89
1	4.36	509	1.35	0.3701	1.50	35211	0.887	0.09	8.52E-07	6.18	1.56	2.37	0.67	0.94
1	4.52	513	1.78	0.5761	2.00	48019	0.886	0.09	8.33E-07	5.60	1.39	2.22	0.58	0.80
1	5.96	546	1.83	0.5660	2.00	57061	0.886	0.09	7.01E-07	4.85	1.36	2.22	0.62	0.86
1	6.24	552	2.85	0.8969	3.00	87848	0.882	0.09	6.83E-07	4.62	1.14	2.00	0.50	0.69

Table 8.4 Initial conditions and corresponding turbulence parameters for iso-octane - air mixtures, $\phi = 1.4$, $p_o = 1$ MPa, $T_o = 358$ K.

p_o (MPa)	p (MPa)	T (K)	u'_k (m/s)	K	u' (m/s)	R_ℓ	Le	u_ℓ (m/s)	ν m^2/s	U Present work	U Bradley	U Gülder	U a Kobay.	U b Kobay.
0.5	0.60	377	0.22	0.0822	0.25	1142	0.416	0.075	4.38E-06	2.08	3.15	2.58	1.07	1.59
0.5	0.62	381	0.22	0.0746	0.25	1160	0.416	0.078	4.31E-06	2.32	3.20	2.61	1.10	1.64
0.5	0.60	378	0.43	0.2323	0.50	2288	0.416	0.075	4.37E-06	2.33	2.36	2.10	0.72	1.05
0.5	0.70	394	0.46	0.1484	0.50	2475	0.416	0.092	4.04E-06	3.40	2.55	2.26	0.83	1.22
0.5	0.71	395	0.67	0.2717	0.75	3741	0.42	0.092	4.01E-06	3.35	2.18	2.04	0.66	0.97
0.5	0.81	410	0.68	0.2659	0.75	3989	0.42	0.092	3.76E-06	3.85	2.16	2.03	0.69	1.00
0.5	0.71	396	0.90	0.4193	1.00	4963	0.417	0.092	4.03E-06	3.17	1.90	1.86	0.56	0.81
0.5	0.80	409	0.91	0.4105	1.00	5291	0.417	0.092	3.78E-06	3.36	1.88	1.85	0.58	0.83
0.5	0.80	409	1.80	1.1580	2.00	10638	0.417	0.092	3.76E-06	3.50	1.40	1.55	0.38	0.55
0.5	0.91	424	1.82	1.1470	2.00	11331	0.417	0.091	3.53E-06	3.60	1.38	1.54	0.40	0.57

Table 8.5 Initial conditions and corresponding turbulence parameters for hydrogen - air mixtures, $\phi = 0.3$, $p_o = 0.5$ MPa, $T_o = 358$ K.

p_o (MPa)	p (MPa)	T (K)	u'_k (m/s)	K	u' (m/s)	R_ℓ	Le	u_ℓ (m/s)	ν m^2/s	U Present work	U Bradley	U Gülder	U a Kobay.	U b Kobay.
0.5	0.71	395	0.22	0.0053	0.25	1208	0.452	0.29	4.14E-06	8.07	7.06	5.84	2.59	3.95
0.5	0.90	423	0.22	0.0056	0.25	1359	0.452	0.28	3.68E-06	8.90	6.77	5.63	2.72	4.11
0.5	0.91	424	0.44	0.0158	0.50	2732	0.452	0.28	3.66E-06	6.27	5.01	4.36	1.81	2.70
0.5	1.02	438	0.45	0.0159	0.50	2915	0.452	0.27	3.43E-06	6.49	4.94	4.33	1.86	2.78
0.5	0.70	394	0.65	0.0279	0.75	3597	0.452	0.29	4.17E-06	5.27	4.35	3.91	1.34	2.00
0.5	0.80	409	0.66	0.0289	0.75	3856	0.452	0.28	3.89E-06	5.87	4.21	3.81	1.37	2.04
0.5	0.81	410	0.85	0.0444	1.00	5155	0.453	0.28	3.88E-06	5.14	3.82	3.58	1.18	1.74
0.5	0.91	424	0.87	0.0447	1.00	5479	0.453	0.28	3.65E-06	5.43	3.74	3.53	1.21	1.78
0.5	1.03	439	0.88	0.0448	1.00	5865	0.453	0.27	3.41E-06	5.59	3.68	3.50	1.25	1.83
0.5	1.29	468	0.90	0.0442	1.00	6579	0.453	0.26	3.04E-06	5.76	3.62	3.47	1.33	1.94
0.5	1.25	464	1.80	0.1253	2.00	12945	0.453	0.26	3.09E-06	5.86	2.65	2.82	0.87	1.25
0.5	1.43	481	1.82	0.1248	2.00	13841	0.453	0.26	2.89E-06	5.90	2.63	2.81	0.90	1.29

Table 8.6 Initial conditions and corresponding turbulence parameters for hydrogen - air mixtures, $\phi = 0.4$, $p_o = 0.5$ MPa, $T_o = 358$ K.

Chapter 9

Conclusions

9.1 Conclusions

The different methods for measuring burning velocities in spherical explosion vessels have been examined. Those involving central ignition were first employed: one predominantly involving optical observation of the flame front, the other involving pressure measurement. The experiments with initially laminar flames have confirmed, first, the effects of flame stretch rate and, second, the onset of flame instabilities with an associated increase in the burning velocity. The latter became more important as the pressure increased. Mixtures with negative Markstein numbers were more prone to instabilities and enhanced burning velocities. There was evidence of related effects in turbulent flames.

In order to measure burning velocities at high pressure a new technique, involving twin imploding kernels with ignition at diametrical opposite points at the combustion vessel wall has been developed. Two different analytical approaches were employed, one based on geometrical quantification of the volume of burned gas, the other on the fractional pressure rise. A knowledge of the flame area then enabled two corresponding expressions to be obtained for the burning velocity. The agreement in values of u_ℓ between these two different approaches and the general consistency of the results showed the technique to be accurate and suitable for obtaining burning velocities at high pressure.

The thesis also has addressed the difficulties in deriving the laminar burning velocity from the measured unstable burning velocities. This derivation has been attempted using an adaptation of the instability theory of Bechtold and Matalon. The validity of the approach has been confirmed for methane – air and iso-octane – air explosions, under conditions where the laminar burning velocities and Markstein numbers at high pressure were known from previous explosions using the central ignition techniques. For very unstable flames it was not possible to measure these parameters and even the

measurement of Pe_{cl} was unreliable. However, with flames that are so unstable that the smallest wavelength of instability is "saturated", the derivation of u_ℓ is simplified by the assumption that $\Lambda_s = 50$.

This implosion technique was also applied to the measurement of turbulent burning velocities in the fan-stirred bomb. For both turbulent and non-turbulent explosions emphasis was placed on the effects of instabilities. The onset of instabilities was facilitated, not only by the use of high pressures and larger diameter flame kernels, but also by the use of mixtures with negative Markstein numbers.

In summary, the principal findings are:

1. Laminar flames became increasingly unstable, as both the distance they had propagated and the pressure increased. This was particularly so for rich mixtures of iso-octane and lean mixtures of H_2 – air. This is explained by the influences of Pe and Ma_{sr}, as explained by the instability theory of Bechtold and Matalon.

2. The agreement between the two different expressions for obtaining u_n with the twin kernel technique and the general consistency of the results showed the technique to be accurate and suitable for obtaining burning velocities at high pressure. The studies also clearly demonstrated the importance of instabilities, even at lower pressures, in enhancing burning velocities.

3. The theory of Bechtold and Matalon (1987), as modified by Bradley (1999) has enabled laminar burning velocities of methane – air ($\phi = 1.0$), iso-octane – air ($\phi = 0.8$ to 1.4) and hydrogen – air ($\phi = 0.3$ to 0.5) mixtures to be obtained over ranges of pressure and temperature in isentropic compressions. There were, however, difficulties with the Bechtold - Matalon approach, in that it is not directly applicable for $Ma_{sr} < 3$ and it requires a knowledge of values of Markstein numbers, which were in some instances sparse at high pressure. The hydrogen flames were so unstable that measurements of Ma_{sr} and Pe_{cl} were almost impossible.

4. The increase in laminar burning velocity due to instabilities is indicated by an enhancement factor F. This is not constant but continually increases as the flame propagates. The value of F was low for a mixture that might otherwise have been assumed to be stable (value of 1.42 at 0.29 MPa, for methane – air, $\phi = 1$). For richer mixtures of iso-octane – air, $\phi = 1.4$, F attained values as high as 6.6, at 2.0 MPa. Similarly with lean mixtures of hydrogen – air flames, $\phi = 0.3$, at 0.9 MPa, also with a negative value of Ma_{sr}, F attained a value of 4.4.

5. The values of u_ℓ for iso-octane mixtures confirmed an earlier study (Bradley *et al.*, 2000) that showed they tended to decrease slightly with isentropic compression and not to increase, as suggested by some previous experimentalists. It also emerged that u_ℓ tended to decrease more sharply for richer mixtures with increasing temperature and pressure during such compressions.

6. The earlier reported increases in u_ℓ in isentropic compressions varied significantly between different researchers and are probably a consequence of flame instabilities. This is not only of practical, but also of theoretical importance, in that laminar burning velocities derived from chemical kinetic, models that omit flame instabilities can only be validated against experimental measurements in which there is either no inherent instability, or the effects of it have been removed.

7. A numerical study based on known "worse case" autoignition delay times, for iso-octane – air mixtures, $\phi = 1.5$ and 1.6, initial pressure 1.0 MPa, showed that autoignition was highly unlikely in the end gas. This conclusion is most probably also true for all other mixtures studied.

8. Further increased values of u_n and u_ℓ at $\phi = 1.5$ and 1.6 are possibly a consequence of the rapid increase in u_n and increased pressure oscillations. These could give rise to further wrinkling of the flame front due to Taylor instabilities.

9. Turbulent burning velocities measured by the new technique, particularly when Ma_{sr} was negative, tended to be higher than those suggested by expressions predominantly based on measurements much closer to atmospheric pressure. These explosions were of

iso-octane – air mixtures (ϕ = 1, 1.4) at initial pressures of 0.5 and 1.0 MPa and hydrogen – air mixtures (ϕ = 0.3, 0.4) at an initial pressure of 0.5 MPa. It was possible for burning velocities to be measured up to a maximum of 6 MPa.

10. The twin kernel technique not only had the advantage of yielding data at high pressures close to the safe working pressure of the bomb but, in addition, the larger kernel diameters gave a greater degree of flame surface development into the longer wavelengths of the turbulent spectrum. As a result, u'_k was closer to u'. In the case of laminar flames the larger diameters gave higher Peclet numbers and increased flame instabilities.

11. There was collaboration with Dr. Sedaghat in his theoretical studies of turbulent burning velocities. These showed that increasingly negative values of Ma_{sr} increased the burning velocity of the stretched flamelets. There was a further increase in the turbulent burning velocity at the smaller values of the Karlovitz stretch factor due to instabilities in the flamelets. However, the range of unstable wavelengths in turbulent burning is less than that in laminar burning and the effects of instabilities are less pronounced. Whereas the largest unstable wavelength is of the order of the flame diameter in laminar flames, it is of the order of the integral length scale in turbulent flames.

9.2 Recommendations

a. A more detailed picture of unstable and turbulent flame structure would be obtained from laser sheet imaging, including Planar Mie Scattering (PMS), and planar laser induced fluorescence (PLIF).

b. Due to the size and position of the optical windows, it was not possible to have complete views of the leading edges of flames. It would be informative to install a small optical window, positioned to observe the flame front. Alternatively, ion probes might be used to map the flame front.

c. It would be advantageous to measure the flow field and u' during flames propagations using laser doppler and particle image velocimetry.

d. Present results should be compared with the findings of related direct numerical simulations in the collaborative work with the Universities of Cambridge (Dr. S. Cant) and Central Lancashire (Dr. V. Kallin), when their studies have been completed.

e. There was a particular difficulty in measuring Markstein lengths and critical Peclet numbers when laminar flames became almost immediately unstable after ignition. It would be useful if a mean of overcoming this could be found, possibly by the measurement of cell sizes.

Appendix A

Typical Computational Results for Flame Radius from ´Edge`, Fortran Program

Appendix A

Briefly, the ´Edge`, program (Kitagawa and Woolley, 2003), performs the following tasks:

1. Finds the edge: identifies the border between white and black and gives a list of coordinates, (Fig A.1).
2. Rejects any coordinates outside the window of the vessel.
3. Splits coordinate into flame 1 and flame 2.
4. For each flame and each point on the flame front (coordinate), it computes the distance from the spark.
5. Calculates the mean radius for each flame.

The program needed the following inputs:
Filename – Number of the first image to be processed and the last one – scaling factor (mm/pixels) – Size of processed images, fixed (256x256 pixels) – Centrr coordinates, fixed (128,128), which is the center of the window – the starting location (point) in the image which the program starts the computation from. The following is an example:

Next line - filname begin
E03d080703

Next line -frame number begin, end
160, 262

Next line - scaling, units = mm/pix
0.574

Next line - Image size: xpix, ypix
256,256

Next line - centre coords x, y
128,128

Next line - start point
255,31

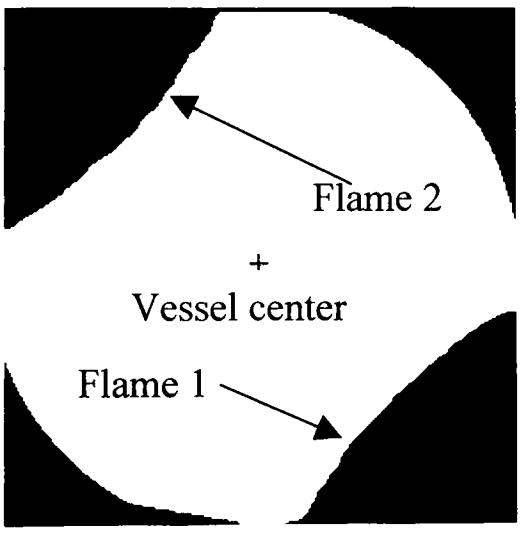

Fig. A.1. Binary image.

A Sample for the computational results preformed by ´Edge`, program is shown in Table A.1.

File name	Bottom flame r1 (mm)		File name	Top flame r2 (mm)
e03d080703166a	122.42		e03d080703166b	126.97
e03d080703172a	128.98		e03d080703172b	131.35
e03d080703178a	134.22		e03d080703178b	135.79
e03d080703184a	138.87		e03d080703184b	140.50
e03d080703190a	143.08		e03d080703190b	144.64
e03d080703196a	147.30		e03d080703196b	148.34
e03d080703202a	151.35		e03d080703202b	151.55
e03d080703208a	154.86		e03d080703208b	154.91
e03d080703214a	157.85		e03d080703214b	158.35
e03d080703220a	160.69		e03d080703220b	161.53
e03d080703226a	163.58		e03d080703226b	164.21
e03d080703232a	166.38		e03d080703232b	166.60
e03d080703238a	168.74		e03d080703238b	169.13
e03d080703244a	170.99		e03d080703244b	171.46
e03d080703250a	173.23		e03d080703250b	173.48
e03d080703256a	175.60		e03d080703256b	175.40
e03d080703262a	177.64		e03d080703262b	177.07

Table A.1 Sample calculations for Edge program.

Appendix B

Additional Experimental Results From Initially Laminar Imploding Flames

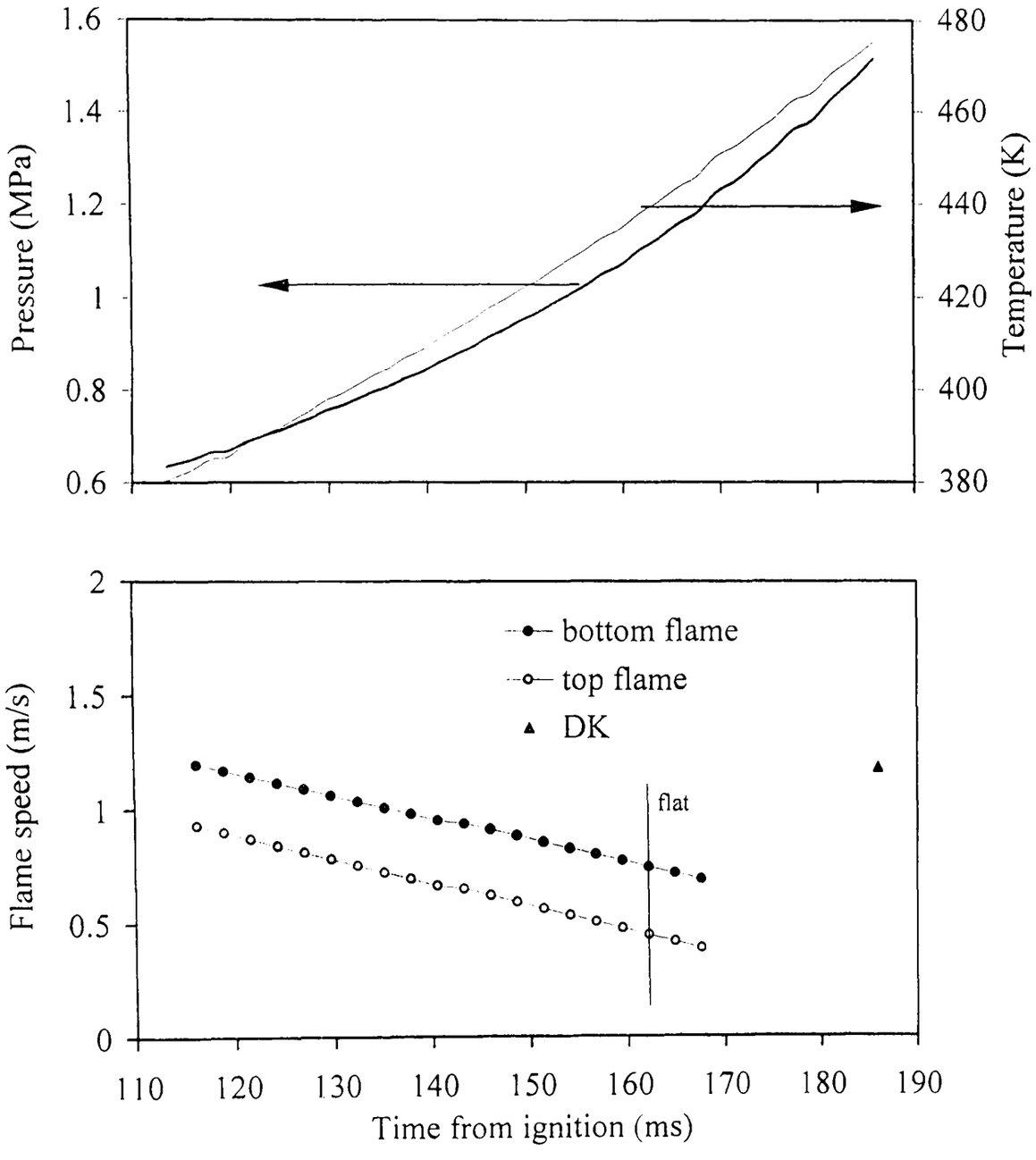

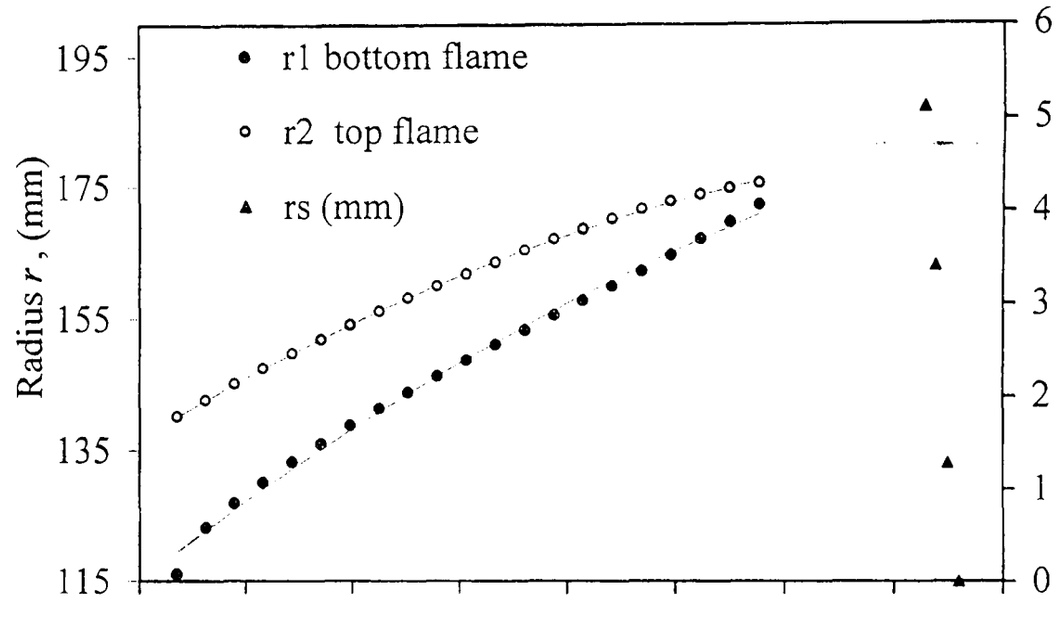

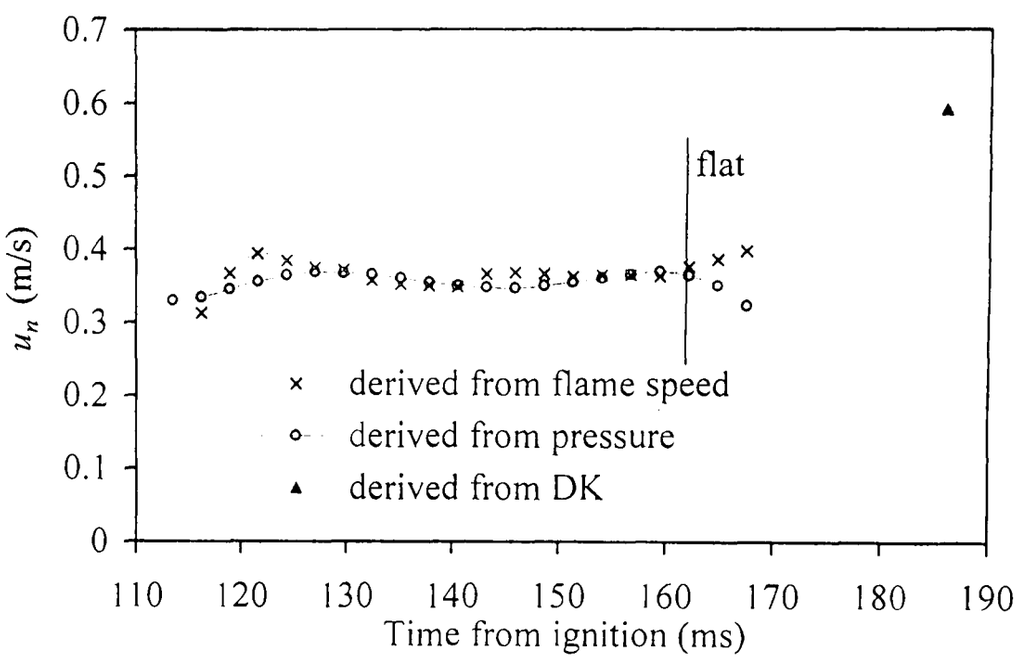

Fig. B.1 Iso-octane - air implosion, $\phi = 0.8, p_o = 0.5$ MPa, $T_o = 358$ K

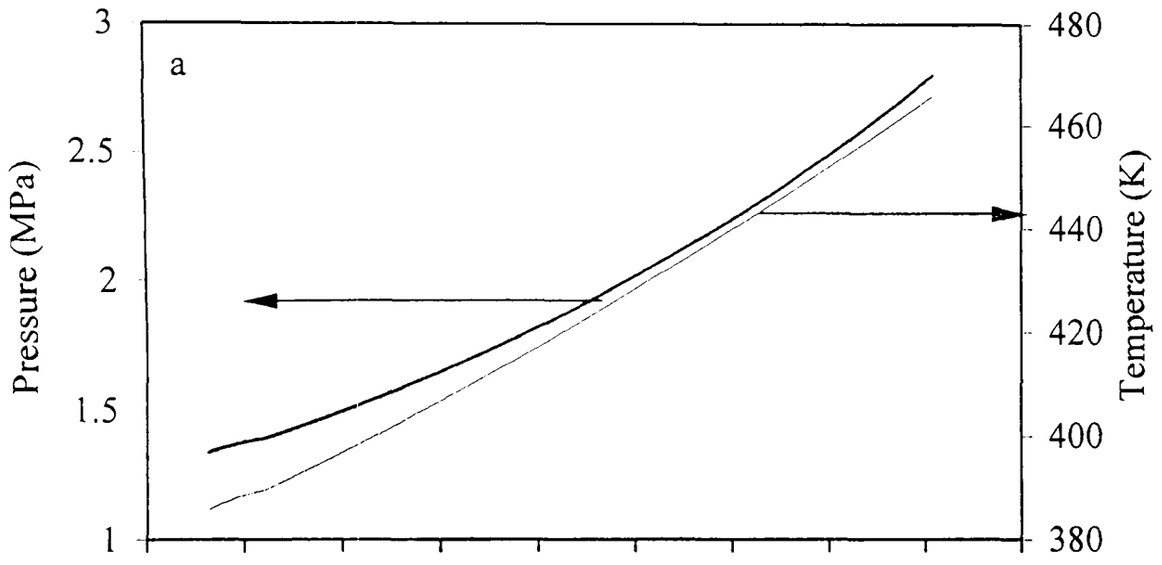

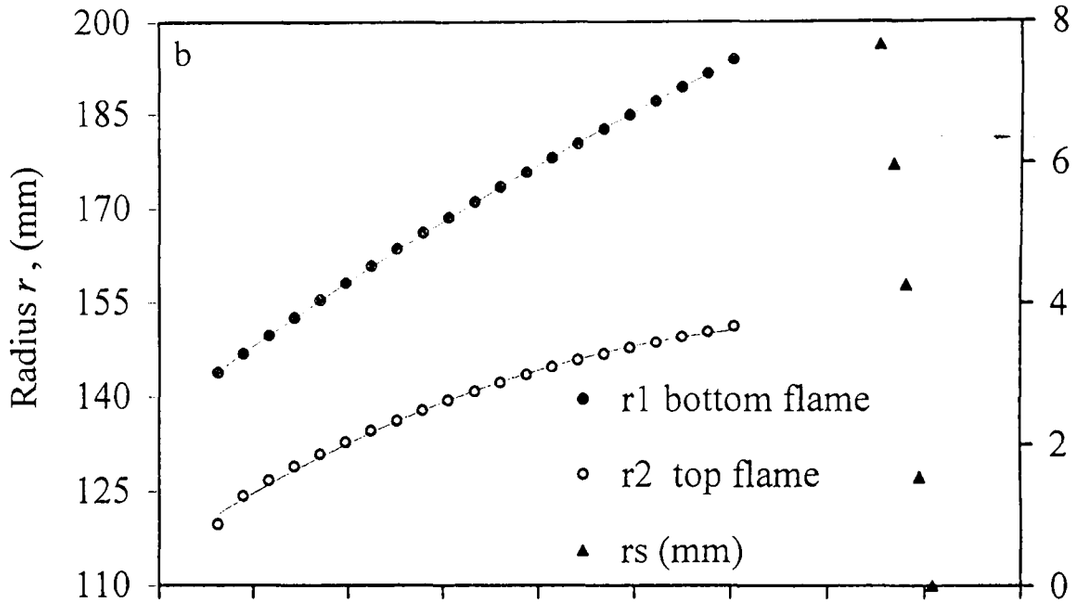

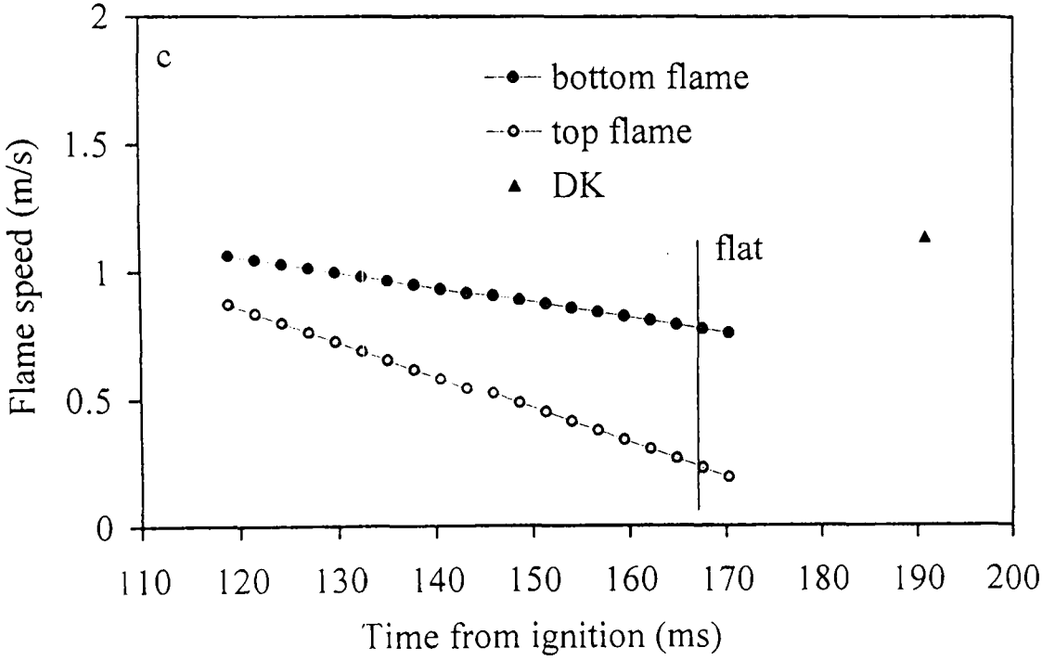

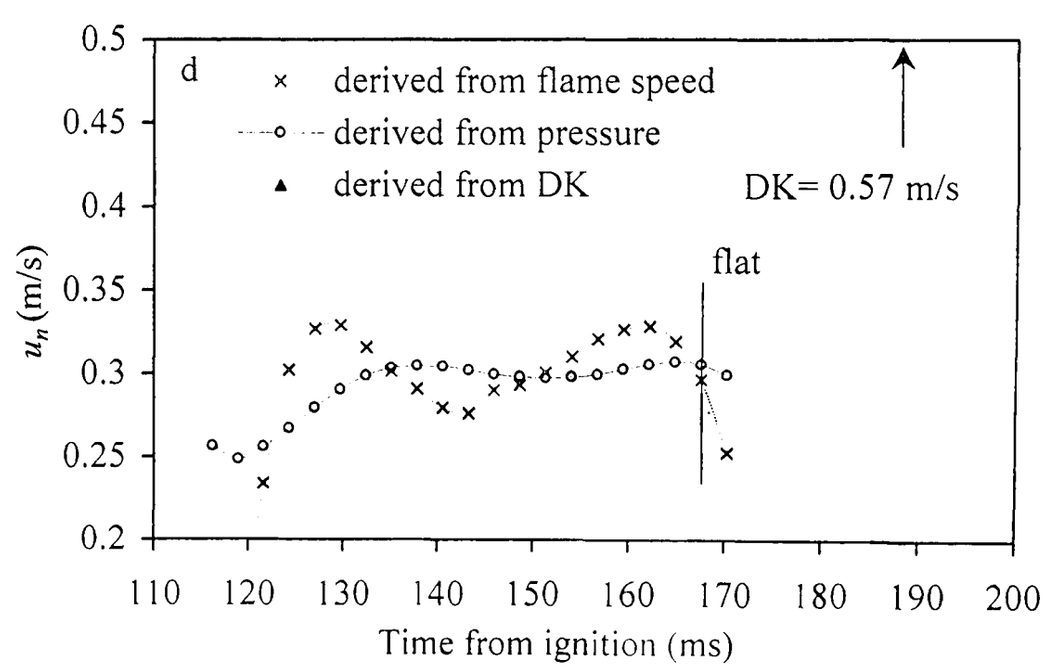

Fig. B.2. Iso-octane - air implosion, ϕ = 0.8, p_o = 1MPa, T_o = 358 K

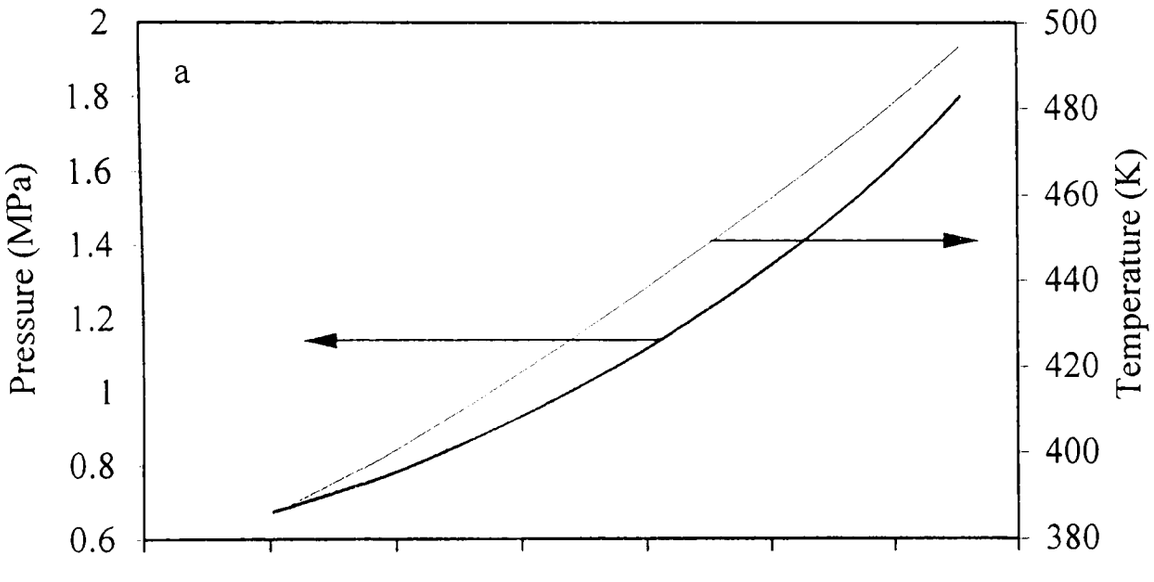

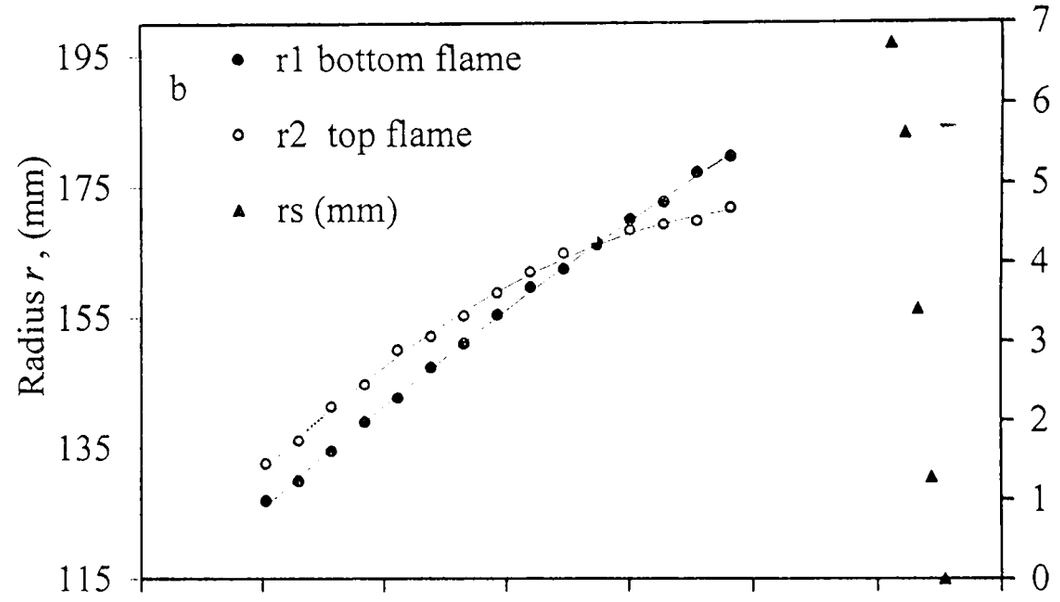

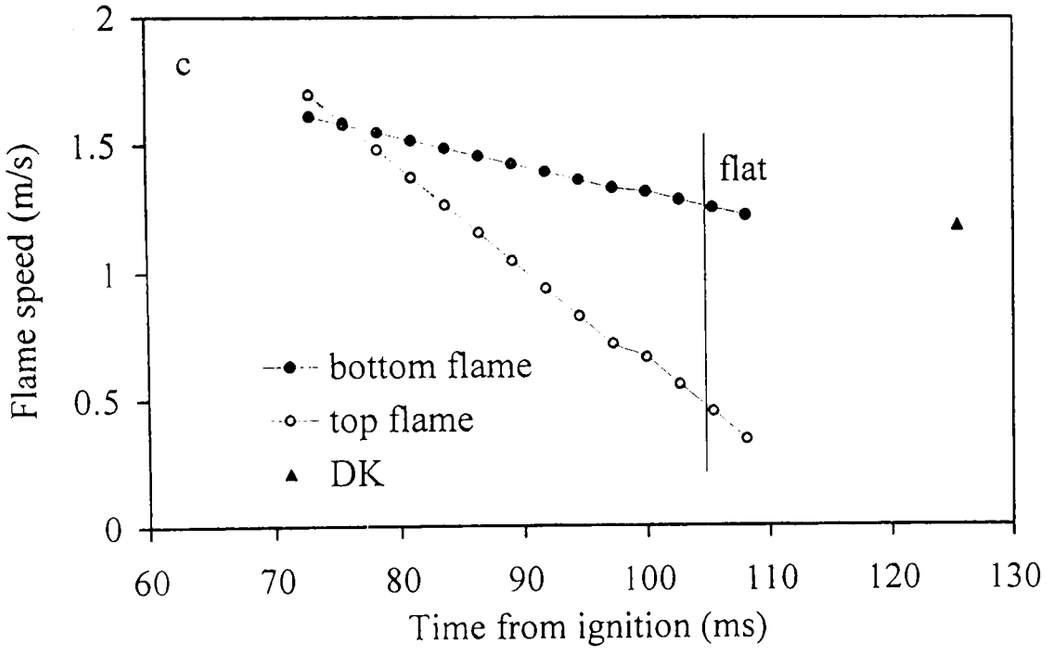

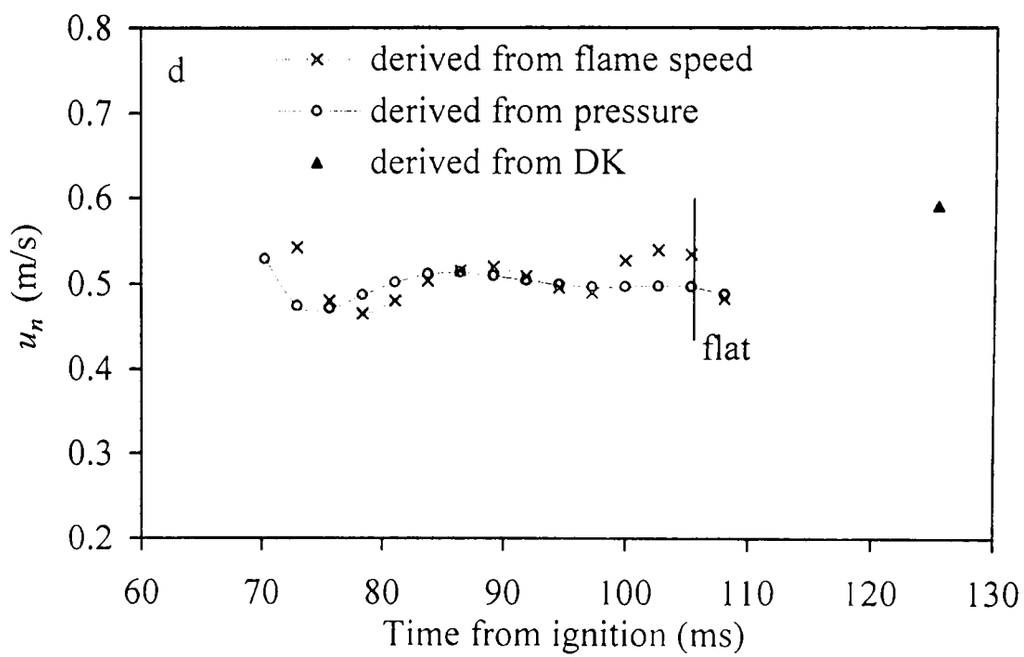

Fig. B.3. Iso-octane - air implosion, ϕ = 0.9, p_o = 0.5 MPa, T_o = 358 K

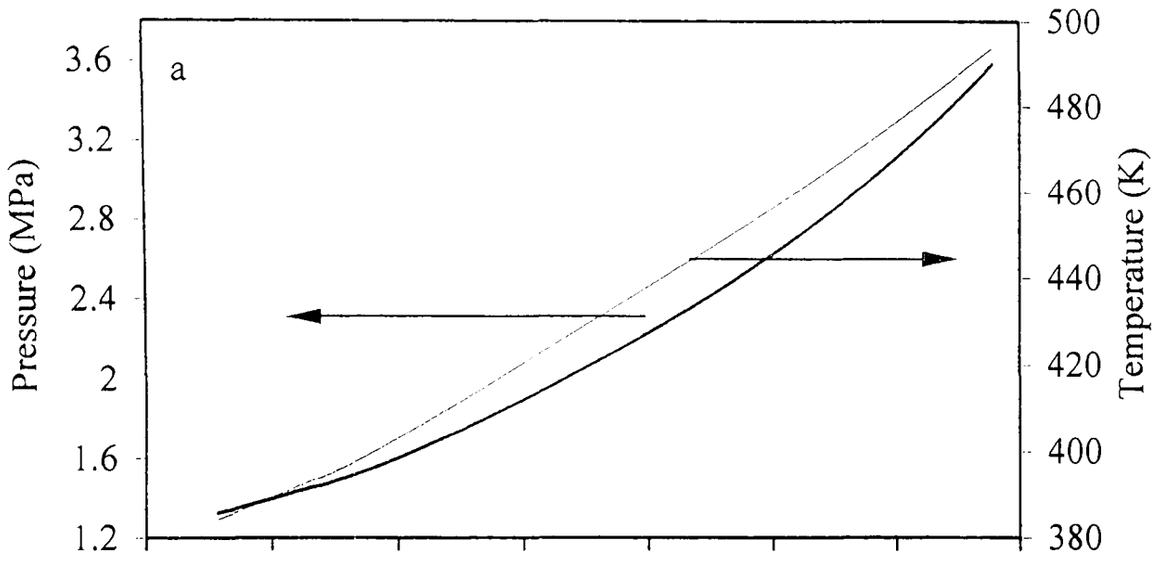

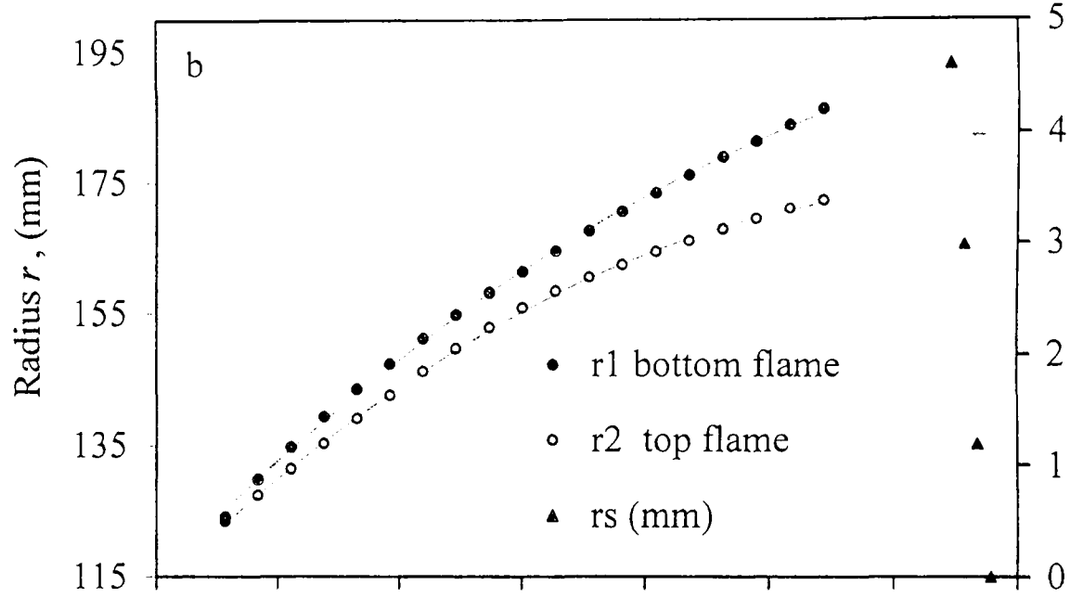

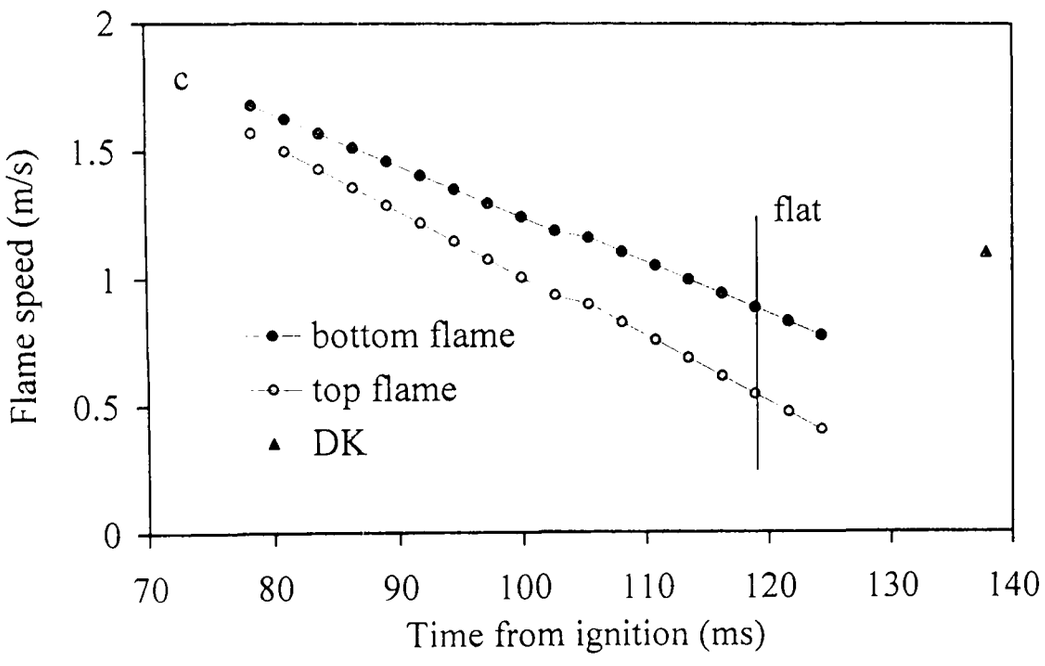

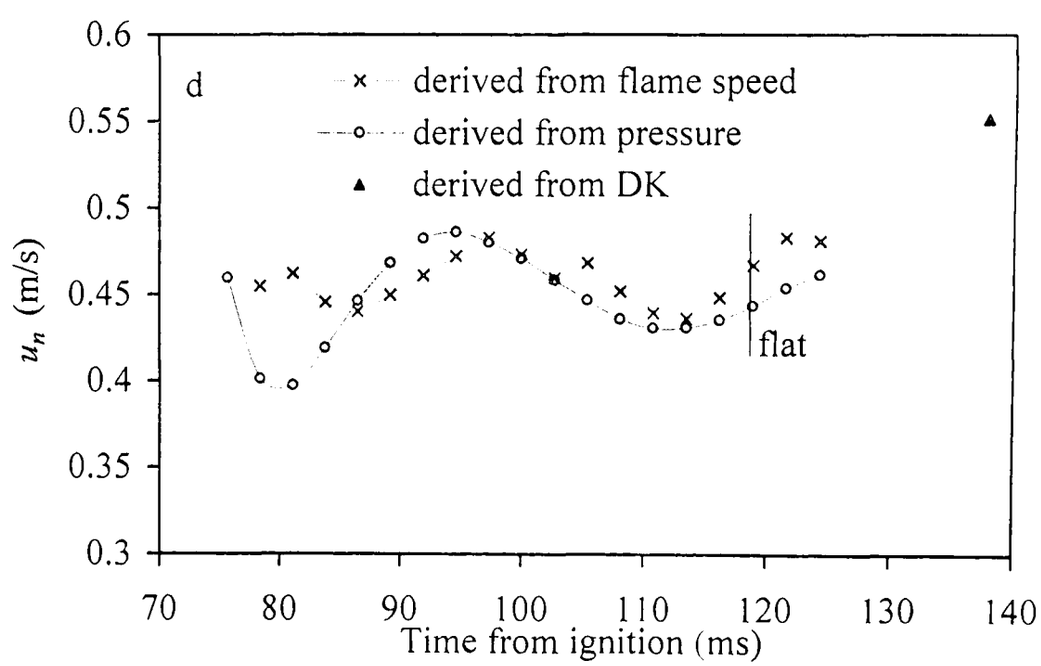

Fig. B.4. Iso-octane - air implosion, ϕ = 0.9, p_o = 1MPa, T_o = 358 K

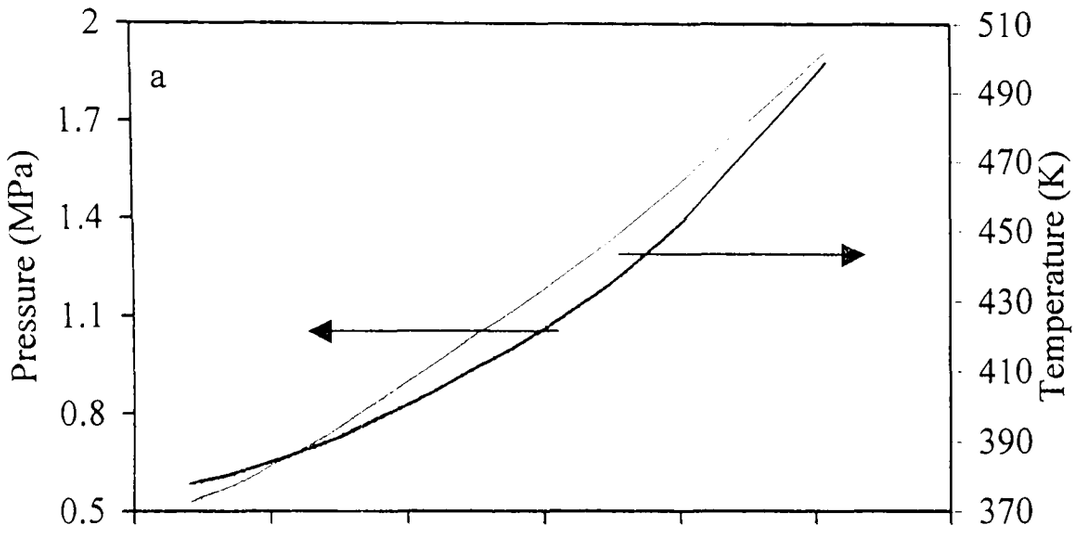

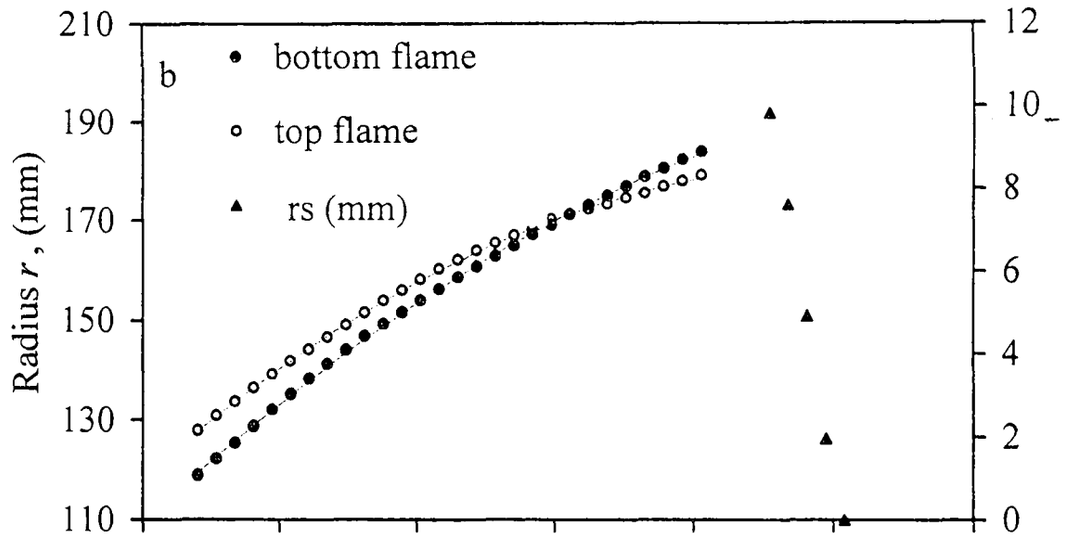

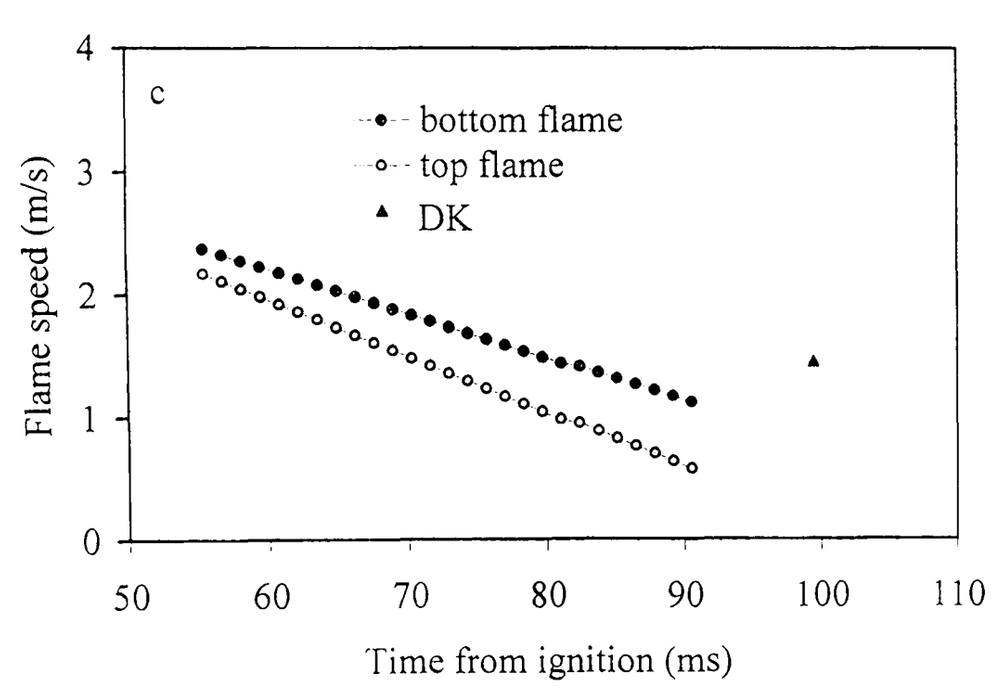

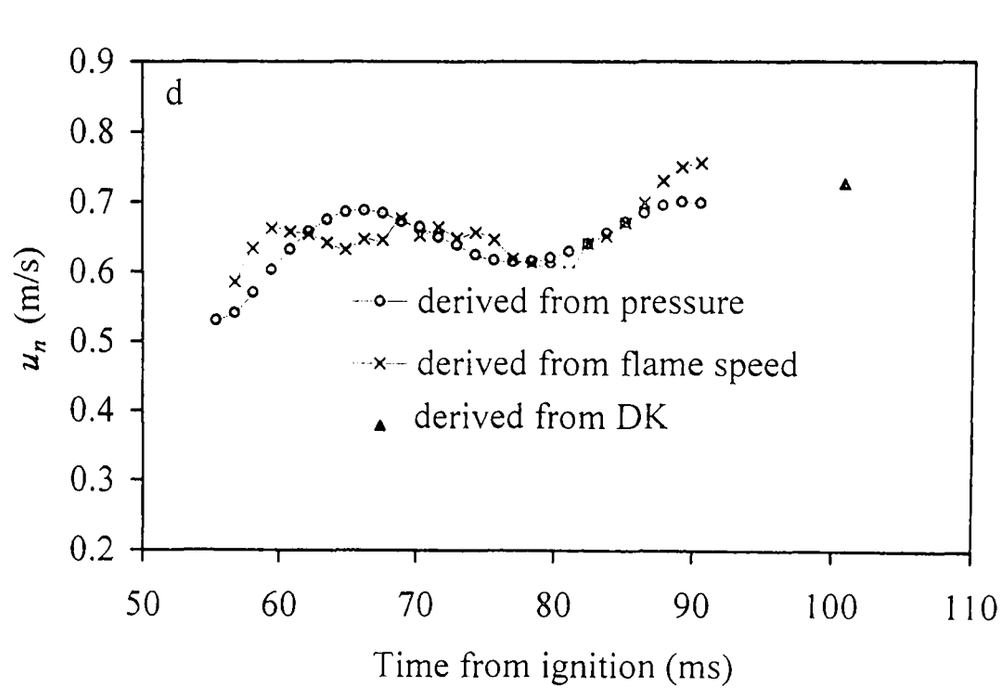

Fig. B.5. Iso-octane - air implosion, $\phi = 1, p_o = 0.5$ MPa, $T_o = 358$ K

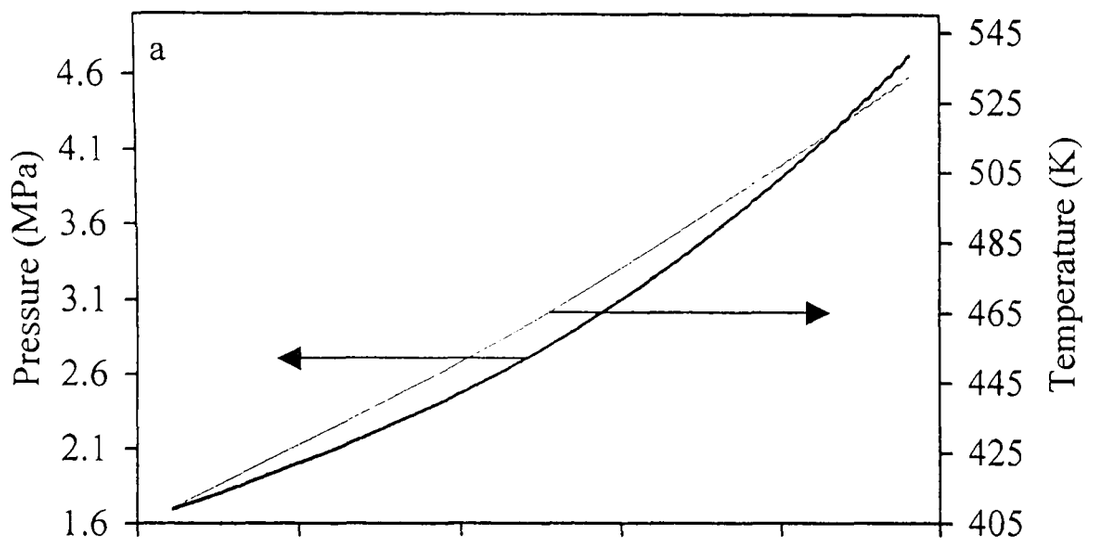

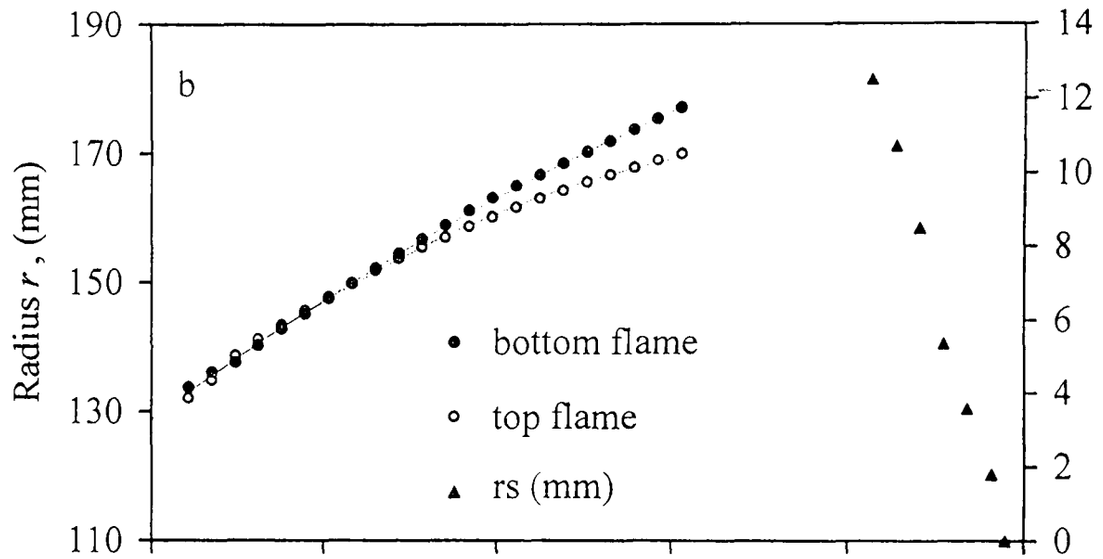

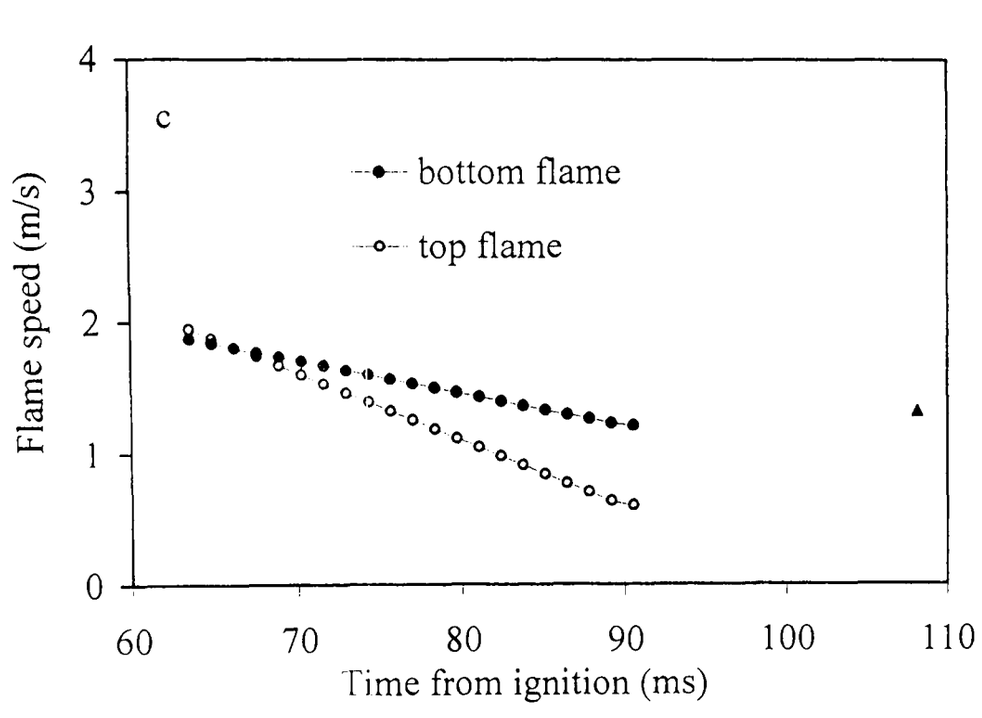

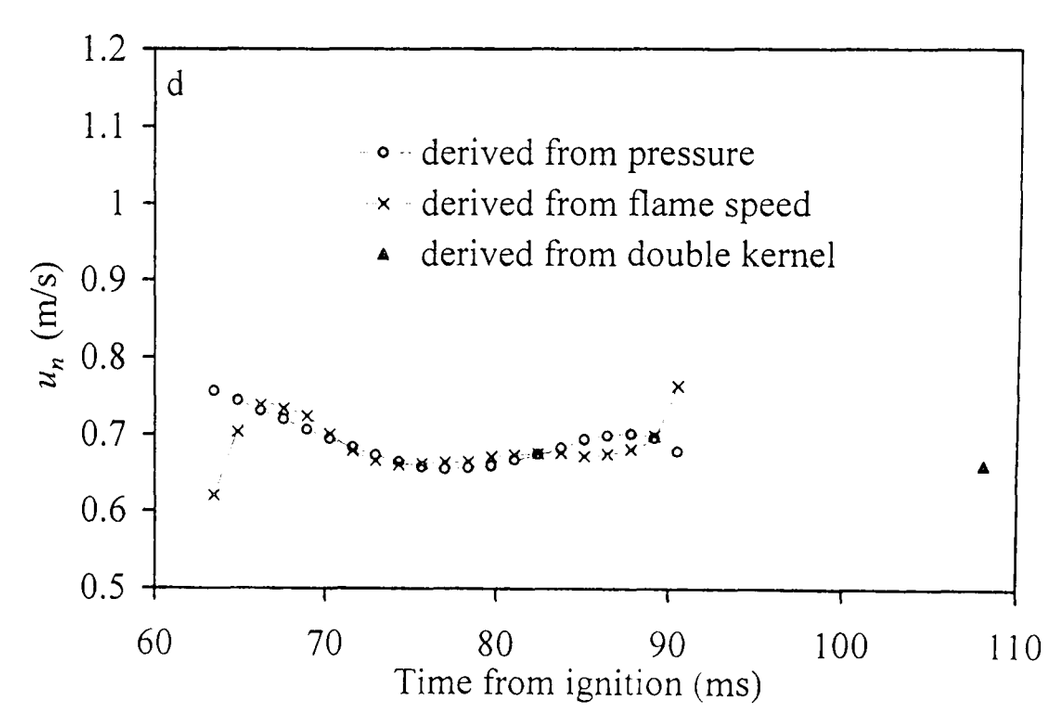

Fig. B.6. Iso-octane - air implosion, ϕ = 1, p_o = 1MPa, T_o = 358 K

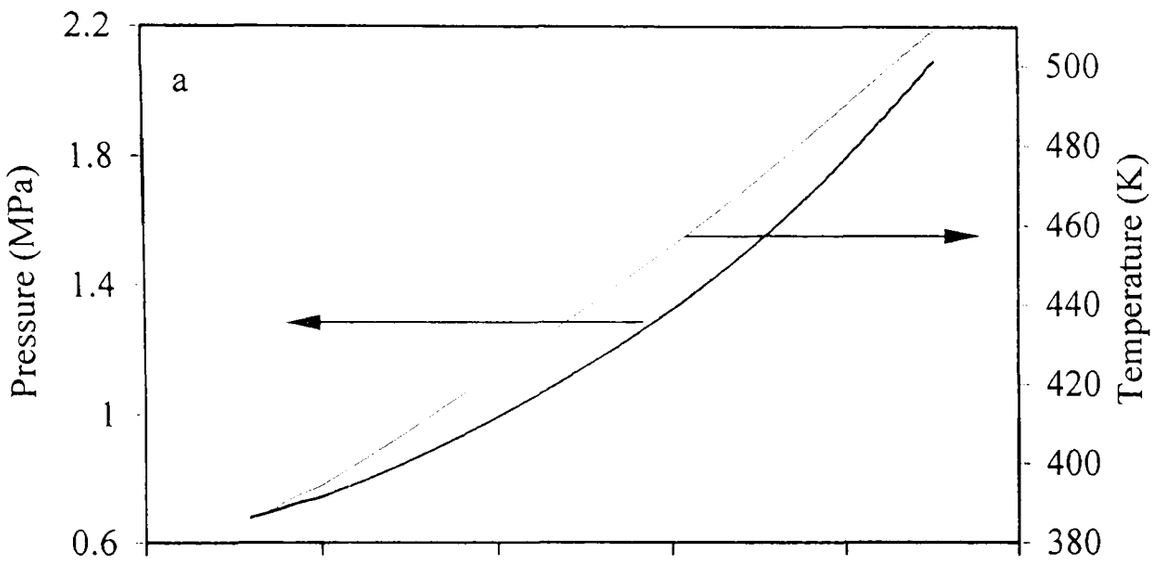

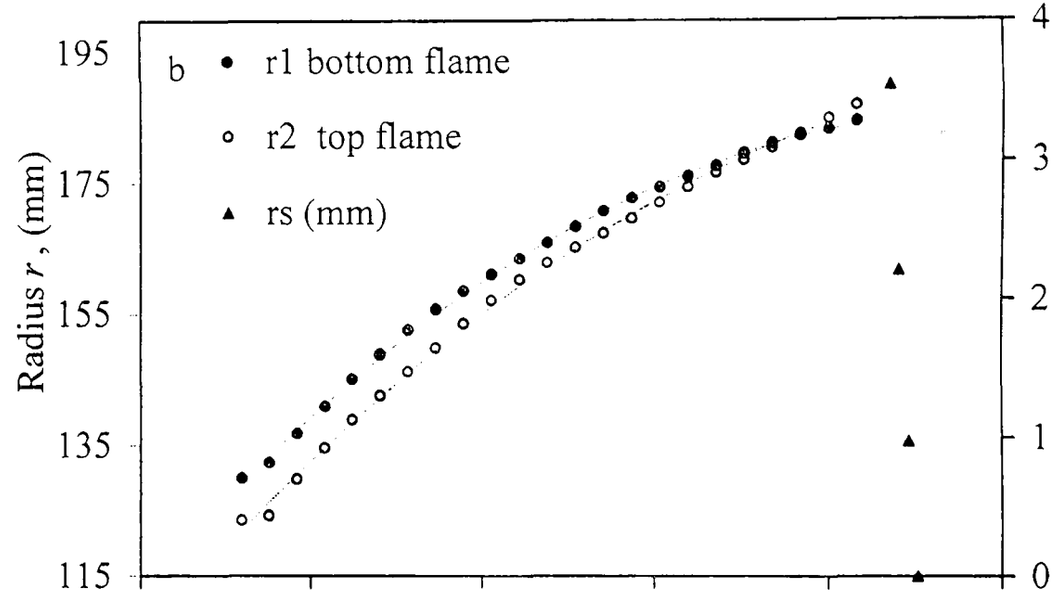

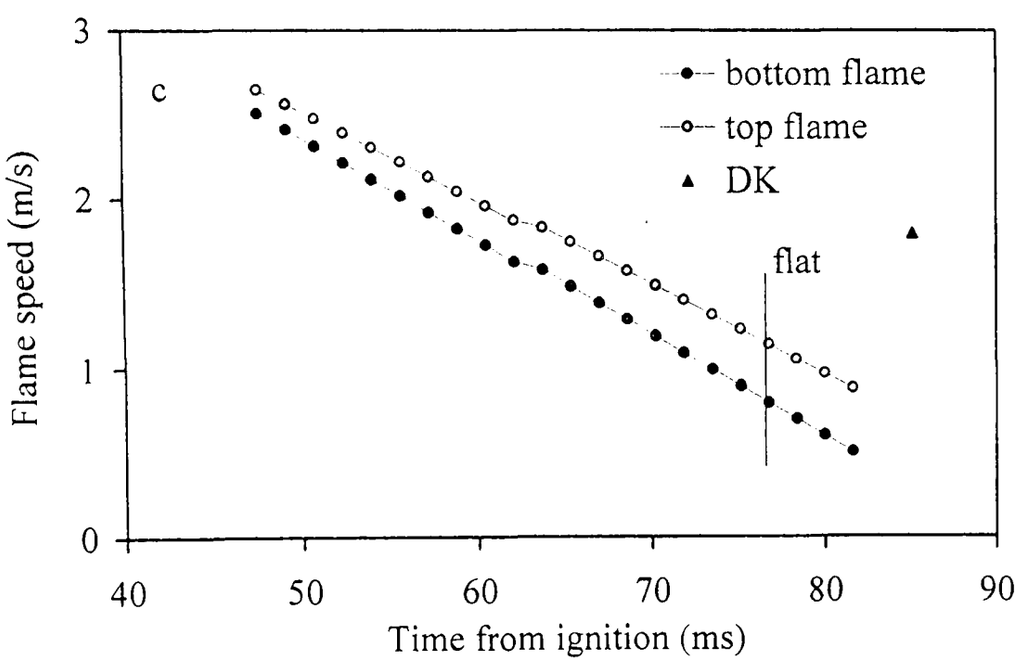

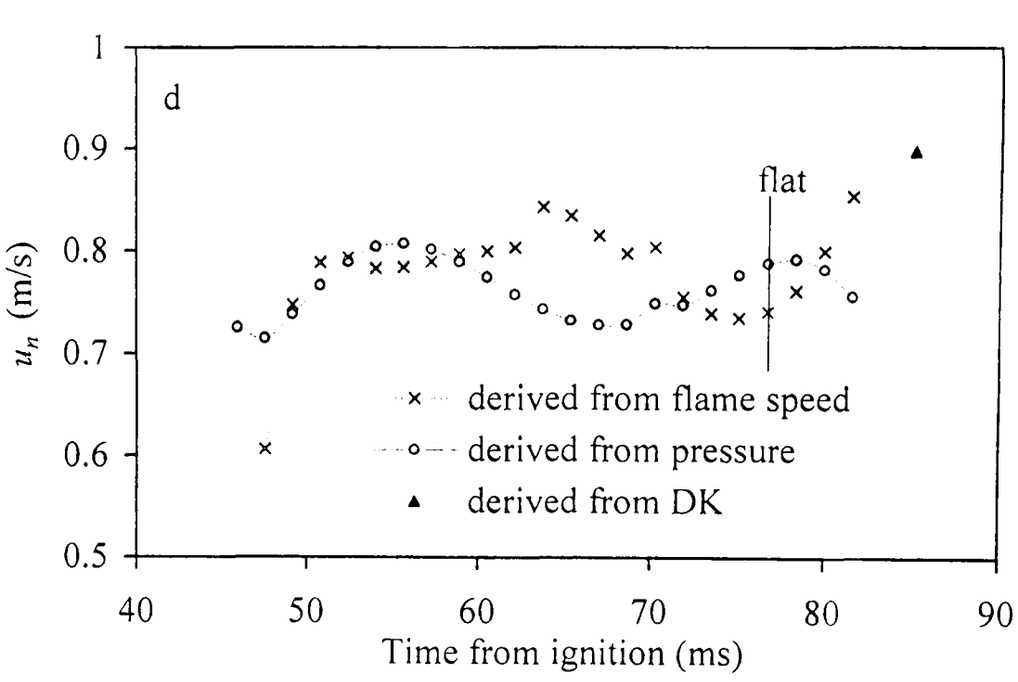

Fig. B.7. Iso-octane - air implosion, ϕ = 1.1, p_o = 0.5 MPa, T_o = 358 K

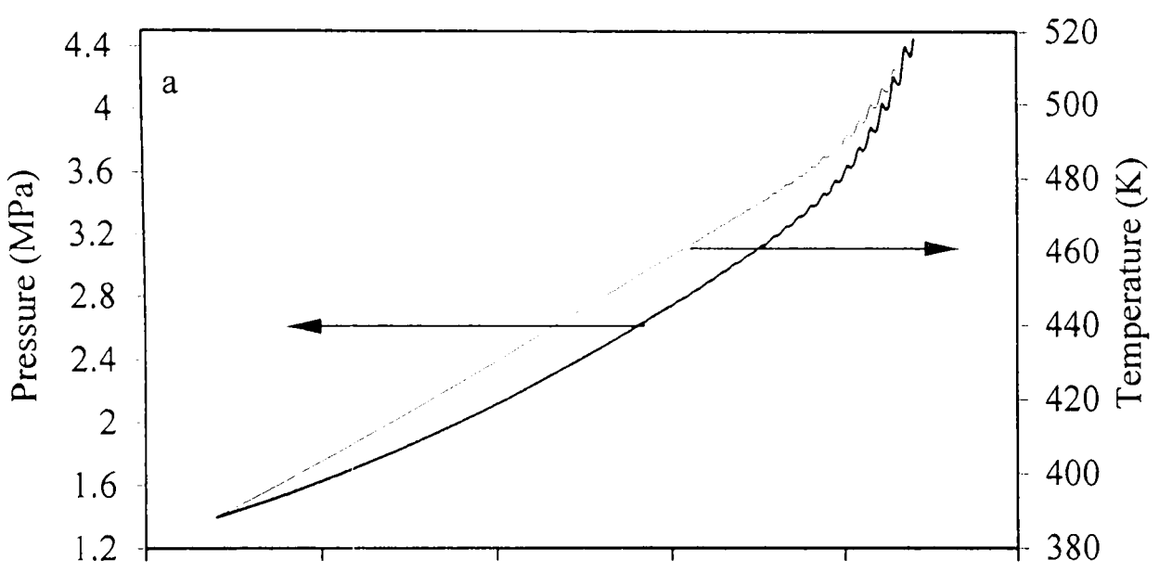

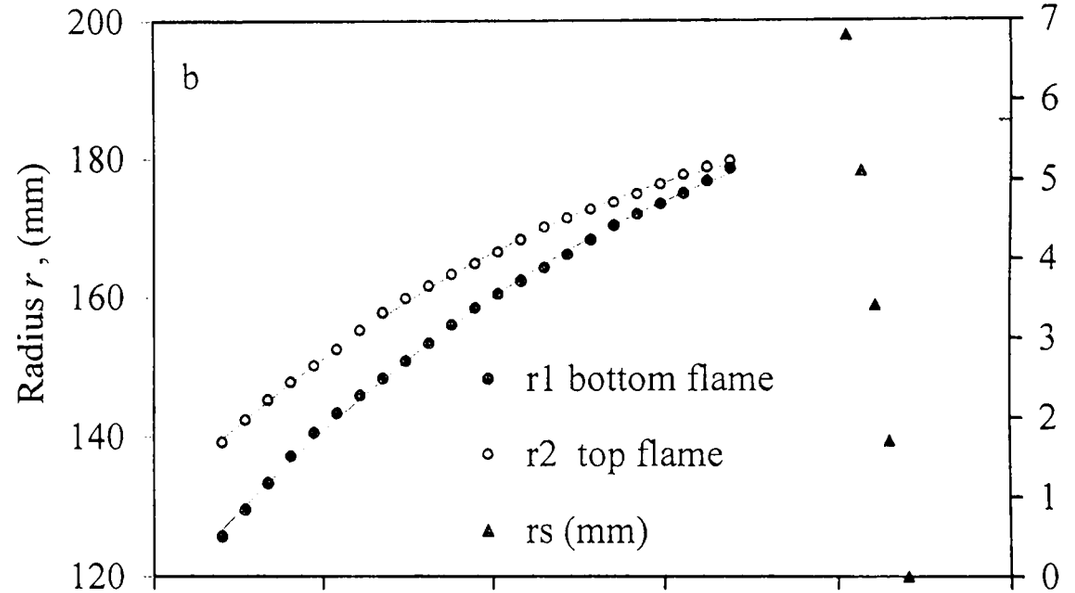

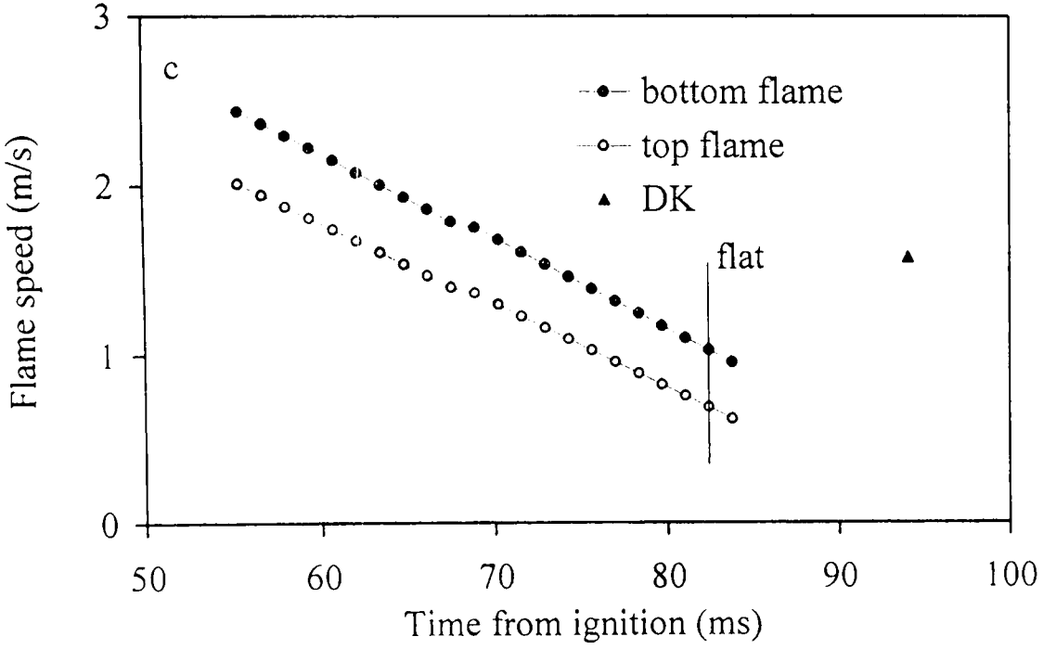

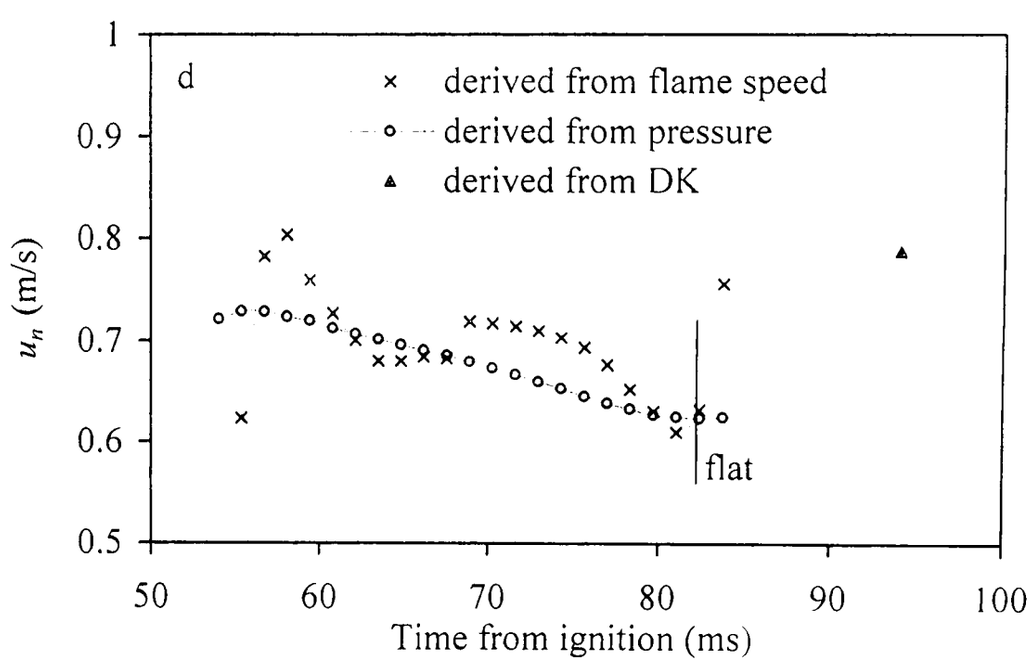

Fig. B.8. Iso-octane - air implosion, $\phi = 1.1, p_o = 1\text{MPa}, T_o = 358\ \text{K}$

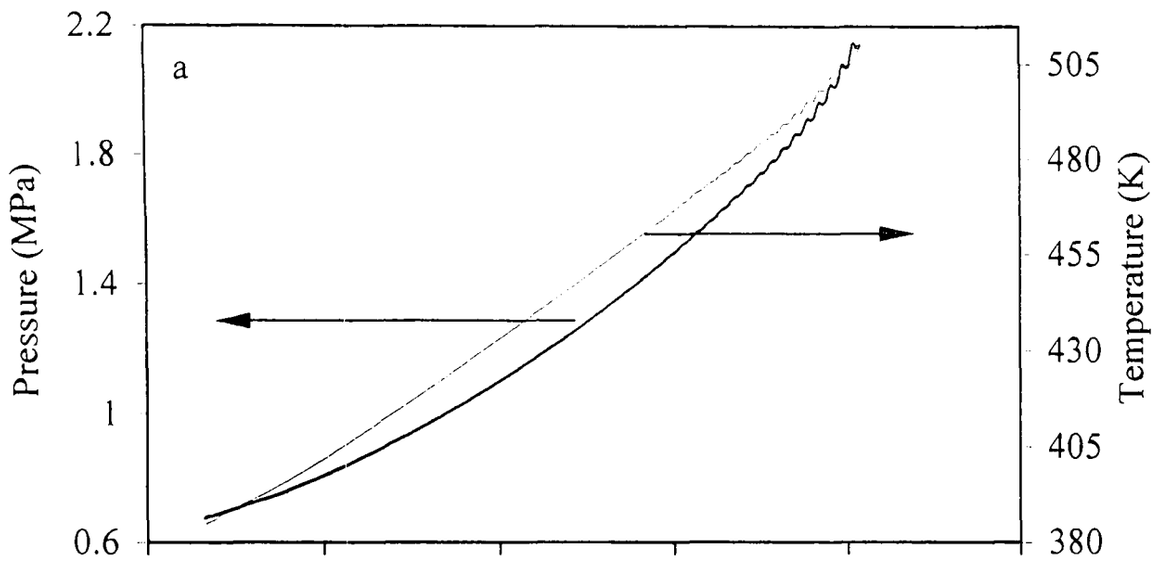

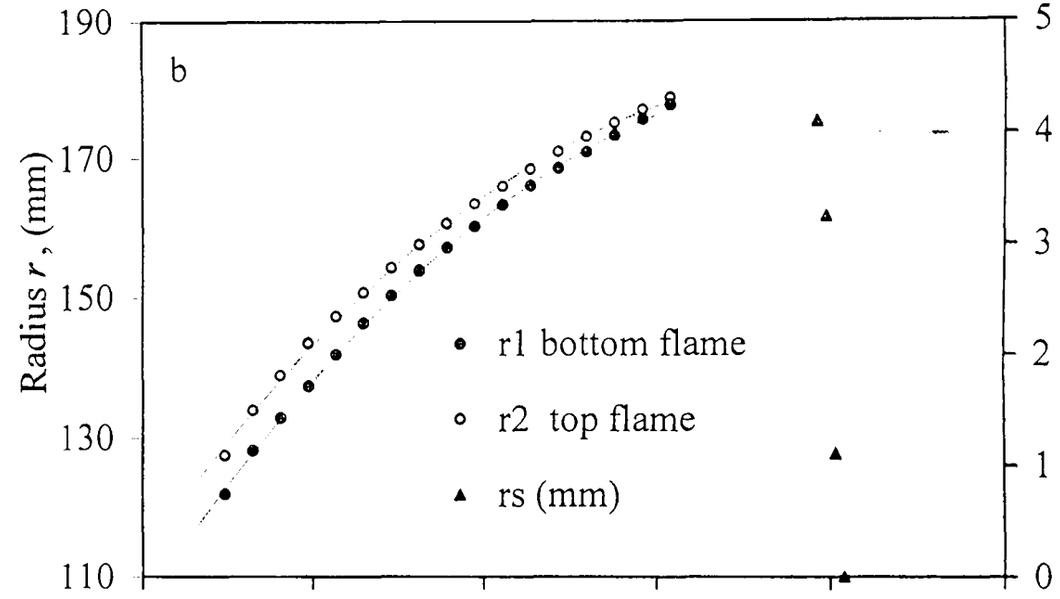

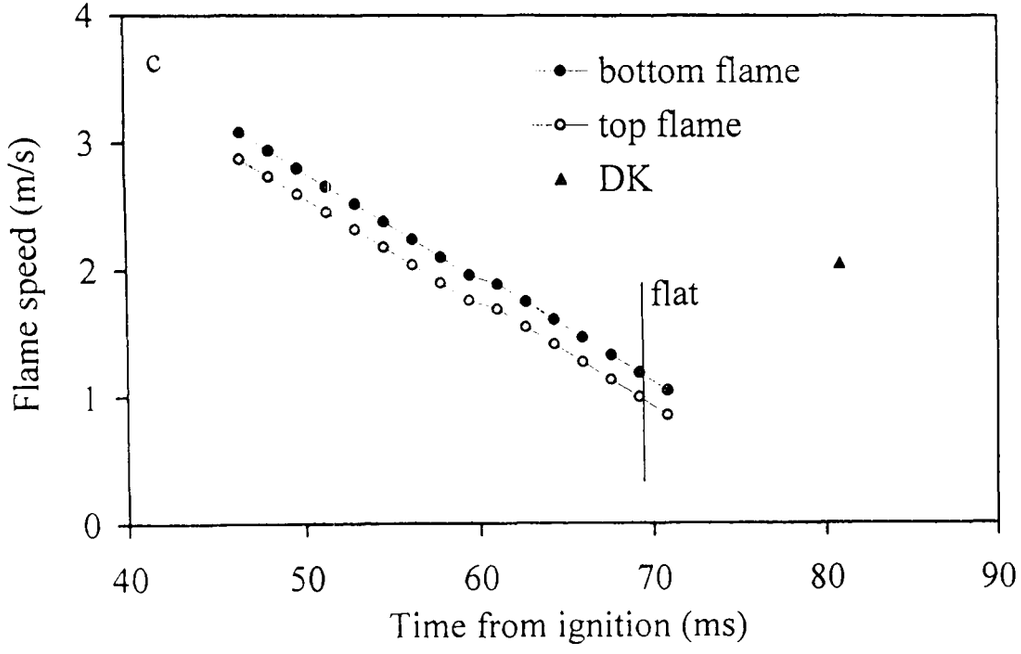

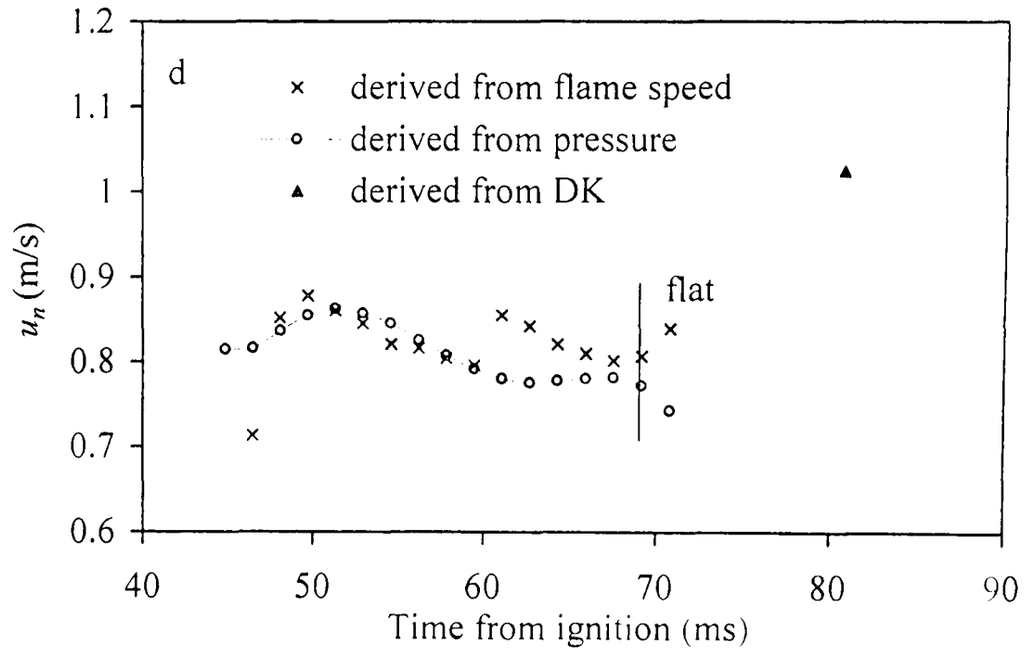

Fig. B.9. Iso-octane - air implosion, ϕ = 1.2, p_o = 0.5 MPa, T_o = 358 K

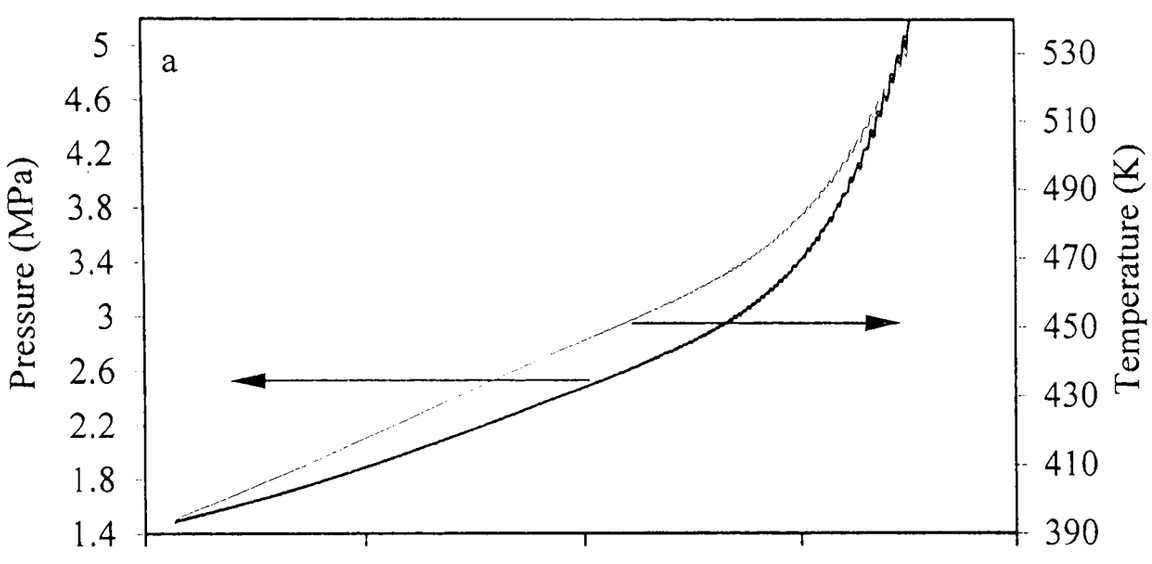

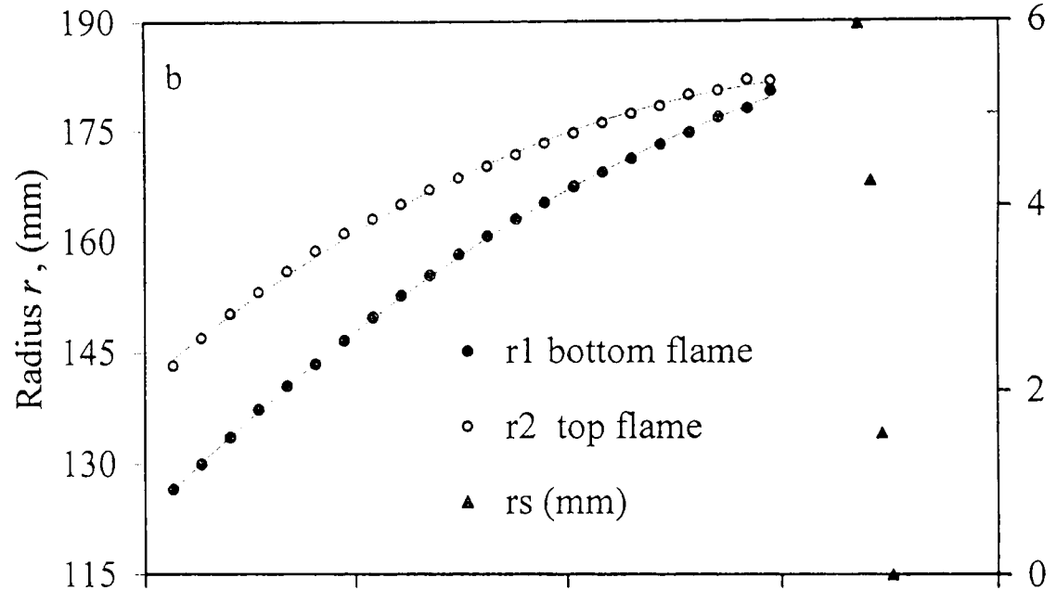

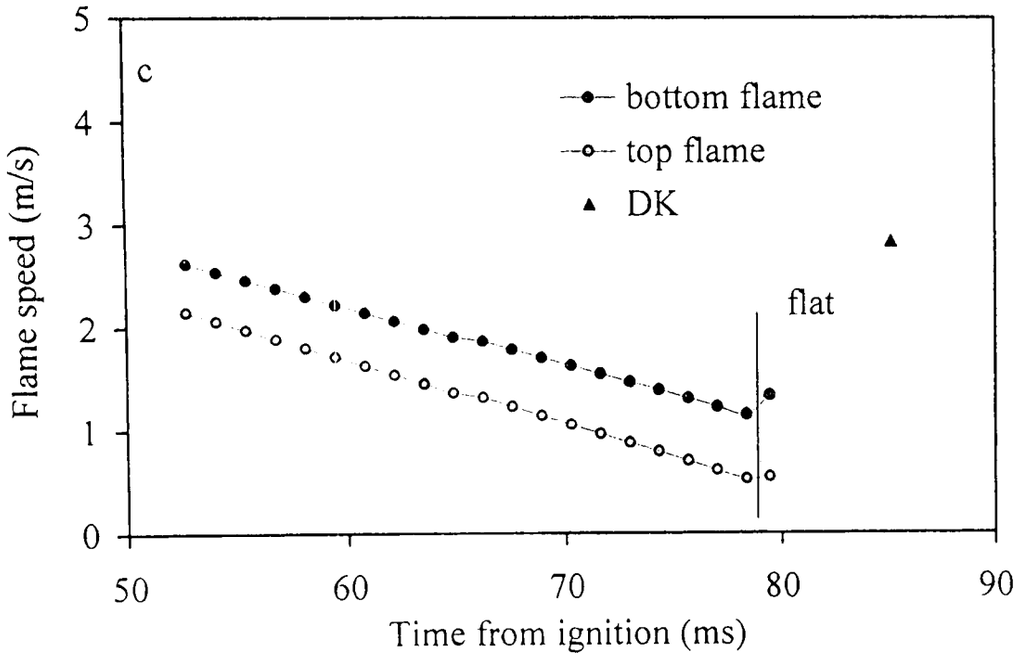

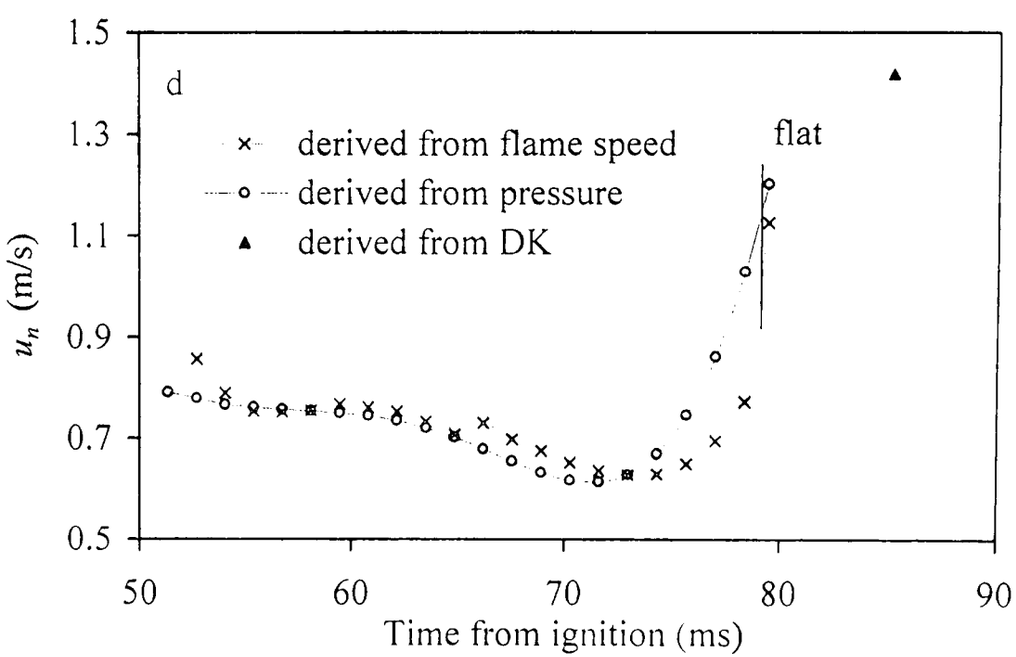

Fig. B.10. Iso-octane - air implosion, ϕ = 1.2, p_o = 1 MPa, T_o = 358 K

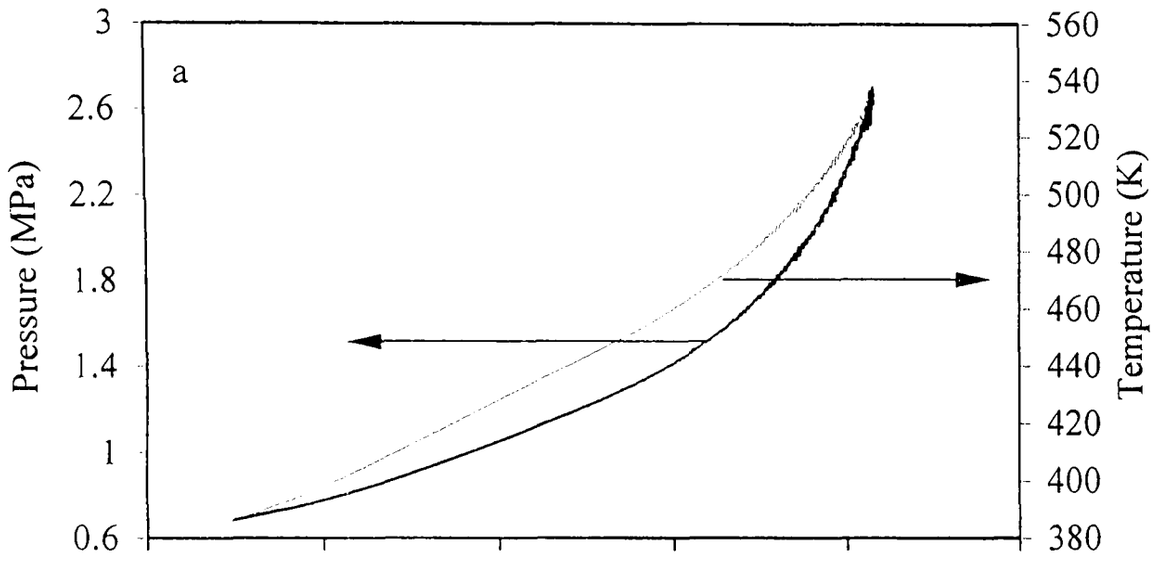

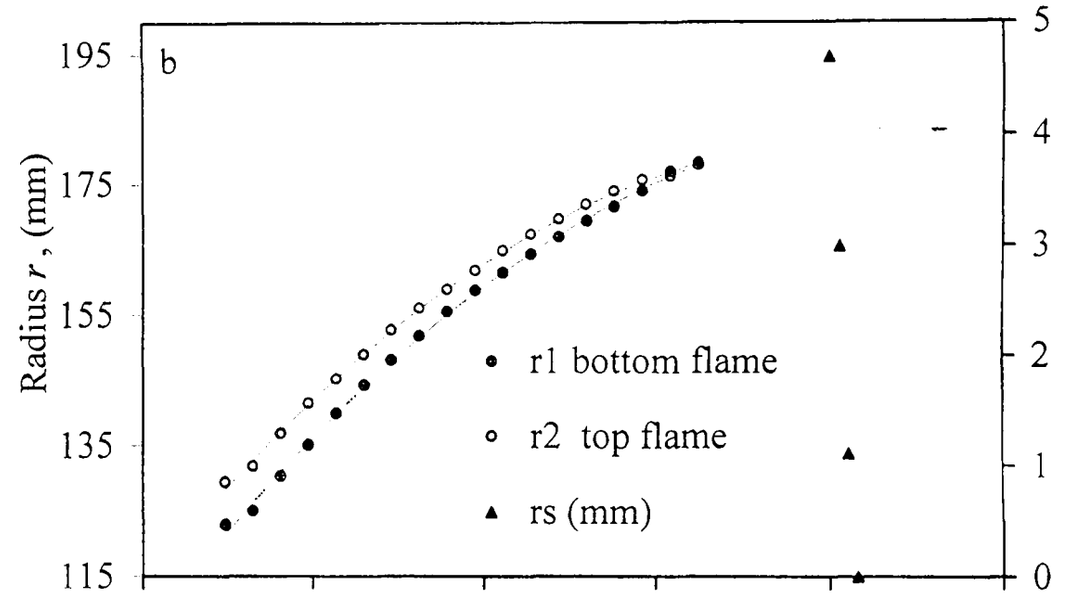

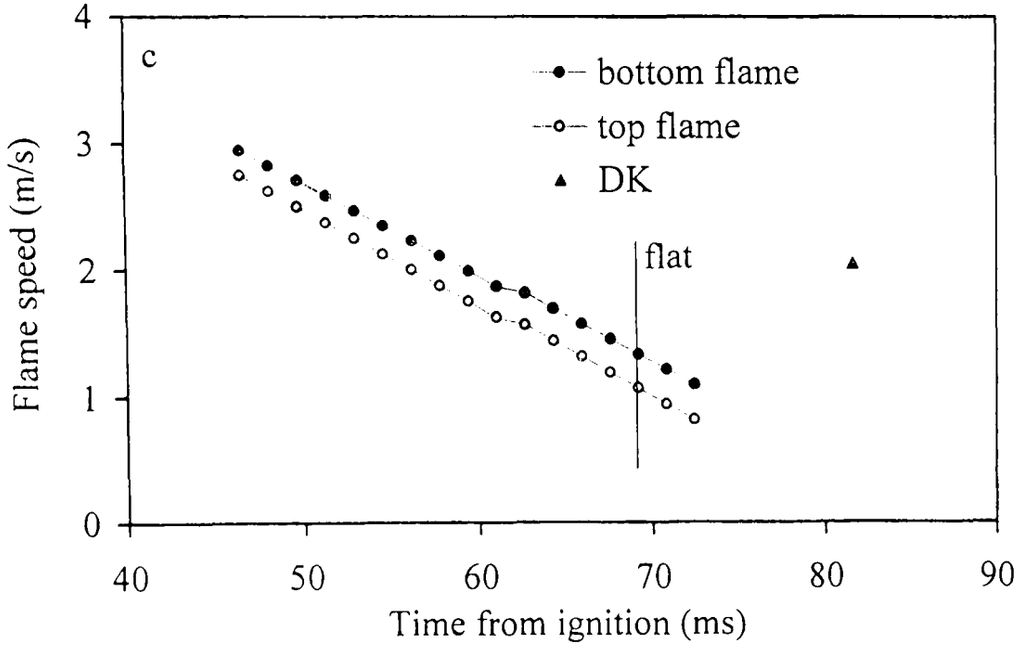

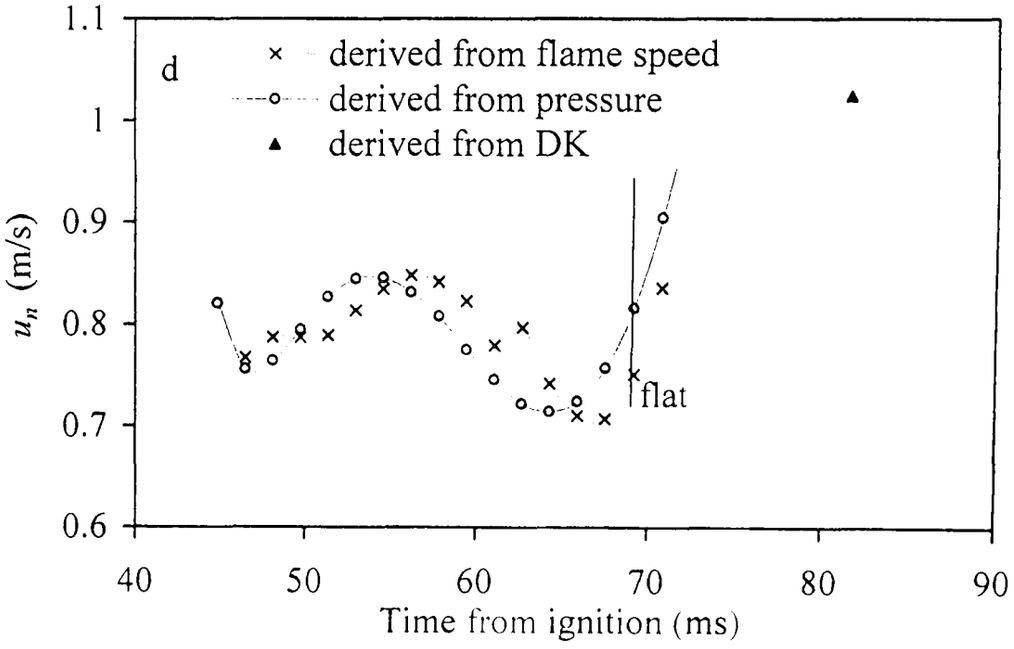

Fig. B.11. Iso-octane - air implosion, ϕ = 1.3, p_o = 0.5 MPa, T_o = 358 K

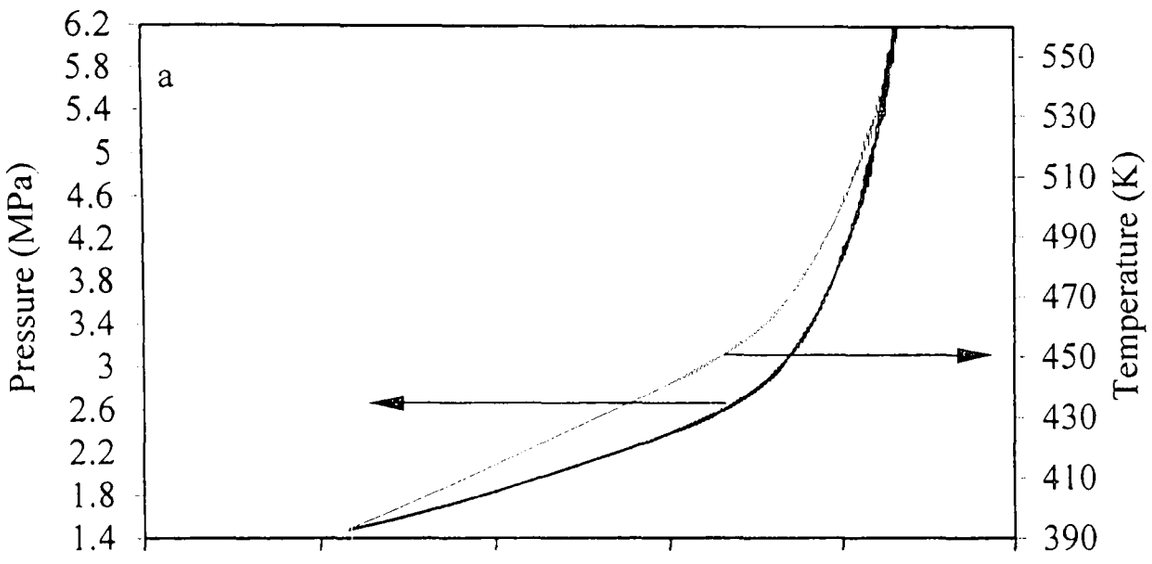

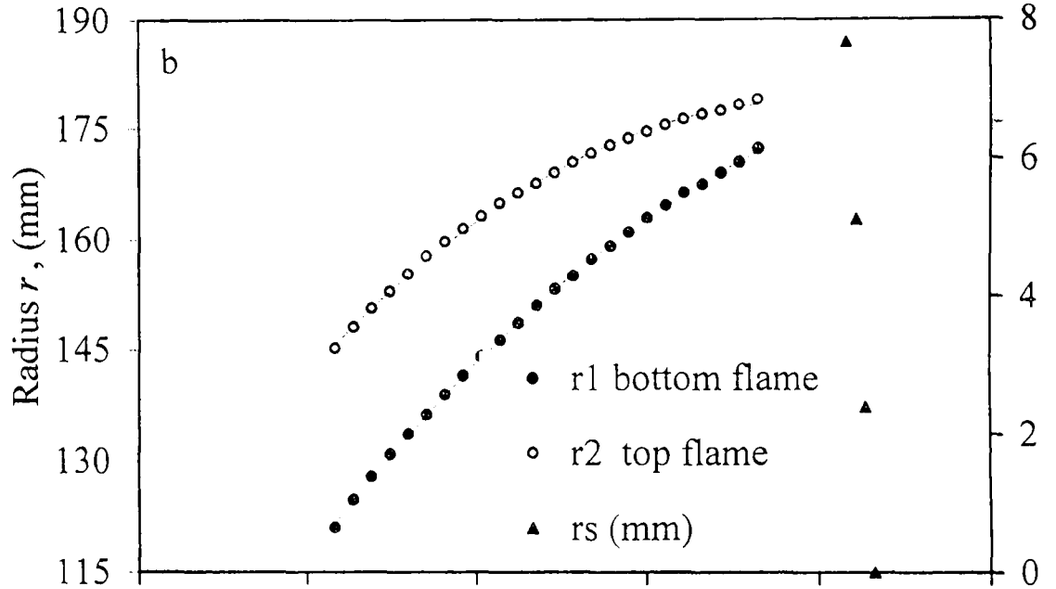

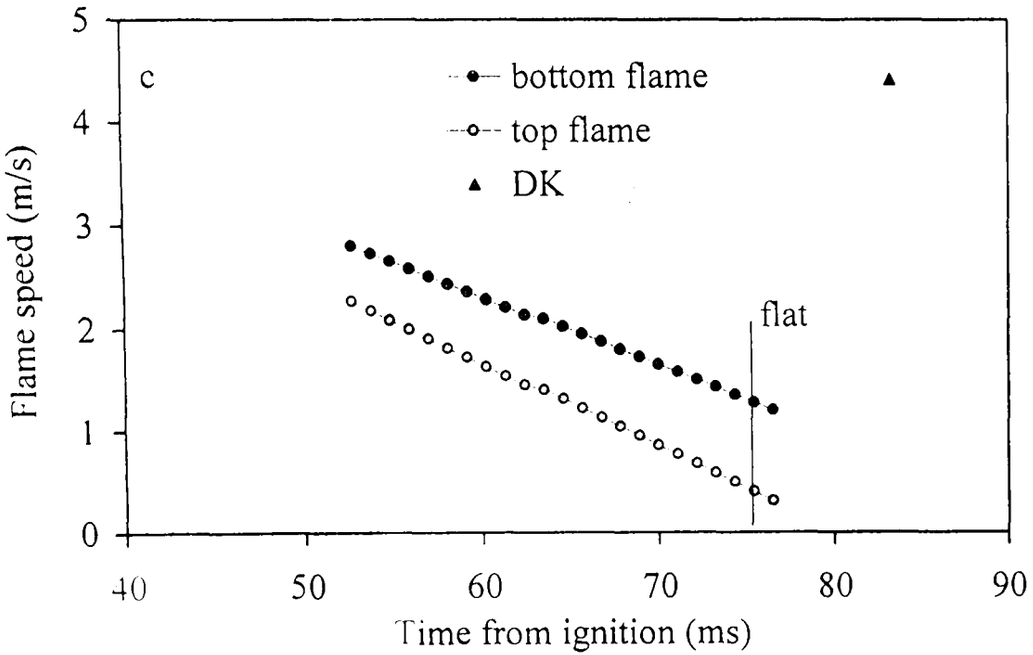

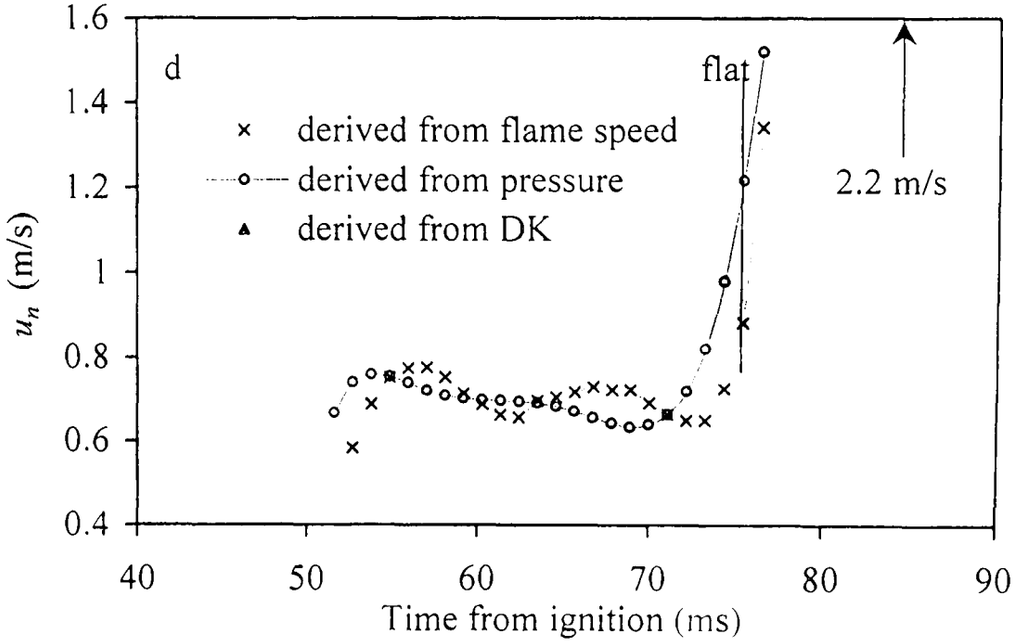

Fig. B.12. Iso-octane - air implosion, ϕ = 1.3, P_o = 1 MPa, T_o = 358 K

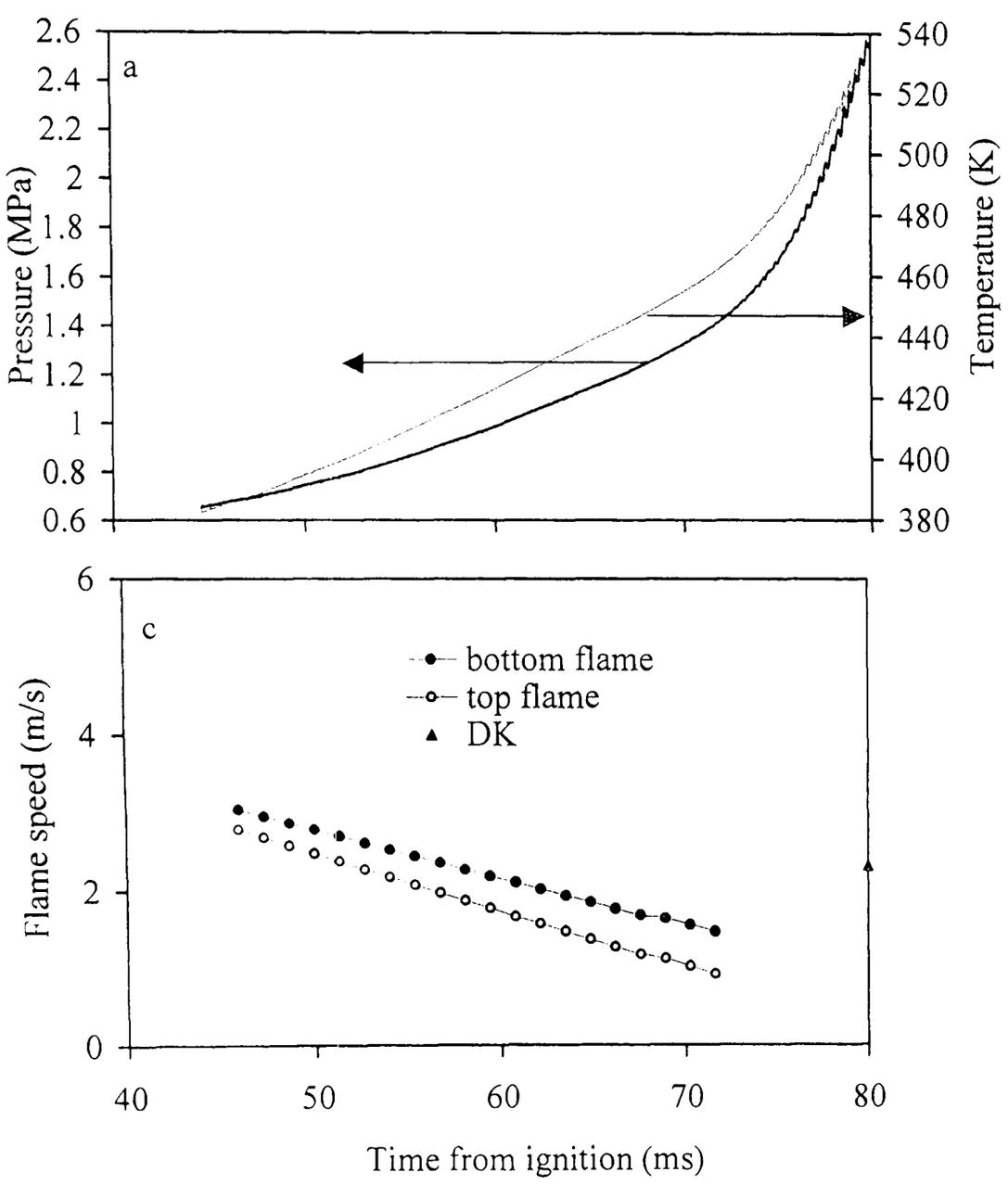

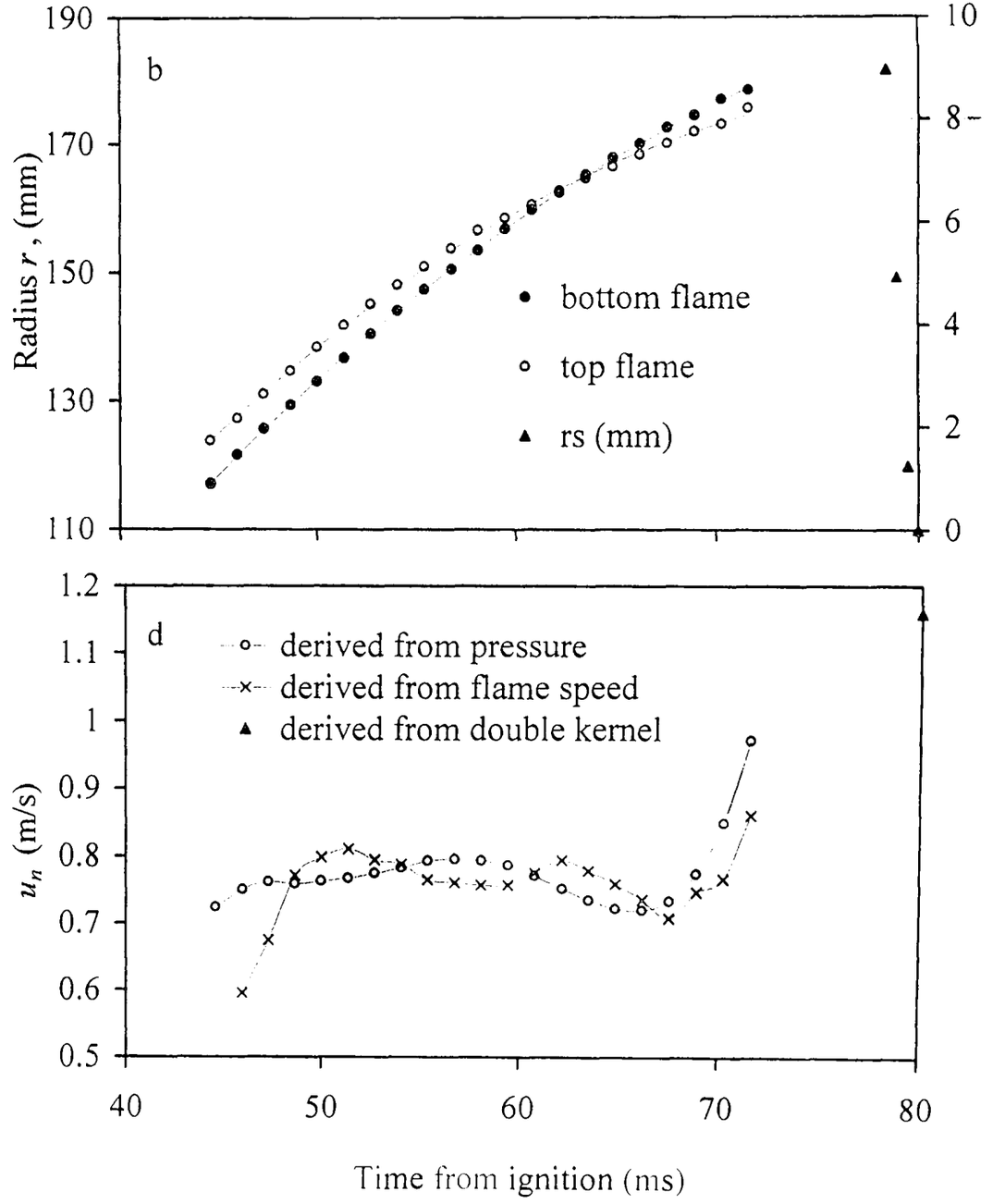

Fig. B.13. Iso-octane - air implosion, ϕ = 1.4, p_o = 0.5 MPa, T_o = 358 K

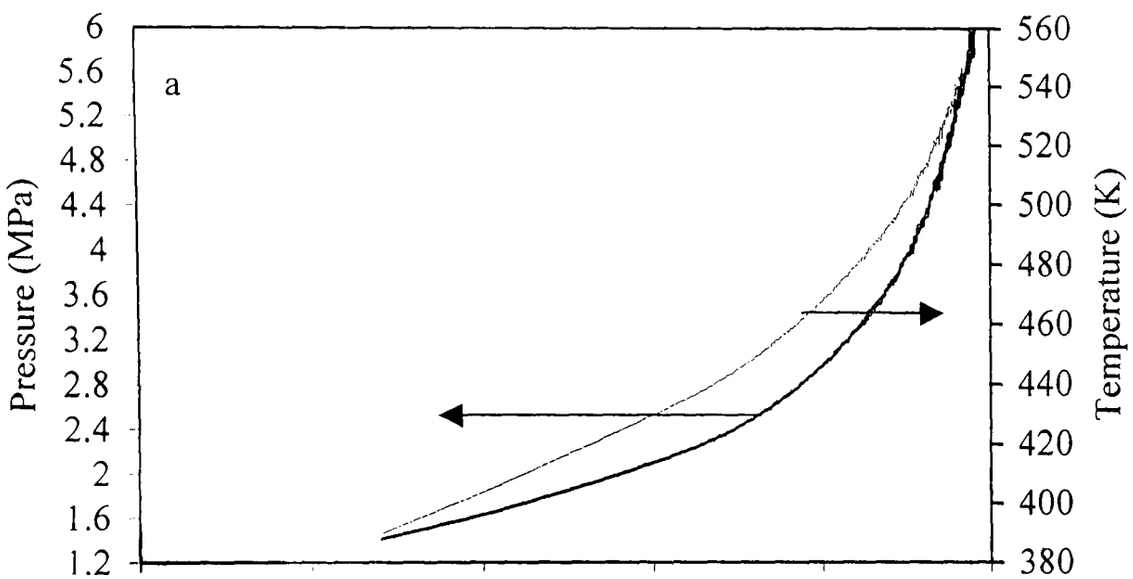

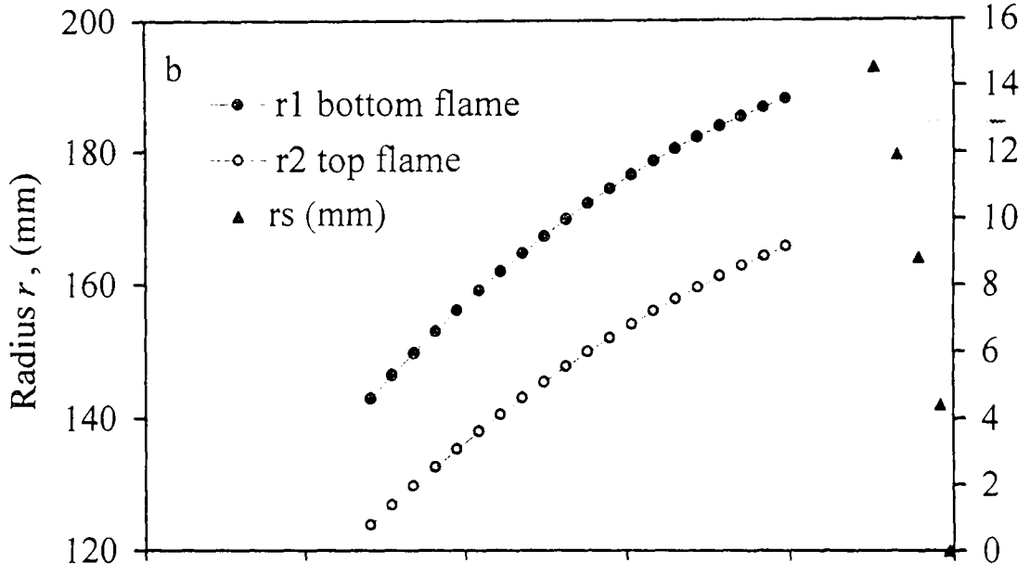

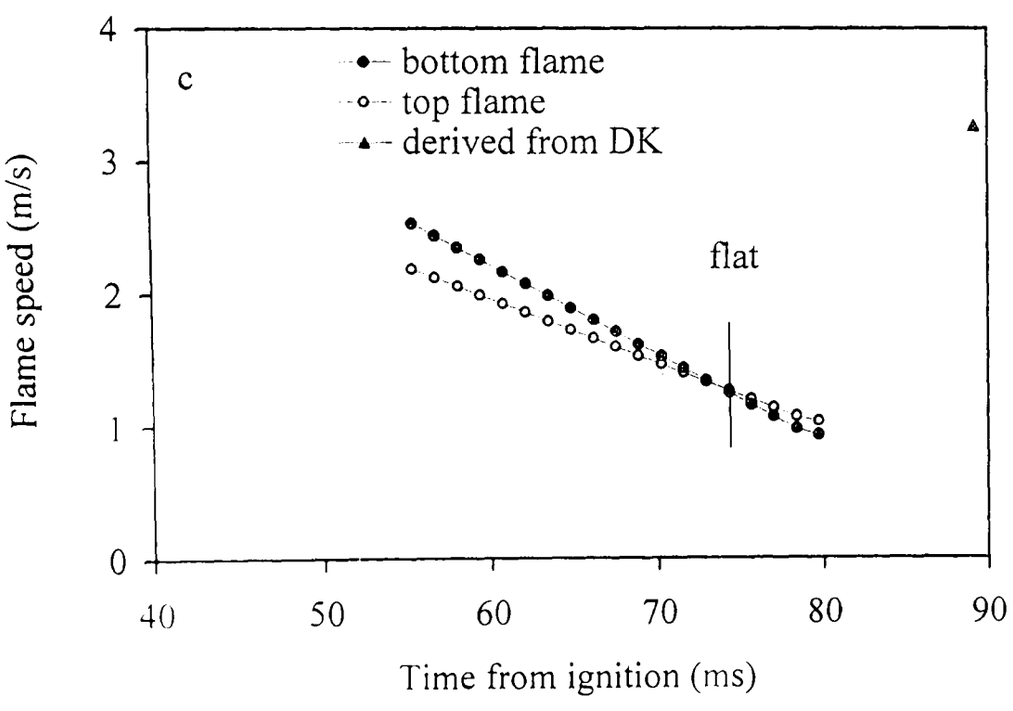

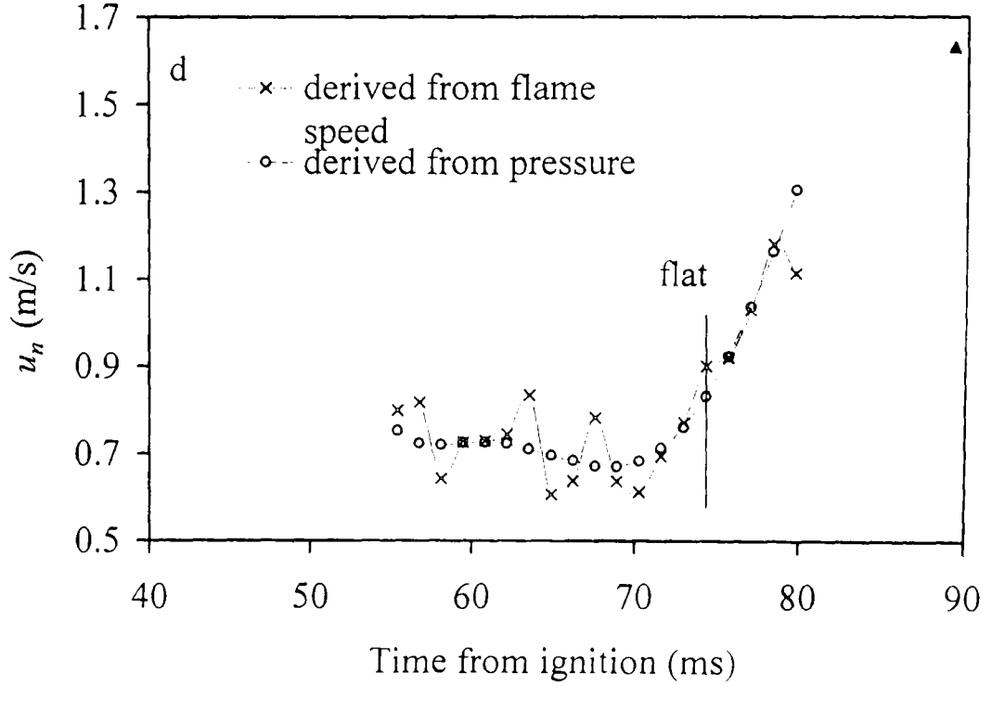

Fig. B.14. Iso-octane - air implosion, ϕ = 1.4, p_o = 1 MPa, T_o = 358 K

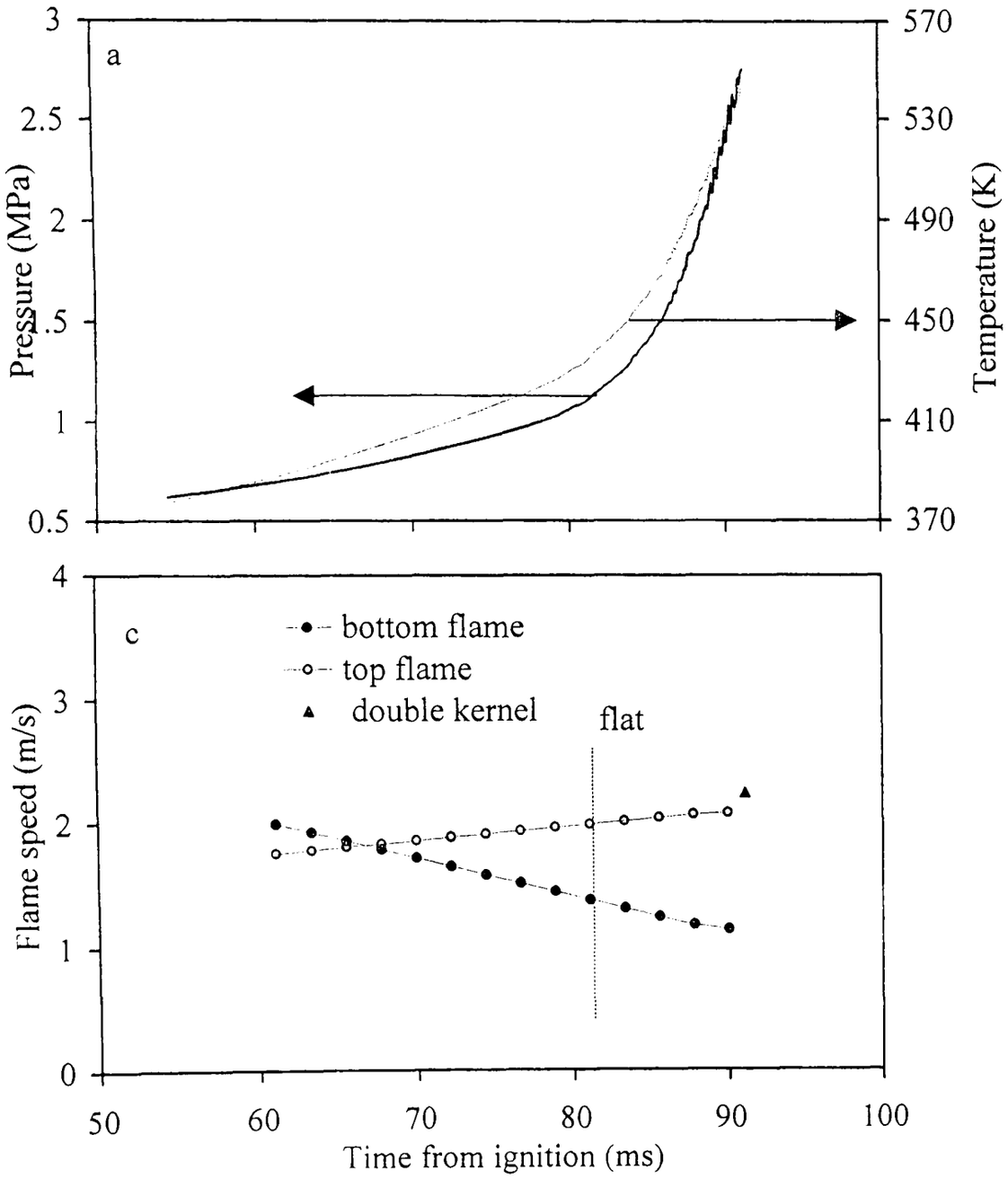

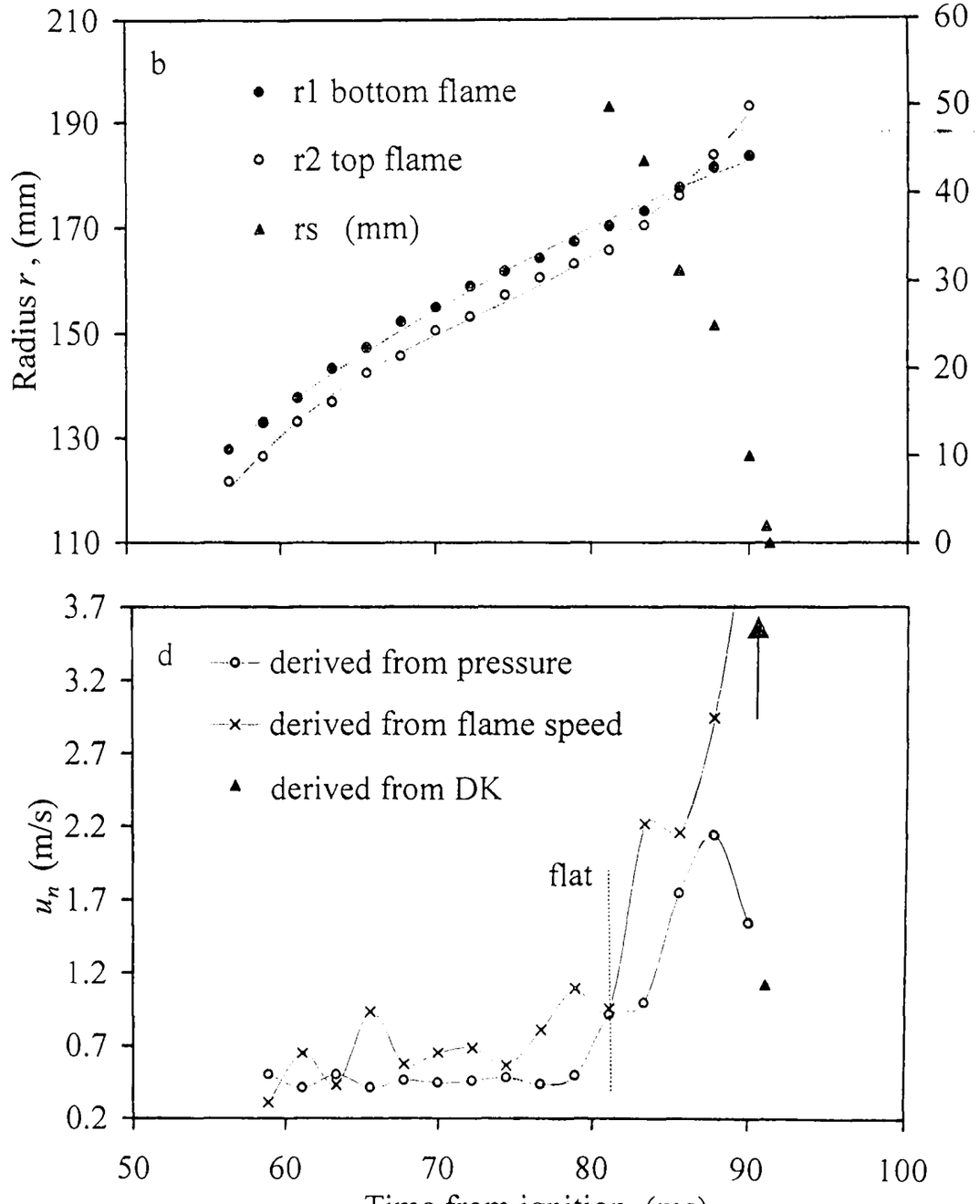

Fig. B.15. Iso-octane - air implosion, ϕ = 1.5, p_o = 0.5 MPa, T_o = 358 K

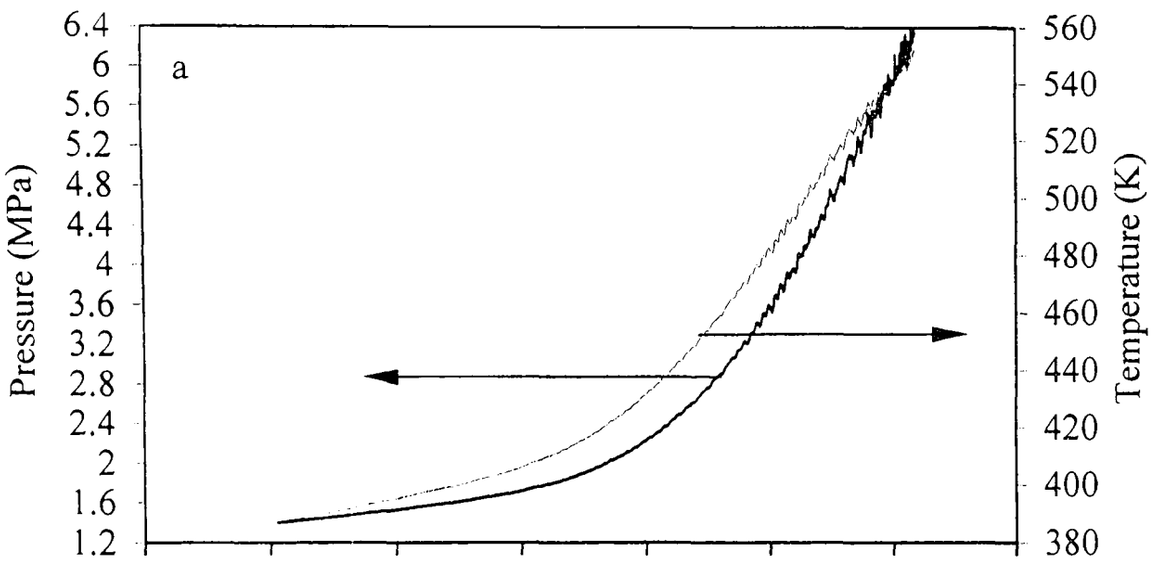

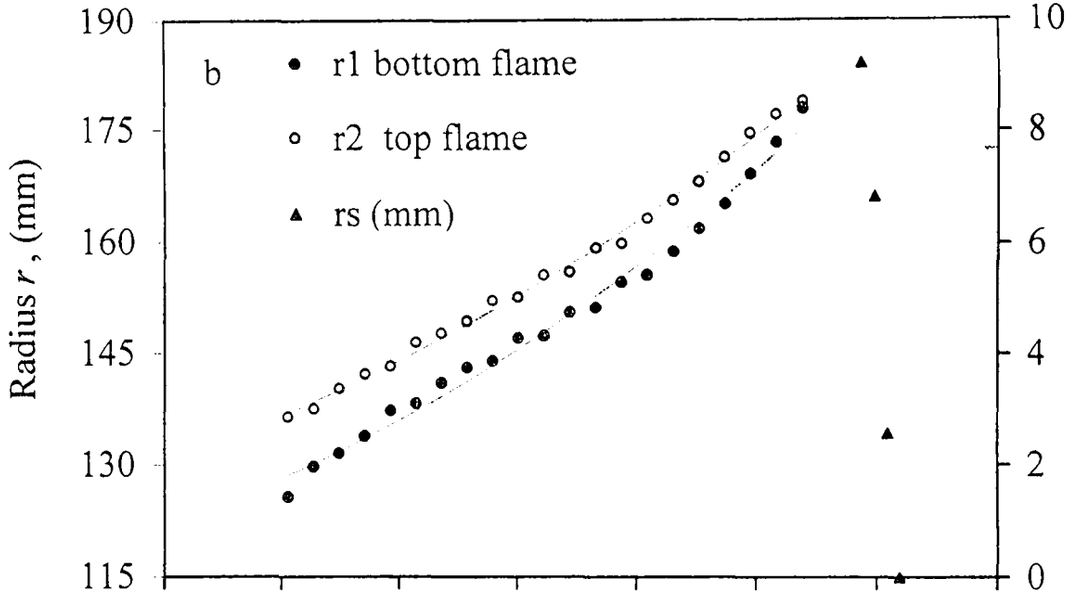

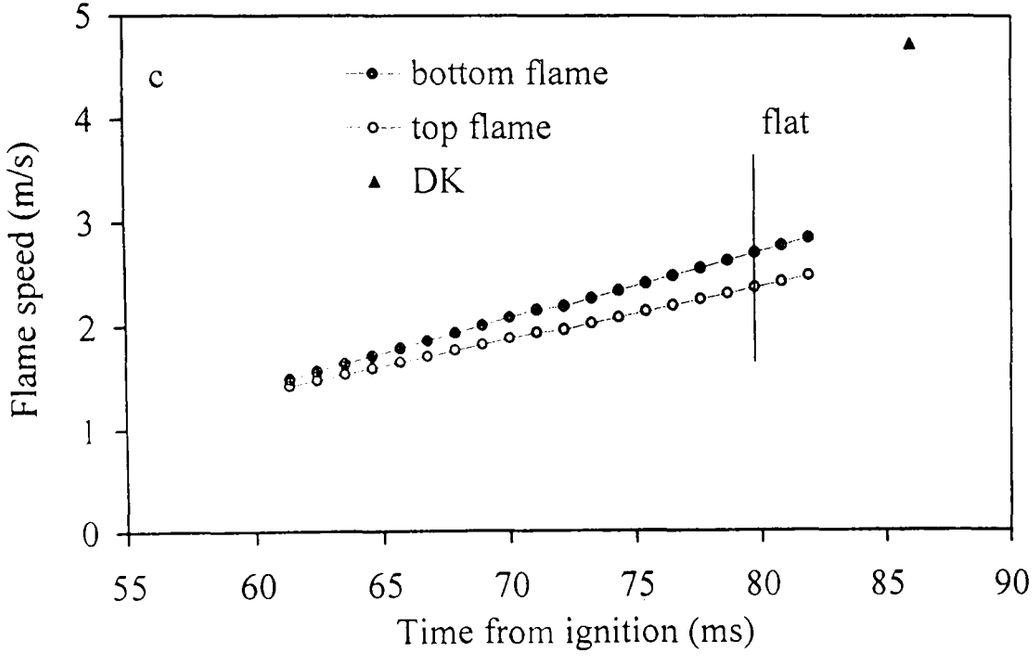

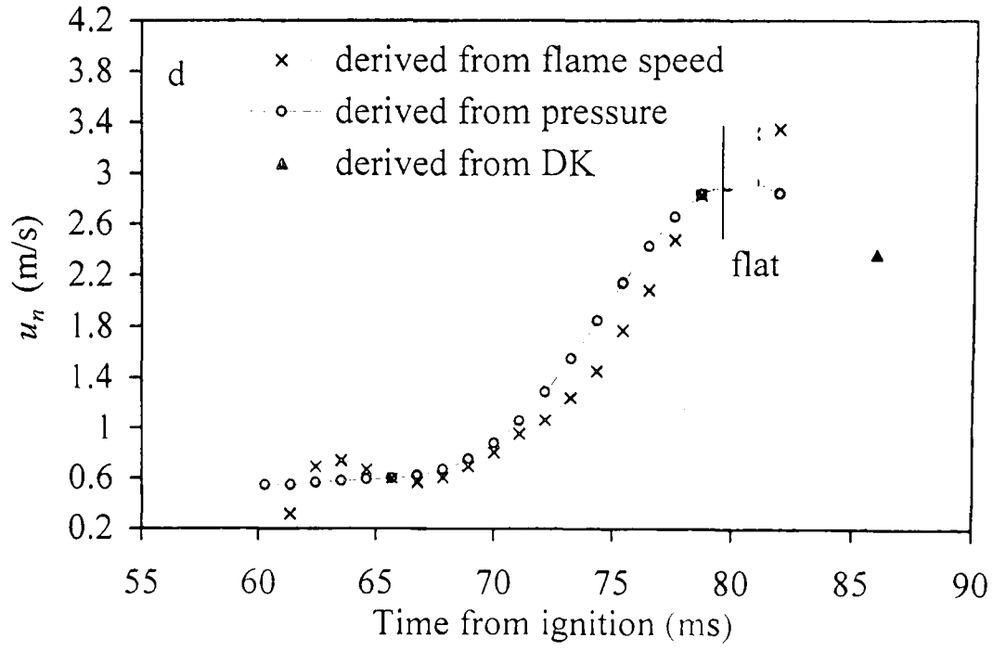

Fig. B.16. Iso-octane - air implosion, ϕ = 1.5, p_o = 1MPa, T_o = 358 K

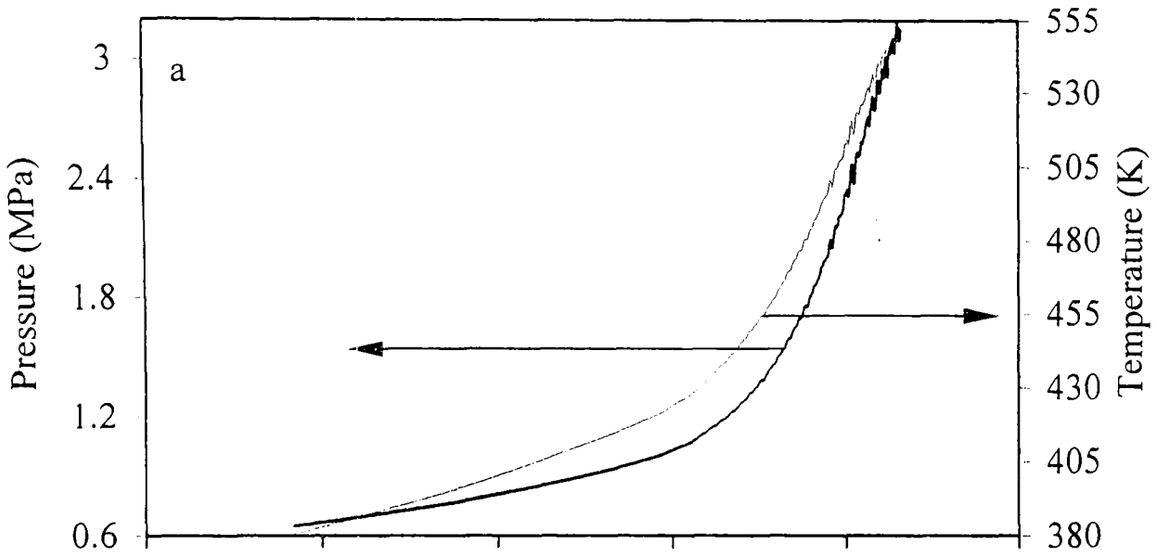

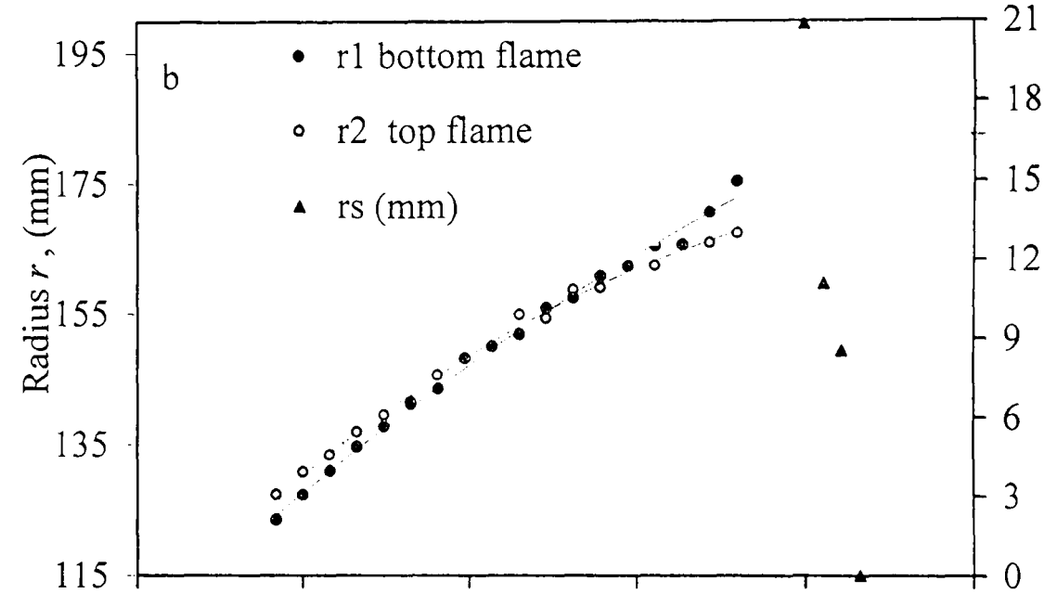

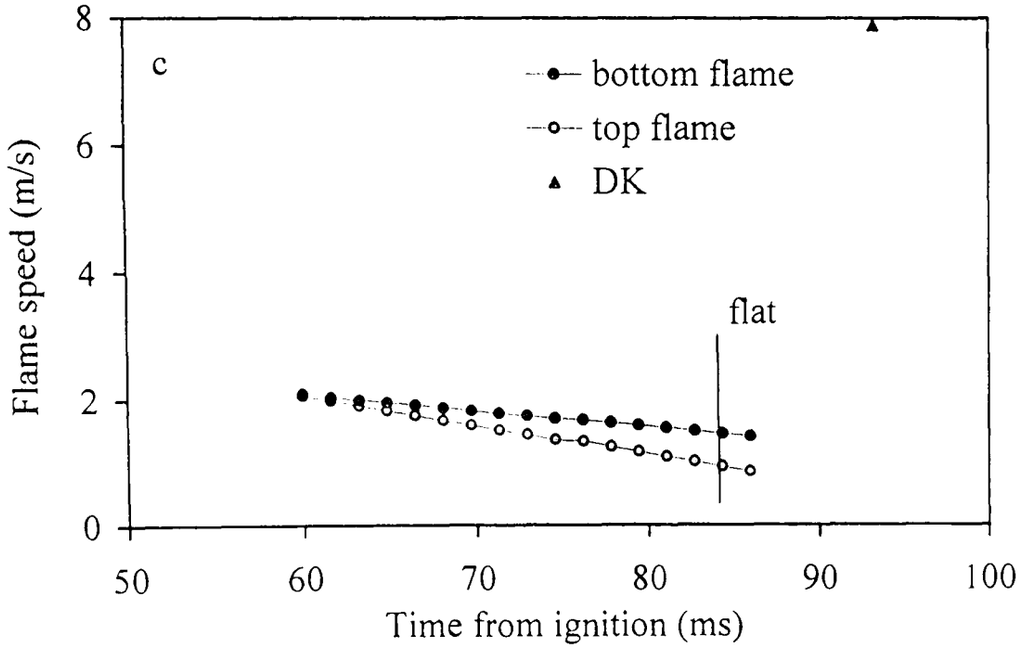

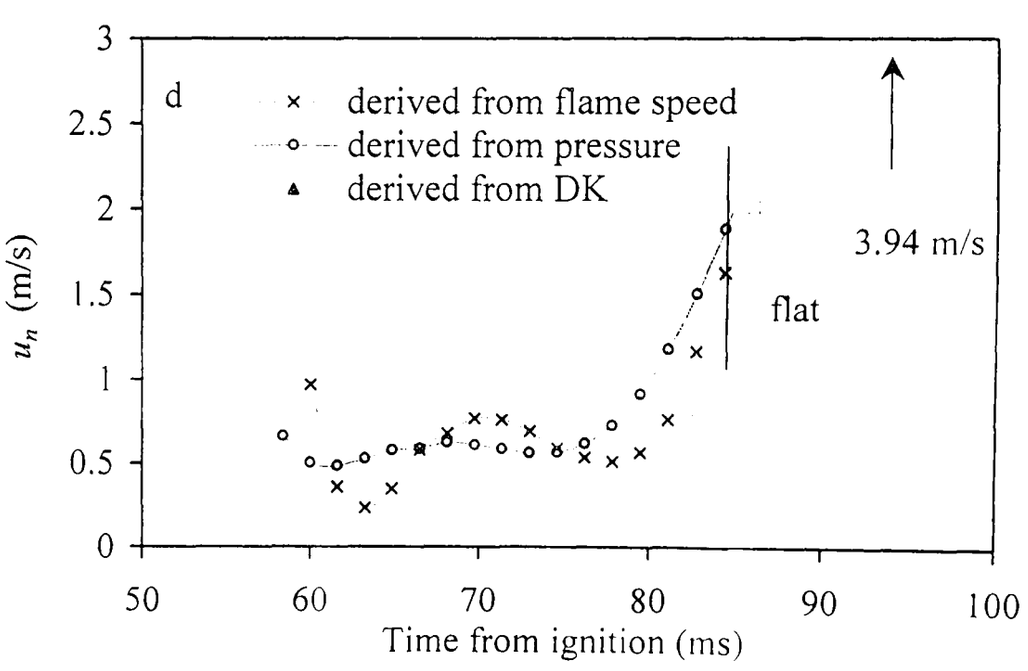

Fig. B.17. Iso-octane - air implosion, ϕ = 1.6, P_o = 0.5 MPa, T_o = 358 K

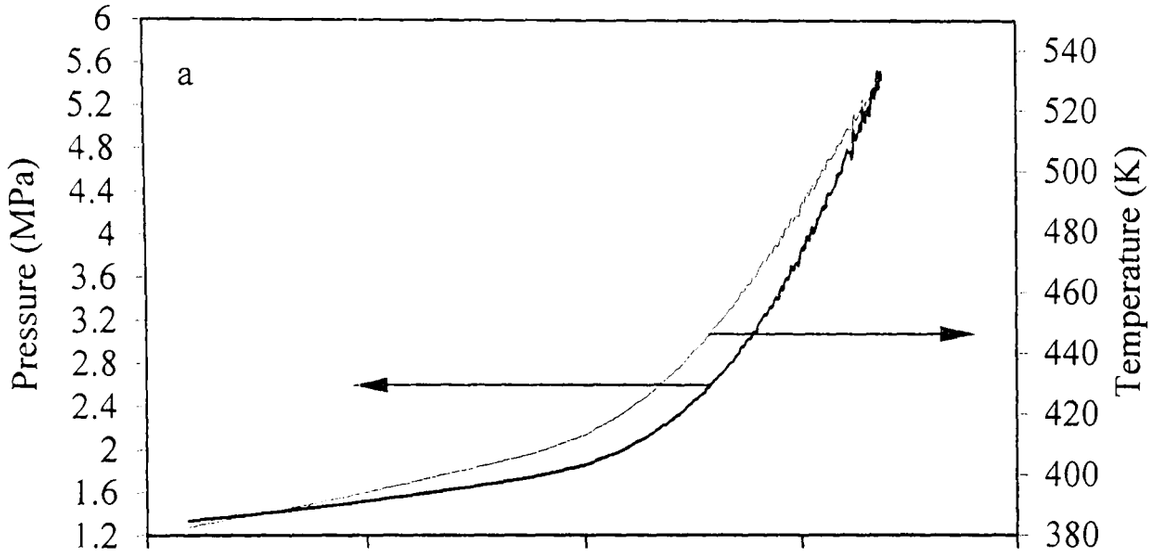

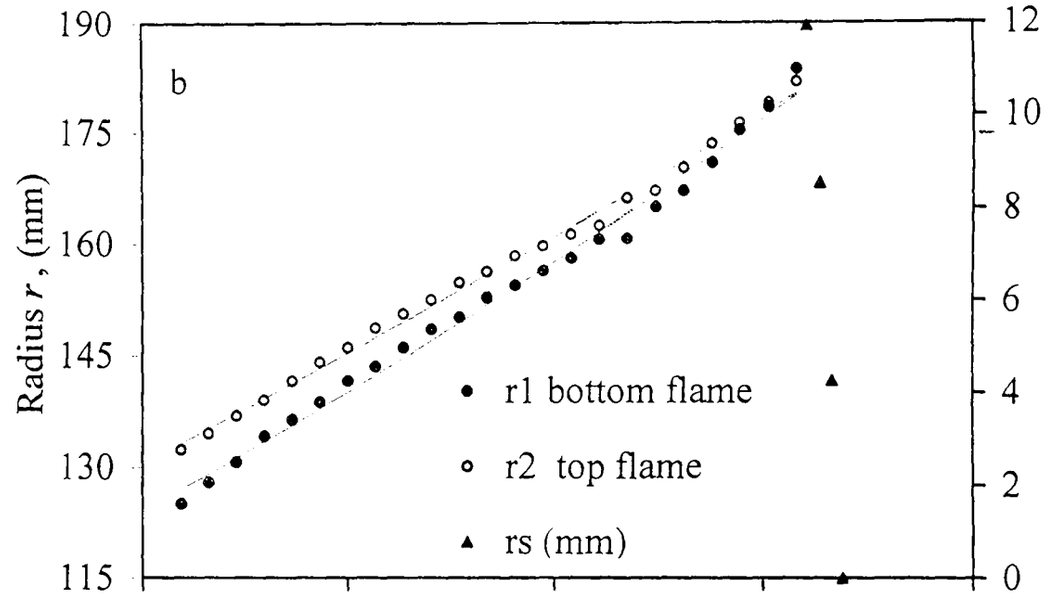

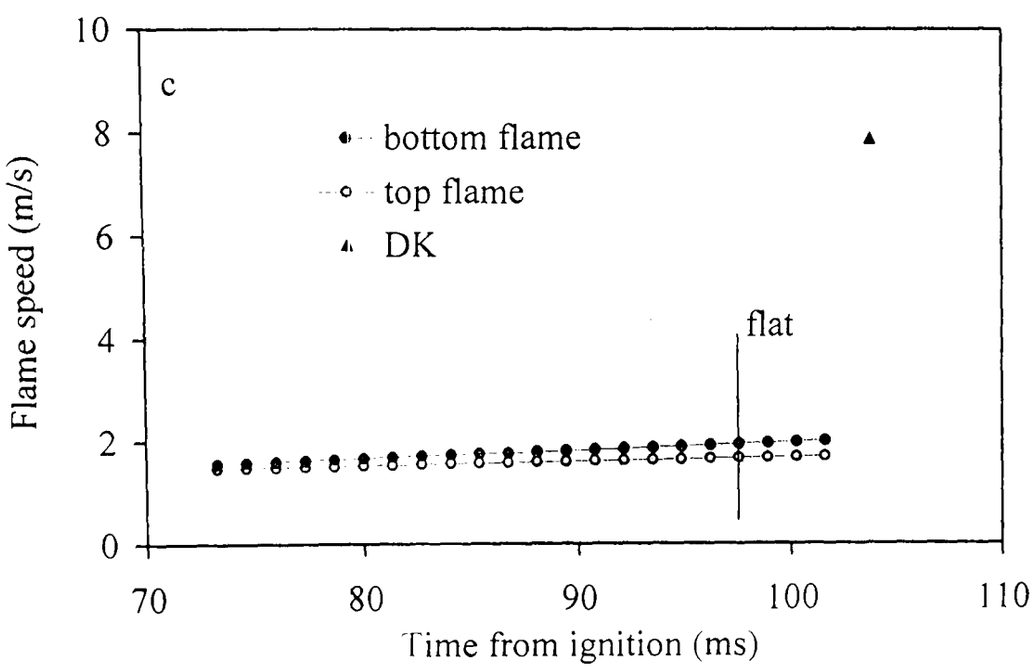

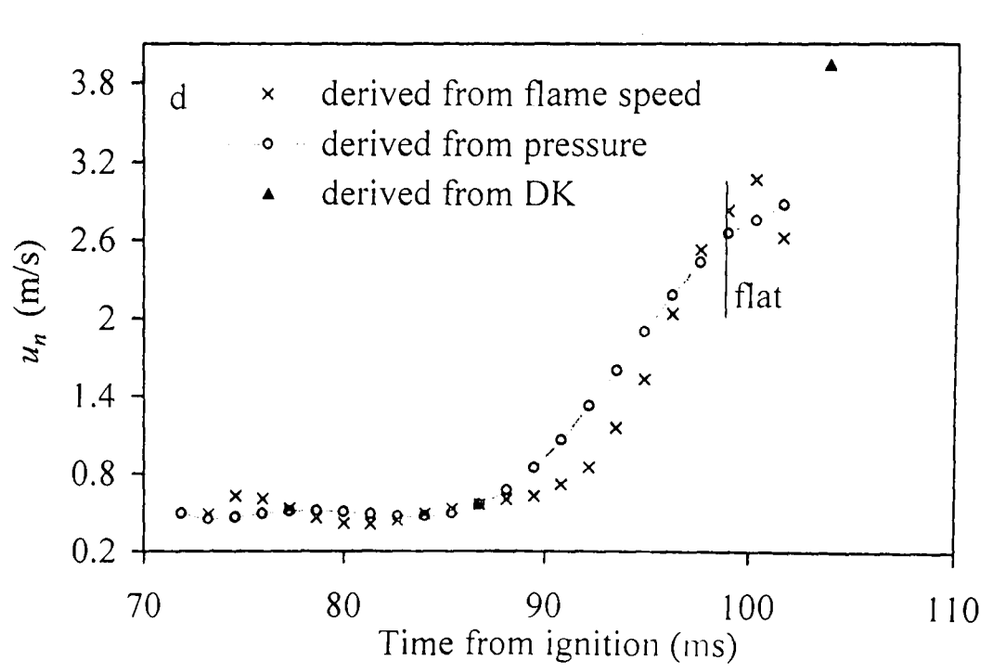

Fig. B.18. Iso-octane - air implosion, ϕ = 1.6, p_o = 1MPa, T_o = 358 K

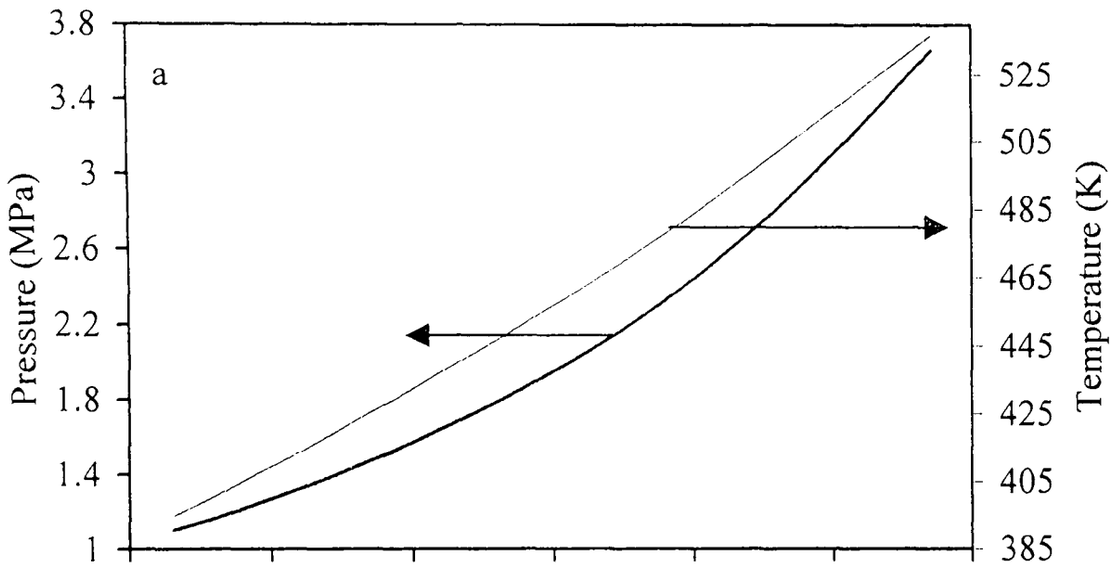

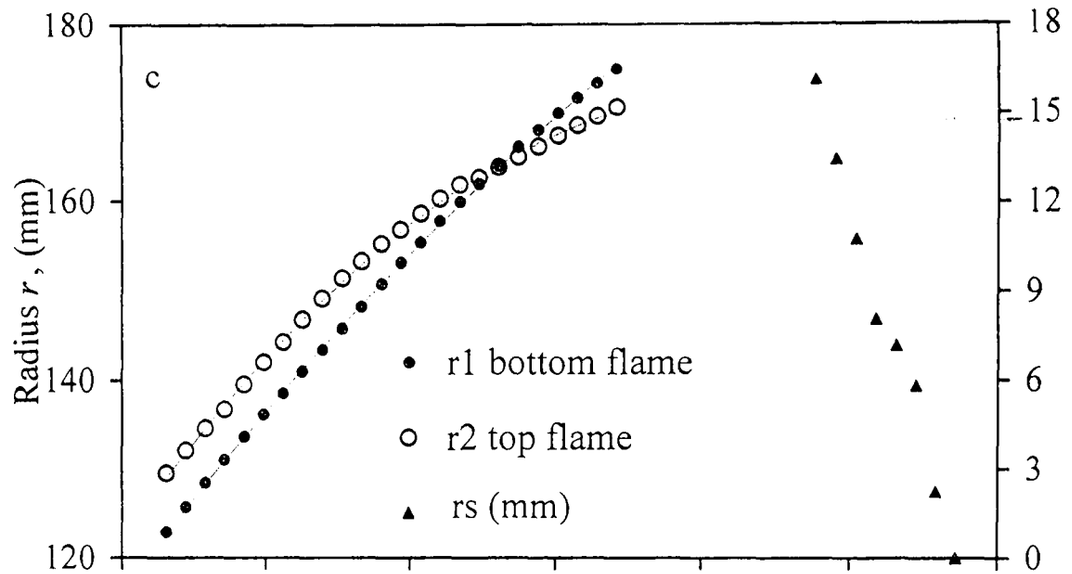

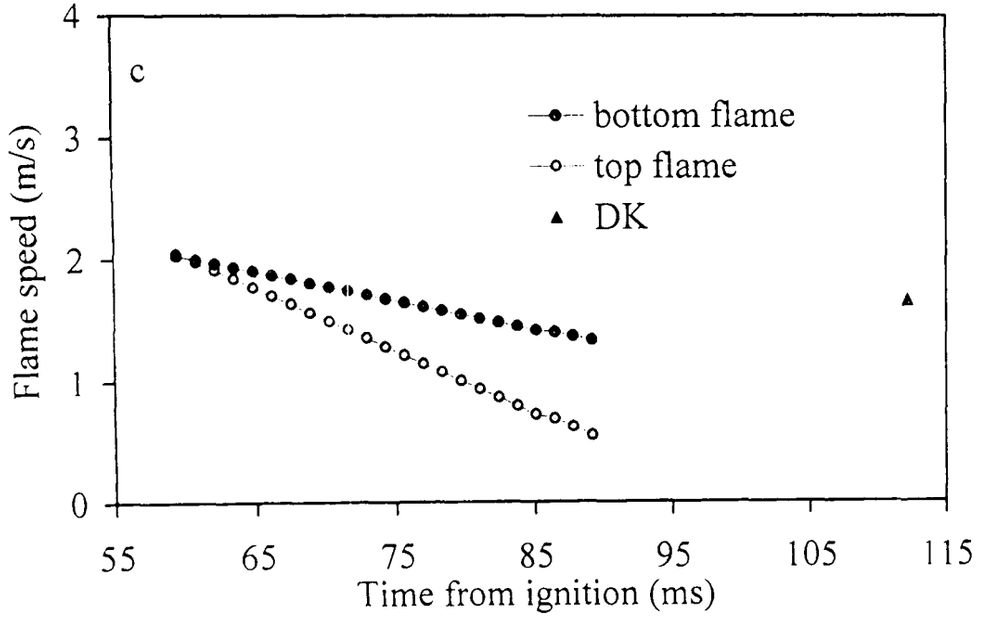

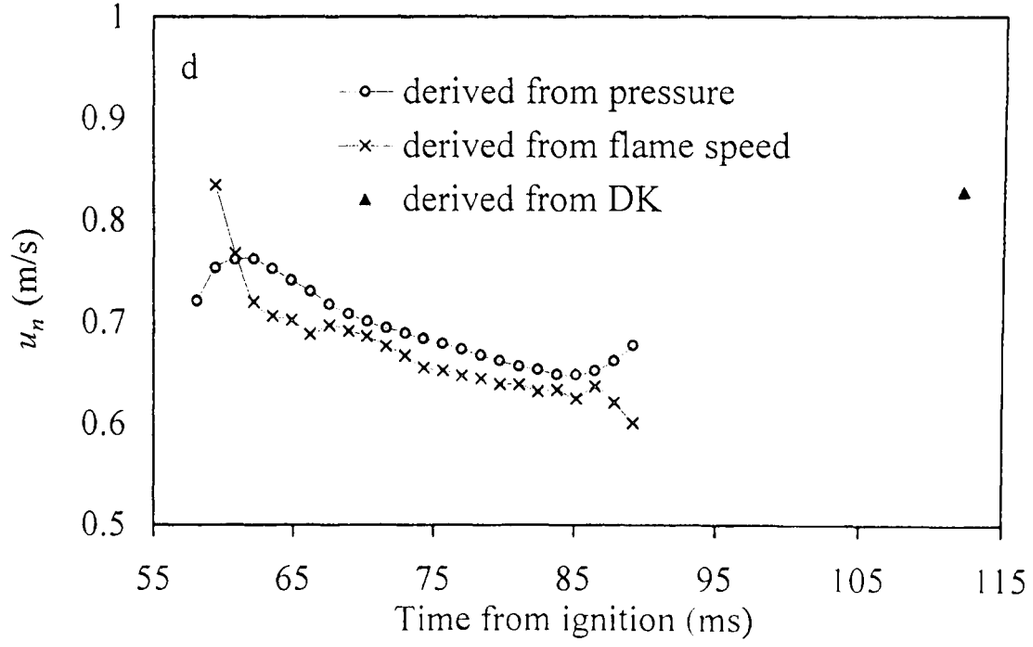

Fig. B.19 Iso-octane - air implosion, $\phi = 1, p_o = 0.75$ MPa, $T_o = 358$ K

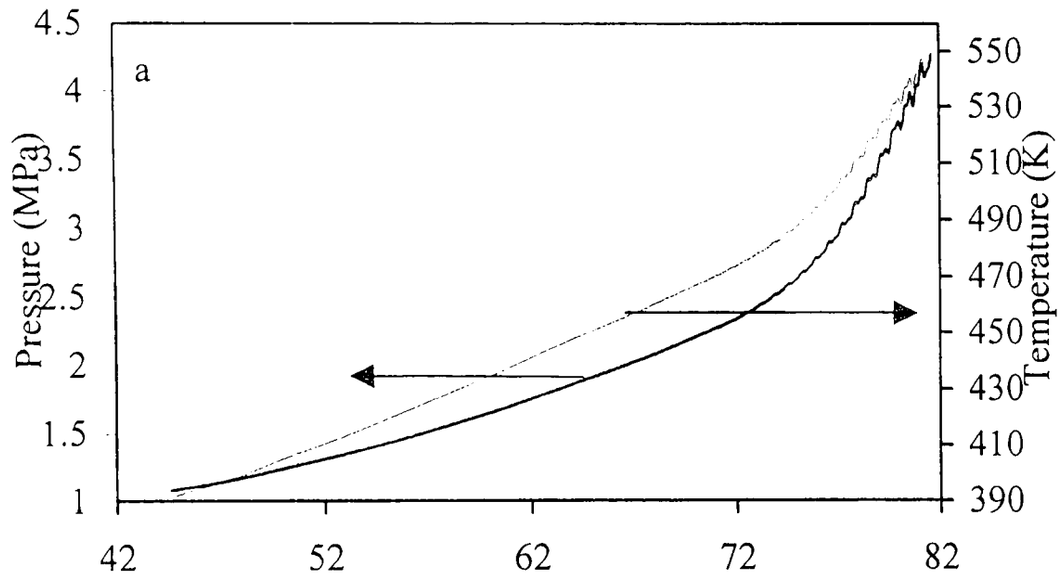

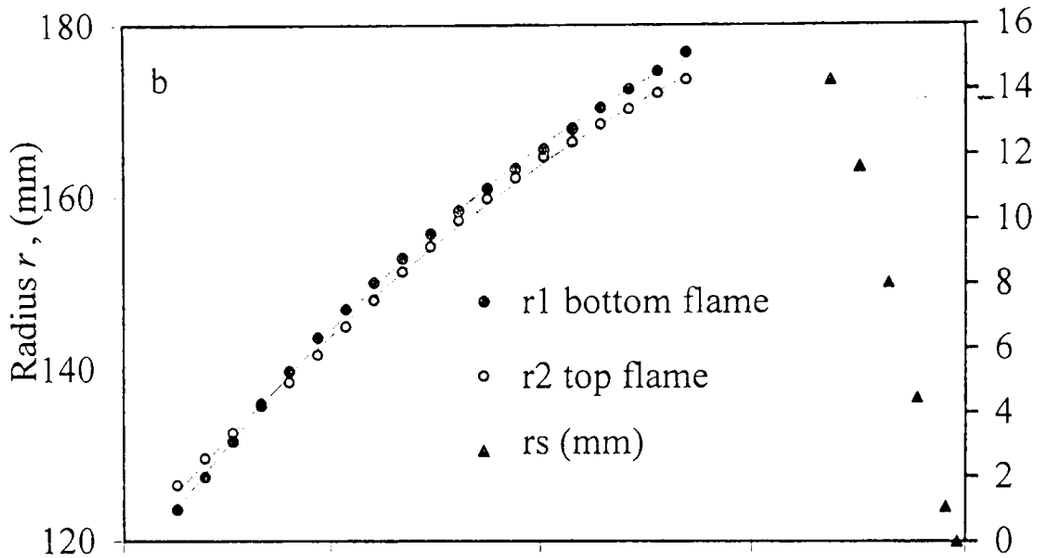

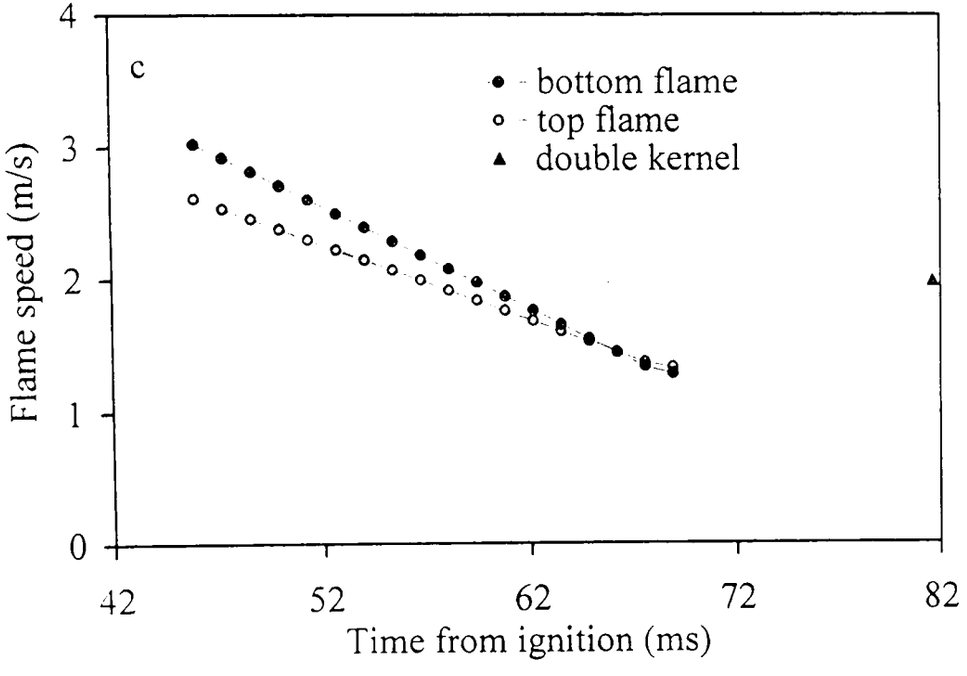

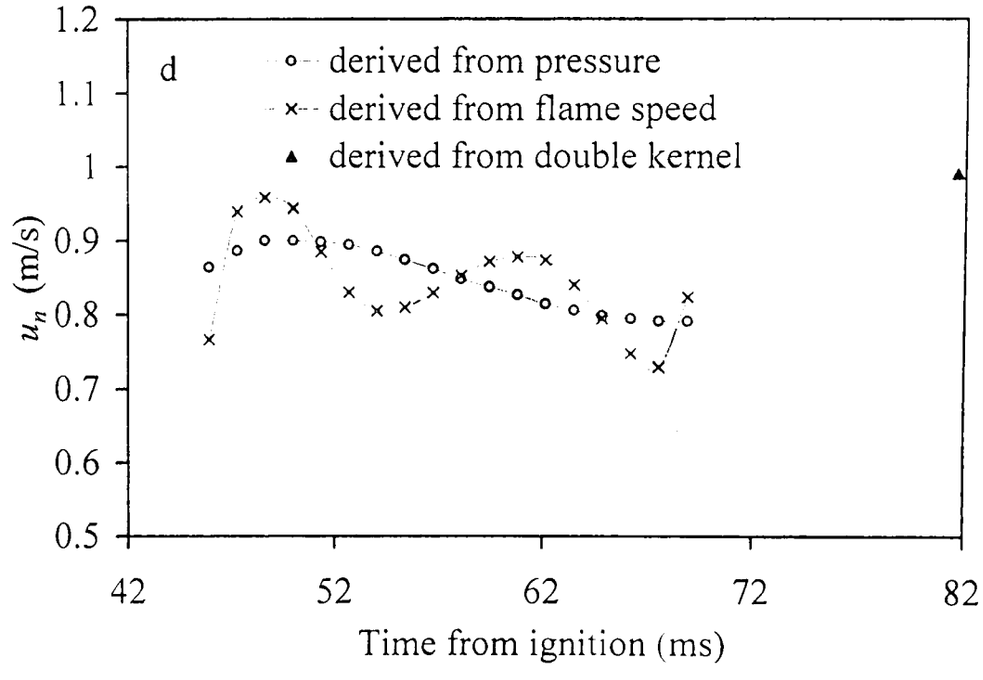

Fig. B.20. Iso-octane - air implosion, ϕ = 1.4, p_o = 0.75 MPa, T_o = 358 K

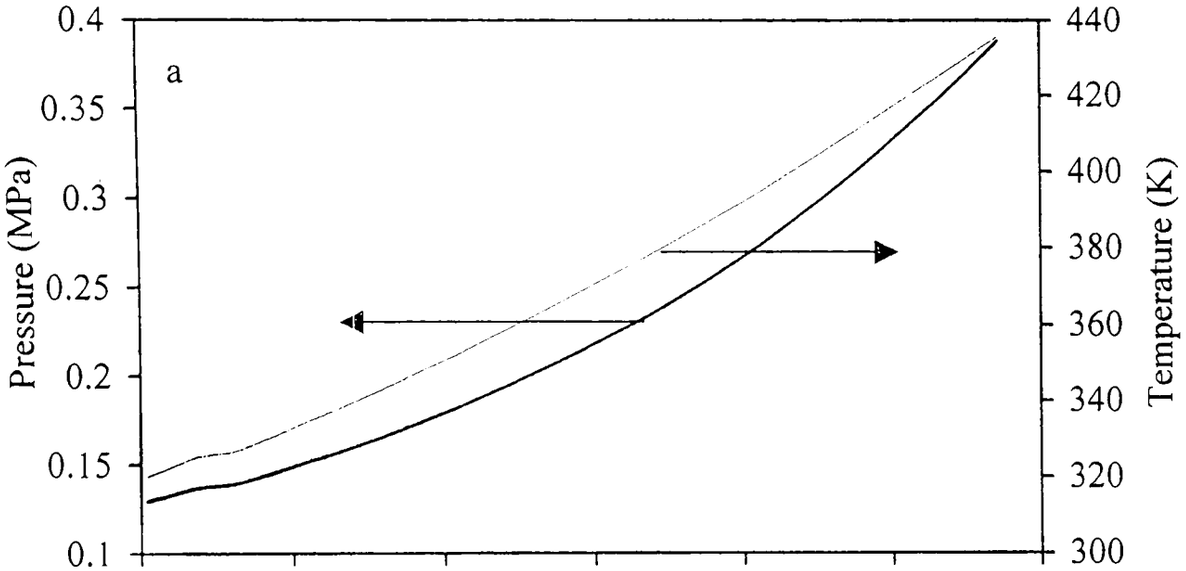

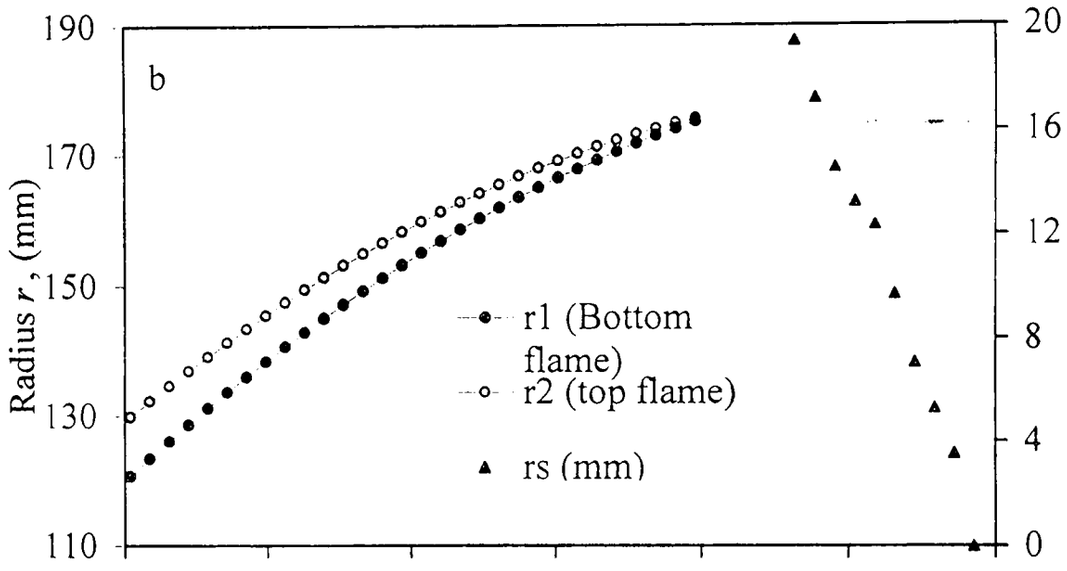

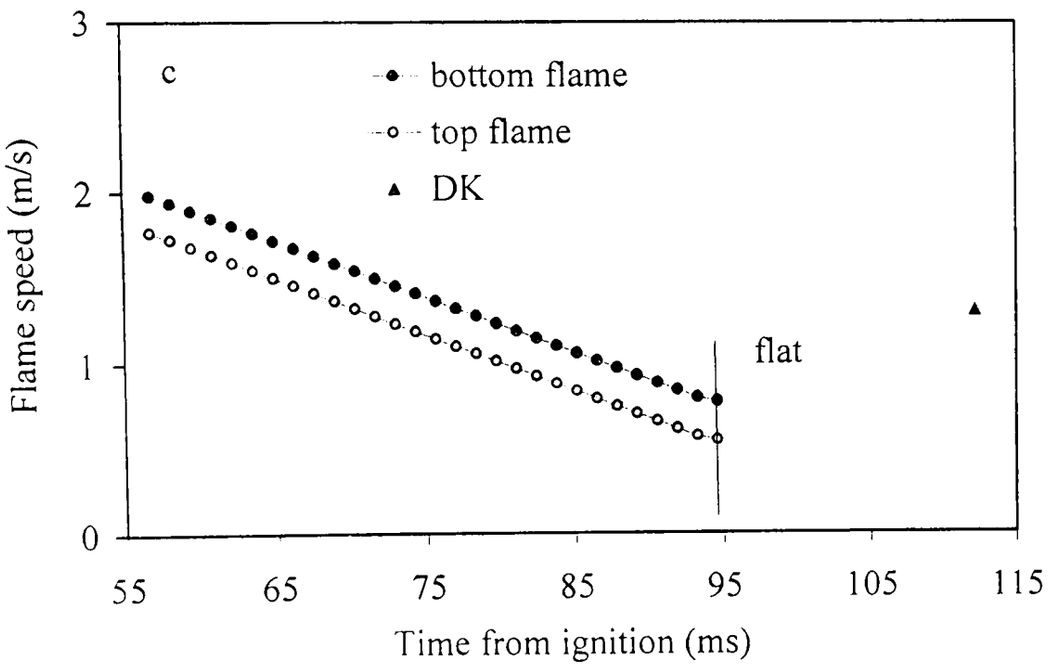

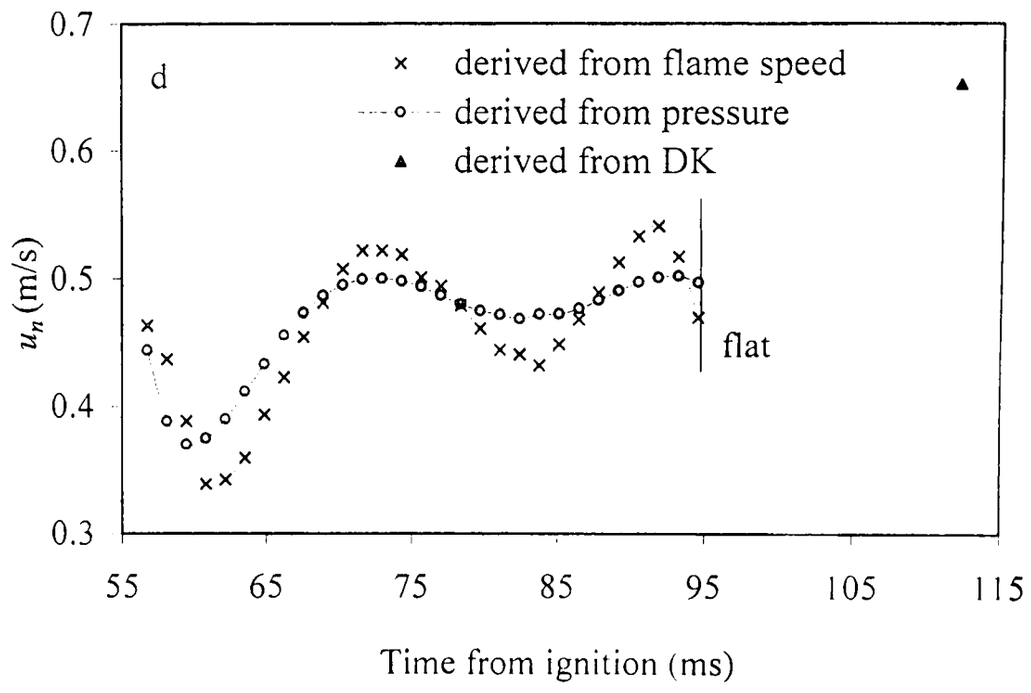

Fig. B.21. Methane - air implosion, $\phi = 1, p_o = 0.1$ MPa, $T_o = 298$ K

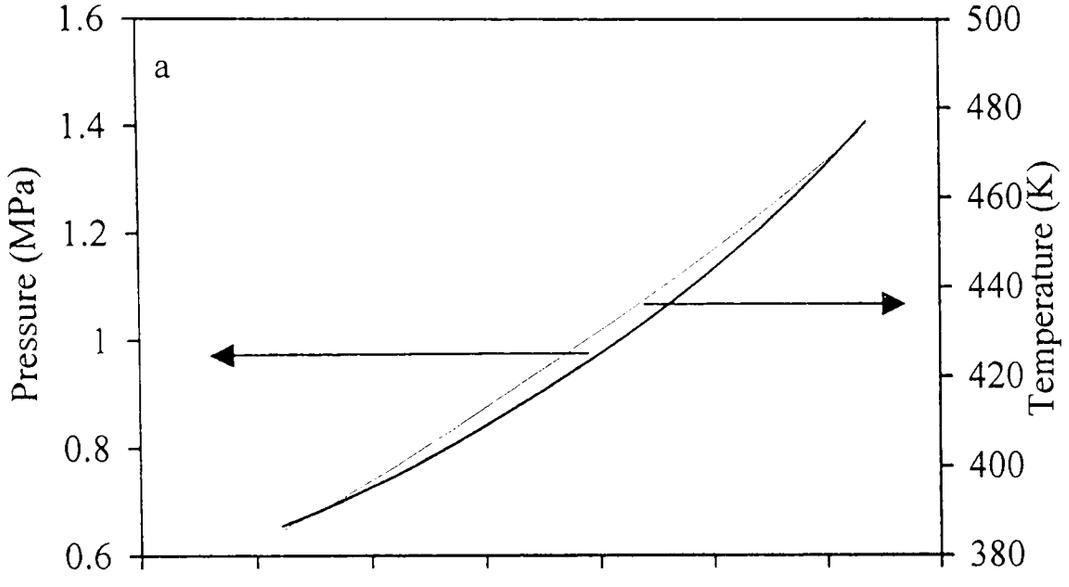

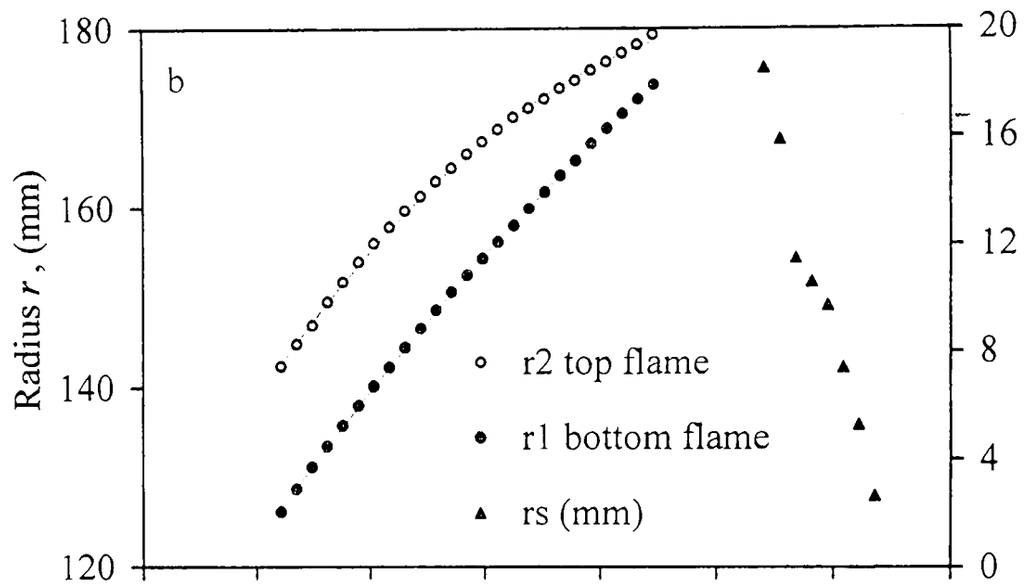

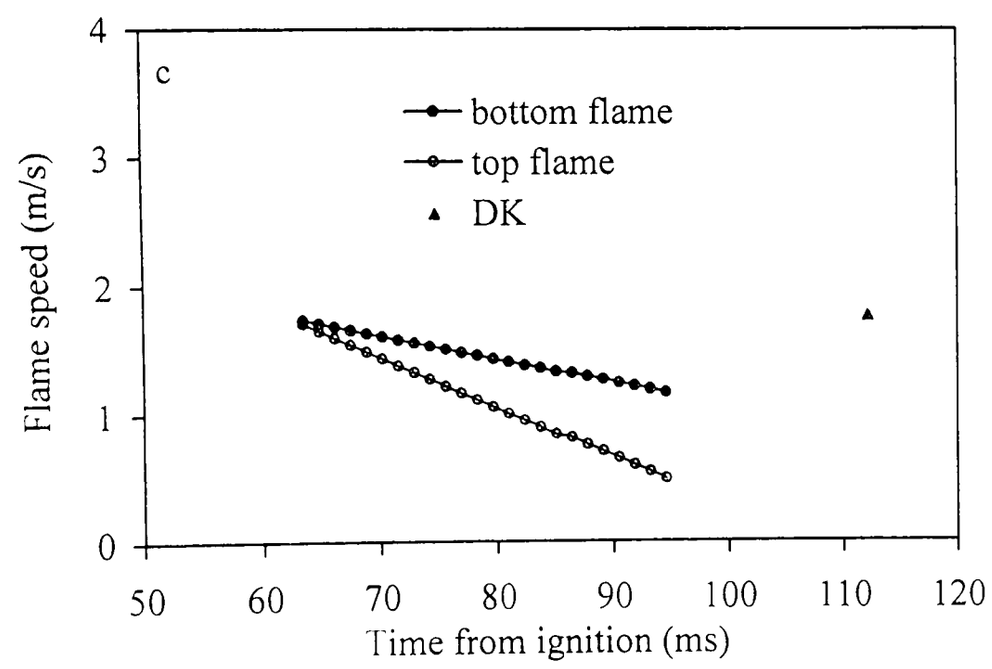

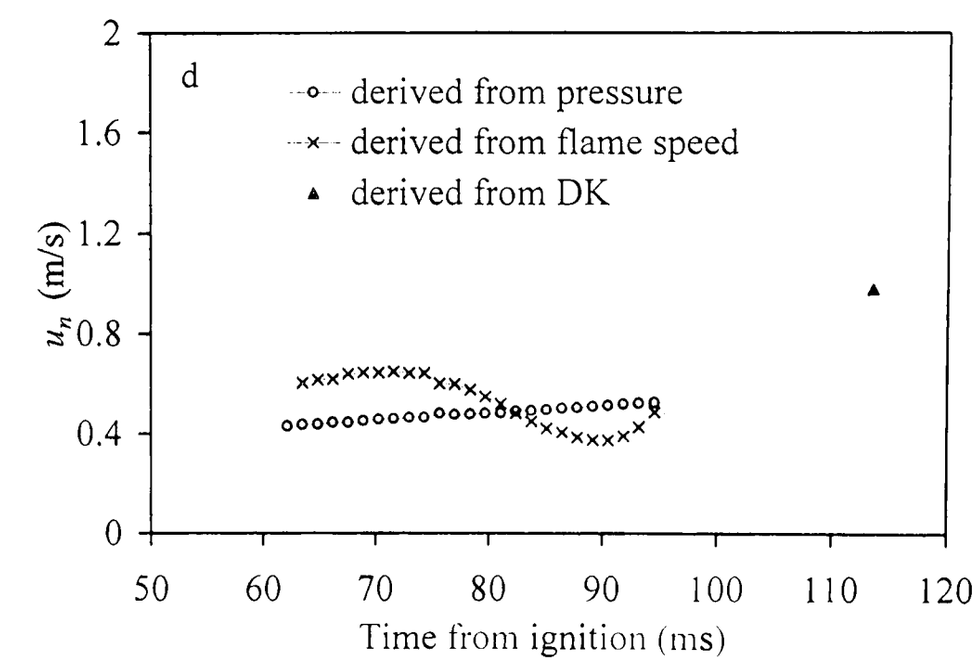

Fig. B.22. Methane - air implosion, ϕ = 1, p_o = 0.5 MPa, T_o = 358 K

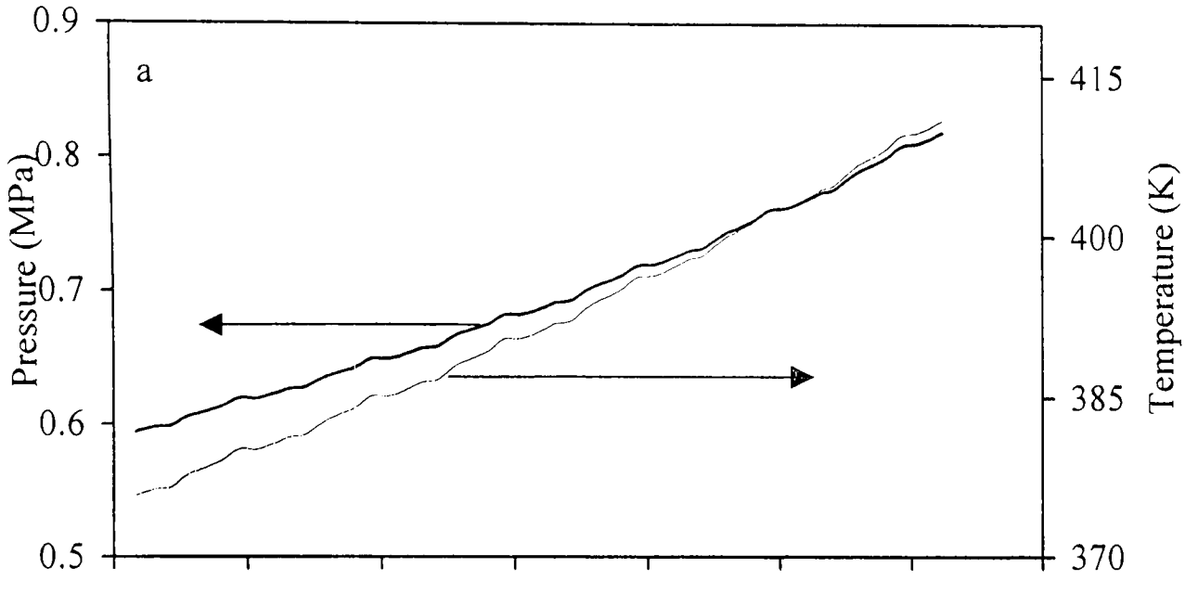

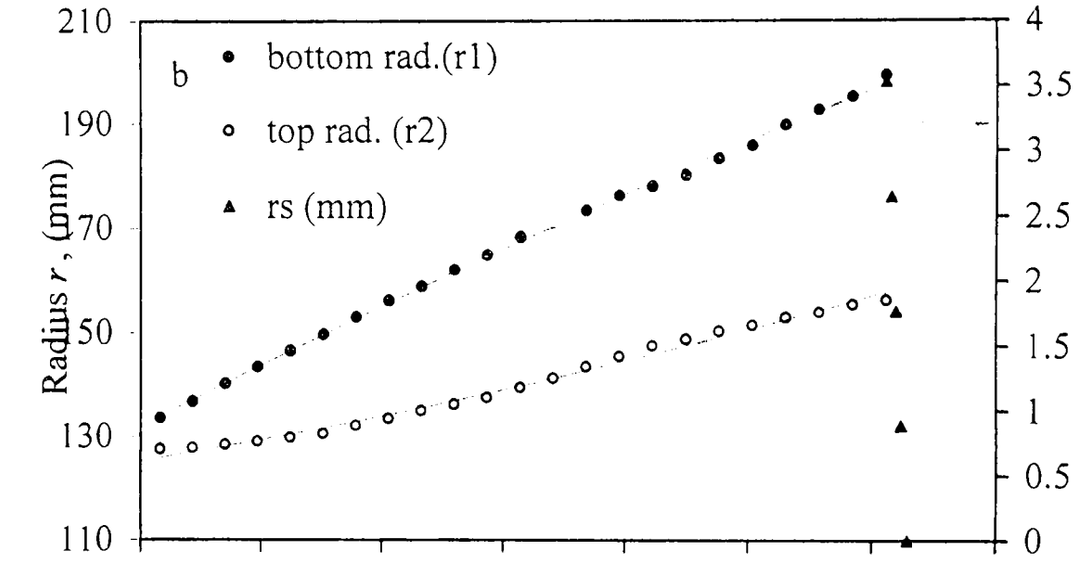

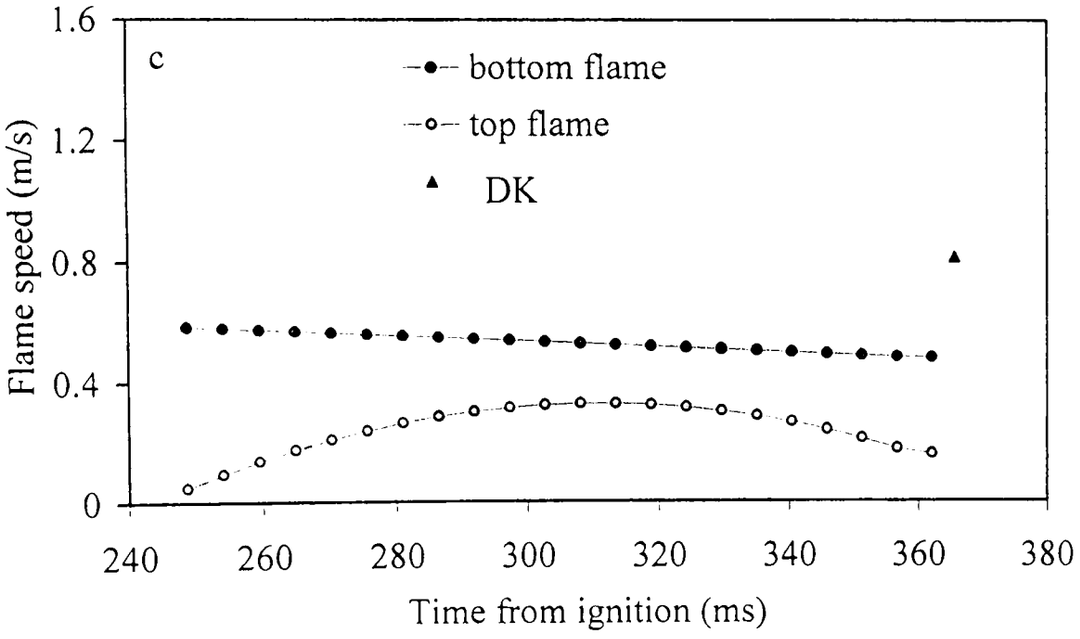

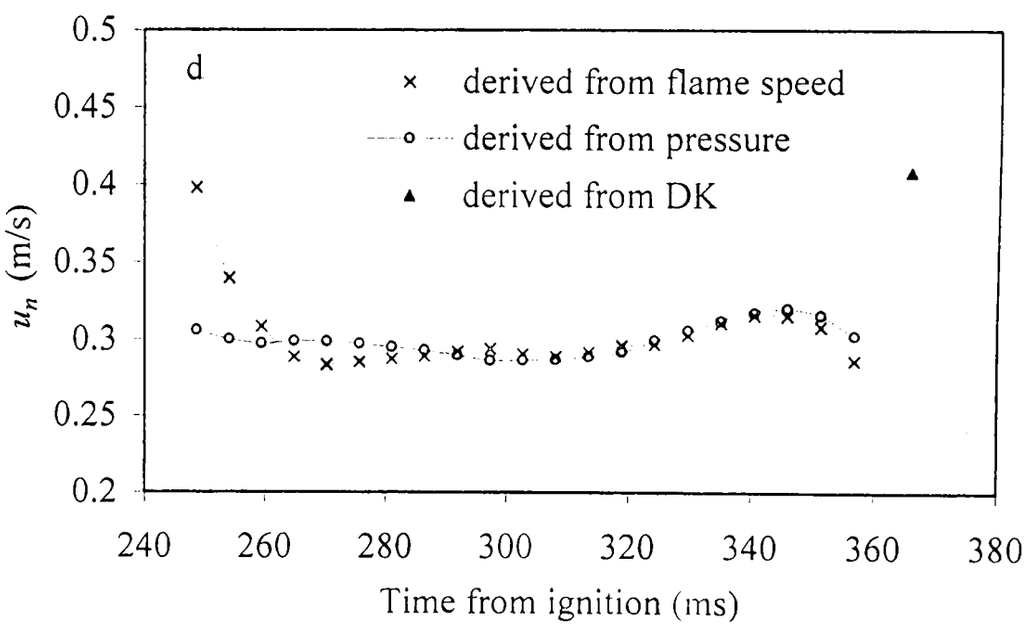

Fig. B.23. Hydrogen - air implosion, ϕ = 0.3, p_o = 0.5 MPa, T_o = 358 K

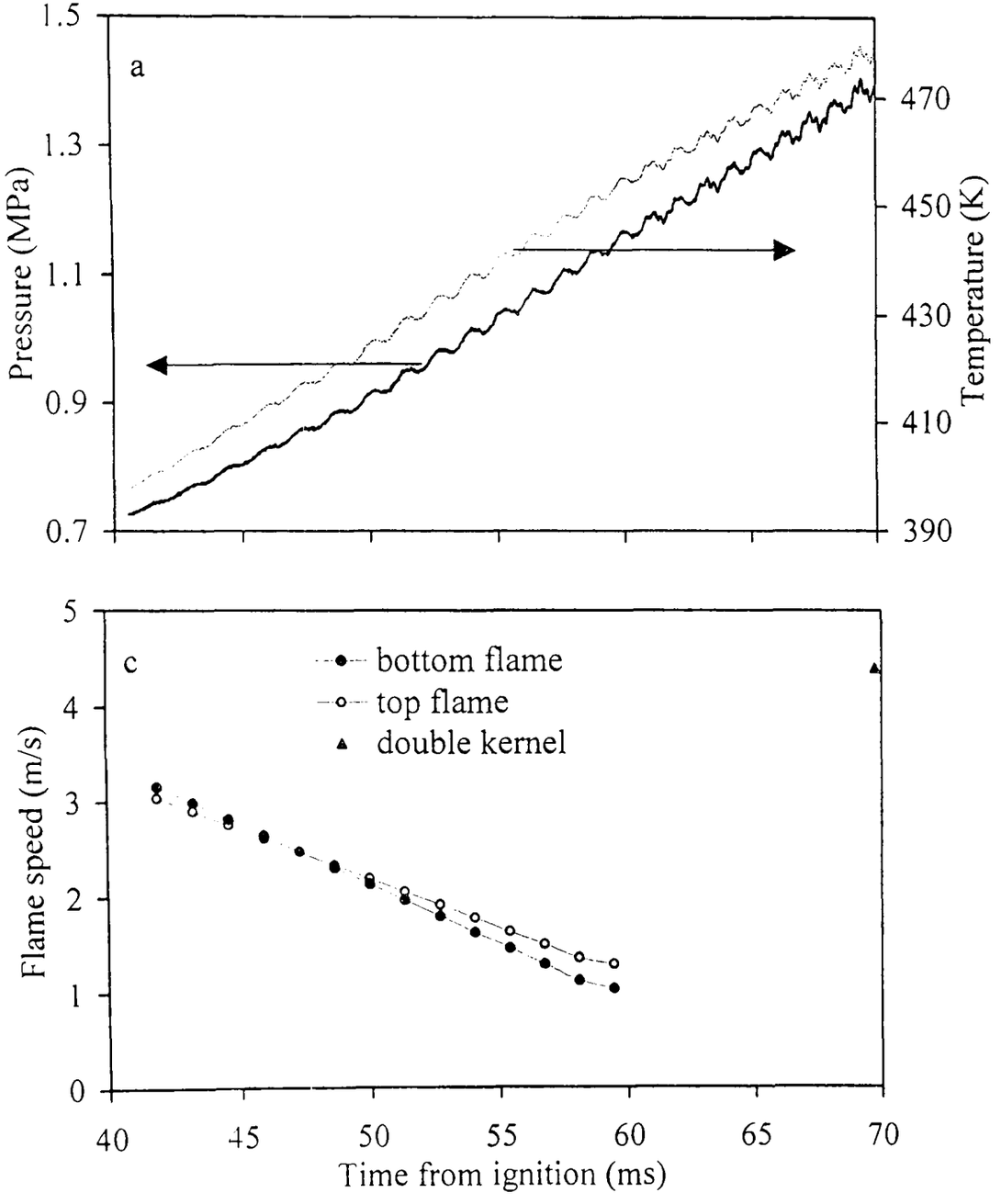

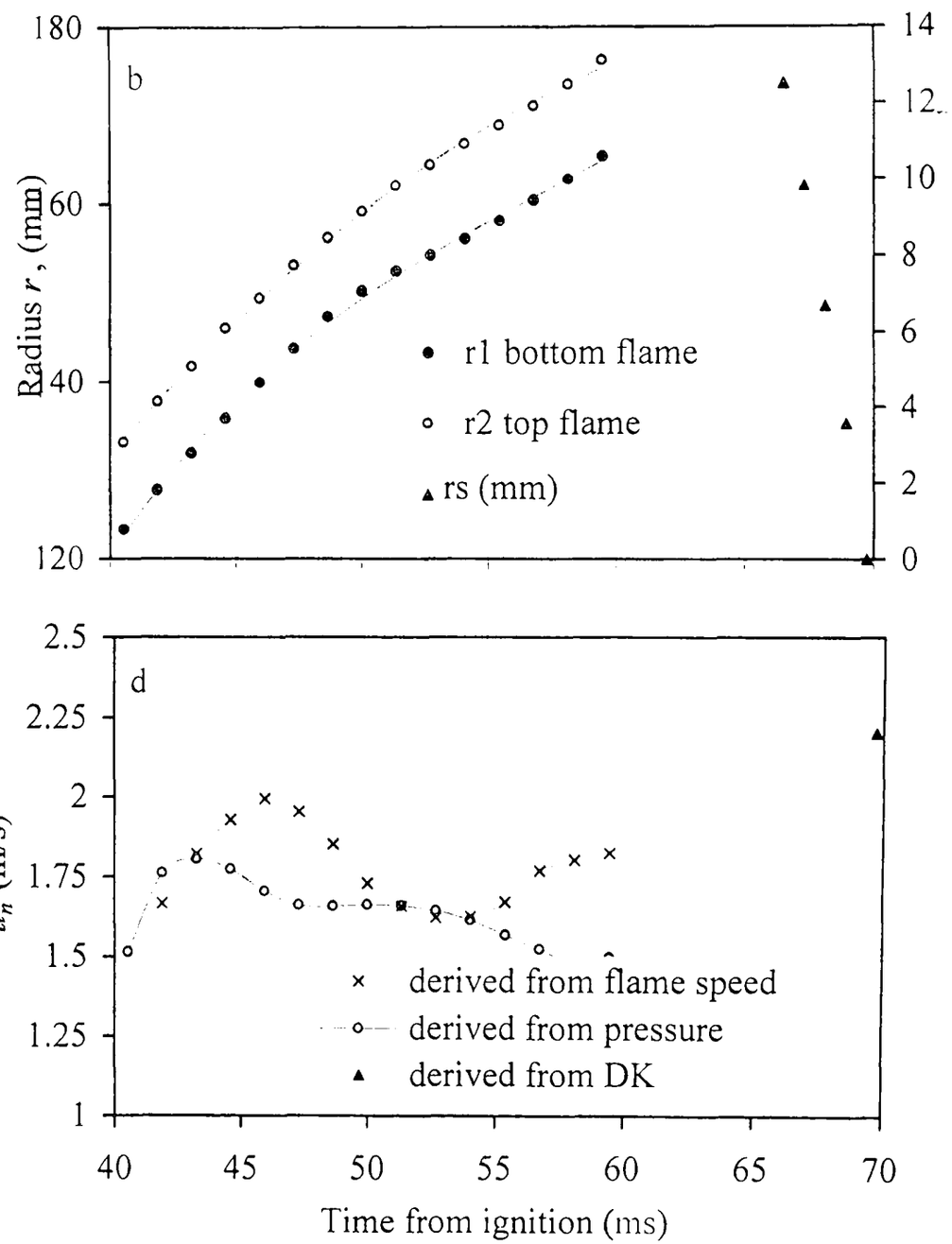

Fig. B.24. Hydrogen - air implosion, ϕ = 0.4, p_o = 0.5 MPa, T_o = 358 K

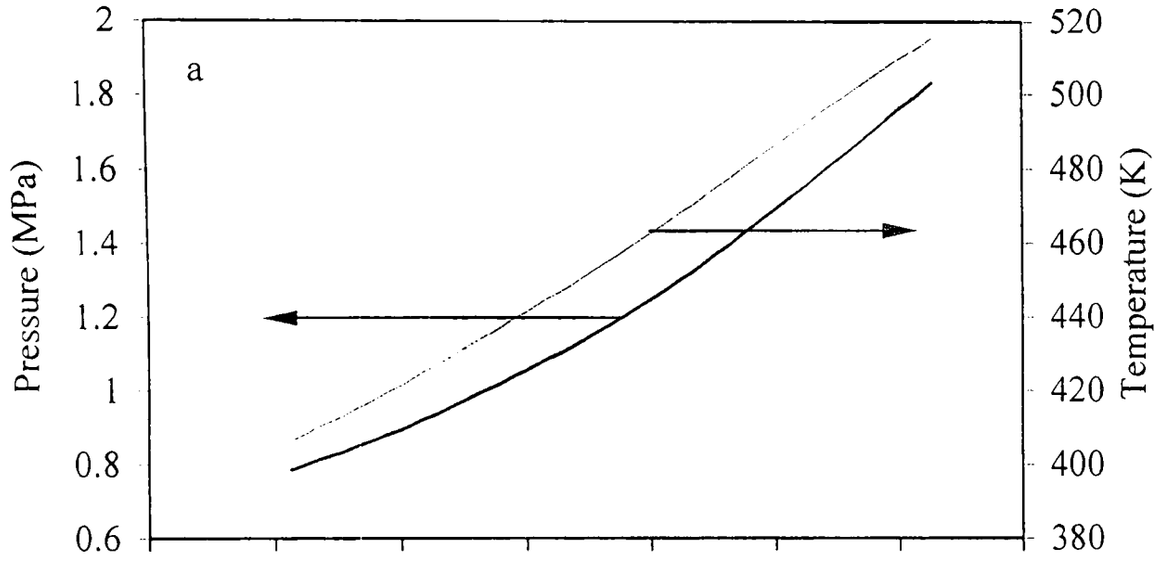

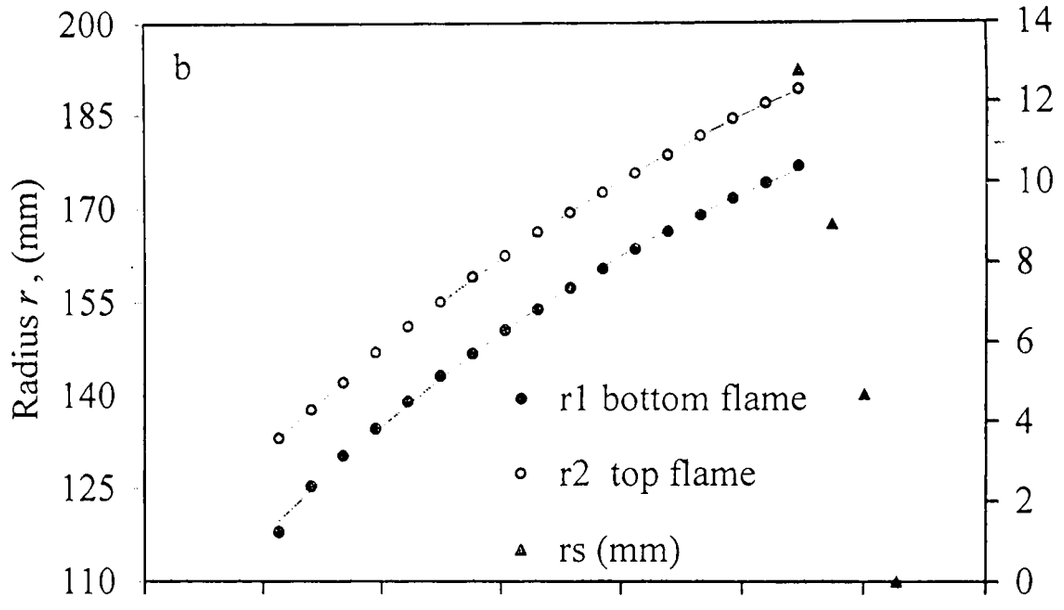

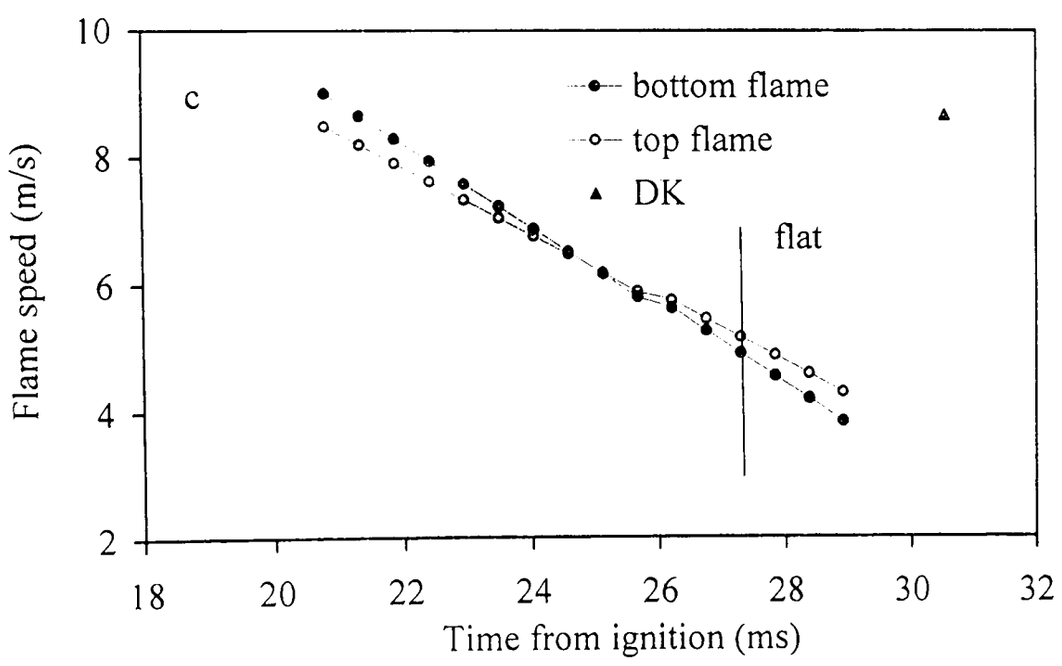

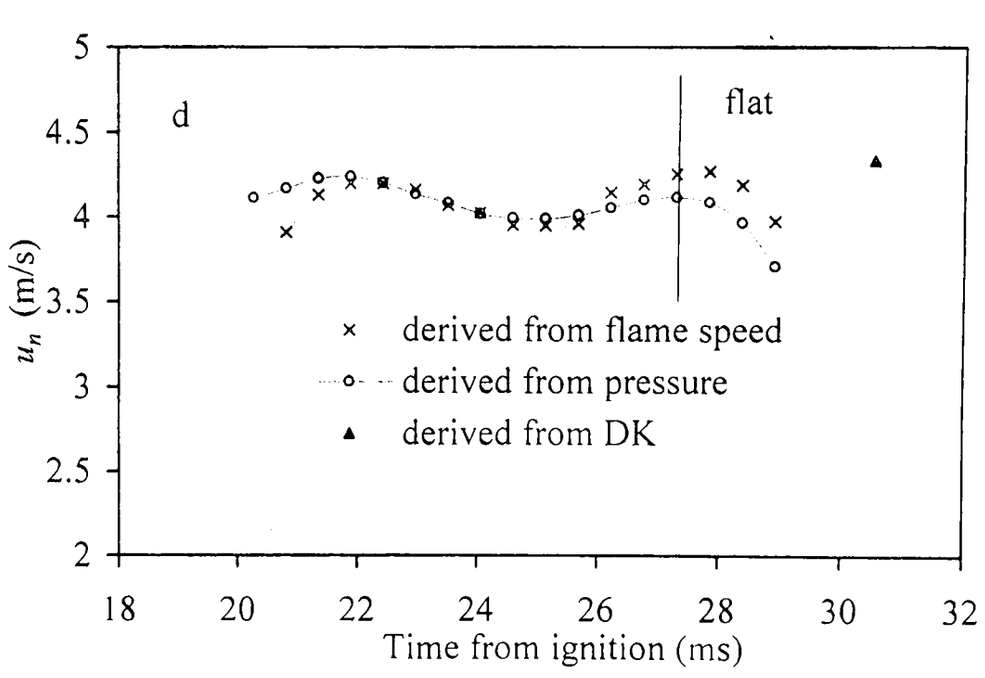

Fig. B.25. Hydrogen - air implosion, $\phi = 0.5$, $p_o = 0.5$ MPa, $T_o = 358$ K

Appendix C

Additional Experimental Results from Turbulent Imploding Flames

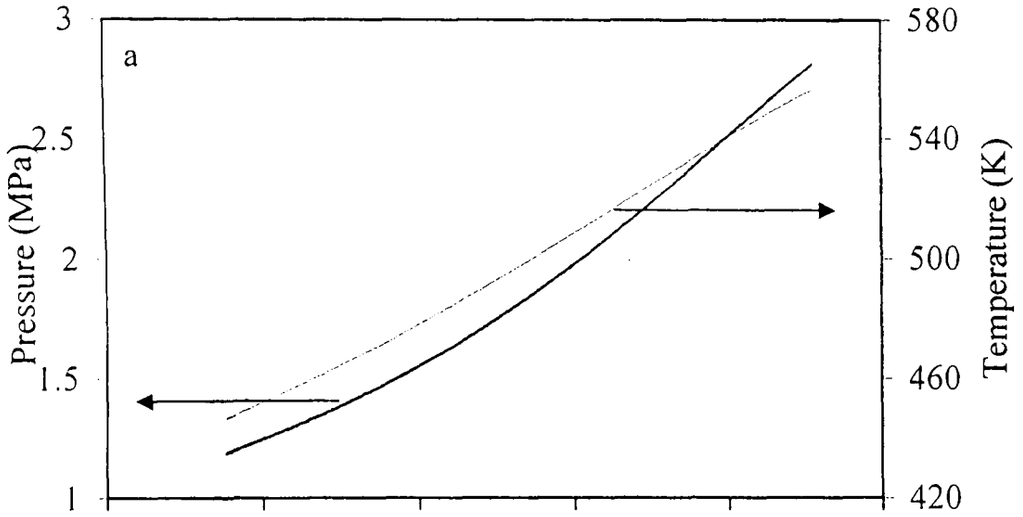

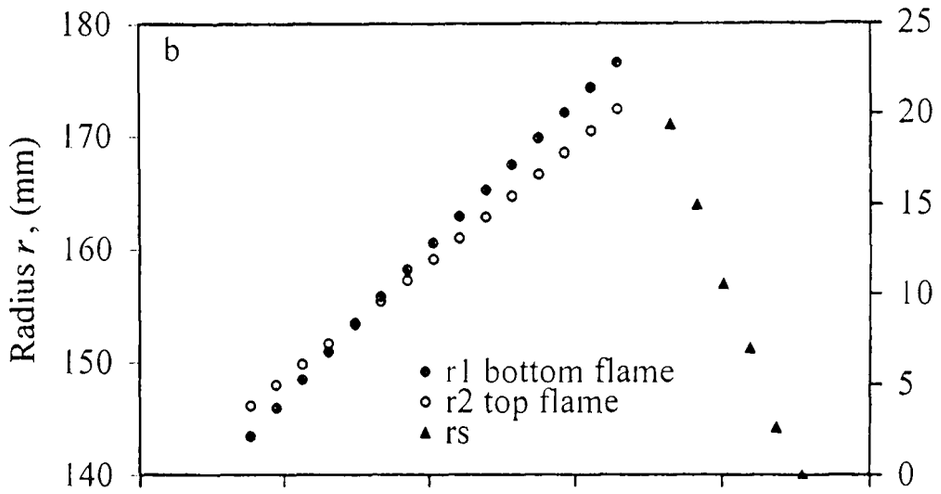

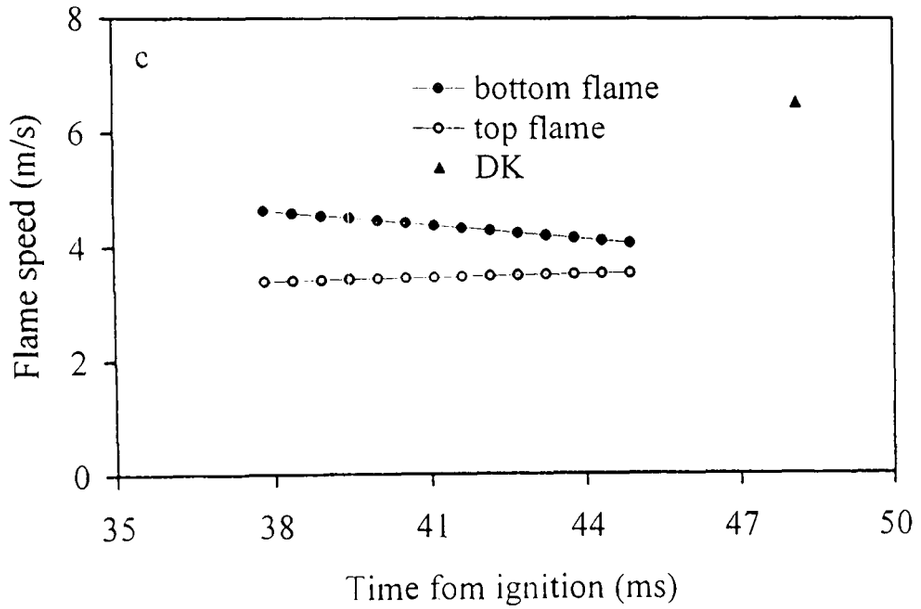

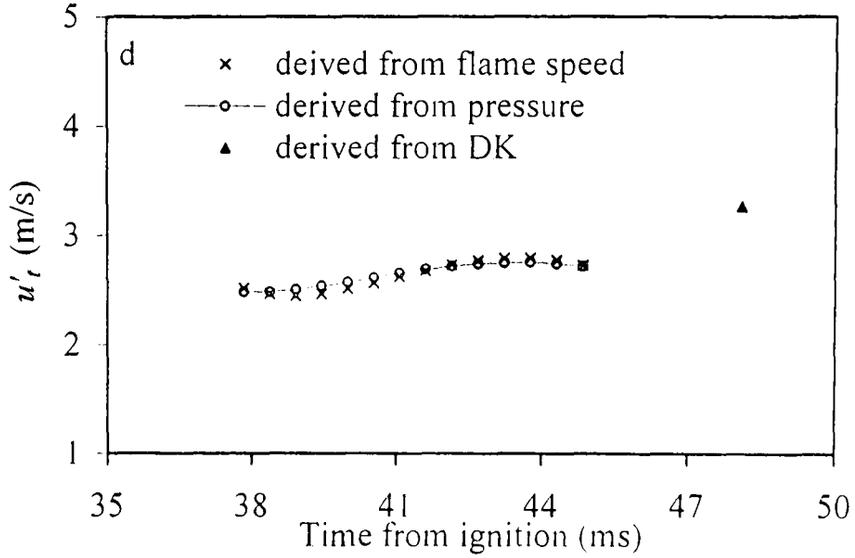

Fig. C.1. Iso-octane - air implosion, $\phi = 1, p_o = 0.5$ Mpa, $T_o = 358$ K, $u' = 0.25$

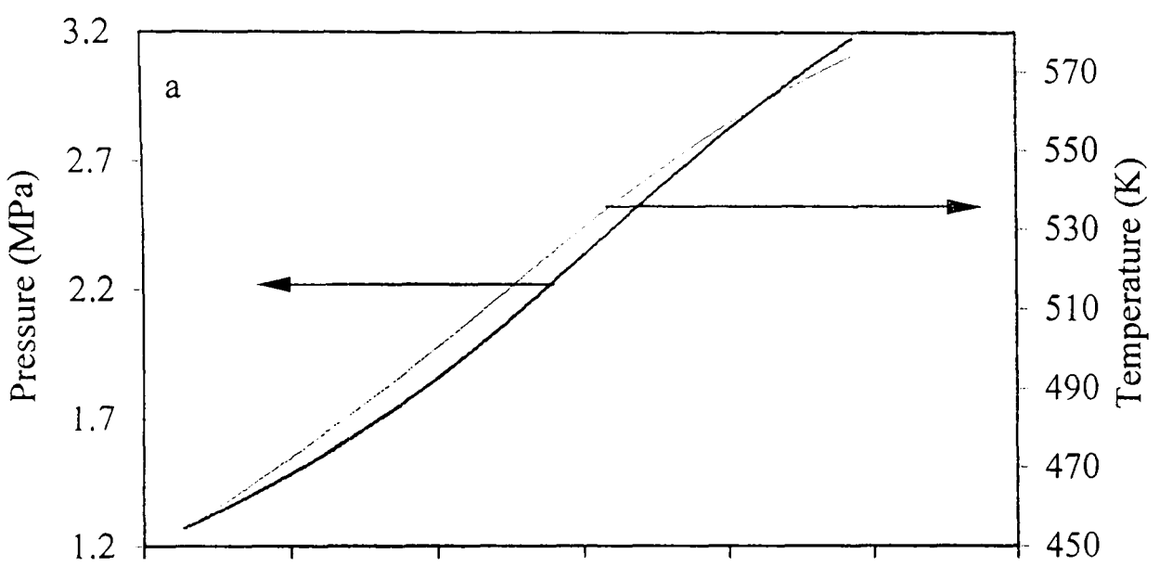

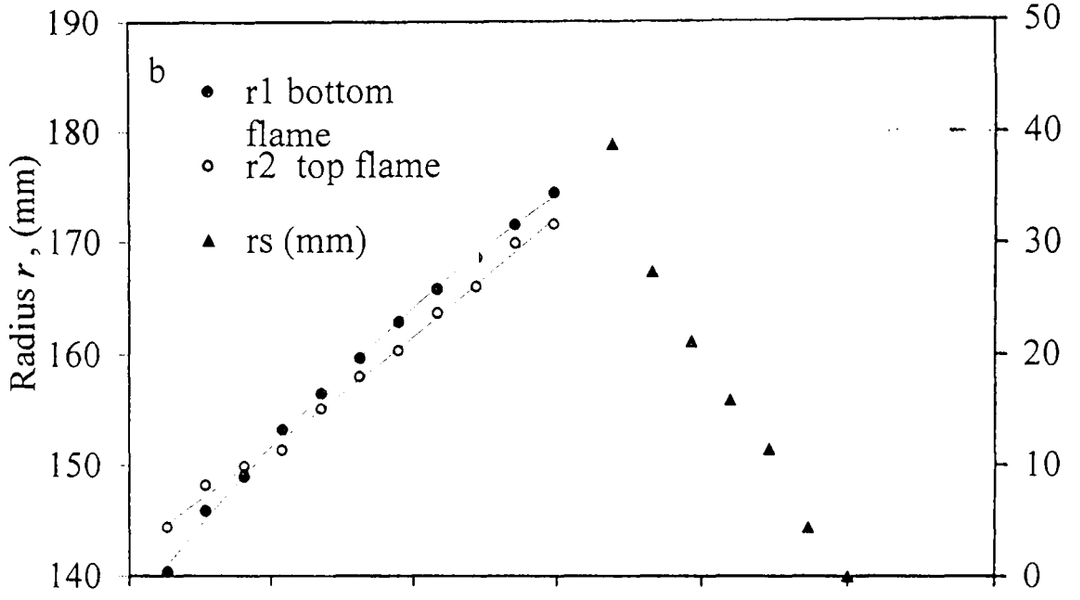

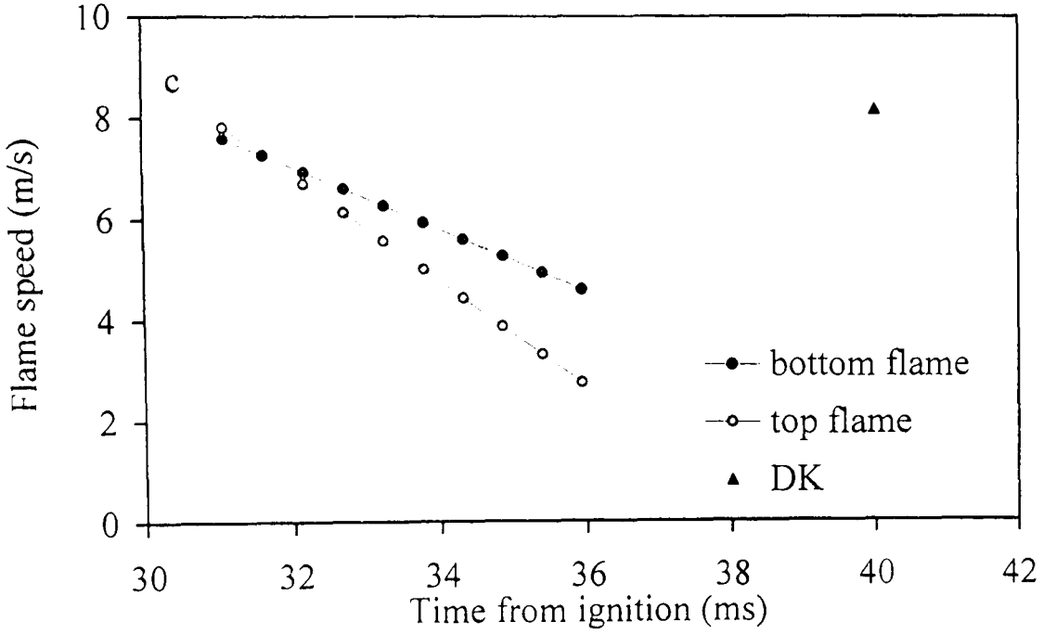

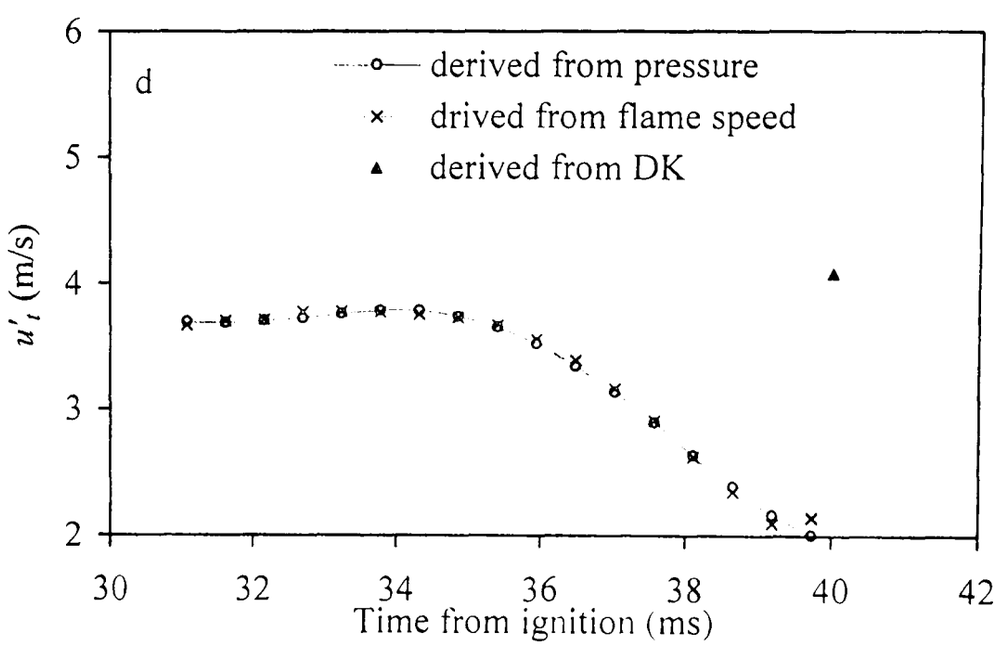

Fig. C.2. Iso-octane - air implosion, $\phi = 1, p_o = 0.5$ MPa, $T_o = 358$ K, $u' = 0.5$

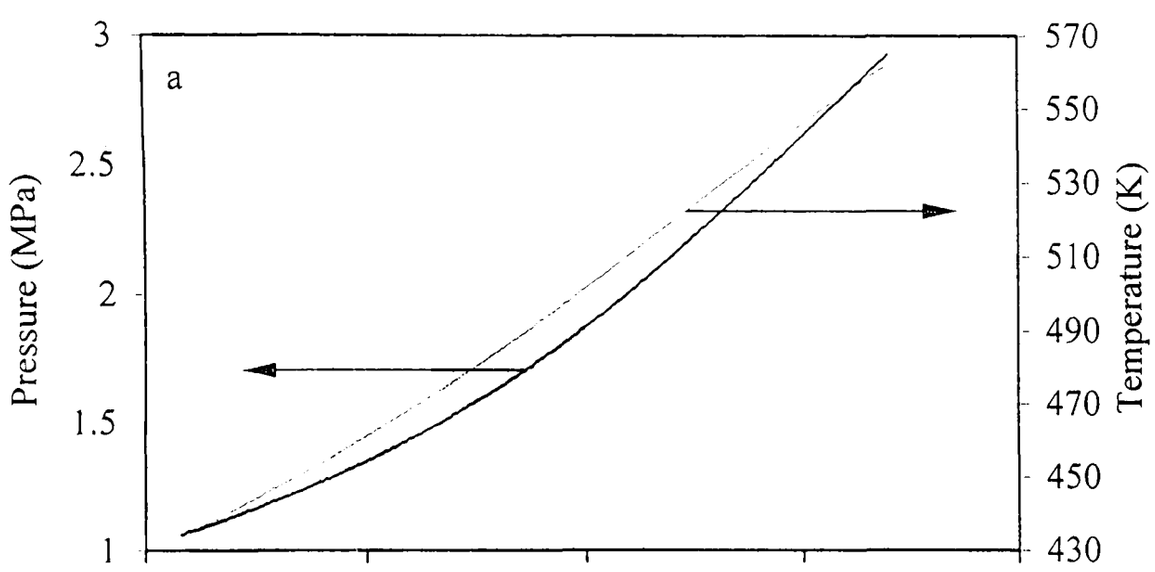

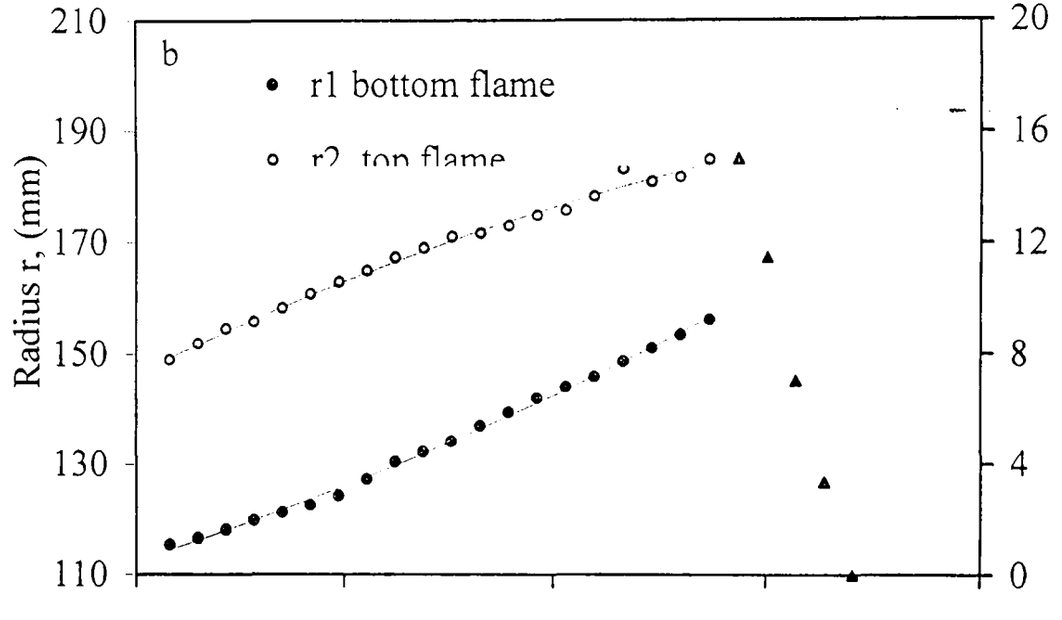

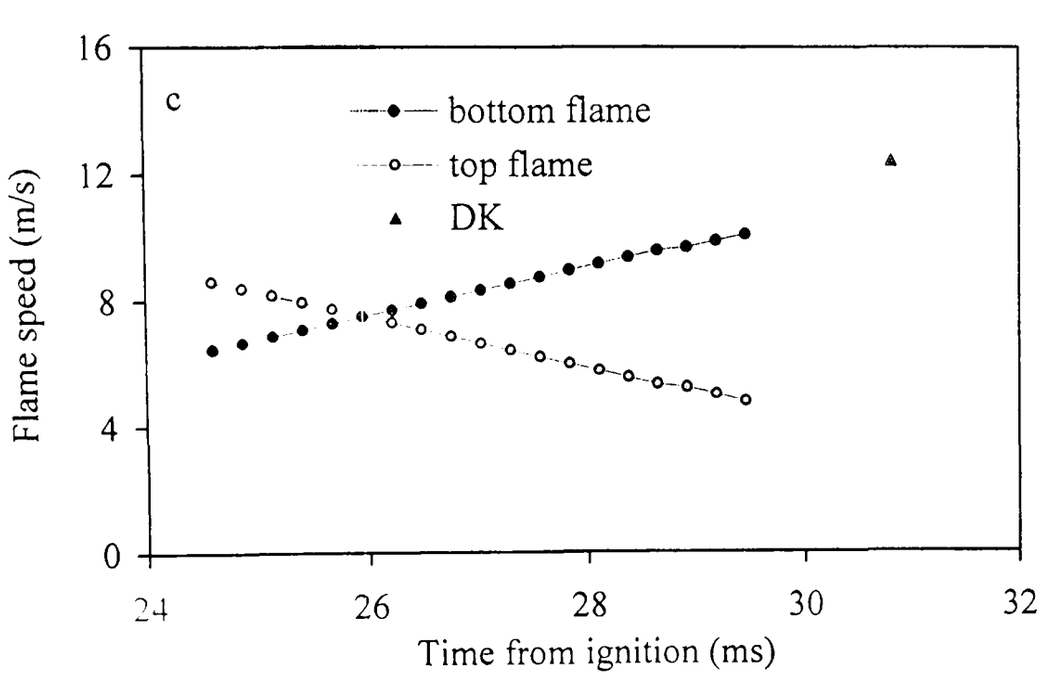

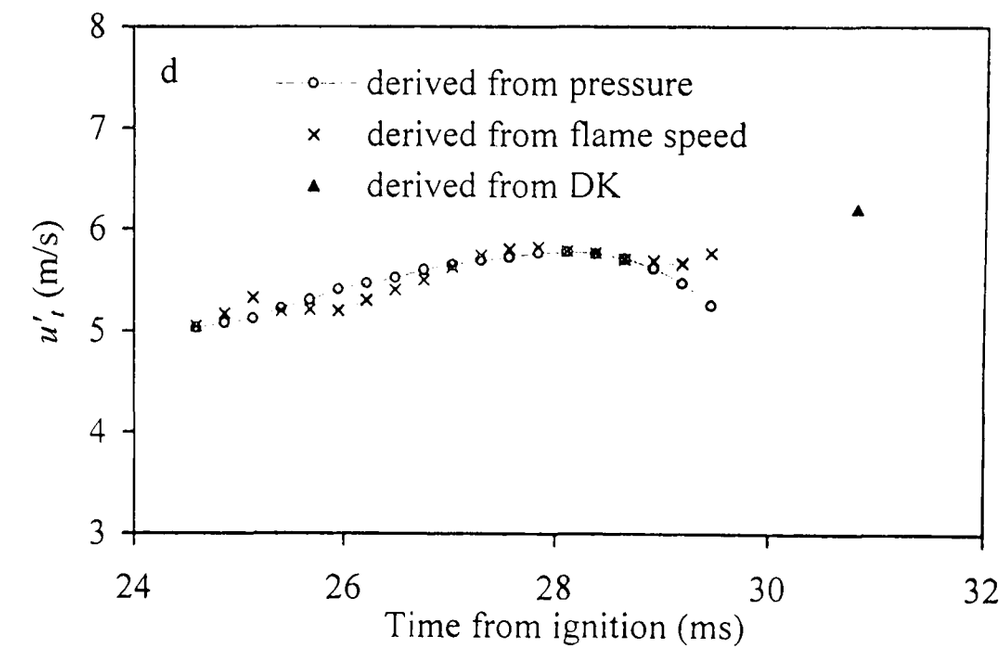

Fig. C.3. Iso-octane - air implosion, $\phi = 1$, $p_o = 0.5$ MPa, $T_o = 358$ K, $u' = 0.75$

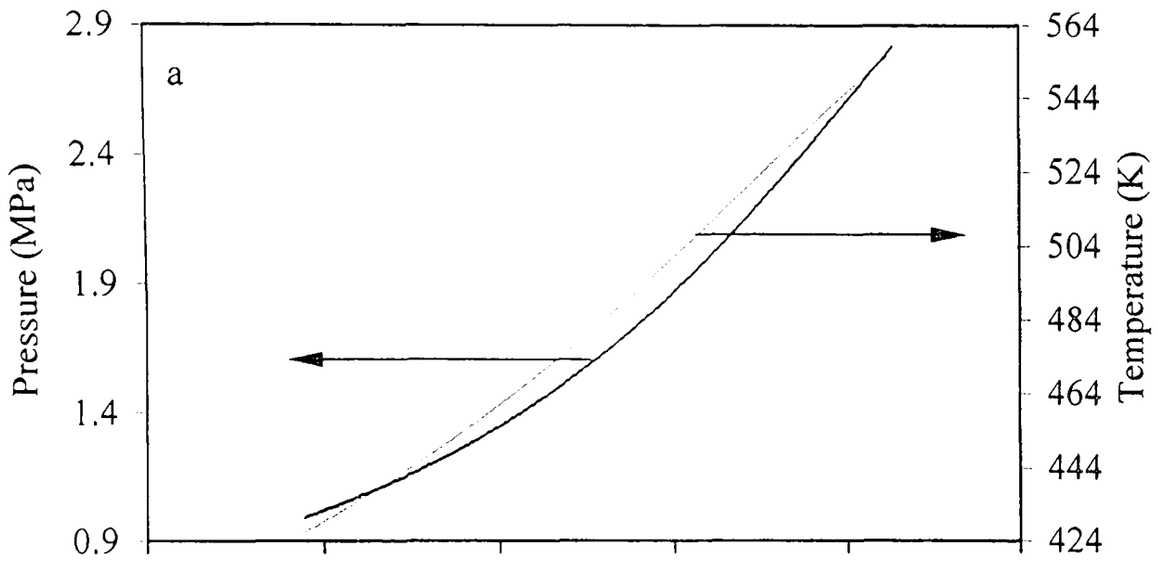

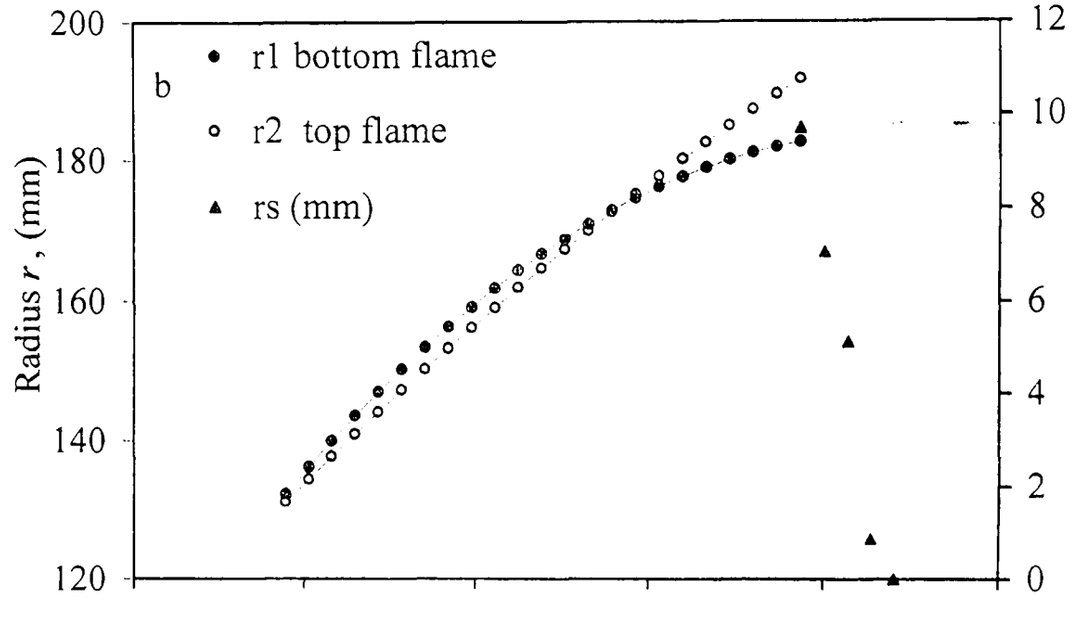

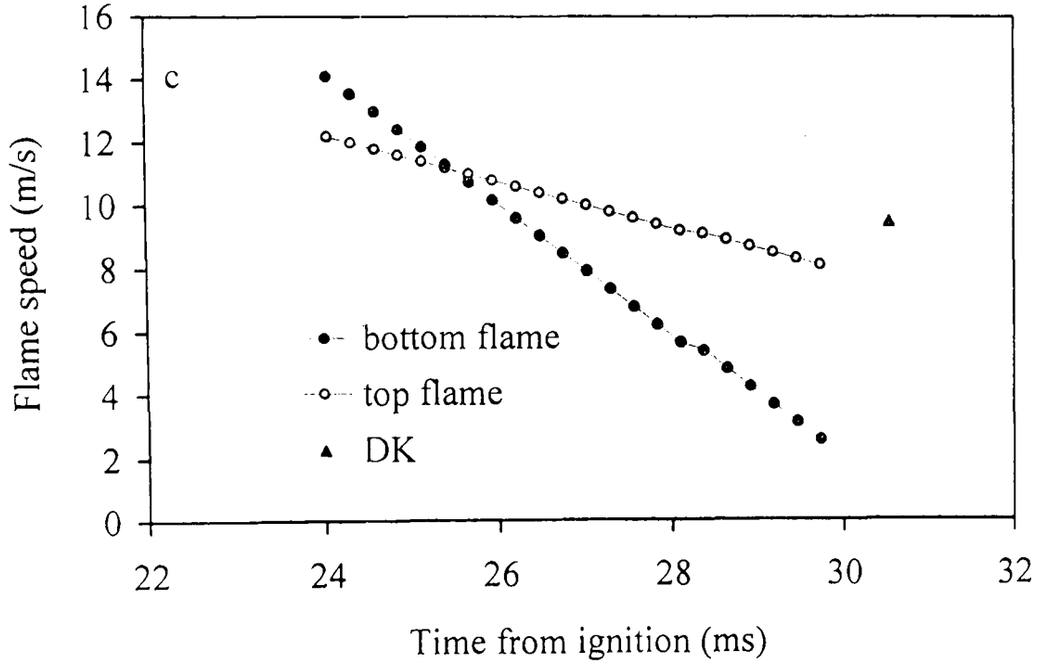

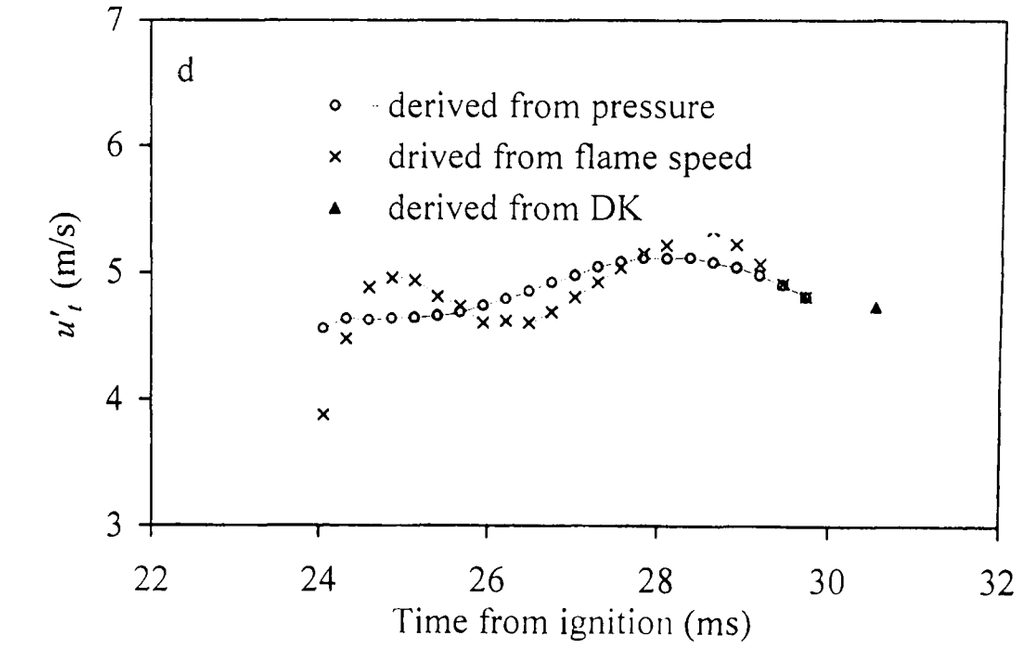

Fig. C.4. Iso-octane - air implosion, $\phi = 1, p_o = 0.5$ MPa, $T_o = 358$ K, $u' = 1$

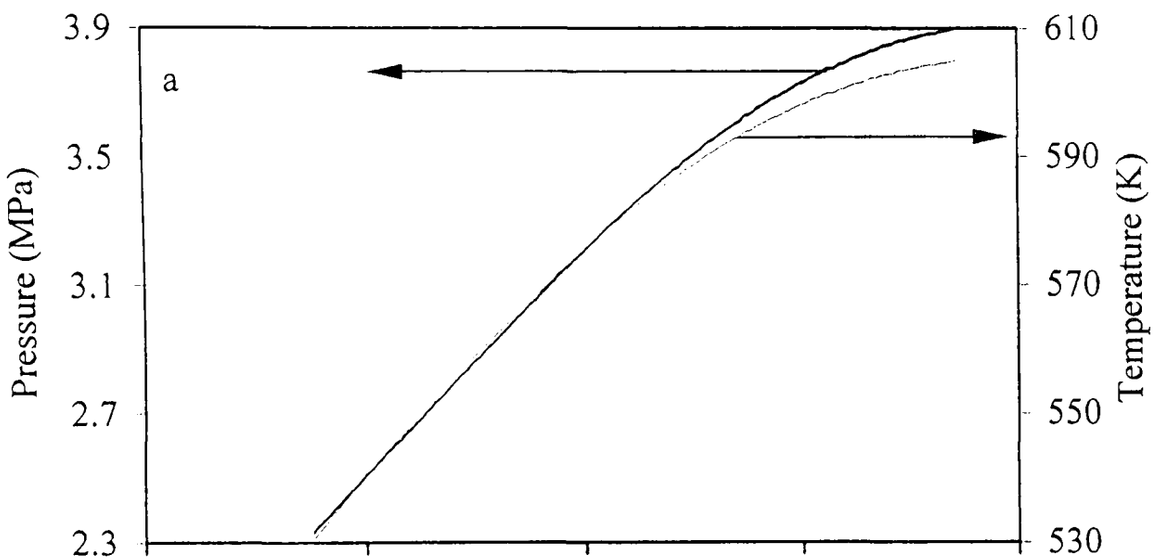

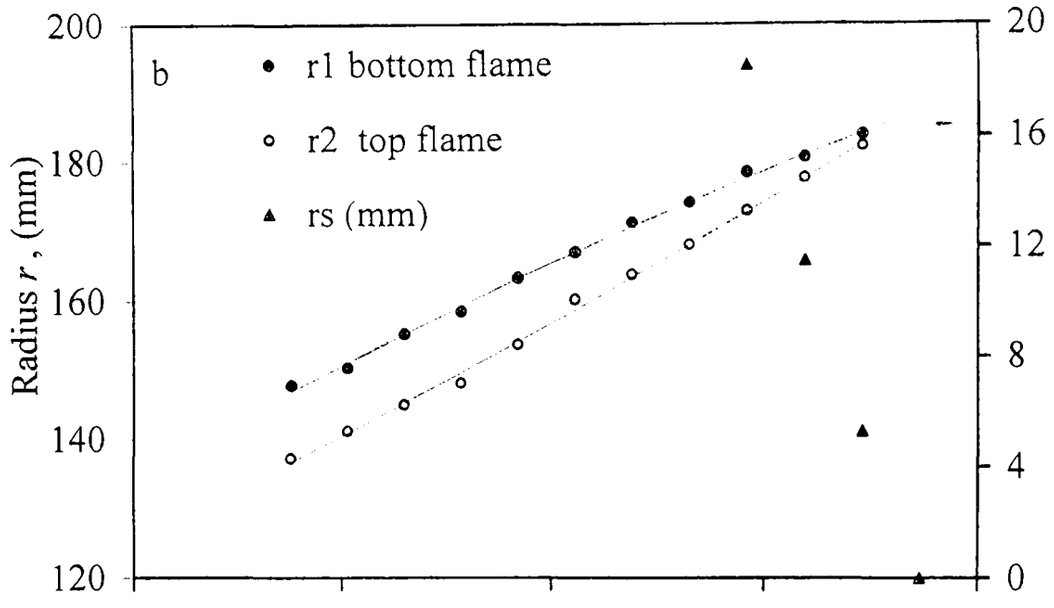

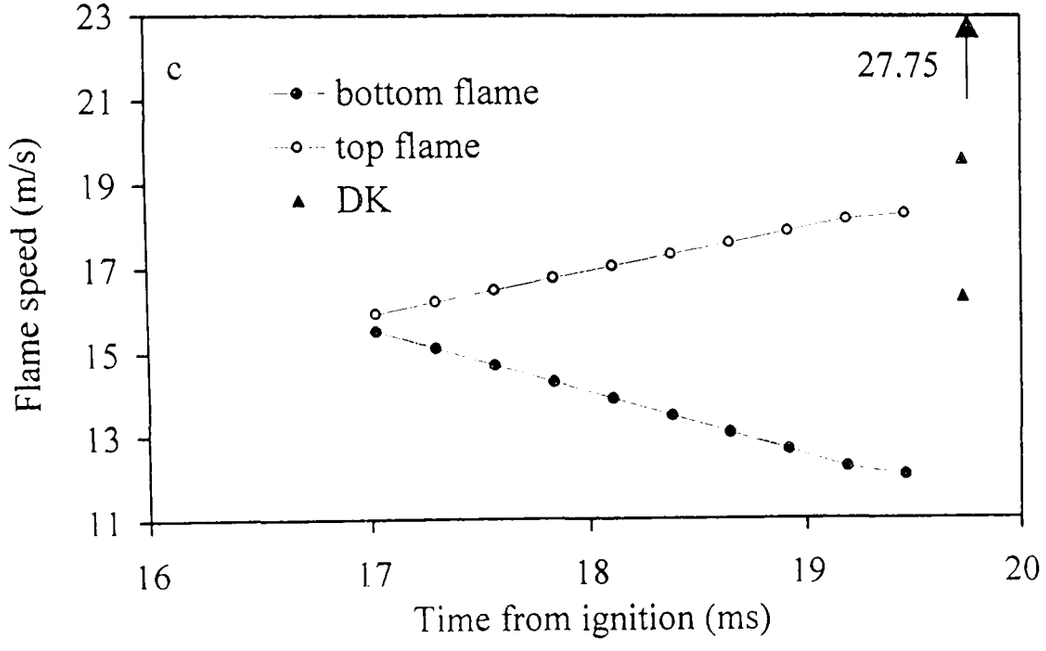

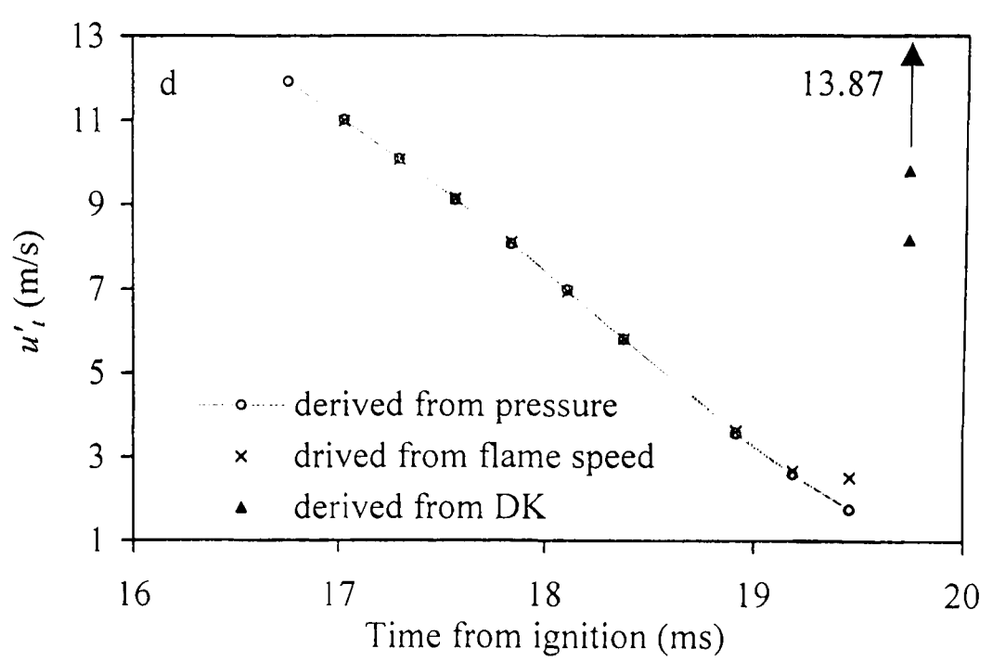

Fig. C.5. Iso-octane - air implosion, $\phi = 1, p_o = 0.5$ MPa, $T_o = 358$ K, $u' = 2$

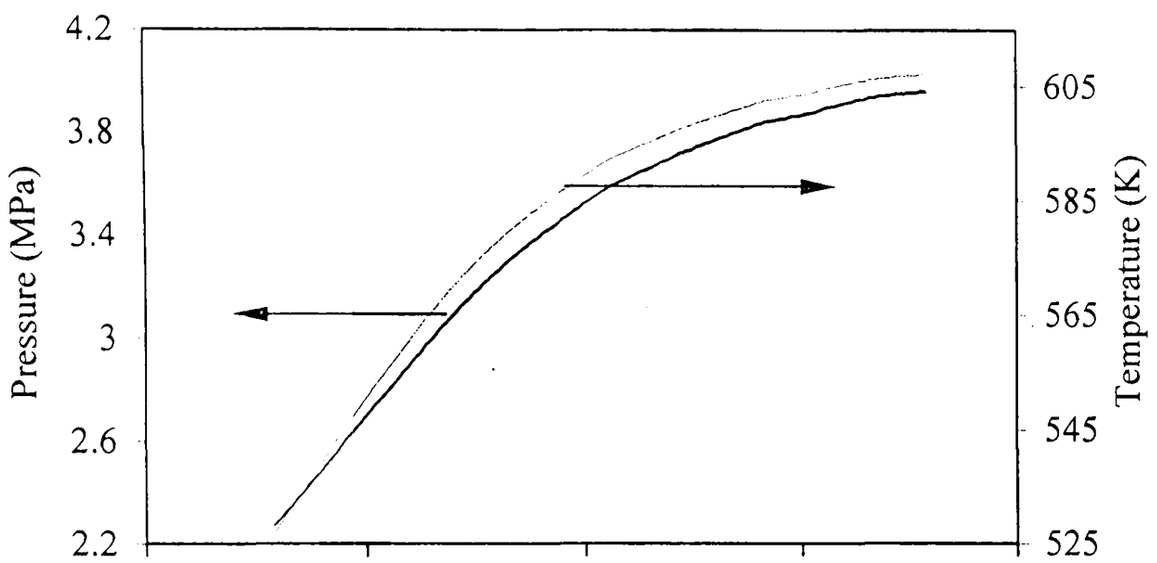

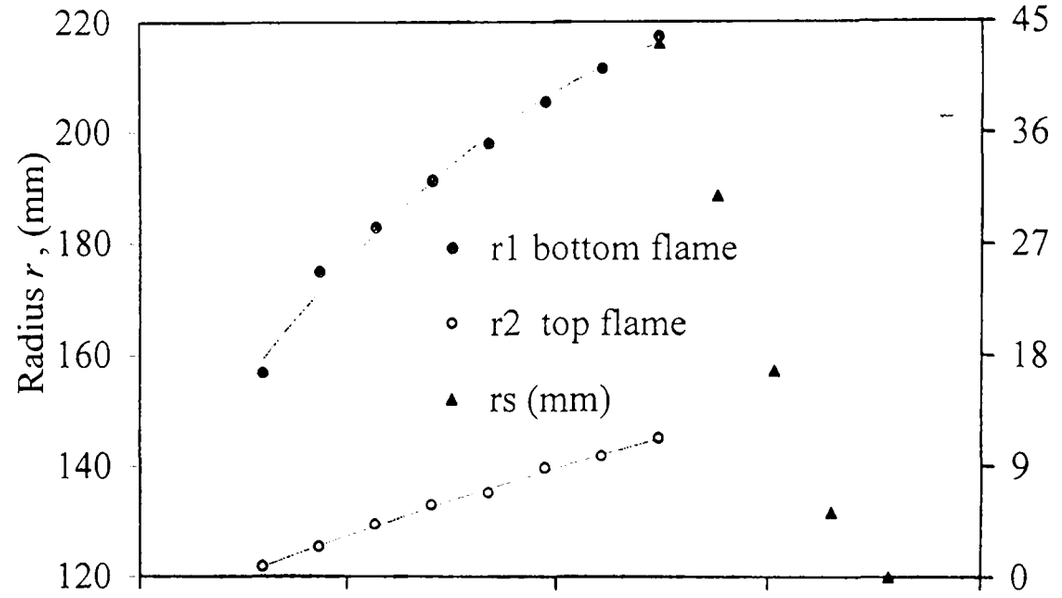

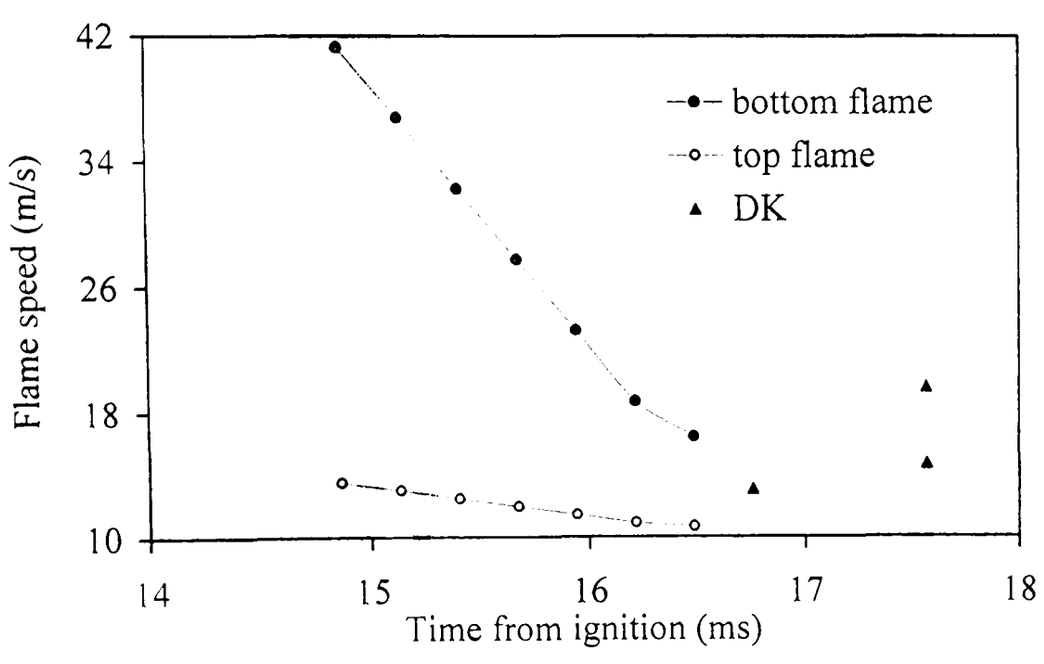

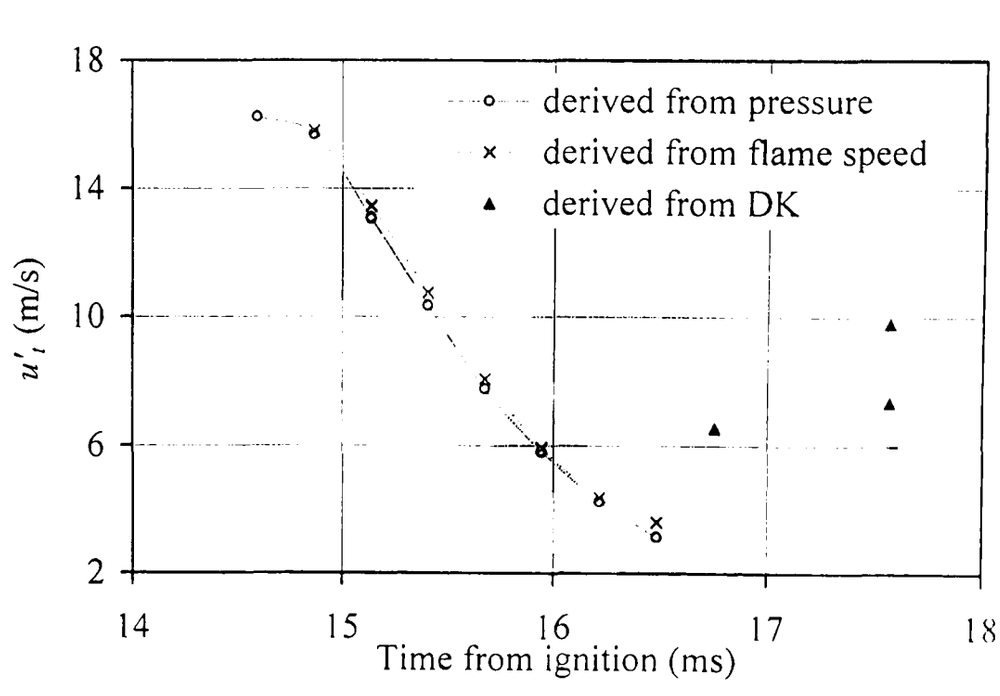

Fig. C.6. Iso-octane - air implosion, $\phi = 1, p_o = 0.5$ MPa, $T_o = 358$ K, $u' = 3$

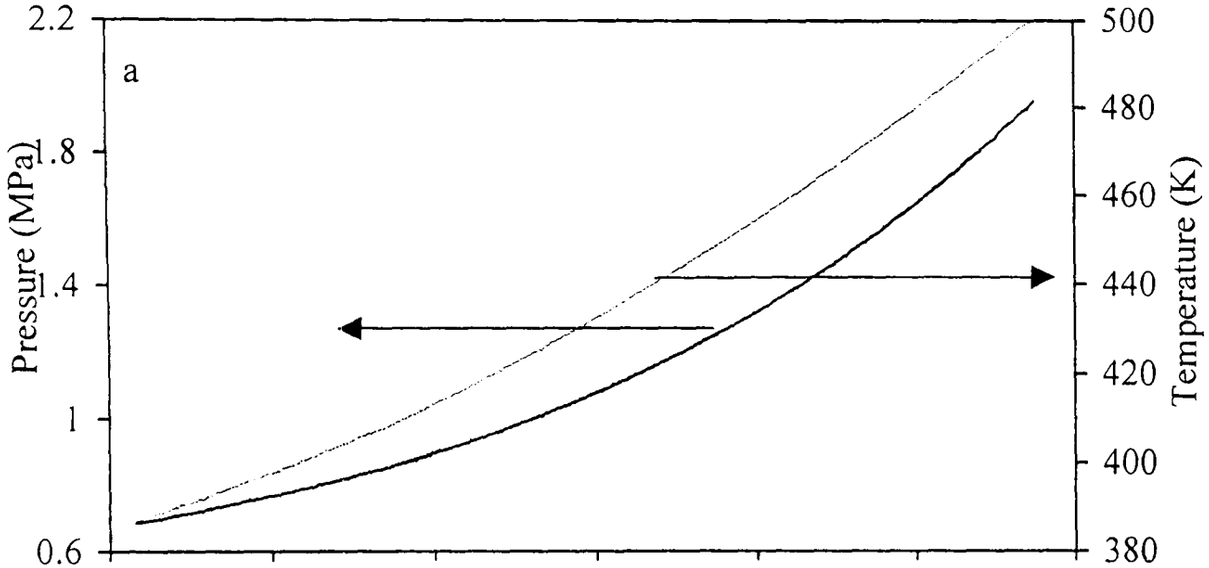

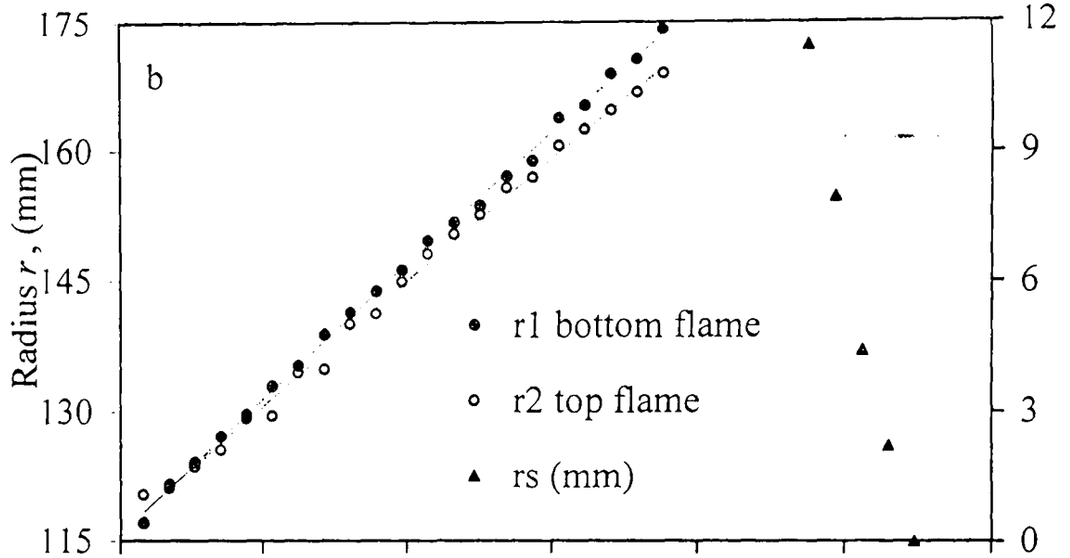

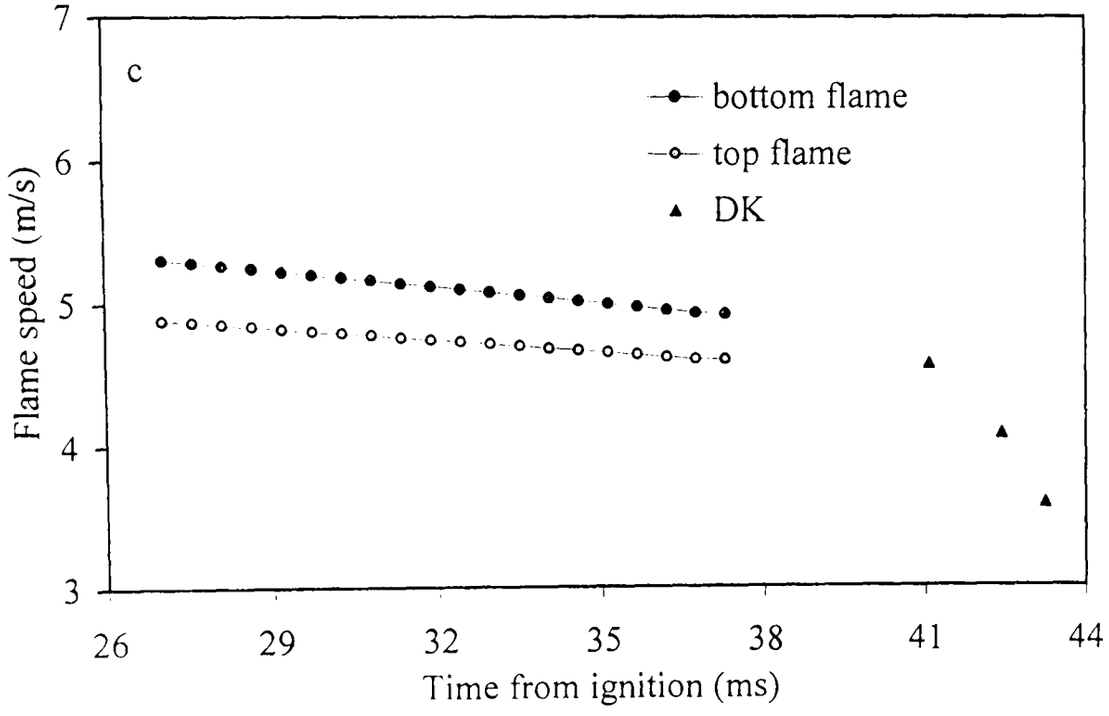

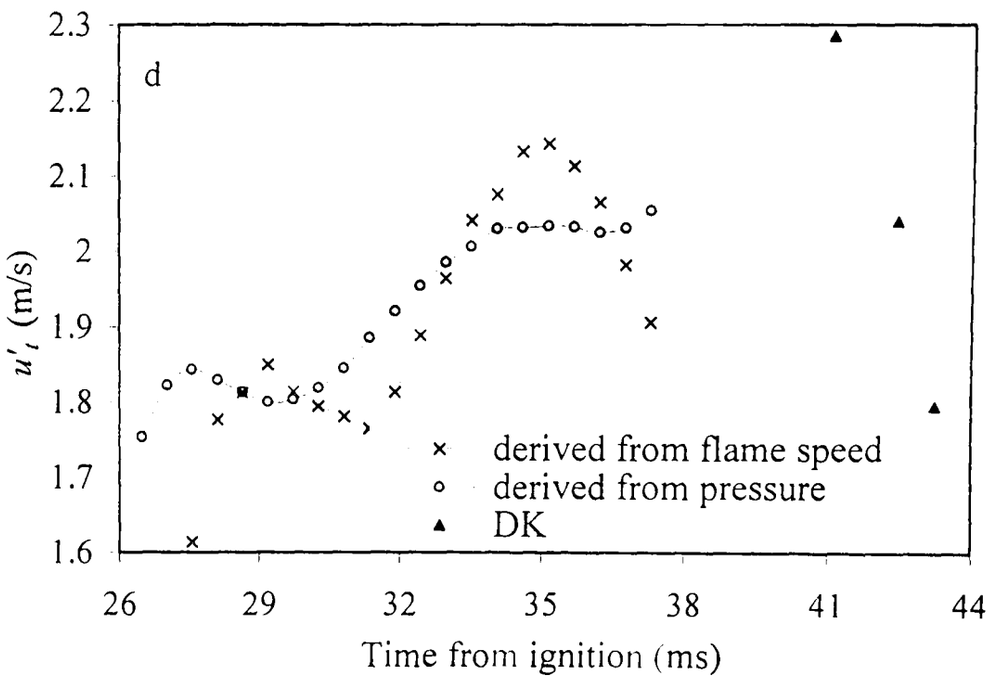

Fig. C.7. Iso-octane - air implosion, ϕ = 1.4, p_o = 0.5 MPa, T_o = 358 K, u' = 0.25

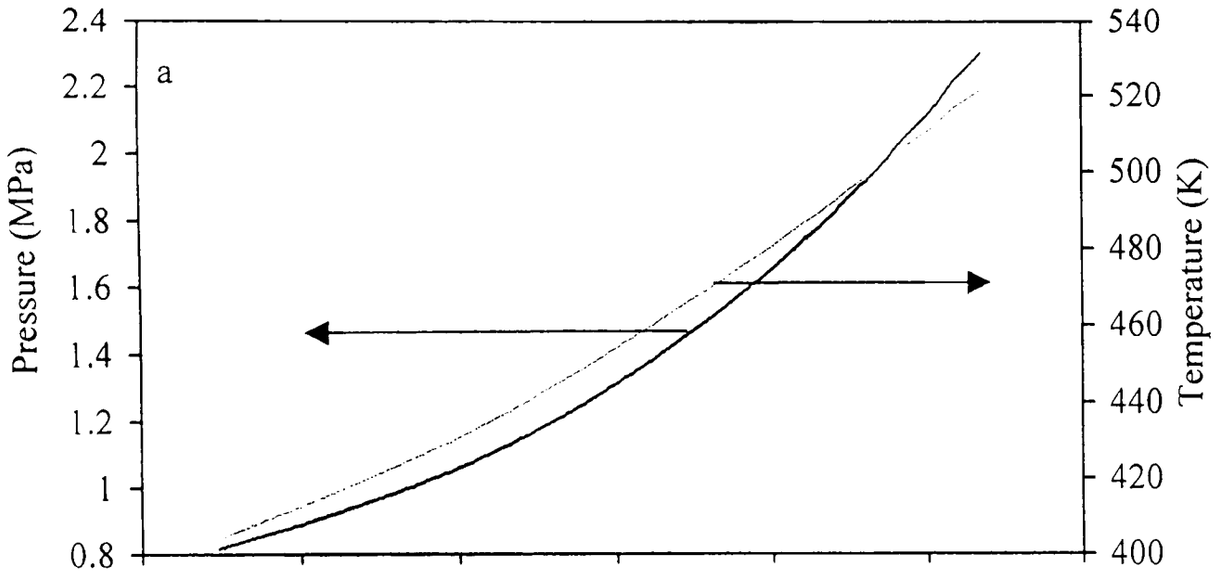

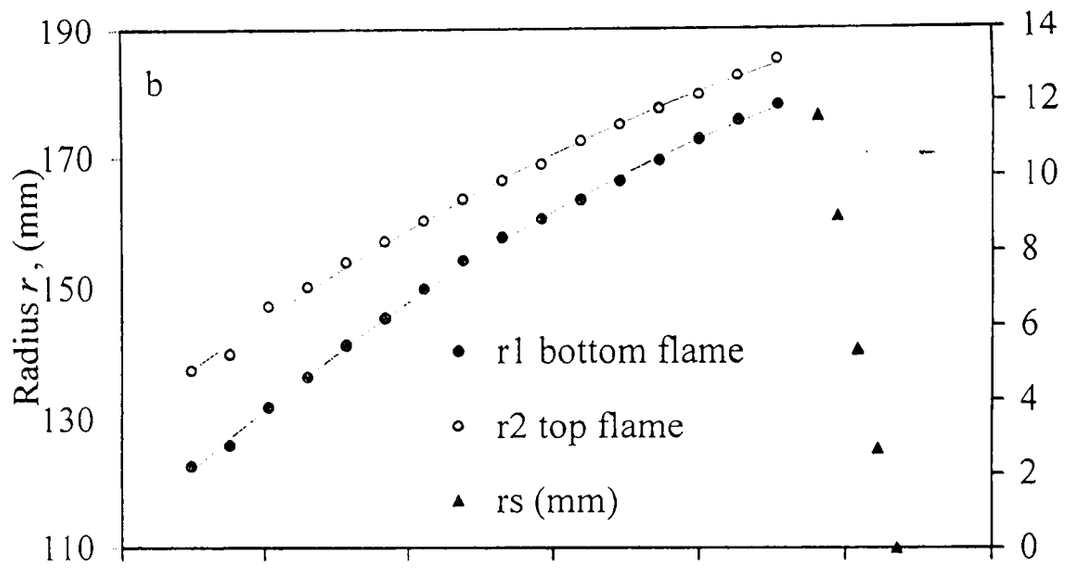

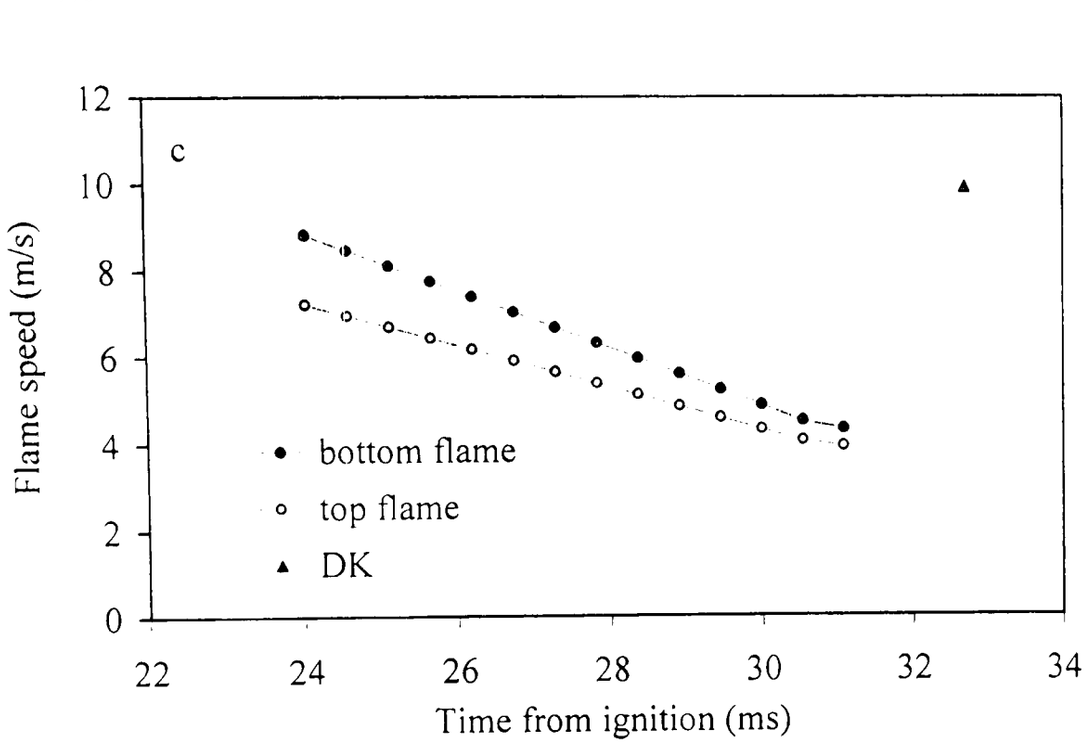

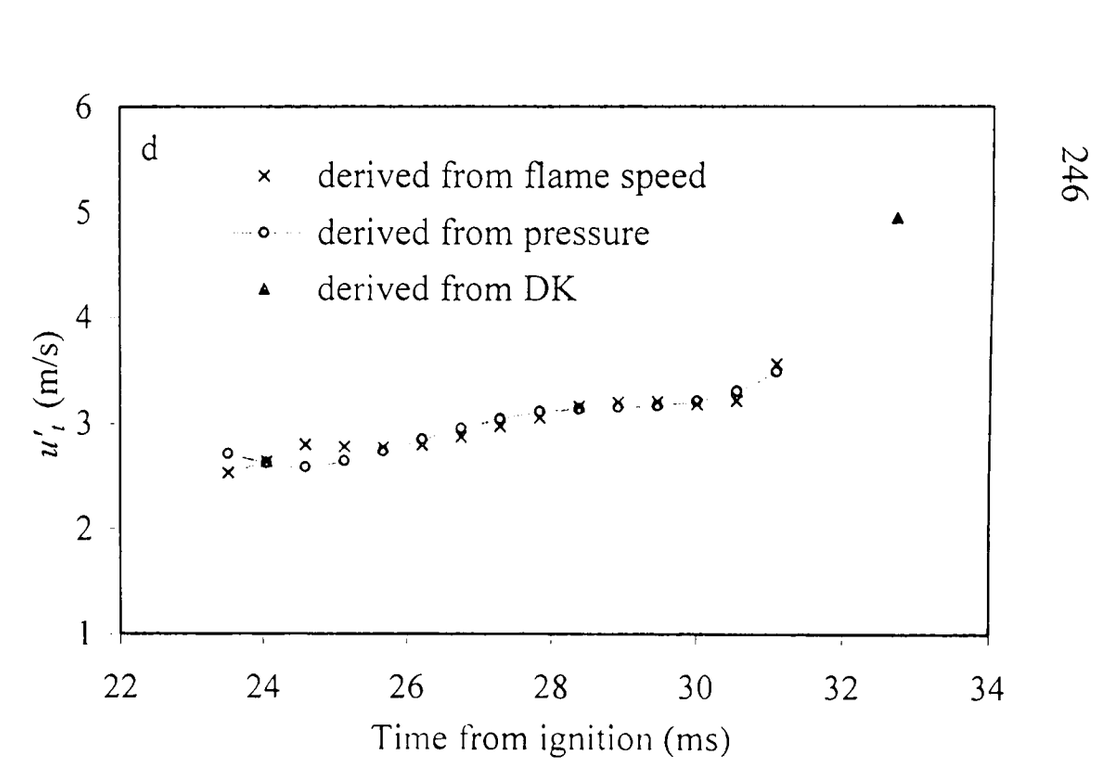

Fig. C.8. Iso-octane - air implosion, ϕ = 1.4, p_o = 0.5 MPa, T_o = 358 K, u' = 0.5

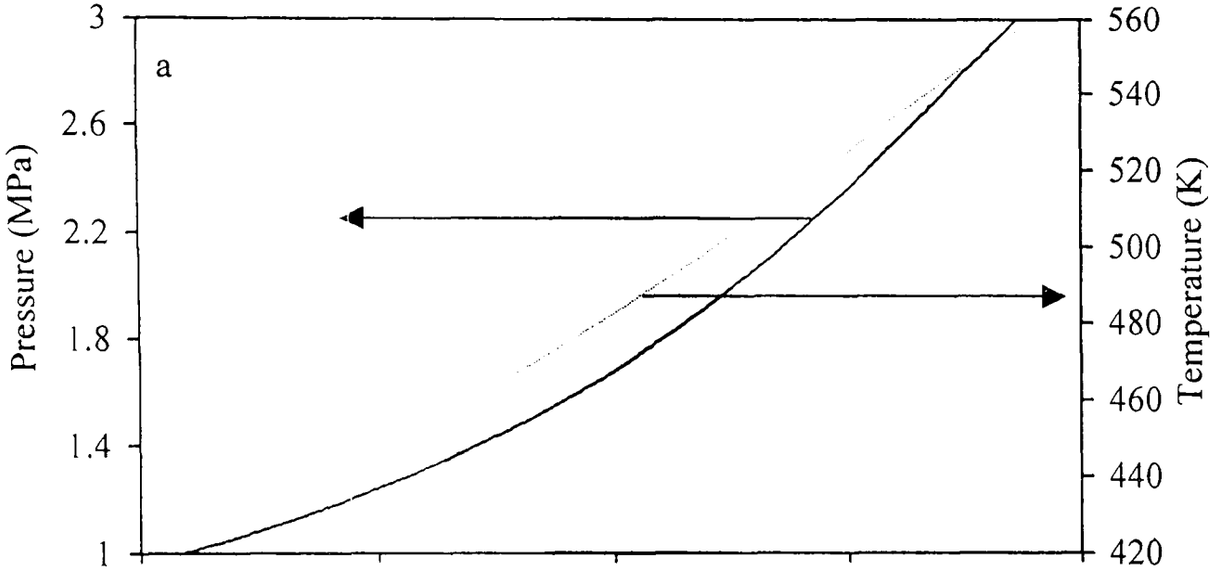

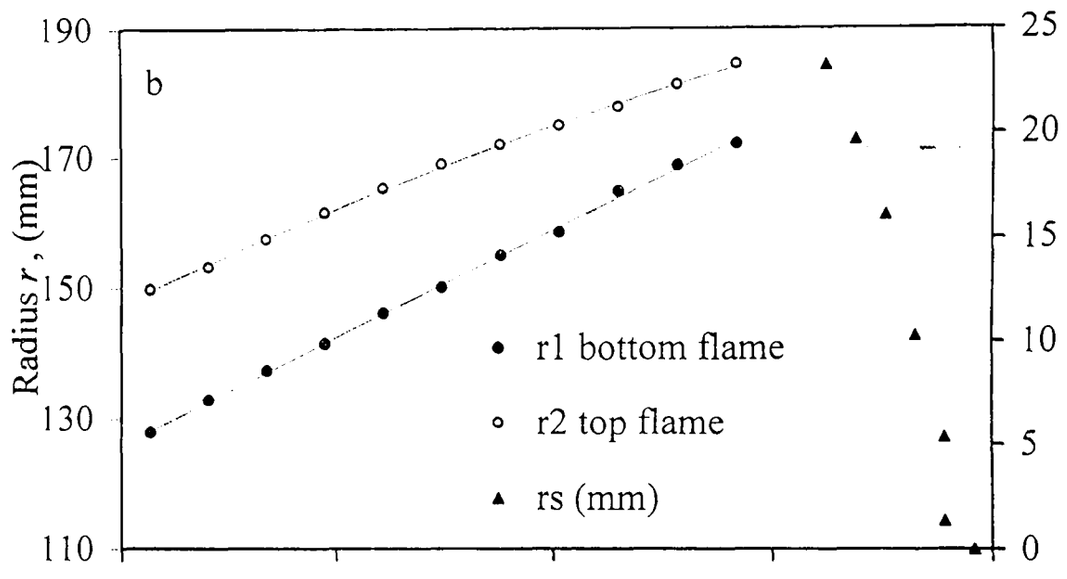

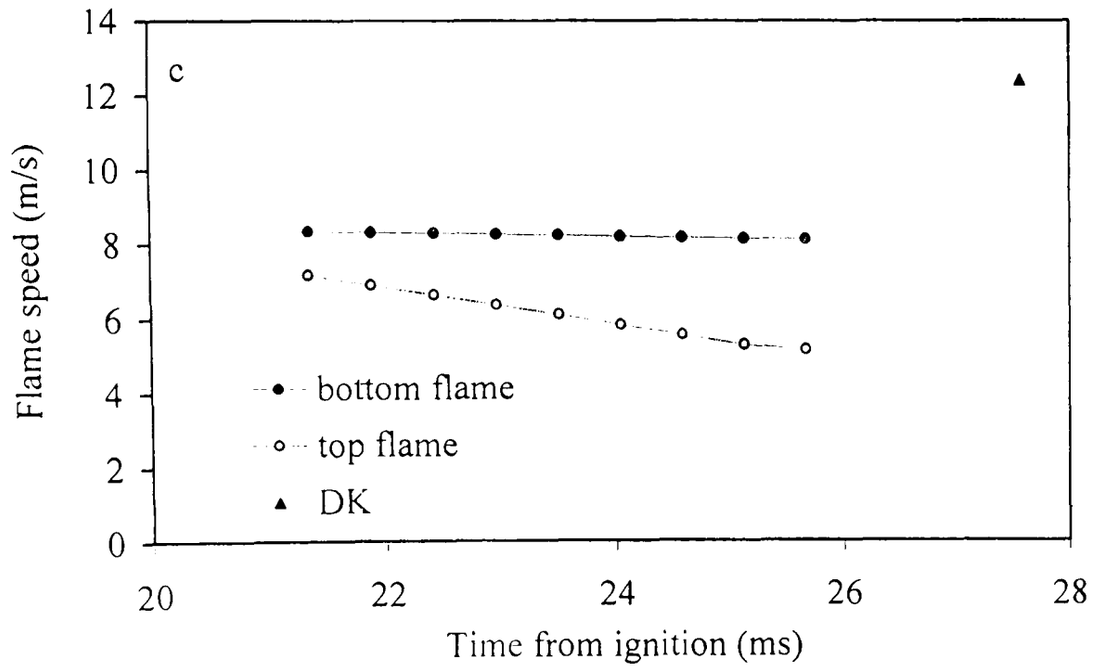

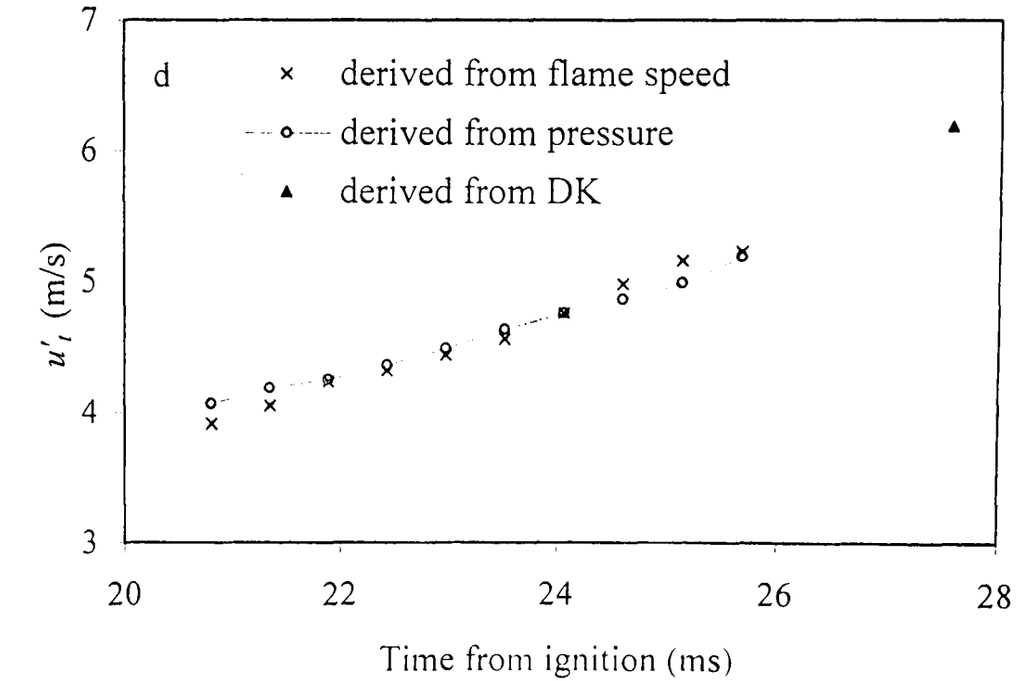

Fig. C.9. Iso-octane - air implosion, ϕ = 1.4, p_o = 0.5 MPa, T_o = 358 K, u' = 0.75

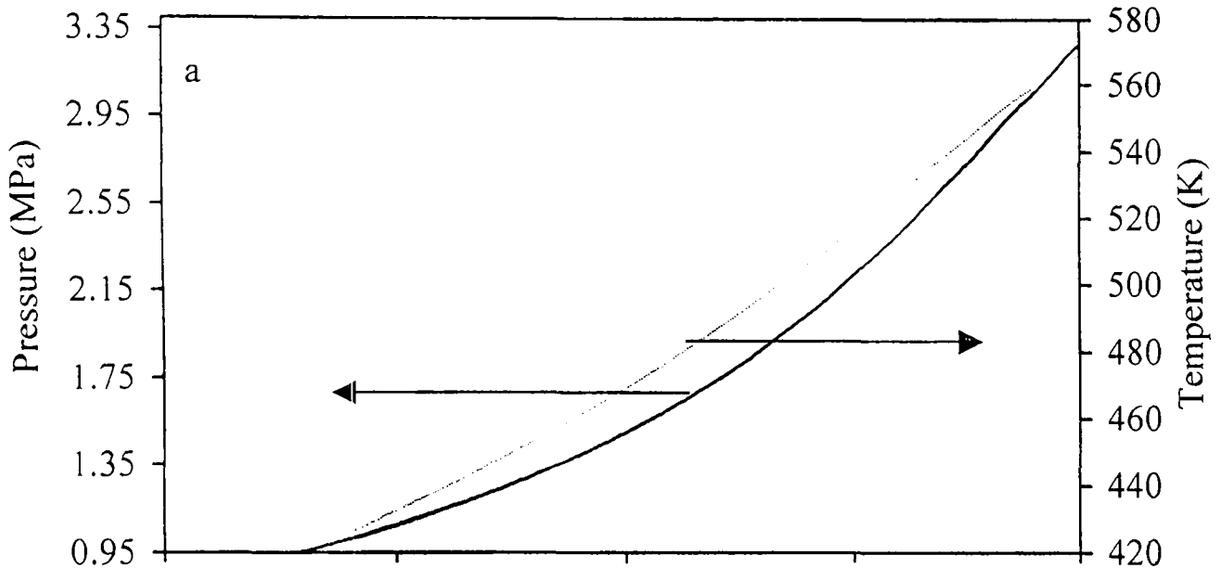

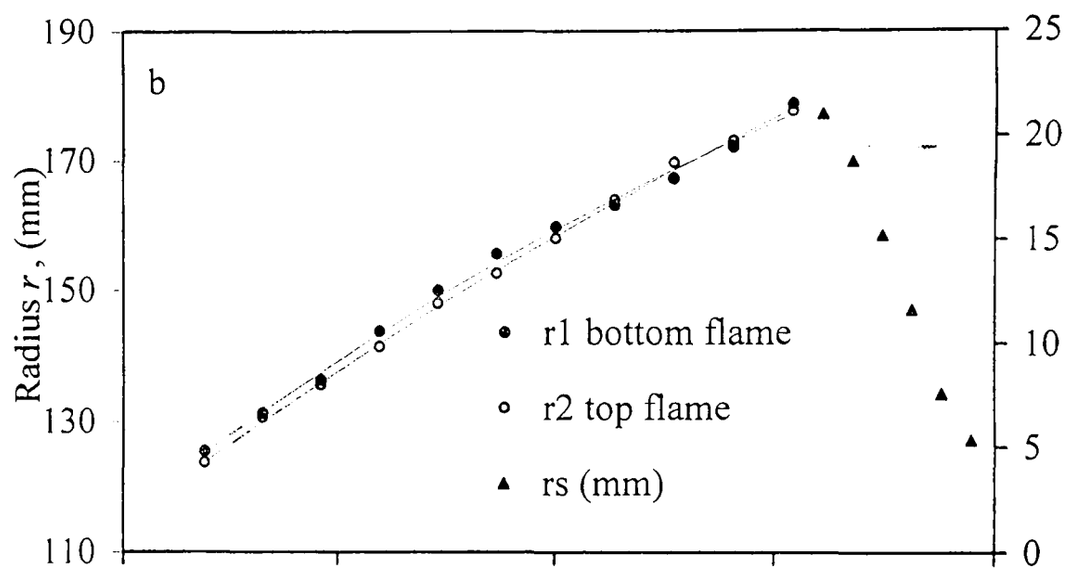

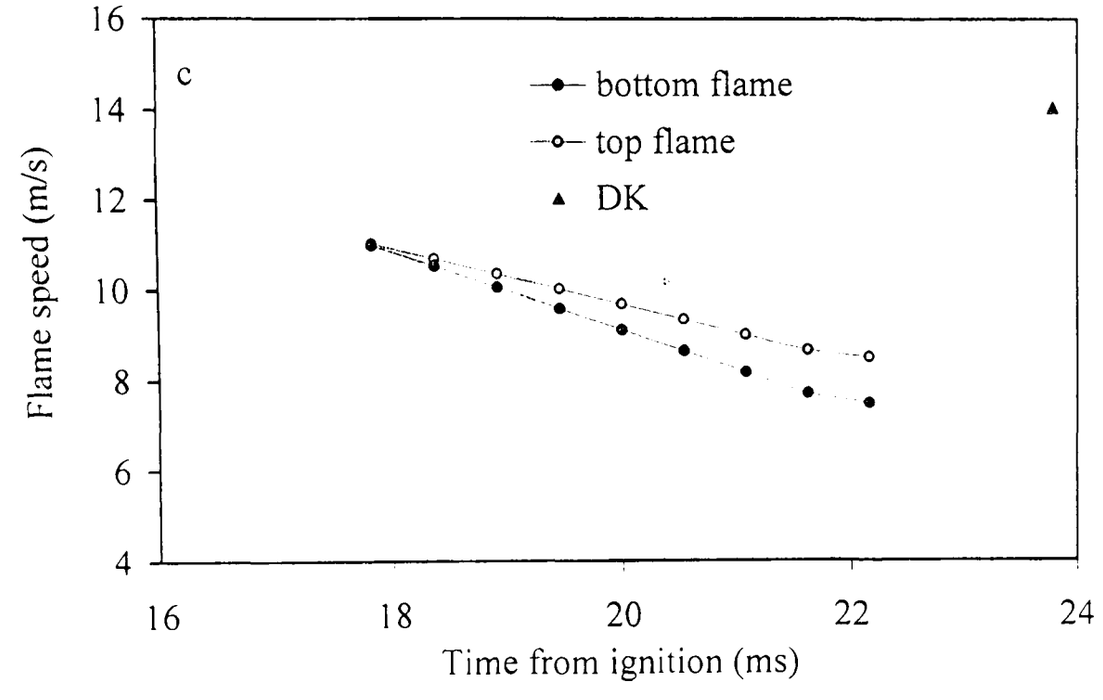

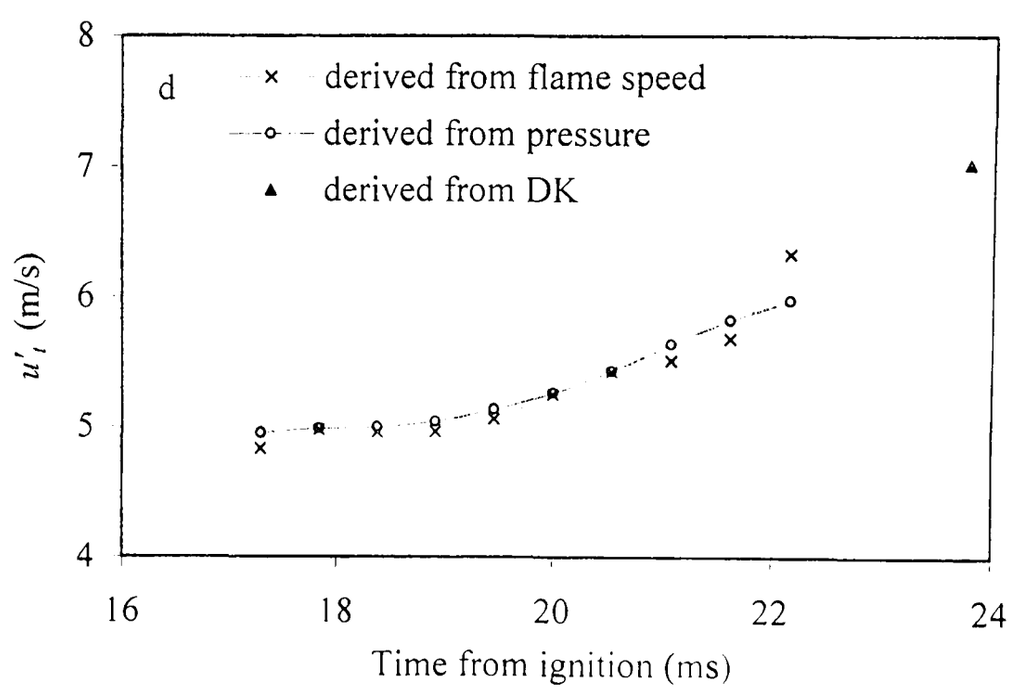

Fig. C.10. Iso-octane - air implosion, ϕ = 1.4, p_o = 0.5 MPa, T_o = 358 K, u' = 1

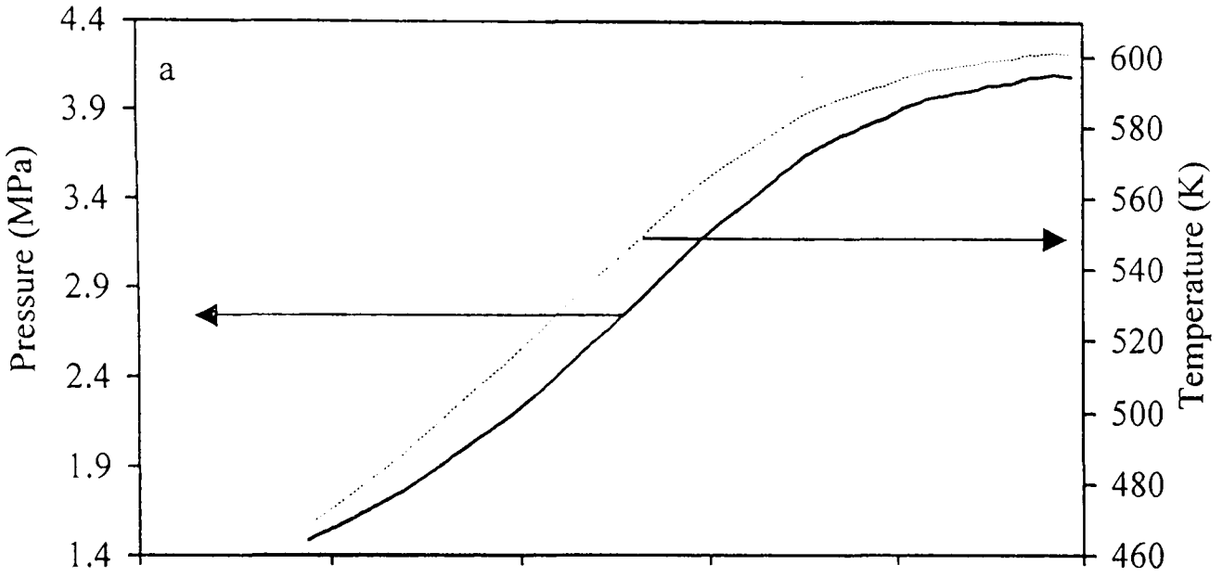

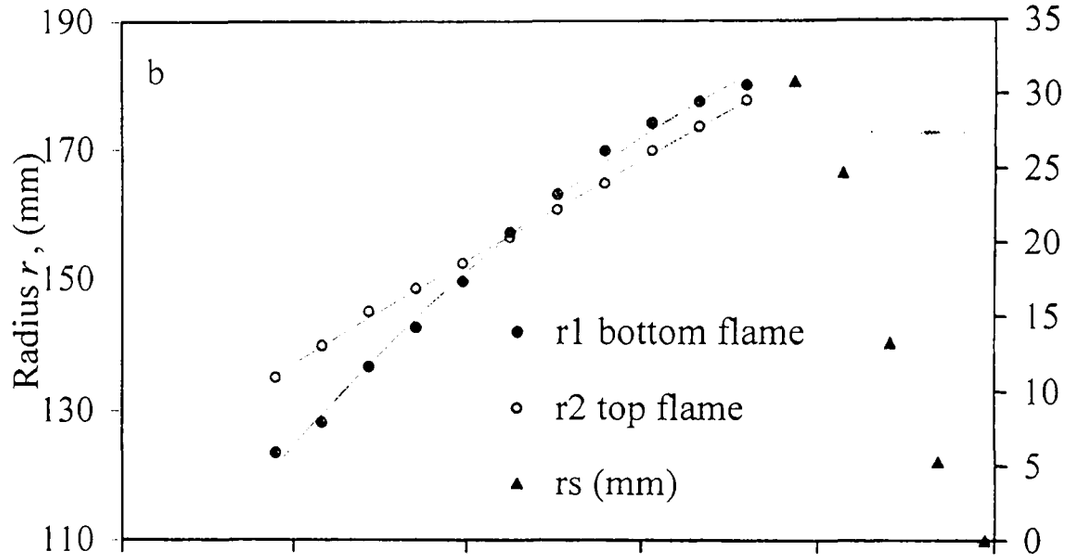

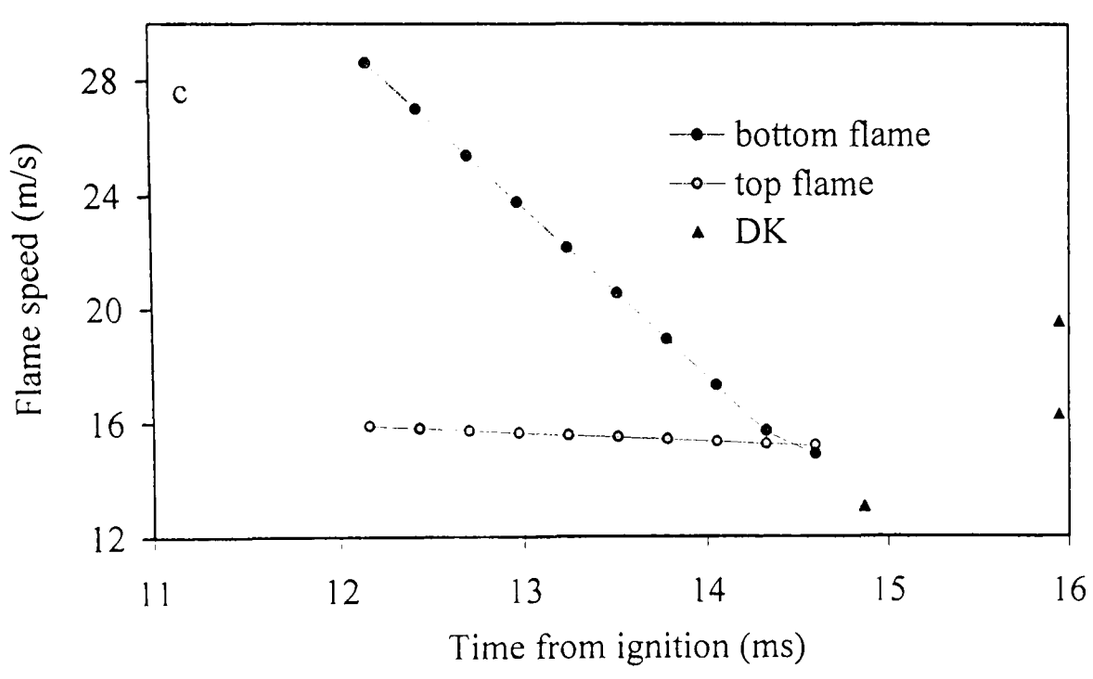

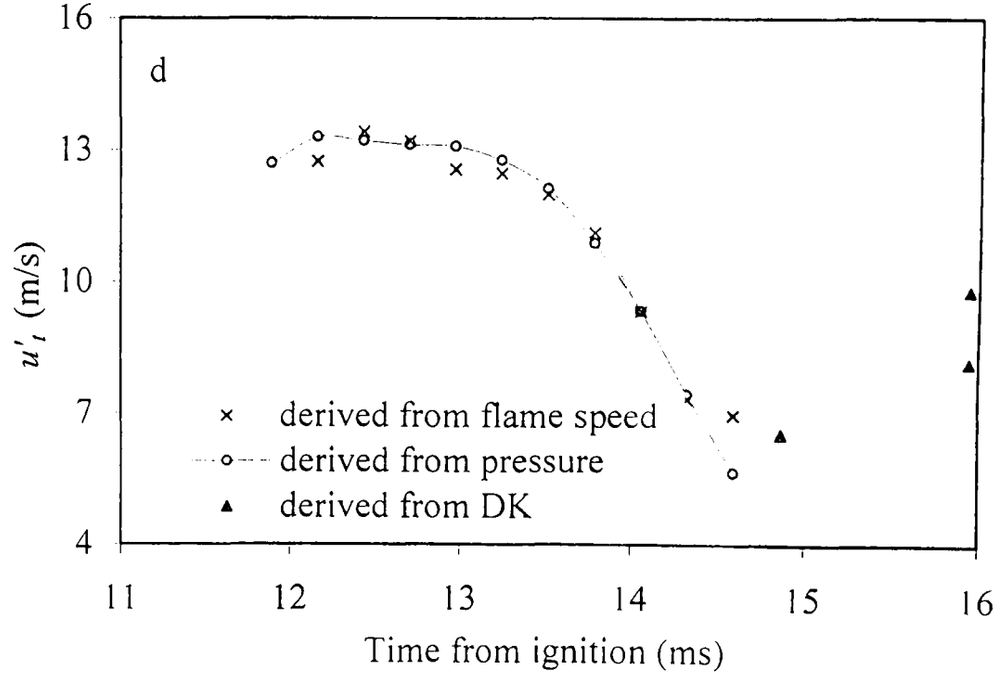

Fig. C.11. Iso-octane - air implosion, ϕ = 1.4, p_o = 0.5 MPa, T_o = 358 K, u' = 2

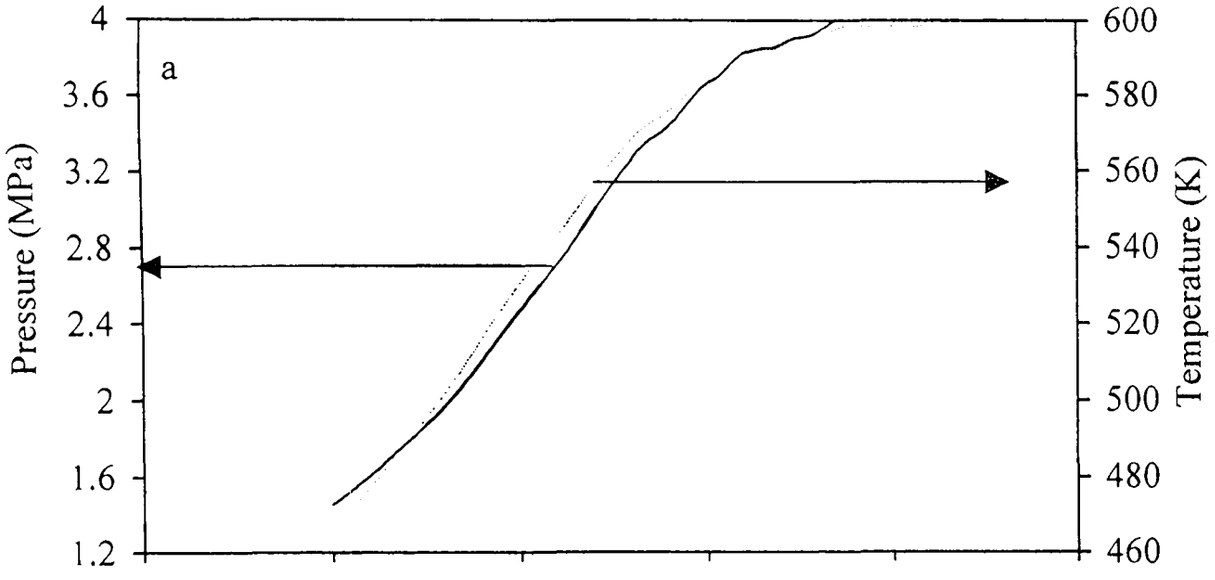

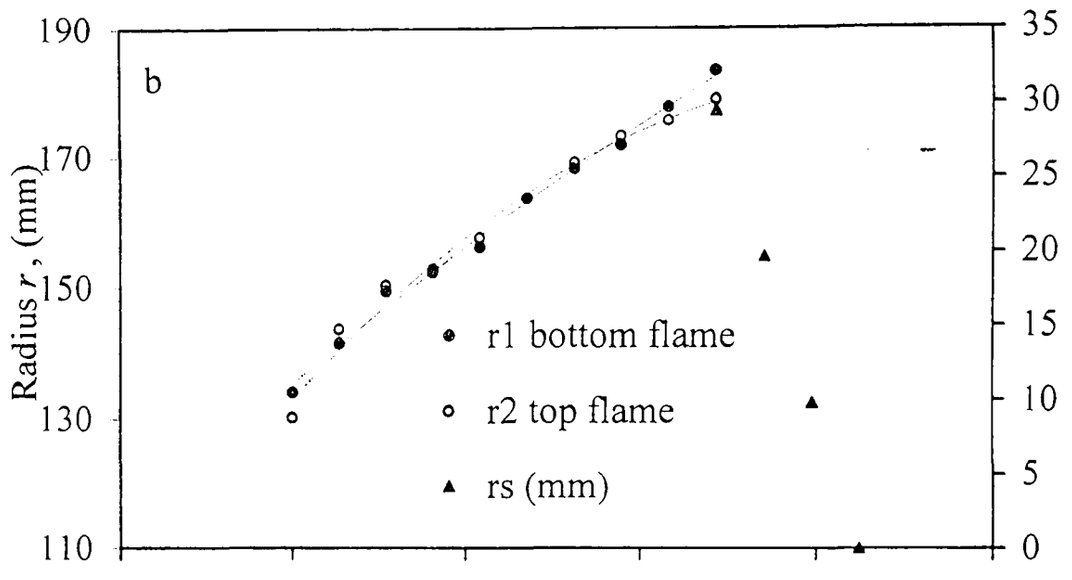

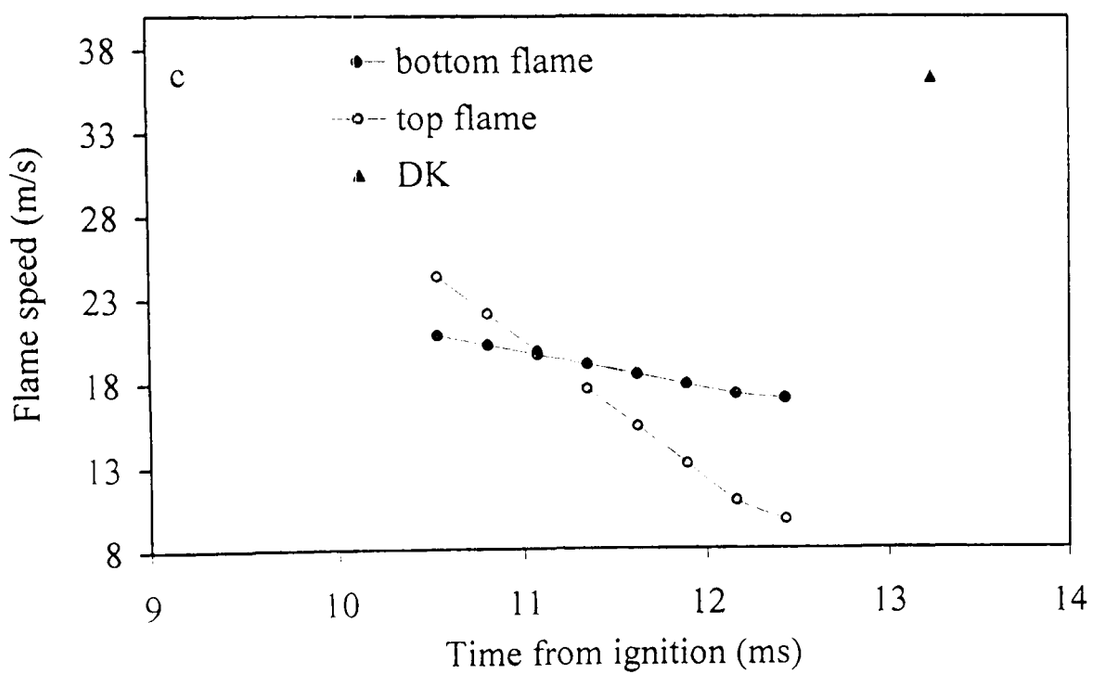

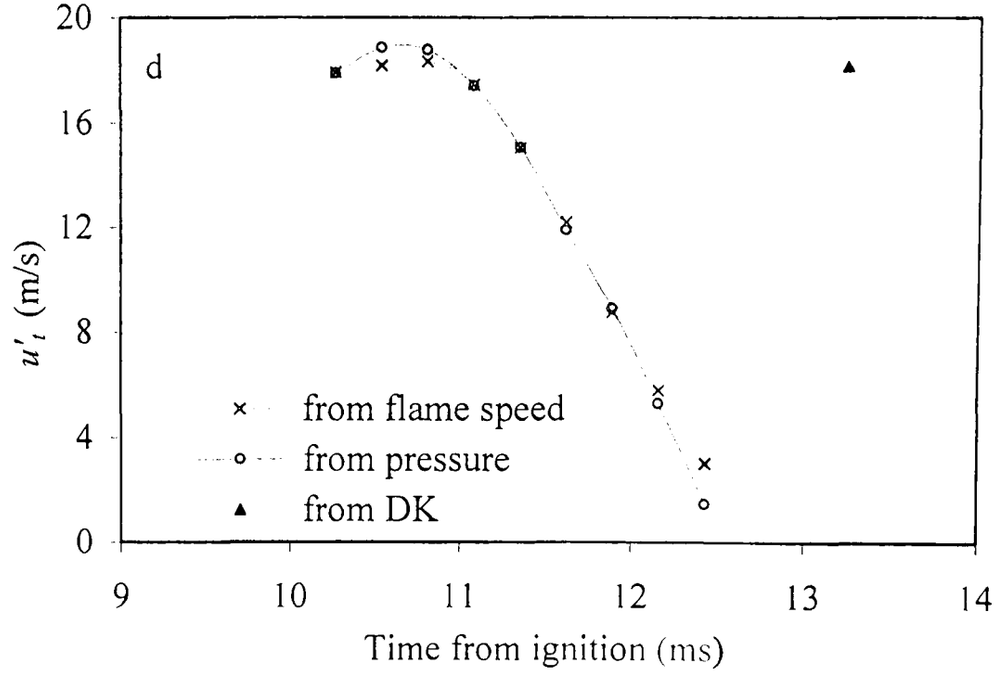

Fig. C.12. Iso-octane - air implosion, ϕ = 1.4, p_o = 0.5 MPa, T_o = 358 K, u' = 3

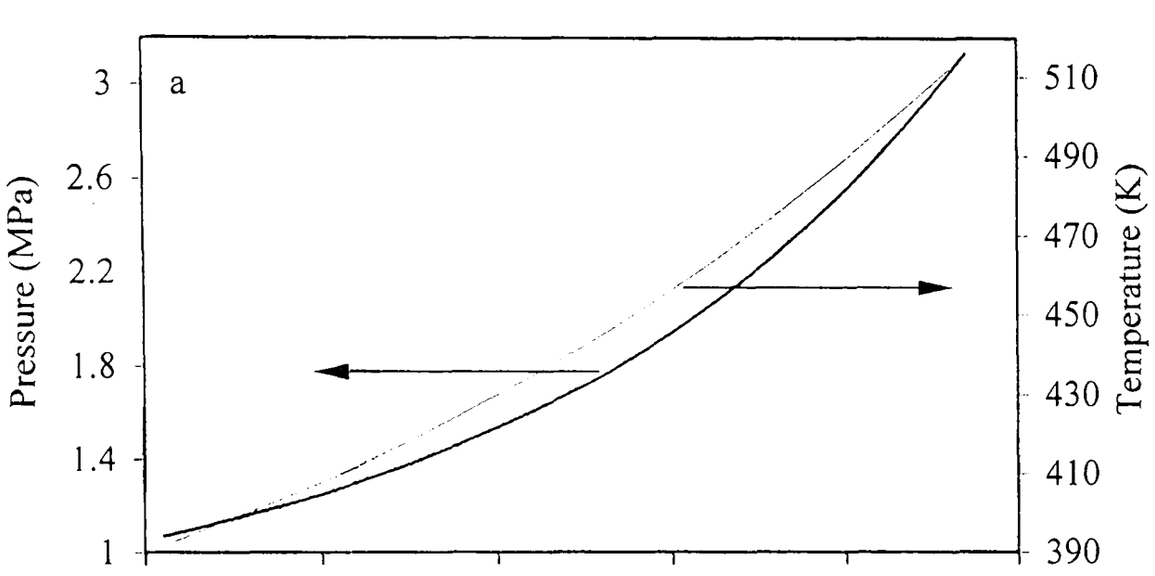

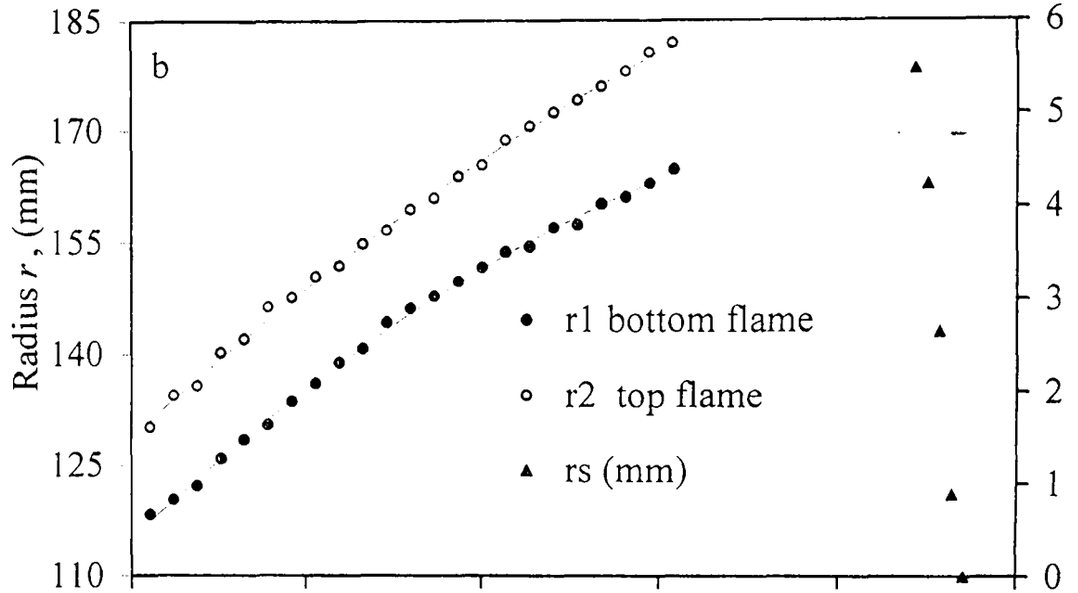

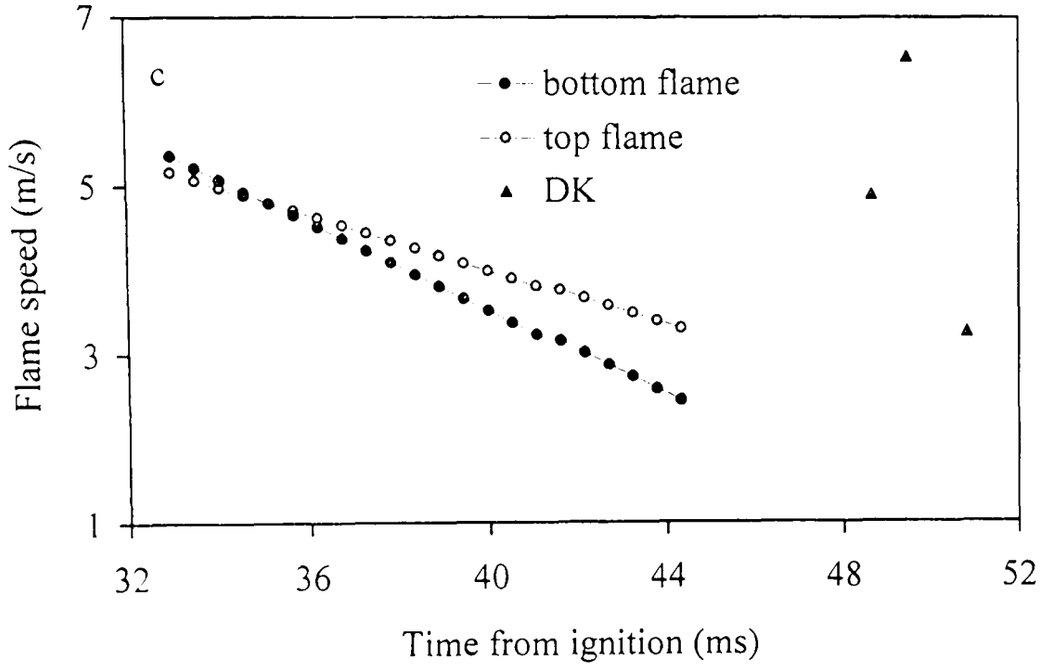

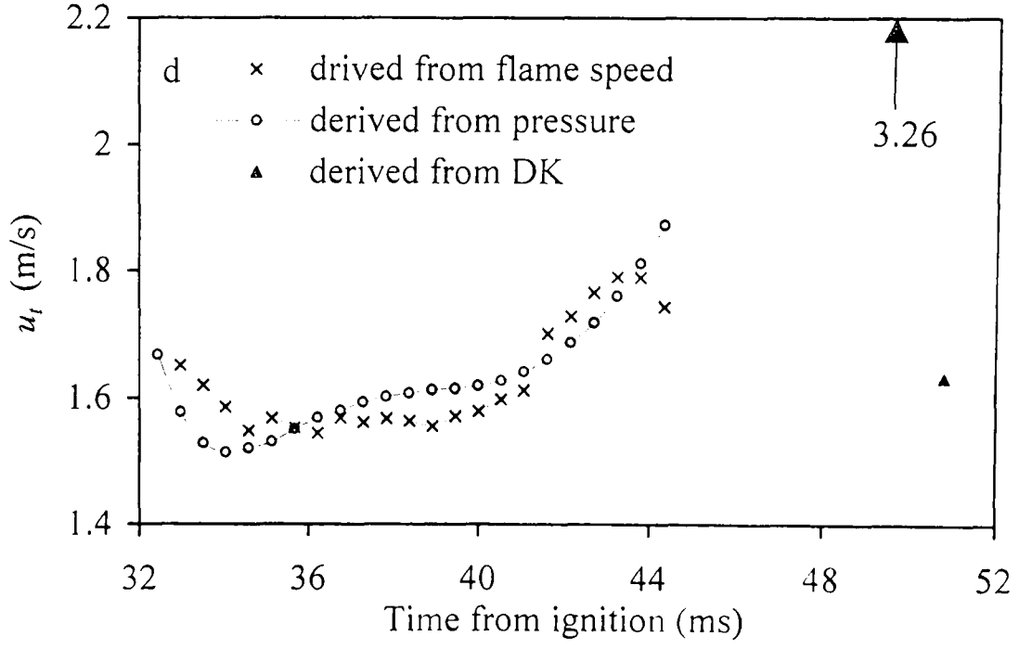

Fig. C.13. Iso-octane - air implosion, $\phi = 1, p_o = 0.75$ MPa, $T_o = 358$ K, $u' = 0.25$

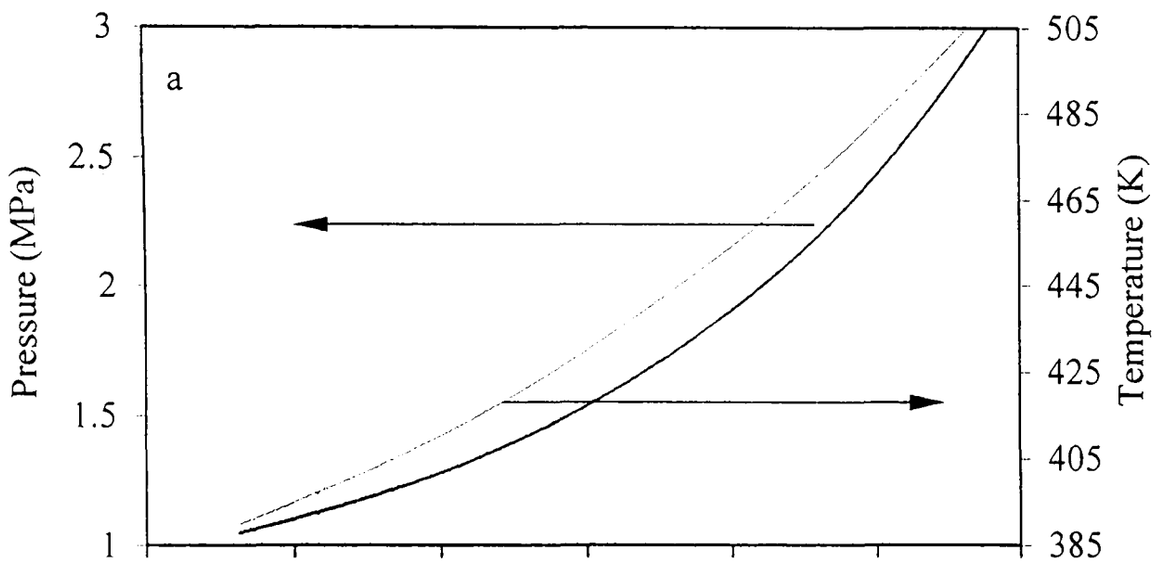

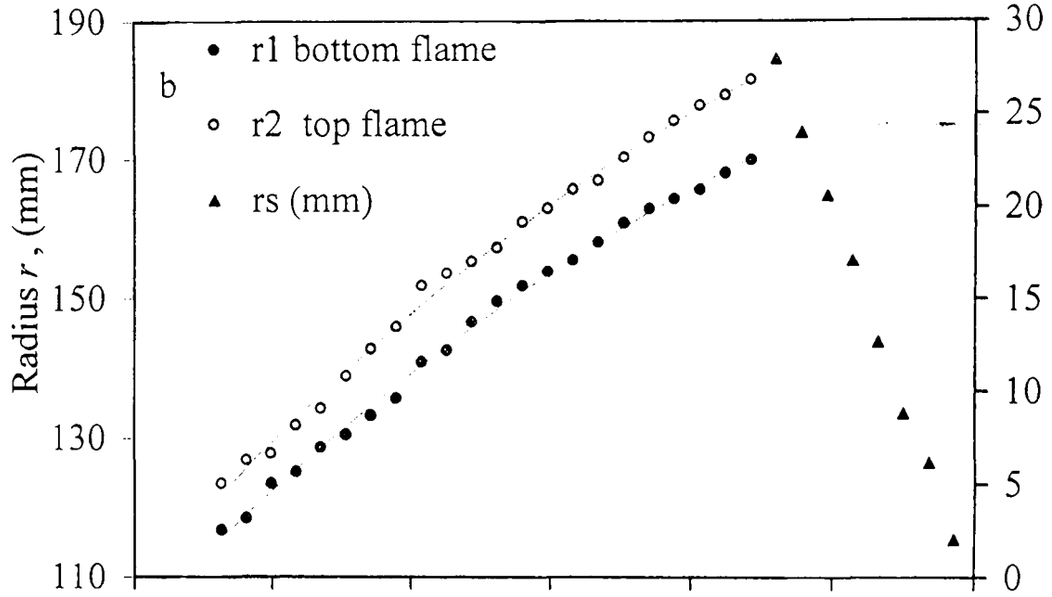

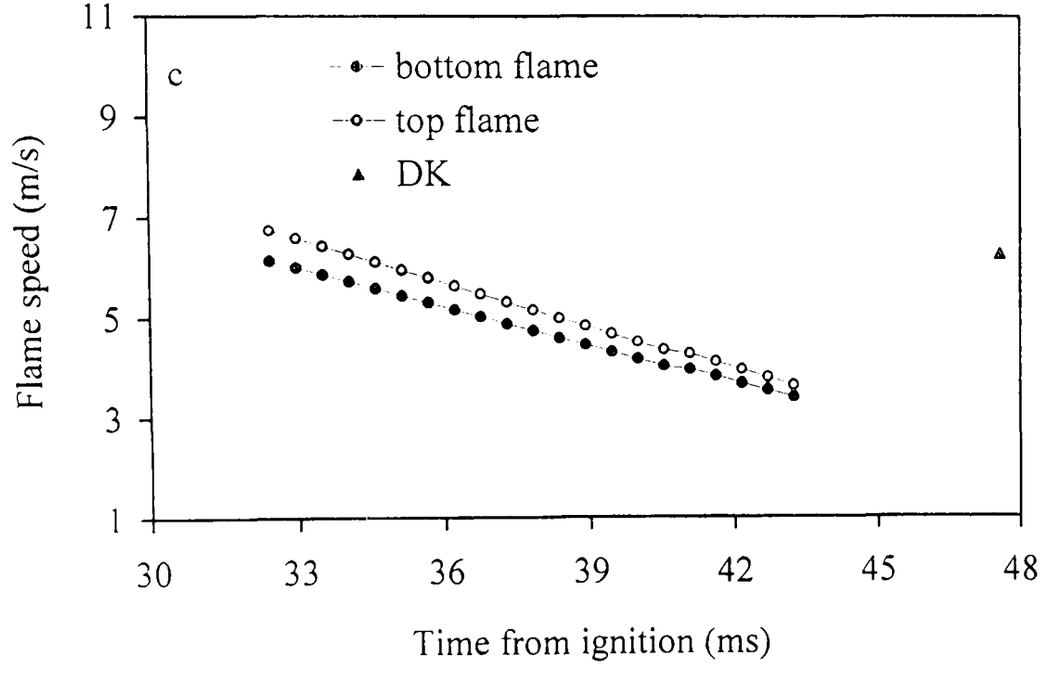

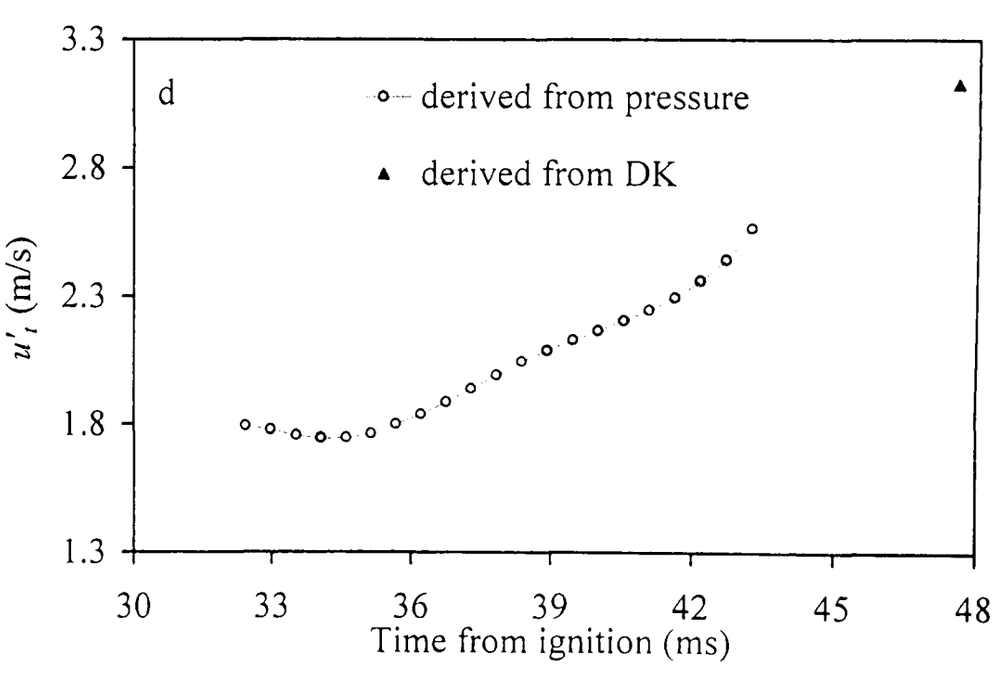

Fig. C.14. Iso-octane - air implosion, $\phi = 1, p_o = 0.75$ MPa, $T_o = 358$ K, $u' = 0.5$

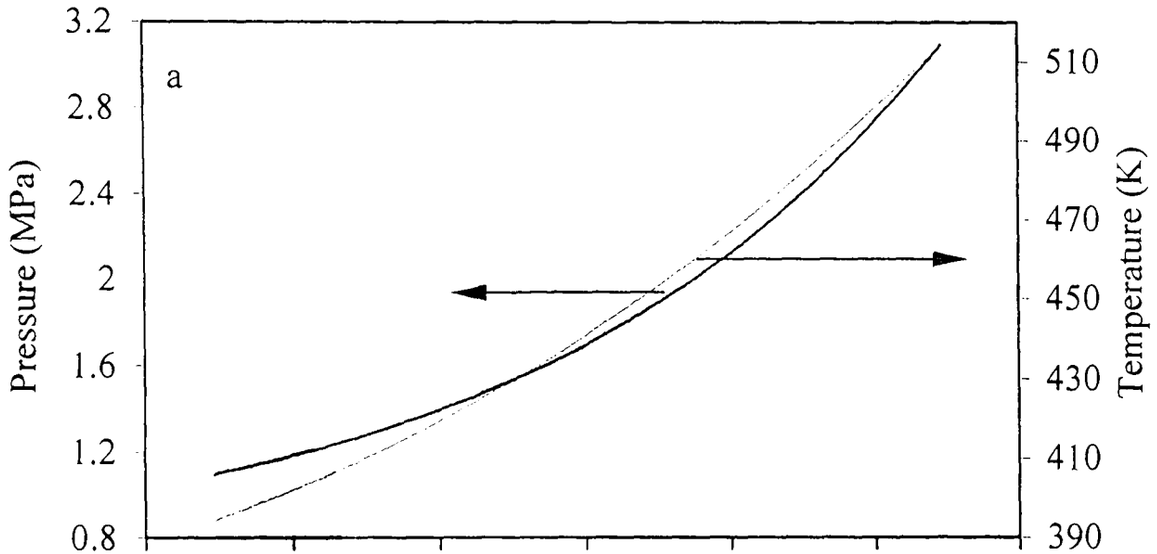

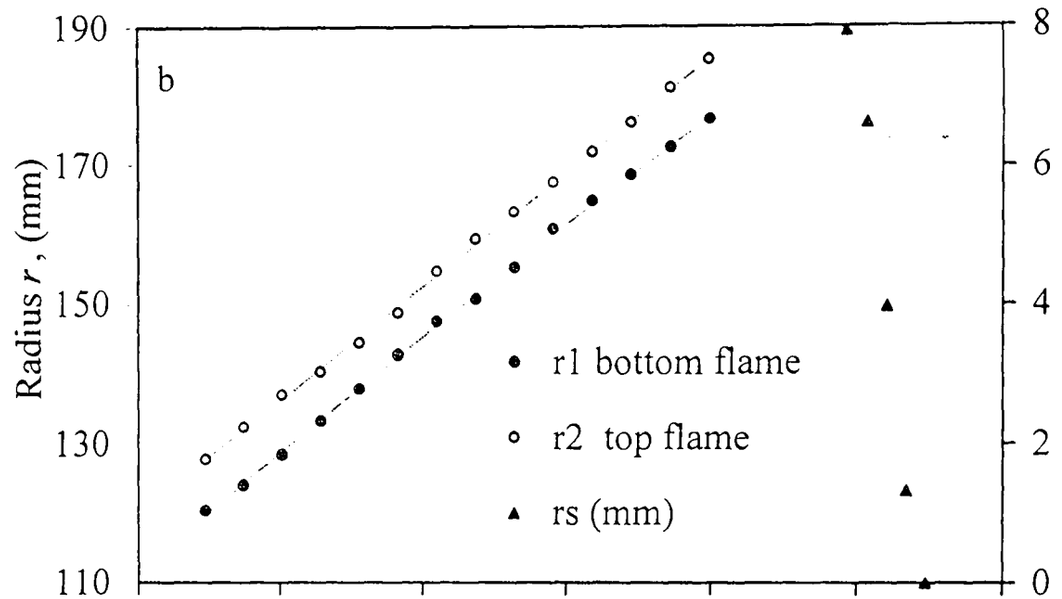

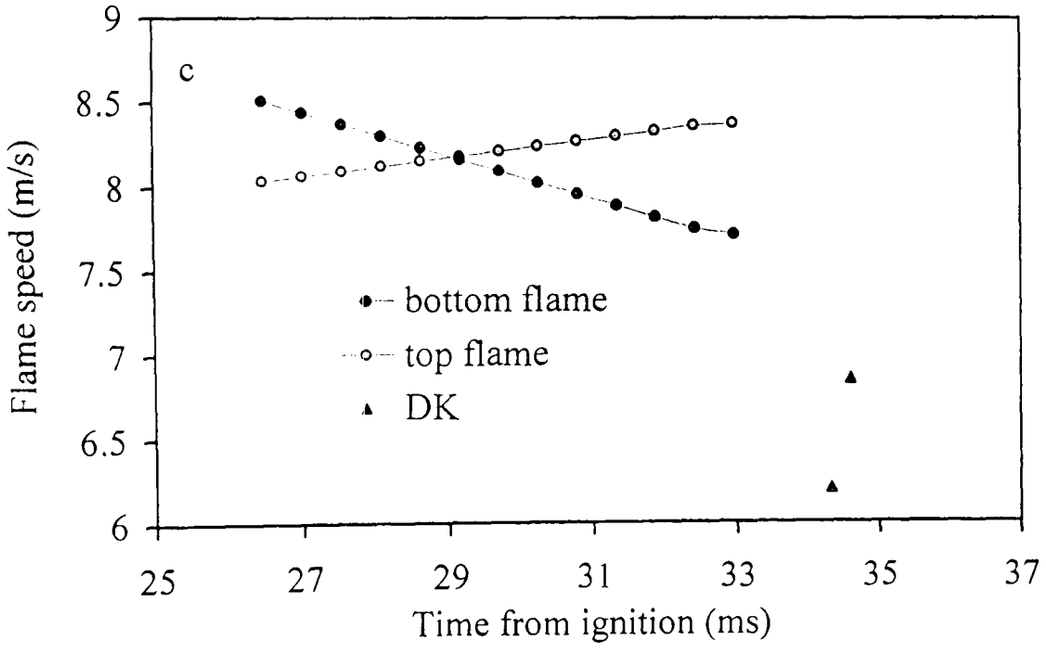

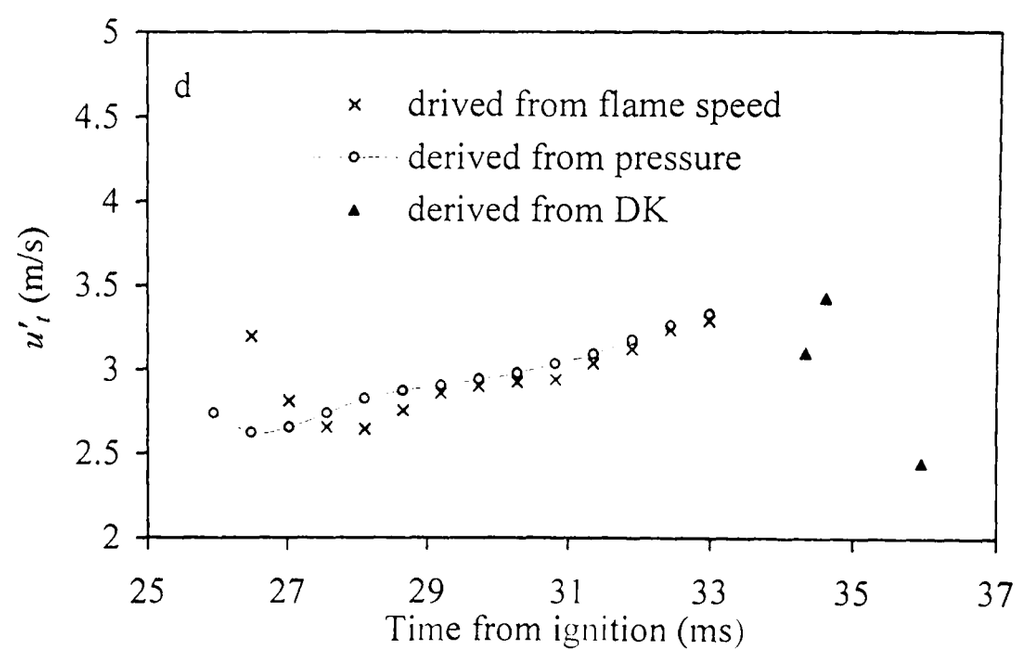

Fig. C.15. Iso-octane - air implosion, $\phi = 1, p_o = 0.75$ MPa, $T_o = 358$ K, $u' = 0.75$

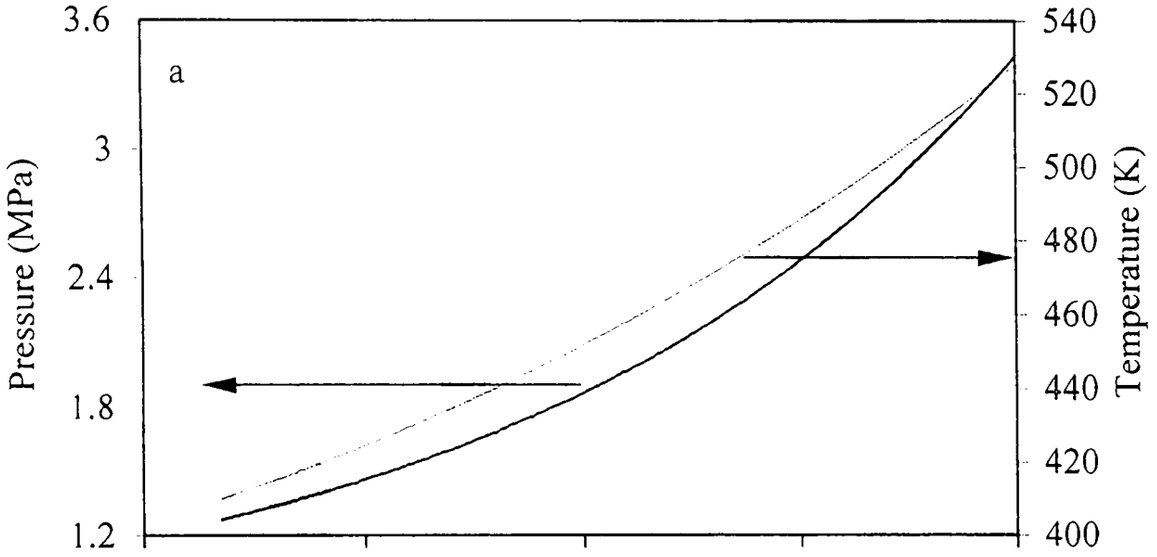

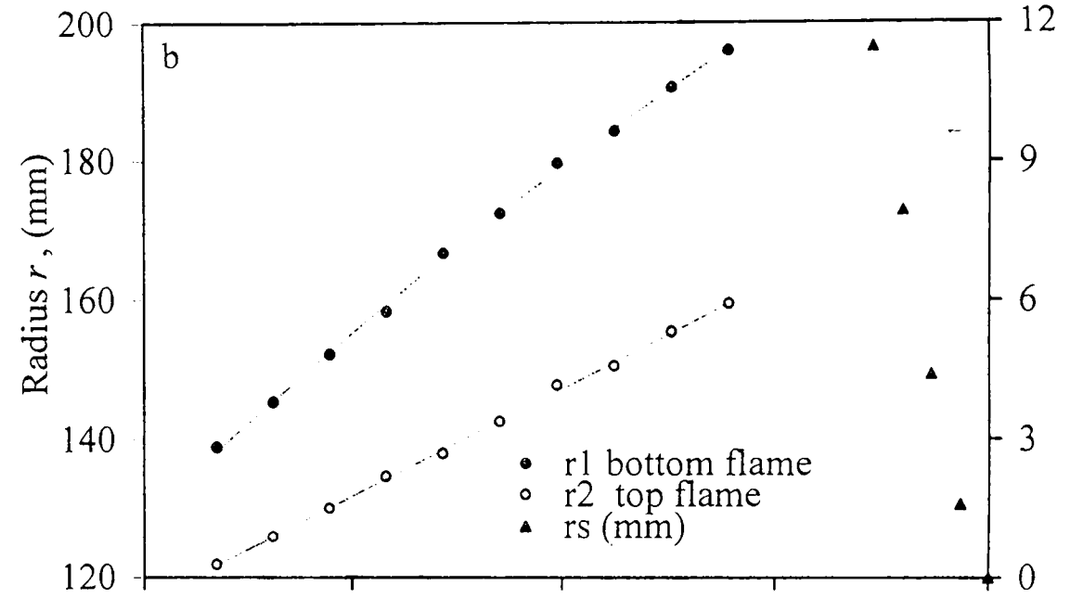

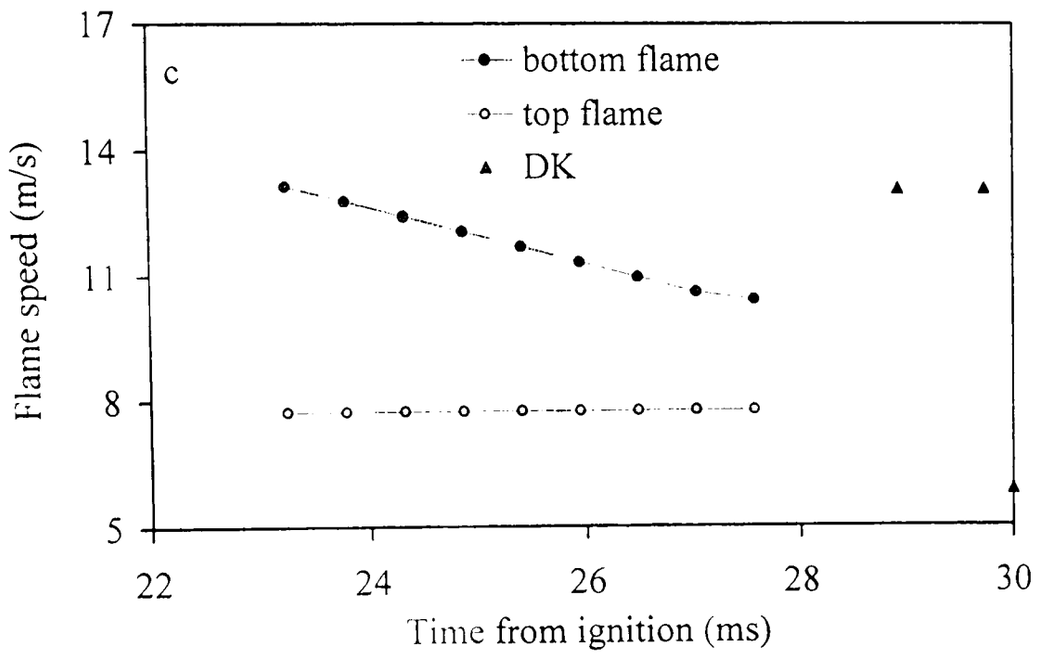

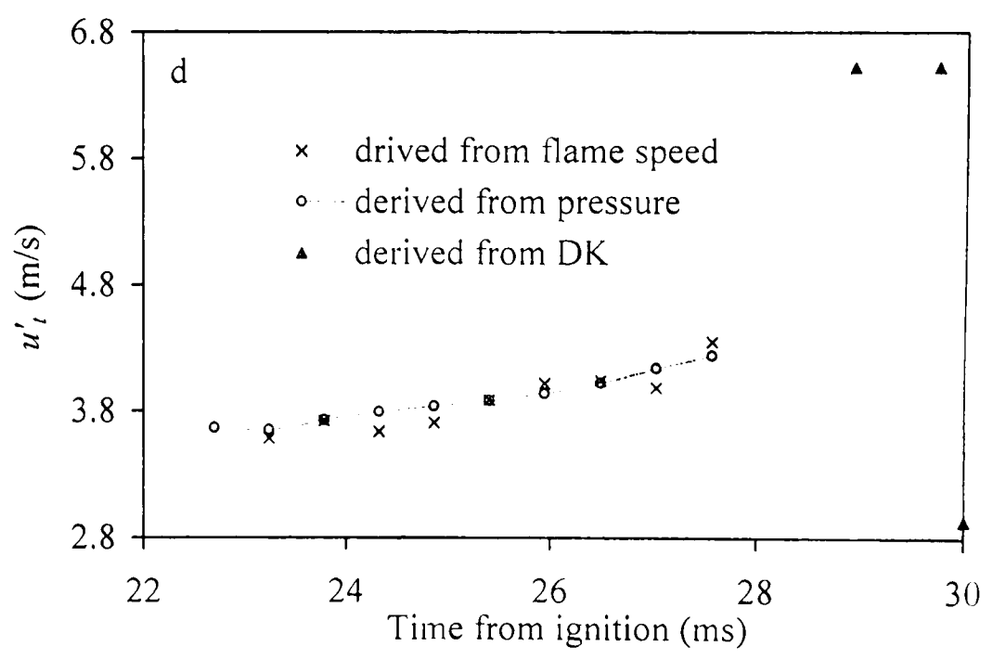

Fig. C.16. Iso-octane - air implosion, $\phi = 1, p_o = 0.75$ MPa, $T_o = 358$ K, $u' = 1$

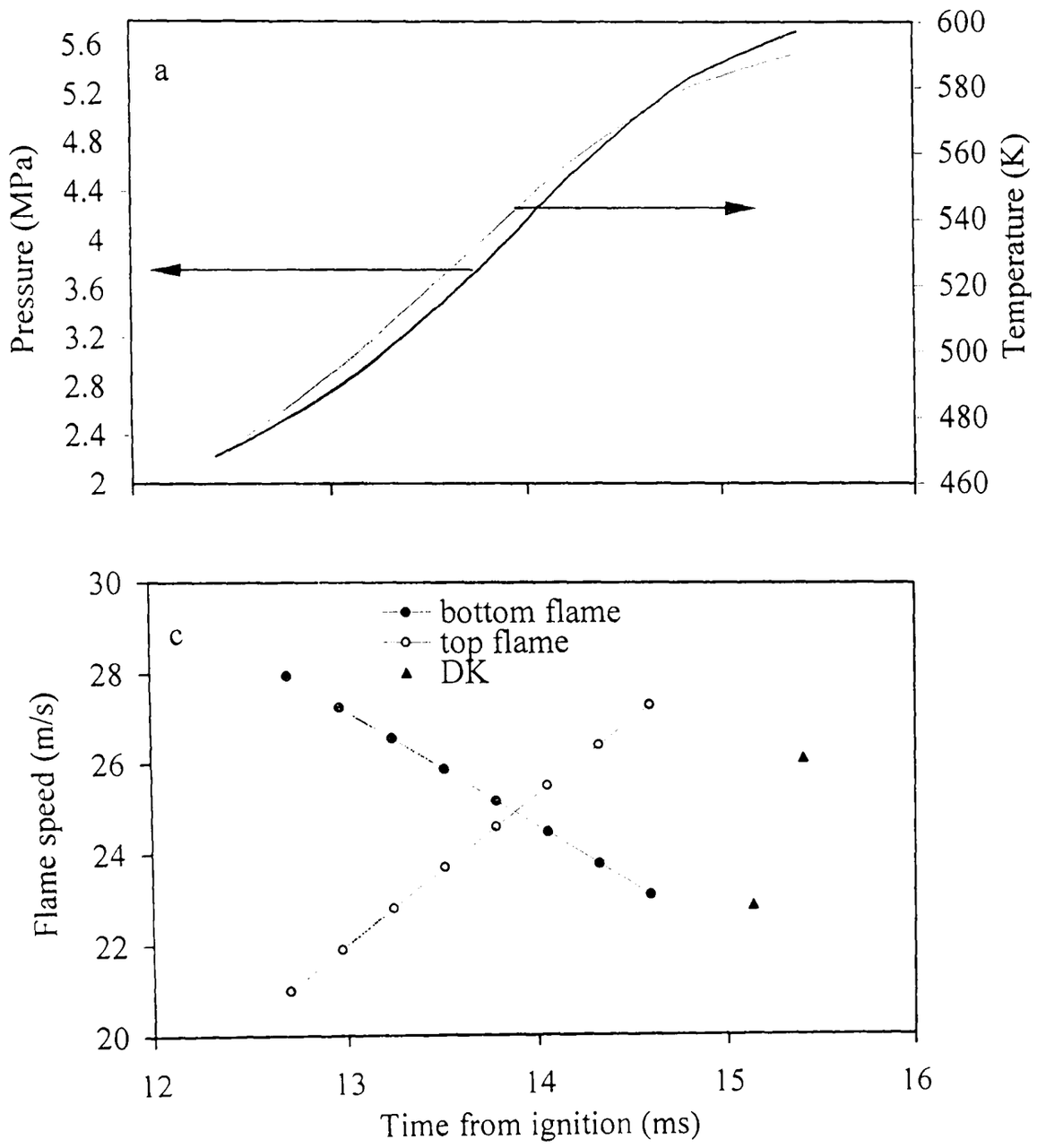

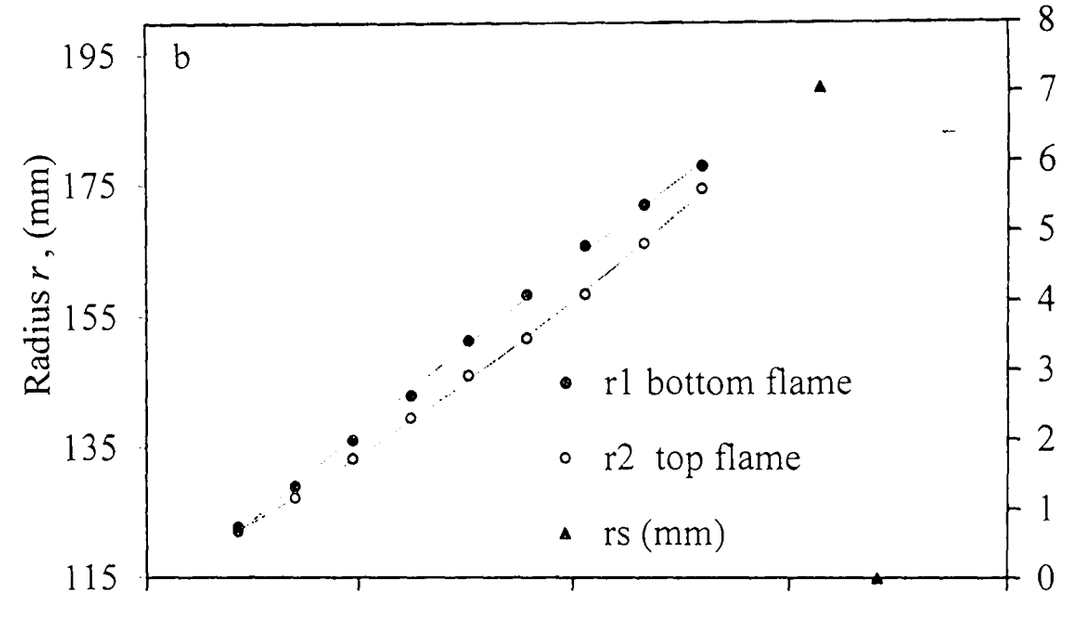

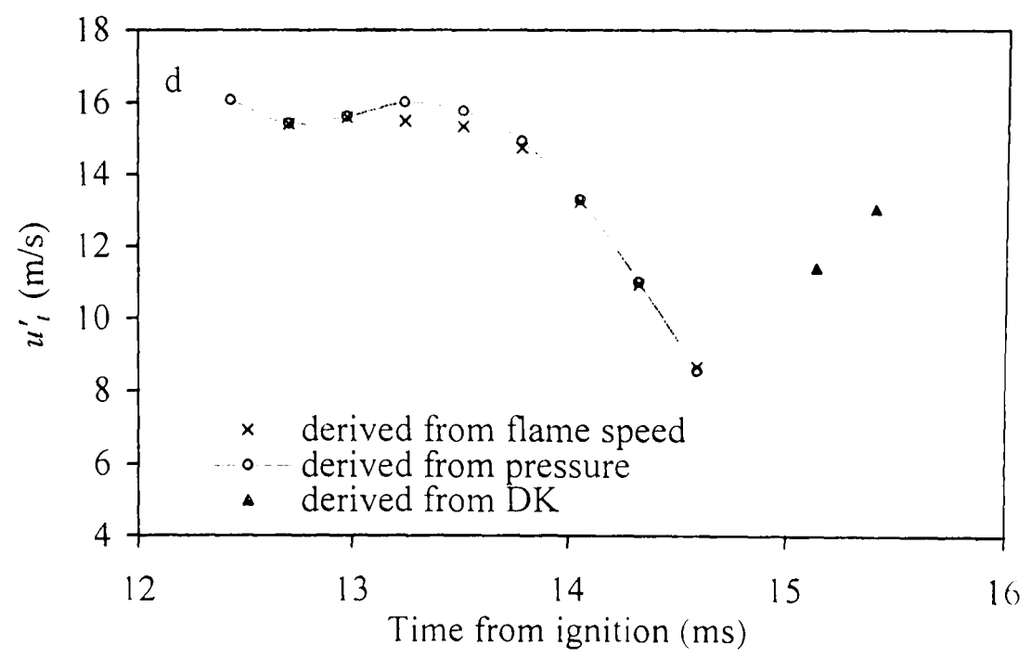

Fig. C.17. Iso-octane - air implosion, $\phi = 1, p_o = 0.75$ MPa, $T_o = 358$ K, $u' = 3$

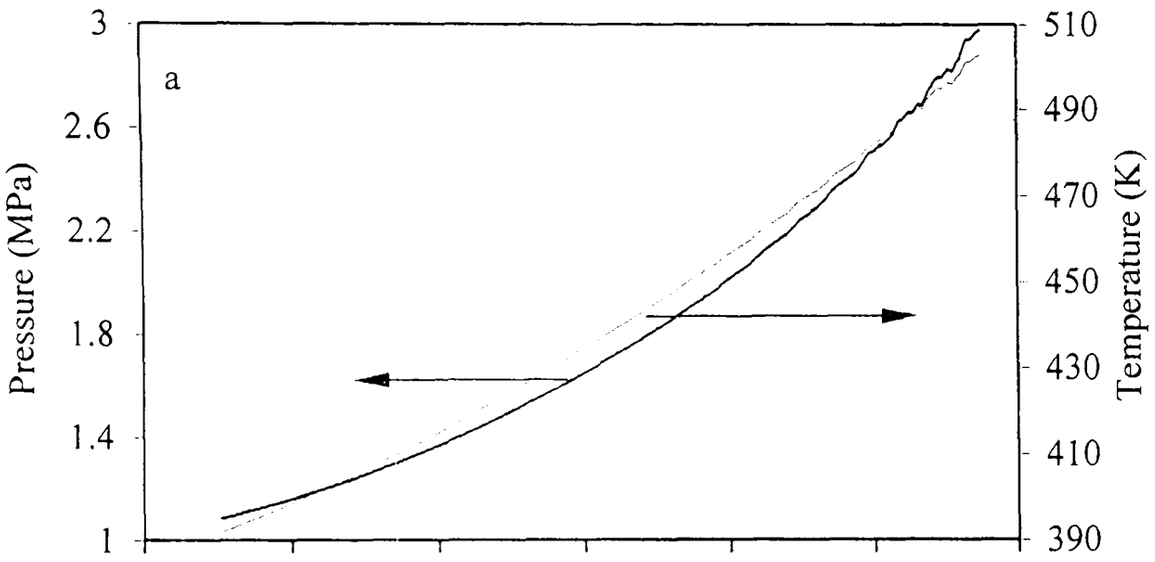

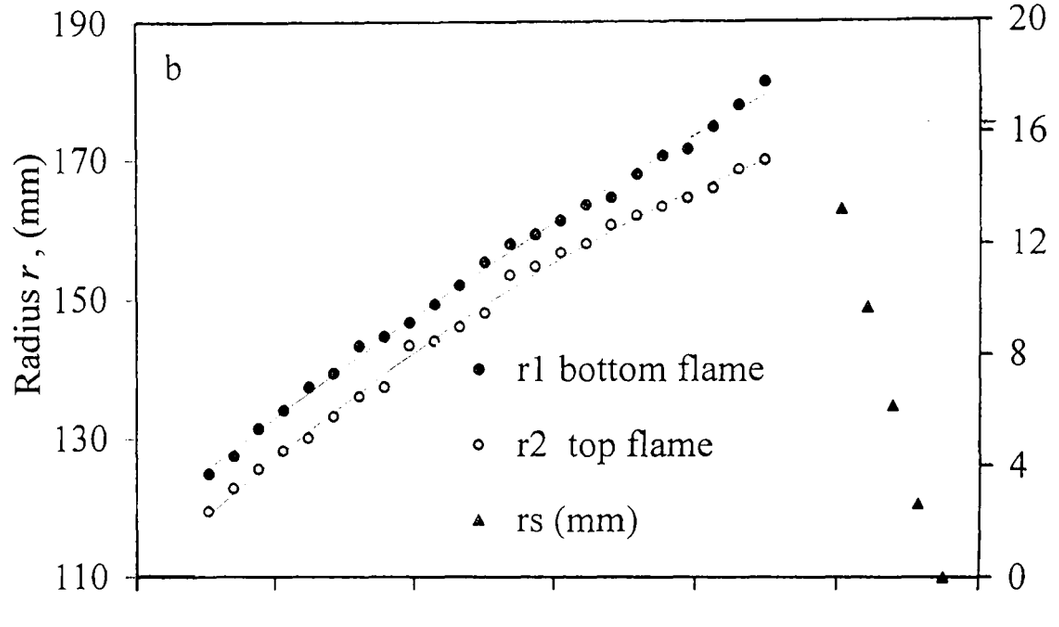

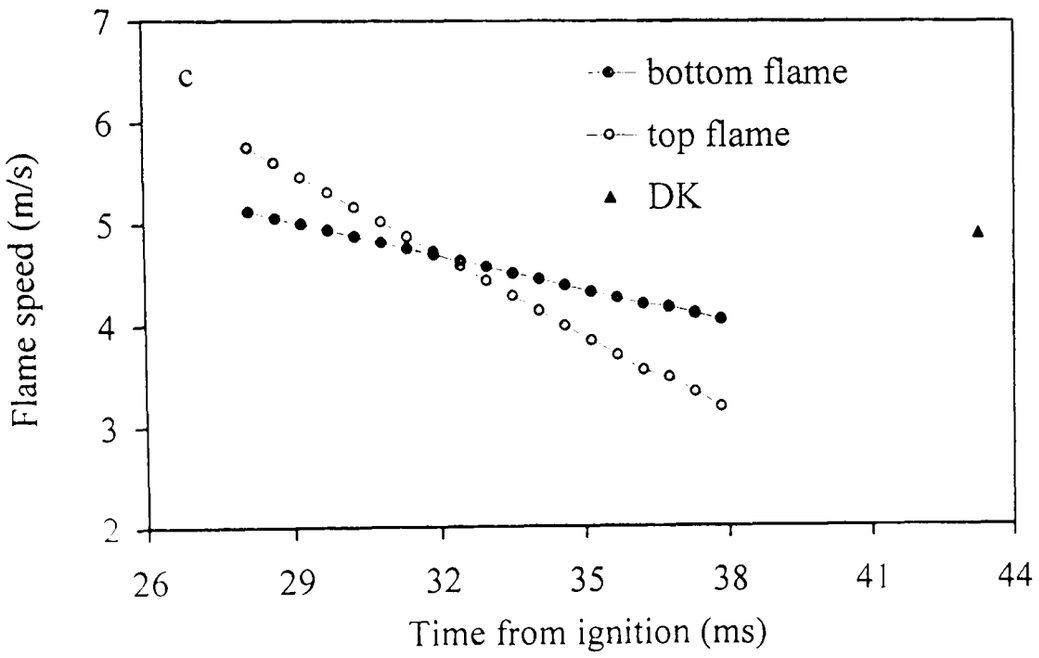

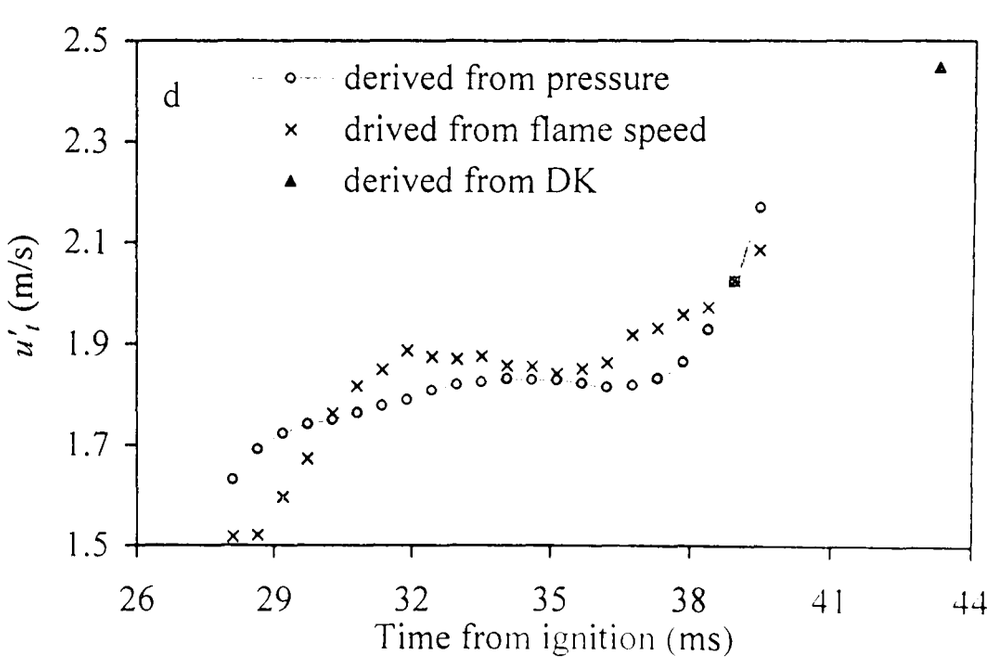

Fig. C.18. Iso-octane - air implosion, ϕ = 1.4, p_o = 0.75 MPa, T_o = 358 K, u' = 0.25

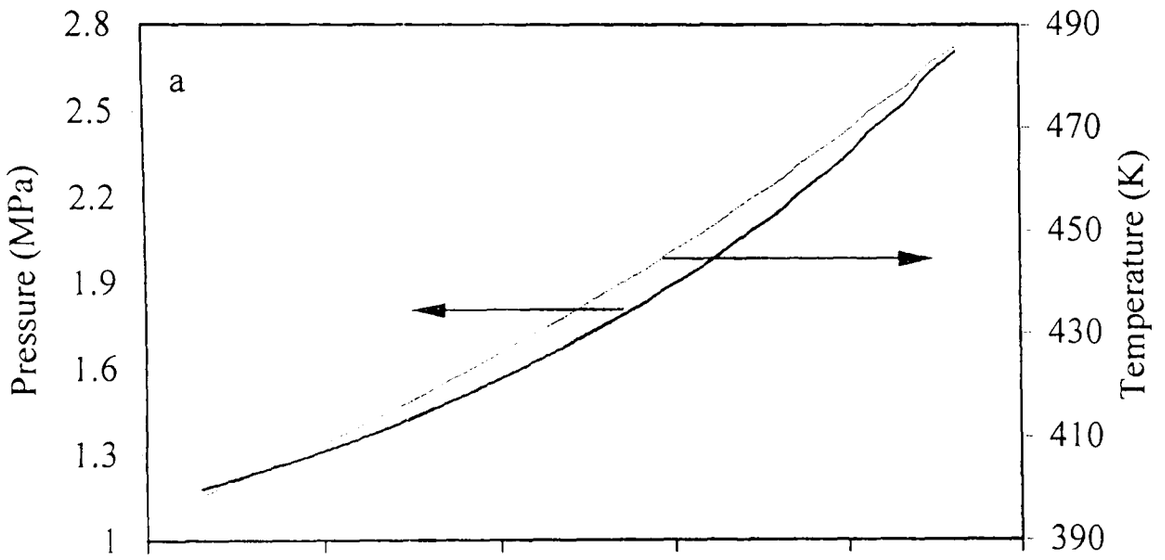

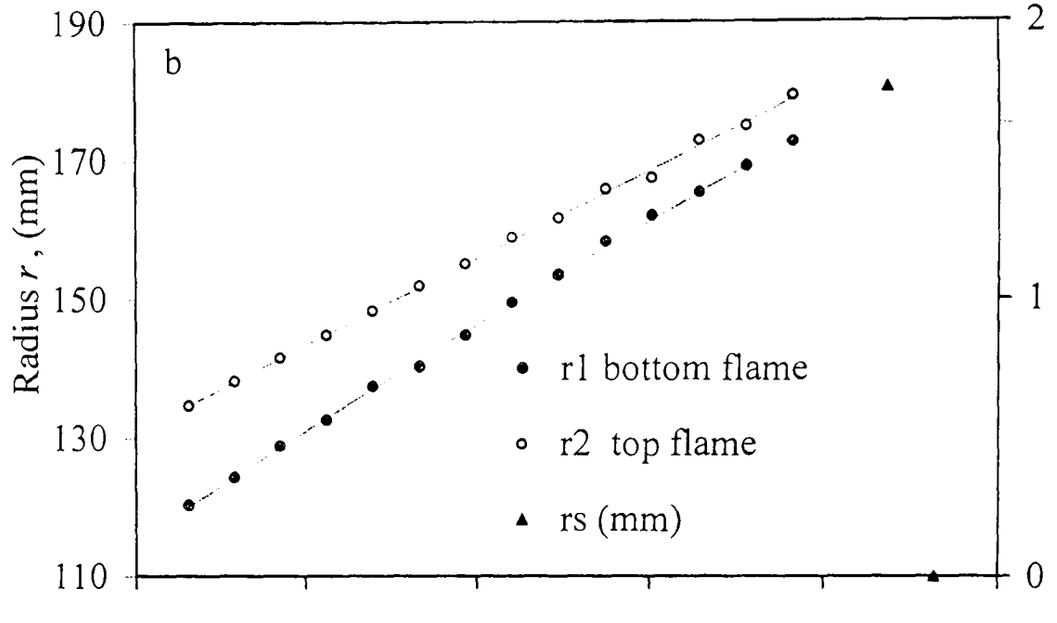

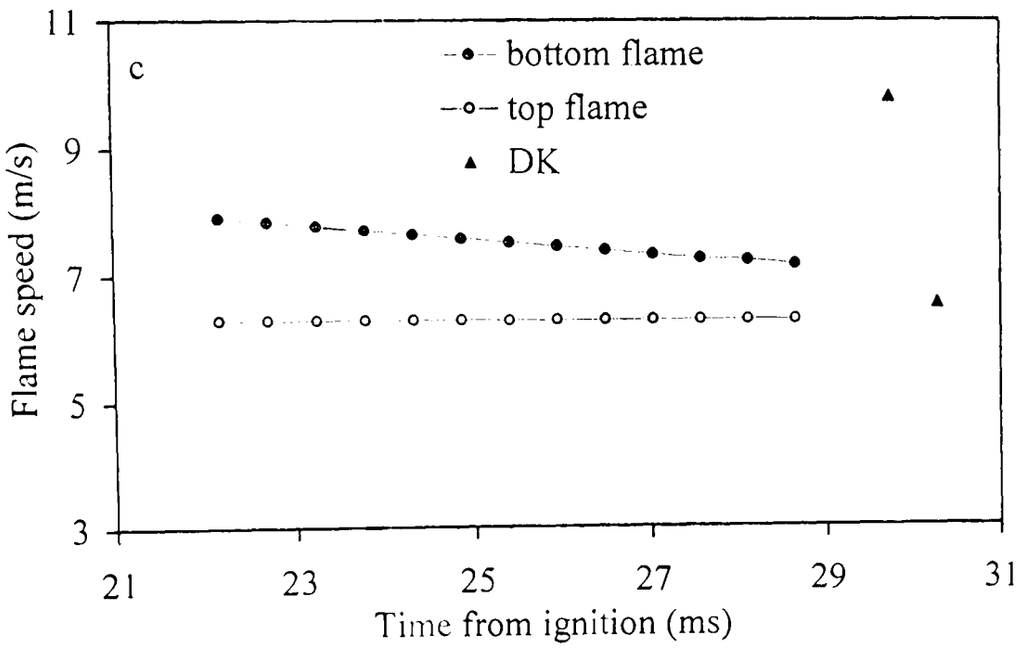

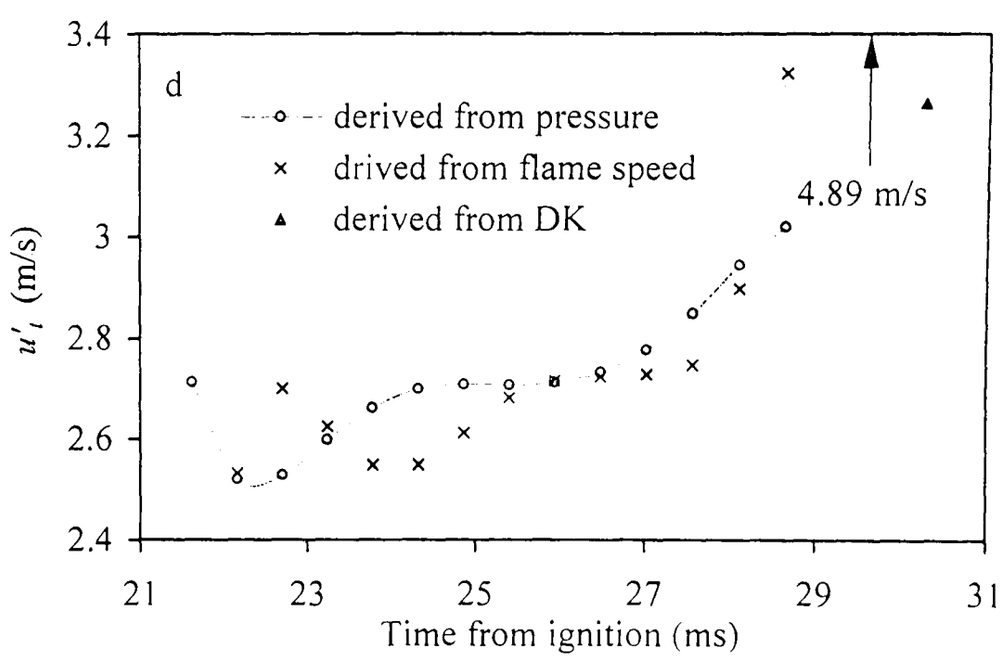

Fig. C.19. Iso-octane - air implosion, ϕ = 1.4, p_o = 0.75 MPa, T_o = 358 K, u' = 0.5

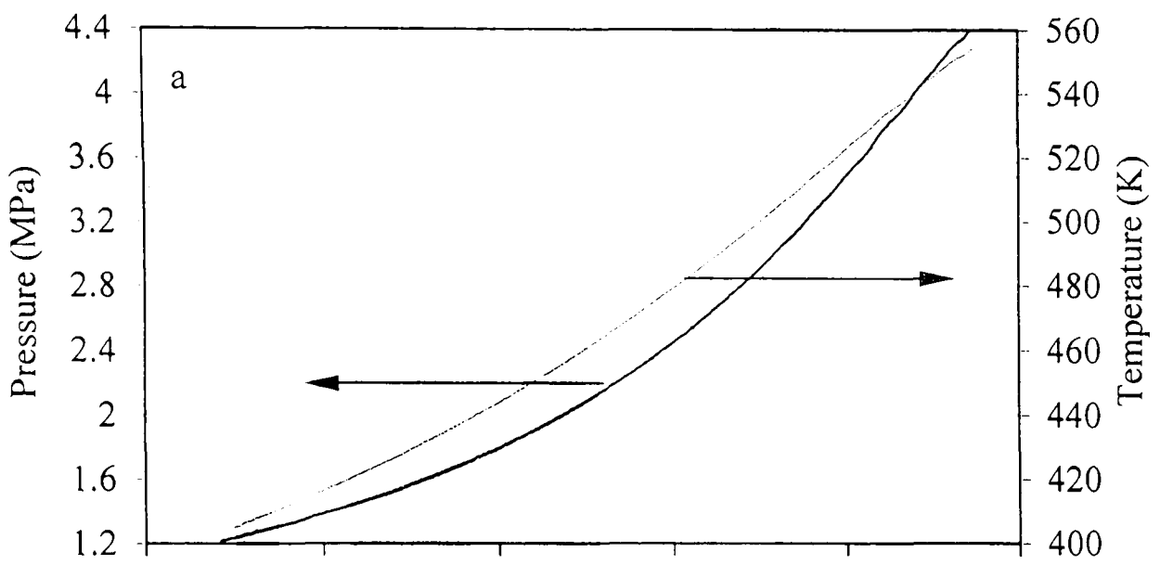

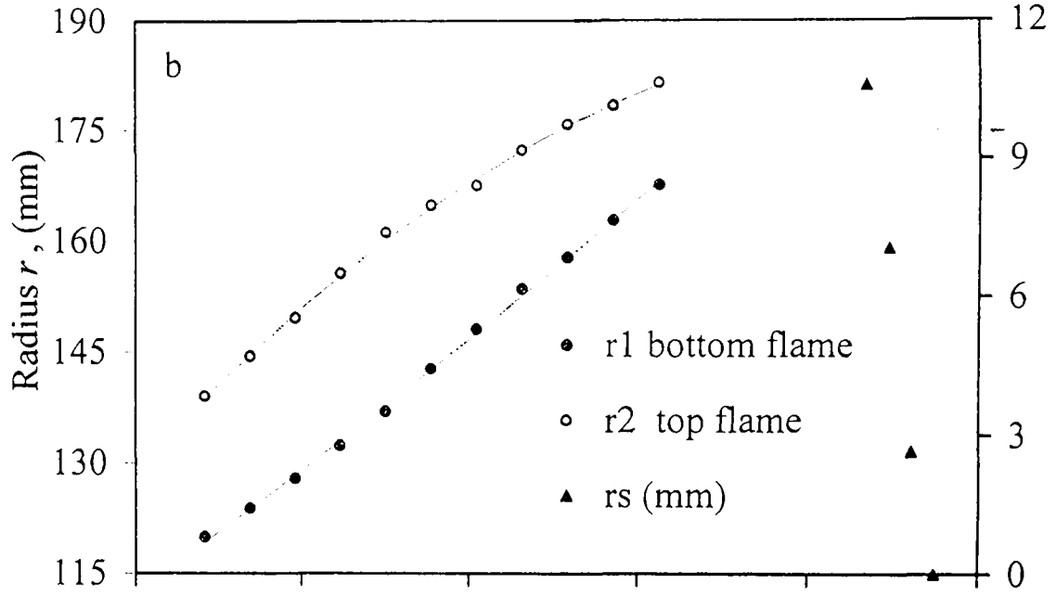

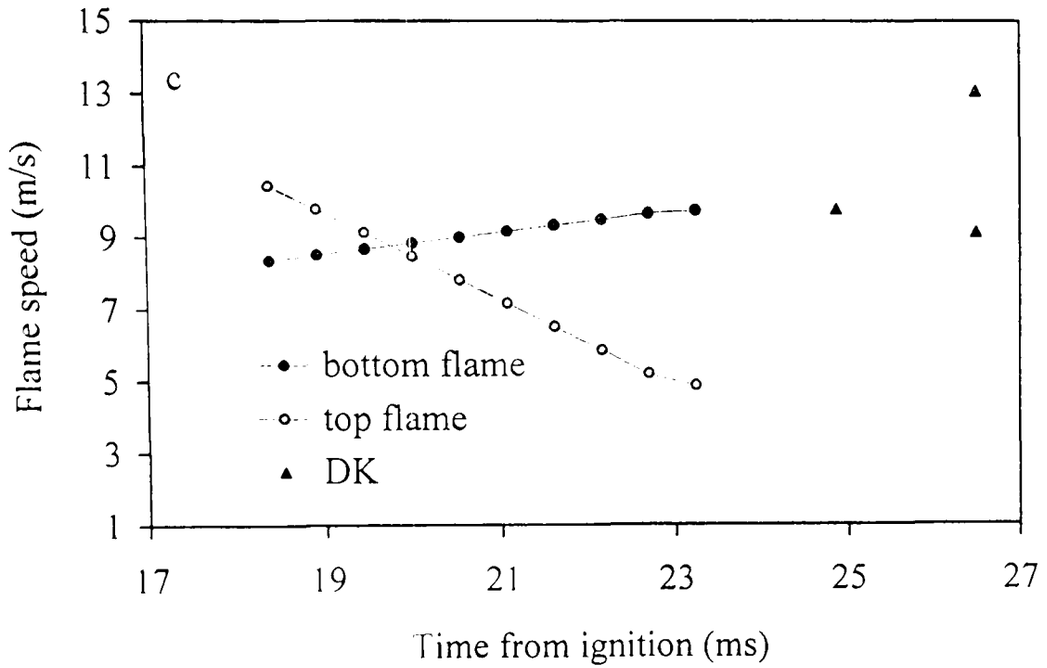

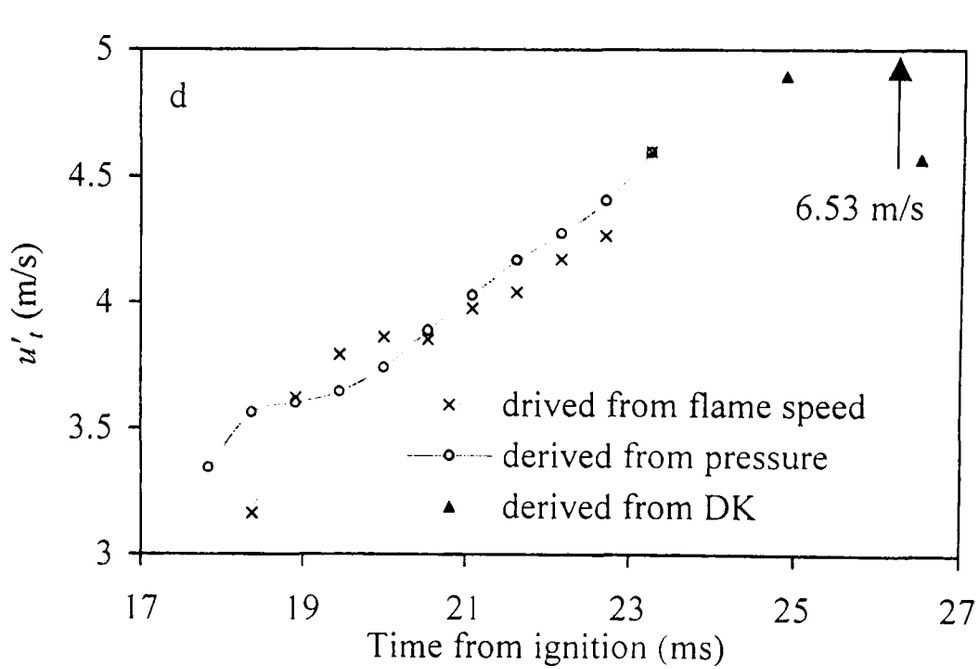

Fig. C.20. Iso-octane - air implosion, ϕ = 1.4, p_o = 0.75 MPa, T_o = 358 K, u' = 0.75

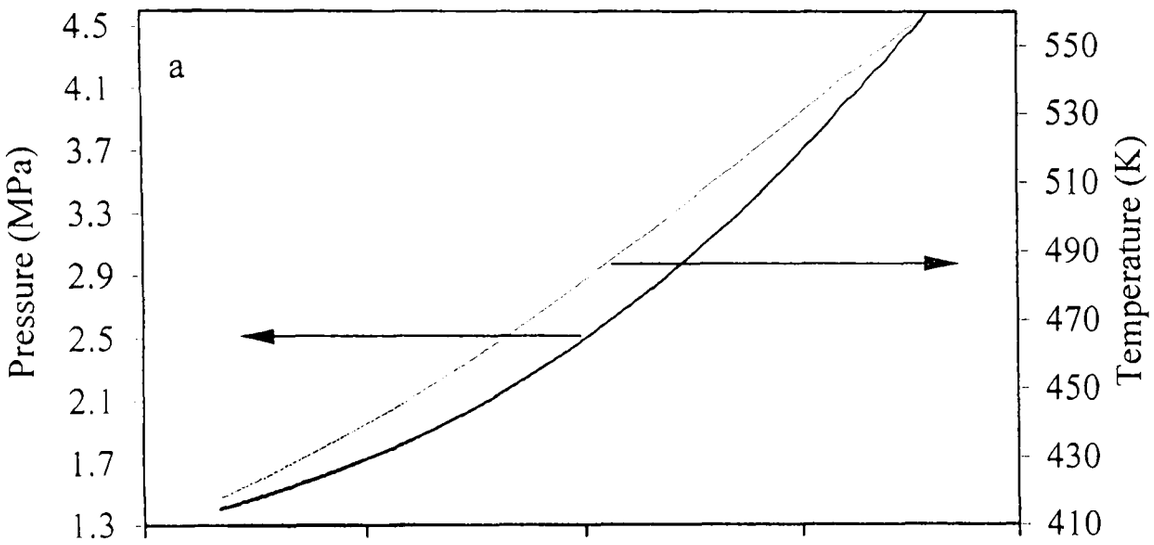

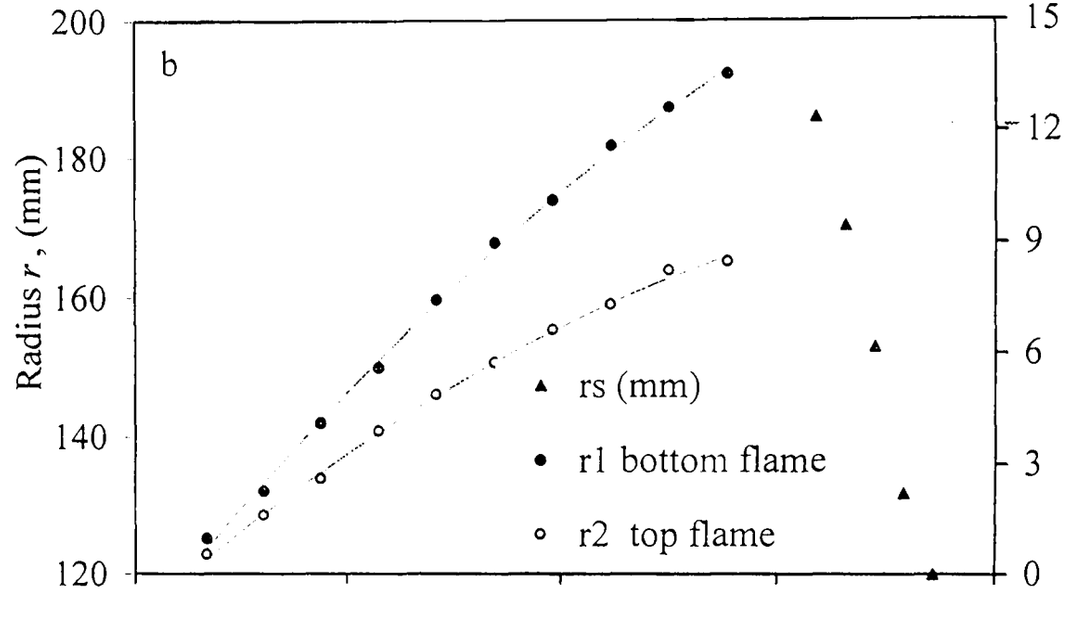

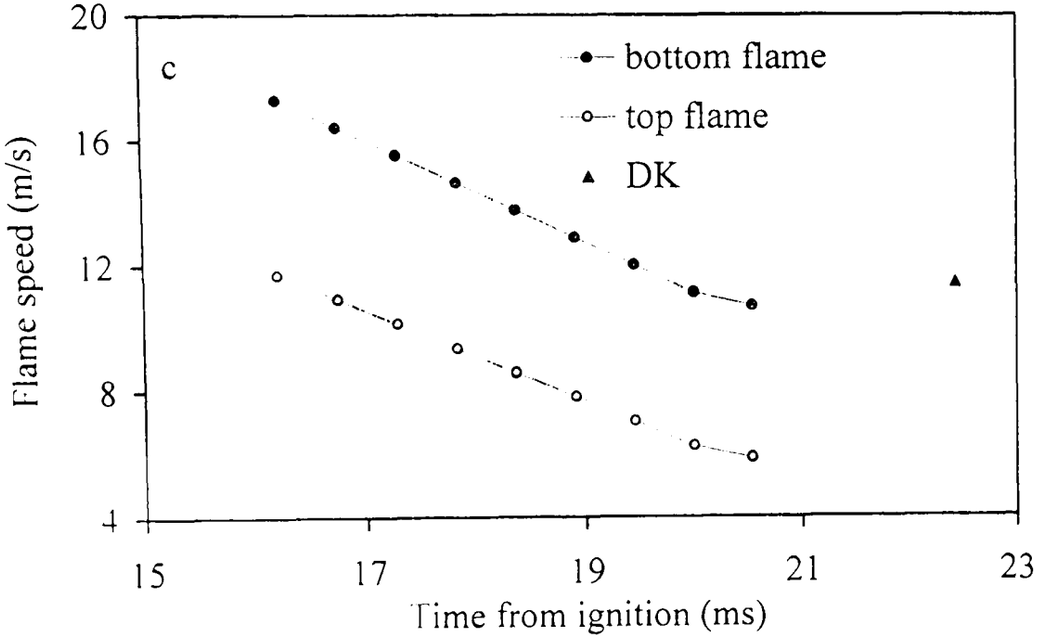

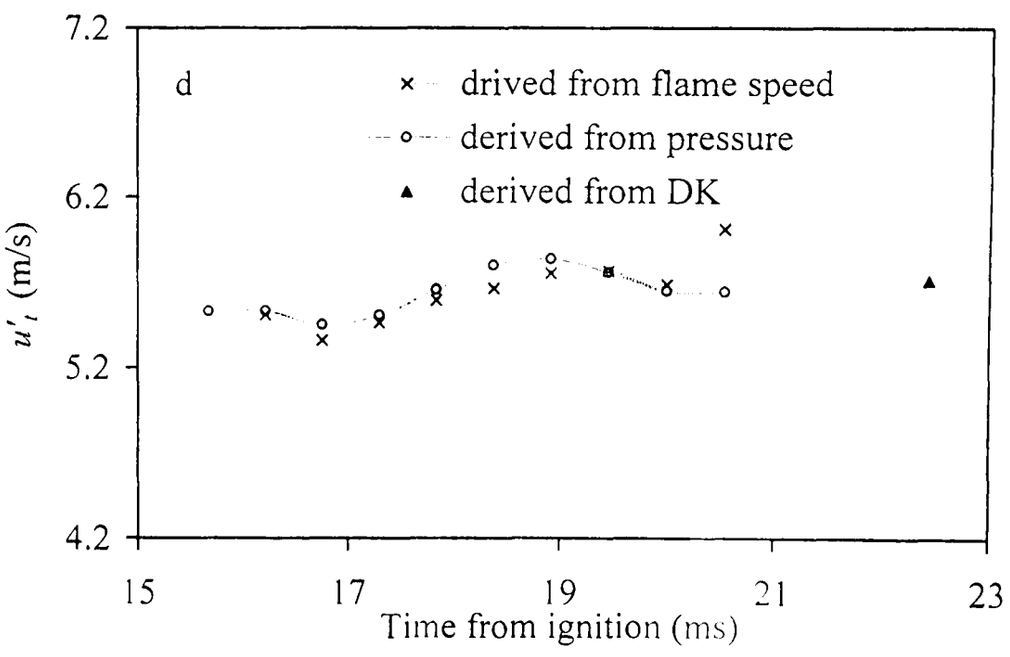

Fig. C.21. Iso-octane - air implosion, $\phi = 1.4$, $p_o = 0.75$ MPa, $T_o = 358$ K, $u' = 1$

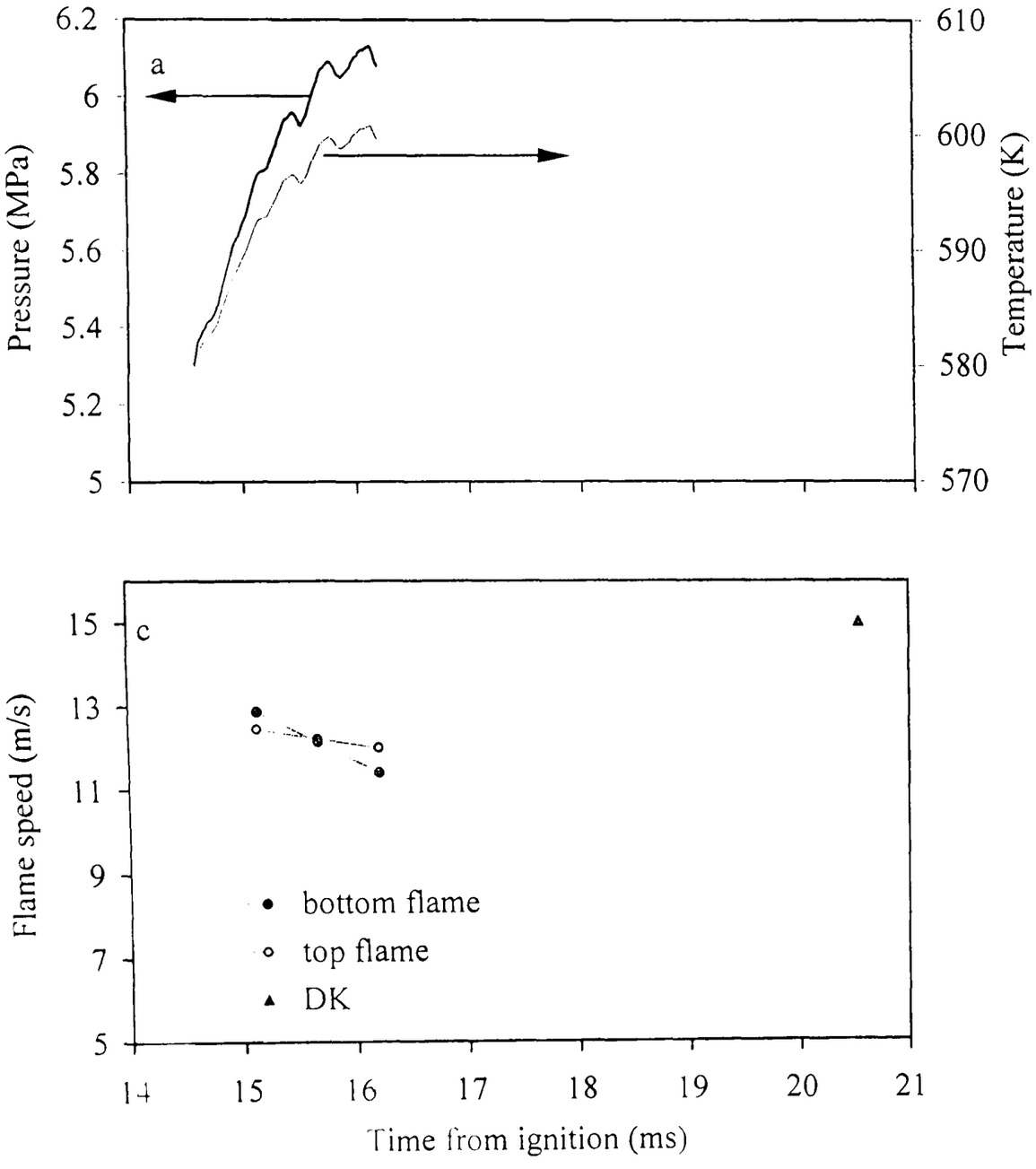

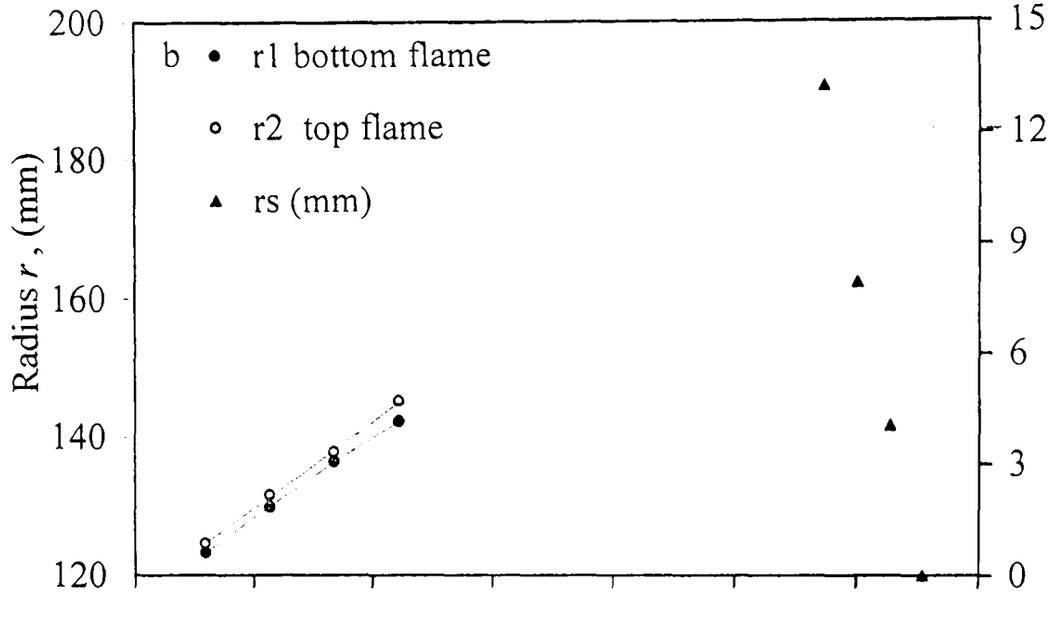

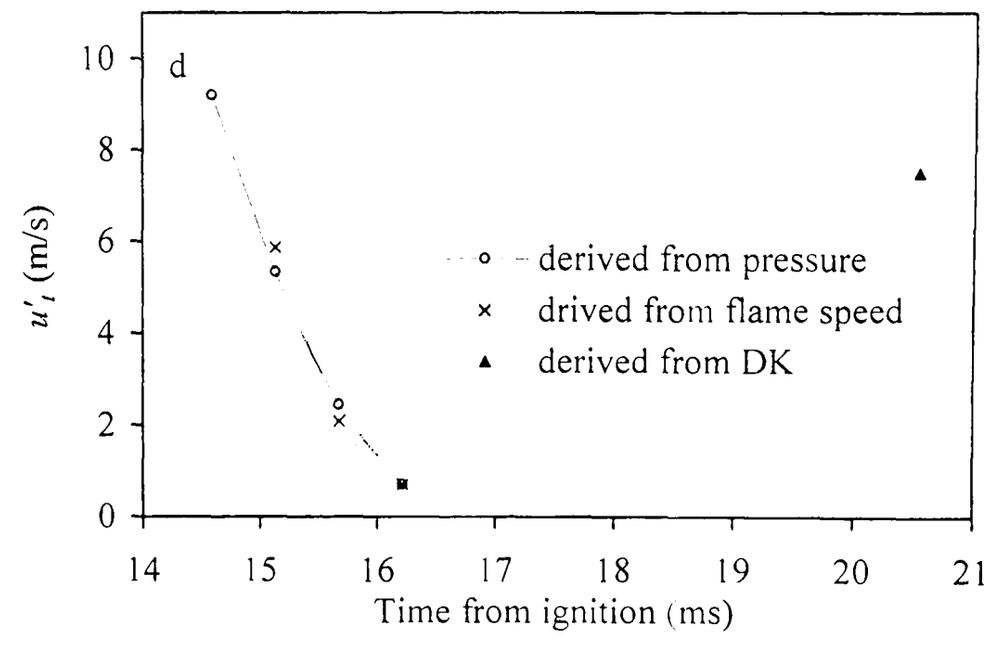

Fig. C.22. Iso-octane - air implosion, ϕ = 1.4, p_o = 0.75 MPa, T_o = 358 K, u' = 2

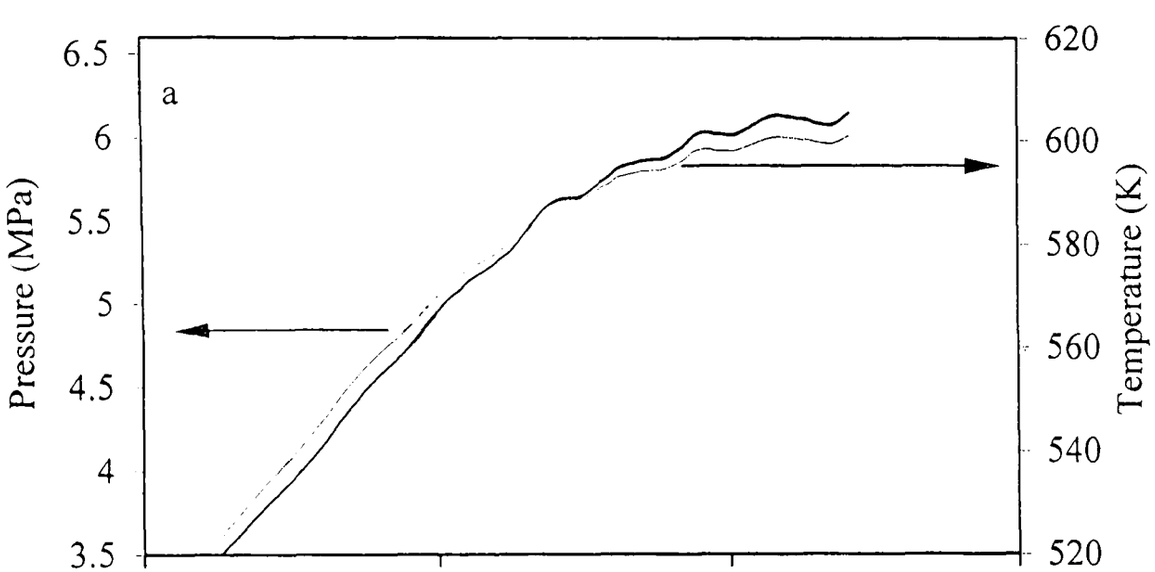

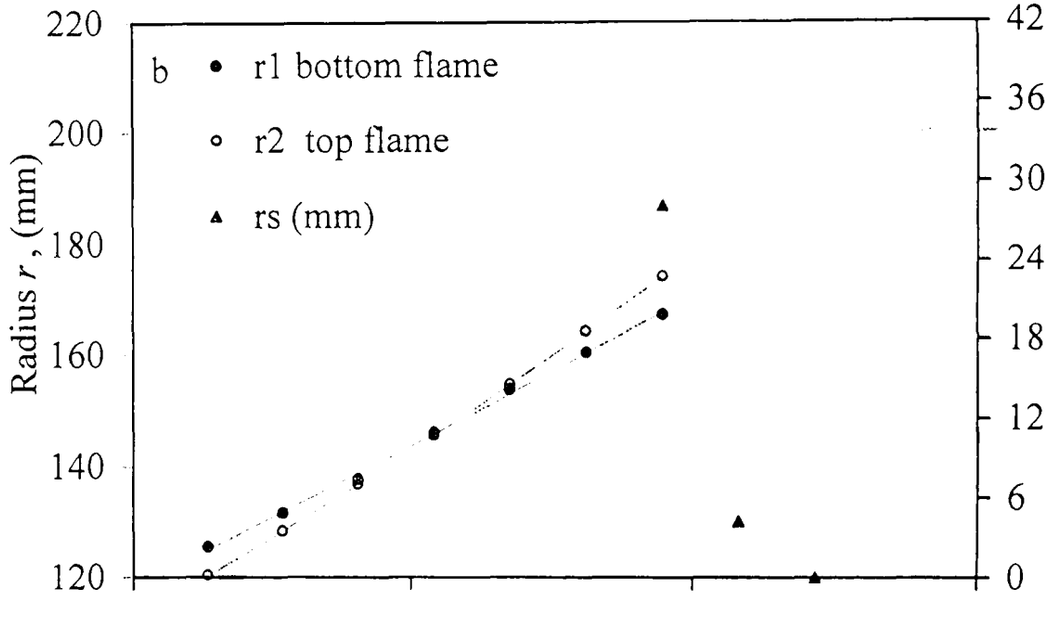

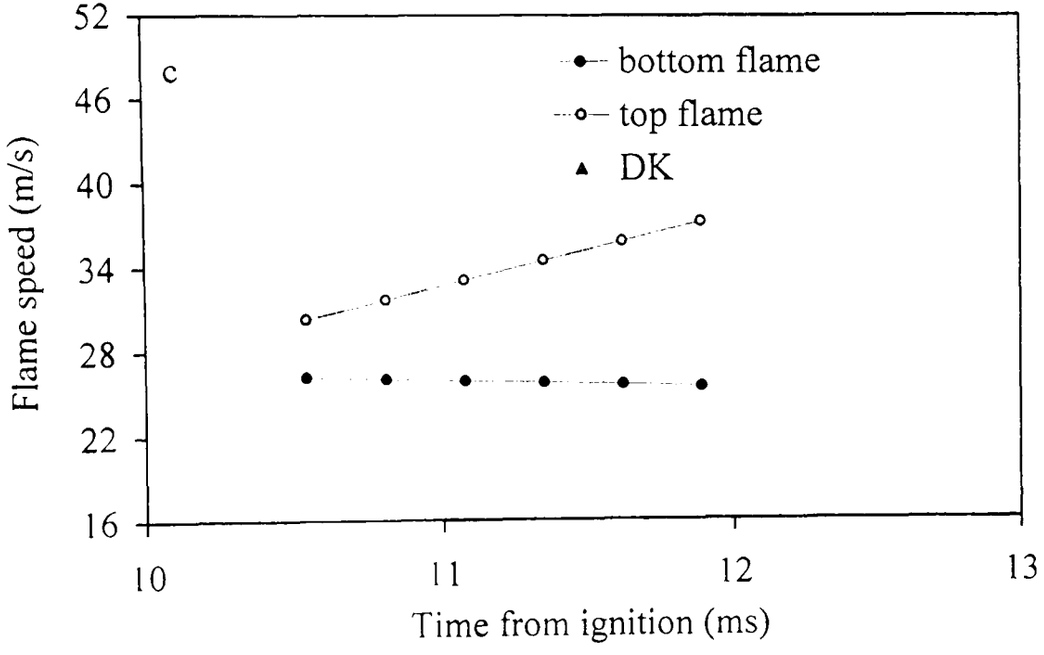

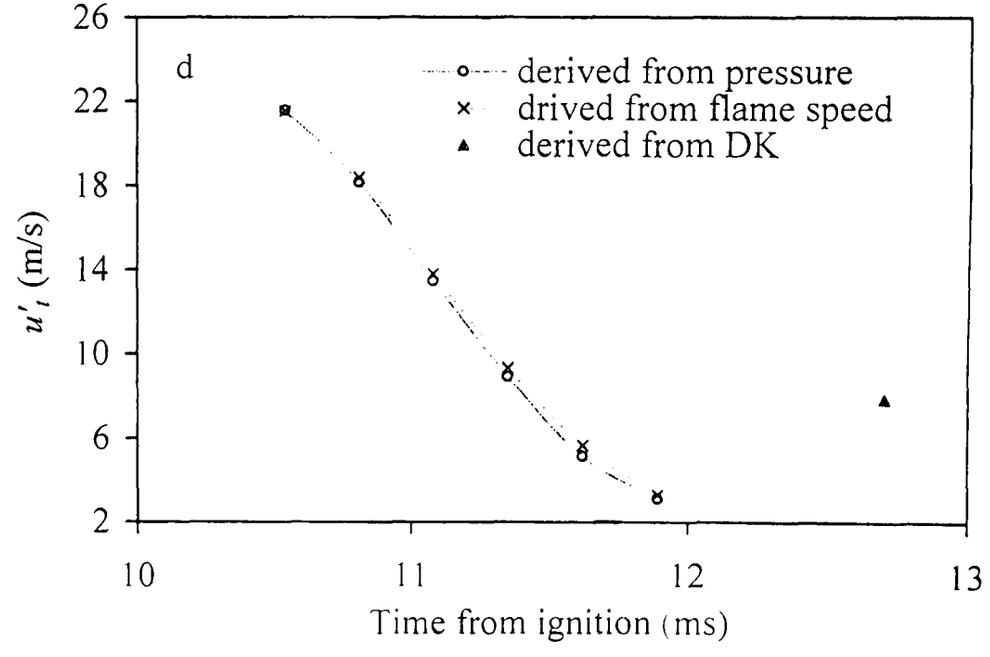

Fig. C.23. Iso-octane - air implosion, ϕ = 1.4, p_o = 0.75 MPa, T_o = 358 K, u' = 3

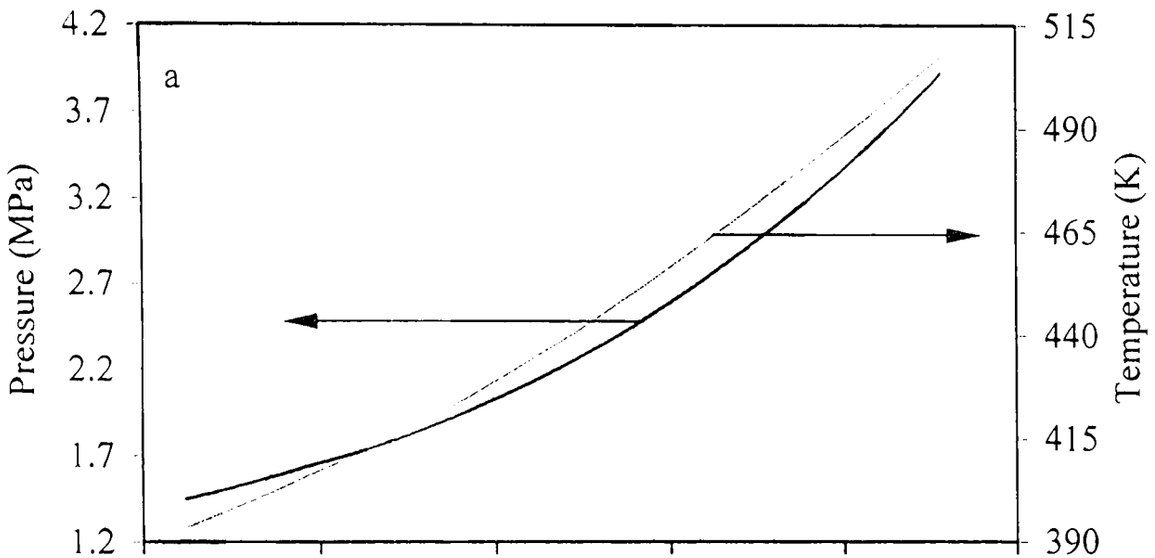

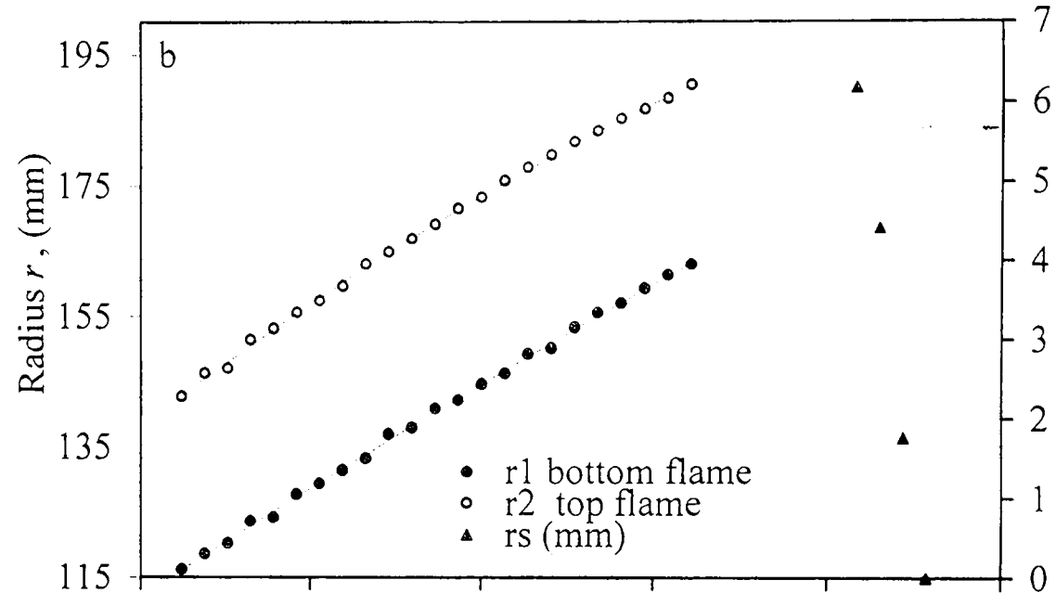

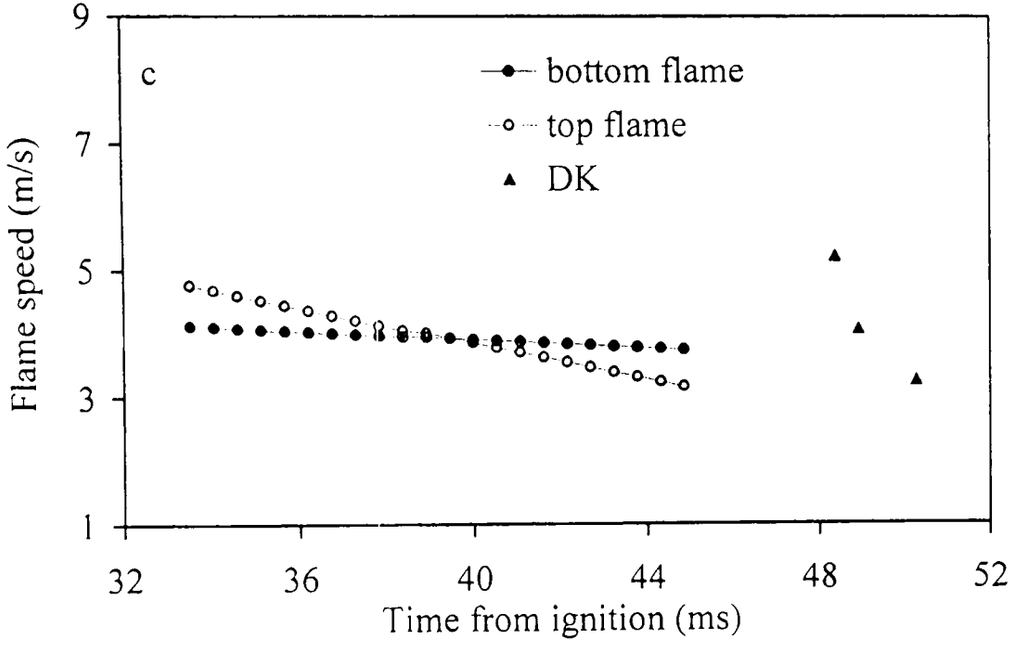

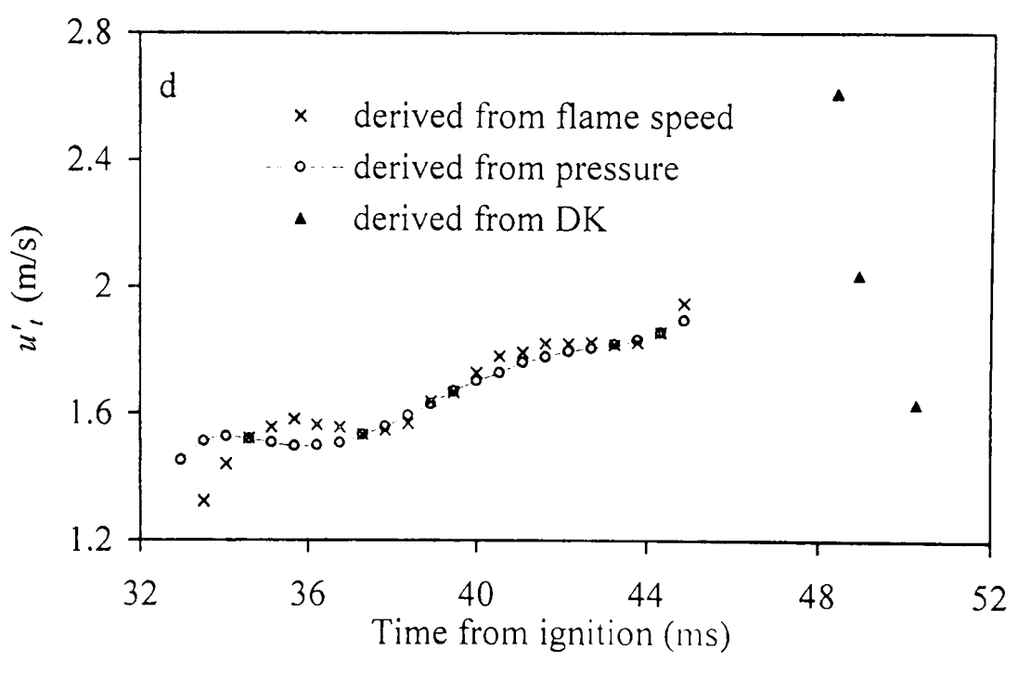

Fig. C.24. Iso-octane - air implosion, $\phi = 1, p_o = 1$ MPa, $T_o = 358$ K, $u' = 0.25$

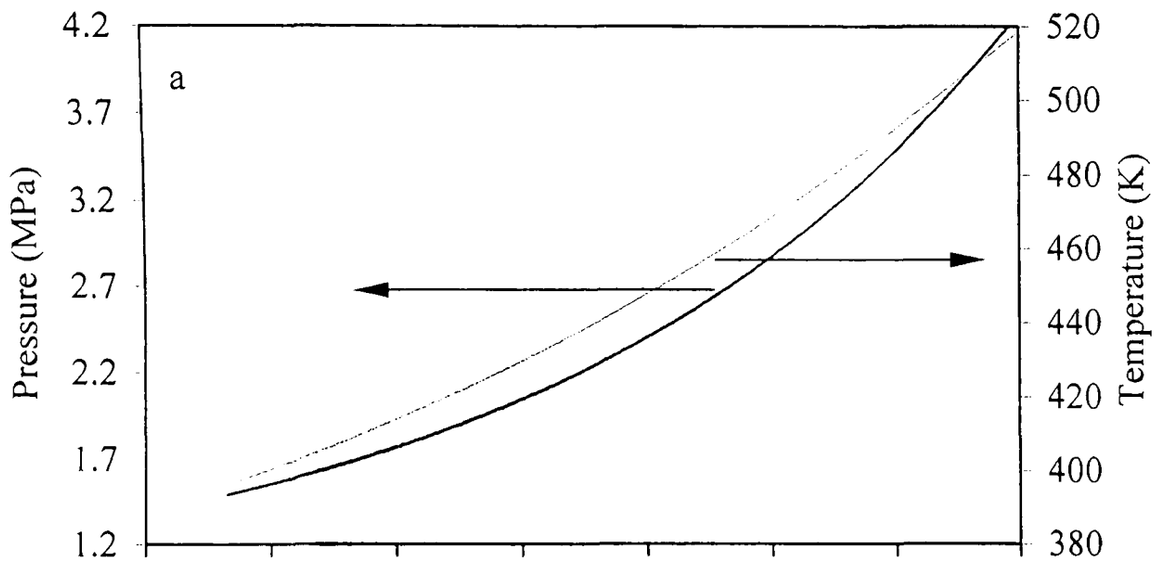

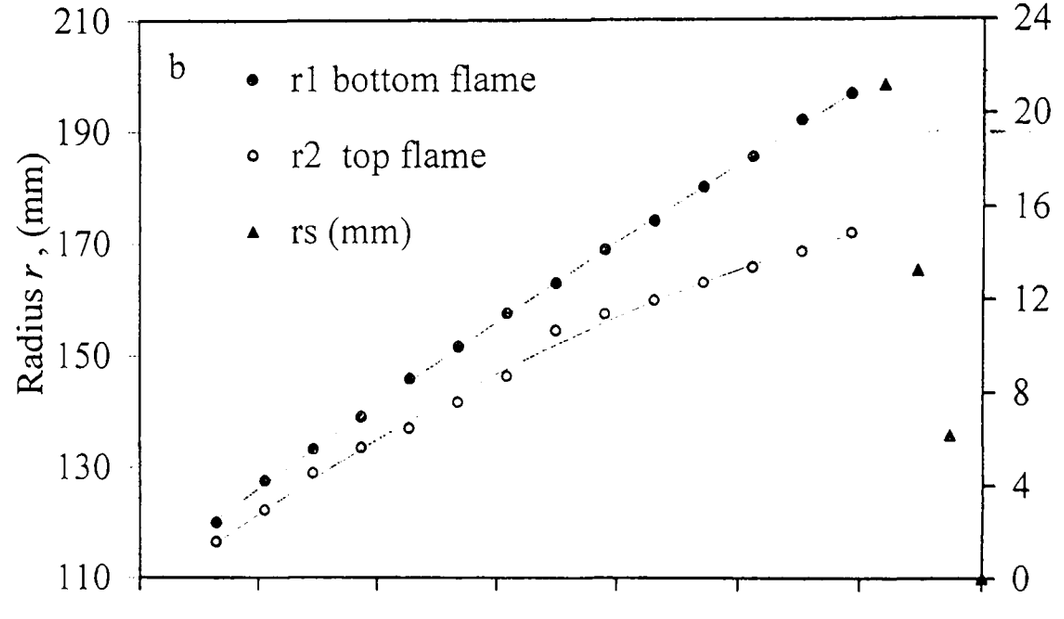

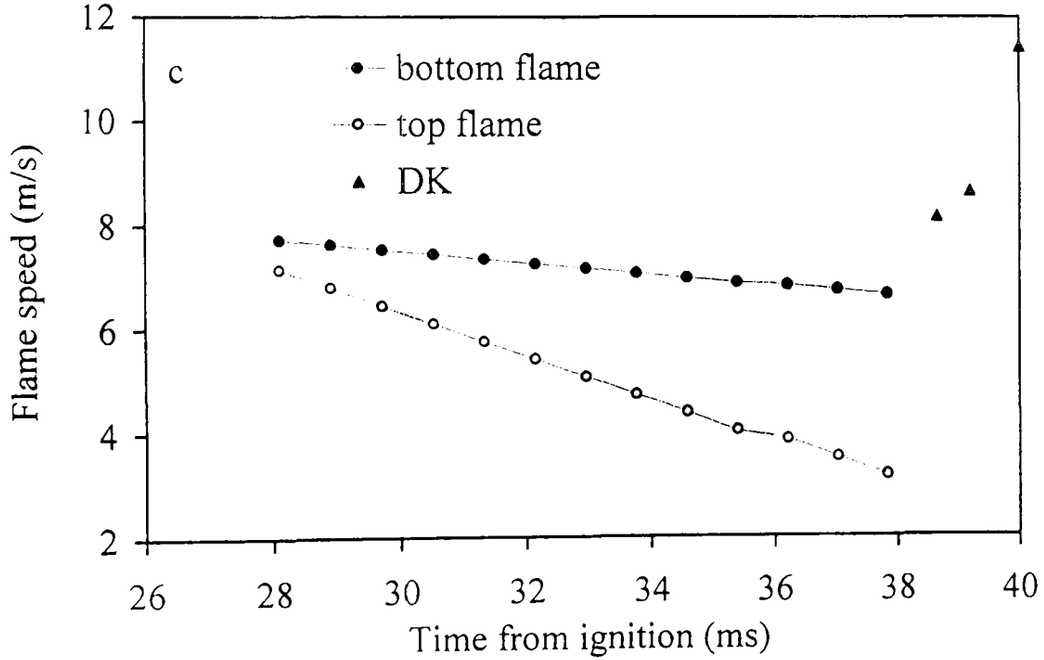

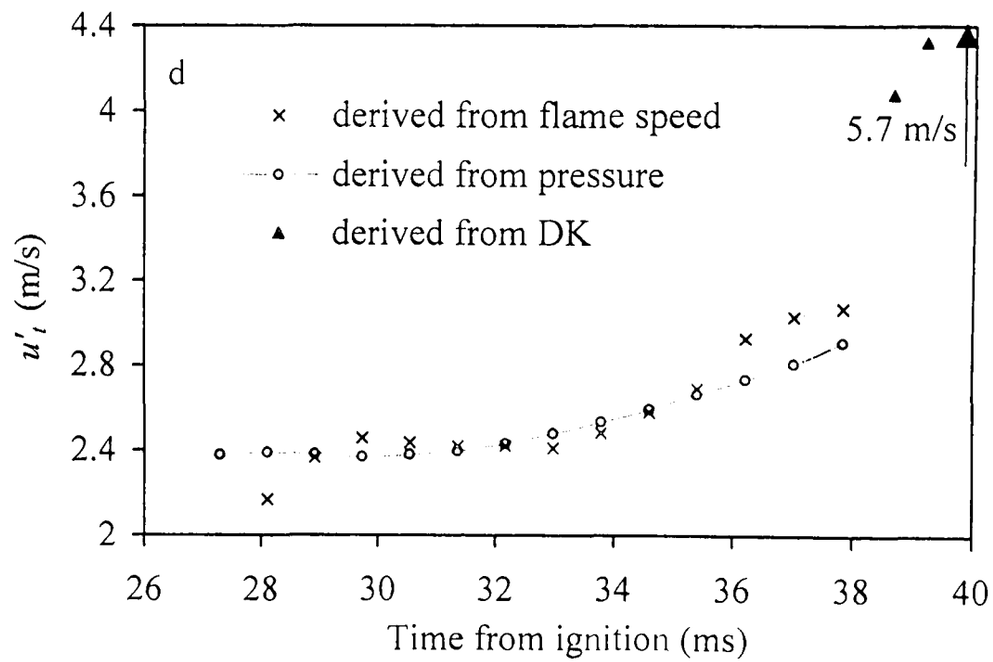

Fig. C.25. Iso-octane - air implosion, ϕ = 1, p_o = 1 MPa, T_o = 358 K, u' = 0.5

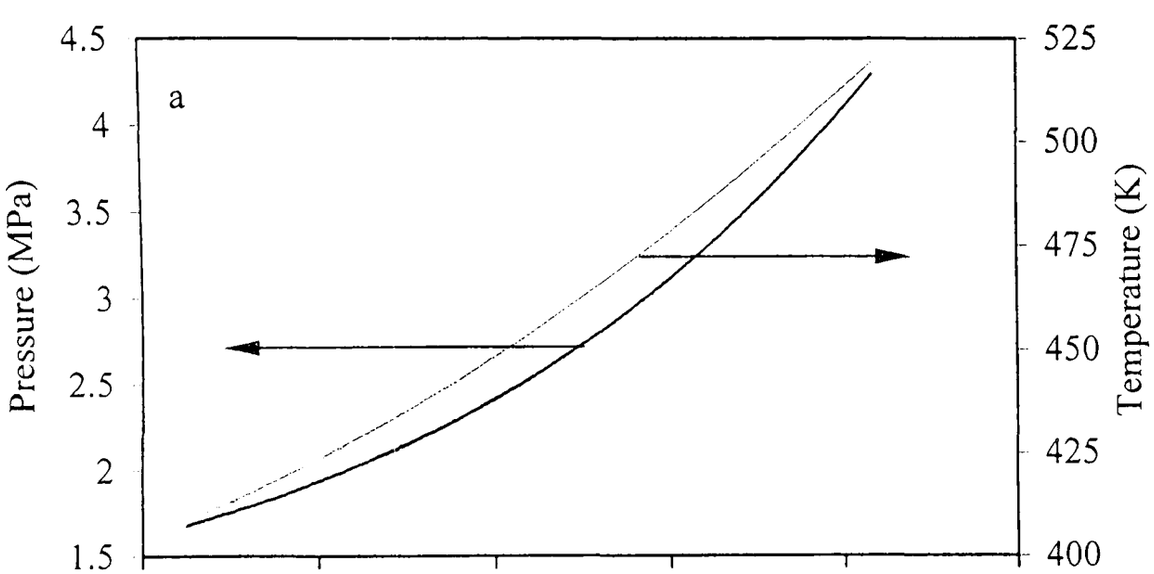

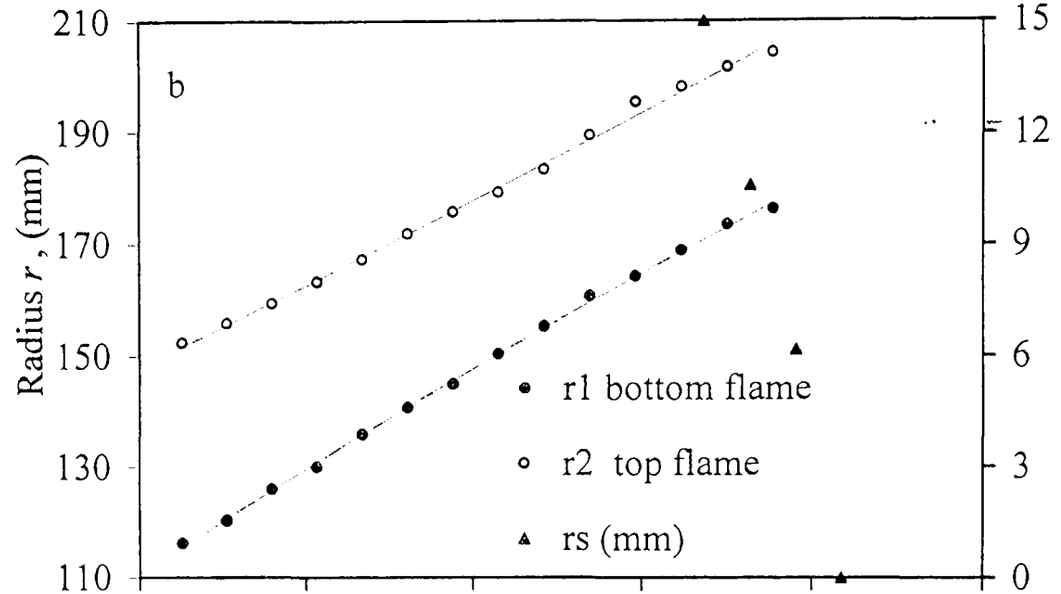

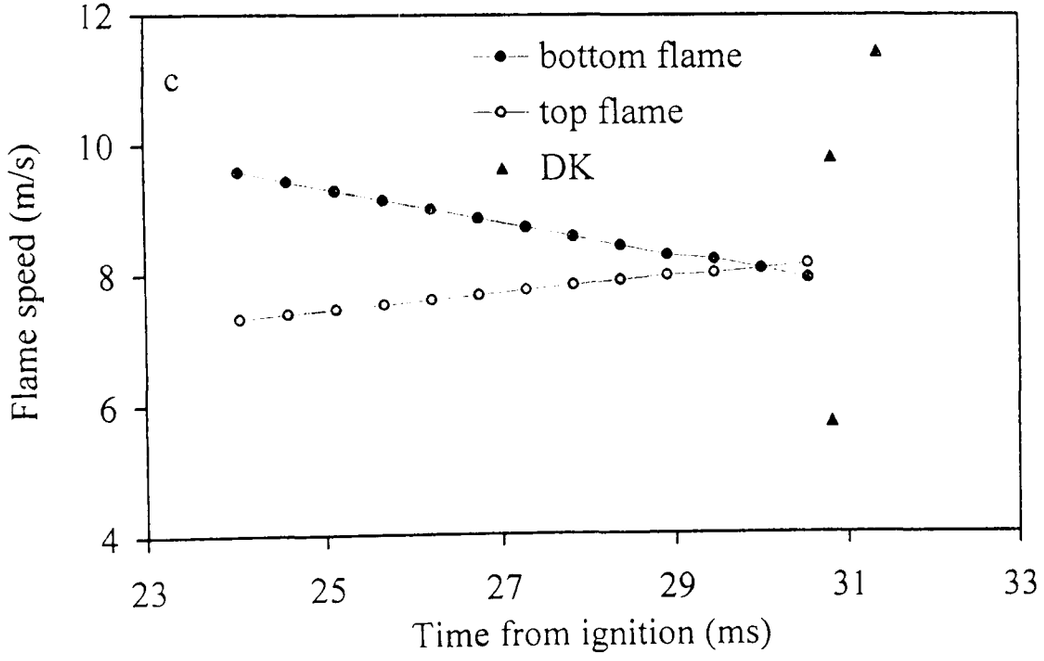

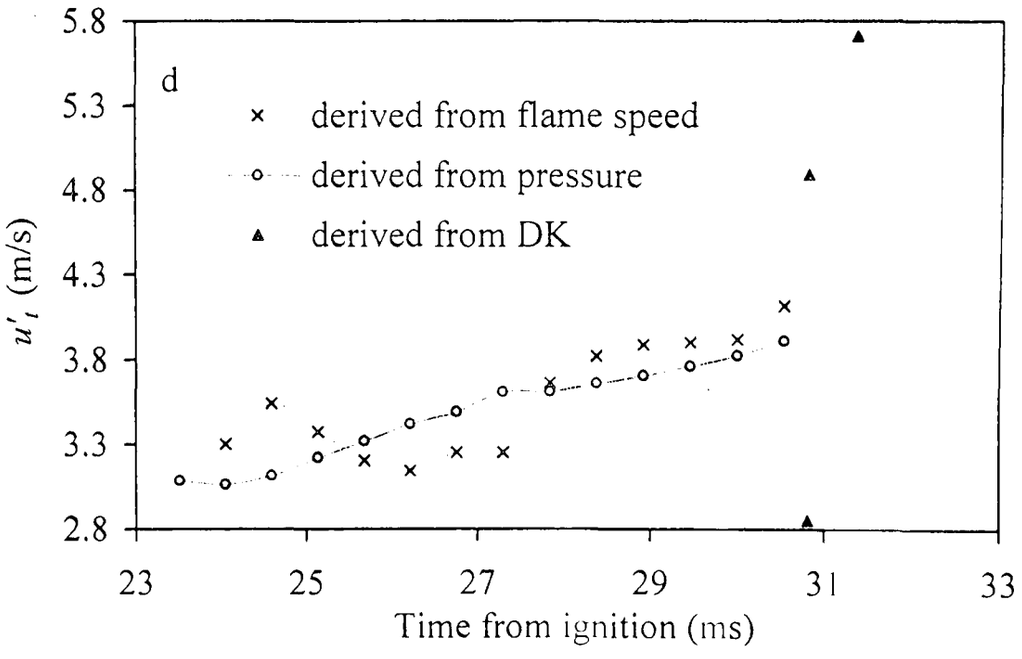

Fig. C.26. Iso-octane - air implosion, $\phi = 1, p_o = 1$ MPa, $T_o = 358$ K, $u' = 0.75$

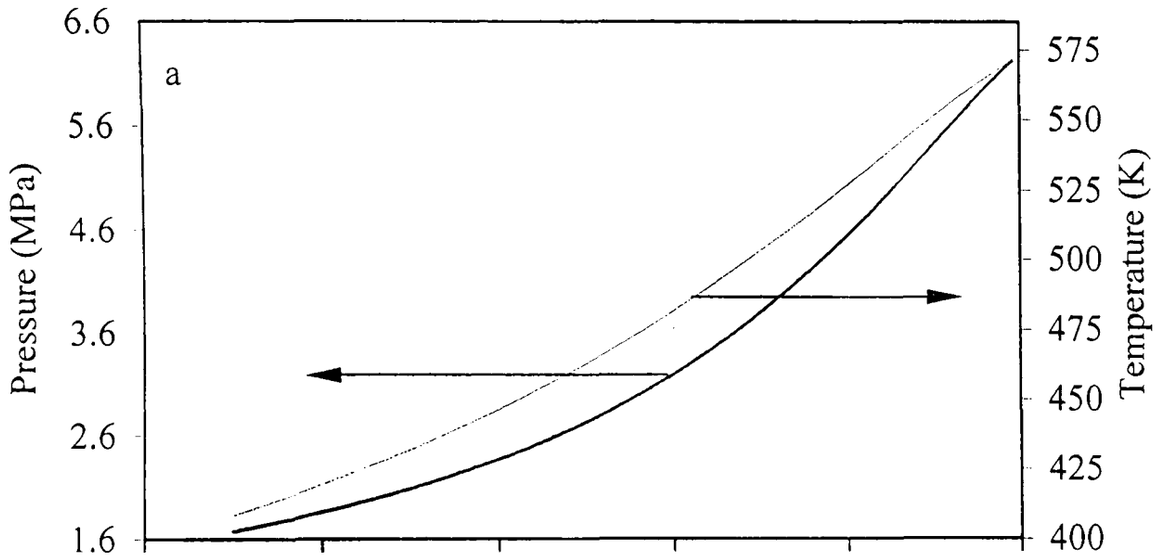

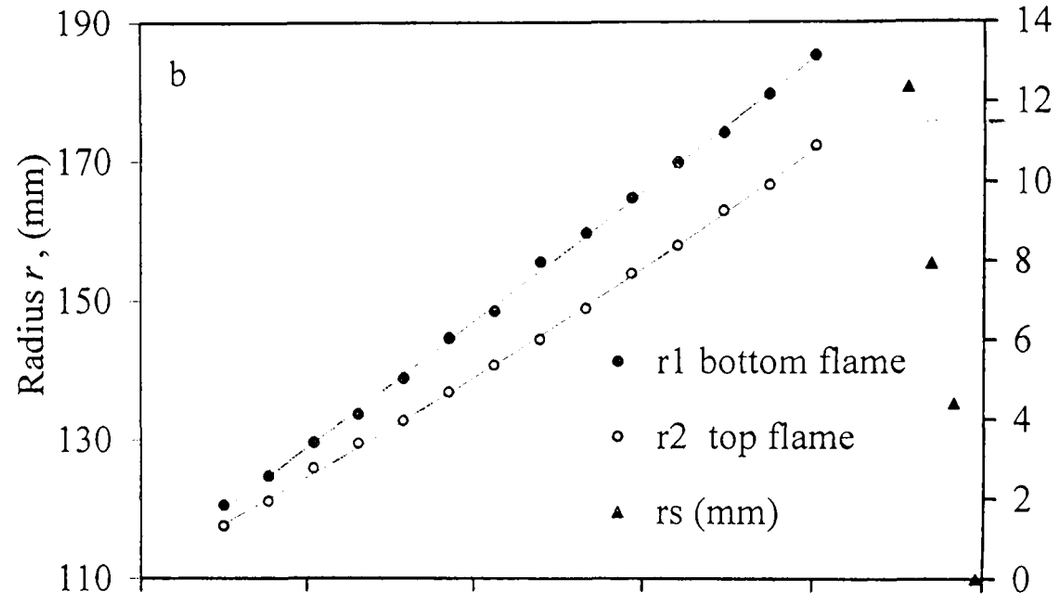

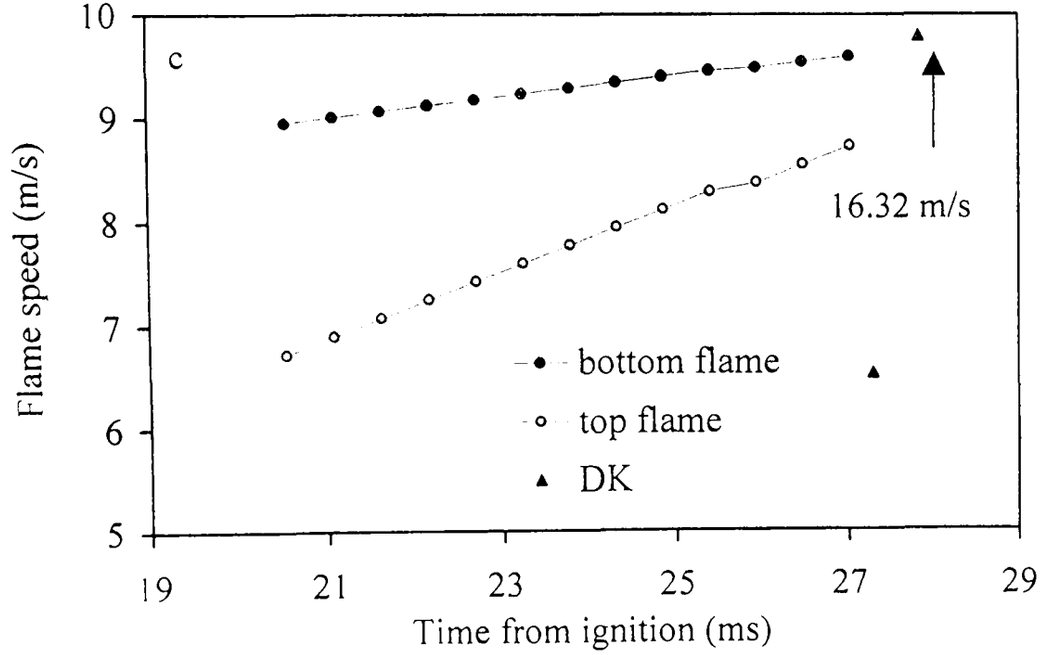

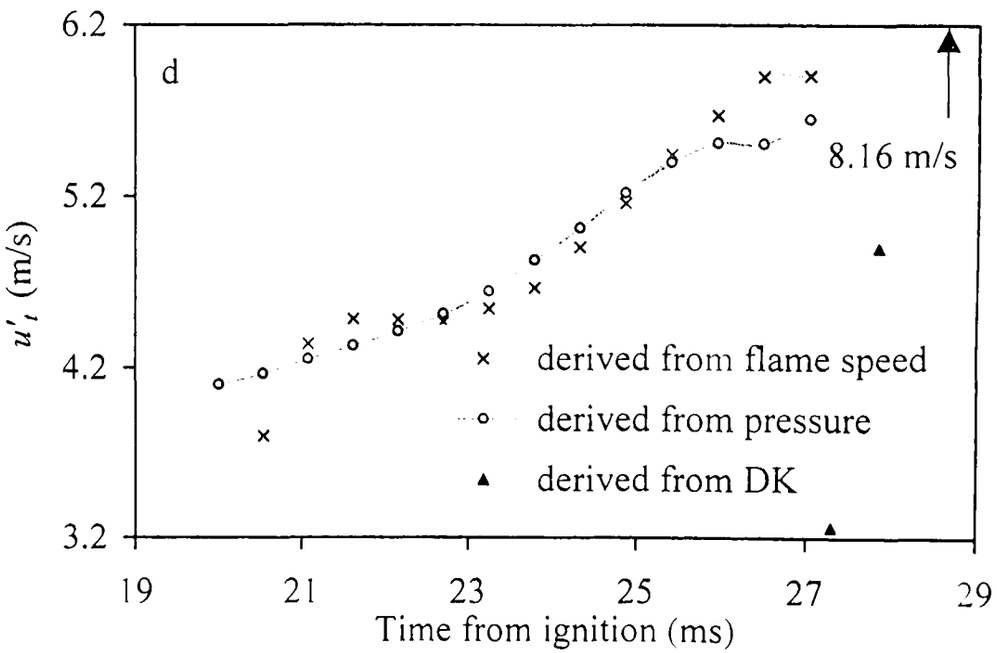

Fig. C.27. Iso-octane - air implosion, $\phi = 1, p_o = 1$ MPa, $T_o = 358$ K, $u' = 1$

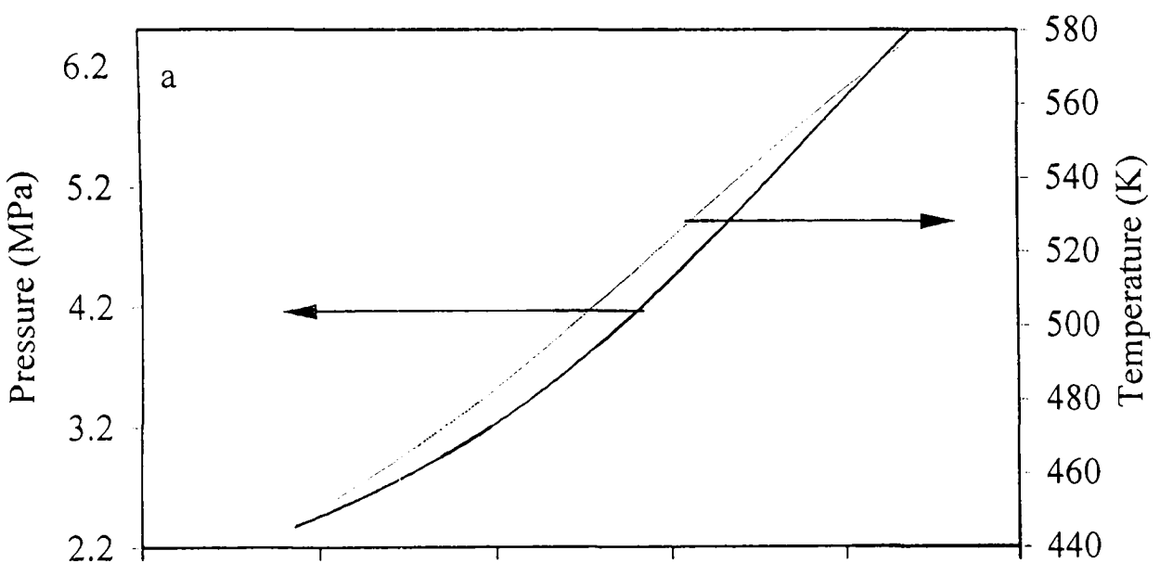

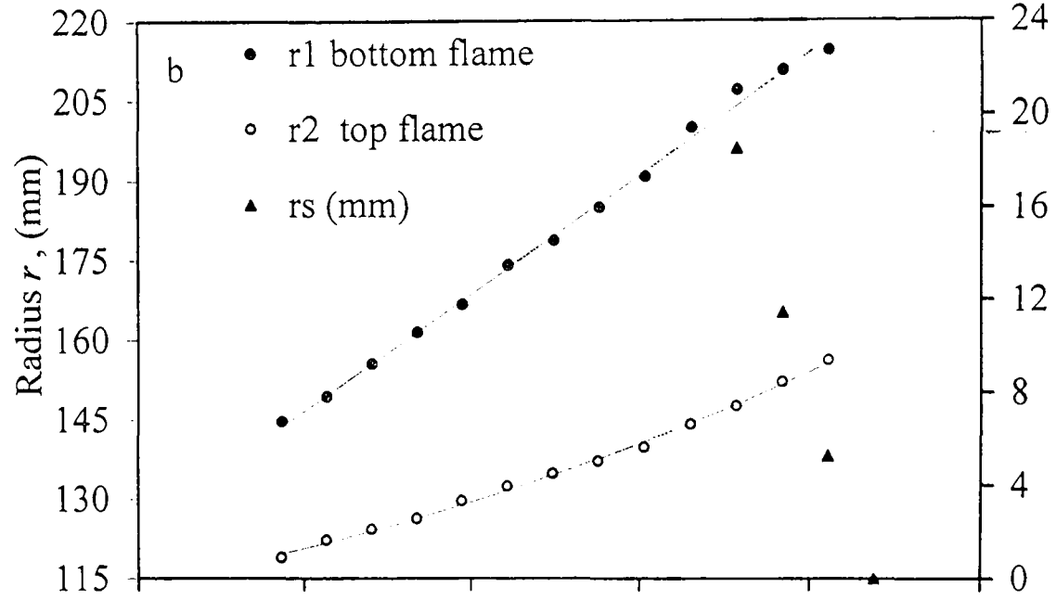

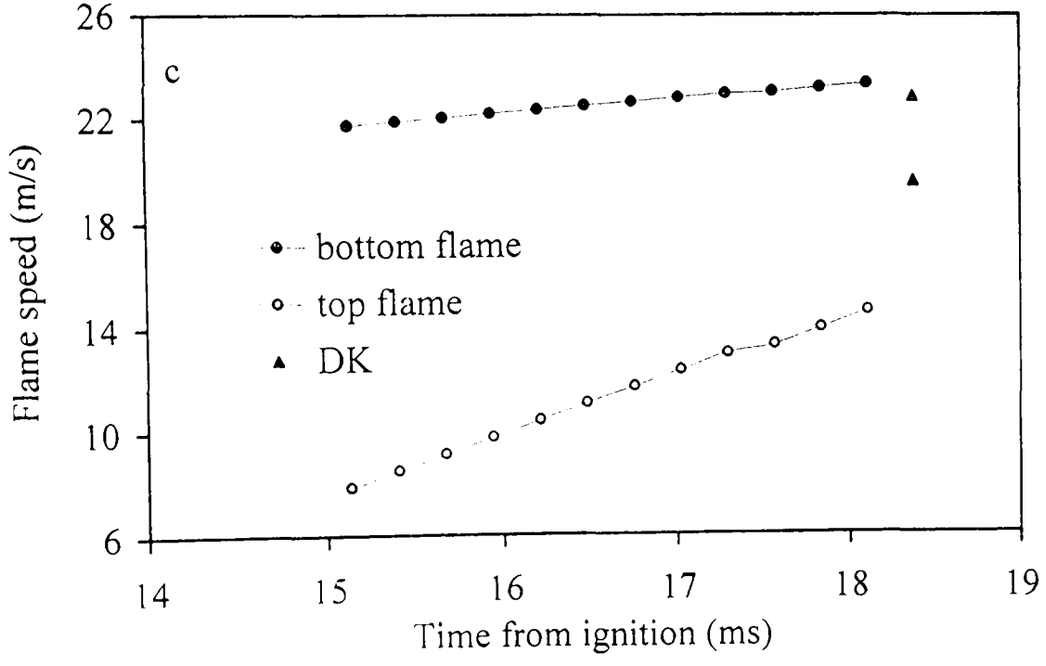

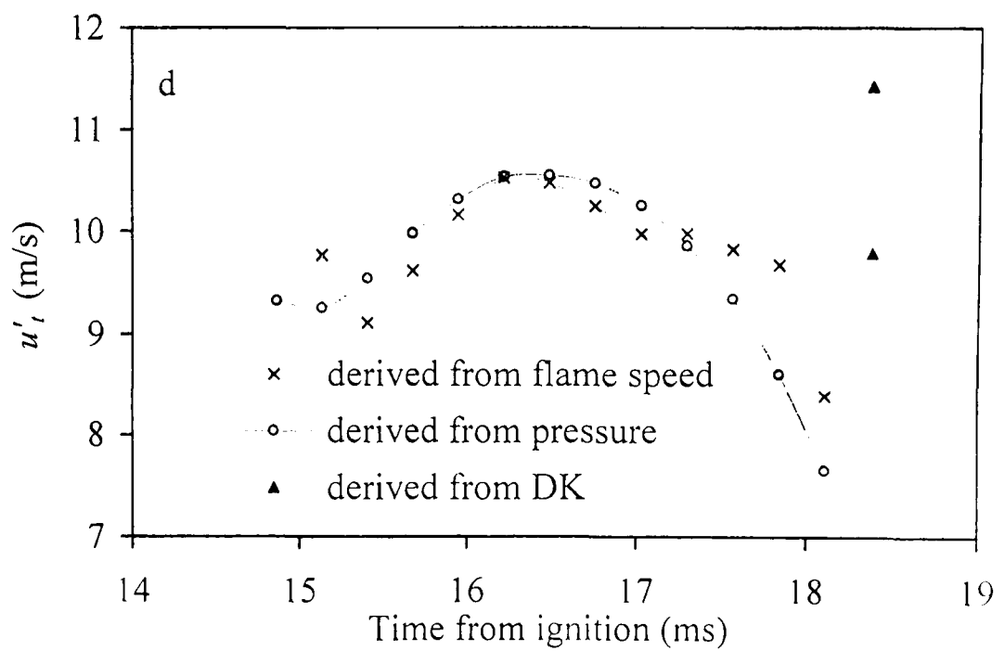

Fig. C.28. Iso-octane - air implosion, $\phi = 1, p_o = 1$ MPa, $T_o = 358$ K, $u' = 2$

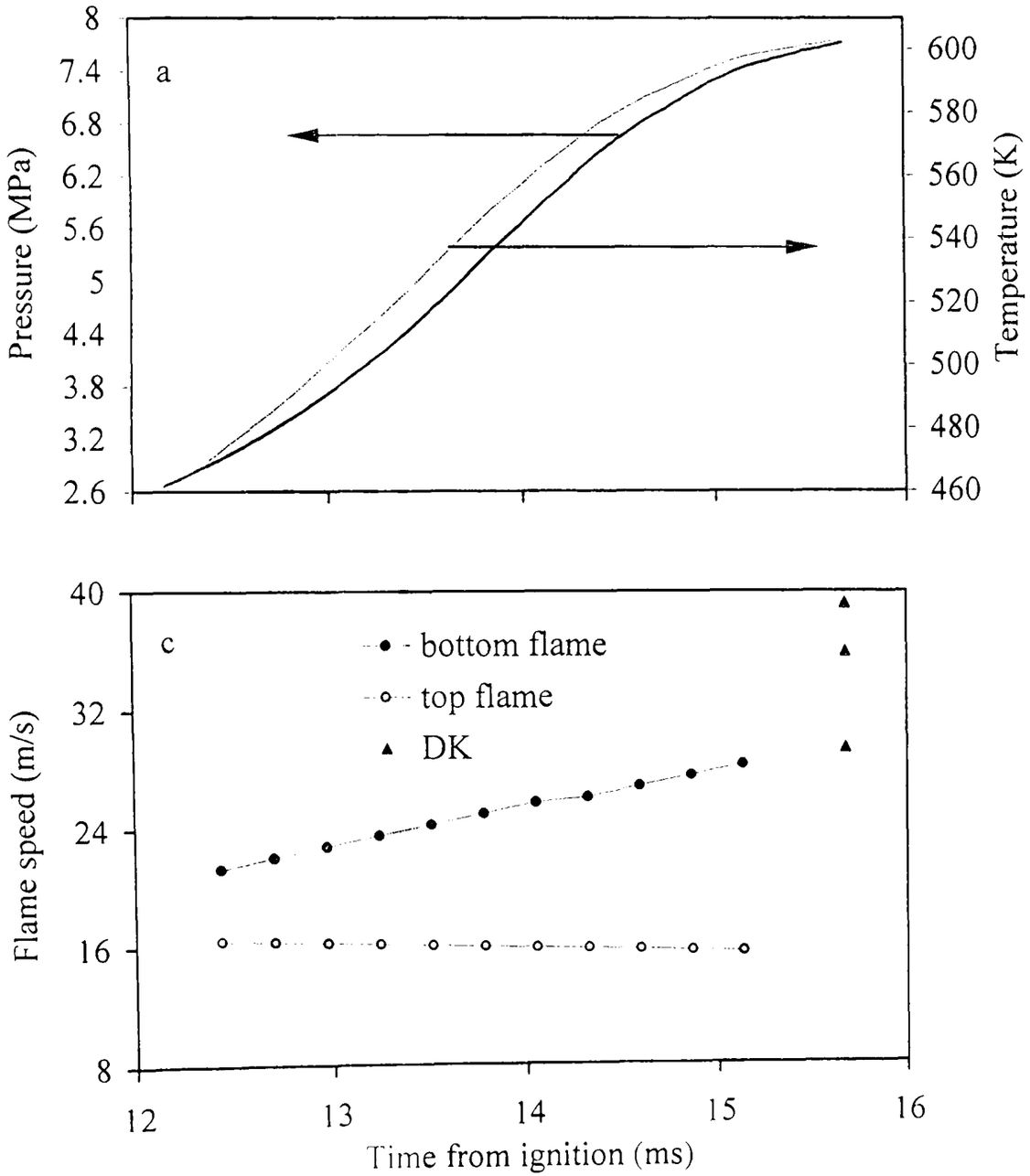

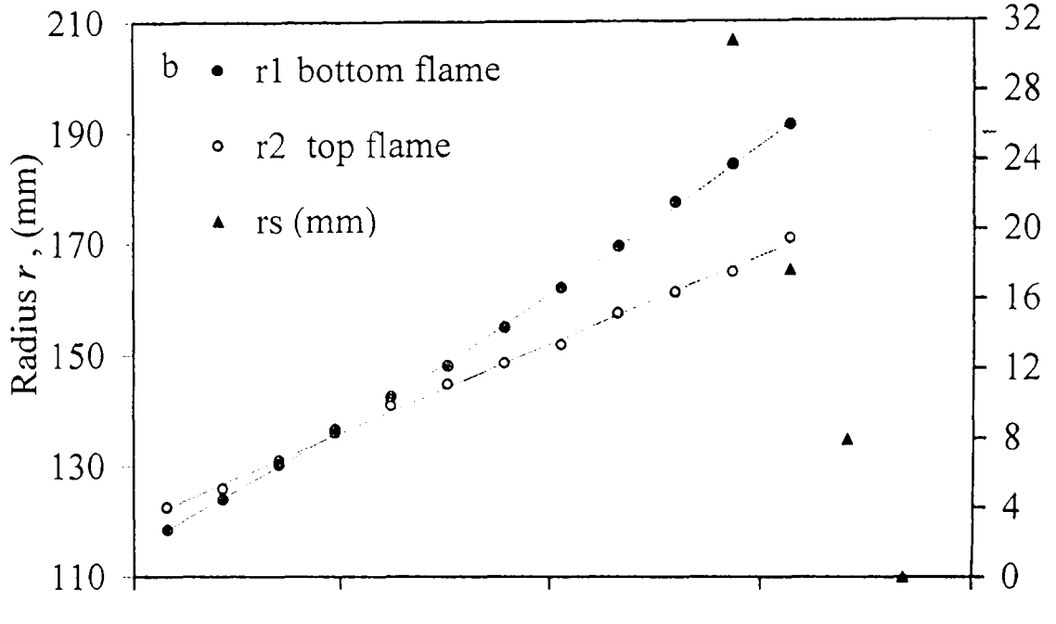

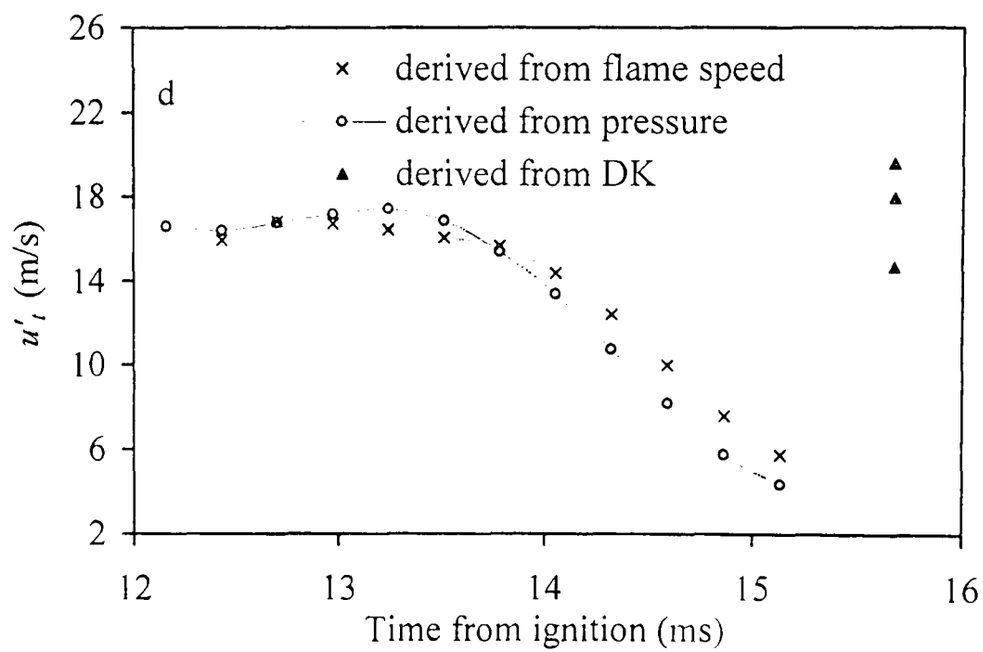

Fig. C.29. Iso-octane - air implosion, $\phi = 1, p_o = 1$ MPa, $T_o = 358$ K, $u' = 3$

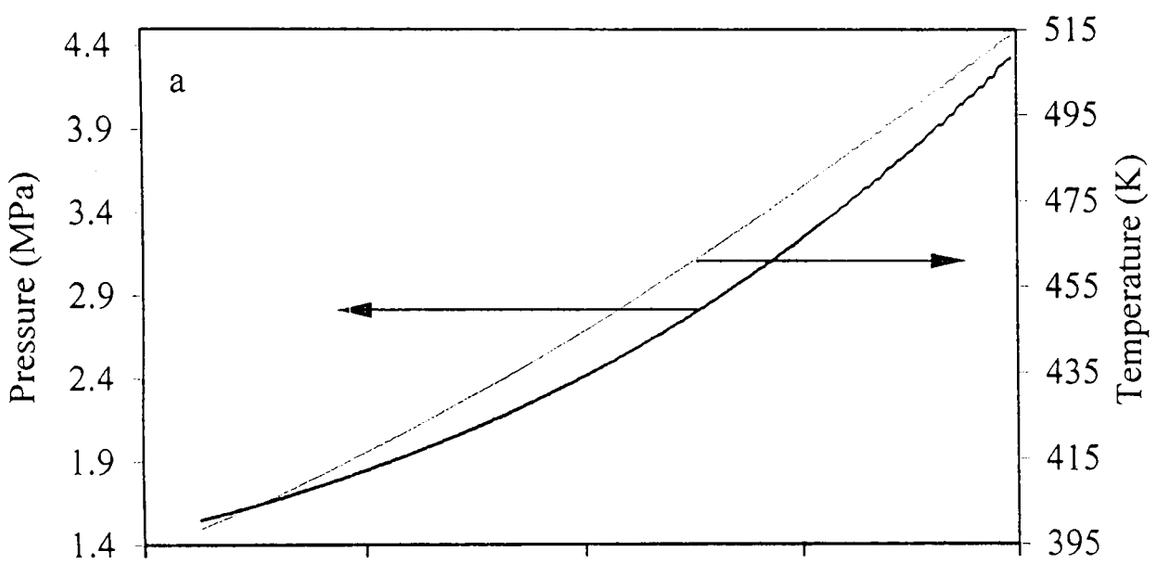

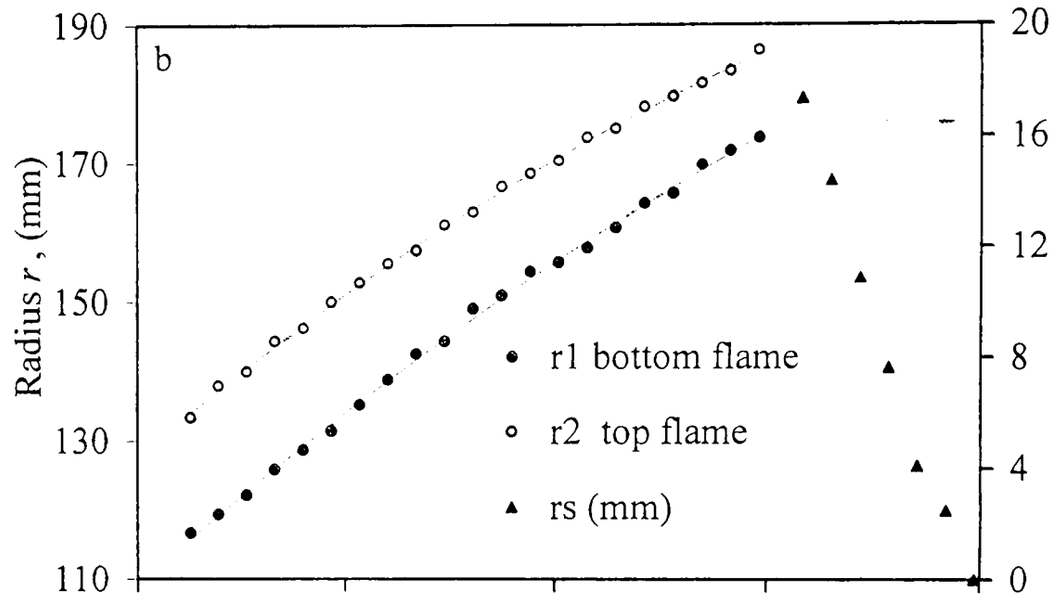

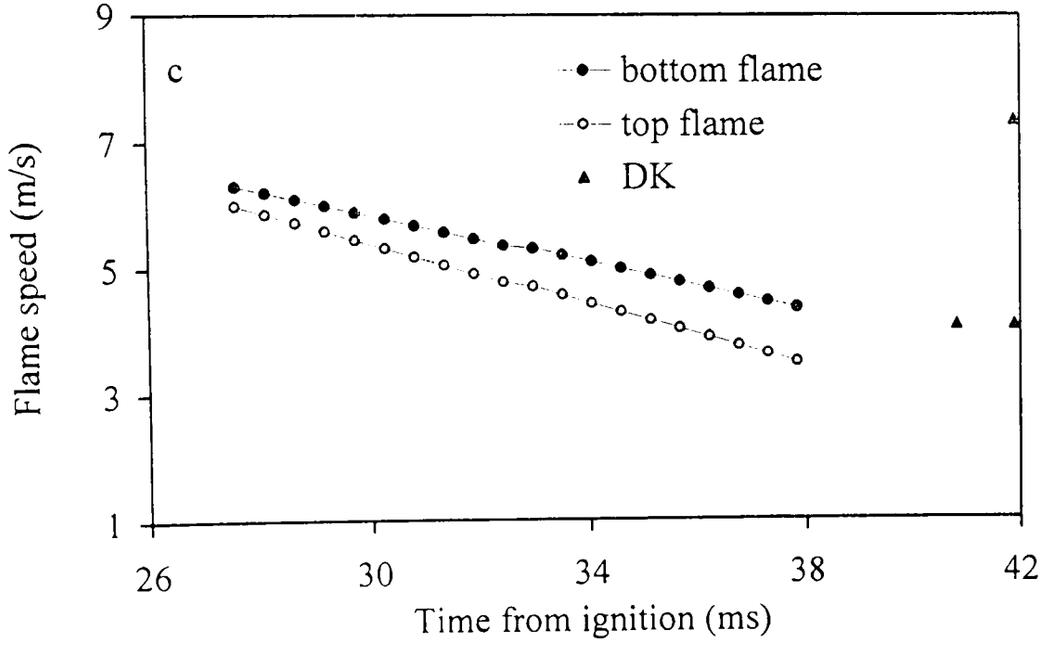

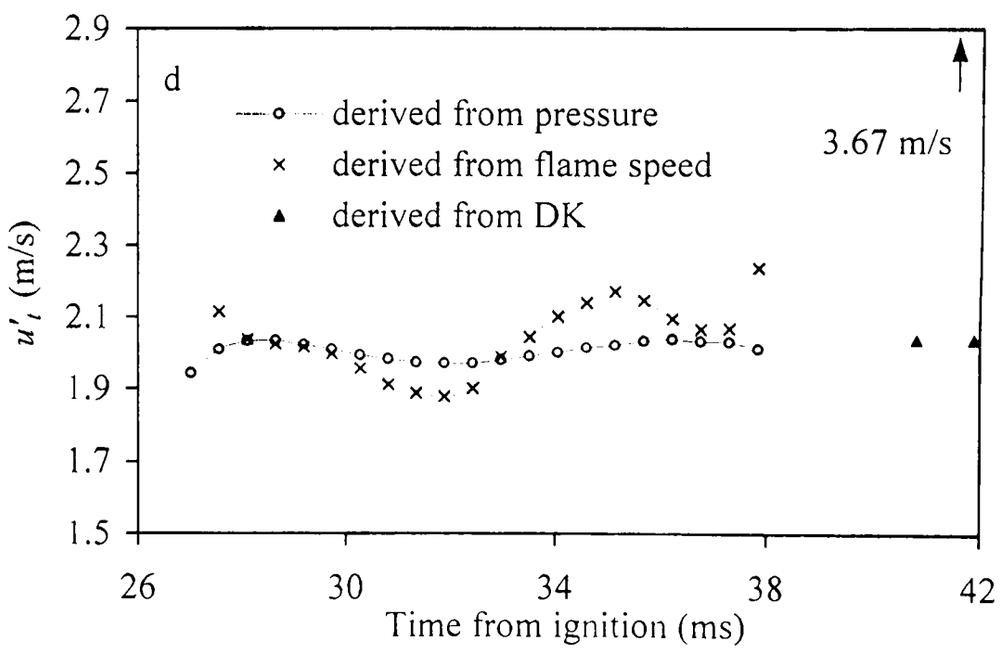

Fig. C.30. Iso-octane - air implosion, ϕ = 1.4, p_o = 1 MPa, T_o = 358 K, u' = 0.25

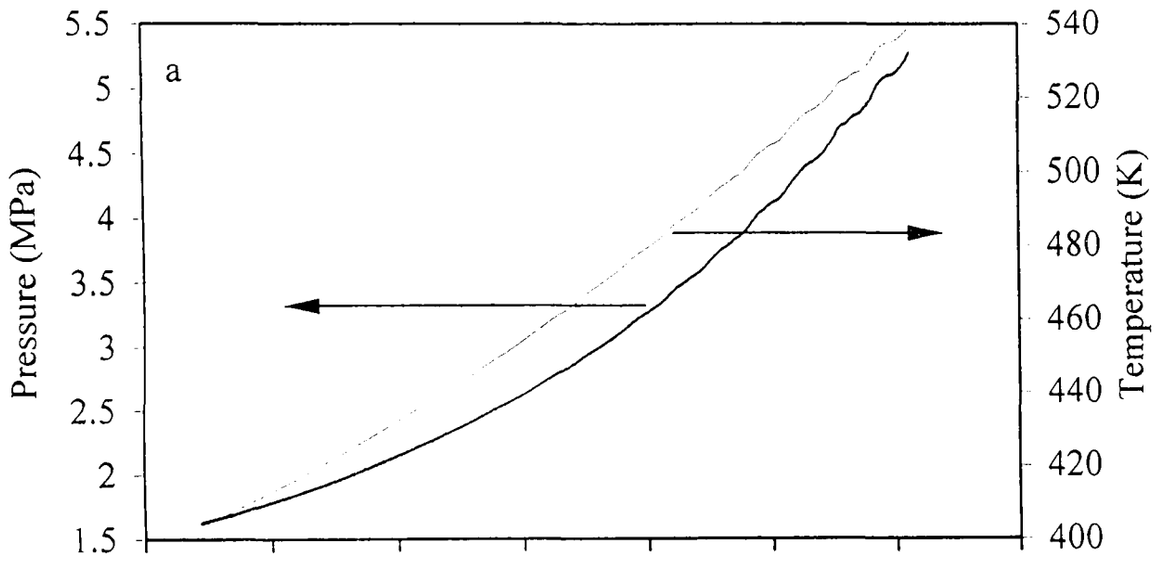

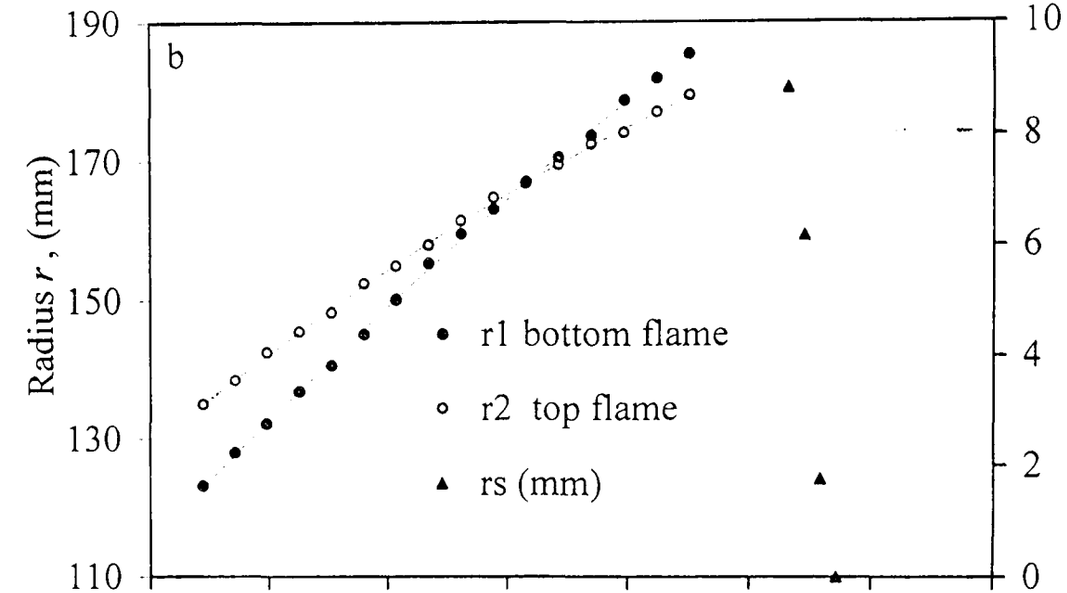

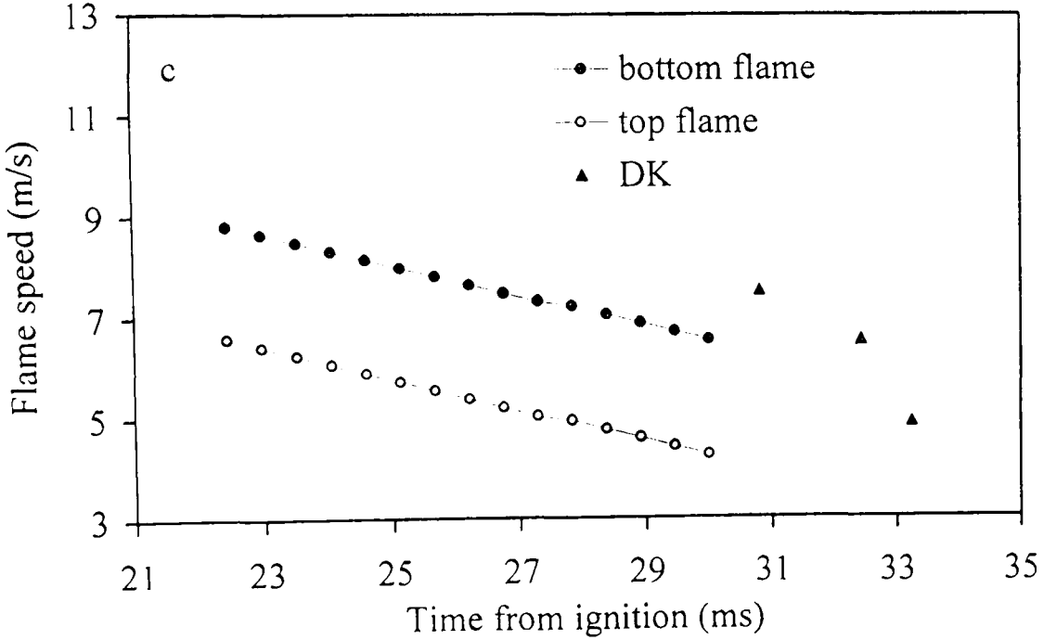

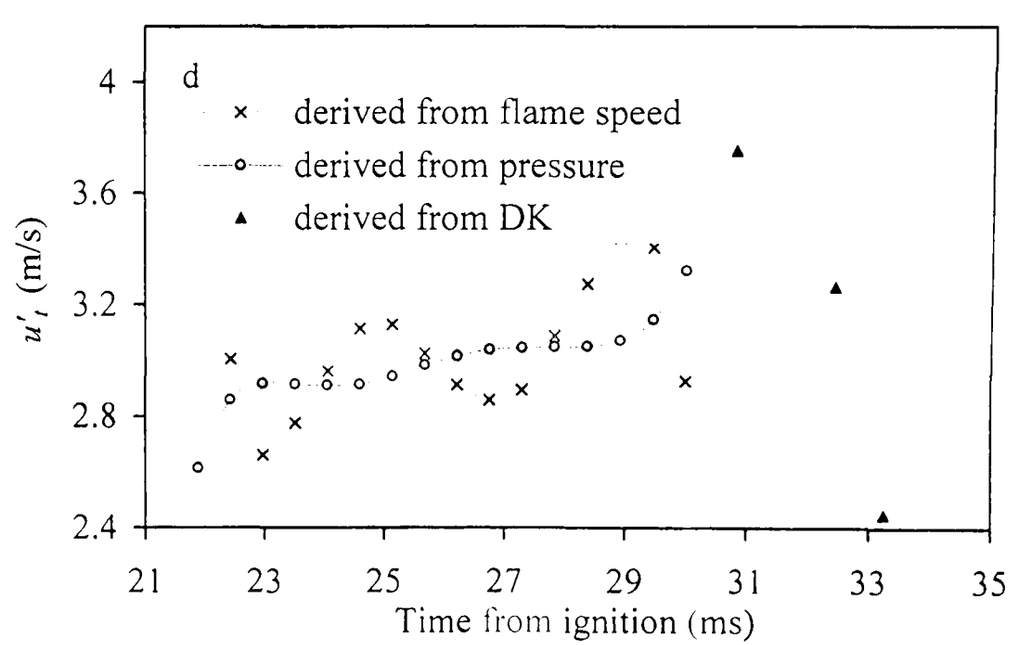

Fig. C.31. Iso-octane - air implosion, $\phi = 1.4, p_o = 1$ MPa, $T_o = 358$ K, $u' = 0.5$

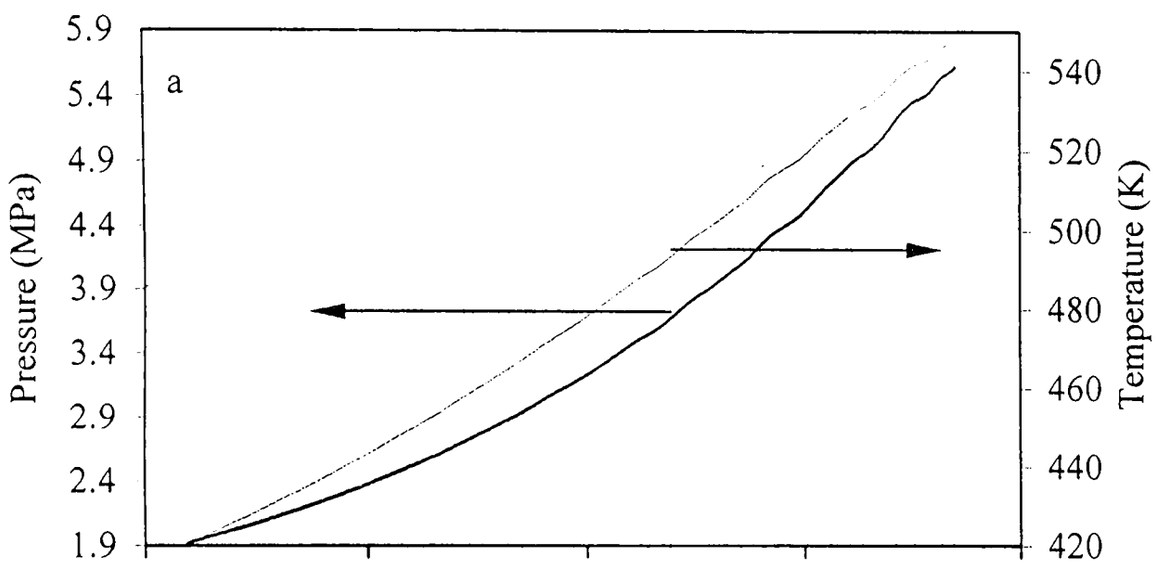

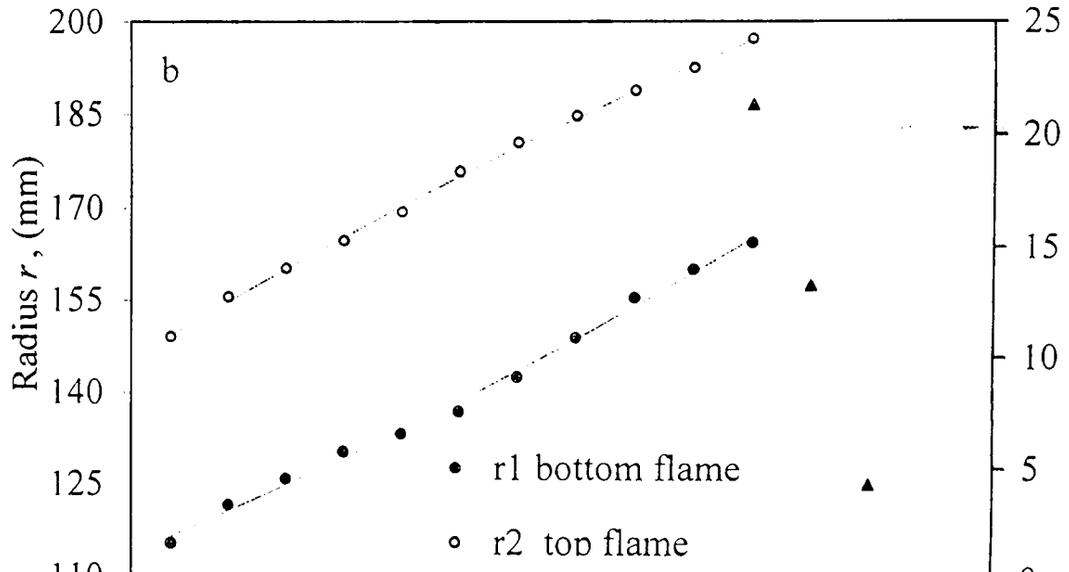

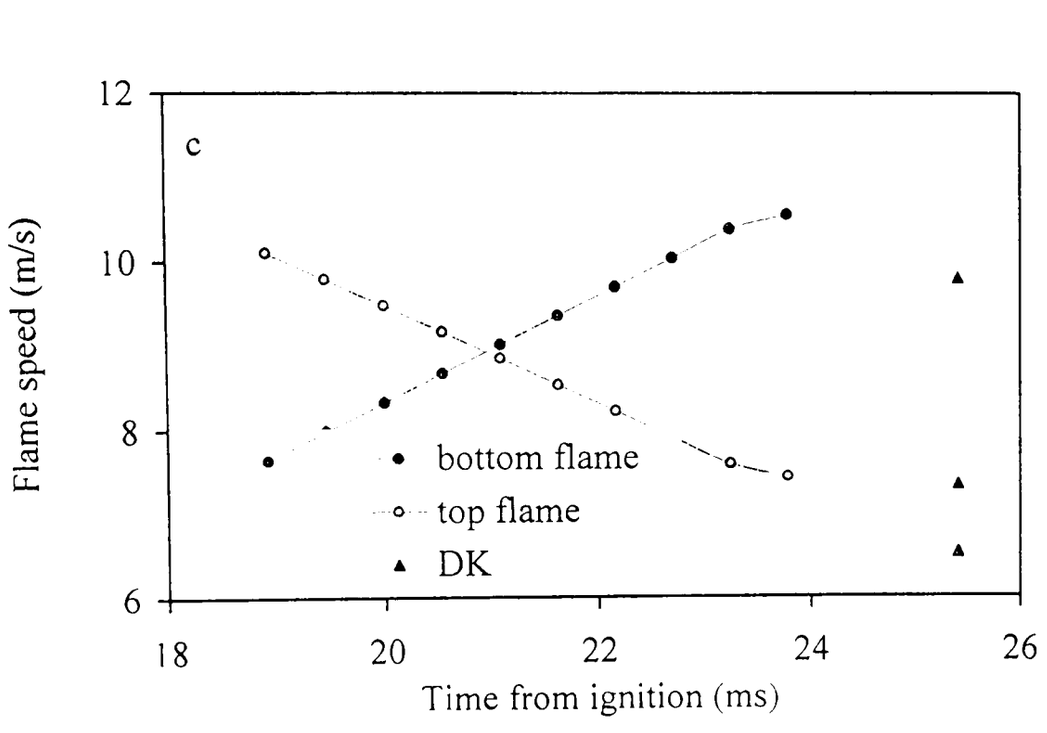

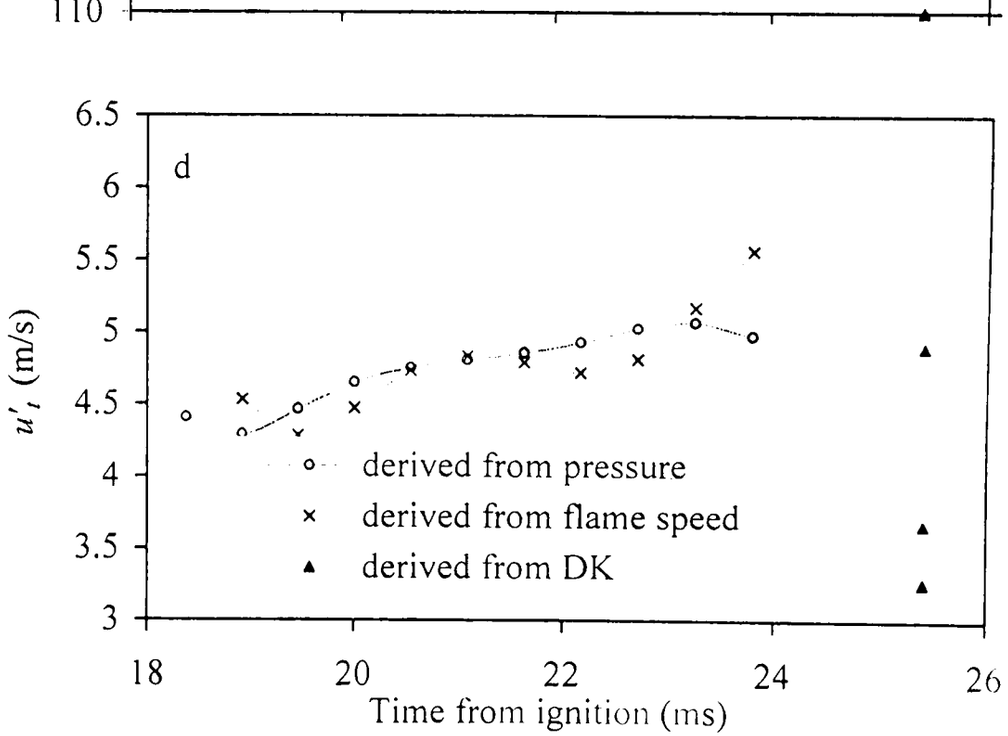

Fig. C.32. Iso-octane - air implosion, ϕ = 1.4, p_o = 1 MPa, T_o = 358 K, u' = 0.75

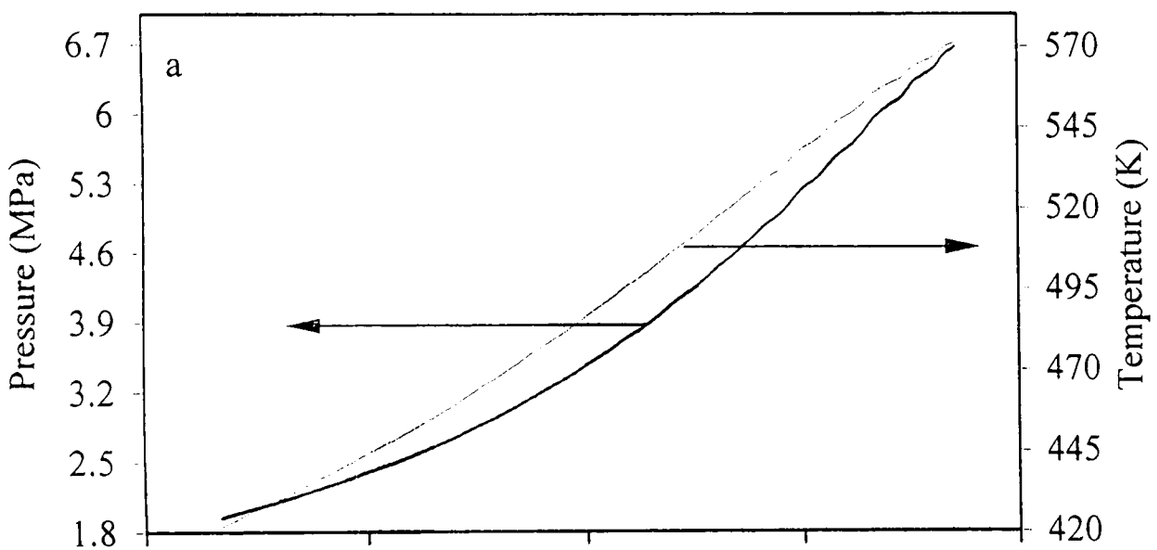

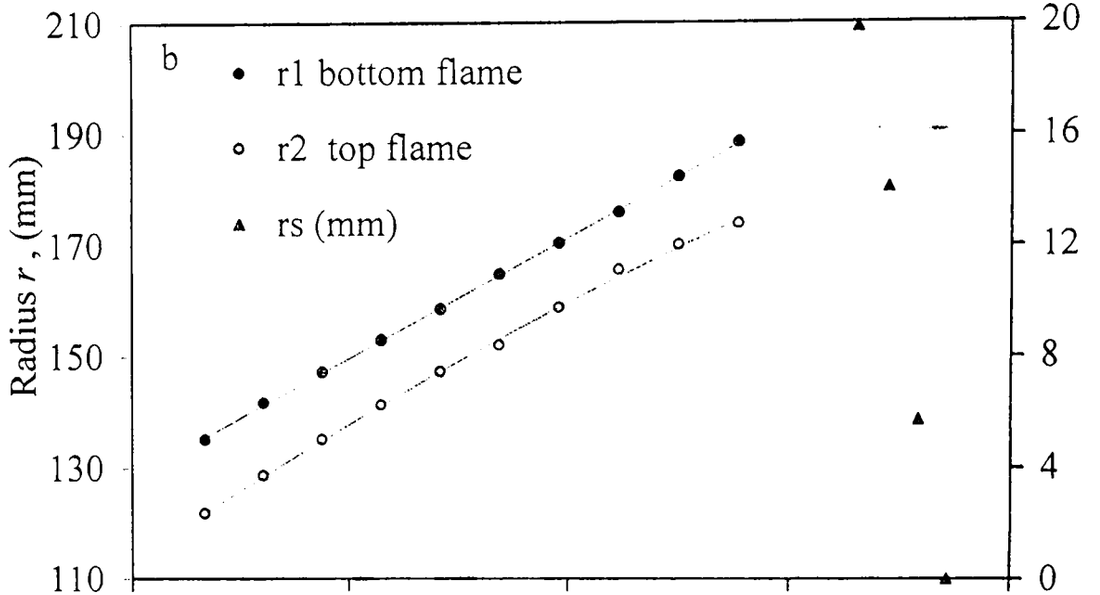

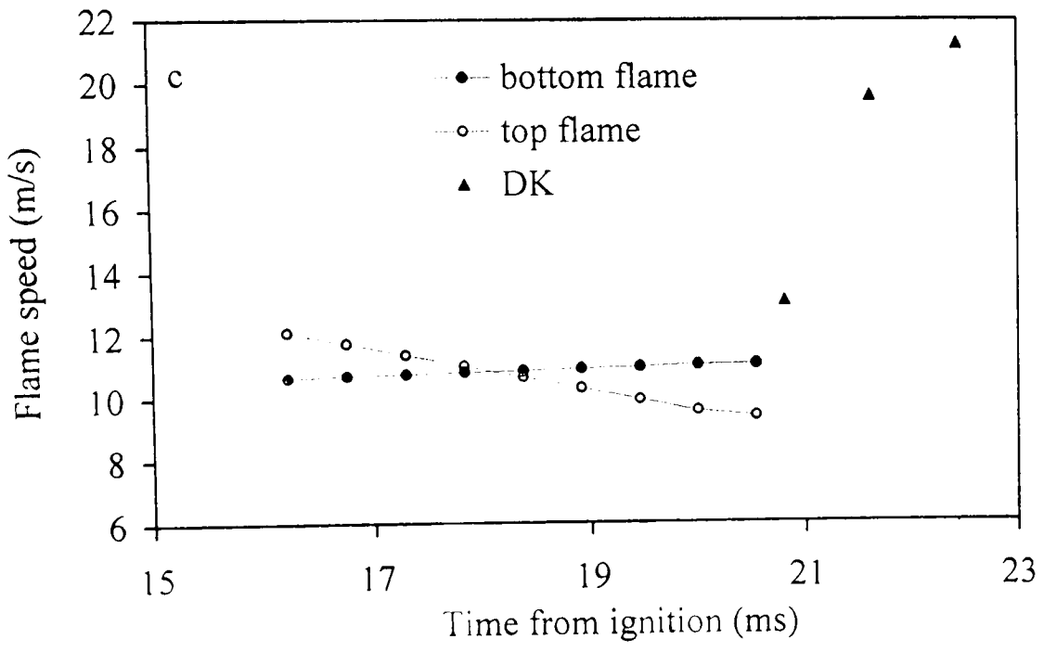

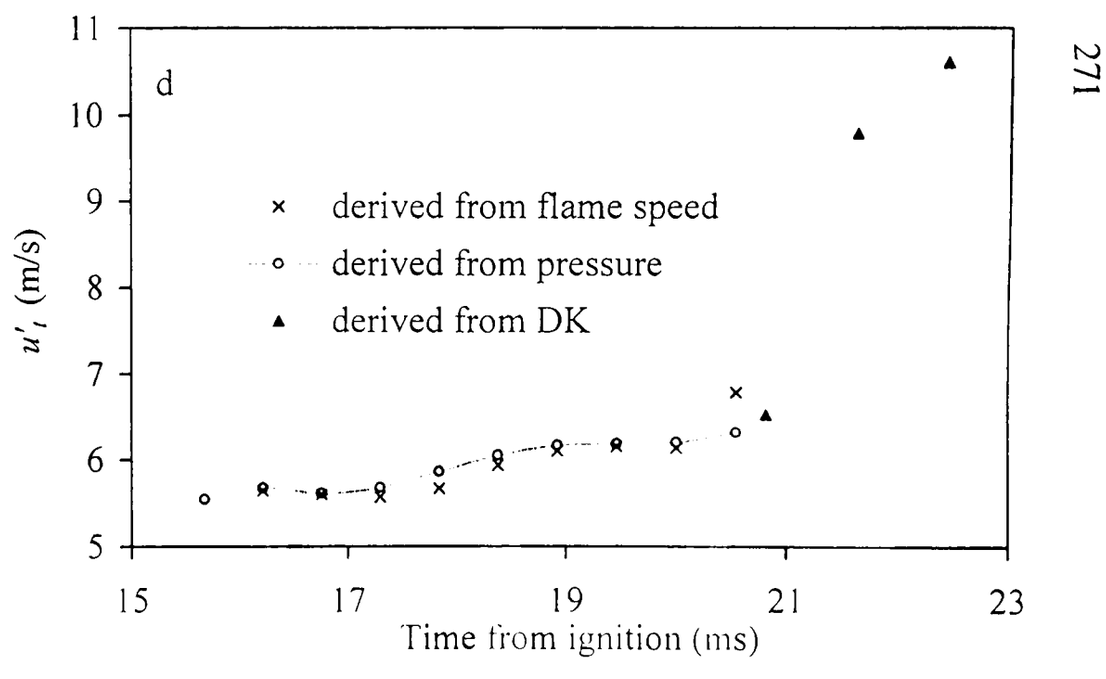

Fig. C.33. Iso-octane - air implosion. ϕ = 1.4, p_o = 1 MPa, T_o = 358 K, u' = 1

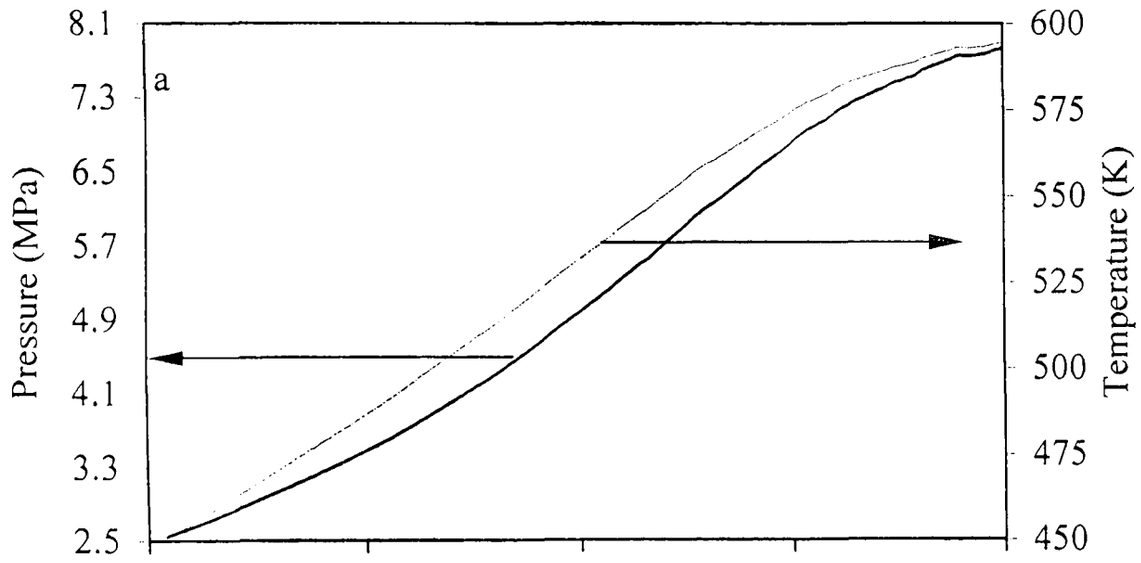

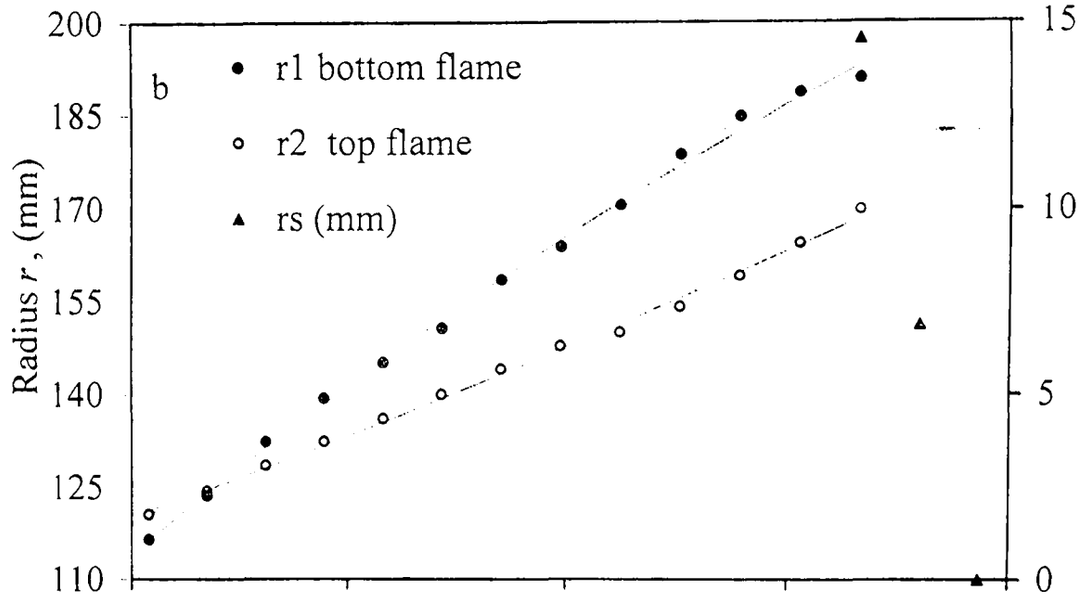

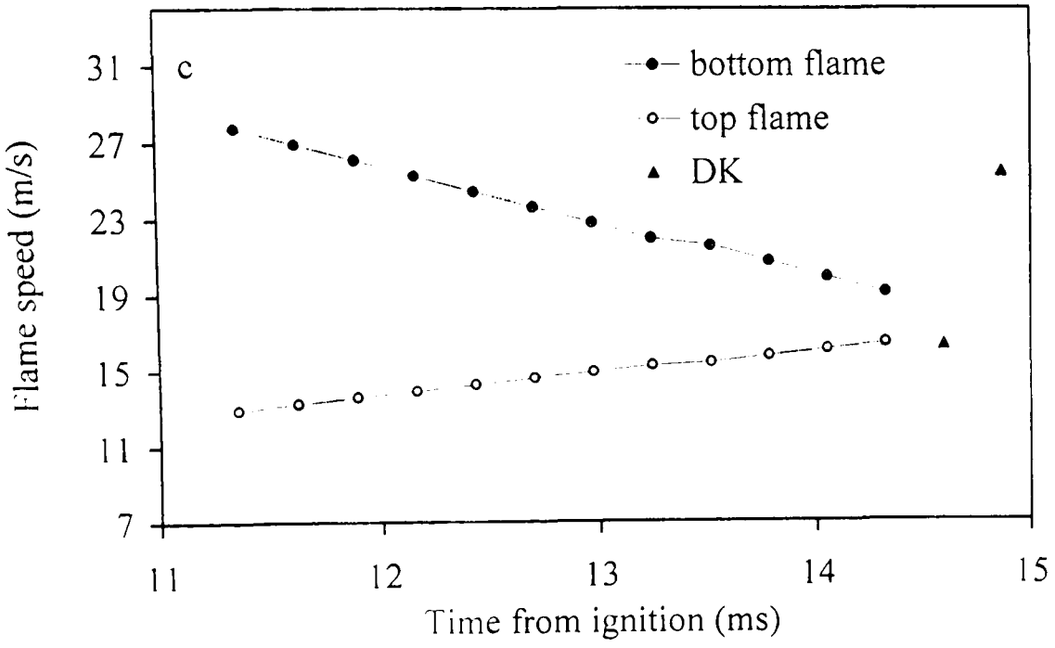

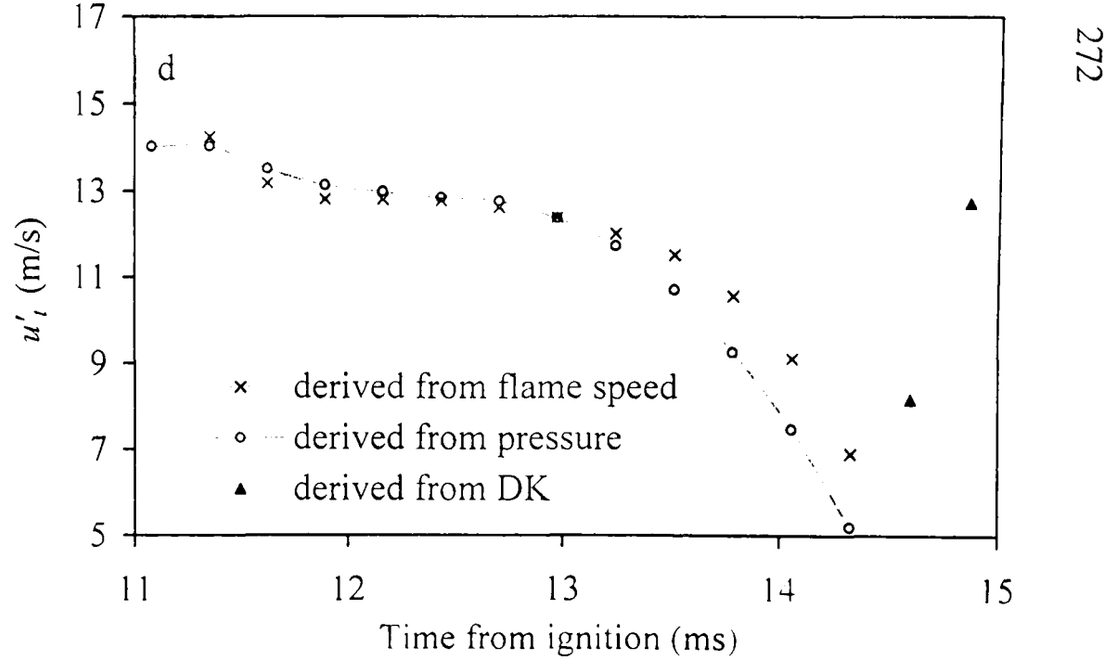

Fig. 7.34. Iso-octane - air implosion, ϕ = 1.4, p_o = 1 MPa, T_o = 358 K, u' = 2

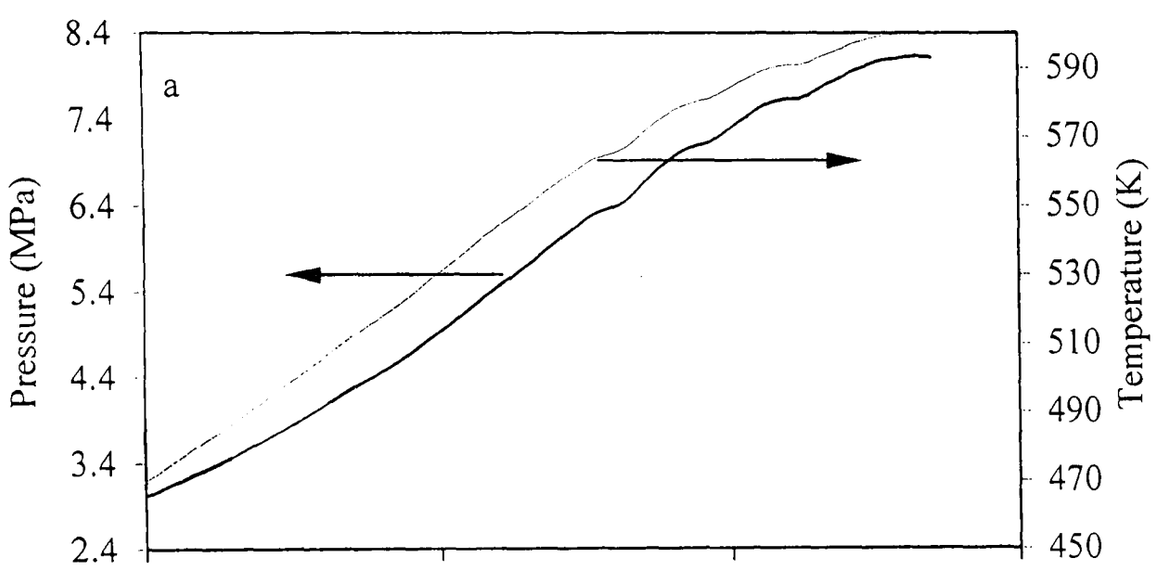

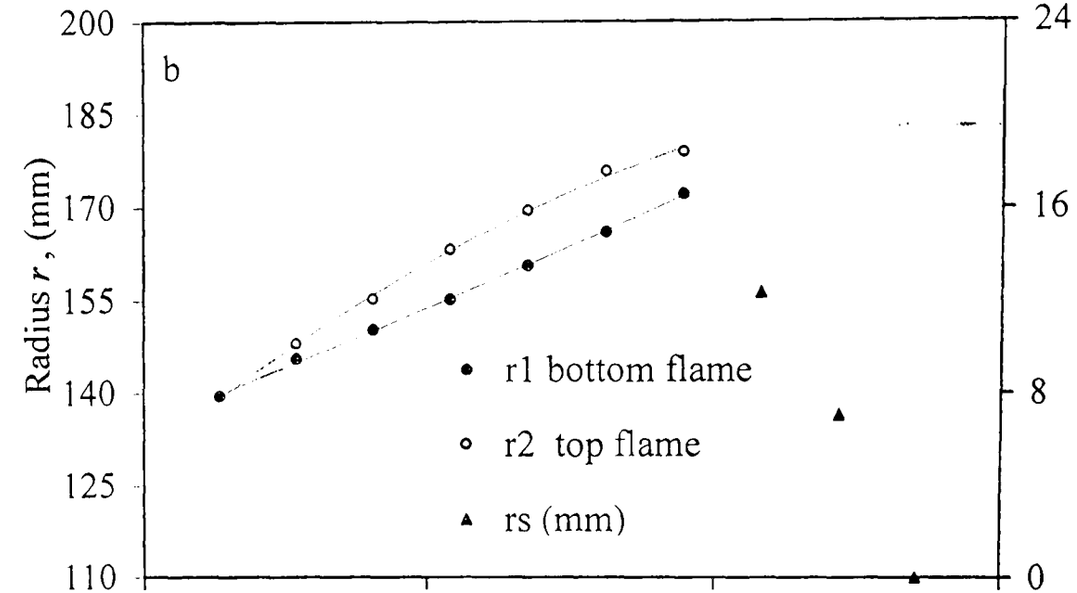

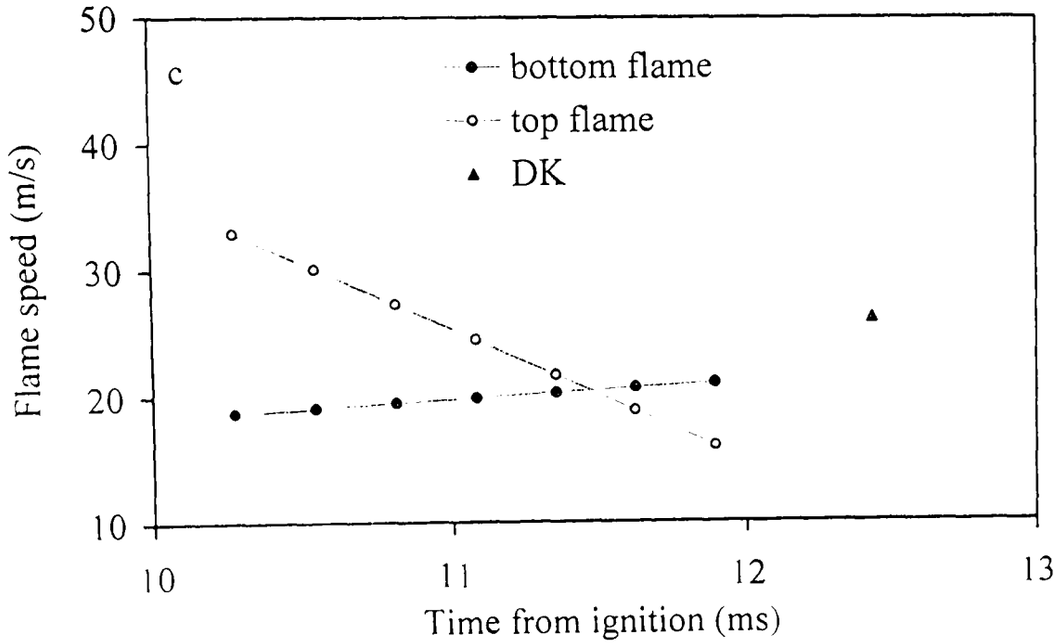

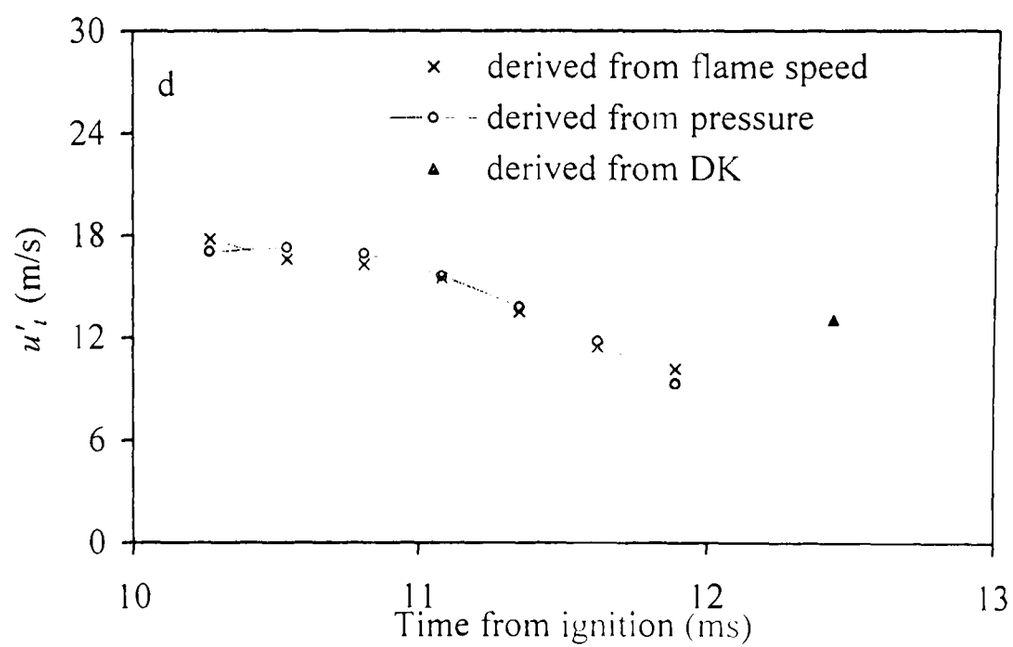

Fig. C.35. Iso-octane - air implosion, $\phi = 1.4, p_o = 1$ MPa, $T_o = 358$ K, $u' = 3$

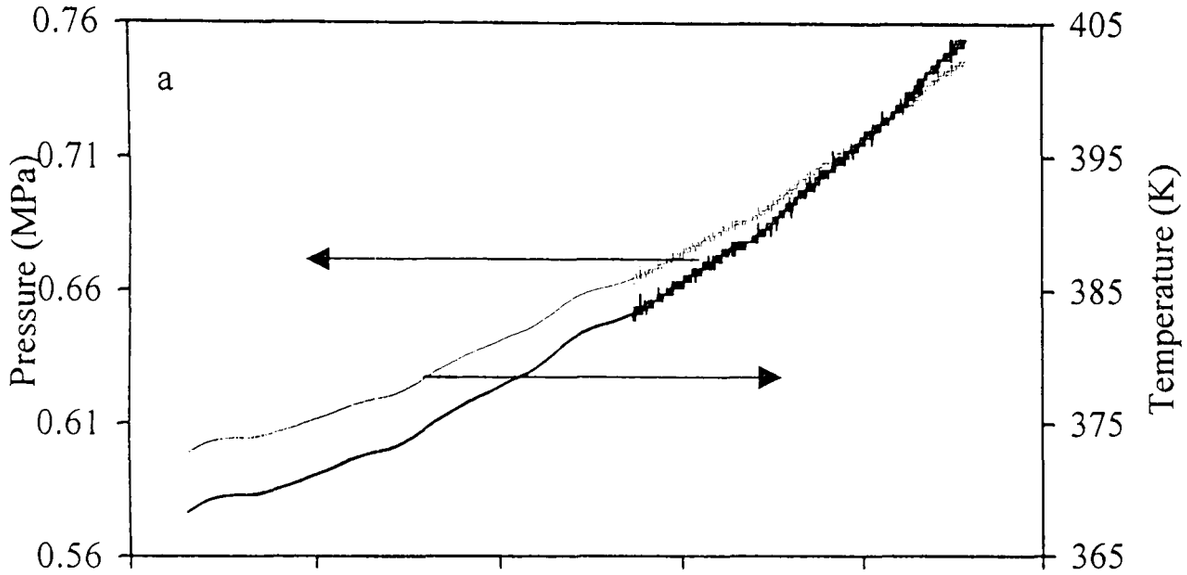

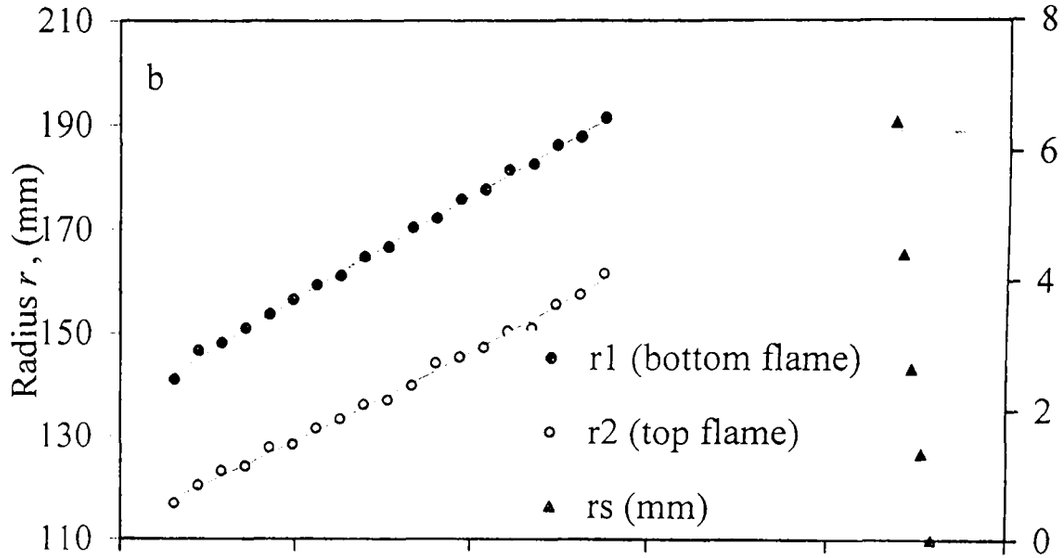

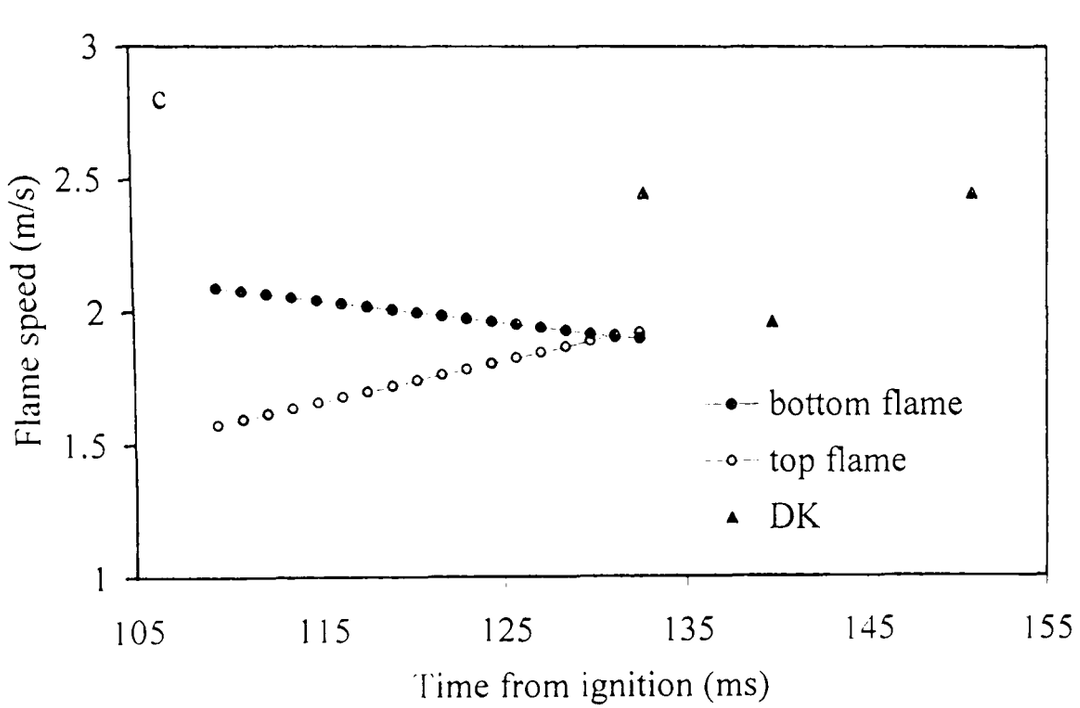

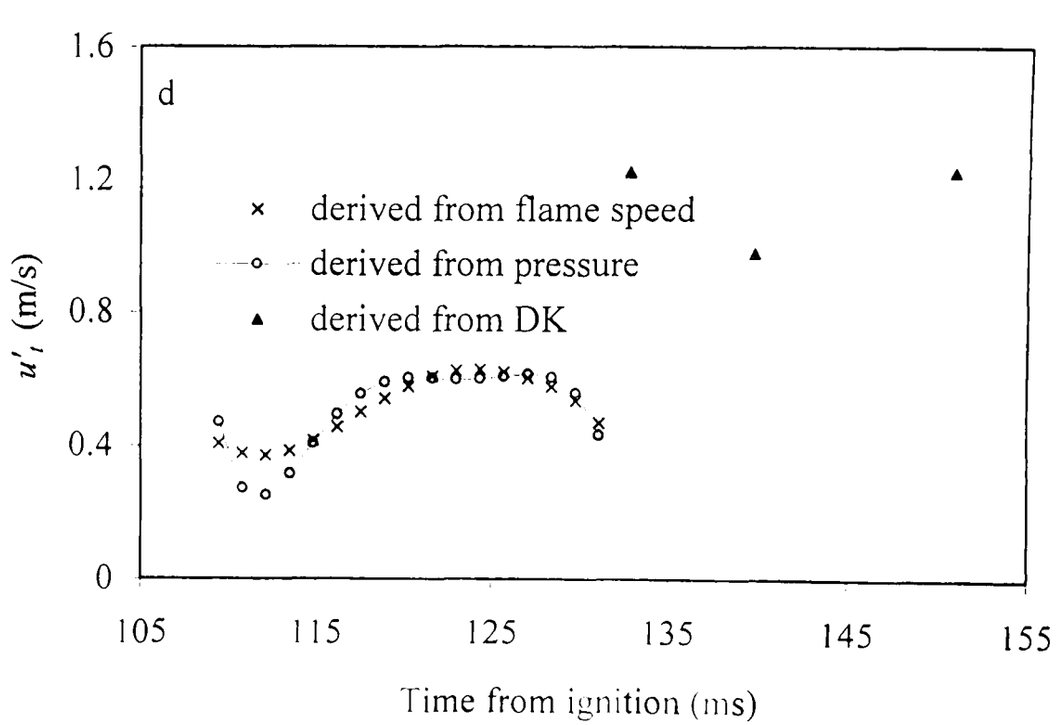

Fig. C.36. Hydrogen - air implosion, ϕ = 0.3, p_o = 0.5 MPa, T_o = 358 K, u' = 0.25

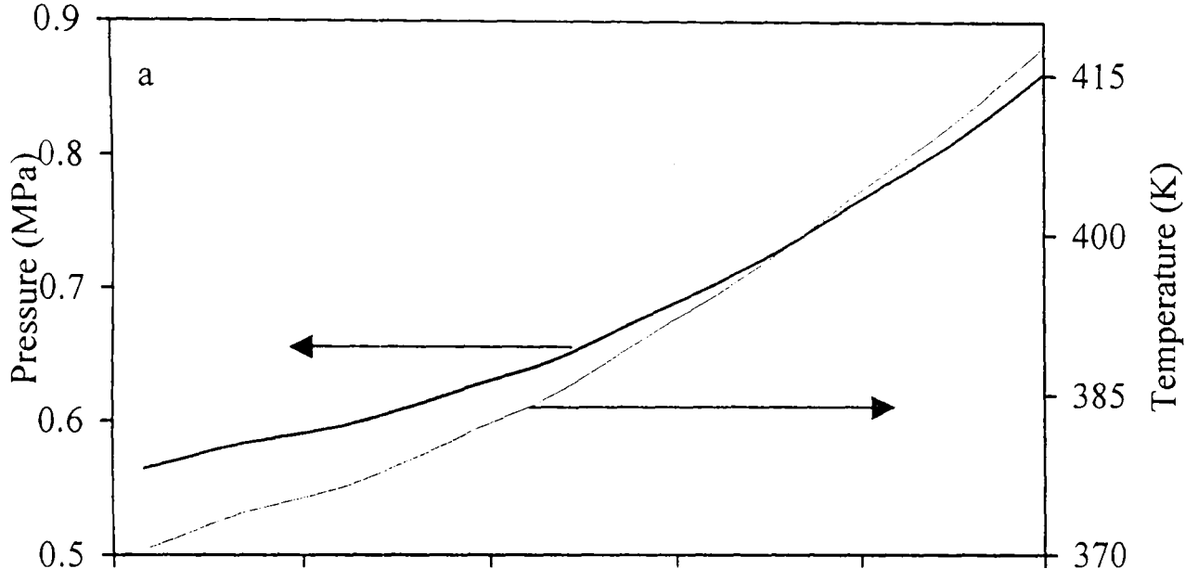

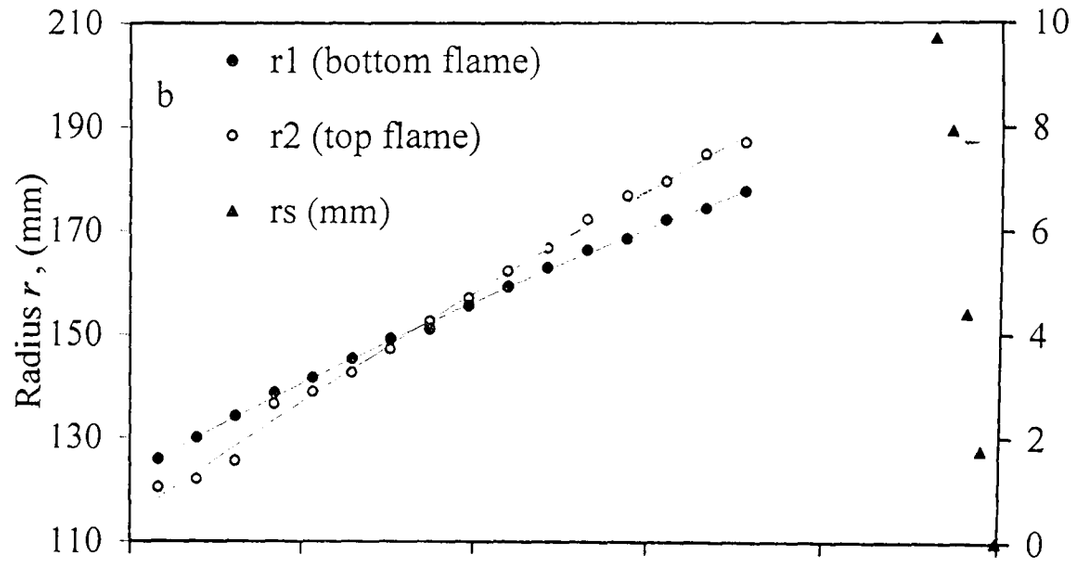

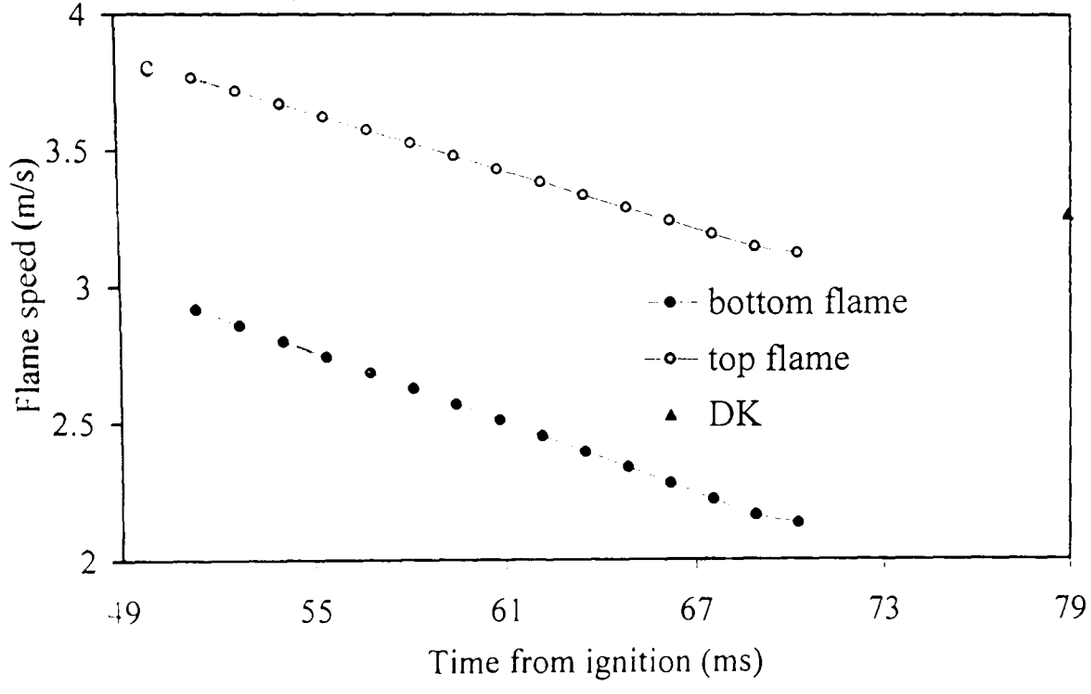

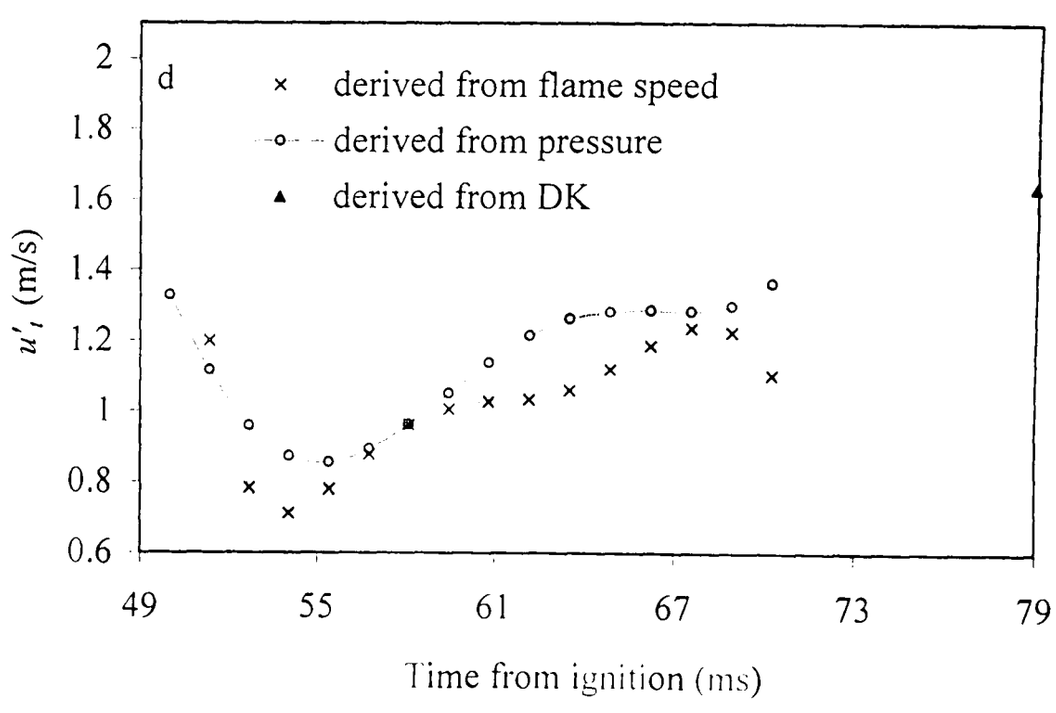

Fig. C.37. Hydrogen - air implosion, $\phi = 0.3$, $p_o = 0.5$ MPa, $T_o = 358$ K, $u' = 0.5$

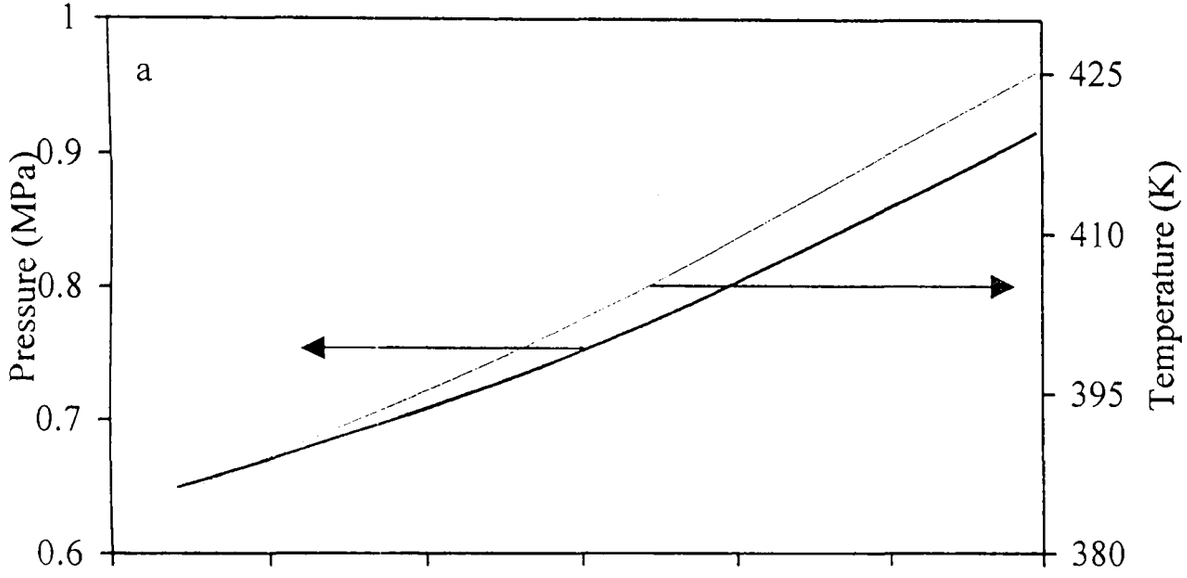

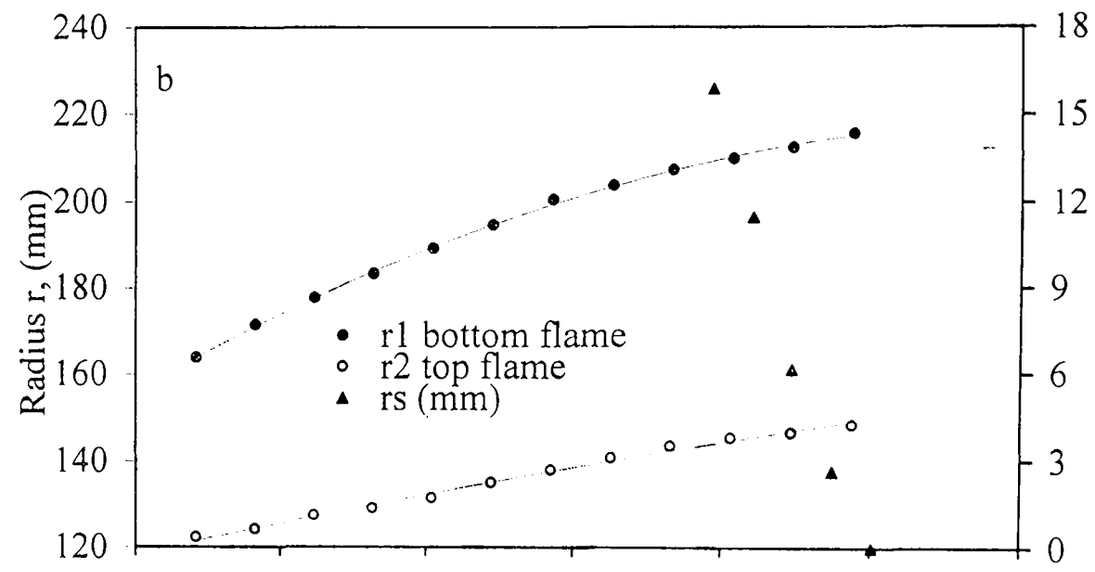

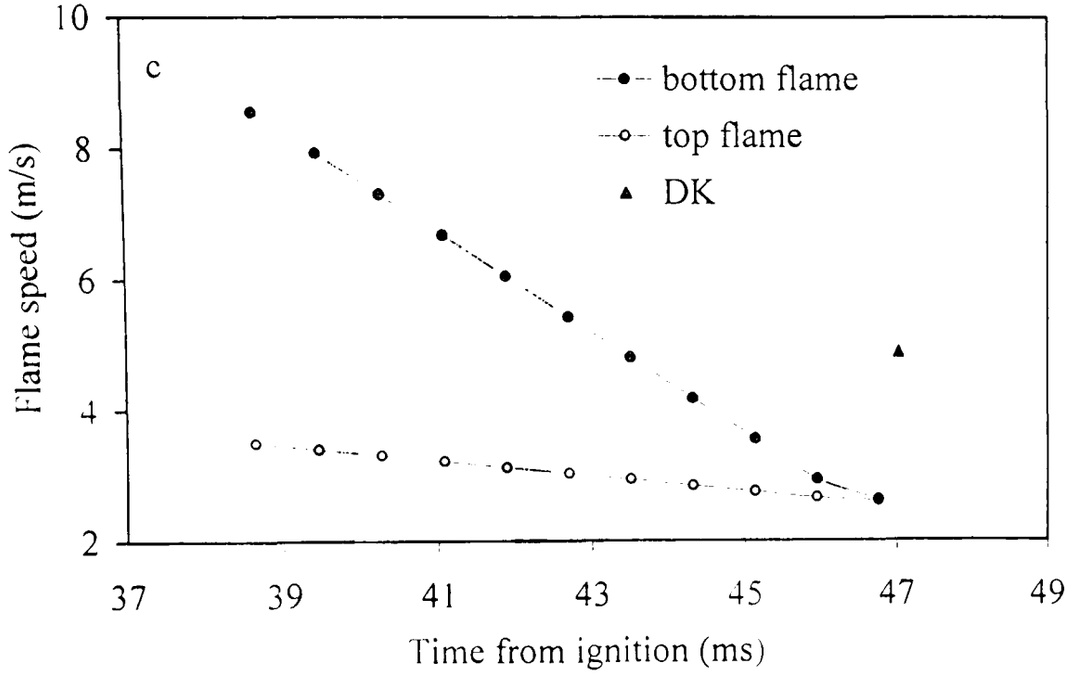

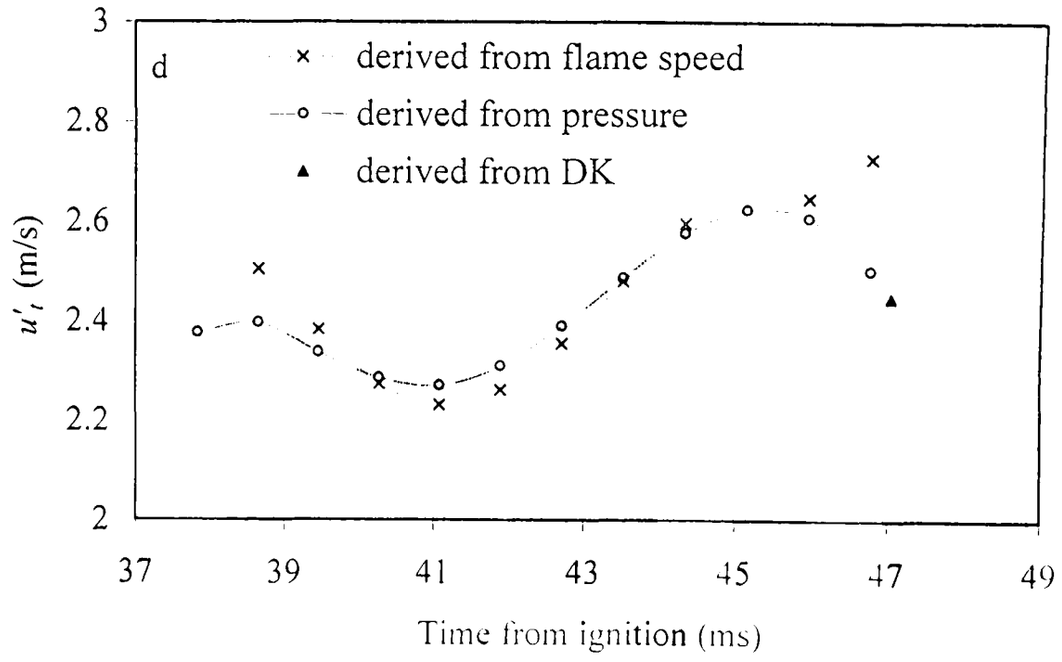

Fig. C.38. Hydrogen - air implosion, ϕ = 0.3, p_o = 0.5 MPa, T_o = 358 K, u' = 0.75

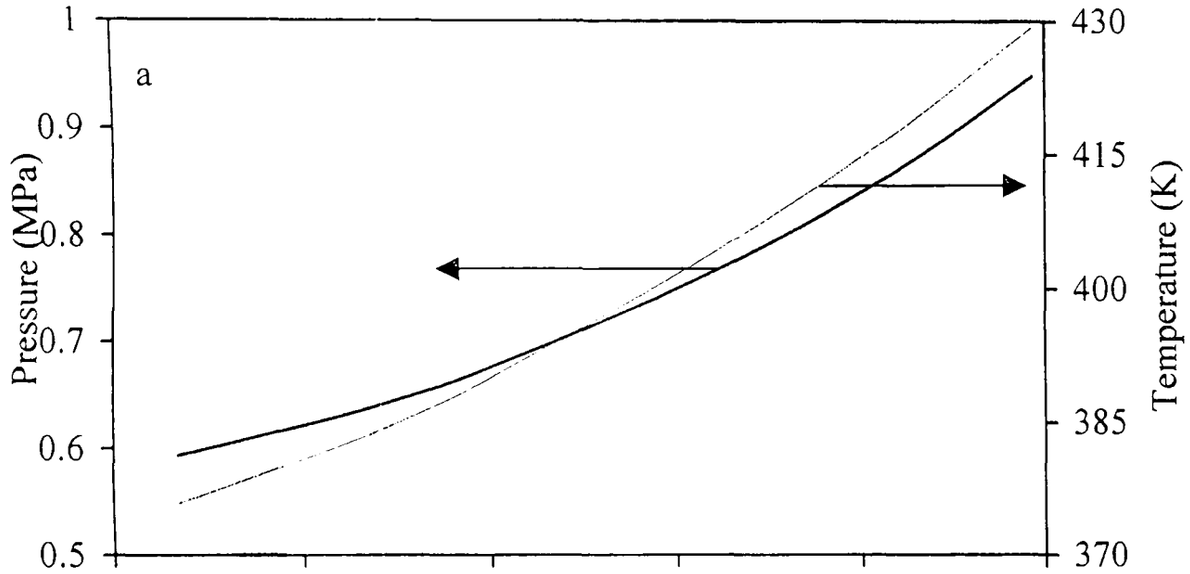

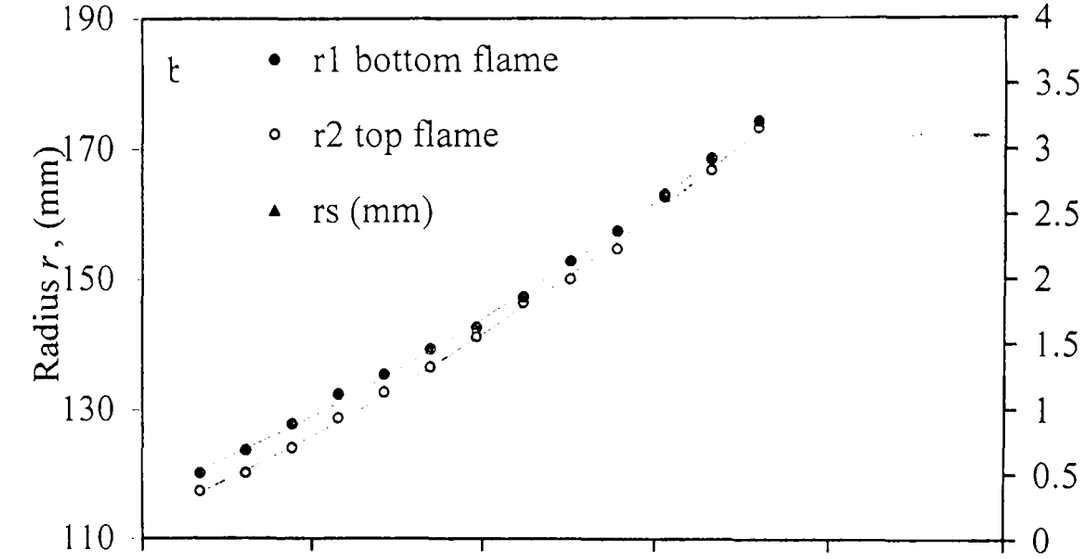

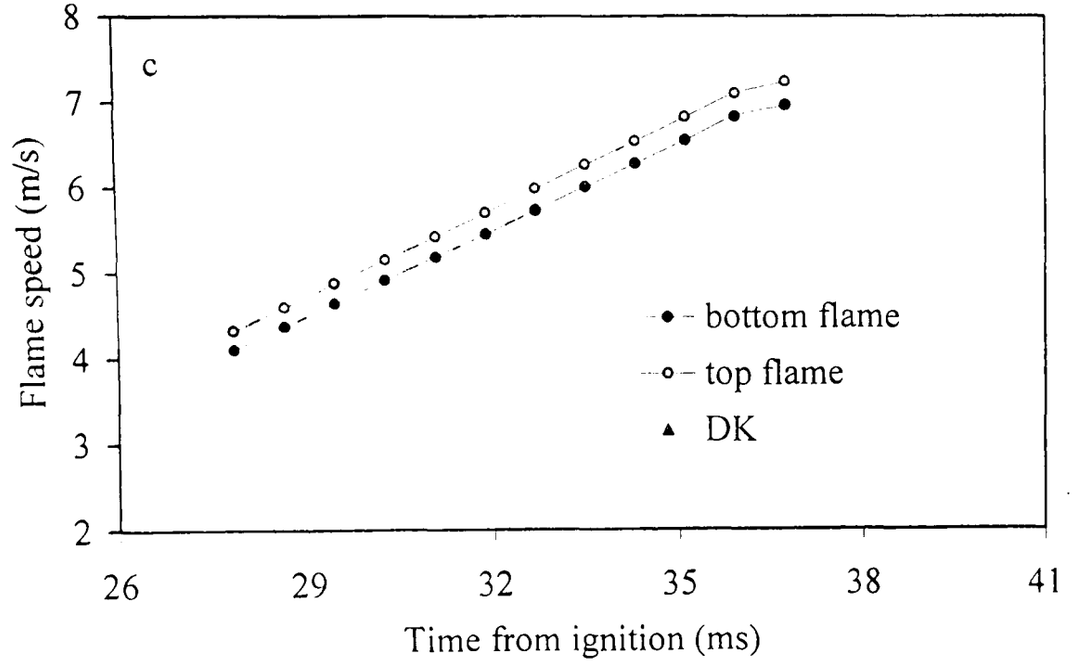

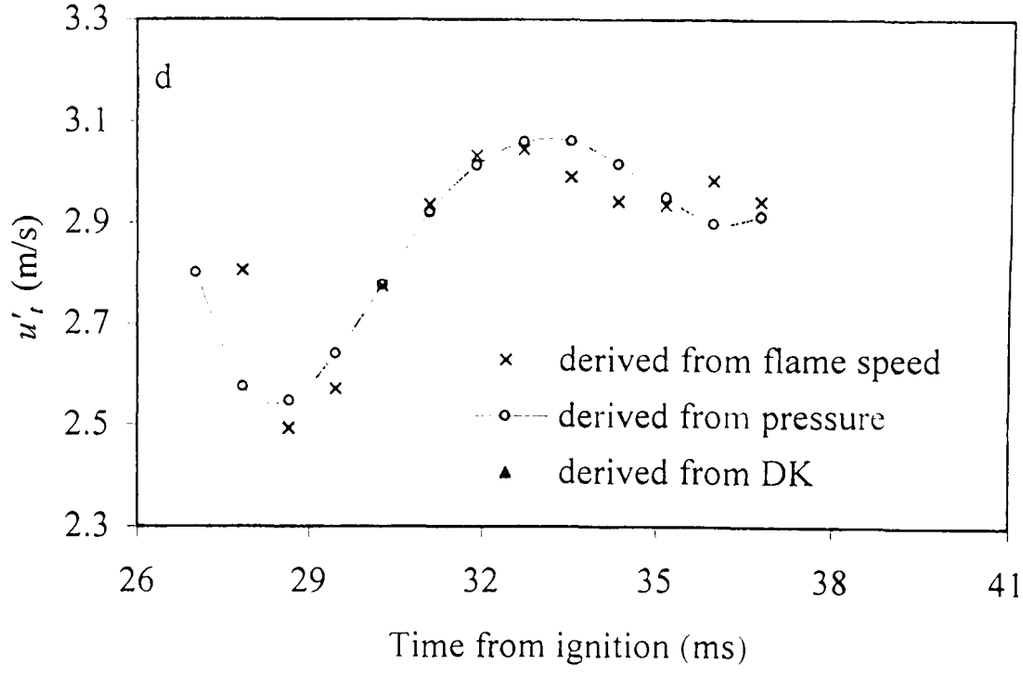

Fig. C.39. Hydrogen - air implosion, ϕ = 0.3, p_o = 0.5 MPa, T_o = 358 K, u' = 1

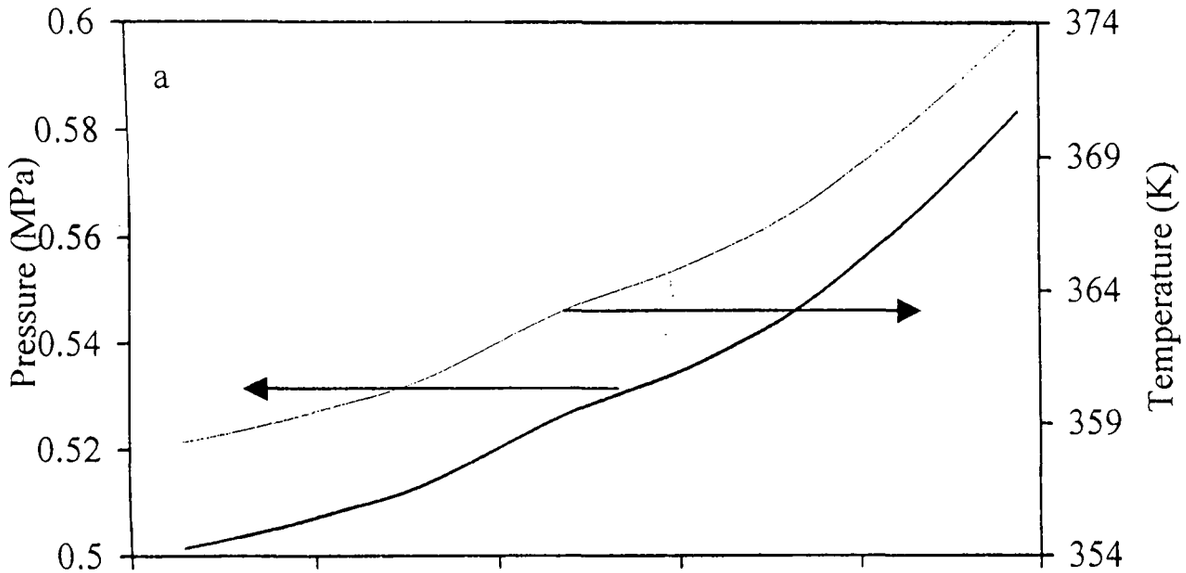

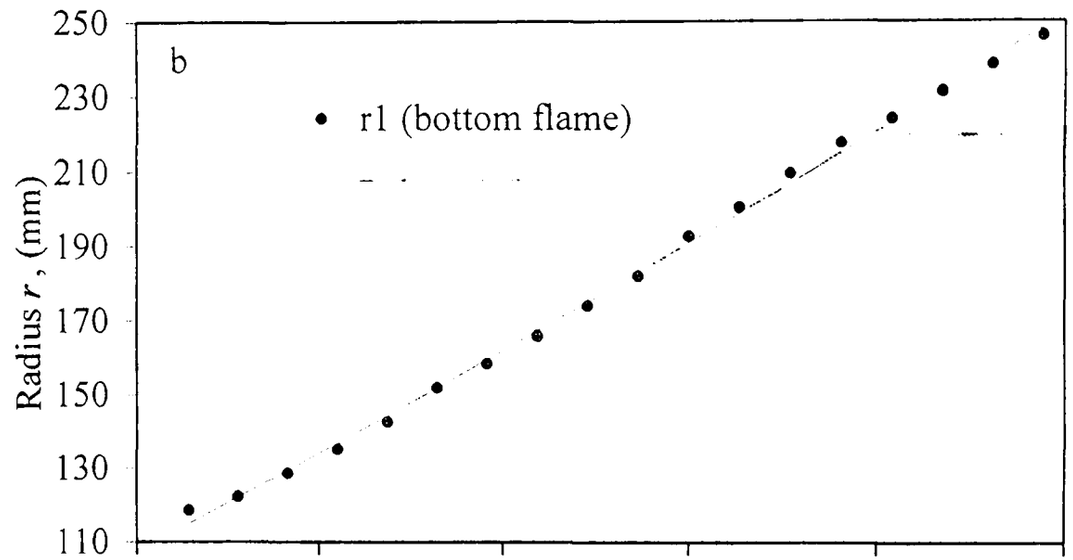

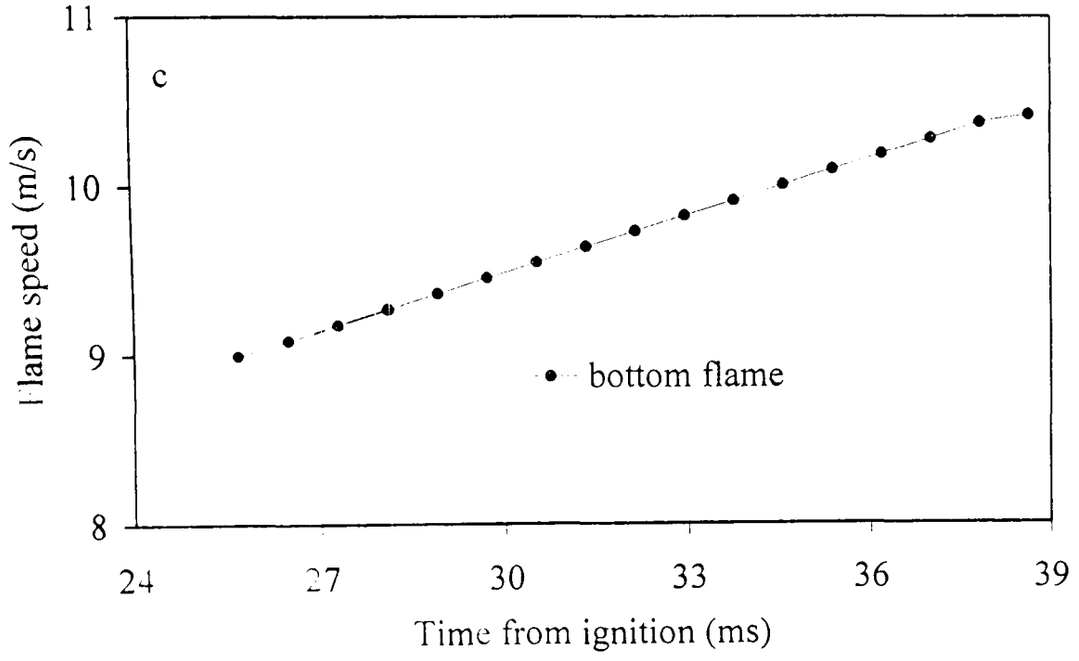

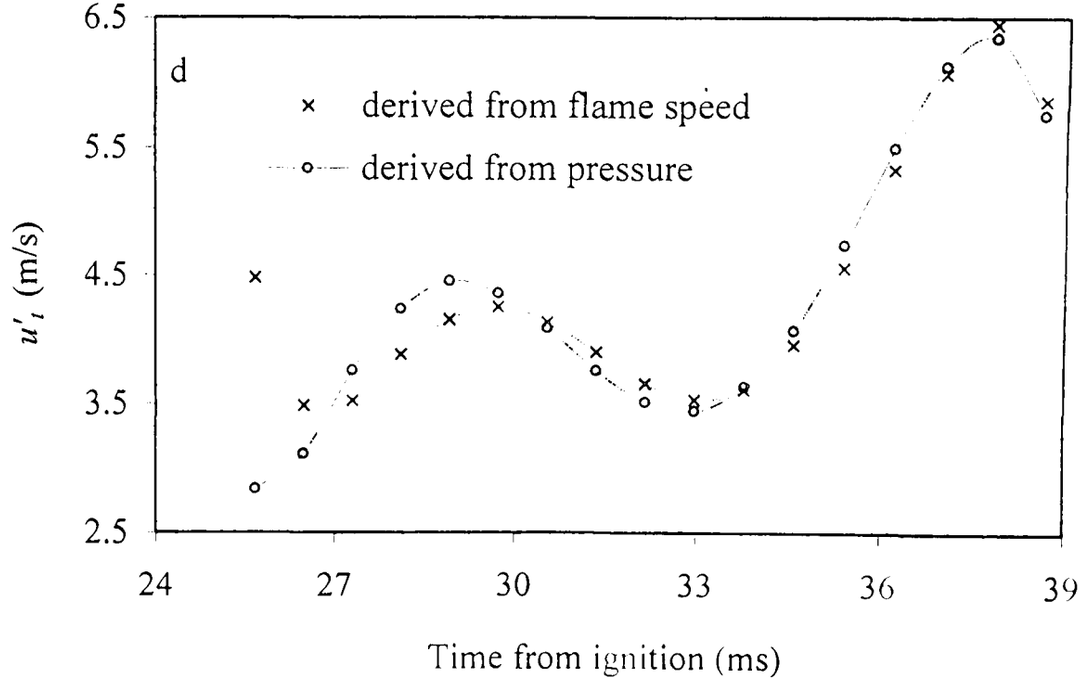

Fig. C.40. Hydrogen - air implosion, $\phi = 0.3, p_o = 0.5$ MPa, $T_o = 358$ K, $u' = 2$ - one kernel implosion

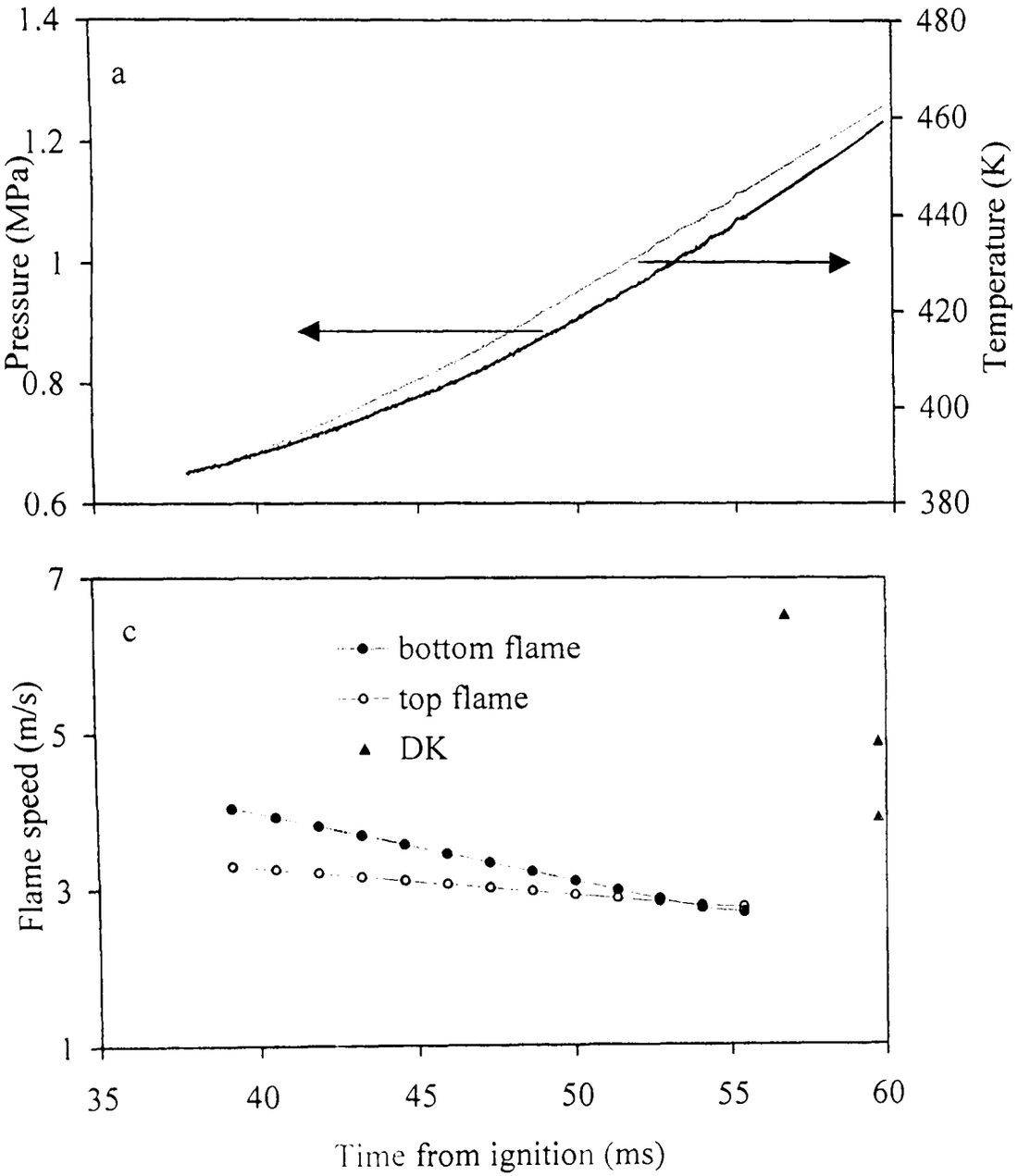

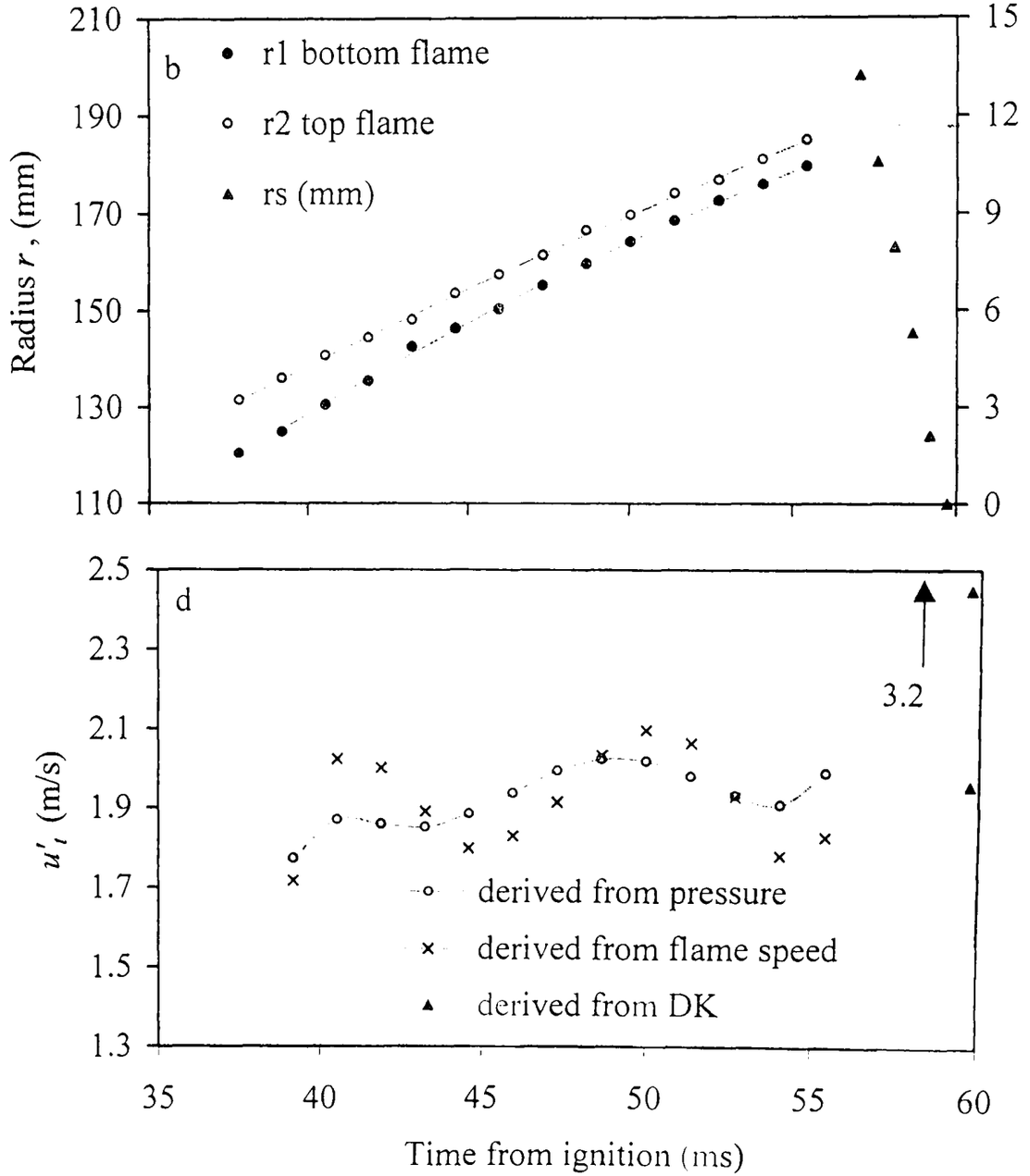

Fig. C.41. Hydrogen - air implosion, $\phi = 0.4$, $p_o = 0.5$ MPa, $T_o = 358$ K, $u' = 0.25$

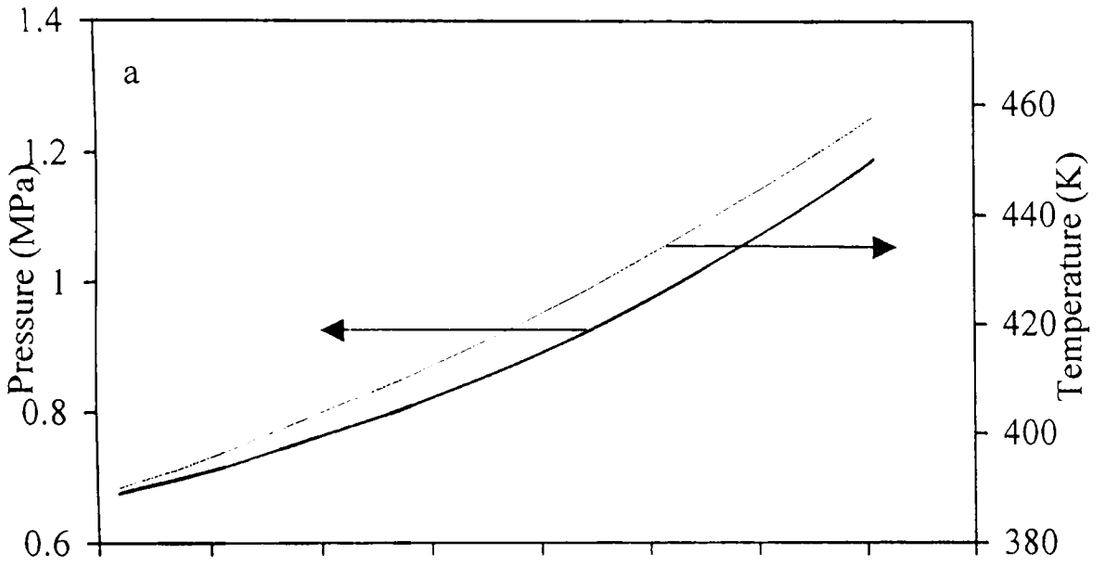

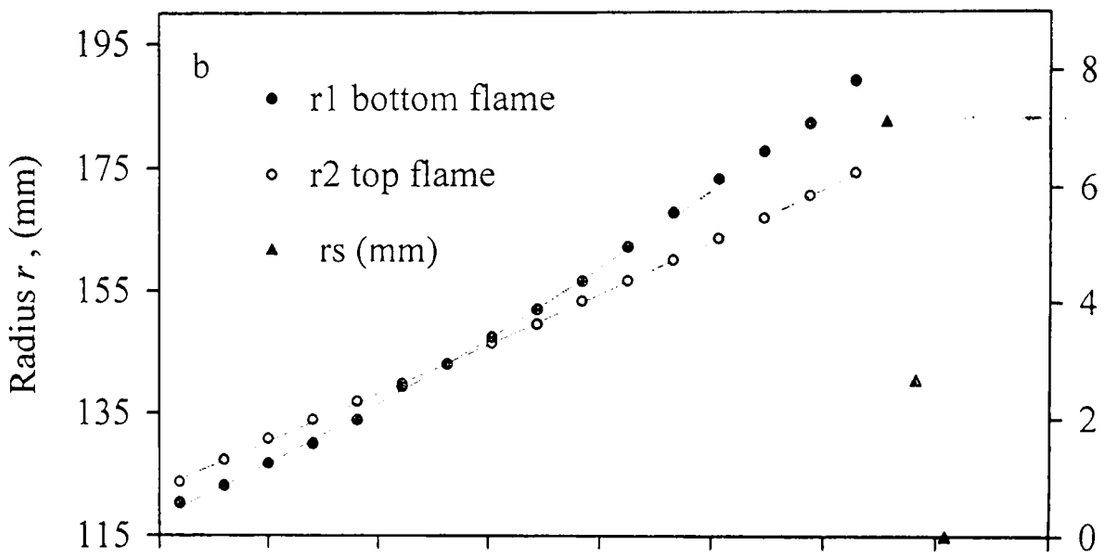

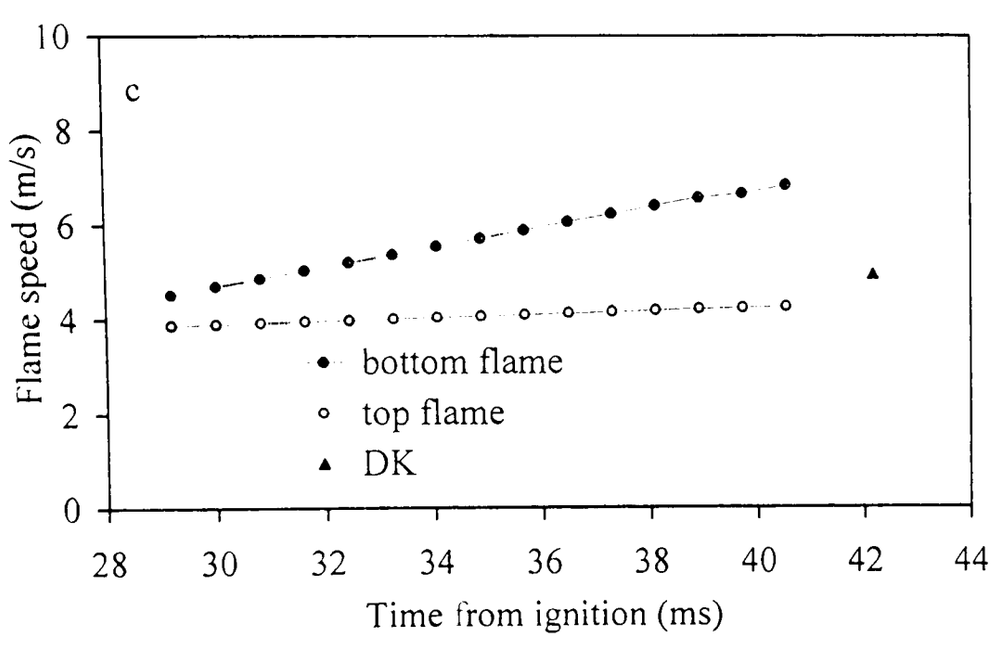

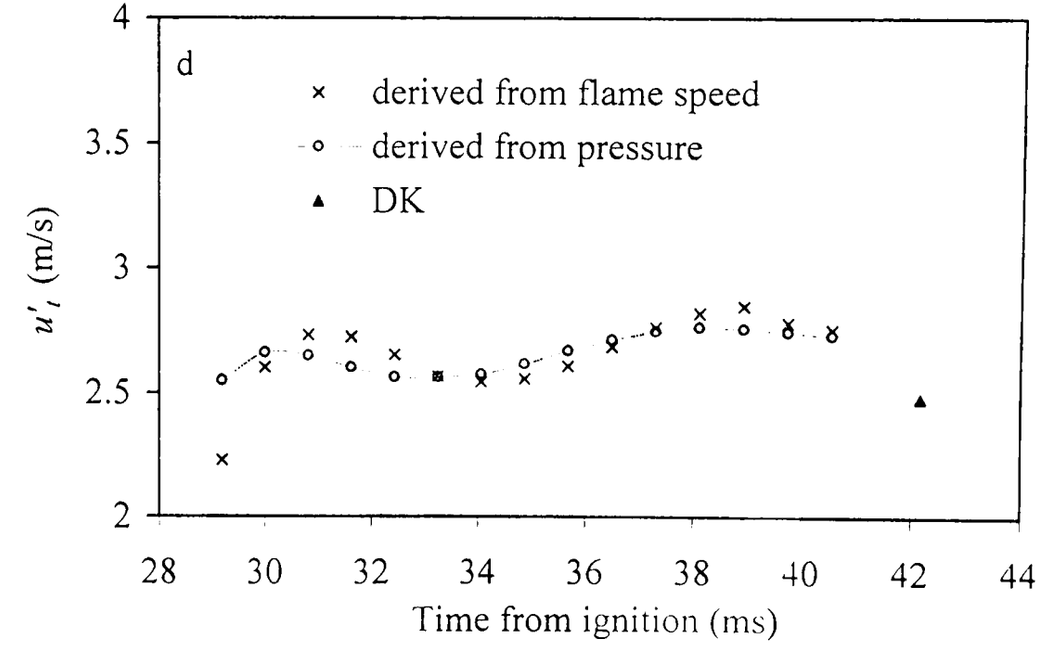

Fig. C.42. Hydrogen - air implosion, $\phi = 0.4, p_o = 0.5$ MPa, $T_o = 358$ K, $u' = 0.5$

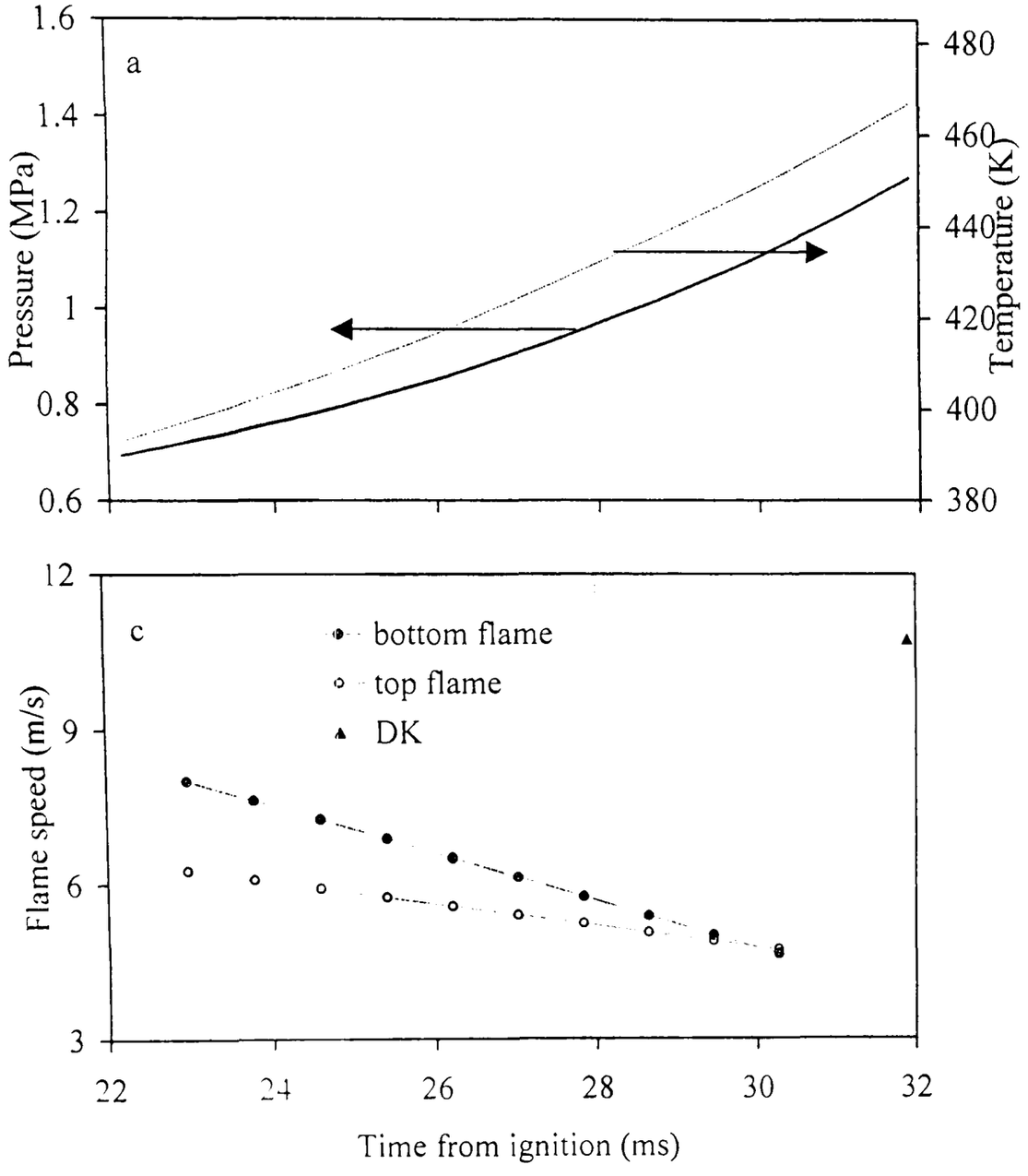

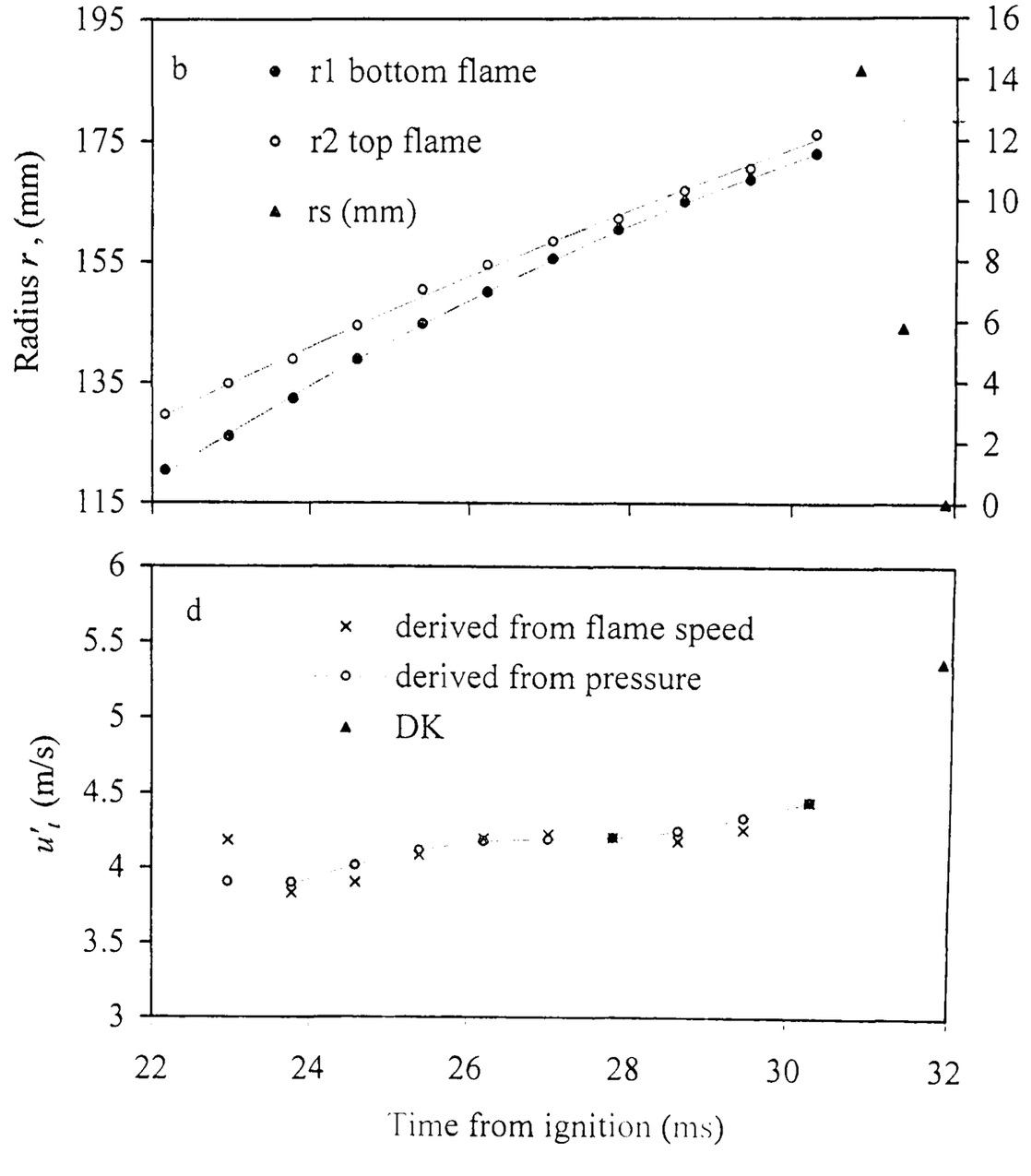

Fig. C.43. Hydrogen - air implosion, ϕ = 0.4, p_o = 0.5 MPa, T_o = 358 K, u' = 0.75

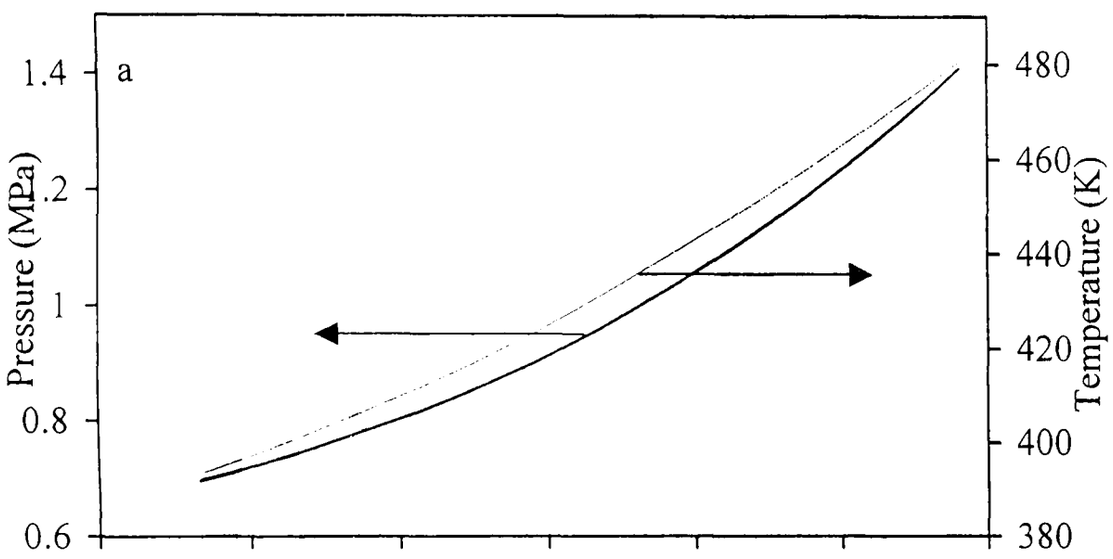

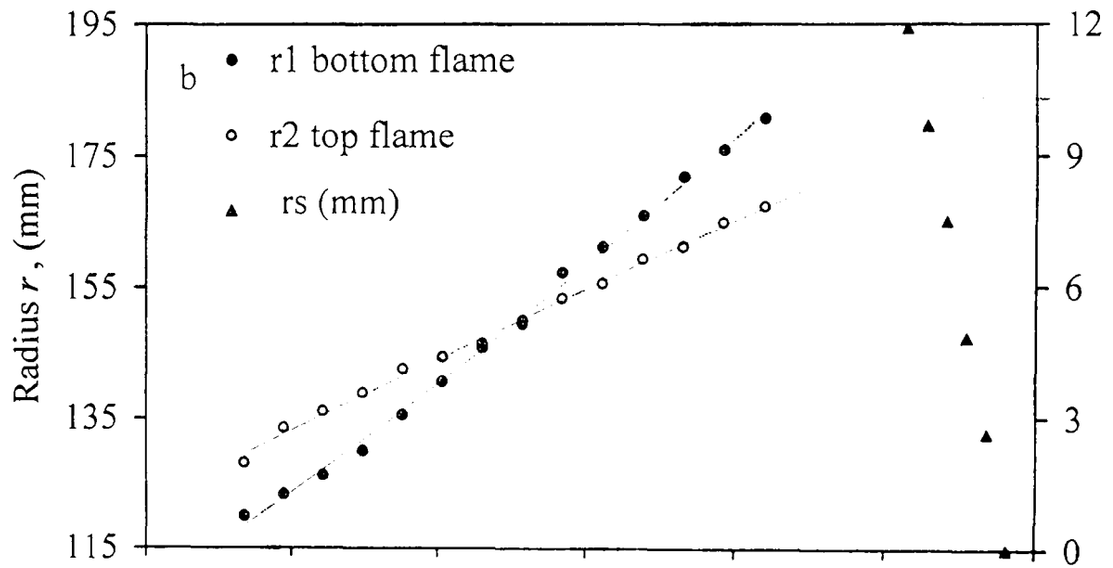

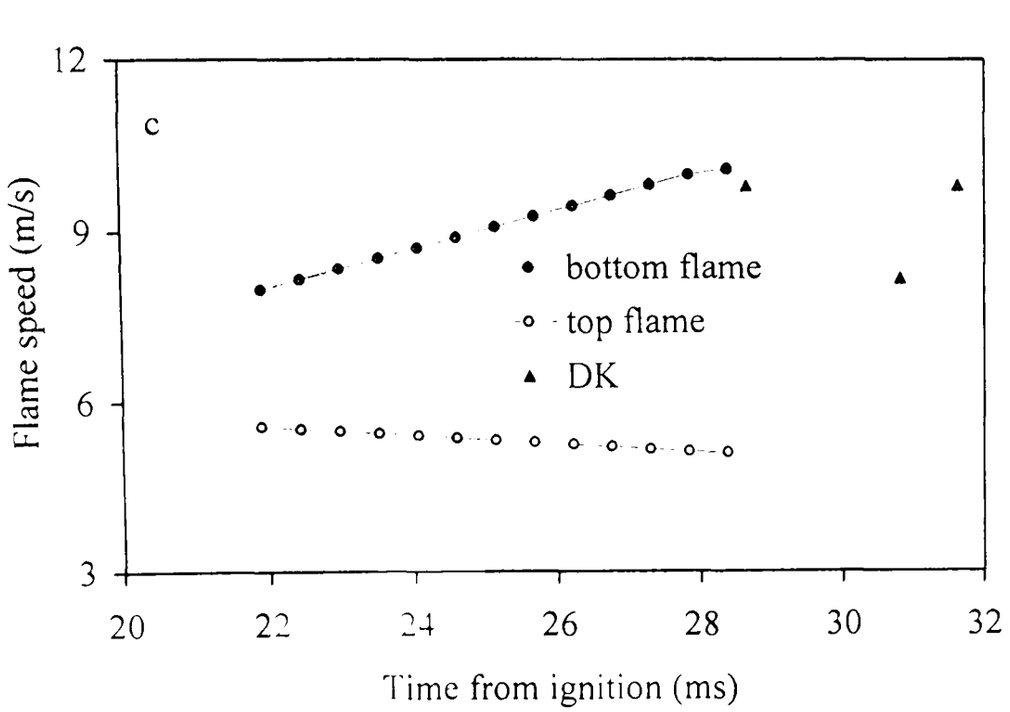

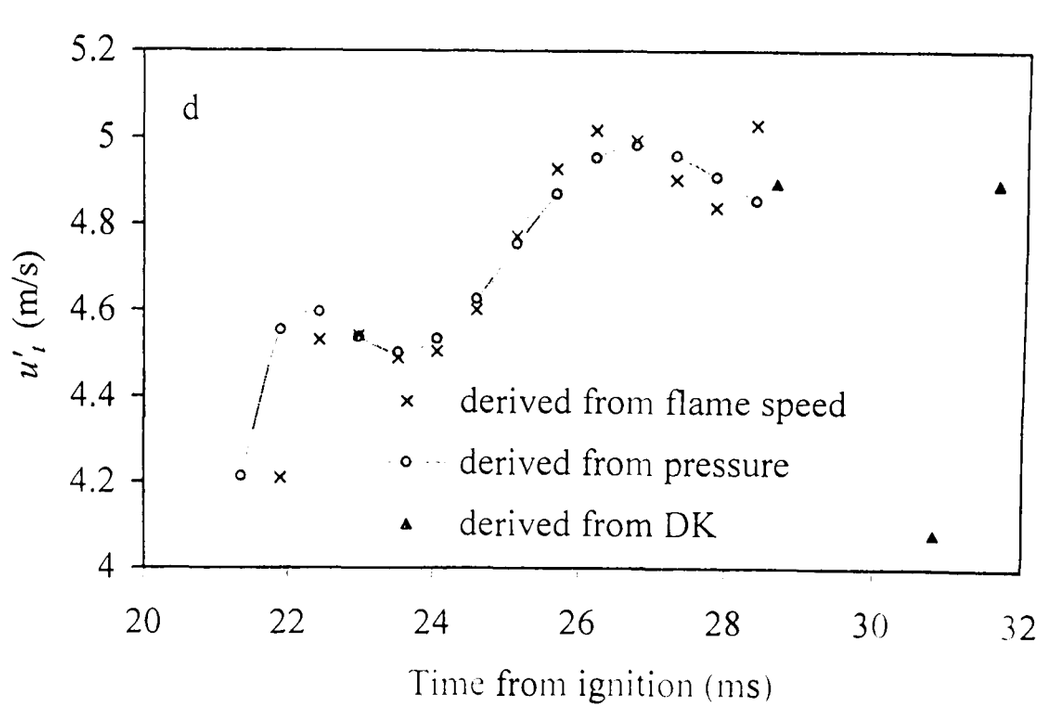

Fig. C.44. Hydrogen - air implosion, ϕ = 0.4, p_o = 0.5 MPa, T_o = 358 K, u' = 1

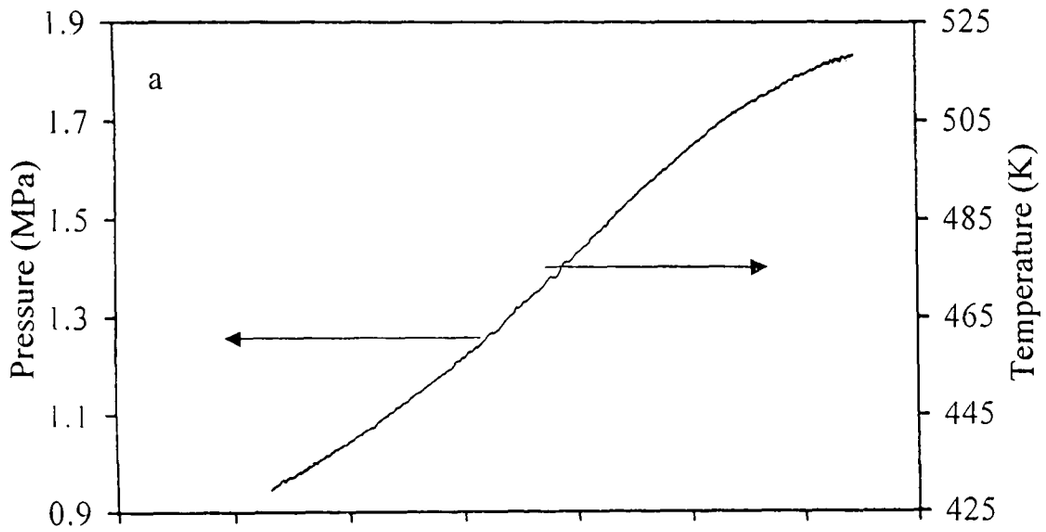

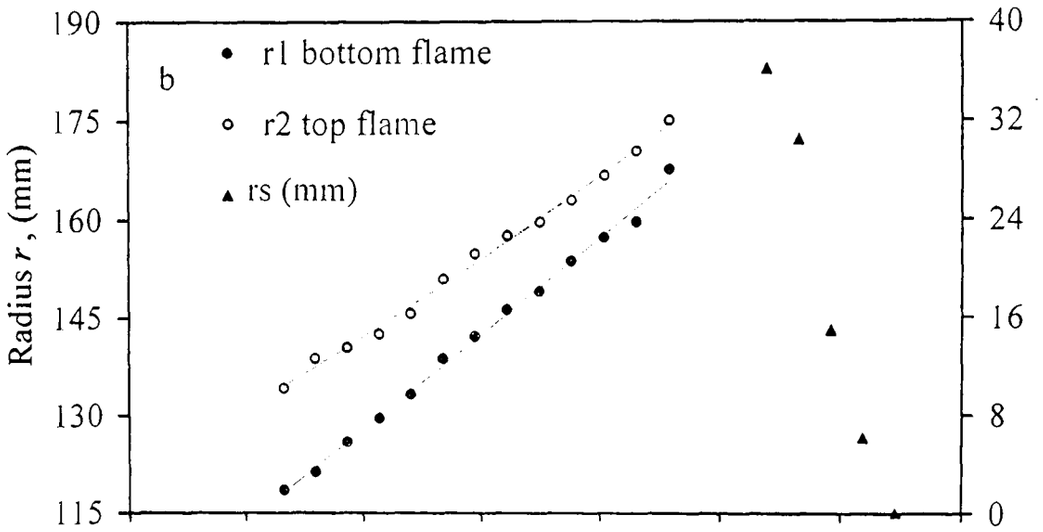

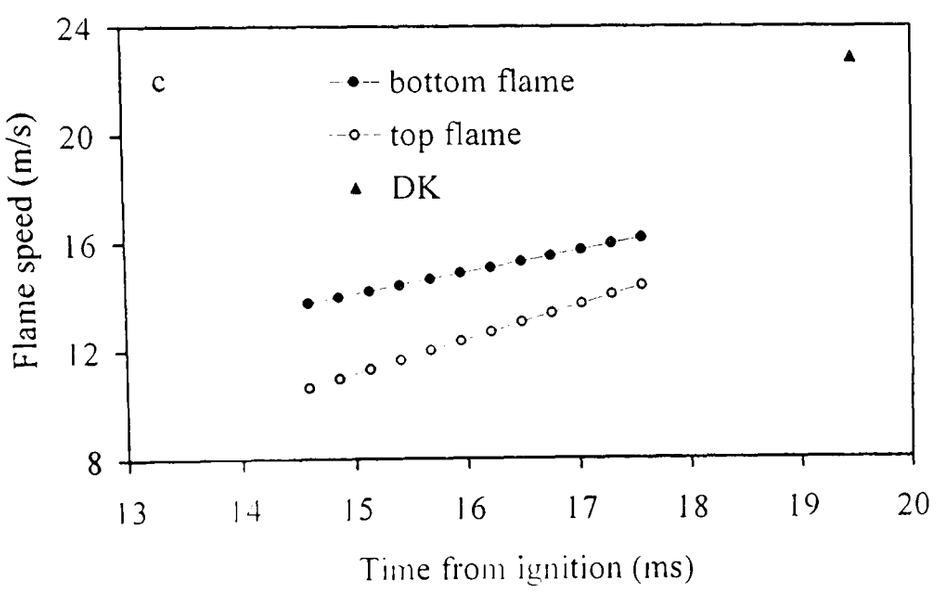

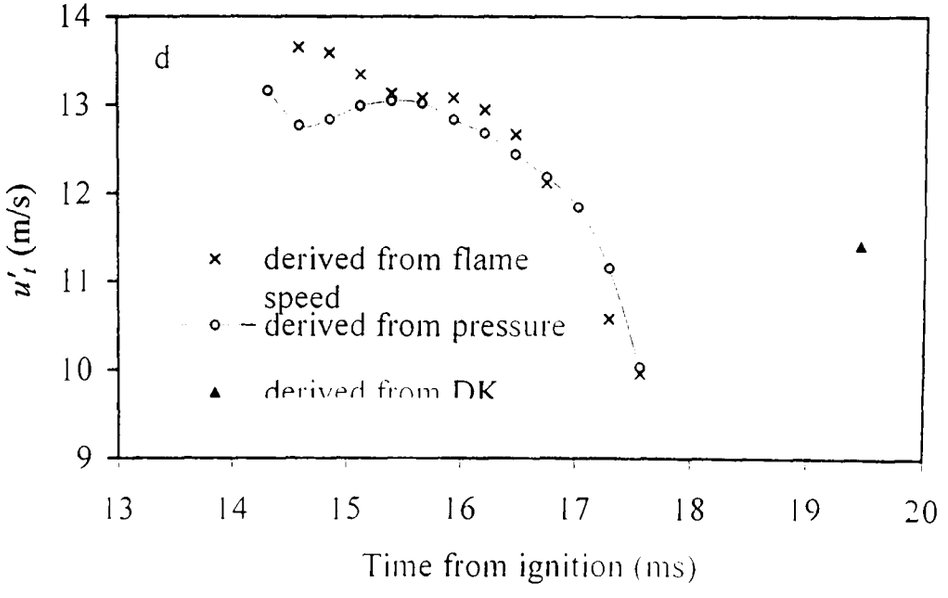

Fig. C.45. Hydrogen - air implosion, $\phi = 0.4$, $p_o = 0.5$ Mpa, $T_o = 358$ K. $u' = 2$

References

Addabbo, R., Bechtold, J. K. and Matalon, M. (2003) Wrinkling of Spherically Expanding Flames, *Proc. Combust. Inst.* 29: 1527-1535.

Andrews, G. E. and Bradley, D. (1972). Determination of Burning Velocities: A Critical Review. *Combust. Flame* 18: 133-153.

Abdel-Gayed, R. G., Bradley, D., and Lawes, M. (1987). Turbulent Burning Velocity: A General Correlation in Terms of Straining Rates. *Proc. R. Soc. Lond.* A 414. 389-413.

Ashurst, W. T. (1997). Darrieus-Landau Instability, Growing Cycloids and Expanding Flame Acceleration. *Combust. Theory Modelling*.1: 405-428.

Aung, K.T., Tseng, L. K., Ismail, M. A. and Faeth, G. M., (1995). Laminar Burning Velocities and Markstein numbers of Hydrocarbons/air Flames. *Combust. Flame* 102: 526.

Bechtold, J. K. and Matalon, M. (1987). Hydrodynamic and Diffusion Effects on The Instability of Spherically Expanding Flame. *Combust. Flame* 6: 77-90.

Bédat, B. and Cheng, R. K. (1995). Experimental Study of Premixed Flames in Intense Isotropic Turbulence. *Combust. Flame* 100: 485-494.

Bolz, R. E. and Burlage, H. (1955). *Jet Propulsion.* 25, 65.

Bolz, R. E. and Burlage, H. (1960). Propagation of Free Flames in Laminar and Turbulent Flow Fields, *NASA Tech.* Note D-551.

Boughanem, H., Trouvé, A., (1998). The Domain of Influence of Flame Instabilities in Turbulent Premixed Combustion. *Twenty-Seventh Symposium (International) on Combustion*, The Combustion Institute, Pittsburgh, 971-978.

Bradley D. and Mitcheson, A. (1976). Mathematical Solutions for Explosions in Spherical Vessels. *Combust. Flame* 26: 201-217.

Bradley D., and Lung, F. K. (1987). Spark Ignition and the Early Stages of Turbulent Flame Propagation. *Combust. Flame* 69: 71-93.

Bradley, D. (1992). How Fast can we Burn? *Twenty-Fourth Symposium (International) on Combustion*, The Combustion Institute, Pittsburgh, p. 247-262.

Bradley, D., Lau, A. K. C., and Lawes, M. (1992). Flame Stretch Rate as a Determinant of Turbulent Burning Velocity. *Phil. Trans. R. Soc.* 338, 359-387. London, UK.

Bradley, D., and Harper C. M. (1994). The Development of Instabilities in Laminar Explosions flames. *Combust. Flame* 99: 562-572.

Bradley, D., Gaskell, P. H., and Gu, X. J. (1996). Burning Velocities, Markstein Length, and Flame Quenching for Spherical Methane-Air Flames: A Computational Study. *Combust. Flame* 104: 176-198.

Bradley, D., Hicks, R. A., Lawes, M., Sheppard, C. G. W. (1996a). Study of Turbulence and Combustion Interaction: Measurement and Prediction of the Rate of Turbulent Burning. Technical Report, Department of Mechanical Engineering, The University of Leeds, UK.

Bradley, D., Hicks, R. A., Lawes, M., Sheppard, C. G. W., and Woolley, R. (1998). The Measurement of Laminar Burning Velocities and Markstein Numbers for Iso-octane-Air and Iso-octane-n-Heptane-Air Mixtures at Elevated Temperatures and Pressures in an Explosion bomb. *Combust. Flame* 115: 126-144.

Bradley, D. (1999). Instability and Flame speed in Large Scale Premixed Gaseous Explosions. *Phil. Trans. R. Soc. Lond.* 357, 3567.

Bradley, D. (2000). Flame Propagation in a Tube: The Legacy of Henri Guénoche. *Combust. Sci. and Tech.* 158, 15-33.

Bradley, D., Lawes, M., and Sheppard, C. G. W. (2000). Combustion and the Thermodynamic Performance of Spark–ignition Engines. *Proc. Instn. Mech. Engrs.* 214 Part C: 257.

Bradley, D., Sheppard, C. G. W., Woolley, R., Greenhalgh, D., A., and Lockett, R., D. (2000a). The Development and Structure of Flames Instabilities and Cellularity at Low Markstein number in Explosions. *Combust. Flame* 122: 195-209.

Bradley, D., Cresswell, T. M, and Puttock, J, S. (2001). The Acceleration Due to Flame-Induced Instabilities in Large-Scale Explosions. *Combust. Flame* 124: 551-559.

Bradley, D., Sheppard, C. G. W. and Woolley, R. (2001). Unstable Explosion Flames and Acoustic Oscillations. Technical report, Department of Mechanical Engineering, The University of Leeds, UK.

Bradley, D., Haq, M. Z., Hicks, R. A., Kitagawa, T., Lawes, M., Sheppard, C. G. W., Woolley, R. (2003). Turbulent Burning Velocity, Burned Gas Distribution, and Associated Flame Surface Definition. *Combust. Flame* 133: 415-430.

Brutscher, T., Zarzalis, N., Bockhorn, H. (2002). An Experimentally Based Approach for the Space –Averaged Laminar Burning Velocity for Modelling Premixed Turbulent Combustion. *Proc. Combust. Inst.* 29: 1825-1832.

Clavin, P. (1985). Dynamic Behavior of Premixed Flame Fronts in Laminar and Turbulent Flows. *Prog. Energy. Combust. Sci.* 11: 1-59.

Cambray, P., Joulain, K., and Joulin, G. (1996). Coalescence Problems in the Theory of Expanding Wrinkled Premixed Flames. *Combust. Sci Tech.* 112: 271-299.

Clarke, A., Stone, R. and Beckwith, P. (1995). Measuring the Laminar Burning Velocity of Methane/Diluent/Air Mixtures within a Constant-Volume Combustion Bomb in a micro-gravity Experiment. *Journ. Inst. Energy*. 68: 130.

Combourieu, J., (1961) In Surugue, J. (Ed.) *Experimental Methods in Combustion Research.* AGARD; Pergamon, Oxford, 25.

Darrieus, G. (1938). Propagation d'un Front de Flamme: Assai de Théorie des Vitesses Anomales de Déflagration par Developpement Spontané de la Turbulence. Presented at 6^{th} *Int.Cong.Appl. Mech. 1946,* Paris.

Davis, S. G. and Law, C. K. (1998). Laminar Flame Speeds and Oxidation Kinetics of Iso-octane – air and n-Heptane – air Flames. *Twenty-Seventh Symposium (International) on Combustion*, The Combustion Institute, Pittsburgh. 521-527.

Dery, R. J. (1949). Development of a Combustion Wave in a Flowing Gas. *Third Symp. on Combustion and Flame and Explosion Phenomena,* p. 235-245, Williams and Wilkins, Baltimore.

Fiock, E. F. and Roeder, C. H. (1935). The Soap Bubble Method of Studying the Combustion of Mixtures of CO, O_2, *NASA Report.*

Gillespie, L., Lawes, M., Sheppard, C. G. W., and Woolley, R. (2000). Aspects of Laminar and Turbulent Burning Velocity Relevant to SI Engines. *SAE Paper* 010192.

Glassman, I. (1996). *Combustion* (Third ed.). San Diego, California: *Academic Press.*

Gostinstev, Yu. A., Istratov, A. G., and Shulenin, Yu. V. (1988). Self-Similar Propagation of a Free Turbulent Flame in mixed gas Mixtures. *Combust. Explosion and Shock Waves.* 5: 63-70.

Griffiths, J. F. and Barnard, J. A. (1995). *Flame and Combustion.* Blackie Academic & Professional: An Imprint of Chapman &Hall.

Groff, E. G. (1982). The Nature of Confined Spherical Propane-Air flames. *Combust. Flame* 48: 51-62.

Gu, X. J., Haq, M. Z., Lawes, M., and Woolley, R. (2000). Laminar Burning Velocity and Markstein Length of Methane-Air Mixtures. *Combust. Flame* 121: 41-58.

Guénoche, H. and Laffitte, P. (1946). Sur la Déflagration des Melanges D'acétyléne et D'oxygéne. *Compt. Rend.* 222: 1394.

Guénoche, H. (1964) In Markstein, G. H. (Ed.) *Non-steady Flame Propagation.* AGARD;Pergamon, Oxford, Chap. E.: 107-181.

Haq, Z. (1998). Fundamental Studies of Premixed combustion. *PhD Thesis*, University of Leeds.

Haniff, M. S., Melvin, A., Smith, D. B. and Williams, A. (1998). The Burning Velocities of Methane and SNG Mixtures with Air. *Journ. Inst. Energy* 62: 229.

Hassan, M. I., Aung, K. T. and Feath, G. M. (1998). Measured and Predicted Properties of Laminar Premixed Methane/Air Flames at Various Pressures. *Combust. Flame* 115: 539.

Hertzberg, M. (1989). Selective Diffusional Demixing: Occurrence and Size of Cellular Flames. *Prog. Ener. Combust. Sci.* 15: 203-239.

Heywood, J. B. (1988*). Internal Combustion Engine Fundamentals*. McGraw-Hill Book Company.

Istratov, A. G., and Librovich, V. B. (1967). *Astronautica Acta.* 14, 453-467.

Ivashchenko, P. F., and Rumyantsev, V. S. (1987*). Fiz. Goreniya Vzryva*. 40, 38-87.

Karpov, V. P., Semenov, E. S., Sokolik, A. S. (1959). *Proc. Acad. Sci. USSR Phys. Chem Sect.*, 128: 871.

Kitagawa and Woolley, (2003). Private communication.

Kobayashi, H., Tamura, T., Maruta, K. and Niioka, T. (1996). Burning Velocity of Turbulent Premixed Flames in a High Pressure Environment. *Twenty-Sixth Symposium (International) on Combustion*, The Combustion Institute, Pittsburgh, p. 389-396.

Kobayashi, H., Kawabata, Y., Maruta, K. (1998). Experimental Study on General Correlation of Turbulent Burning Velocity at High Pressure. *Twenty-Seventh Symposium (International) on Combustion*, The Combustion Institute, Pittsburgh. 941-948.

Kobayashi, H., Kawazoe, H. (2000). Flame Instability Effects on the smallest Wrinkling Scale and Burning Velocity of High-Pressure Turbulent Premixed Flames. *Proc. Combust. Inst.* 28: 375-382.

Koroll, G. W., Kumar, R. K., and Bowles, E. M. (1993). Burning Velocities of Hydrogen – Air Mixtures. *Combust. Flame* 94, 330-340.

Kwon, S., Tseng, L. K., Faeth, G. M. (1992). Laminar Burning Velocities and Transition to Unstable Flames in $H_2/O_2/N_2$ and $C_3H_8/O=/N_2$ Mixtures. *Combust. Flame* 90: 230-246.

Laffitte, P. (1961) In Surugue, J. (Ed.) *Experimental Methods in Combustion Research.* AGARD; Pergamon, Oxford,: 5.

Landau, L. D. (1944). *Act Physicohimica URSS.* 19, 77-85.

Landau, L. D., and Lifshitz, E. M. (1987). *Fluid Mechanics.* Oxford: Pergamon.

Law, C. K. and Sung, C. J. (2000). Structure, Aerodynamics, and Geometry of Premixed Flamelets. *Progress in Energy and Combustion Science* 26. 459-505.

Law, C. K. (1988). Dynamics of Stretched Flames. *Twenty-Second Symposium (International) on Combustion*, The Combustion Institute, Pittsburgh, p. 1381-1402.

Lewis, B. and Von Elbe, G. (1987). Combustion, Flames and Explosions of Gases. *Academic Press,* London.

Lind, C. D., and Whitson. J. C. (1977). Explosive Hazards Associated With Spills of Large Quantities of Hazardous Materials Phase II. Department of Transportation, Rep. No. CG-D-85-77. *D.O.T.US Coast Guard Final Rep.* ADA-047585.

Linnett, J. W., Pickering, H. S. and Wheatley, P. J. (1951). Burning Velocity Determinations. *Trans. Faraday Soc.* 47, 974-980.

Liu, K., Burluka, A. A., Woolley, R., and Sheppard, C. G. W. (2001). On the Development of the Mass Burning Rate. *The Third Asia-Pacific Conference on Combustion.* Seoul, Korea.

Mallard, E. and Le Chatelier, H. L. (1883). Recherche sur la Combusion des Mélanges Gazeux Explosives. *Ann. Mines* , 8eme serie., t IV , 274.

Manton, J., Von Elbe, G., and Lewis, B. (1952). *J. Chem. Phys.* 30: 153-157.

Markstein, G. H. (1951). Experimental and Theoretical studies of Flame-Front stability. *J. Aero, Sci.* 18, 199-209.

Markstein, G. H. (1964). *Nonsteady Flame Propagation.* New York: Pergamon Press.

Metghalchi, M. and Keck, J. C. (1982). Burning Velocities of Mixtures of Air with Methanol, Isooctane and Indolene at High Pressure and Temperature, *Combust. Flame.* 48: 191-210.

Mitani, T., and Williams, F. A. (1980). Studies of Cellular Flames in Hydrogen-Oxygen-Nitrogen Mixtures. *Combust. Flame.* 39: 169-190.

Morely, C. (2001). GASEQ Program. (www.C.Morley.u kgateway.net/ver 061.htm).

Nwagwe, K., Weller, H. G., Tabor, G. R., Gosman, A. D., Lawes, M., Sheppard, C. G. W., and Woolley, R. (2000). Measurements and Large Eddy Simulations of Turbulent Premixed Flame Kernel Growth. *Pro. Combust. Inst.* 28, 59-65.

Palm-Leis, A., and Strethlow, R. A. (1969). On the Propagation of Turbulent Flames. *Combust. Flame* 13: 111-129.

Peters, N. (2000). *Turbulent Combustion*, Cambridge University Press. UK.

Peters, N., Paczko, G., Seiser, R. and Seshadri, K. (2002). Temperature Cross-Over and Non-Thermal Runaway at Two-Stage Ignition of N-Heptane. *Combust. Flame* 128: 38-59.

Raezer, S. D., and Olsen, H. L. (1962). Measurement of Laminar Flame Speeds of Ethylene - Air and Propane - Air Mixtures by the Double Kernel Method. *Combust. Flame* 6: 227-232.

Rallis, C. J. and Garforth, A. M. (1980). The Determination of Laminar Burning Velocity. *Prog. Energy Combust. Sci.* 6, 303-329.

Sedagaht, A. (2004). Private communication.

Schetinkov V. M. (1970). *Physics of Gaseous Combustion*. Izdov Nauka, Moscow.

Scott, M. J. (1992). Distribution of Strain Rate and Temperature in Turbulent Combustion. *PhD Thesis*, University of Leeds.

Semenov, N. N. (1951). *NACA Tech. Memo.* No. 1282.

Simon, D. M. and Wong, E. L. (1954). An Evaluation of the Soap Bubble Method for Burning velocity Measurements using Ethylene-Oxygen-Nitrogen and Methane-Oxygen-Nitrogen Mixtures, *NASA Tech.* Notes 3106.

Sivashinsky, G. I. (1977). Diffusional – Thermal Theory of Cellular Flames. *Combust. Sci. Technol.* 15: 137-146.

Sivashinsky, G. I. (1983). Instabilities, Pattern Formation and Turbulence in Flames. *A. Rev. Fluid Mech.* 15: 197-199.

Stevens, F. W. (1929). The Gaseous Explosive Reactions: A Study of the Kinetics of Composite Fuels. *NASA Report,* 305.

Stevens, F. W. (1932). The Gaseous Explosive Reactions: The Effect of Pressure on the Rate of Propagation of the Reaction Zone and upon the Rate of Molecular Transformation. *NASA Report,* 372.

Taylor, S. C. (1991). Burning Velocity and the Influence of Flame Stretch. *PhD Thesis*, University of Leeds.

Torshin, Y. K., and Skchelkin, K. I. (1955). *Akad. Nauk.* USSR, OTN 9: 160-166.

Tse, S.D., Zhu, D.L., Law, C.K. (2000). Morphology and Burning Rates of Expanding Spherical Flames in H2/O2/Inert Mixtures up to 60 Atmospheres, *Proc. Combust. Inst.* 28: 1793-1800.

Turns, S. R. (1996). *An Introduction to Combustion: Concepts and Applications.* McGraw-Hill Book Company.

Vagelopoulos, C. M., Egolfopoulos, F. N. and Law, C. K. (1994). Further Considerations on the Determination of Laminar Flame Speeds with Counterflow Twin-Flame Technique. *Twenty-Fifth Symposium (International) on Combustion*. The Combustion Institute, Pittsburgh, p. 1341.

Vagelopoulos, C. M. and Egolfopoulos, F. N. (1998). Direct Experimental Determination of Laminar Flame speed. *Twenty-Seventh Symposium (International) on Combustion*, The Combustion Institute, Pittsburgh, p. 513.

Van Maaren, A., Thung, D. S. and De Goey, L.P.H. (1994) Measurment and Adiabatic Burning Velocity of Methane/Air Mixtures. *Combust. Sci. Tech.* 96, p. 327.

Verhelst, S., Woolley, R., Lawes, M. and Sierens, R. (2004). Laminar and Unstable Burning Velocities and Markstein Lengths of Hydrogen-air Mixtures at Engine-Like Conditions. To be presented at the Thirtieth Symposium (International) on Combustion, The Combustion Institute, Chicago.

Williams, F. A. (1985). *Combustion Theory* (Second ed.). Menlo Park, California: Addison-Wesley Publishing Company.

Woolley, R. (2001). Private communication.

Wu, J. (2003). Study Related to Downsize of Production Engine. *PhD Thesis*, University of Leeds. (anticipated submission date 2004).

Wu, C. K. and Law, C. K. (1984). On the Determination of Laminar Flame Speeds from Stretched Flames. *Twentieth Symposium (International) on Combustion*, The Combustion Institute, Pittsburgh, p. 1941.

Yamaoka, I. And Tsuji, H. (1984). Determination of Burning Velocity Using Counterflow Flames. *Twentieth Symposium (International) on Combustion*, The Combustion Institute, Pittsburgh, p. 1883.

Zel'dovich, Y. B. and Frank-Kamenetskii, D.A. (1938). *Dokl. Akad. Nauk.* SSSR, 19: 693.

Zel'dovich, Y. B. and Barenblatt, G. I. (1959). Theory of Flame Propagation. *Combust. Flame* 3: 61-74.